Konstantin Sobolev · Surendra P. Shah
Editors

Nanotechnology in Construction

Proceedings of NICOM5

Springer

Nanotechnology in Construction

Konstantin Sobolev • Surendra P. Shah
Editors

Nanotechnology in Construction

Proceedings of NICOM5

Springer

Editors
Konstantin Sobolev
Department of Civil Engineering
and Mechanics
University of Wisconsin-Milwaukee
Milwaukee, WI, USA

Surendra P. Shah
Center for Advanced Cement Based
Materials
Northwestern University
Evanston, IL, USA

ISBN 978-3-319-17087-9 ISBN 978-3-319-17088-6 (eBook)
DOI 10.1007/978-3-319-17088-6

Library of Congress Control Number: 2015940117

Springer Cham Heidelberg New York Dordrecht London

Printed on acid-free paper

Springer International Publishing AG Switzerland is part of Springer Science+Business Media (www.springer.com)

Preface

I'm glad you found a new name for chemistry. Now you have the incentive to learn what you didn't want to learn in college.

R. Hoffman, 1981 Nobel Prize Laureate (Chemistry)

The Proceedings of 5th International Symposium on Nanotechnology in Construction open a new window in the development of the next generation of nano-enabled construction materials and advanced technologies. Nanotechnology has recently become one of the most active research and development subjects in science, medicine, and engineering. It has already demonstrated surprising potential for improving the performance of construction materials, and many of these recent developments were facilitated by NICOM symposia. NICOM5 is bringing together international leaders to discuss the emerging opportunities and future of the use of nanotechnology in construction. Characterizing, understanding, and manipulating material at nanolevel, the dimension compared to distance between the atoms, or 10^{-9} m, have led to unprecedented possibilities to develop new materials with novel and enhanced properties.

Governments and industry have allocated considerable funds towards nanotechnology development. Recent work in nanotechnology and nanoscience promises exciting opportunities for the field of construction materials. It is imperative that we take advantage of this, enabling technology to advance the state of knowledge and to achieve new levels of technological breakthroughs. Understanding the structure at the nanolevel helps to modify, synthesize, and design a new generation of high-performance construction materials. With new advanced instruments, it is possible to observe the structure of composites at the atomic level and even to measure the mechanical response of different phases at a nanolevel. For example, the application of Atomic Force and Transmission Electron Microscopy reveals that the "amorphous" C–S–H gel at nanoscale has a distinct ordered structure. Advanced instruments such as Tribo-Indenters can both observe and measure the mechanical properties at a nanoscale. To improve the performance of composites, one can use

the principle of particle packing at the nanoscale. This concept has led to research on nano-silica particles and nano-$Al2O_3$ fibers with the aim of improving processing characteristics, strength, and durability. Researchers are studying whether nanofibers such as multiwall carbon nanotubes drastically alter the fracture properties of cement paste to produce smart and ductile concrete composites. Incorporation of nano-sized TiO_2 particles introduces new characteristics such as self-cleaning, due to their photocatalytic properties.

We believe that further research in nanotechnology promises very real breakthroughs in the field of construction composites. We hope that this publication will be of great value for many researchers from academic institutions and research organizations and will help them to apply their research findings in the rapidly changing materials world.

This Proceedings volume is based on contributions to be presented at the NICOM5 symposium held at the Trump Tower Chicago, USA, which features high-performance concrete and is the first application of 110 MPa high-performance self-consolidating concrete, elevating the state of the art and science of concrete materials. This event will become the catalyst for interdisciplinary research on construction materials on the micro- and nanoscale. Now, this work is coordinated by the newly formed ACI 241 committee on "Nanotechnology of Concrete" and the Task Force on Nanotechnology-Based Concrete Materials of Transportation Research Board of National Academies. The organization of NICOM5 is supported by American Concrete Institute, RILEM, Transportation Research Board of National Academies, and the International Federation for Structural Concrete. The editors wish to thank the authors for their outstanding contributions and congratulate them for their pioneering work. The editors would also like to acknowledge the excellent work of the program committee, reviewers, and the continuous support of our colleagues at ACI 241.

We welcome all engineers, scientists, and students from around the world attending NICOM5 symposium. Your contributions are vital for the progress of technology and scientific development. NICOM5 will convey the research results to the world community and allow engineers and scientists to evaluate the results of investigations. It is anticipated that the symposium in 2015 will facilitate global connections and lead to new ideas and innovation, active collaborations, and greater interactions.

The publication of this Proceedings volume was made possible by the generous contributions from our sponsors: We Energies, Active Minerals, Portland Cement Association, University of Wisconsin-Milwaukee, and the University of Wisconsin-Milwaukee Foundation. Their financial support is greatly appreciated.

Chicago, IL, USA
May 24–26, 2015

Konstantin Sobolev
Surendra P. Shah

Organization

Scientific Committee

Carmen Andrade
Peter J. M. Bartos
Nele de Belie
Björn Birgisson
Klaas van Breugel
Ignasi Casanova
Georgios Constantinides
Henri van Damme
Frank Dehn
Jorge S. Dolado
Horacio D. Espinosa
Vyacheslav R. Falikman
Liberato Ferrara
Ismael Flores-Vivian
Juan J. Gaitero
Edward J. Garboczi
Al Ghorbanpoor
Brian Green
Boris V. Gusev
Frederick D. Hejl
Hamlin M. Jennings
Maria S. Konsta-Gdoutos
Steven H. Kosmatka
Kimberly Kurtis
Zongjin Li
Yolanda R. de Miguel
Harald S. Müller
Jose F Munoz
Jiri Nemecek
Michael J Nosonovsky
Jan Olek
Roland J.-M. Pellenq
Johann Plank
Aantonio Porro
Laila Raki
Pradeep K. Rohatgi
Aly Said
Florence Sanchez
Michael Schmidt
Karen Scrivener
Surendra P. Shah
Lok P. Singh
Mohammed Sonebi
Dietmar Stephan
Mahmoud Reda Taha
Jussara Tanesi
Leticia M. Torres-Martínez
Pavel Trtik
Franz-J. Ulm
Kejin Wang
Charles A. Weiss

Proceedings Review Committee

Warda Ashraf
Mohamed Bassuoni
Haroldo Bernardes
G. Quercia Bianchi
Mohammad Bolhassani
Yiwen Bu
Elena Cerro-Prada
Samir Chidiac
Panagiotis Danoglidis
Hongjian Du
Edurne Erkizia
Yingfang Fan
Ana Guerrero
David Harbec
Pengkun Hou
Shiho Kawashima
Bérengère Lebental
Zhibin Lin
Gilson Lomboy
Yang Lu
Zoi Metaxa
Juhyuk Moon
Anol Mukhopadhyay
Scott Muzenski
Moncef Nehdi
Narayanan Neithalath
Sulapha Peethamparan
Bekir Yilmaz Pekmezci
Alva Peled
Gloria Perez
Amirpasha Peyvandi
Lin Shen
Caijun Shi
Jessica Silva
Peter Stynoski
Zhihui Sun
Serkan Tapkin
Kay Wille
Erik Wotring
Ardavan Yazdanbakhsh
Min Hong Zhang

Contents

Part I
Modern Trends

Nanotechnology and Nanoengineering of Construction Materials

Konstantin Sobolev

Abstract This paper reviews the state of the field of nanotechnology of construction materials. The impact of recent advances in instrumentation and design of advanced composite materials is discussed. Main directions, historical milestones and recent progress in nanoengineering and nanomodification of cement-based materials are presented.

Keywords Nanotechnology • Construction • Materials • Cement • Composite • C-S-H gel • Nanoparticles • Silicon dioxide • Nanofibers • Self-cleaning • Photocatalyst • Stress-sensing • Self-compacting

1 Introduction

While the science related to nanotechnology is new, nanosized devices and objects have existed since ancient times when humans began to use nanosized materials in glass [1], to modern times where "classic" photography employed silver nanoparticles sensitive to light. It has been proven that the exceptional mechanical performance of biomaterials such as bones or mollusk shells is due to the presence of nanocrystals of calcium compounds [2, 3]. The nanocomposite material of the abalone shell consists of nanosized particles of calcium carbonate bound together by a glue composed of a carbohydrate protein mix [3]. This type of nanostructure leads to the very high strength and toughness of the shell due to the interlocking of nanoblocks of calcium carbonate and is responsible for crack arrest and dissipation of energy. Better understanding and mimicking the processes of "bottom-up" assembly used by nature is one of promising directions in nanotechnology [1, 3].

K. Sobolev (✉)
Department of Civil and Environmental Engineering, University of Wisconsin-Milwaukee, Milwaukee, WI, USA

Department of Civil and Environmental Engineering, Concrete Sustainability Hub, Massachusetts Institute of Technology, Cambridge, MA, USA
e-mail: sobolev@uwm.edu

K. Sobolev, S.P. Shah (eds.), *Nanotechnology in Construction*,
DOI 10.1007/978-3-319-17088-6_1

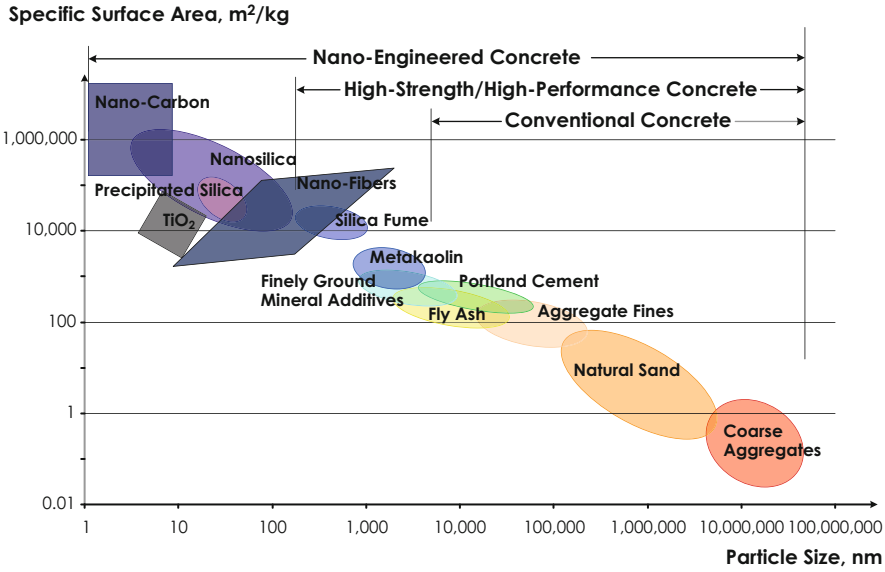

Fig. 1 The particle size and specific surface area scale related to concrete materials

The elementary building unit in nanotechnology is a quantum dot or nanoparticle, which can be represented as a cluster of tens to thousands of atoms of 1–100 nm in diameter. When nanoparticles are created by the "bottom-up" approach, the size and shape of a particle can be controlled by production conditions. These particles can also be considered as nanocrystals because the atoms within the particle are perfectly ordered. When the dimensions of a material are reduced from macro- to nano-size, significant changes occur in conductivity, optical absorption, chemical reactivity, and mechanical properties. In reducing the size, more atoms are located on the surface of each particle, and this, in addition to remarkable surface area of nanopowders (Fig. 1), imparts a considerable change to the particles' surface energies and morphologies. These factors alter the basic properties and the chemical reactivity of nanomaterials [1, 2, 4]. The shift in properties helps to improve catalytic ability and to design better pigments and paints with self-cleaning and self-healing features [1, 5]. Nanosized particles have also been used to enhance the mechanical performance of plastics and rubbers [1–3], as they help to make cutting tools harder and ceramic materials ductile. New nanomaterials based on metal and oxides of silicon and germanium demonstrate superplastic behavior, undergoing elongations up to 1,000 % before failure [6].

The most promising contemporary developments include the synthesis of the new forms of carbon: fullerene (C_{60}), carbon nanotubes (e.g., single-wall nanotubes, SWNT) and graphene. The synthesis of SWNTs is achieved under precisely con-

trolled conditions in the presence of a catalyst; the multi-wall carbon nanotubes (MWNTs) are formed in the case of deviation from the optimal production route [1]. Application areas for nanotubes vary widely from nanoelectronic devices and tips for scanning-probe microscopes to bio/chemical sensors, catalyst support, gas storage/separation, drug delivery, self-healing technologies, and, especially, strength enhancement in composite materials. For example, the super-high tensile strength of nanotubes (calculated to be 20 times higher than that of steel, at the level of 45 GPa) makes these materials an ideal reinforcing component for modern fibers and films with possible applications to the cables supporting long-span or high-rise structures.

The combination of carbon nanotubes and conventional polymer based fibers and films is another challenge. For example, the incorporation of 10 % SWNTs into the strongest man-made fiber, Zylon, resulted in anew material with 50 % greater strength [7]. It is expected that better exfoliation along with improved dispersing and alignment of the individual nanotubes can boost the performance of composite fibers or, alternatively, reduce the volume of the nanotubes used. Dalton et al. [8] introduced a breakthrough related to SWNT-reinforced fibers and achieved strength of 1.8 + GPa. These fibers match the energy-absorbing capacity of spider silk up to the breaking point of silk at 30 % (165 J/g) and continue absorbing energy until reaching a toughness of 570 J/g, compared with 50 and 33 J/g for Spectra and Kevlar fibers, respectively [8]. Because of these properties, the application of new fibers in construction composites is very promising.

The nanoscience and nanoengineering(nanomodification) of construction composites are terms that describe two main directions related to nanotechnology [9]. *Nanoscience* deals with the measurement and characterization of the nano- and micro-scale structure of materials used to understand how this structure affects the macroscale properties and performance through the use of advanced characterization techniques and atomistic modeling. *Nanoengineering* encompasses the techniques of manipulation at the nanometer scale to develop new multifunctional composites with superior mechanical performance and durability potentially having a range of novel properties such as low electrical resistivity, self-sensing capabilities, self-cleaning and self-healing [9]. Composites can be nano-engineered by the incorporation of nano-sized building blocks or objects (e.g., nanoparticles and nanofibers) to control material behavior and add novel properties or by the grafting of molecules onto cement particles, aggregates, additives (including nano-sized additives) to provide surface functionality, which can be tuned to promote the specific interfacial interactions [9, 10].

The majority of recent nano-research in construction has investigated the structure of cement-based materials and their fracture mechanisms [3, 9–11]. With new advanced equipment, it is possible to observe the structure at its atomic level and even measure the strength, hardness and other basic properties of the micro- and nanoscopic phases of materials [1–4]. The application of atomic force microscopy (AFM) for investigating the “amorphous” C-S-H gel led to the discovery that this product has a highly ordered structure at the nanoscale [12]. Considerable progress

over recent years has been achieved by the employment of nano-scale characterization techniques to understand nano-scale structure and processes such as:

- Nuclear magnetic resonance;
- Atomic force microscopy;
- Micro-and nano-indentation;
- Neutron and X-ray scattering;
- Ultrasonic force microscopy;
- Focus-ion-beam (FIB) nanotomography.

Better understanding the structure of these new nano-engineered materials at the nano-level can influence the important processes related to the production and use of construction materials: strength, fracture, corrosion and even tailoring of the desired properties. For instance, for façade and interior applications, the development of paints and finishing materials with new self-cleaning properties, discoloration resistance, anti-graffiti protection, and high-scratch and wear-resistance is important. The existing self-cleaning concrete, mortars, and water-based paints were developed based on photocatalyst technology [13]. The self-cleaning effect related to the decomposition of organic pollutants and gases is achieved when a TiO_2 photocatalyst thin film is set on a surface and can emit active oxygen under UV light. Another aspect of self-cleaning is provided by the hydrophilicity of the surface, which helps to rinse away dust and dirt. Photocatalytic properties can also be used to engineer cement based materials for energy harvesting applications [14]. Nano-SiO_2 has proved to be a very effective additive to polymers to improve strength, flexibility, and durability [15, 16].

2 Nanotechnology of Concrete

Concrete, the most ubiquitous man-made material, is a nano-structured, multiphase, composite material that ages over time [9, 10]. The properties of concrete exist in, and the degradation mechanisms occur across, multiple length scales (nano to micro to macro) where the properties of each scale derive from those of the next smaller scale [10]. The amorphous phase, calcium-silicate-hydrate (C–S–H) is the "glue" that holds concrete together and is itself a nanomaterial [12].

With its "bottom-up" possibilities, nano-chemistry offers new products that can be effectively applied in concrete technology. One example is related to the development of new admixtures for concrete, such as polycarboxylic ether (PCE)superplasticizers designed for extended slump retention of concrete mixtures [9]. It was proposed that, when nanoparticles are incorporated into conventional building materials, such materials can possess advanced properties required for the construction of high-rise, long-span or intelligent civil and infrastructure systems [9–11]. For example, SiO_2 nanoparticles (Figs. 1 and 2) can be used as an additive for high-performance and self-compacting concrete, improving workability and strength [9]. The particle size and specific surface area scale related to concrete materials reflect the general trend to use finer materials [9]. For decades, major developments in concrete perfor-

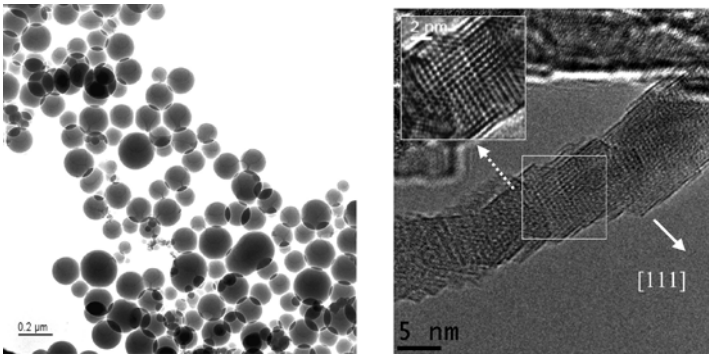

Fig. 2 TEM images of nanosilica particles (*left*) and Al_2O_3 nanofibers (*right*, courtesy of ANF Development OU)

mance have been achieved with the application of ultrafine particles such as silica fume, and now, with nanosilica. Nanofibers(such as nano-Al_2O_3) are also promising component for application in composites.

3 Concrete with Nanoparticles

Nano-binder was proposed as a material designed with a nano-dispersed cement component to fill the gaps between the particles of mineral additives [9]. The nano-sized cementitious component can be obtained by the colloidal milling of portland cement (the top-down approach) or by self-assembly using mechano-chemically induced to po-chemical reactions (the bottom-up approach).

Chemically precipitated C-S-H was suggested as an effective admixture to improve the performance of concrete [17]. It was proposed that nano-sized C-S-H particles with an average size of 5–10 nm act as nucleation seeds for the hydration products of portland cement. The positive effect of the C-S-H is attributed to the significant reduction of porosity, the size of the pores, and permeability.

Most of the experimental work has been conducted using nano-SiO_2 particles. Collepardi et al. were among the first to study the performance of low-heat self-compacting concrete (SCC) produced with nano-SiO_2. Nanosilica (5–50 nm) was used in a form of slurry as a viscosity modifying agent at a dosage of 1–2 % of cementitious materials [18]. The design of SCC with a low-heat release was achieved by using blended cement (with 60 % of blast furnace slag) and incorporating limestone and fly ash powders. It was reported that the addition of nano-SiO_2 makes the concrete mixture more cohesive and reduces bleeding and segregation. The best performance was demonstrated by concrete with ground fly ash, 2 % nano-silica, and 1.5 % superplasticizer. This concrete had the desired behavior in a fresh state and the highest compressive strength [18]. Similarly, nano-SiO_2 was used as an effective viscosity modifying agent in high-density, high-strength cementitious

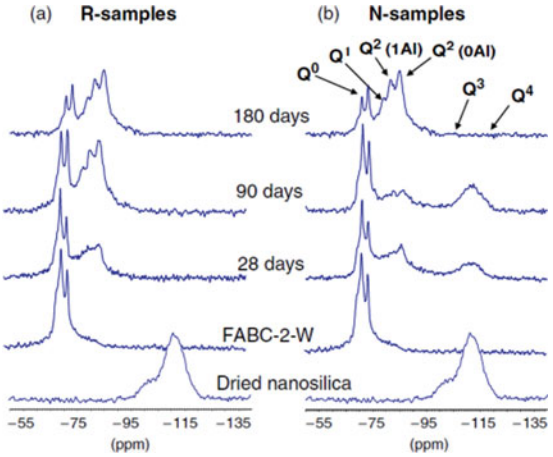

Fig. 3 ^{29}Si MAS NMR spectra for C–S–H gels of (**a**) reference (*R*) and nanosilica (*N*) samples (**b**) samples after exposure to a sulfate solution (0.5 M $NaSO_4$) [23]

grout [19]. The accelerating effect of nano-SiO_2 on the hydration of C_3S was reported by Björnström et al. [20]. The increased rates of C_3S phase dissolution, subsequent accelerated formation of C-S-H gel, and the removal of non-hydrogen bonded OH^- groups were revealed with DR FTIR spectroscopy and DSC for samples containing up to 5 % of colloidal silica. Li [21] performed a laboratory study of superplasticized high-strength concrete incorporating 4% nano-SiO_2 and 50% class F fly ash. It was demonstrated that the pozzolanic reaction of nano-SiO_2 is very quick, reaching 70 % of its ultimate value within 3 days; and, in a 2-week period, up to 95 %. The investigation of the hydration process confirmed the assumption that the pozzolanic activity of fly ash can be significantly improved by the application of nano-SiO_2. The use of nano-SiO_2 at small dosages (3 %) enables to reduce the amount of CH formed at the aggregate's interface and the size of CH [22]. The addition of nano-SiO_2 was effective way to improve the compressive and bond strength, especially at the early ages of hardening. Porro et al. [23], reported on the effect of different dosages and types of nano-SiO_2 on the performance of portland cement pastes. The compressive strength of the cement pastes increased with the reduction of the dosage and the particle size of the nanoparticles. This improvement of strength and durability was attributed to the formation of larger silicate chains of the C-S-H gel in mixtures with nano-SiO_2 (Fig. 3).

The relatively small quantities of nano-sized materials, less than 1 % by weight of cement, are sufficient to improve the performance of nanocomposites [9, 10]; yet, the commercial success of nanomaterials depends on the ability to manufacture these materials in large quantities and at a reasonable cost relative to the overall effect of the nanoadditives. Nanomaterial technologies, which could lead to industrial outputs, involve plasma arcing, flame pyrolysis, chemical vapor deposition, electrodeposition, sol-gel synthesis, mechanical attrition, and the use of natural nanosystems [1]. Among chemical technologies, sol-gel synthesis is one of the widely used "bottom-up" production methods for nano-sized materials such as nano-silica. The process involves the formation of a colloidal suspension (sol) and

gelation of the sol to form a network in a liquid phase (gel). Usually, tetraethoxysilane (TEOS) is applied as a precursor for synthesizing nanosilica [4]. The details of the "bottom-up" sol-gel synthesis of nano-SiO_2 particles with a size range of 5–100 nm and the effect of this material on the performance of cement systems was reported [24]. It was demonstrated that the performance of nano-SiO_2 in cement system depends on the conditions of synthesis (molar ratios of the reagents, type of the reaction media, pH and the duration of the reaction). The best nano-SiO_2 products with particle sizes ranging from 5 to 20 nm were synthesized at the highest molar concentrations of water. The addition of developed nano-SiO_2 to portland cement mortars improved the compressive strength. The distribution of nano-SiO_2 particles within the cement paste is an important factor governing its performance; therefore, the disagglomeration of nanoparticles is essential for the design of composite materials. The application of superplasticizer, ultrasonification and high-speed mixing was an effective approach to use nano-SiO_2 [24].

Based on the available data, the beneficial action of nano-particles on the microstructure and the performance of cement-based materials can be explained by the following factors [9, 10]:

- Well-dispersed nano-particles increase the viscosity of the liquid phase, helping to suspend the cement grains and aggregates and improving the segregation resistance and workability of the system;
- Nano-particles fill the voids between cement grains, resulting in the immobilization of "free" water (the "filler" effect);
- Well-dispersed nano-particles act as centers of crystallization of cement hydrates, thereby accelerating hydration;
- Nano-particles favor the formation of small-sized crystals (such as $Ca(OH)_2$ and AF_m) and small-sized uniform clusters of C-S-H;
- Nano-SiO_2 participates in the pozzolanic reactions, resulting in the consumption of $Ca(OH)_2$ and formation of an "additional" C-S-H;
- Nano-particles improve the structure of the aggregates' contact zone, resulting in a better bond between aggregates and the cement paste;
- Crack arrest and interlocking effects between the slip planes provided by nano-particles improve the toughness, shear, tensile, and flexural strength of cement based materials.

4 Application of Carbon Nanostructures

Carbon nanostructures (CNS) such as nanotubes(CNT), nanofibers(CNF) and graphene are potential candidates for nano-reinforcement of cement-based composites. CNS exhibit extraordinary strength with moduli of elasticity on the order of TPa and tensile strength in the range of GPa, and they have unique electronic and chemical properties [9–11]. Compared to CNT, vapor grown CNF have a lower production cost and are suitable for mass production. While CNT/CNF have been extensively

studied in polymeric composites, their use in cement composites has remained limited. Most research efforts have focused on CNT rather than CNF and have been performed on cement pastes and mortars [9, 10, 25–27].

5 Developing New Functionalities

Carbon nanofiber-reinforced composites may function as piezoresistive strain sensors. The introduction of carbon nanofibers into a composite decreases its electrical resistivity due to the high conductivity of the carbon fibers compared to plain cementitious material. In addition to providing strain-sensing ability, the addition of CNFs increases tensile and flexural strengths, tensile ductility and flexural toughness, which make the self-sensing feasible. Han et al. introduced a self-sensing material with multi-walled carbon nanotubes for traffic monitoring [28]. A self-sensing CNT-cement composite was used for the detection of mechanical stresses induced by traffic flow in laboratory and field experiments.

Architectural concrete needs to maintain its aesthetic characteristics, such as color, over its entire service life, even in highly polluted urban environments. The incorporation of photocatalytic materials is a smart solution for oxidizing and destroying organic pollutants and, subsequently, removing inorganic matter from the surface of architectural concrete. Photocatalytic TiO_2 was applied in white cement-based concrete with self-cleaning and air-purification features [9, 29]. One of the best photocatalystsis based on anatase polymorph of nano-sized TiO_2.

It was proved that the cement-TiO_2 composite is a very effective photocatalytic couple. Accelerated 8-h irradiation stimulating intensive solar light (corresponding to 1 month of sunlight exposure) of phenanthroquinonecolored TiO_2 cement based specimens resulted in restoration of an original white color. It was reported that the photocatalytic cement matrix is very effective for NO_x abatement. Under solar radiation, NO in the air is oxidized and converted to nitrate. A photocatalytic cement technology has been used for a number of construction projects including the “Dives in Misericordia” Church (architect Richard Meier) located in Rome, Italy.

6 Future Developments

Vast progress in construction materials, especially concrete, is expected in coming years by the adaptation of new knowledge generated from the rapidly growing field of nanotechnology. Development of the following concrete-related nanoproducts can be anticipated:

- Catalysts for low-temperature clinker synthesis and accelerated hydration;
- Grinding aids for superfine grinding and mechano-chemical activation;
- Binders reinforced with nano-particles, nano-rods, nano-tubes, graphene, nano-nets, nano-dampers, or nano-springs;

- Binders with nano-engineered bonds between the hydration products;
- Binders modified by nanopolymer particles or films;
- Bio-inspired materials (e.g., imitating the structure of mollusk shells);
- Cement-based composites reinforced with nano-engineered fibers;
- Superplasticizers for supreme workability control;
- Cement-based materials with supreme strength, ductility, and toughness;
- Binders with controlled internal moisture supply to control micro-cracking;
- Materials with engineered nanostructures exhibiting supreme durability;
- Superhydrophobic materials for extreme durability;
- Self-healing materials and repair technologies;
- Photocatalyst materials with self-cleaning and air-purifying features;
- Materials with controlled electrical conductivity, deformative properties, non-shrinking and low thermal expansion;
- Smart materials, such as temperature-, stress-sensing or stress-responding;
- Nanomodifiedeco-binders with substantially reduced volumes of portland cement component (down to 15 %);
- Alternative nanobinder systems (MgO-phosphate, geopolymers).

Mechano-chemistry and nano-catalysts could change the face of the modern cement industry by significantly reducing clinkering temperature and even realizing the possibility of cold-sintering clinker minerals in mechano-chemical reactors.

7 Conclusions

Nanotechnology has changed and will continue to change our vision, expectations, and abilities to control the material world. These developments will greatly affect construction and the field of construction materials. The major achievements in this domain include:

- The ability to observe nano-structures at the atomic level and measure the strength and hardness of nanoscopic phases of composite materials;
- Discovery of an ordered crystal nanostructure of “amorphous” C-S-H gel;
- Nanoparticles, nanofibers, nanomeshes for performance enhancement;
- Development of paints and finishing materials with self-cleaning properties, discoloration resistance, anti-graffiti protection, and high scratch-and-wear resistance;
- Self-cleaning materials based on photocatalyst technology;
- Nanometer-thin coatings that protect carbon steel against corrosion and enhance thermal insulation of window glass;
- Smart stress-sensing composites.

Among the new nano-engineered polymers are highly efficient superplasticizers for concrete and high-strength fibers with exceptional energy-absorbing capacity. Nanoparticles, such as silicon dioxide, were found to be a very effective additive to polymers and concrete, a development recently realized in high-performance and self-compacting concrete with improved workability and strength.

Portland cement, one of the largest commodities consumed by humankind, has significant, but not completely explored potential. Better understanding and precise engineering of an extremely complex structure of cement-based materials at the nanolevel will result in a new generation of concrete that is stronger and more durable, with improved stress-strain behavior and possibly possessing a range of newly introduced "smart" properties, such as electrical conductivity and temperature-, moisture-, and stress-sensing abilities. At the same time, this new concrete should be sustainable, cost and energy effective—in essence exhibiting the qualities modern society demands. Nano-binders or nano-engineered cement-based materials with nano-sized cementitious components or other nano-sized particles will be the next ground-breaking development.

Nanotechnology is still in its pre-exploration stage—it is just emerging from fundamental research onto the industrial floor; thus its full-scale applications, especially in construction, are currently very limited. However, the tremendous potential for nanotechnology to improve the performance of conventional materials and processes is extremely promising.

References

1. Bhushan, B. (Ed.). (2004). *Handbook of nanotechnology*. Berlin: Springer.
2. Poole, C. P., & Owens, F. J. (2003). *Introduction to nanotechnology*. Hoboken: John Wiley & Sons.
3. Gann, D. (2002). *A review of nanotechnology and its potential applications for construction*. SPRU, University of Sussex.
4. Klabunde, K. J. (Ed.). (2004). *Nanoscale materials in chemistry* (p. 304). New York: Wiley.
5. Bauer, B. J., Liu, D., Jackson, C. L., et al. (1996). Epoxy/SiO_2 interpenetrating polymer networks. *Polymers for Advanced Technologies, 7*, 333–339.
6. Calderón-Moreno, J. M., Schehl, M., & Popa, M. (2002). Superplastic behavior of zirconia-reinforced alumina nanocomposites from powder alcoxide mixtures. *Acta Materialia, 50*(16), 3973–3983.
7. Kumar, S., et al. (2002). Synthesis, structure, and properties of PBO/SWNT composites. *Macromolecules, 35*(24), 9039–9043.
8. Dalton, A. B., et al. (2003). Super-tough carbon-nanotube fibres. *Nature, 423*, 703.
9. Sobolev, K., & Ferrada-Gutiérrez, M. (2005). How nanotechnology can change the concrete world: Part 1. *American Ceramic Society Bulletin, 10*, 14–17.
10. Sanchez, F., & Sobolev, K. (2010). Nanotechnology in concrete – A review. *Construction and Building Materials, 24*(11), 2060–2071.
11. Trtik, P., & Bartos, P. J. M. (2001). *Nanotechnology and concrete: What can we utilise from the upcoming technologies?* Proceeding of the 2nd Anna Maria workshop: Cement & Concrete: Trends & Challenges, pp. 109–120. Anna Maria, FL, USA.
12. Plassard, C., Lesniewska, E., Pochard, I., & Nonat, A. A. (2004). Investigation of the surface structure and elastic properties of calcium silicate hydrates at the nanoscaled. *Ultramicroscopy, 100*(3–4), 331–338.
13. Watanabe, T., Kojima, E., et al. (2001). *Multi-functional material with photocatalytic functions and method of manufacturing same*. U.S. Pat. No. 6 294 247.
14. Hosseini, T., Flores-Vivian, I., Sobolev, K., & Kouklin, N. (2013). Concrete embedded dye-synthesized photovoltaic solar cell. *Nature Scientific Reports, 3*, 2727.

15. Kang, S., Hong, S.-I., Choe, C.-R., Park, M., Rim, S., & Kim, J. (2001). Preparation and characterization of epoxy composites filled with functionalized nanosilica particles obtained via sol-gel process. *Polymer, 42*, 879–887.
16. Li, H., Xiao, H.-G., Yuan, J., & Ou, J. (2004). Microstructure of cement mortar with nano-particles. *Composites: Part B, 35*, 185–189.
17. Thomas, J. J., Jennings, H. M., & Jeffrey, J. (2009). Chen influence of nucleation seeding on the hydration mechanisms of tricalcium silicate and cement. *The Journal of Physical Chemistry C, 113*, 4327–4334.
18. Collepardi, M., Ogoumah-Olagot, J. J., Skarp, U., & Troli, R. (2002). Influence of amorphous colloidal silica on the properties of self-compacting concretes. Proceedings of the international conference. *Challenges in concrete construction – Innovations and developments in concrete materials and construction* (pp. 473–483). Dundee: Thomas Telford.
19. Green, B. H. (2008). Development of a high-density cementitious rock-matching grout using nano-particles, SP-254. In K. Sobolev & S. P. Shah (Eds.), *Nanotechnology of concrete: Recent developments and future perspectives* (pp. 121–131). Farmington Hills: American Concrete Institute.
20. Bjornstrom, J., Martinelli, A., Matic, A., Borjesson, L., & Panas, I. (2004). Accelerating effects of colloidal nano-silica for beneficial calcium-silicate-hydrate formation in cement. *Chemical Physics Letters, 392*(1–3), 242–248.
21. Li, G. (2004). Properties of high-volume fly ash concrete incorporating nano-SiO_2. *Cement and Concrete Research, 34*, 1043–1049.
22. Qing, Y., Zenan, Z., Deyu, K., & Rongshen, C. (2007). Influence of nano-SiO_2 addition on properties of hardened cement paste as compared with silica fume. *Construction and Building Materials, 21*(3), 539–545.
23. Porro, A., Dolado, J. S., Campillo, I., Erkizia, E., de Miguel, Y., Sáez de Ibarra, Y., & Ayuela, A. (2005). *Effects of nanosilica additions on cement pastes* (Applications of nanotechnology in concrete design). London: Thomas Telford.
24. Flores, I., Sobolev, K., Torres, L. M., Valdez, P. L., Zarazua, E., & Cuellar, E. L. (2010, May 5–7). Performance of cement systems with nano-SiO_2 particles produced using sol-gel method. *TRB first international conference in North America on Nanotechnology in Cement and Concrete*, Irvine.
25. Makar, J. M., Margeson, J., & Luh, J. (2005, August 22–24). Carbon nanotube/cement composites – Early results and potential applications. *Proceedings of 3rd international conference on Construction Materials: Performance, Innovations and Structural Implications*, Vancouver, pp. 1–10.
26. Sanchez, F., Zhang, L., & Ince, C. (2009). Multi-scale performance and durability of carbon nanofiber/cement composites. In Z. Bittnar, P. J. M. Bartos, J. Nemecek, V. Smilauer, & J. Zeman (Eds.), *Nanotechnology in construction: Proceedings of the NICOM3 (3rd international symposium on Nanotechnology in Construction)* (pp. 345–350), Prague. Berlin: Springer.
27. Shah, S. P., Konsta-Gdoutos, M. S., Metaxa, Z. S., & Mondal, P. (2009). Nanoscale modification of cementitious materials. In Z. Bittnar, P. J. M. Bartos, J. Nemecek, V. Smilauer, & J. Zeman (Eds.), *Nanotechnology in construction: Proceedings of the NICOM3 (3rd international symposium on Nanotechnology in Construction*) (pp. 125–130), Prague. Berlin: Springer.
28. Han, B., Yu, X., & Kwon, E. (2009). A self-sensing carbon nanotube/cement composite for traffic monitoring. *Nanotechnology, 20*, 1–5.
29. Cassar, L., Pepe, C., Tognon, G., Guerrini, G. L., & Amadelli, R. (2003). White cement for architectural concrete possessing photocatalytic properties. *Proceedings of the 11th international congress on the Chemistry of Cement (ICCC)*, Durban.

Durability of Cement-Based Materials and Nano-particles: A Review

Surendra P. Shah, Pengkun Hou, and Xin Cheng

Abstract The development of modern cement and concrete industry calls for the improvement of the durability. By addition of a small amount of nano-particles nano structure of cement based materials can be modified and a higher durability can be achieved. In this paper, a review of the investigation of the effect of the frequently used nanoparticles, i.e., nano-silica, nano-clay and carbon nanotube on the durability of cement and concrete is presented. It is concluded that nanomodification of cementitious materials with nano-particle would make them durable through alteration of the physicochemical properties of the binder. Although intensive study on the usage of nano-silica has been conducted, more work is needed to get a better knowledge on the influencing mechanism. Surface-treatment of cementitous materials with nano-particles shows great potential for acquiring a durable concrete surface, and study on the selection of the treatment agent and treatment technique has been suggested. In addition, potential of using nano-clay in decreasing the transport property and the effect of carbon nanotube in optimizing the microstructure, as well as in decreasing the volume instability of cement-based materials are also discussed.

Keywords Cement and concrete • Durability • Nano-particles • Nanomodification

S.P. Shah (✉)
Department of Materials Science & Engineering, Northwestern University,
Evanston, IL 60201, USA
e-mail: s-shah@northwestern.edu

P. Hou
School of Materials Science & Engineering, University of Jinan,
Jinan, Shandong 250022, China
e-mail: pkhou@163.com

X. Cheng
Shandong Provincial Key Laboratory of Preparation and Measurement of Building Materials,
Jinan, Shandong 250022, China
e-mail: ujn_chengxin@163.com

K. Sobolev, S.P. Shah (eds.), *Nanotechnology in Construction*,
DOI 10.1007/978-3-319-17088-6_2

1 Introduction

Since the last decades, with the invention of chemical agents used in concrete, especially the water-reducer, as well as the addition of pozzolans into cement-based materials, the quality of concrete mix has been greatly improved. It is generally agreed that a compact microstructure and an optimized composition/C-S-H gel structure are one of the key issue that govern the durability of a concrete structure. Considering the nano-scale feature of the C-S-H gel, researchers have been recently using nano-technology for the improvement of the durability [1–3].

In this paper, the influences of the most widely used nanoparticles in cement and concrete, i.e. nano-silica, nano-clay, carbon-nanotube on the durability of cement-based materials are reviewed. Effects of these nano-particles on the improvement of concrete durability are exhibited and the potential directions of further investigation are discussed.

2 Nano-silica Particle

Among all the nano-materials used in cement-based materials, nano-silica of different forms, for example, powder(nano silica), colloidal solution (colloidal nano silica) and even its precursor (tetraethoxysilane), have been investigated [4–10]. By exploring its effects on the hydration and hardening properties of cementitious materials, many researchers have reported the benefits that have been introduced, including the enhanced pozzolanic reactivity and the seeding effect.. Kong and his co-workers reported a greater $Ca(OH)_2$-consuming capability of nano-silica as compared to that of silica fume. The current authors have reported one order of magnitude higher pozzolanic reaction rate of nano-silica particle than that of silica fume [11]. Singh recently reviewed the application of nano-silica in concrete [5], and his recently published paper quantitatively assessed the additional C-S-H gel formed by nano-silica hydration [12]. The alterations of the hydration and hardening processes of cementitious materials in the presence of nano-silica particle as revealed by various workers improve the durability of cementitious materials.

2.1 On the Early Age Properties of High-Volume Industrial By-Product Cementitious Materials

Using more industrial by-products, such as fly ash, in cementitious material has been considered desirable for making cement based materials more sustainable. Although great advantages such as low-carbon footprint, smaller hydration heat, greater strength gain at later ages and higher resistivity to the surrounding environment are acquired when fly ash is added into cementitious materials, the slow property gain at

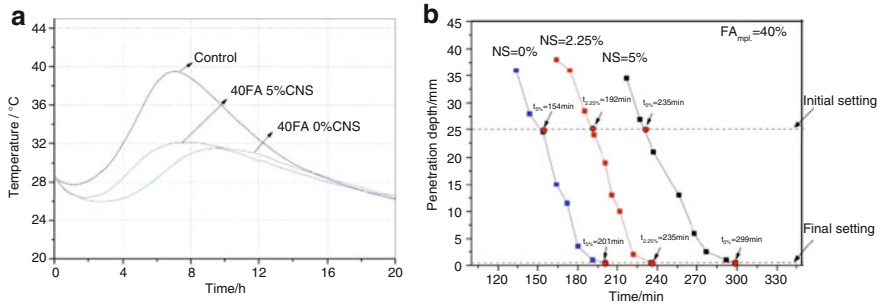

Fig. 1 Influences of nano-silica on the early age hydration of HVFA system [3]. (**a**) Hydration temperature (**b**) setting time measured by Vicat needle

early ages such as prolonged setting time, low early-age mechanical property are considered to the major drawbacks [13]. By taking the advantages of the acceleration effect of nano-silica particles on the hydration of cement [14], various researchers have investigated the influences of nanosilica on high volume fly ash system (HVFA) [3, 15]. Hou et al. have measured the hydration heat of HVFA system after addition of nano-silica [3], as shown in Fig. 1. It can be seen that the slowed hydration processes of HVFA system, i.e. lower hydration temperature and slower hydration rate, are accelerated when 5 % colloidal nano-silica (CNS) is added. Acceleration effect of nano-silica is more apparently demonstrated in the setting time measurement: it can be seen in Fig. 1 that the initial and final setting time of HVFA system was greatly shortened, and the setting times of 40 % FA replacement system were comparable to that of plain cement paste [3].

Zhang and his co-authors studied the influence of nano-silica particle on the mechanical property development of high volume fly ash/pulverized blast furnace slag cementitious materials, whose results supported the great increase of the mechanical properties of the systems, especially at early ages [16, 17].

By analyzing the hydration extents of the pozzolans at various ages, Li [18] and Hou [3] have studied the influences of nano-particles on the pozzolanic reaction. Li reported an increased hydration degree of fly ash in the presence of nano-silica. Hou et al. showed that the increase was seen in the early age, but a reduced hydration degree was the result at later ages.

2.2 On the Gel Property

As a silicate material, the pozzolanic reaction of nano-silica with the hydration product of $Ca(OH)_2$ forming additional C-S-H gel has often been ascribed to the benefits that nano-silica introduced into cement-based materials. Moreover, it has been reported that the alteration of the physicochemical properties of C-S-H gel

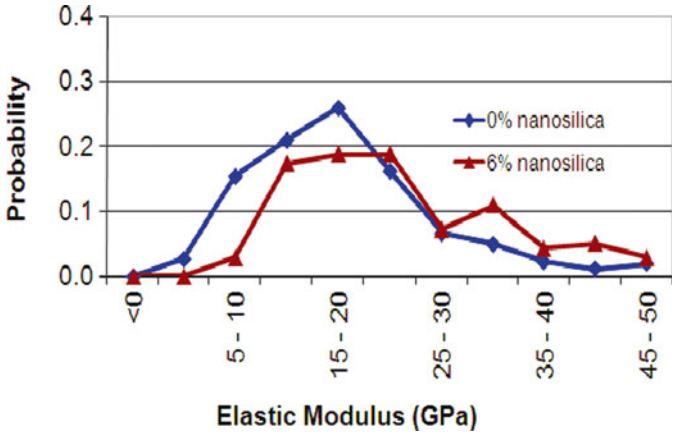

Fig. 2 Elastic modulus of plain cement paste (CP) vs CP modified with nano-silica [19]

contributed to the improvement of durability of cement-based materials. Gaitero and his co-authors investigated the calcium-leaching resistivity of nano-silica-added cement-based materials [6]. They observed that degradation due to accelerated calcium leaching was significantly less for nano-silica addition as compared to that by micro-silica addition. They reported that nano-silica particles increase the average length of the silicate chains of C-S-H gel. In addition, it was reported that addition of nanosilica modified the nano structure of C-S-H as measured by nano indentation (Fig. 2). Bosque studied the morphology of C-S-H gel after the addition of nano-silica particle into cement paste under different temperatures and their results suggested that C-S-H gel of longer average length of the silicate chains was achieved [20].

The current authors made an in-depth study of the hydration properties of nano-silica particles. SEM images (Fig. 3) showed that a compacter micro-structure (with a lower calcium to silica ratio) of the pozzolanic reaction products is formed when compared to that of silica fume, and this has been attributed to the improvement of the durability of cementitious materials. A compacter C-S-H gel structure formed by nano-silica particle has also been reported by Thomas [22] and Singh [12].

Although nano-silica has been intensively used in cement and concrete, its reaction mechanism and the influence on C-S-H gel still need to be clarified.

2.3 On the Surface-Treatment

More recently, the high pozzolanic reactivity and its nano-sized feature of nano-silica has been used for the surface-treatment of hardened cementitious materials [7, 8, 23]. Due to its closeness to the environment, the surface of concrete structure exposed to the environment is the most vulnerable part and an improvement of the

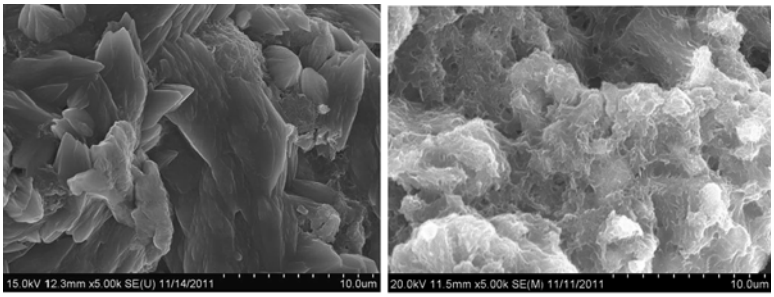

Fig. 3 Morphology of pozzolanic hydration products of CNS and silica fume (CNS/SF:CH = 5:20; w/b = 2.0, 4 months old) [21]

Table 1 Initial water absorption coefficients of cement pastes before and after surface treatment/ ($mg/cm^2 * s^{1/2}$) [8]

w/c	0.26	0.38	0.6	1.0
Control	2.5(100 %)	5.7(100 %)	6.9(100 %)	8.3(100 %)
CNS	2.5(100 %)	5.7(100 %)	5.7(82.6 %)	6.3(75.9 %)
TEOS	2.5(100 %)	4.2(73.7 %)	5.2(75.4 %)	5.5(66.3 %)

surface would be beneficial for the improvement of the durability. Cardenas and his coworkers investigated the influence of nano particle treatment on the properties of reinforced concrete, whose results supported that the quality of the surface concrete can be improved by nanoparticle-treatment through an electrokinetic technique [24, 25]. More recently, Franzoni et al. used colloidal nano-silica in treating hardened concrete; their results did not support the positive effectiveness of surface-treatment of nano-silica [23], but they found that the precursor of producing nano-silica, tetraethoxysilane (TEOS), which hydrolyzes in the pore structure forming a silica sol [26], was effective in making more compacter and more durable concrete. The current authors recently reported the mechanism of nano-silica for the surface-treatment of hardened cement-based materials under different curing regimes [7]. Results showed that the pozzolanic reaction of nano-silica contributes to the densification of the surface micro-structure (reduction of the water absorption as shown in Table 1), meanwhile the alteration of the C-S-H gel, i.e. the increase of the polymerization degree was also ascribed to the improvement of the calcium-leaching resistivity as shown in Fig. 4. All the results demonstrate the possibility of surface-treatment of cement-based materials with nano-particles. All the results demonstrated the potential of using nano particles, in various forms, of improving the surface quality. However, work on the selection of nano particle type, the reaction mechanism and the treatment technique still needed.

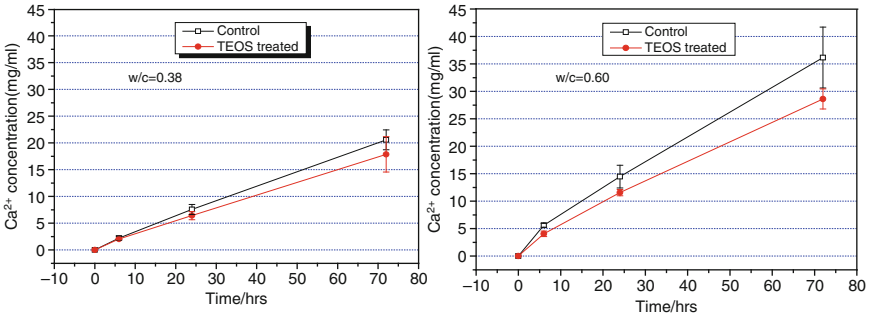

Fig. 4 Decalcification of hardened cement pastes [27]

Table 2 Effect of nano-clay on the chloride diffusion coefficients of concrete [28]

Series	Clay additive wt/%	Diffusion coefficient/m^2/s	Reduction diffusion coefficient/%
Plain	0	1.98262e-11	0.00
CC1	1	1.81058e-11	8.68
CC2	3	1.81343e-11	8.53
CC3	5	1.60840e-11	18.87

Note: Mix proportion of the concrete mixtures (in kg/m^3): cement:water:sand:aggregate = 350: 175:619:1,256

3 Nano-clay

Due to the low price, as well as the benefits introduced, nano-clay is considered to be a promising alternative for the modification of cement-based materials. Compared to the control, the flexural strength of cement paste with 1 % kaolinite clay increased by 30.41 %, 39.04 %, 36.27 % and 38.32 % at 1, 3, 7 and 90 days, respectively. The increase in compressive strength of the cement concrete with clay is 12 %, 13.5 %, and 28.4 % compared to the control at 1 %, 3 % and 5 % addition, respectively [28].

Nano-clay has a two-layer structure and it has been suggested that water molecules transport through the sheets can be blocked and a lowered permeability of cement mortar can be achieved. Fan et al. [28] investigated the effects of nano-clay on the chloride ion diffusion and freezing-thawing resistivity of concrete and the results are shown in Table 2 and Fig. 5. It can be seen in Table 2 that the reduction of chloride diffusion coefficient of cement concrete is 8.68 % and 18.87 % at 1 % and 5 % clay, respectively. After 125 freeze-thaw cycles, the relative dynamic elastic modulus loss is 33 % of the plain concrete, while only 5 % is seen in the 3 % nano-clay added concrete.

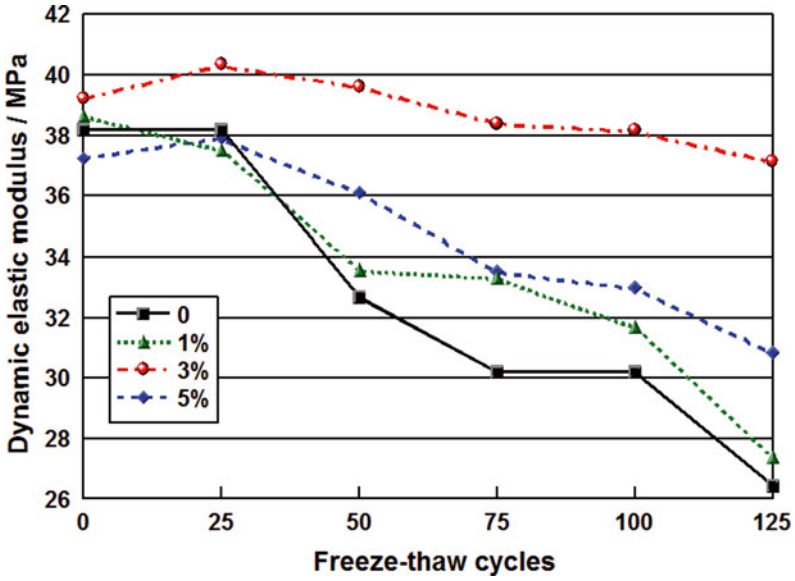

Fig. 5 Influence of nano-clay on the dynamic elastic modulus of concrete after freeze-thaw cycling [28]

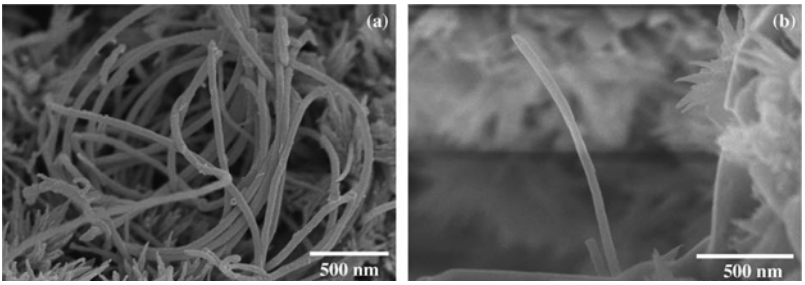

Fig. 6 SEM images of cement paste fracture surfaces reinforced with undispersed (**a**) and dispersed (**b**) MWCNTs, respectively [29]

4 Multi-wall Carbon-Nanotube (MWCNT)

The excellent mechanical properties of CNT make it the candidate for the improvement of the volume stability of cement-based materials. An uniform dispersion of CNT in cementitious materials can be achieved with the aid of sonication and surfactant (as seen in Fig. 6). With the addition of a small amount of CNT, various researchers reported a significant improvement of the mechanical properties. For example, Li et al reported that the addition of 0.5 wt% MWCNTs into cement matrix

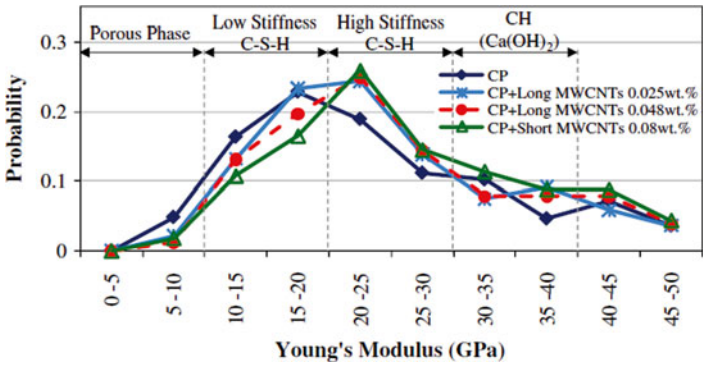

Fig. 7 Probability plots of the Young's modulus of 28 days cement paste (w/c = 0.3) and cement paste reinforced with 0.025 wt% long, 0.048 wt% long and 0.08 wt% short MWCNTs [29]

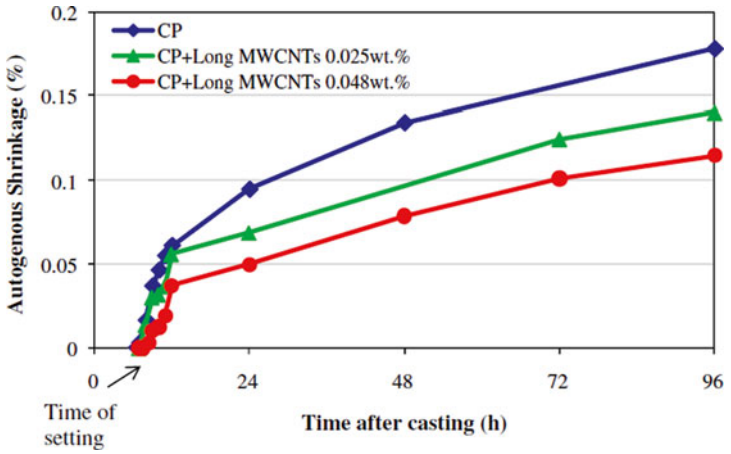

Fig. 8 Autogenous shrinkage of cement paste (w/c = 0.3) and cement paste reinforced with 0.025 and 0.048 wt% long MWCNTs [29]

resulted in a 25 % increase in flexural strength and a 19 % increase in compressive strength. Some other work demonstrated cement hydration acceleration of CNT [30]. Konsta-Gdoutos et al. [29] conducted nano-indentation on CNT-added cement pastes and revealed that the use of highly dispersed small amount (0.05 %) of MWCNTs can increase the amount of high stiffness C–S–H and decrease the porosity (see Fig. 7). The alteration of the nano-structure results in an improvement of the volume stability of cement-based materials at very early age: it can be seen in Fig. 8 that the autogenous shrinkage of cement paste was reduced by about 25 %, and this could be ascribed to the reduction of the capillary stresses induced by the reduction of the porosity.

5 Conclusions

This paper presents a review of the influences of nanoparticle on the durability of cement-based materials. The following conclusions can be drawn.

1. The hydration and hardening properties of cement-based materials can be altered by nano-particles, resulting in a stronger and compacter micro-structure, as well as a modified C-S-H gel structure, all of which contribute to the improvement of the durability. However, the hydration mechanism still needs more work;
2. Modification of the surface of cement-based materials with nano-particles is a promising way to improve the durability of concrete structure, and the selection of the treatment agent and treatment technique needs more work;
3. Application of nano-material (such as CNT) in cement-based materials would contribute to a better performance of the transport and deformation resistivity, through which the durability of concrete structures can be improved.

Acknowledgements Supports from National High Technology Research and Development Program ("863 Program", 2015AA034701) and Natural Science Foundations of China (Grant No. 51302105) are greatly acknowledged.

References

1. Yu, R., Spiesz, P., & Brouwers, H. (2014). Effect of nano-silica on the hydration and micro-structure development of Ultra-High Performance Concrete (UHPC) with a low binder amount. *Construction and Building Materials, 65*, 140–150.
2. Shekari, A., & Razzaghi, M. (2011). Influence of nano particles on durability and mechanical properties of high performance concrete. *Procedia Engineering, 14*, 3036–3041.
3. Hou, P., Wang, K., Qian, J., et al. (2012). Effects of colloidal nanoSiO_2 on fly ash hydration. *Cement and Concrete Composites, 34*, 1095–1103.
4. Sánchez, M., Alonso, M., & González, R. (2014). Preliminary attempt of hardened mortar sealing by colloidal nanosilica migration. *Construction and Building Materials, 66*, 306–312.
5. Singh, L., Karade, S., Bhattacharyya, S., et al. (2013). Beneficial role of nanosilica in cement based materials – A review. *Construction and Building Materials, 47*, 1069–1077.
6. Gaitero, J., Campillo, I., & Guerrero, A. (2008). Reduction of the calcium leaching rate of cement paste by addition of silica nanoparticles. *Cement and Concrete Research, 38*, 1112–1118.
7. Hou, P., Cheng, X., Qian, J., et al. (2014). Effects and mechanisms of surface treatment of hardened cement-based materials with colloidal nanoSiO_2 and its precursor. *Construction and Building Materials, 53*, 66–73.
8. Hou, P., Cheng, X., Qian, J., et al. (2014). Characteristics of surface-treatment of nano-SiO_2 on the transport properties of hardened cement pastes with different water-to-cement ratios. *Cement and Concrete Composites, 55*, 26–33.
9. Sanchez, F., & Sobolev, K. (2010). Nanotechnology in concrete – A review. *Construction and Building Materials, 24*, 2060–2071.
10. Kim, K., Heo, Y., Kang, S., et al. (2014). Effect of sodium silicate- and ethyl silicate-based nano-silica on pore structure of cement composites. *Cement and Concrete Composites, 49*, 84–91.

11. Kong, D., & Shah, S. (2012). Effect of nano-silica agglomeration on hydration and hardening of cement. *Chinese Ceramic Society, 40*, 1599–1606.
12. Singh, L., Bhattacharyya, S., Shah S., et al. (2015). Studies on early stage hydration of tricalcium silicate incorporating silica nanoparticles: Part I. *Construction and Building Materials, 74*, 278–286.
13. Hou, P., Kawashima, S., Wang, K., et al. (2013). Effects of colloidal nanosilica on rheological and mechanical properties of fly ash–cement mortar. *Cement and Concrete Composites, 35*, 12–22.
14. Hou, P., Kawashima, S., Kong, D., et al. (2013). Modification effects of colloidal nanoSiO_2 on cement hydration and its gel property. *Composites Part B: Engineering, 45*, 440–448.
15. Shaikh, F., Supit, S., & Sarker, P. (2014). A study on the effect of nano silica on compressive strength of high volume fly ash mortars and concretes. *Materials and Design, 60*, 433–442.
16. Zhang, M., Islam, J., & Peethamparan, S. (2012). Use of nano-silica to increase early strength and reduce setting time of concretes with high volumes of slag. *Cement and Concrete Composites, 34*, 650–662.
17. Zhang, M., & Islam, J. (2012). Use of nano-silica to reduce setting time and increase early strength of concretes with high volumes of fly ash or slag. *Construction and Building Materials, 29*, 573–580.
18. Li, G. (2004). Properties of high-volume fly ash concrete incorporating nano-SiO_2. *Cement and Concrete Research, 34*, 1043–1049.
19. Mondal, P. (2010). *Nanomechanical properties of cementitious materials*. Ph.D Thesis, Northwestern University, Evanston, USA.
20. Bosque, S., Martin-Pastor, M., Martínez-Ramírez, S., et al. (2013). Effect of temperature on C_3S and C_3S + nanosilica hydration and C-S-H structure. *American Ceramic Society, 96*, 957–965.
21. Hou, P., Cheng, X., Qian, J., et al. (2015). Effects of the pozzolanic reactivity of nanoSiO2 on cement-based materials. *Cement and Concrete Composites, 55*, 250–258.
22. Thomas, J., Jennings, H., & Chen, J. (2009). Influence of nucleation seeding on the hydration mechanisms of tricalcium silicate and cement. *Physical Chemistry, 113*, 4327–4334.
23. Franzoni, E., Pigino, B., & Pistolesi, C. (2013). Ethyl silicate for surface protection of concrete: Performance in comparison with other inorganic surface treatments. *Cement and Concrete Composites, 44*, 69–76.
24. Cardenas, H., & Struble, L. (2006). Electrokinetic nanoparticle treatment of hardened cement paste for reduction of permeability. *Journal of Materials in Civil Engineering, 18*, 554–560.
25. Cardenas, H. (2012). *Nanomaterials in concrete: Advances in protection, repair, and upgrade*. Lancaster: DEStech Publications.
26. Pigino, B., Leemann, A., Franzoni, E., et al. (2012). Ethyl silicate for surface treatment of concrete – Part II: Characteristics and performance. *Cement and Concrete Composites, 34*, 313–321.
27. Pengkun Hou, Yamei Cai, Xin Cheng, et al. In-situ $Ca(OH)_2$ consumption of TEOS and its influences on the calcium-leaching resistivity of hardened cement-based materials. Paper submitted to Cement and Concrete Composites for review.
28. Fan, Y., Zhang, S., Kawashima, S., et al. (2014). Influence of kaolinite clay on the chloride diffusion property of cement-based materials. *Cement and Concrete Composites, 45*, 117–124.
29. Konsta-Gdoutos, M., Metaxa, Z., & Shah, P. (2010). Multi-scale mechanical and fracture characteristics and early-age strain capacity of high performance carbon nanotube/cement nanocomposites. *Cement and Concrete Composites, 32*, 110–115.
30. Li, G., Wang, P., & Zhao, X. (2007). Pressure-sensitive properties and microstructure of carbon nanotube reinforced cement composites. *Cement and Concrete Composites, 29*, 377–382.

The Role of Calcium Hydroxide in the Elastic and Viscoelastic Response of Cementitious Materials: A Nanoindentation and SEM-EDS Study

Yiwen Bu, Christopher Saldana, Carol Handwerker, and Jason Weiss

Abstract Calcium hydroxide (CH) typically comprises 20–25 % of the volume of ordinary portland cement (OPC) paste. CH is generally considered as an elastic phase that restrains the viscoelastic responses of calcium silicate hydrates (CSH). In this study, nanoindentation was used to study both the indentation modulus and the short-term viscoelastic responses of CSH/CH mixtures using an OPC paste made using a low water to cement ratio. A scanning electron microscope, equipped with energy dispersive X-ray spectroscopy, was used to identify the phase compositions in the matrix at the individual indentation locations. This study showed that CH increased both the indentation modulus and the contact creep modulus of the CSH/CH mixtures when compared with more pure CSH phases. However, such enhancement did not depend strongly on the volumetric concentration of CH. When the CH volume exceeded 20 %, no further enhancement of the indentation modulus and contact creep modulus was observed.

Keywords Nanoindentation • SEM-EDS • Calcium hydroxide • Viscoelastic response • Cementitious materials

Y. Bu (✉) • C. Handwerker
School of Materials Engineering, Purdue University, West Lafayette, IN, USA
e-mail: bu@purdue.edu

C. Saldana
George W. Woodruff School of Mechanical Engineering, Georgia Institute of Technology, Georgia, GA, USA

J. Weiss
School of Materials Engineering, Purdue University, West Lafayette, IN, USA

Lyles School of Civil Engineering, Purdue University, West Lafayette, IN, USA

K. Sobolev, S.P. Shah (eds.), *Nanotechnology in Construction*,
DOI 10.1007/978-3-319-17088-6_3

1 Introduction

Calcium hydroxide (CH) is an important constituent in portland cement paste. Typically CH occupies 20–25 % of the volume of ordinary portland cement (OPC) paste [1]. Together with calcium silicate hydrates (CSH), CH influences both the durability [2, 3] and mechanical properties [4] of cementitious materials. The mechanical behavior of both CSH [5–10] and CH [11, 12] has been studied. CH was observed to behave elastically with a higher elastic modulus than that of CSH [13–15]. It is generally believed that CSH is the major phase that contributes to the viscoelastic behavior of cementitious materials, while unhydrated clinker, aggregate, and CH are generally non-viscoelastic phases that act to restraint the time-dependent response of cement pastes, mortars and concretes [8, 16, 17].

The restraining effects of both the clinker and aggregate phases on the viscoelastic response of concrete usually increases with their volumetric content [18, 19]. This increase with volumetric concentration however may not hold true for CH due to its complex morphology. CH can form within capillary pores with crystals sizes in the order of tens or hundreds of micrometers, or it could mix intimately with CSH with a size in the range of one micrometer or less to form CSH/CH mixtures [20]. Such CSH/CH mixtures could be nanocomposites of CSH and CH phases, where CH nucleates within the gel pores of CSH as nano-sized crystals [21]. Allen et al. [22] detected the co-existance of nano-sized CH crystals with CSH using small-angle neutron and X-ray scattering.

In this study, nanoindentation was used to study the indentation modulus and short-term viscoelastic response of CSH/CH mixtures in an OPC paste with a low water to cement ratio (w/c). SEM-EDS was used to identify the phase compositions at the individual indentations. The indentation modulus and contact creep modulus was related to volumetric concentration of CH in the CSH/CH mixtures. This study attempts to determine whether CH enhances the indentation modulus and contact creep modulus of CSH/CH mixtures and whether such enhancement increases with the volume percent of CH in the mixtures.

2 Materials and Specimen Preparation

An OPC paste was prepared with a w/c of 0.27 using a Type V cement (ASTM C150 −12). The cement had an estimated Bogue composition of 64 % C_3S, 13 % C_2S, 0 % C_3A, 13 % C_4AF, an Na_2O_{eq} of 0.21 %, and a Blaine fineness of 316 m^2/kg. Paste specimens were prepared using a vacuum mixer to reduce entrapped air voids. The paste specimens were cast into cylindrical molds (0.5 in. diameter and 2 in. height). The specimens were cured in a sealed condition at 23 ± 1 °C for 1 year.

At an age of 1 year, the paste specimens were demolded and cut into 15 mm thick slices with a wet diamond tipped saw blade using water as the cutting/cooling fluid. The specimens were then ground and polished following the steps described in [23] using an automated polishing machine for at least 8 h. After polishing, the specimen

surface was wiped with acetone to remove any diamond slurry. The surface roughness (R_q) of the polished specimens was checked with atomic force microscope (AFM) to be 41 nm over a scan size of 50×50 μm. According to [23], the obtained surface roughness was sufficient for nanoindentation on cementitious materials with a maximum indentation depth of 250 nm.

3 Experimental Procedures

3.1 Nanoindentation

The nanoindenter used in this study was a Hysitron TI-750. Nanoindentation tests were performed with a typical diamond Berkovich indenter at 23 ± 1 °C and at a relative humidity of approximately 50 %. Two loading schemes (Scheme 1 and Scheme 2) were adopted. For both loading schemes, the maximum load was set to be 2,000 μN and the loading and unloading speed was 200 μN/s. The holding (dwelling) time at the maximum load were set to be 5 s for Scheme 1 and 100 s for Scheme 2. Scheme 1 (with a holding time of 5 s) was used to determine the indentation hardness (H) and the indentation modulus (M):

$$H = P_{\max} / A_c \tag{1}$$

$$M = S / 2\sqrt{A_c / \pi} \tag{2}$$

where P_{max} is the maximum indentation load, A_c is the projected area of the elastic contact, and S is the initial unloading stiffness. Both A_c and S were determined according to the Oliver and Pharr methods [24].

The short dwell time of 5 s (Scheme 1) was used to minimize the influence of viscoelastic behaviour of cementitious materials on the determination of elastic modulus M [25] and was short enough so that indentation hardness H does not include an increase of A_c (Eq. 1) due to viscoelastic response [6]. With Scheme 1, an indentation grid of 10×10 with 5 μm spacing was made on two areas at least 5 mm apart, resulting in a total of 200 indentations. Such large indentation number was designed to provide statistical information about the distribution of H and M.

Scheme 2 incorporates a longer dwell time of 100 s, which enables the measurement of viscoelastic response of the specimen. An indentation grid of 6×6 with 5 μm spacing was used, with a total of 36 indentations. The change of indentation depth during the holding period ($\Delta h(t) = h(t) - h_0$, where h_0 is the indentation depth at the end of the loading period, and $h(t)$ is the indentation depth at time t (0–100 s) of the holding period) was fitted with the following logarithmic creep function:

$$\Delta h(t) = x_1 \ln(x_2 t + 1) + x_3 t + x_4 \tag{3}$$

where x_1, x_2, x_3 and x_4 are fitting parameters [6, 9]. Vandamme et al. showed that of these four fitting parameters, only x_1 is material related and therefore the contact creep modulus (C) could be calculated using Eq. 4 [6]:

$$C = P_{\max} / \left(2x_1\sqrt{A_c / \pi}\right) \tag{4}$$

Before nanoindentation tests were performed, a standard quartz specimen with known mechanical properties was used to calibrate the indenter contact area function. The quartz standard was loaded with Scheme 2 to quantify the thermal drift of the instrument. Considering the non-viscoelastic nature of the quartz specimen, any change of indentation depth during the dwelling period was attributed to the inherent drift of the indenter. The thermal drift rate was calibrated to be 0.0226 ± 0.0075 nm/s. Accordingly, the recorded indentation depth *h(t)*was adjusted for instrument drift before any further analysis.

3.2 SEM-EDS

A Quanta® FESEM equipped with an energy dispersive X-ray spectroscopy system was used to analyze the indentation area of 6×6 indents following loading Scheme 2. The specimen was coated with carbon prior to the SEM-EDS examination. The indentation area was located under secondary electron mode since it emphasizes topography information of the specimen surface. Subsequently, with an accelerating voltage of 20 kV and a working distance of 10 mm, both EDS mapping and spot analysis were performed. EDS mapping helps identify regions of unhydrated clinker, while spot analysis provides quantification of the composition of the indentation impression. EDS mapping signal was collected for a duration of 6 min over the entire indentation area, while EDS spot signal was collected for 60 s in close approximation to the individual indentation to avoid the interference of surface roughness with the signal collection.

4 Results and Discussions

4.1 Loading Scheme 1: Indentation Modulus and Hardness

Under loading Scheme 1, the maximum indentation depth at all indentation locations was found to be less than 210 nm. Such indentation depth satisfies the scale separability condition that is used to ensure that nanoindentation provides phase properties [7]. Of the total 200 indents performed (using Scheme 1), 28 were excluded from the analysis based on the irregular nanoindentation curves, which may be due to cracks and/or voids in the specimen [26]. The frequency distribution of the indentation modulus (*M*) and indentation hardness (*H*) calculated from the 172 valid indentations were plotted in Fig. 1a, b.

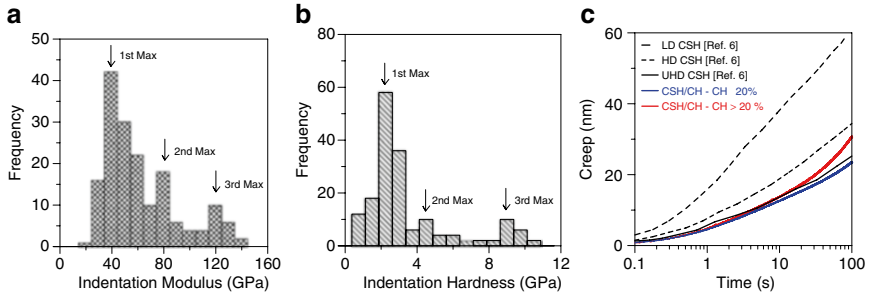

Fig. 1 Frequency distribution of (**a**) indentation modulus (M) and (**b**) indentation hardness (H) with bin number of 16 for both M and H. determined using Scheme 1. (**c**) Creep during the 100 s hold period at maximum load of 2,000 μN for CSH/CH mixtures using Scheme 2

In both frequency plots (Fig. 1a, b), three local maximums could be identified. These local maximums could be assigned to characteristic phase properties [27]. The 1st local frequency maximum, centred at approximately (M = 40 GPa, H = 2.5 GPa), corresponds to the hydrated phases [21]. The 3rd local frequency maximum, centred at about (M = 120 GP, H = 9 GPa), is attributed to the presence of unhydrated clinker phases [17, 21]. The 2nd local frequency maximum, at around (M = 80 GPa, H = 4.5 GPa), is usually attributed to a mixture of the hydrated phases and the clinker phases [21]. Interestingly, the 1st frequency maximum which corresponds to the hydrated phases centred at a modulus and hardness value that is higher than both low density CSH (LD CSH, M = 18.2 GPa, H = 0.45 GPa) and high density CSH (HD CSH, M = 29.1 GPa, H = 0.83 GPa) [14]. Similar observations was made by Chen et al. on an OPC paste specimens with a w/c of 0.20 [21]. If both LD CSH and HD CSH were purely CSH phases [14, 21], the hydrated phases in the specimen could be CSH phases intermixed with other constituents.

4.2 Loading Scheme 2: Short-Term Viscoelastic Behaviour

Under loading Scheme 2, the maximum indentation depth at all indentation spots was found to be less than 250 nm, still satisfying the scale separability condition [7]. The short-term creep parameters were identified at each indentation position. The elemental compositions of each indentation were identified with EDS spot analysis. The location of each indentation relative to unhydrated clinker was determined according to EDS mapping as shown in Fig. 2.

The phase compositions of all 36 indentations (using Scheme 2) were summarized together with their indentation modulus in Table 1 (note that the indentation hardness was not considered in this case due to the significant increase of A_c during the dwell periods of 100 s [6]). The indentation modulus of clinker phases or mixed clinker/CSH phases are comparable to the values obtained in other nanoindentation studies [15, 17]. However, the hydrated phases were observed again to have a mean

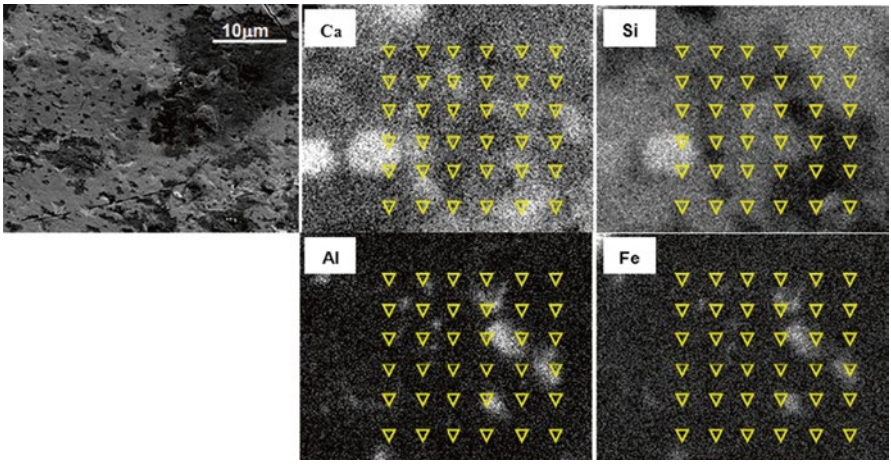

Fig. 2 SE topography image showing grids of indents (*top left*) and EDS element mapping of the corresponding indentation area. The indentation positions are located on the element maps with grids of triangles. The size of the triangles is only an approximation of the true indentation size. Maps of other relatively unimportant elements are not shown here. The contrast and brightness of the element maps may be adjusted for better visualization

Table 1 Phase identification and corresponding indentation modulus of indents subject to scheme 2

Phase ID	Counts	Indentation modulus (GPa)	
		Mean	Std. dev.
Hydrated phases (CSH/CH mixtures)	28	44.13	4.84
C_2S clinker	1	126.46	–
C_2S clinker – CSH	4	84.15	12.90
C_4AF clinker – CSH	3	68.00	24.22
$C_3(A,F)H_6$ – CSH	1	32.14	–

indentation modulus (44.13 GPa) that is higher than both LD CSH ($M = 18.2$ GPa) and HD CSH ($M = 29.1$ GPa) [14], as also observed through the statistical approach (Fig. 1a, b). EDS spot analysis at these 28 indents of hydrated phases showed a calcium to silicate ratio (Ca/Si) greater than 1.96, which is higher than the usual Ca/Si of 1.80 for CSH alone [28]. The possibility that the elevated Ca/Si may be due to a mixture of CSH with the clinker phases was ruled out since the calculated total oxide content was less than 0.76 [21]. Ca/Si of the CSH phases may also be increased due to the co-presence of C_4AF hydrates. The low reactivity of C_4AF, however, makes this possibility unlikely as well, especially considering the general presence of elevated Ca/Si. For this reason, the increased Ca/Si of the hydrated phases is likely explained by an intermixing of CSH and CH.

Nonetheless, within the 28 indents of CSH/CH mixtures, a large variation of Ca/Si is present with the Ca/Si ranging from 1.97 to 11.59. This corresponds to a wide range of CH volume percent within the CSH/CH mixtures. The volume percent of

Table 2 Further division of the CSH/CH mixtures according to the volume percent of CH

V_{CH} of CSH/CH mixtures	Counts	Indentation modulus (GPa)	
		Mean	Std. dev.
≤20 % (8.48–19.83 %)	23	44.92	4.38
>20 % (38.71–77.25 %)	5	39.58	3.32

CH (V_{CH}) could be calculated from the Ca/Si assuming a CSH gel particle compositions of $(CaO)_{1.7}(SiO_2)(H_2O)_{1.8}$ with a density of 2.604 g/cm^3 [22], an intrinsic CSH gel porosity of 0.25 [29], and a density of 2.24 g/cm^3 for portlandite. A volume range of 8.48–77.25 % is calculated for CH in the CSH/CH mixtures.

As to the morphology of CSH/CH mixtures, Chen et al. proposed the existence of both CSH/CH nanocomposites and CSH/CH microcomposites [21]. The nanocomposites could present alone when V_{CH} is below a critical value $V_{CH\text{-}crit}$ that is determined by the intrinsic gel porosity of CSH. Above the critical value $V_{CH\text{-}crit}$, CH has filled all the gel porosity of CSH and thus has to also precipitate outside the CSH gel as micro-sized crystals. Assuming an intrinsic gel porosity of 0.25 for CSH [29], $V_{CH\text{-}crit}$ is determined to be 20 %. Accordingly, the CSH/CH mixtures are further divided into two groups as shown in Table 2.

Twenty three indentations (out of 28) of CSH/CH mixtures resided in locations where the V_{CH} is less than 20 %. These locations have an indentation modulus of 44.92 ± 4.38 GPa. Five indentations (out of 28) located in positions where the V_{CH} is greater or even three times greater than 20 %, yet the indentation modulus was tested to be 39.58 ± 3.32 GPa, similar to, if not lower than the other twenty three indentations. The indentation modulus of both groups are higher than that of either LD CSH (M = 18.2 GPa) or HD CSH (M = 29.1 GPa), but are close to the indentation modulus of CH (M = 38 ± 5 GPa) [14]. This suggests that the co-presence of CH indeed have increased indentation modulus of CSH/CH mixtures when compared to more pure CSH phases. However, it is also clear from Table 2 that such an enhancing effect does not depend strongly on the volume percent of the CH in the CSH/CH mixtures.

The short-term creep during the 100 s hold at 2,000 μN for CSH/CH mixtures were plotted in Fig. 1c for the two groups of CSH/CH mixtures in Table 2. Creep results were also compared with the statistical nanoindentation results obtained in [6], since the same loading rates (200 μN/s) and peak loads (2,000 μN) were adopted in both studies. It is noticed that the CSH/CH mixtures creep less than LD CSH and HD CSH, but similarly as the UHD CSH, which was identified by a separate peak in the statistical nanoindentation study [6]. This indicates that UHD CSH, observed through statistical approach, likely corresponds to CSH/CH mixtures according to resembling viscoelastic responses. Similar observation has been made by Chen et al. between UHD CSH and CSH/CH mixtures through comparison of indentation modulus and hardness [21].

The creep fitting parameters (x_1, x_2, x_3, and x_4) and the calculated contact creep modulus C for the two groups of CSH/CH mixtures are listed in Table 3. The parameter x_1 describes the logarithmic creep behaviour of the materials and is shown to be similar between the two groups. The contact creep modulus C, calculated using x_1, is also similar for both groups considering standard deviation. The slightly greater

Table 3 Creep fitting parameters and creep modulus for two groups of CSH/CH mixtures

	$V_{CH} \leq 20$ %		$V_{CH} > 20$ %	
	Mean	Std. dev.	Mean	Std. dev.
x_1	3.538	0.468	3.660	0.090
x_2	2.965	0.005	3.147	1.228
x_3	0.108	0.015	0.029	0.016
x_4	−0.322	0.145	−0.480	0.047
Creep modulus C (GPa)	405.151	29.868	384.815	37.139

creep for CSH/CH mixtures with a V_{CH} greater than 20 % was reflected in a corresponding increase in the fitting parameter x_3, which captures the linear component of the creep. However, only five indents were analyzed for V_{CH} greater than 20 % and thus observations about x_3 are not definitive.

4.3 Discussion

Even though CH was the reason of enhanced mechanical properties of CSH/CH mixtures when compared with pure CSH phases, neither indentation modulus nor contact creep modulus showed a distinct dependence on the volume percent of CH in the mixture. The indentation results suggest that the lower volume fractions of CH (8.48–19.83 %) could stiffen the CSH/CH mixtures just as effectively as higher volume fractions of CH (38.71–77.25 %). This could be explained by the two possible ways in which CH can exist in OPC pastes, especially at a lower w/c [21]. CH could precipitate within the gel pores of CSH to form CSH/CH nanocomposites with a reduced gel porosity compared to more pure CSH phases [21, 22]. CH could also precipitate as micro-sized crystals in the capillary pores outside the CSH gel pores and act simply as a stronger inclusion. Through either mechanism, the indentation modulus and contact creep modulus could be increased. It is likely that nanocomposites were formed in areas where V_{CH} is at 8.48–19.83 %, while at 38.71–77.25 % the extra CH has to precipitate outside the CSH/CH nanocomposites as a crystalline inclusion as well. The CSH/CH mixtures at V_{CH} = 8.48–19.83 % (possibly CSH/CH nanocomposites) already has an indentation modulus (44.92 ± 4.38 GPa) that is close to that of CH crystals (38 ± 5 GPa). Thus any extra volume of CH does not enhance the mechanical properties any further.

5 Conclusions

Nanoindentation was coupled with SEM/EDS to study the effects of CH on the indentation modulus and short-term viscoelastic response of an OPC specimen with a w/c of 0.27. It was noticed that when CSH was intermixed with CH to form CSH/CH

mixtures, a higher indentation modulus and higher contact creep modulus was found when compared to that of more pure CSH phases. It was also found that the observed enhancement in mechanical properties (indentation modulus and contact creep modulus) does not necessarily increase with the volume percent of CH in the CSH/CH mixtures. This could be explained by the morphology of the CH present in the cementitious matrix. Below a critical volume content (20 %), CH appears to fill in the gel pores of CSH to form CSH/CH nanocomposites, while at higher volume content (above 20 %) the extra volume of CH precipitates as a crystalline inclusion outside the CSH/CH nanocomposites and therefore does not continue to enhance the indentation modulus or contact creep modulus, since the CSH/CH nanocomposites appear to have similar mechanical properties as CH crystals.

Acknowledgements The work described in this paper was conducted in the Pankow Laboratory and Michael Golden Laboratories at Purdue University, and the authors would like to acknowledge the support that has made its operation possible.

References

1. Mindess, S., Young, J., & Darwin, D. (2003). *Concrete* (2nd ed.). Upper Saddle River: Prentice Hall.
2. Marchand, J., Odler, I., & Skalny, J. (2003). *Sulfate attack on concrete*. New York: CRC Press.
3. Farnam, Y., Wiese, A., Dick, S., Davis, J., Bentz, D., & Weiss, J. (2014). *The deleterious effects of CaCl2 deicing salt on concrete exposed to freeze-thaw* (Working Paper).
4. Manzano, H., Dolado, J. S., & Ayuela, A. (2009). Elastic properties of the main species present in Portland cement pastes. *Acta Materialia, 57*, 1666–1674.
5. Jennings, H. M. (2003). Colloid model of C-S-H and implications to the problem of creep and shrinkage. *Materials and Structures, 37*, 59–70.
6. Vandamme, M., & Ulm, F.-J. (2009). Nanogranular origin of concrete creep. *Proceedings of the National Academy of Sciences of the United States of America, 106*, 10552–10557.
7. Constantinides, G., & Ulm, F.-J. (2007). The nanogranular nature of C–S–H. *Journal of the Mechanics and Physics of Solids, 55*, 64–90.
8. Šmilauer, V., & Bažant, Z. P. (2010). Identification of viscoelastic C-S-H behavior in mature cement paste by FFT-based homogenization method. *Cement and Concrete Research, 40*, 197–207.
9. Nguyen, D.-T., Alizadeh, R., Beaudoin, J. J., Pourbeik, P., & Raki, L. (2014). Microindentation creep of monophasic calcium–silicate–hydrates. *Cement and Concrete Composites, 48*, 118–126.
10. Garci Juenger, M. C., & Jennings, H. M. (2002). Examining the relationship between the microstructure of calcium silicate hydrate and drying shrinkage of cement pastes. *Cement and Concrete Research, 32*, 289–296.
11. Beaudoin, J. J. (1983). Comparison of mechanical properties of compacted calcium hydroxide and portland cement paste systems. *Cement and Concrete Research, 13*, 319–324.
12. Monteiro, P. J. M., & Chang, C. T. (1995). The elastic moduli of calcium hydroxide. *Cement and Concrete Research, 25*, 1605–1609.
13. Hughes, J. J., & Trtik, P. (2004). Micro-mechanical properties of cement paste measured by depth-sensing nanoindentation: A preliminary correlation of physical properties with phase type. *Materials Characterization, 53*, 223–231.

14. Constantinides, G., & Ulm, F.-J. (2004). The effect of two types of C-S-H on the elasticity of cement-based materials: Results from nanoindentation and micromechanical modeling. *Cement and Concrete Research, 34*, 67–80.
15. Trtik, P., Münch, B., & Lura, P. (2009). A critical examination of statistical nanoindentation on model materials and hardened cement pastes based on virtual experiments. *Cement and Concrete Composites, 31*, 705–714.
16. Illston, J. M., & Domone, P. L. J. (2001). *Construction materials: Their nature and behaviour* (3rd ed.). London/New York: CRC Press.
17. Velez, K., Maximilien, S., Damidot, D., Fantozzi, G., & Sorrentino, F. (2001). Determination by nanoindentation of elastic modulus and hardness of pure constituents of Portland cement clinker. *Cement and Concrete Research, 31*, 555–561.
18. Neville, A. M. (1964). Creep of concrete as a function of its cement paste content. *Magazine of Concrete Research, 16*, 21–30.
19. Kameswara Rao, C. V. S., Swamy, R. N., & Mangat, P. S. (1974). Mechanical behaviour of concrete as a composite material. *Matériaux Construction, 7*, 265–271.
20. Stutzman, P. E. (2001). Scanning electron microscopy in concrete petrography. *Materials Science Concrete Special Volume Calcium Hydroxide Concrete*, Proceeding (pp. 59–72).
21. Chen, J. J., Sorelli, L., Vandamme, M., Ulm, F.-J., & Chanvillard, G. (2010). A coupled nanoindentation/SEM-EDS study on low water/cement ratio Portland cement paste: Evidence for C-S-H/Ca(OH) 2 nanocomposites. *Journal of the American Ceramic Society, 93*(5), 1484–1493.
22. Allen, A. J., Thomas, J. J., & Jennings, H. M. (2007). Composition and density of nanoscale calcium-silicate-hydrate in cement. *Nature Materials, 6*, 311–316.
23. Miller, M., Bobko, C., Vandamme, M., & Ulm, F.-J. (2008). Surface roughness criteria for cement paste nanoindentation. *Cement and Concrete Research, 38*, 467–476.
24. Oliver, W. C., & Pharr, G. M. (2011). An improved technique for determining hardness and elastic modulus using load and displacement sensing indentation experiments. *Journal of Materials Research, 7*, 1564–1583.
25. Němeček, J. (2009). Creep effects in nanoindentation of hydrated phases of cement pastes. *Materials Characterization, 60*, 1028–1034.
26. Konsta-Gdoutos, M. S., Metaxa, Z. S., & Shah, S. P. (2010). Multi-scale mechanical and fracture characteristics and early-age strain capacity of high performance carbon nanotube/cement nanocomposites. *Cement and Concrete Composites, 32*, 110–115.
27. Ulm, F.-J., Vandamme, M., Bobko, C., Alberto Ortega, J., Tai, K., & Ortiz, C. (2007). Statistical indentation techniques for Hydrated nanocomposites: Concrete, bone, and shale. *Journal of the American Ceramic Society, 90*, 2677–2692.
28. Taylor, H. F. W. (1997). *Cement chemistry*. London: Thomas Telford.
29. Powers, T. C., & Brownyard, T. L. (1948). Studies of the physical properties of hardened Portland cement paste. *Portland Cement Association Research Bulletin, 22*, 249–336.

Silica Aerogels: A Multifunctional Building Material

Tao Gao and Bjørn Petter Jelle

Abstract Silica aerogels are a nanoporous material with extremely high porosity (up to ~99.8 %), low density (as low as ~0.005 g/cm^3), and low thermal conductivity (~0.010–0.020 W/(mK)). Aerogels can also be made with a translucent or transparent state. These structural and functional features make aerogels a multifunctional material for many important applications. In this work, we discuss the perspective of aerogels as super insulation materials and window glazings in the building and construction sector. It shows that different research and development (R&D) strategies of aerogels shall be considered when aiming for different applications; reducing the manufacture cost, improving the service durability, and minimizing the environmental impacts of aerogels are important factors to be addressed. We show also the R&D potentials of developing aerogel-like materials with improved structural or functional performance for building related applications.

Keywords Nanomaterial • Construction • Building material • Aerogel • Glazing • Insulation

1 Introduction

The past couple of decades have witnessed an exponential growth of research and development activities in nanotechnology, which has been making a ground-breaking impact on several science and engineering sectors. The building and construction industry has recently started seeking out a way to advance conventional building

T. Gao (✉)
Department of Architectural Design, History and Technology, Norwegian University of Science and Technology (NTNU), Trondheim NO-7491, Norway
e-mail: tao.gao@ntnu.no

B.P. Jelle
Department of Civil and Transport Engineering, Norwegian University of Science and Technology (NTNU), Trondheim NO-7491, Norway

Department of Materials and Structures, SINTEF Building and Infrastructure, Trondheim NO-7465, Norway
e-mail: bjorn.petter.jelle@sintef.no

K. Sobolev, S.P. Shah (eds.), *Nanotechnology in Construction*,
DOI 10.1007/978-3-319-17088-6_4

Table 1 Typical physical properties of silica aerogels

Density	Porosity	Mean pore size	Thermal conductivity	Tensile strength
~0.1 g/cm^3	~95 %	~20 nm	~13 mW/(mK)[a]	~10 kPa

[a]Monolithic aerogels

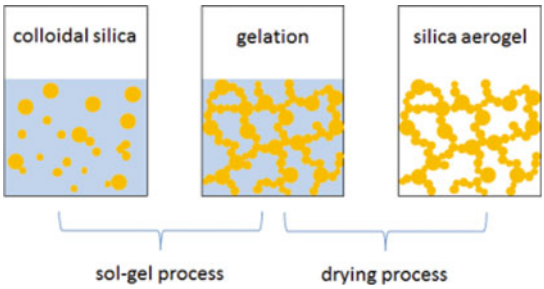

Fig. 1 Typical synthetic process of aerogels

materials or components by using a variety of nanomaterials. It has been revealed that the application of nanotechnology can enhance many vital characteristics of building materials, such as strength and durability, and endow them with new and useful properties, hence leading to new building materials or components, e.g., self-cleaning façades, smart windows, and super insulation materials [1, 2]. Silica aerogels (denoted as aerogels hereafter), for example, are a nanoporous material with very low density and low thermal conductivity (Table 1) [3]. Aerogels can also be made with a transparent or translucent state. These properties make aerogels a multifunctional material for various applications in the building and construction sector, e.g., as thermal insulation materials or window glazings [4, 5].

2 Synthesis of Aerogels

The synthesis of aerogels in general involves two major steps: the formation of a colloidal gel and the extraction of the liquid from the solid framework, as shown schematically in Fig. 1. The drying process is challenging since the loss of the pore liquid maintaining the liquid-vapor interface will generate very high capillary pressure that can shrink and collapse the solid skeleton. Effective drying technologies such as supercritical fluids drying have therefore been developed to preserve the nanoporous network of aerogels [3]. Moreover, the drying process represents the most energy intensive step during the synthesis and has a great impact on the environmental features of aerogels [6].

The nanoporous network endows also aerogels a poor mechanical strength (see Table 1), which limits their applications as a structural component in buildings. In fact, the commercial available aerogels are usually in forms of granules (particle size of 1–5 mm) due to the difficulties of making large pieces of monolithic aerogels (see Fig. 2) [7]. Different synthetic strategies have therefore been developed to improve the mechanical performance of aerogels, such as using flexible silica

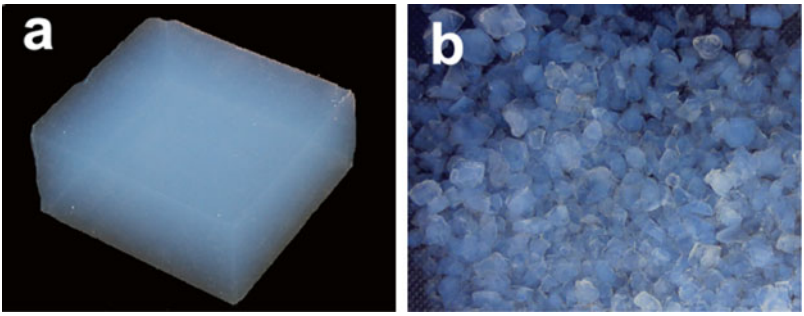

Fig. 2 Monolithic (**a**) and granular (**b**) silica aerogels

precursors in the silica gel backbone [8], conformal coating of silica backbone via surface cross-linking with polymers [9], and dispersing reinforced fibers into the initial sol of aerogels [10]. The reinforced aerogels may have some extended applications due to their newly empowered structural and functional properties.

3 Aerogels as Thermal Insulation Materials

As shown in Table 1, aerogels are lightweight and thermally insulating and have good sound and fire resistance; moreover, the materials can be treated to obtain a hydrophobic surface [3]. These properties are ideal for building thermal insulation applications. However, aerogels are usually available as small sized granules and are also very fragile. For building related applications, aerogels need to be mixed with other mechanically supporting materials to form a multi-phased composite with improved workability. For example, the commercial insulation products made of aerogels, such as Aspen Spaceloft®, are blanket-like materials consisting of aerogel granules and fibrous reinforcements. Typical thermal conductivity of these insulation products are about 20–30 mW/(mK), depending on the content of aerogel granules. Aerogel blankets can be cut to meet the dimension and insulation requirements at the building site; though healthy and safety issues shall be considered during the process since the materials are relatively dusty.

Aerogel-based composites with interesting insulation properties can also be prepared by incorporating aerogel granules into a certain matrix, where the properties can be controlled by adjusting the content of aerogel granules. For example, by mixing aerogel granules with cement and water, lightweight and thermally insulating aerogel concrete has been prepared (Fig. 3) [11, 12]. Stahl et al. have prepared an aerogel-based render by mixing aerogel granules with a mineral based binder [13]. The obtained aerogel-based renders have excellent workability and show potentials in retrofitting of buildings.

Since the mechanical strength of aerogels is very low (see Table 1), it is almost unavoidable that some large aerogel granules would break into small particles during the fabrication process of the aerogel-based composites. The change of granule

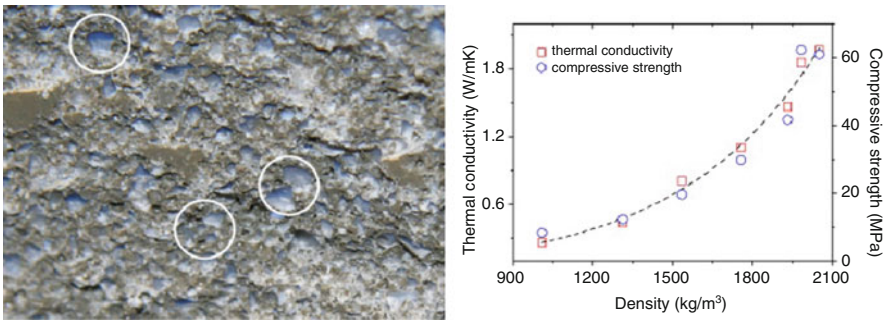

Fig. 3 Aerogel incorporated concrete: structure (*left*, circles show the aerogel granules) and property (*right*)

size and the exposure of new, fresh silica surfaces would affect the physical and chemical properties of aerogels [14], and consequently those of the resulting composites. In this regard, effective synthetic strategies are important to prepare aerogel-based composites with controlled properties.

4 Aerogels as Window Glazing Materials

The fact that aerogels can be made in form of monolithic panes with a transparent/translucent state makes them very attractive for window glazings. Previously, Schultz et al. reported an aerogel window consisting of a 15 mm monolithic aerogel pane sandwiched in between two layers of clear glass [5], which shows a centre heat loss coefficient (i.e. *U*-value) of about 0.7 W/(m^{2}K) and a solar transmittance of 76 %. The aerogel window can reduce heat loss ~42 % with respect to a conventional double glazed window (*U*-value 1.2 W/(m^{2}K)), thus being very promising for energy efficient buildings.

However, the fact that aerogels are very fragile (i.e. typical flexural strength of about 10 kPa, Table 1) may limit the application of monolithic aerogel panes as window glazings, e.g., the risk of failure under tensile/bending stresses due to wind load and/or external mechanical forces. In practice, aerogel glazings are usually assembled with aerogel granules (Fig. 4) [14]. Although the loss of a clear view through the glazing aperture may represent a drawback, granule-based aerogel windows have some interesting features. For example, they may provide high quality diffused light to minimize/avoid the potential glare and privacy problems that are related to specular glazing techniques (e.g. clear glass or monolithic aerogel panes). Furthermore, optical and thermal performance of granule-based aerogel windows can be readily determined at their production; a larger thermal resistance is usually achieved with a thicker layer of aerogel granules, whereas a larger optical transmittance is achieved with a thinner layer of aerogel granules.

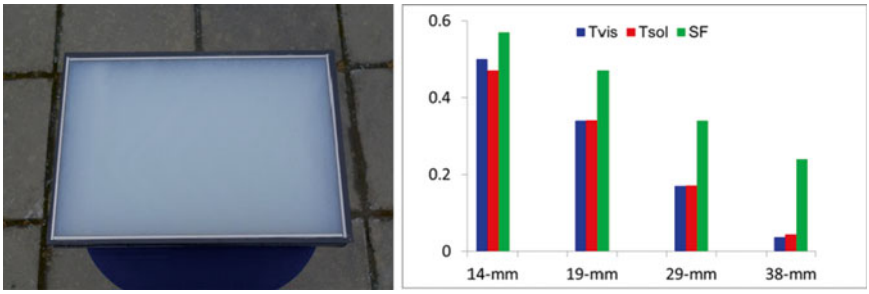

Fig. 4 Aerogel glazing unit (*left*) and its solar radiation glazing factors (*right*)

Aerogel glazings may experience challenges related to volume shrinkage. Being a particle aggregation system, the volume of aerogel granules inside the cavity tends to decrease along with time to reach the highest possible packing density, where external forces such as vibrations may speed up such a process. Eventually, an air gap may be developed at the top of the aerogel glazing unit [14]. The air gap may, on the one hand, act as a thermal bridge and decrease the thermal insulation performance of aerogel glazings; on the other hand, call for a challenging window frame design. Therefore, the building integration of aerogel glazings needs further investigation.

5 New Aerogel-Like Materials

The novel structural and functional properties of silica aerogels inspire also considerable research efforts on other aerogel-like materials, such as carbon nanotube aerogels [15] and oxide nanotube aerogels [16]. These aerogel-like materials have usually low density and high porosity and exhibit novel structural and electrical properties, hence offering possibilities for various applications.

Another example is nano insulation materials (NIM) [17], which can be assembled with hollow silica nanospheres (HSNSs) and exhibit low thermal conductivities that are comparable to silica aerogels [18]. One distinctive advantage of HSNS NIMs over their aerogel counterparts for thermal insulation applications is their controllability, *i.e.*, by modifying the particle size and porosity, their thermal and/or other properties can be specified and controlled over a wide range. Nevertheless, turning the conceptual HSNS NIMs into practical thermal insulation materials may require substantial research efforts dedicated to this field.

6 Conclusions

How silica aerogels and other nanomaterials can be used in building applications depends on many factors, such as their physical properties, finishing characteristics, maintenance requirements, costs, and availability; whereas other considerations

such as carbon footprints and environmental impacts are also important. It is therefore critical to evaluate these newly developed building materials or components according to different criteria to provide a full perspective.

Silica aerogels are very promising for building related applications. It is therefore important to reduce the manufacture costs and minimize the environmental impacts of these materials. Moreover, the development of aerogel-like materials with improved structural and functional performance is of particular interest for building related applications.

Acknowledgements This work has been supported by the Research Council of Norway and several partners through "The Research Centre on Zero Emission Buildings" (ZEB).

References

1. Zhu, W., Bartos, P. J. M., & Porro, A. (2004). Application of nanotechnology in construction. Summary of a state-of-the-art report. *Materials and Structures, 37*, 649–658.
2. Lee, J., Mahendra, S., & Alvarez, P. J. (2010). Nanomaterials in the construction industry: A review of their applications and environmental health and safety considerations. *ACS Nano, 4*, 3580–3590.
3. Pierre, A. C., & Pajonk, G. M. (2002). Chemistry of aerogels and their applications. *Chemical Reviews, 102*, 4243–4265.
4. Baetens, R., Jelle, B. P., & Gustavsen, A. (2011). Aerogel insulation for building applications: A state-of-the-art review. *Energy and Buildings, 43*, 761–769.
5. Schultz, J. M., Jensen, K. I., & Kristiansen, F. H. (2005). Super insulating aerogel glazing. *Solar Energy Materials and Solar Cells, 89*, 275–285.
6. Dowson, M., Grogan, M., Birks, T., Harrison, D., & Craig, S. (2012). Streamlined life cycle assessment of transparent silica aerogel made by supercritical drying. *Applied Energy, 97*, 396–404.
7. http://www.cabotcorp.com/solutions/products-plus/aerogel
8. Nadargi, D. Y., Latthe, S. S., Hirashima, H., & Rao, A. V. (2009). Studies on rheological properties of methyltriethoxysilane (MTES) based flexible superhydrophobic silica aerogels. *Microporous and Mesoporous Materials, 117*, 617–626.
9. Randall, J. P., Meador, M. A., & Jana, S. C. (2011). Tailoring mechanical properties of aerogels for aerospace applications. *ACS Applied Materials and Interfaces, 3*, 613–626.
10. Meador, M. A. B., Vivod, S. L., McCorkle, L., Quade, D., Sullivan, R. M., Ghosn, L. J., Clark, N., & Capadona, L. A. (2008). Reinforcing polymer cross-linked aerogels with carbon nanofibers. *Journal of Materials Chemistry, 18*, 1843–1852.
11. Gao, T., Jelle, B. P., Gustavsen, A., & Jacobsen, S. (2014). Aerogel-incorporated concrete: An experimental study. *Construction and Building Materials, 52*, 130–136.
12. Kim, S., Seo, J., Cha, J., & Kim, S. (2013). Chemical retreating for gel-typed aerogel and insulation performance of cement containing aerogel. *Construction and Building Materials, 40*, 501–505.
13. Stahl, T., Brunner, S., Zimmermann, M., & Ghazi Wakili, K. (2012). Thermo-hygric properties of a newly developed aerogel based insulation rendering for both exterior and interior applications. *Energy and Buildings, 44*, 114–117.
14. Gao, T., Jelle, B. P., Ihara, T., & Gustavsen, A. (2014). Insulating glazing units with silica aerogel granules: The impact of particle size. *Applied Energy, 128*, 27–34.
15. Zou, J., Liu, J., Karakoti, A. S., Kumar, A., Joung, D., Li, Q., Khondaker, S. I., Seal, S., & Zhai, L. (2010). Ultralight multiwalled carbon nanotube aerogel. *ACS Nano, 4*, 7293–7302.

16. Korhonen, J. T., Hiekkataipale, P., Malm, J., Karppinen, M., Ikkala, O., & Ras, R. H. A. (2011). Inorganic hollow nanotube aerogels by atomic layer deposition onto native nanocellulose templates. *ACS Nano, 5*, 1967–1974.
17. Jelle, B. P. (2011). Traditional, state-of-the-art and future thermal building insulation materials and solutions – Properties, requirements and possibilities. *Energy and Buildings, 43*, 2549–2563.
18. Gao, T., Jelle, B. P., Sandberg, L. I. C., & Gustavsen, A. (2013). Monodisperse hollow silica nanospheres for nano insulation materials: Synthesis, characterization, and life cycle assessment. *ACS Applied Materials and Interfaces, 5*, 761–767.

Part II
Nanoscale Investigation

Nanoscale Characterization of Cementitious Materials

Gilson R. Lomboy, Kejin Wang, and Sriram Sundararajan

Abstract The present study investigates the adhesion properties and coefficient of friction of various cementitious particles using atomic force microscopy (AFM). The cementitious materials studied are Portland cement (PC), fly ash (FA) and ground granulated blast furnace slag (GGBFS). AFM probes used were commercial silicon nitride tips and cementitious particles attached to the tips of AFM cantilevers. The adhesion force is determined from pull-off force measurements, which is then used to calculate effective Hamaker constants according to JKR or DMT contact models. The coefficient of friction is determined by sliding the tip of the AFM probes on another material and increasing the normal loads and friction forces. The results in dry air indicate that FA can have a high Hamaker constant; also when in contact with other cementitious materials. The results in fluid environments have showed high Hamaker constants for PC and FA. The results for the friction test in dry air indicate that the coefficient of friction of PC is lower than fly ashes, which is attributed to the asperities present on the particle surface. However, the coefficient of friction of PC becomes much higher in fluid environments.

Keywords Atomic for microscopy • Adhesion • Friction • Cement • Fly ash • Ground granulated blast furnace slag

1 Introduction

Rheological behavior of a cement-based material is primarily controlled by the particle interactions in the system. In addition to collisions, the adhesion and friction forces involved in the interactions of particles in a flowing system are present

G.R. Lomboy (✉) • K. Wang
Department of Civil, Construction and Environmental Engineering, Iowa State University, Ames, IA, USA
e-mail: grlomboy@iastate.edu; kejinw@iastate.edu

S. Sundararajan
Department of Mechanical Engineering, Iowa State University, Ames, IA, USA
e-mail: srirams@iastate.edu

K. Sobolev, S.P. Shah (eds.), *Nanotechnology in Construction*,
DOI 10.1007/978-3-319-17088-6_5

at the nanometer-scale. Adhesion is due to the attraction between materials and friction depends on the properties of the sliding surfaces.

The present study investigates the adhesion properties and coefficient of friction of various cementitious particles using atomic force microscopy (AFM). The adhesion force is determined from pull-off force measurements, which is then used to calculate effective Hamaker constants according to JKR or DMT contact models. The coefficient of friction is determined by sliding the tip of the AFM probes on another material and increasing the normal loads and friction forces.

2 Materials and Methods

2.1 Materials

Three types of commercially available cementitious materials were used in the adhesion and friction studies, ordinary Portland Cement (PC), Ground Granulated Blast Furnace Slag (GGBFS) and Class C Fly Ash (CFA). Reference materials with known Hamaker constants [1] were also used in the development and verification of the validity of the methodology for measuring adhesion forces; these were mica, silica, and calcite and silicon nitride (Si_3N_4).

2.2 Adhesion Force Measurement

The schematic illustration of the pull-off deflection measurement is shown in Fig. 1. Measurements were made between and among reference and cementitious materials. To conduct the test, samples must first be prepared on a glass slides. PC, GGBFS, silica and calcite were mixed in fast setting epoxy and polished to have exposed particles with flat surfaces, Fig. 2a. Fly ashes can have different properties on the surface compared its inside; it may also be hollow spheres. FA was therefore fixed on glass slides with a very thin layer of epoxy and without polishing, Fig. 2b. Mica only needed to be freshly cleaved before testing.

For measurements between cementitious particles, AFM probes were prepared by attaching PC and FA particles to the ends of AFM cantilevers. Figure 3 shows an AFM probe with PC attached on its tip.

The AFM measurements were conducted in both dry N_2 gas for an air environment, and Milli-Q ultrapure water for a fluid environment. The normal stiffness of each probe used was determined according to the method outlined by Torii et al. [7]. Probe tips were imaged with the AFM to determine its radius using a diffraction grating TGT1 from NT-MDT or AFM tip mounted to face the AFM probe, as shown in Fig. 4a.

Force measurements were performed by acquiring force-distance curves using the AFM, shown in Fig. 5. The pull-off force (F) between the two particles tested was calculated from the cantilever pull-off deflection (δ) and normal stiffness (k) as $F = k\delta$. The pull-off force may also be expressed in terms of work of adhesion (W)

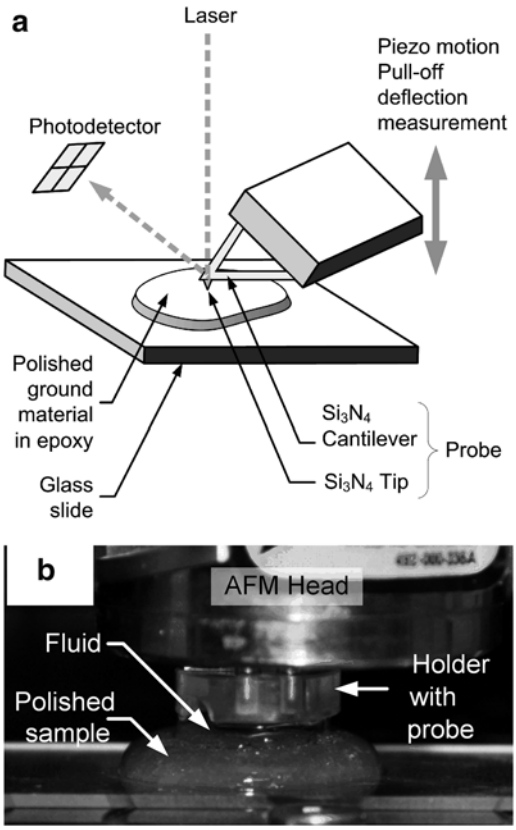

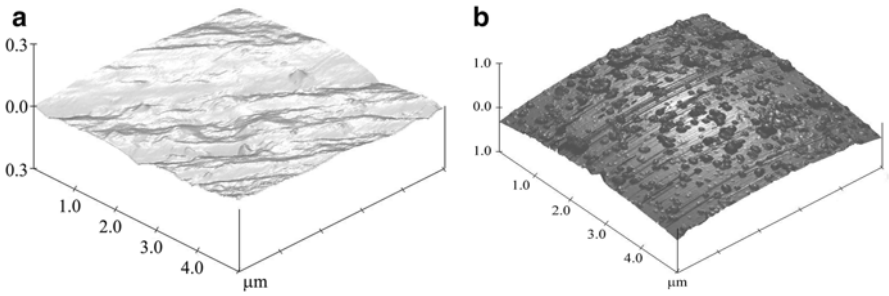

Fig. 1 (**a**) Schematic of pull-off deflection measurement and (**b**) set up for test in fluid

Fig. 2 (**a**) Schematic of pull-off deflection measurement and (**b**) set up for test in fluid

of the interface and AFM probe tip radius (R) as $F = c\pi R W_{12}$. The constant c is 3/2 for the JKR model [4] and is 2 for the DMT [2] model. The work of adhesion can be expressed as a function of Hamaker constant (A_{12}) between two contacting bodies and cut-off distance (D_0); $W_{12} = A_{12}/12\pi D_0^2$. The cut-off distance is the interfacial separation between two contacting materials [3]. The two models are usually chosen based on the Tabor parameter [6].

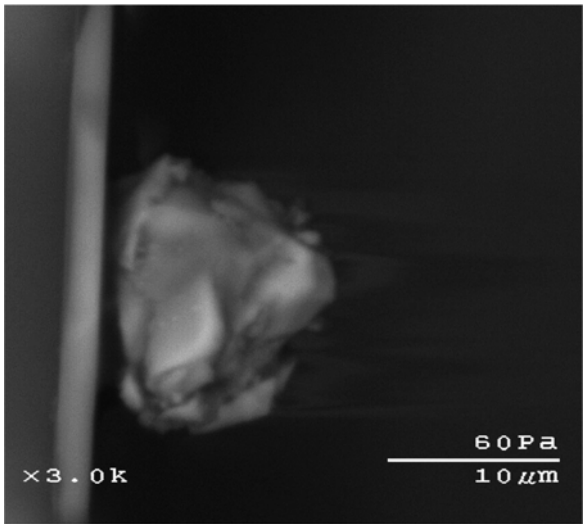

Fig. 3 SEM image of PC particle attached to the end of the rectangular AFM cantilever

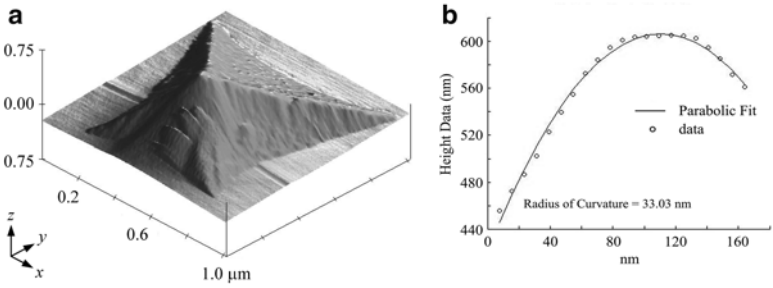

Fig. 4 (**a**) Image of Si3N4 tip using AFM and (**b**) parabolic curve fit of tip scan data points along the y direction

For measurements in dry air, the AFM chamber was closed and purged with N_2 gas to reach experimental conditions of RH (relative humidity) ≤ 8 % to eliminate the effects of humidity on the measured forces. To test the samples in fluid, a droplet of fluid was placed on the polished sample surface. The droplet was then approached by the probe until it was fully submerged. Then, probe approached the particle until it contacted and it was then pulled off from the particle in the same manner as the test in air.

2.3 Friction Force Measurement

The test method introduced by Ruan and Bhushan [5] using friction force microscopy was used for determining the coefficient of friction. To measure the friction force, the probe is lowered until the tip comes to contact with the sample and the

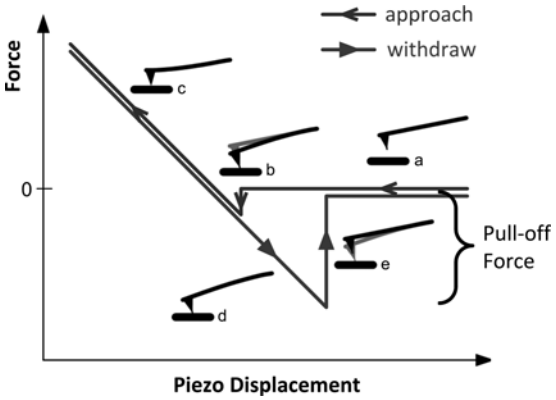

Fig. 5 Sketch of a typical force curve

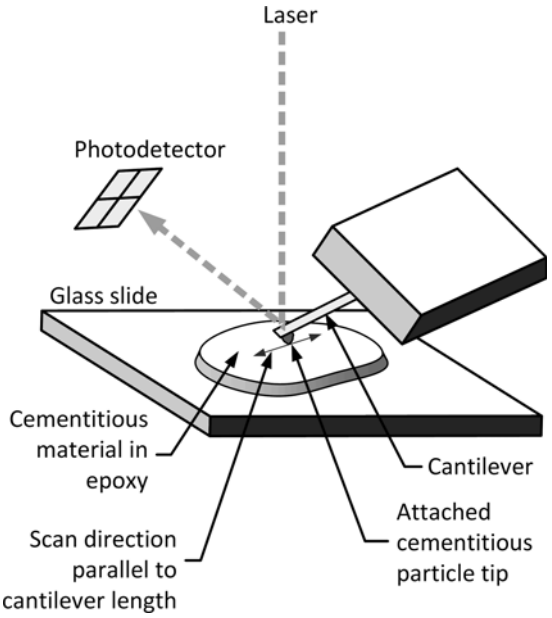

Fig. 6 Schematic of set-up for friction measurement using AFM

cantilever deflects to apply a normal force (N_0) between the two contacting materials. The AFM is engaged in a scanning motion where the probe is moved parallel to the cantilever's long axis, as shown in Fig. 6. The cantilever deflects due to the sample surface topography and also due to the friction force between the probe and the sample surface.

The friction force acts in the opposite direction of the probe motion. To maintain the deflection of the cantilever to a given value or set-point, the AFM piezo adjusts by retracting or extending, thus decreasing or increasing the normal load by ΔN_1 or ΔN_2, respectively. The coefficient of friction can be solved with equation as $\mu = f/N_0 = (\Delta N_1 + \Delta N_2)(L)/(2N_0 l)$. L and l are functions of the distance of the probe tip to the root of the cantilever L_c and the height of the tip h_t.

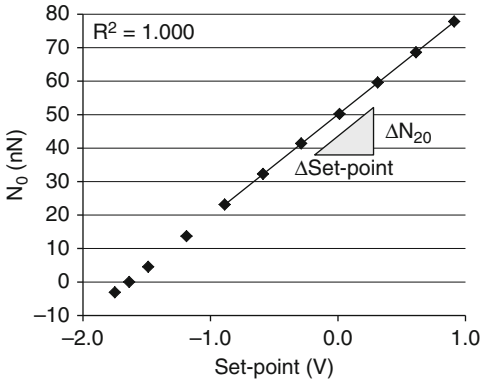

Fig. 7 Normal force due to cantilever deflection with increasing deflection set-point

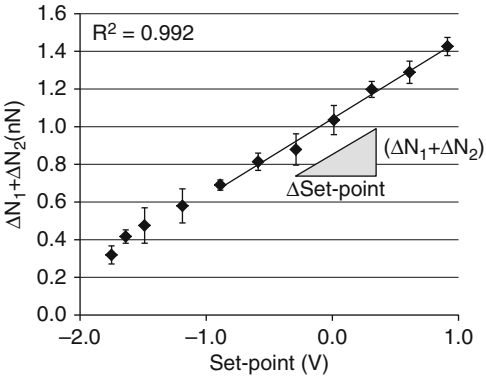

Fig. 8 Normal force changes when probe is traveling parallel with the probe long axis with increasing deflection set-point

The sliding distance of the tips for the friction measurements was 5 μm. The deflection set-point was varied for an increasing normal load, from a set-point less than zero (adhesion regime) to ~100 nN exerted by the cantilever. Figure 7 shows the increase in normal load with increasing set-point. Figure 8 shows the increase $(\Delta N_1 + \Delta N_2)$ with increasing set-point (normal load) and friction force. It can be observed that near the adhesion regime, there is a non-linear increase in $(\Delta N_1 + \Delta N_2)$. This is due to the change in contact area at very low normal loads.

3 Results

With consideration of the random errors in the experimental measurement, the Hamaker constants of the reference and cementitious materials with its interaction with silicon nitride (the probe) in air and water are given in Table 1. The DMT model is well suited for mica and silica, but it resulted in a lower Hamaker constant for calcite when compared with the value published by previous researchers. We attribute the difference to the relatively high RMS roughness of the calcite sample.

Table 1 Hamaker constants of materials interacting with Si3N4 in air (×10–20 J)

Tested material	DMT	JKR	Reference	DMT	JKR	Reference
	Air			Water		
Mica	10.76 ± 2.60	–	12.80		–	–
Silica	12.16 ± 2.97	–	10.38	1.96 ± 0.58	–	1.90
Calcite	8.45 ± 2.09	–	12.90	1.03 ± 0.34		2.53
PC (Group A)	24.06 ± 5.95	32.08 ± 7.93	–	2.89 ± 1.25	3.85 ± 1.67	–
(Group B)	7.64 ± 1.87	10.19 ± 2.49	–	0.50 ± 0.13	0.67 ± 0.18	–
GGBFS	5.15 ± 1.25	6.88 ± 1.67	–	0.78 ± 0.25	1.04 ± 0.71	–

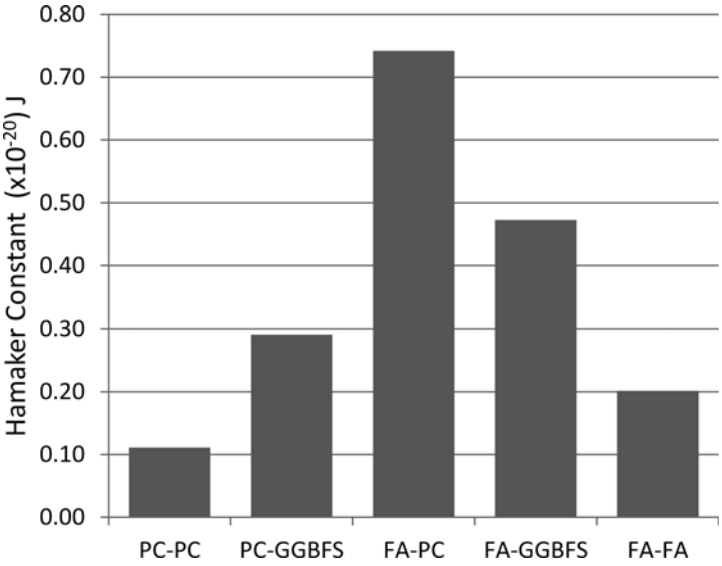

Fig. 9 Hamaker constants of cementitious materials in dry air

PC exhibits two distinct values of pull-off forces (indicated as group A and group B). This is most likely due to the different phases in the particles of Portland cement. The groupings were also observed in the tests in fluid.

The computed Hamaker constants between cementitious materials in dry air and fluid environments are shown in Figs. 9 and 10, respectively. The Hamaker constants between dissimilar materials were higher that the individual materials. This may be due to the large difference in the interatomic distance D_0 between similar and dissimilar materials. The Hamaker constants of fly ashes are generally lower than PC at high pH levels and decreases at the pH of 13. Similar to the tests in air, the Hamaker constant of FA-PC in water is higher than PC-PC and FA-FA.

The coefficient of friction for different cementitious material combinations are given in Fig. 11. In dry air, it can be observed that coefficient of friction involving

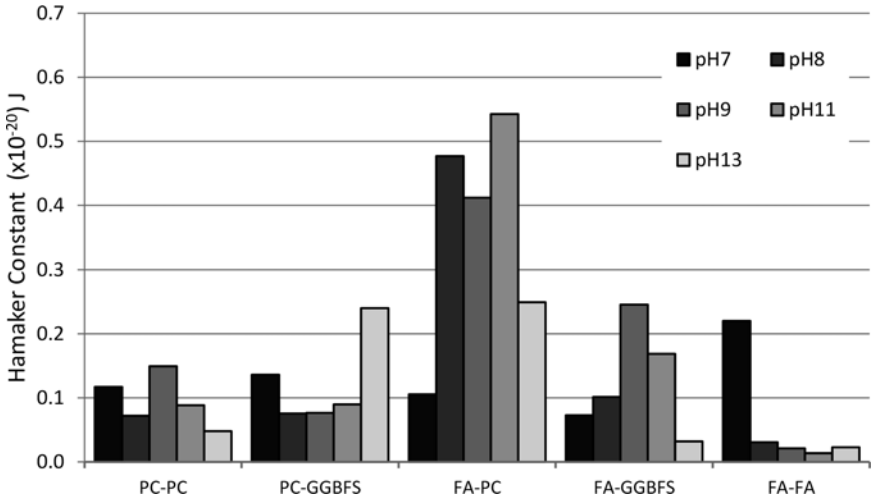

Fig. 10 Hamaker constants of cementitious materials in water (pH 7) and solution of sodium hydroxide (pH 8, 9, 11, 13)

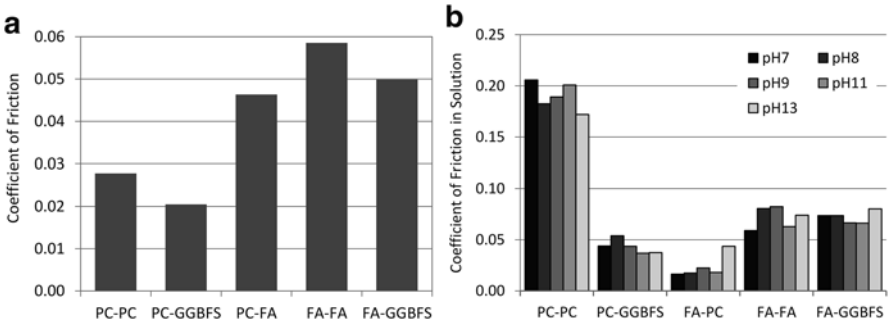

Fig. 11 Coefficient of friction of cementitious materials in (**a**) dry air and (**b**) fluid

FA is high. FA against FA has the highest coefficient of friction among the material combinations tested. This may be due to the asperities on the surface of the fly ash particles. In fluid, there is no significant change in coefficient of friction with change in pH. The coefficient of friction of PC is higher than other cementitious materials tested. The coefficient of friction of FA and FA with GGBFS is second highest compared to PC, which may be due to high surface roughness.

4 Conclusion

The atomic force microscope is powerful tool that can be used in characterizing the adhesion and friction properties of cementitious materials. From the study, Hamaker results of reference materials indicates that the present method is valid and reliable. In the both air and water, the Hamaker constants of PC determined from the present study fall into two different groups, one with a high value and the other with a low value. These results may be attributed to the different phases in PC and the early-age cement hydration effect. It was also found that sample surface roughness can have a significant effect on the adhesion force measurement.

The microscale coefficients of friction of tested cementitious materials are lower than the macroscale coefficients of friction. The results for the friction test in dry air indicate that the coefficient of friction of PC is lower than fly ashes, which is attributed to the asperities present on the particle surface. However, the coefficient of friction of PC becomes much higher in fluid environments.

Acknowledgement This research is sponsored by the National Science Foundation (GRANT NO. 0927660).

References

1. Bergstrom, L. (1996). Hamaker constants of inorganic materials. *Advances in Colloid and Interface Science, 70*, 125–169.
2. Derjaguin, B. V., Muller, V. M., & Toporov, Y. P. (1975). Effect of contact deformation on the adhesion of particles. *Journal of Colloid and Interface Science, 53*(2), 314–320.
3. Israelachvili, J. (1991). *Intermolecular and surface forces*. San Diego: Academic.
4. Johnson, K. L., Kendall, K., & Roberts, A. D. (1971). Surface energy and the contact of elastic solids. *Proceedings of the Royal Society of London A, 324*, 301–313.
5. Ruan, J. A., & Bhushan, B. (1994). Atomic-scale friction measurements using friction force microscopy: part I – General principles and new measurement techniques. *Journal of Tribology, 116*(2), 378–389.
6. Tabor, D. (1977). The hardness of solids. *Journal of Colloid and Interface Science, 58*(2), 145–179.
7. Torii, A., Sasaki, M., Hane, K., & Okuma, S. (1996). A method for determining the spring constant of cantilevers for atomic force microscopy. *Measurement Science and Technology, 7*, 179–184.

Formation of Nano-Sized Ettringite Crystals Identified as Root Cause for Cement Incompatibility of PCE Superplasticizers

Alex Lange and Johann Plank

Abstract Recently, nano materials including nanoclays, nano-TiO_2 or nano-sized CSH-PCE seed crystals have gained considerable attention in building materials. It is however frequently overlooked that particularly nano-sized crystals can also form during cement hydration. This study investigates on the early ettringite formation in cement, and on the interaction of polycarboxylate-based superplasticizers with such ettringite. Two different cements and five different polycarboxylate-based superplasticizers were analyzed. It was found that the formation of nano-sized ettringite instigated by common PCE superplasticizers presents the root cause for cement-PCE incompatibility which is frequently observed in concrete exhibiting low water-to-cement ratio. Experiments revealed that PCE superplasticizers act as morphological catalyst and transform common micro-meter sized ettringite into nano-sized crystals (l–200 nm). This effect can cause incompatibility between PCE and cements possessing elevated C_3A content (>7 wt.-%) and high amounts of immediately soluble sulfates. The nano-scale ettringite was identified via X-ray diffraction, elemental analysis and thermogravimetry. It can be separated from a cement paste by centrifugation where it appears as a gel-like, viscous top layer. Almost all PCE polymers, independent of their chemical nature, produce particularly small, nano-sized ettringite and thus require exceptionally high dosages with these cements. Such phenomenon is commonly referred to as "cement incompatibility" of PCE. Only one specific molecular structure of PCE was identified which produces micro-meter sized ettringite, therefore requires low dosages.

Keywords Cement • Hydration • Ettringite • Superplasticizer • Incompatibility

A. Lange • J. Plank (✉)
Department of Chemistry, Technische Universität München,
Lichtenbergstraße 4, Garching 85747, Germany
e-mail: sekretariat@bauchemie.ch.tum.de
http://www.bauchemie.ch.tum.de

K. Sobolev, S.P. Shah (eds.), *Nanotechnology in Construction*,
DOI 10.1007/978-3-319-17088-6_6

1 Introduction

Nano materials are used in considerable amounts in construction. Typical examples include nanoclays for asphalt pavements and polymer nanocomposites [1, 2]. Titanium dioxide nanoparticles are widely used in applications such as photocatalytically active tile grouts, concrete, coatings, roof tiles or wall paints. TiO_2 can also produce self-cleaning surfaces because organic material is oxidized to CO_2 and H_2O [3]. Furthermore, the early strength of concrete can be increased by implementing seed crystals consisting of a composite of calcium silicate hydrate (CSH) nanocrystals and polycarboxylate superplasticizers which acts as crystal nucleus to speed up CSH formation in cement [4].

In mortar or concrete, hydration products from cement crystallize almost immediately after water is added to the mixture. In many cases, generally in high performance concrete with low water-to-cement (w/c) ratio, superplasticizers are added to provide sufficient workability at such low water contents. The most effective superplasticizers are polycarboxylates (PCEs) which possess an anionic polymer trunk with polyglycol pendants. Their dispersing force originates from the ability to adsorb onto sites of the cement particles exhibiting positive surface charge, i.e. mainly on the aluminate and ferrite phases (C_3A and C_4AF) and their initial hydration products such as e.g. ettringite or monosulfo aluminate [5–7]. It has been established before that the speed of C_3A hydration and ettringite formation presents a key parameter which significantly influences the compatibility of a PCE superplasticizer with various cements. Some authors suggest that such incompatibility might be owed to the interaction of PCE with these early hydration products [8].

The incompatibility phenomenon between PCE and specific cements is most frequently observed in concretes possessing low w/c ratio such as e.g. ultra-high strength concrete (UHSC), where the PCE polymer commonly is added to the mixing water to reduce the mixing time [9].

In this study, the effect of several structurally different PCE superplasticizers on the crystal morphology and size of early ettringite was analyzed. For this purpose, cement pastes including these PCE superplasticizers were prepared from two different ordinary Portland cements (OPCs) and the instantaneously formed ettringite was extracted. Finally, the impact of PCE superplasticizers on the morphology of ettringite synthesized from solution was studied to confirm the results obtained in actual cement.

2 Materials and Methods

2.1 Cements

Two different ordinary Portland cements were selected for this study. One sample (CEM I 52.5 R HS) had a very low C_3A content of 1.56 wt.-% whereas the other sample (CEM I 32.5 R) had a much higher content of 9.85 wt.-%. Their phase compositions were analyzed by quantitative XRD (*Rietveld*) analysis. The samples were selected such as to represent cements possessing a very low and a very high amount of C_3A.

Table 1 Analytical properties of the synthesized PCE samples

Polymer	M_w [g/mol]	M_n [g/mol]	PDI [M_w/M_n]	n_{EO} [mol]
MPEG-7	44,300	23,300	1.9	7
MPEG-45	35,900	18,200	2.0	45
APEG-23	69,000	23,700	2.9	23
APEG-34 AM	78,400	24,500	3.2	34
IPEG-50	101,200	40,100	2.5	50

M_w being the mass average molar mass, M_n the number average molar mass, *PDI* the polydispersity index, n_{EO} the average number of ethylene oxide units present in the side chain

2.2 PCE Samples

A total of five PCE samples were studied. Two of them (samples MPEG-7 and MPEG-45) were methacrylic acid-co-ω-methoxy polyethylene glycol (MPEG) methacrylate ester polymers with side chains holding 7 and 45 EO units respectively. The molar ratio of methacrylic acid and MPEG-MA ester was adjusted in such a way that optimal dispersing performance (i.e. lowest dosage) was achieved. For MPEG-7, the MA : MPEG-MA ratio was 1.2:1 while for MPEG-45 it was 6:1.

Furthermore, two PCE samples (denominated as APEG-23 and APEG-34 AM) were allyl ether (APEG) based polycarboxylates with a side chain holding 23 or 34 EO units. APEG-34 AM contained allyl maleate as additional monomer. The molar ratios between allyl ether, maleic anhydride and allyl maleate were 1:1:0 (for APEG-23) or 1:1:1 (for APEG-34 AM) respectively. The effect of molecular architecture on the dispersing performance has been discussed before [10].

The fifth PCE sample (IPEG-50) was a copolymer of acrylic acid and ω-hydroxy polyethylene glycol isoprenyl ether (IPEG) with 50 EO units in the side chain. Again, the molar ratio was adjusted for maximum dispersing performance and was 6:1 (acrylic acid:IPEG ether).

The synthesis of these polymers has been described in detail before [11–14]; their analytical properties are shown in Table 1.

2.3 Separation of Early Ettringite Crystals

The initial hydration products (mainly ettringite) formed within the first minutes of cement hydration were separated from the cement via centrifugation (20 min at 10,000 g). There, they form a gel-like, colloidal top layer above the cement residue. For the separation, a cement paste was prepared at a w/c ratio of 0.5 and PCE dosages were set constant at 1 % by weight of cement. At this high w/c ratio and PCE dosage, the cement pastes exhibit strong bleeding. After mixing manually for 4 min with a spoon, the cement paste rested for 5 min. Then the bleeding water (which is where a significant portion the nano-sized ettringite accumulates) was taken up by

using a pipette and centrifuged as described above. A gel-like top layer with ~85 wt.-% solids content was obtained. The gel layer was carefully removed and dried at 30 °C under atmospheric pressure. It is highly important to mildly dry the product, as ettringite easily can dehydrate to meta-ettringite which is X-ray amorphous [15]. The gel was also separated from cement pastes with a w/c ratio of 0.3, but there only ~5 mL of bleeding water could be skimmed. The ettringite concentration in this small amount of bleeding water was even higher than that obtained at w/c = 0.5, but the absolute amount was much smaller because of the much smaller volume. For this reason, a w/c ratio of 0.5 was selected. The resulting colorless powder was analyzed using X-ray diffraction (Bruker AXS D8 Advance, Karlsruhe, Germany), elemental analysis (Elementar vario EL, Hanau, Germany) and thermogravimetry (Netzsch STA 409 TG-MS, Selb, Germany).

2.4 Preparation of Synthetic Ettringite

Ettringite was precipitated from solution following the method of *Struble* [16] by dissolving 0.255 g of $Al_2(SO_4)_3 \cdot 18H_2O$ in 10 mL of water. To this solution, 100 mL of a saturated $Ca(OH)_2$ solution (~1.6 g/L) were rapidly added under vigorous stirring. Instantaneous precipitation of ettringite was evident as the solution turned turbid. Influence of the PCE samples on ettringite crystallization was analyzed by dissolving the PCE in the aluminum sulfate solution. The amount of PCE was kept constant at 0.35 g (~10 wt.-% of the amount of ettringite formed). One half of the resulting dispersion was centrifuged for 20 min at 10,000 g and carefully dried under atmospheric pressure. The resulting colorless powder was characterized using X-ray diffraction and scanning electron microscopy (SEM). The other part of the dispersion was immediately analyzed for particle size distribution using dynamic light scattering (ZetaSizer Nano ZS, Malvern Instruments, Worcestershire, United Kingdom).

3 Results and Discussion

3.1 Analysis of Ettringite Gel Obtained from Cement Pastes

At first it was observed that pastes prepared from the C_3A rich cement (CEM I 32.5 R) and all PCE samples except APEG-34 AM form a white, gelous top layer when centrifuged for 20 min at 10,000 g. This layer did not occur when the cement was mixed without PCE. Especially PCE samples MPEG-7, MPEG-45 and APEG-23 produced significant amounts of this layer.

For example, from 300 g of cement sample CEM I 32.5 R ~6 g of a transparent, waxy gel with a solids content of ~85 wt.-% were obtained. The opaque appearance of the gel indicates that the ettringite crystals must be extremely small and thus can

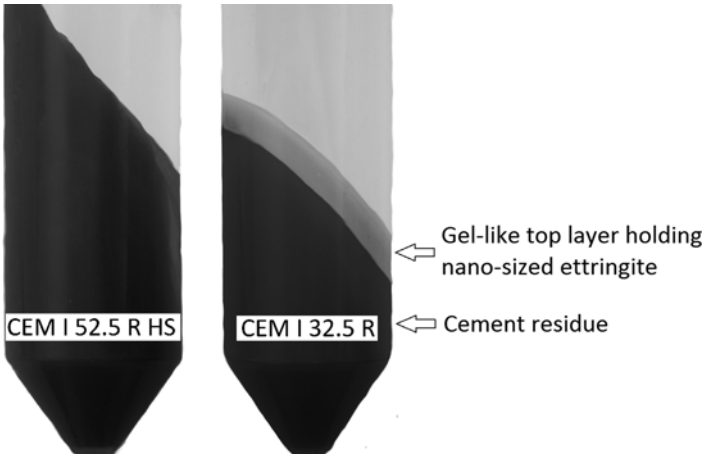

Fig. 1 Comparison of the amounts of ettringite gel obtained as top layer after centrifugation of cement paste (w/c = 0.5) prepared from two different cements in the presence of 1 % bwoc of PCE sample MPEG-7

adsorb large amounts of PCE. Figure 1 displays how the amount of gel can vary with cement composition (i.e. the C_3A content) when PCE polymer MPEG-7, a PCE with strong impact on ettringite crystallization, is used.

The gel-like phase was carefully removed, dried and analyzed using X-ray diffraction. This gel contains pure ettringite, as was confirmed also by elemental analysis of the dried powder. Furthermore, in the presence of 1 % by weight of cement of PCE sample MPEG-7, a carbon content of 6.51 wt.-% was detected in the gel, thus indicating significant adsorption of PCE on the surface of this colloidal ettringite. Additionally, TG-MS analysis of the ettringite gel containing PCE was performed. Dehydration of ettringite occurs in the temperature range between 100 and 180 °C while the PCE begins to decompose above 200 °C as evidenced by the mass signal of m/z = 44 corresponding to the release of CO_2.

Extraction of colloidal ettringite was also attempted at delayed addition of the PCE. Surprisingly, the gel layer was no longer observed when the PCE was added only 1 min after beginning of the mixing. Apparently, when PCE is added in delayed mode ettringite can grow to its normal micro-meter size and thus sediments during centrifugation.

Opposite to cement sample CEM I 32.5 R, sample CEM I 52.5 R HS never showed an ettringite gel under the conditions described before. Thus, the amount of initial ettringite is closely linked to the C_3A content of the cement samples.

The crystallization of ettringite appears to be a process which occurs within the very first seconds of cement hydration. This gave reason to study the effect of the PCEs on pure ettringite prepared via crystallization from solution. This system was chosen to eliminate any effects derived from cement impurities and to obtain a pure reference sample without any superplasticizer.

3.2 Impact of PCE on Ettringite Crystallization

Following the method of *Struble* [16], synthetic ettringite was prepared via precipitation from an aluminum sulfate solution combined with a saturated calcium hydroxide solution. Ettringite precipitates were collected from two batches, one without PCE and one prepared in the presence of PCE which was added to the aluminum sulfate solution. XRD analysis confirmed that pure ettringite was formed in all cases. Visual inspection of the samples already revealed substantial differences in the crystal sizes of ettringite. The product obtained in the absence of PCE settled quickly and appeared as milky white suspension. Large agglomerates were visible to the naked eye. On the other hand, the ettringite suspensions produced in the presence of PCEs, especially of the MPEG PCEs and of APEG-23, were stable, did not settle and exhibited only slight turbidity or were almost transparent. Concentration of these samples via centrifugation yielded the same viscous and opaque gel as found before when using cement paste.

The suspensions holding the precipitated ettringite were characterized by dynamic light scattering and SEM. For the sample where no PCE was present, laser granulometry produced particle sizes of ~10 µm (d_{50} value). Opposite to this, the sizes of the ettringite samples obtained in the presence of PCEs were much smaller: MPEG-7 718 ± 14 nm; MPEG-45 981 ± 24 nm; APEG-23 1,238 ± 27 nm; IPEG-50 1,936 ± 86 nm and APEG-34 AM 2,050 ± 65 nm.

SEM imaging confirmed these differences. For synthetic ettringite produced in the absence of PCE, large micrometer-sized (l = 1–10 µm), needle like crystals characteristic for ettringite were found (Fig. 2).

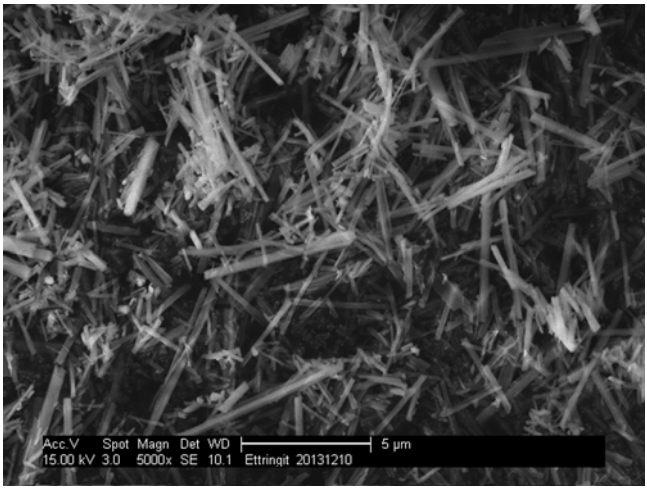

Fig. 2 Synthetic ettringite crystals precipitated in the absence of PCE

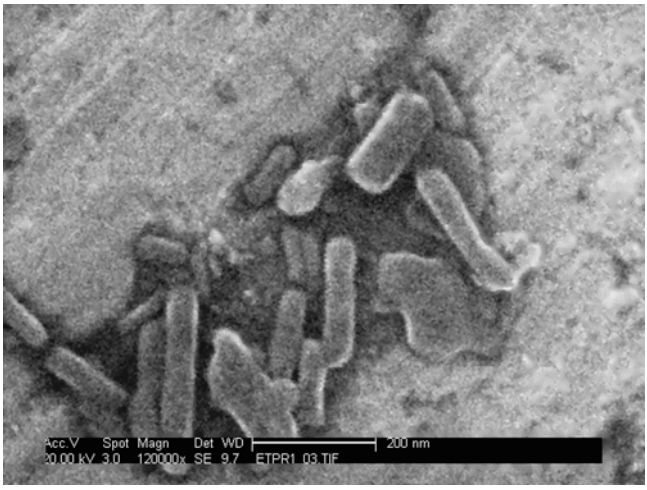

Fig. 3 Nano-sized synthetic ettringite crystals precipitated in the presence of PCE sample MPEG-7

When the ettringite was precipitated in the presence of polymer sample MPEG-7, the crystal size was drastically reduced. As is shown in Fig. 3, the length of the ettringite needles was reduced to ~200 nm or even less and their width typically was below 50 nm. SEM imaging of these small crystals was particularly difficult, as under the vacuum and due to the energy inferred by the electron beam ettringite quickly dehydrated into meta-ettringite, thus losing its original morphology. The results suggest that PCE polymers act as morphological catalysts which significantly reduce the aspect ratio of ettringite crystals from ~20 (without PCE) to ~3–5 in the presence of PCE.

The experiments on ettringite precipitation from solution also revealed that ettringite formation and precipitation is instantaneous, i.e. turbidity occurs immediately when aluminum sulfate and calcium hydroxide come into contact. Even more, precipitation was complete within ~10 s. This observation is consistent with the results on delayed PCE addition to cement paste because there, no gel-like top layer holding ettringite had occurred. After only 1 min of hydration, formation of ettringite was complete and no nano-sized crystals were obtained when the PCE was added in a delayed mode.

4 Conclusions

The study reveals that PCE superplasticizers can strongly impact ettringite morphology. They act as morphological catalysts and transform micrometer-sized ettringite which is commonly found in cement prepared in the absence of PCE into

nano-sized crystals. SEM imaging clearly shows the differences in crystal size of synthetic ettringite prepared with and without PCE. It ranges from several micrometers without PCE to less than 500 nm in the presence of PCEs.

The nano-sized ettringite crystals possess a huge surface area and are able to adsorb significantly larger amounts of PCE, compared to common, micrometer-sized ettringite. Furthermore, cements exhibiting high C_3A contents generate especially large amounts of ettringite during the first seconds of hydration. Thus, when such C_3A rich cements are used in combination with almost any PCE product present in the mixing water, excessive amounts of PCE are taken up by the nano-sized ettringite resulting in complete failure of the PCE to disperse such cements at normal dosages (<0.5 % bwoc). This phenomenon is commonly referred to as incompatibility between a PCE and cement. Only very few PCE polymers such as APEG-34 AM or – less effective – IPEG-50, have less influence on ettringite morphology. These specific PCEs are able to disperse the "difficult" cement sample CEM I 32.5 R possessing high C_3A content at reasonable dosages. At present, no experimental evidence exists which can explain why those specific PCE molecules have less influence on ettringite morphology. Even from PCEs within the same chemical group, very different ettringite morphologies can be obtained. Adsorption measurements showed that the adsorbed amounts of PCEs are not correlated with their effectiveness as morphological catalyst. One possible explanation is that the PCE molecules can occupy the different faces of the ettringite crystal in variable manner and thus impact the direction of crystal growth.

References

1. Patel, H. A., Somani, R. S., Bajaj, H. C., & Jasra, R. V. (2006). Nanoclays for polymer nanocomposites, paints, inks, greases and cosmetics formulations, drug delivery vehicle and waste water treatment. *Bulletin of Materials Science, 29*(2), 133–145.
2. You, Z., Mills-Beale, J., Foley, J. M., Roy, S., Odegard, G. M., Dai, Q., & Goh, S. W. (2011). Nanoclay-modified asphalt materials: Preparation and characterization. *Construction and Building Materials, 25*(2), 1072–1078.
3. Fujishima, A., Rao, T. N., & Tryk, D. A. (2000). Titanium dioxide photocatalysis. *Journal of Photochemistry and Photobiology, C: Photochemistry Reviews, 1*(1), 1–21.
4. Nicoleau, L., Jetzlsperger, E., Friedrich, D., Vierle, M., Lorenz, K., Albrecht, G., Schmitt, D., Wohlhaupter, T., Dorfner, R., Leitner, H., Bräu, M., Hesse, C., Montero Pancera, S., Zürn, S., & Kutschera, M. (2010). *Plasticizer-containing hardening accelerator composition*, WO2010026155, assigned to Construction Research & Technology GmbH (BASF).
5. Plank, J. (2012, September 12–15). *PCE superplasticizers – Chemistry, application and perspectives* 18 (Vol. 1, pp. 91–102). Weimar: ibausil.
6. Yoshioka, K., Tazawa, E., Kawai, K., & Enohata, T. (2002). Adsorption characteristics of superplasticizers on cement component minerals. *Cement and Concrete Research, 32*, 1507–1513.
7. Aitcin, P.-C., Jolicoeur, C., & MacGregor, J. G. (1994). Superplasticizers: How they work and why they occasionally don't. *Concrete International, 16*, 45–52.
8. Prince, W., Espagne, M., & Aïtcin, P.-C. (2003). Ettringite formation: A crucial step in cement superplasticizer compatibility. *Cement and Concrete Research, 33*, 635–641.

9. Plank, J., Schröfl, C., Gruber, M., Lesti, M., & Sieber, R. (2009). Effectiveness of polycarboxylate superplasticizers in ultra-high strength concrete: The importance of PCE compatibility with microsilica. *Journal of Advanced Concrete Technology, 7*, 5–12.
10. Winnefeld, F., Becker, S., Pakusch, J., & Götz, T. (2007). Effects of the molecular architecture of comb-shaped superplasticizers on their performance in cementitious systems. *Cement and Concrete Composites, 29*, 251–262.
11. Yuasa, T., Tanaka, H., Sakamoto, N., Nishikawa, T., Izukashi, H., & Uno, T. (2002). *Polycarboxylic acid type copolymer and method for producing the same, and use of the same*. WO 02/053611 A1. *Polycarboxylic acid copolymer, production method and use thereof*, US 2002/0193547 A1, 2002, both patents assigned to Nippon Shokubai LTD.
12. Plank, J. K., Pöllmann, N., Zouaoui, P. R., Andres, C., & Schaefer, C. (2008). Synthesis and performance of methacrylic ester based polycarboxylate superplasticizers possessing hydroxy terminated poly(ethylene glycol) side chains. *Cement and Concrete Research, 38*, 1210–1216.
13. Yamamoto, M., Uno, T., Onda, Y., Tanaka, H., Yamashita, A., Hirata, T., & Hirano, N. (2004, April 27). *Copolymer for cement admixtures and its production process and use*, US patent 6,727,315, assigned to Nippon Shokubai LTD.
14. Lange, A., Hirata, T., & Plank, J. (2014). Influence of the HLB value of polycarboxylate superplasticizers on the flow behavior of mortar and concrete. *Cement and Concrete Research, 60*, 45–50.
15. Zhou, Q., Lachowski, E. E., & Glasser, F. P. (2004). Metaettringite, a decomposition product of ettringite. *Cement and Concrete Research, 34*, 703–710.
16. Struble, L. J. (1986). *Synthesis and characterization of ettringite and related phases*. In: Proceedings of the 8th International Congress on the Chemistry of Cement, Rio de Janeiro, 6, pp. 582–588.

A Nanoindentation Study of Portland Cement Pastes Exposed to a Decalcifying Environment

Lesa Brown and Florence Sanchez

Abstract The effect of decalcification on the micromechanical properties of cement pastes was investigated using nanoindentation coupled with statistical methods. Portland cement pastes were subjected to accelerated decalcification via exposure to ammonium nitrate solution for 125 days. A grid nanoindentation technique was performed in the degraded zones found in the cement paste cross-section to evaluate the differences in the local mechanical properties. Results showed that while the hardness and modulus values decreased as a function of the extent of degradation, the rate of decrease was influenced by the cement phases present.

Keywords Decalcification • Nanoindentation • Cement • Micromechanical properties

1 Introduction

During their lifetime, cement-based materials are exposed to a variety of aggressive environments, leading to progressive degradation of the material. Degradation processes generally begin on the nano-scale and evolve over time to affect the macroscale properties of the material by causing loss of strength and structural integrity, cracking, and expansion. Traditional mechanical testing for cement-based materials typically examines only the macroscale response of the material and often involves 'averaging' the response [1, 2]. While the 'averaged' macroscale response provides useful information about the overall behavior of the material, it does not allow for identification of the mechanisms causing the mechanical property change. Nanoindentation coupled with scanning electron microscopy (SEM)/ energy dispersive x-ray spectroscopy (EDS), scanning probe microscopy, and statistical methods

L. Brown • F. Sanchez (✉)
Department of Civil and Environmental Engineering, Vanderbilt University, Nashville, TN, USA
e-mail: lesa.brown@vanderbilt.edu; florence.sanchez@vanderbilt.edu

K. Sobolev, S.P. Shah (eds.), *Nanotechnology in Construction*,
DOI 10.1007/978-3-319-17088-6_7

has proven to be a valuable technique in determining the local mechanical properties of cement-based materials at the microscale [3–7] and provides a unique opportunity to analyze the mechanical differences in degraded materials presenting high heterogeneity at the microscale.

In this paper, Portland cement pastes were subjected to decalcification through exposure to ammonium nitrate solution for 125 days. A grid nanoindentation technique was performed on the degraded zones found in the cement paste cross-section, and the influence of the extent of degradation on the changes in the micromechanical properties was evaluated. Statistical methods were then used to provide segmentation of the indentation data based on the cement phase(s) present at each location to provide a better understanding of the micromechanical behavior of the cement paste during exposure to a decalcifying environment.

2 Experimental

2.1 Sample Preparation and Exposure Conditions

Portland cement pastes were prepared using Type I/II Portland cement (Lafarge, Nashville, Tennessee) and Glenium 7500 (BASF, Ludwigshafen, Germany), a polycarboxylate-based high range water reducer. A water to cement ratio of 0.28 and a Glenium loading of 1 % per mass of cement was used. After mixing, the pastes were poured into beam molds and compacted by hand. The beams were allowed to cure at room temperature and 100 % relative humidity for 28 days.

After curing, the beam specimens ($2.54 \times 2.54 \times 11.5$ cm) were exposed to an ammonium nitrate (NH_4NO_3) solution to accelerate decalcification. Each specimen was immersed in 1 L of NH_4NO_3 solution at a concentration of 480 g/L (6 M) for 125 days. After exposure, cross-sections of the specimens were cut using a low-speed Buehler diamond saw. The cross-sections were prepared for nanoindentation by epoxy-mounting and polishing using a series of grinding and polishing steps, with the final polishing step utilizing a 50 nm alumina powder suspension on specialized polishing cloths.

2.2 Micromechanical Testing

Nanoindentation was performed using an Agilent Nanoindenter G200 Testing System (Agilent Technologies, Santa Clara, California, USA) and a diamond Berkovich tip. Three grids of 200 indents were collected in each visible degraded zone of the cross-section. Spacing between indents was 10 μm in both the X and Y directions. During testing, a maximum force of 2 mN was applied with a targeted

strain rate of 0.050 s^{-1}. The maximum load was held for 15 s followed by a 10 s unloading period. Each indentation curve was then evaluated, and abnormal curves were discarded so as to not interfere with the determination of the micromechanical properties. The elastic modulus and hardness were then calculated using the Oliver and Pharr method [8]. A statistical method (similar to that found in [9]) was used to further segment the nanoindentation data into different phases. This method involved fitting n Gaussian distributions to the experimental probability density function (PDF), calculating the parameters for each fitted distribution, and generating the theoretical PDF for the nanoindentation data. A least squares minimization procedure was then used to compare the experimental and theoretical PDF in order to find the best fit.

3 Results and Discussion

After exposure to ammonium nitrate solution, the cement pastes exhibited three clearly defined visible degradation zones (Fig. 1): a light colored outer layer, a slightly darker middle layer, and a dark interior core. Nanoindentation grids were collected in the outer layer and middle layer as these two zones encompassed a majority of the cross-section surface area and represented the most degraded areas of the cross-section.

Elastic modulus and hardness for the outer and middle layers of the degraded specimen are presented in Table 1 along with the values from [4] for a non-degraded Portland cement paste cast under the same conditions and analyzed using the same

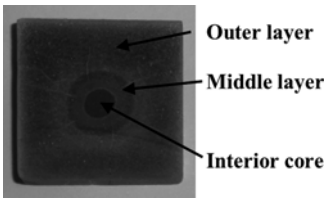

Fig. 1 Representative image of the cement paste cross-section after 125 days of exposure to ammonium nitrate solution

Table 1 Elastic modulus and hardness for non-degraded and degraded cement pastes (average of all valid curves)

Sample	Elastic modulus (GPa)	Hardness (GPa)
No exposure	39.5	1.86
125 days of exposure – middle layer	27.9	1.29
125 days of exposure – outer layer	12.7	0.66

method. In both degraded layers, the elastic modulus and hardness clearly decreased after exposure to ammonium nitrate solution. The middle layer experienced a 29 % decrease in modulus, while the outer layer experienced a more significant decrease of 68 % relative to the non-degraded cement paste. The hardness appeared to decrease at a similar rate to the modulus with a 31 % decrease for the middle layer and a 65 % decrease for the outer layer.

The nanoindentation data of each layer were further analyzed using a statistical Gaussian fitting method. Given the number of characteristic peaks seen in the experimental PDF, the number of Gaussian distributions to be fitted to the data was set at three. While these peaks do not necessarily correlate with chemically distinct phases, they can be discussed in general terms of hydration products as shown in [9]. The three mechanically distinct phases considered were:

Phase A: Majority of the main hydration products (e.g., CSH)
Phase B: High stiffness hydration products (e.g., CH or high stiffness CSH)
Phase C: Unhydrated cement particles, CH, or a combination of the two

While the modulus values of all three phases decreased in the degraded middle and outer layers (Fig. 2a), their rate of decrease was different. In the middle layer, Phase A experienced a minimal decrease in the modulus (9 %), while Phase B and C showed a sharp decrease (37 % and 58 %, respectively) relative to the non-degraded cement paste. These results indicated that the predominant chemical mechanisms in that layer were most likely the dissolution of calcium hydroxide (CH) and possibly a partial dissolution/hydration of the unhydrated cement particles. The calcium silicate hydrates (CSH) had, however, been minimally affected. Given that this middle layer surrounded a dark, likely non-degraded core, the leading edge of the calcium leaching front after 125 days of exposure was thought to be located in this layer. In contrast, the outer layer modulus values of the different phases all experienced drastic decreases (65 %, 72 %, and 76 % for Phases A, B, and C, respectively). Since this layer represented the most degraded portion of the cross-section, it was expected that the CH had already dissolved and the progressive decalcification of CSH had occurred. The similar decrease seen for all three phases may further indicate that only the residual strength of the cement paste was left vs. distinctive mechanical properties for each phase.

With the exception of Phase A in the middle layer, the hardness values of all of the phases followed the same trends as the modulus values (Fig. 2b). In the middle layer, Phase A experienced an increase in hardness relative to the non-degraded cement paste. This increase in hardness was thought to be due to a change in the phase mineralogy. However, this necessitates further investigations of the microstructure and chemical changes that occurred in this layer during exposure.

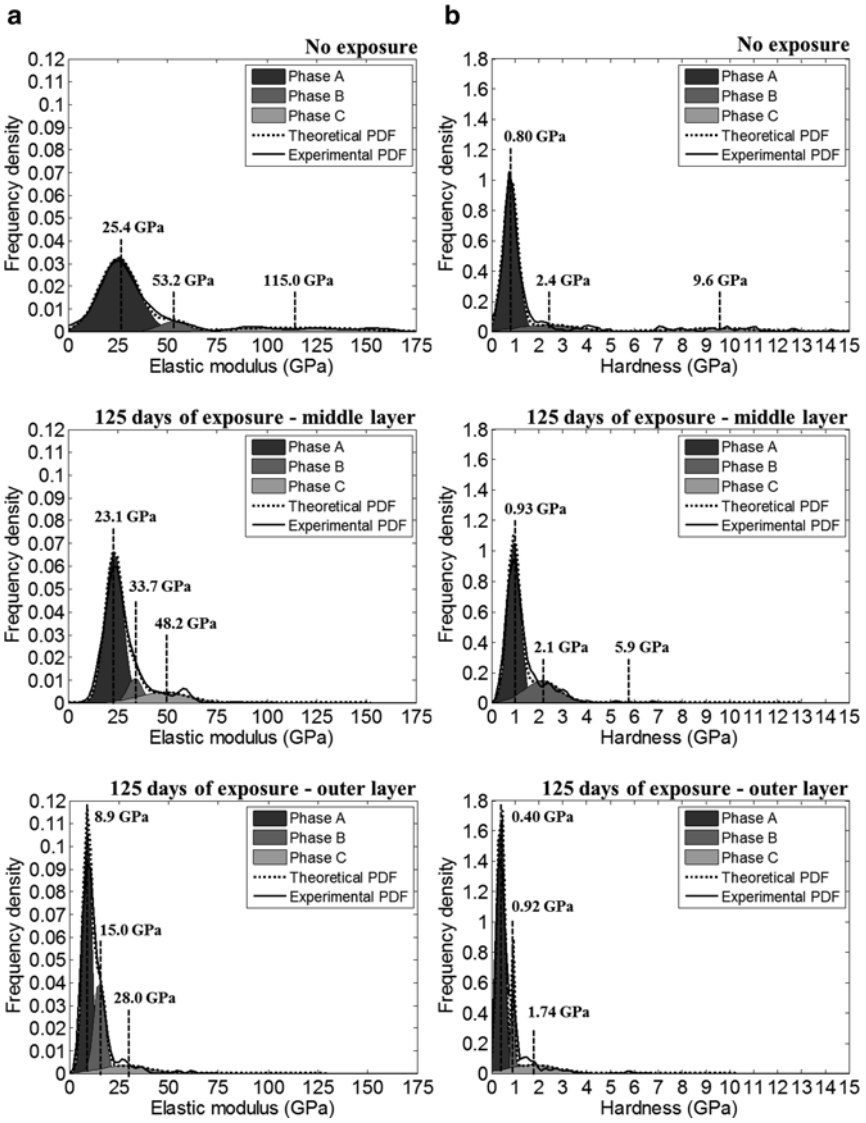

Fig. 2 (**a**) Elastic modulus and (**b**) hardness for the non-degraded cement paste and the middle and outer layers of the degraded cement paste

4 Conclusions

The micromechanical properties (modulus and hardness) of decalcified cement pastes were investigated. The results can be summarized as follows:

- The hardness and elastic modulus followed, overall, the same decreasing trend relative to the non-degraded cement paste as a function of the extent of degradation, with a much greater decrease seen for the outer layer than the middle layer.

- Segmentation of the nanoindentation data from each layer into mechanically distinct phases indicated that the phases behaved differently during decalcification with respect to their micromechanical properties.

Future work involves identification of the cement phases present at each indent location using SEM-EDS coupled with the nanoindentation data. This will allow the micromechanical data to be correlated to chemical data and provide a better understanding of the chemo-mechanical behavior of cement pastes exposed to a decalcifying environment.

Acknowledgments This research was supported through funding from the National Science Foundation (NSF) CMMI 0547024 and GRFP DGE-0946822 as well as the DOE funded Consortium for Risk Evaluation with Stakeholder Participation III (CRESP III). Opinions, findings, conclusions, or recommendations expressed herein are those of the authors and do not necessarily reflect the views of the NSF, DOE, or CRESP III. The authors also gratefully acknowledge Dr. Paul Allison and Dr. Robert Moser from the US Army Corps of Engineers Engineering Research and Development Center, Vicksburg, MS, for the use of the nanoindentor and their help with the nanoindentation experiments.

References

1. Sanchez, F., & Borwankar, A. (2010). Multi-scale performance of carbon microfiber reinforced cement-based composites exposed to a decalcifying environment. *Materials Science & Engineering, A: Structural Materials: Properties, Microstructure and Processing, 527*(13–14), 3151–3158.
2. Nguyen, V. H., et al. (2007). Chemo-mechanical coupling behaviour of leached concrete: Part I: Experimental results. *Nuclear Engineering and Design, 237*(20–21), 2083–2089.
3. Chen, J. J., et al. (2010). A coupled nanoindentation/SEM-EDS study on low water/cement ratio portland Cement paste: Evidence for C–S–H/Ca(OH)2 nanocomposites. *Journal of the American Ceramic Society, 93*(5), 1484–1493.
4. Stephens, C. (2013). Multiscale performance of cement-based composites with carbon nanofibers. PhD dissertation, Civil and Environmental Engineering Department, Vanderbilt University, Nashville.
5. Allison, P., et al. (2011). Nanomechanical structure–property relations of dynamically loaded reactive powder concrete. In A. A. Mammoli, C. A. Brebbia, & A. Klemm (Eds.), *Materials characterization V: Computational methods and experiments* (pp. 287–298). Southampton: WIT Press.
6. Constantinides, G., & Ulm, F. J. (2004). The effect of two types of C-S-H on the elasticity of cement-based materials: Results from nanoindentation and micromechanical modeling. *Cement and Concrete Research, 34*(1), 67–80.
7. Mondal, P., Shah, S. P., & Marks, L. (2007). A reliable technique to determine the local mechanical properties at the nanoscale for cementitious materials. *Cement and Concrete Research, 37*(10), 1440–1444.
8. Oliver, W. C., & Pharr, G. M. (2004). Measurement of hardness and elastic modulus by instrumented indentation: Advances in understanding and refinements to methodology. *Journal of Materials Research, 19*(01), 3–20.
9. da Silva, W. R. L., Němeček, J., & Štemberk, P. (2013). Application of multiscale elastic homogenization based on nanoindentation for high performance concrete. *Advances in Engineering Software, 62–63*, 109–118.

Nanomechanical Characterization of the Carbonated Wollastonite System

Warda Ashraf, Jan Olek, and Nannan Tian

Abstract This paper focuses on the nano-mechanical characterization of carbonated calcium silicate mineral (wollastonite ($CaSiO_3$)) using nanoindentation technique. While exposed to carbon dioxide (CO_2), the calcium component of wollastonite undergoes carbonation reaction which results in formation of two main products: calcium carbonate ($CaCO_3$) and silica (SiO_2). The mechanical properties of these partially reacted wollastonite systems were evaluated using the nanoindentation technique from which the reduced elastic modulus (E_r) of silicate phase found to be around 38 GPa. For calcium carbonate phase this value was around 60 GPa.

Keywords Wollastonite • Calcium silicate • Carbonation • Nanoindentation • Characterization

1 Introduction

Carbonation of calcium silicate minerals is a well-known phenomenon as observed in cases involving CO_2 sequestration and studies of ordinary portland cement (OPC). Calcium silicates produce silica gel and calcium carbonate phases during carbonation processes and hence capture the CO_2 within the microstructure. This concept is widely utilized to capture and store the CO_2 in calcium/magnesium silicate minerals and it is known as 'mineral carbonation' process [1–3].

W. Ashraf (✉) • J. Olek
Lyles School of Civil Engineering, Purdue University, West Lafayette, IN, USA
e-mail: washraf@purdue.edu; olek@purdue.edu

N. Tian
School of Materials Engineering, Purdue University, West Lafayette, IN, USA
e-mail: ntian@purdue.edu

K. Sobolev, S.P. Shah (eds.), *Nanotechnology in Construction*,
DOI 10.1007/978-3-319-17088-6_8

The investigation of carbonation process of wollastonite mineral is thoroughly described in [4–6]. The set of equations presented below can be used to explain the carbonation process of wollastonite ($CaSiO_3$):

$$CO_2 + H_2O \rightleftharpoons H^+ + HCO_3^- \quad (1)$$

$$CaSiO_3 + H^+ + HCO_3^- \rightleftharpoons SiO_2 \downarrow + CaCO_3 \downarrow + H_2O \quad (2)$$

Similar reaction mechanism can also be observed during the carbonation process of OPC based construction materials [7, 8]. The microstructural phases of hydrated OPC system, such as CSH, C_2S and C_3S were also found to produce silica gel and calcium carbonate as the reaction products while subjected to carbonation process. In this paper, the silicate and calcium carbonate phases produced during the carbonation process of wollastonite were nanomechanically characterized with the aid of nanoindentation technique.

2 Experimental Study

2.1 Sample Preparation

Carbonated wollastonite sample was prepared according to the patent US20130122267 A1 [9]. Powdered natural wollastonite sample was first mixed with a small amount of water (water to solid ratio ~0.25) and compacted in 50 mm cube molds. These compacted cubes were then subjected to carbonation process by being exposed for 65 h to pure CO_2 (100 % concentration) at the temperature of 60 °C.

After the carbonation process was completed approximately 10 mm cube samples were removed from the 50 mm cubes for experimental investigation. These 10 mm cube samples were polished on successively smaller mesh sizes (upto 0.25 μm) to obtain a very flat surface with minimal roughness.

2.2 Test techniques

2.2.1 SEM/EDS Analysis

Scanning electron microscope (SEM) along with energy-dispersive spectroscopy (EDS) analyses were performed using a FEI NOVA nanoSEM field emission scanning electron microscope (FESEM) which was operated in high vacuum mode. The accelerating voltage was 20 kV and the working distance was 10.00 mm.

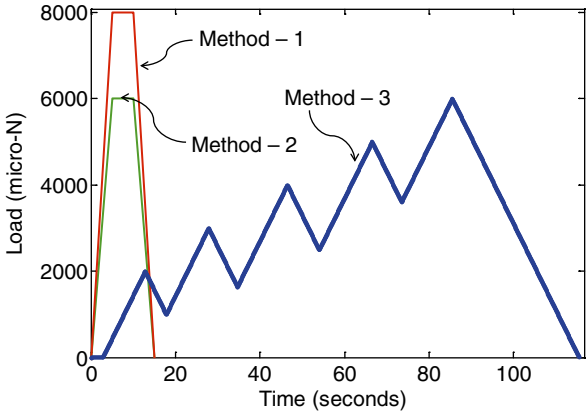

Fig. 1 Loading cycles of nanoindentation tests

2.2.2 Nanoindentations

For nanomechanical characterization of the carbonated wollastonite, nanoindentations were performed using three different methods (later referred to as: method – 1, method – 2 and method – 3). In the first method, indentations were performed over a small area, mainly focusing on an unreacted grain and the surrounding area. In this case, a trapezoidal loading cycle with 8,000 μN maximum load was used (shown in Fig. 1). In the next method (method-2), nanoindentations were carried out in a grid pattern for using so called statistical nanoindentation technique [10, 11]. In order to do so, four areas of 80 μm × 80 μm were selected on the polished samples surface and a total of 256 indentations were performed (i.e., 64 indents on each area). For the last part of this experimental study (method – 3), a repetitive and consecutively increasing loading cycle was applied on 98 indentation points to identify the short term creep behavior of this system. In this case, for each indent point a total 5 loading cycles were applied with loads increasing from 2,000 to 6,000 μN (Fig. 1). Nanoindentation tests were performed using a Hysitron Triboindenter 950 system fitted with a Berkovich diamond indenter probe.

3 Results and Discussions

3.1 Microstructural Investigation Using SEM/EDS

Figure 2 shows a SEM image of the carbonated wollastonite system along with the EDS patterns for individual microstructural phases. The brightest parts of the SEM image represents the unreacted grains of wollastonite as confirmed by 1:1 atomic ratio of Ca: Si. Silica gel primarily forms as a rim around the wollastonite grains and the calcium carbonate phase is mostly found to fill up the inter-particle spaces.

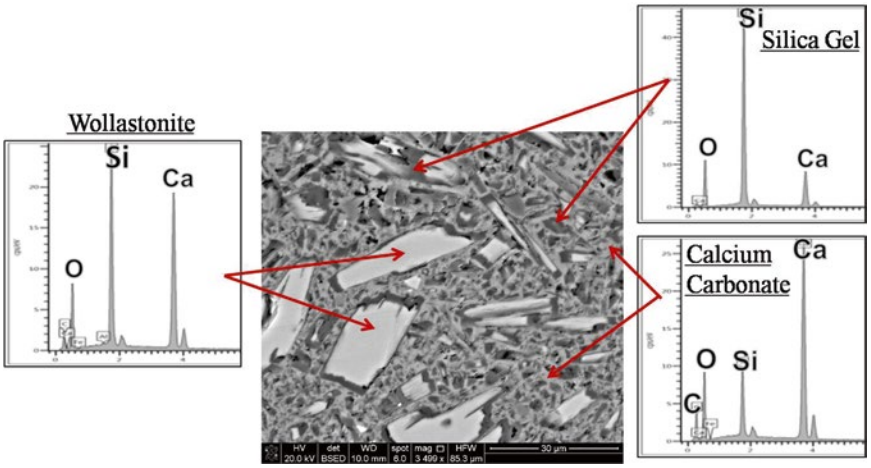

Fig. 2 SEM image and EDS patterns identifying different microstructural phases of carbonated natural wollastonite system

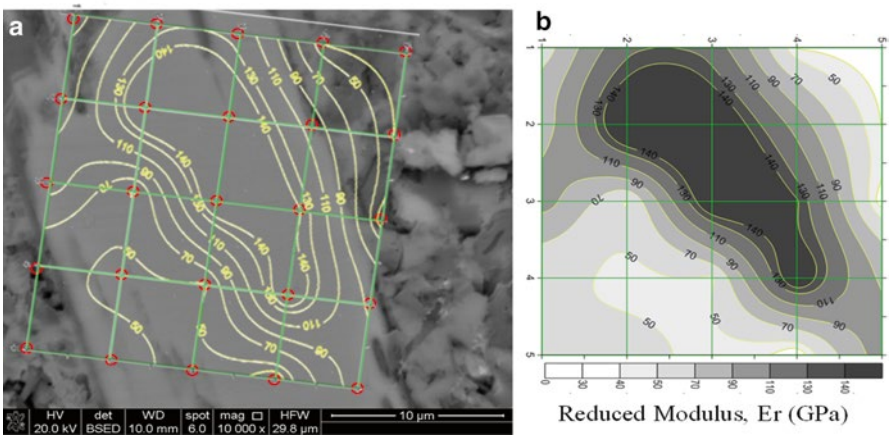

Fig. 3 Contour map of reduced modulus, Er (*GPa*) around carbonated wollastonite grain showing as (**a**) transparent overlay on BSED image of actual indented area and (**b**) color filled contour with corresponding color scale

3.2 Nano Mechanical Characterization

3.2.1 Method – 1: Identification of the Phases

In this method, the main objective was to use the SEM analysis to identify the nanoindentation marks so that a relative comparison of the reduced elastic modulus for the microstructural phases can be obtained. Figure 3 shows the variation of reduced elastic modulus on and around a wollastonite grain. The center region of the unreacted grain is associated with high values (~160 GPa) of the reduced elastic

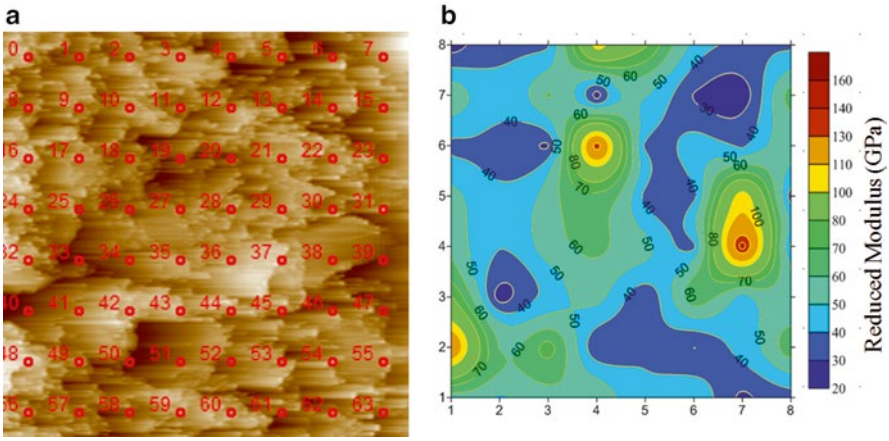

Fig. 4 (**a**) SPM image showing locations of 64 indentation points on an 80 μm × 80 μm area and (**b**) corresponding contour map of the moduli (*GPa*)

modulus. That value was found to be smaller around the edges of the grain. Few indentation points were also identified in regions occupied by the silica gel and calcium carbonate phases. Based on the findings of this test, the approximate values of reduced elastic modulus for silica and calcium carbonate phases were determined to be in the range, respectively, of about 40 and 60 GPa.

3.2.2 Statistical Nanoindentation

To obtain the mean reduced modulus of individual microstructural phases, statistical nanoindentation technique [10, 11] was applied. Figure 4 shows a scanning probe microscope (SPM) image identifying the locations of 64 indentation points and the corresponding contour map of reduced elastic modulus values. This map was used to illustrate the locations of the unreacted grains and the pores. The Gaussian frequency distributions of the reduced modulus values for individual microstructural phases are given in Fig. 5a. These distributions were determined from the statistical deconvolution of cumulative frequency distributions as given in Fig. 5b.

3.2.3 Short Term Creep Behavior

The load-depth responses of the silica gel, calcium carbonate and unreacted wollastonite phases while subjected to repetitive and increasing loading cycles are given in Fig. 6a. The blunting of the tip of load-depth curve with increased and repetitive load reflects the creep behavior of silica gel and calcium carbonate phases [12]. However, the minimal variation of the modulus values with increasing load (Fig. 6b) also indicates that the effect of the indentation size was not significant at least within this load range.

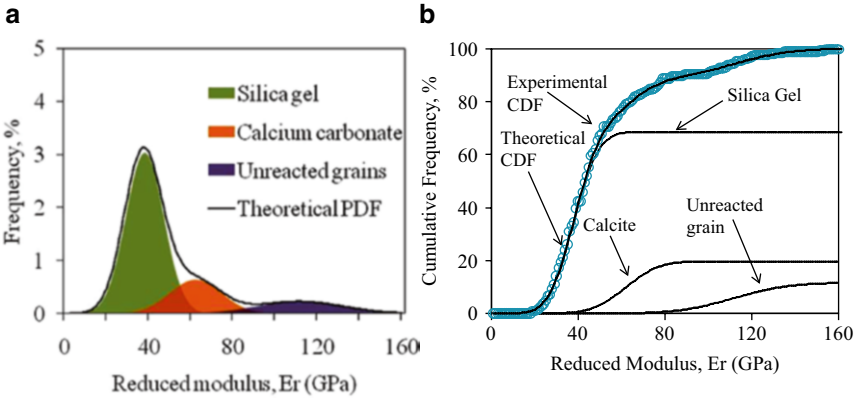

Fig. 5 (**a**) Frequency distribution and (**b**) cumulative frequency distribution plots of reduced modulus, Er (GPa) for carbonated wollastonite sample

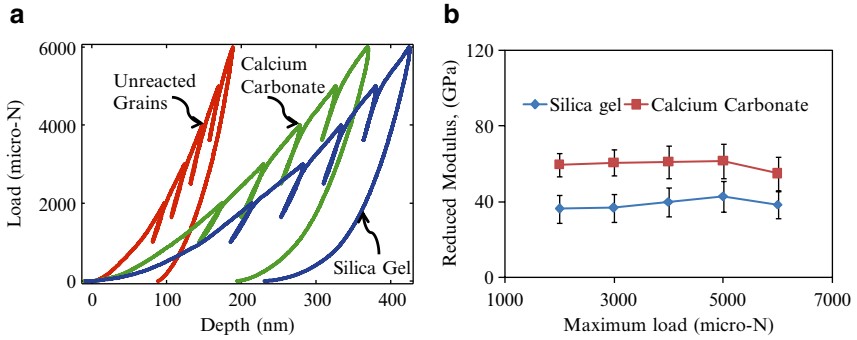

Fig. 6 (**a**) Load depth response of microstructural phases for different loading functions, (**b**) variation of moduli (*GPa*) with increasing loads

4 Conclusions

In this paper, the silica gel and calcium carbonate phases that formed during the carbonation of calcium silicate minerals were characterized using nanoindentation technique. The reduced elastic modulus for silica gel and calcium carbonate found to be 38 ± 10 GPa and 61 ± 16 GPa, respectively. The creep effect of silica gel phases was found to be higher than that of calcium carbonate phase.

Acknowledgement Solidia technologies are gratefully acknowledged for providing testing materials required for this study. Authors would also like to acknowledge the Rutger University, NJ, USA for the development of the technology.

References

1. Huijgen, W. J. J., & Comans, R. N. J. (2005). *Carbon dioxide sequestration by mineral carbonation: literature review update 2003–2004* (Report). Energy Research Centre of the Netherlands.
2. Goff, F., & Lackner, K. (1998). Carbon dioxide sequestering using ultramafic rocks. *Environmental Geosciences, 5*(3), 89–101.
3. Lackner, K. (2003, June). A guide to CO_2 sequestration. *Science*, *300*, 1677–1678.
4. Daval, D., Martinez, I., Corvisier, J., Findling, N., Goffé, B., & Guyot, F. (2009, July). Carbonation of Ca-bearing silicates, the case of wollastonite: Experimental investigations and kinetic modeling. *Chemical Geology*, *265*(1–2), 63–78.
5. Daval, D., Martinez, I., Guigner, J. M., Hellmann, R., Corvisier, J., Findling, N., et al. (2009, November). Mechanism of wollastonite carbonation deduced from micro- to nanometer length scale observations. *American Mineralogist, 94*(11–12), 1707–1726.
6. Tai, C. Y., Chen, W. R., & Shih, S. M. (2006, January). Factors affecting wollastonite carbonation under CO_2 supercritical conditions. *AIChE Journal, 52*(1), 292–299.
7. Chun, Y., Naik, T., & Kraus, R. (2007). Carbon dioxide sequestration in concrete in different curing environments. In *Conference: Sustainable Construction Materials and Technologies, Coventry, Special Papers Proceedings* pp. 18–24.
8. Papadakis, V., Vayenas, C., & Fardis, M. (1991). Fundamental modeling and experimental investigation of concrete carbonation. *ACI Materials Journal, 88*, 363–373.
9. Riman, R. E., Gupta, S., Atakan, V., & Li, Q. (2013). *U.S. 20130122267 A1: Bonding element, bonding matrix and composite material having the bonding element, and method of manufacturing thereof*.
10. Constantinides, G., Ravi Chandran, K. S., Ulm, F. J., & Van Vliet, K. J. (2006, August). Grid indentation analysis of composite microstructure and mechanics: Principles and validation. *Materials Science and Engineering: A, 430*(1–2), 189–202.
11. Ulm, F. J., Vandamme, M., Bobko, C., Alberto Ortega, J., Tai, K., & Ortiz, C. (2007, September). Statistical indentation techniques for hydrated nanocomposites: Concrete, bone, and shale. *Journal of the American Ceramic Society*, 90(9), 2677–2692.
12. Němeček, J. (2009, September). Creep effects in nanoindentation of hydrated phases of cement pastes. *Materials Characterization, 60*(9), 1028–1034.

Atom Probe Tomography for Nanomodified Portland Cement

Gilson R. Lomboy, Dieter Isheim, and Surendra P. Shah

Abstract The study presents the use of Atom Probe Tomography (APT) to investigate the interaction between nanolimestone and Portland cement. APT is an analytical imaging technique that generates a three-dimensional atom-by-atom image of a specimen, with sub-nanometer spatial resolution. For the APT tests, a polished Portland cement clinker with nanolimestone on the surface was hydrated between 2 and 4 h. The hydrated Portland cement clinker was then imaged with a scanning electron microscope to visually determine the degree of hydration. Tip specimens for APT were then formed by FIB lift-out in a FEI Helios Nanolab, followed by annular ion-beam milling to form APT tips targeted on the nanolimestone/cement clinker interface, so that the nanolimestone is located at the apex of the specimen. The results show that the nanolimestone had reacted with the cement clinker. This demonstrates that the use of nanolimestone may not be only providing nucleation sites for cement hydration but is also chemically reacting with the Portland cement clinker within the first few hours of hydration.

Keywords Atom probe tomography • Cement • Clinker • Nanolimestone

1 Introduction

There is a great interest for use of nanoparticles in cement-based materials because of its wide and almost exclusive use in construction, and the potential for nanoscale manipulation has profound effects for altering performance of cement-based

G.R. Lomboy (✉)
Department of Civil, Construction and Environmental Engineering, Iowa State University, Ames, IA, USA
e-mail: grlomboy@iastate.edu

D. Isheim
Center for Atom Probe Tomography, Northwestern University, Evanston, IL, USA
e-mail: isheim@northwestern.edu

S.P. Shah
Center for Advanced Cement Based Materials, Northwestern University, Evanston, IL, USA
e-mail: s-shah@northwestern.edu

K. Sobolev, S.P. Shah (eds.), *Nanotechnology in Construction*,
DOI 10.1007/978-3-319-17088-6_9

materials [1, 2]. Atom-probe tomography (APT) is uniquely suited to the study of nanoparticles and reactions between nanoparticles and in nanostructured materials. It is an analytical imaging technique that generates a three-dimensional atom-by-atom image of a specimen, with sub-nanometer spatial resolution [3–9]. Local compositions, composition gradients, and concentration profiles across interfaces or inhomogeneity and second-phase particles can be determined. Modern APT is applied routinely for the analysis of nanostructured materials such as metals and alloys, semiconductors and semiconductor devices, nanowires, thin-film functional materials, geological specimens, and bio-minerals [10, 11].

The accelerated hydration by nanolimestone modification has been thought to be caused by seeding or reduction of the nucleation barrier during the early stages, but other researchers have reported that the nanoparticles chemically react with Portland cement to form new hydration compounds [12, 13]. The study uses APT to investigate the interaction between nanolimestone and Portland cement. The following explains a method of testing hydrated clinker with nanolimestone using APT. The method of preparing atom probe tips and APT testing parameters used are presented. Finally, the APT data are reconstructed and analyzed. Based on the results of the concentration distributions, nanolimestone was found to interact with Portland cement clinker during the early stage of the hydration process.

2 Materials and Methods

The materials used are Portland cement clinker and nanolimestone. The Portland cement clinker is used for production of Type I cement. The nanolimestone has an average particle diameter of 100 nm. Other materials used are nickel, as protective and conductive coating on the surface of the hydrated clinker, deposited by ion-beam sputtering; and platinum for marking particle locations and further protection during cutting and milling.

A disk is cut from a Portland cement clinker and affixed on an SEM mount. The clinker disk was then sanded flat and polished with sandpaper and lapping. After polishing, the disk was cut into several rectangular pieces and remounted separately as shown in Fig. 1. The clinker was then viewed with a scanning electron microscope (SEM) to verify a clean flat surface.

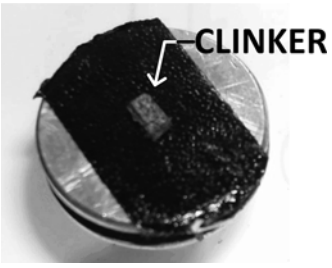

Fig. 1 Polished and cut clinker, mounted on a 12.7 mm SEM mount

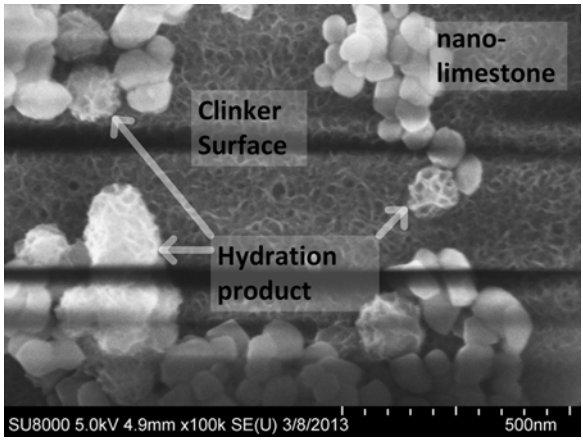

Fig. 2 SEM image of clinker surface hydrated with nanolimestone solution (×100 k magnification) hydrated for 4 h

Nanolimestone particles were dispersed in deionized water in a ultrasonic bath to make a suspension. The solution was rested for 24 h to allow large agglomerates to settle. A sample of the solution was extracted from near the surface of the solution using a pipette. Drops of the solution were placed on the clinker until it was completely covered. The clinker was hydrated up to 4 h. After the hydration period, the clinker was washed with ethanol and dried with pressurized line air to halt the hydration process.

An SEM micrograph of the clinker surface that were hydrated with nanolimestone solution for 4 h is shown in Fig. 2. The clinker surface shows formation of gel-like hydration products and the nanolimestone particles. They also show some nanoparticles that have similar formations of hydration products as the surface, which is likely due to nucleation or seeding [13].

The tip was fabricated using a FEI Helios Nanolab 600 Focused Ion Beam (FIB) microscope, equipped with SEM, micromanipulator, and gas-injection systems (GIS) for metal deposition. Nanoparticles were selected by SEM imaging and their locations marked by platinum deposition as shown in Fig. 3.

Additional Pt deposition served as a protective layer during the subsequent cutting of a section of the surface that was marked with the ion beam. That section was then attached to the micromanipulator, lifted out, and then mounted on prefabricated Si microtips. Each APT tip was then sharpened with an annular ion-beam pattern until an end radius of approximately 20–35 nm was obtained. A typical tip is shown in Fig. 4.

Atom probe tomography was performed utilizing a LEAP 4000X Si tomograph (Cameca Instruments, Madison, WI). Specimens were evaporated, atom-by-atom and atomic-plane-by-atomic-plane, employing a picosecond ultraviolet laser with a 355 nm wavelength. The laser was pulsed at a repetition rate of 500 kHz. The samples were analyzed at a specimen temperature of 40 K or 80 K in a vacuum of $\leq 4 \times 10^{-10}$ Torr. Laser pulse energies of 40–80 pJ pulse^{-1} and an evaporation rate of 1.0–0.1 % were utilized. The data was recorded and reconstructed in three-dimensions (3-D) using the program IVAS 3.4 (Cameca Instruments) [14].

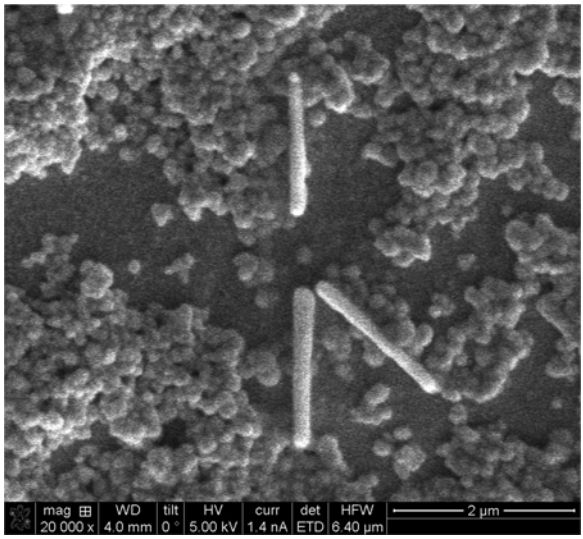

Fig. 3 Hydrated clinker surface with nanolimestone; line markers are placed to locate selected particles

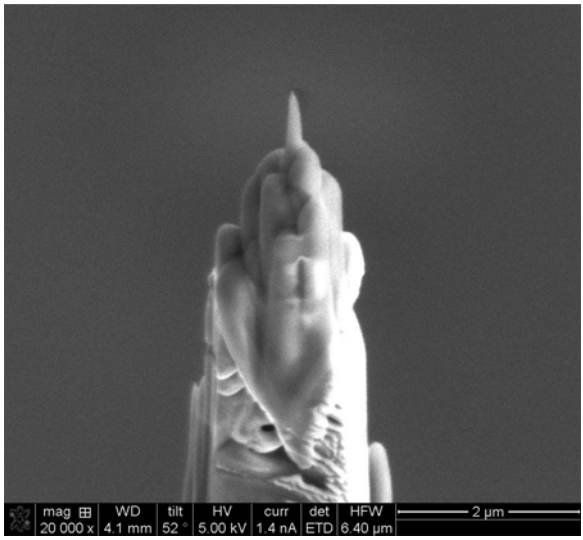

Fig. 4 Atom probe tip made from hydrated clinker with nanolimestone particle at the tip

3 Results

The APT reconstruction of the sampled tip volume is presented in Fig. 5, with a total of 1,600,838 atoms and a height of 60 nm. Individual atoms or small molecules are represented by colored dots. Not all atoms are drawn to allow for visibility of the carbon isoconcentration-surface used to delineate the nanolimestone (nanometer sized particle of calcium carbonate) particle which is of limited amount in clinker.

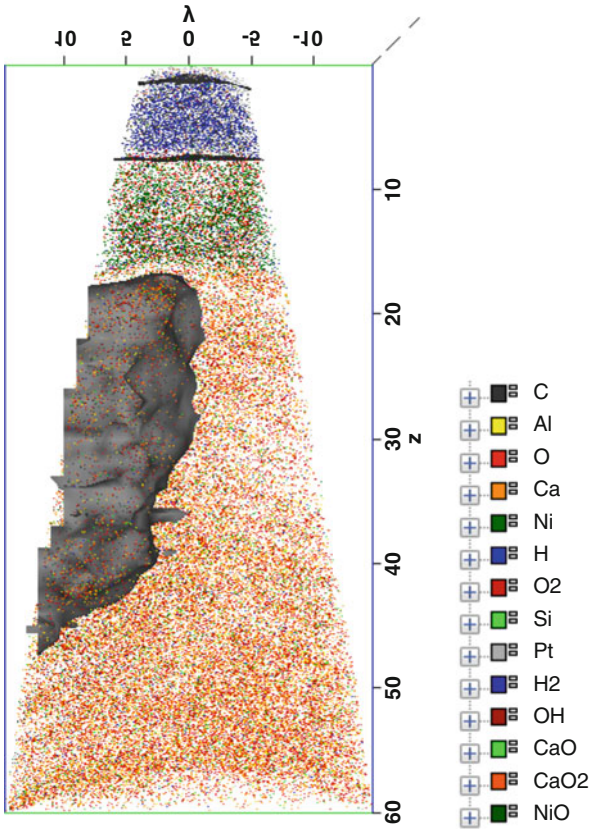

Fig. 5 Reconstruction of Tip

The APT reconstruction consist of three distinct layers. The top-most layer (blueish) is the residue from the protective platinum deposit in the FIB. Next is the nickel layer and the entire bottom part is the hydrated clinker with Ca atoms shown in orange. The carbon isoconcentration-surface delineating the nanolimestone particle is drawn at 15 at.% and is shaped as a segment of a spheroid. The shape suggests that tip sample was extracted within the vicinity of a nanolimestone particle. Concentration profiles were obtained along different directions through the reconstruction: first, vertically through the entire height of the APT sample, from top to bottom (Fig. 6); second along the side of the APT reconstruction passing through the 15 at.% C isoconcentration-surface, Fig. 7; and third horizontally across the APT sample (Fig. 8), also passing through the 15 at.% C iso-surface. From Fig. 6, the remaining platinum layer after tip sharpening is about 6 nm, while the nickel layer deposit is about 10 nm. The most abundant element in the volume sampled from the clinker is oxygen, followed by calcium, then by aluminum.

In the concentration profile in Fig. 7, the average concentration of carbon in the section from 19.5 to 36 nm is 23.2 at.%, while that of calcium is 12.4 at.%. In the profile Fig. 8, the proportion of carbon to calcium was found to be greater than 2

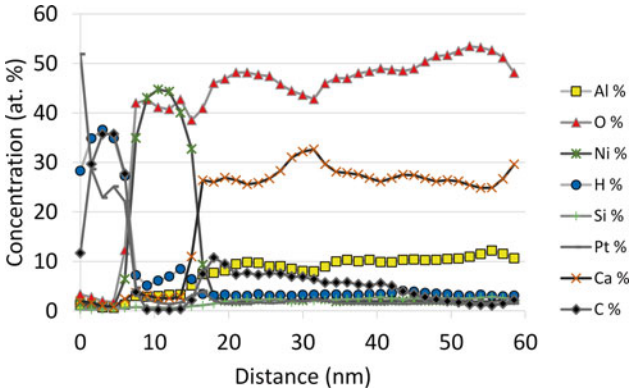

Fig. 6 Concentration distribution of atoms along the height, distance zero is the apex

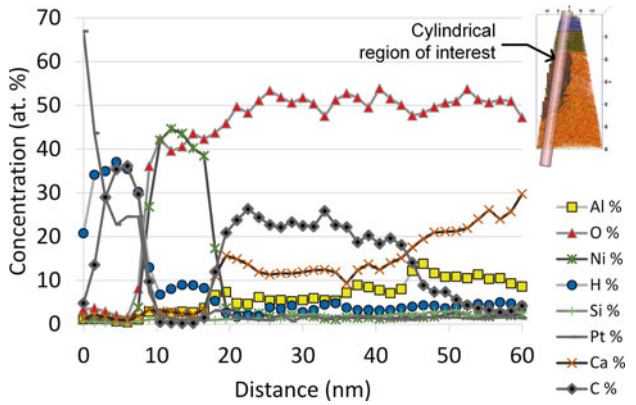

Fig. 7 Concentration distribution of atoms through a 5 nm diameter cylindrical region along the; distance 0 is the apex

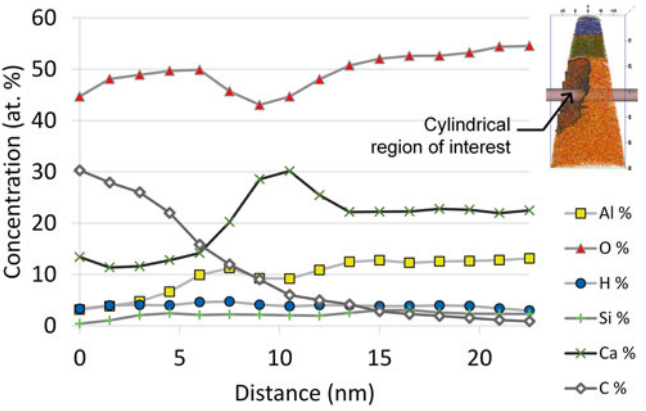

Fig. 8 Concentration distribution of atoms through a 5 nm diameter cylindrical region across the tip

within the 15 at.% C iso-surface, and diminishes as the profile continues to the right-hand side of the APT reconstruction. Stoichiometric calcium carbonate ($CaCO_3$) has the same number of carbon atoms as the number of calcium atoms, while oxygen will be three times of either element. This was not found within the 15 at.% C iso-surface. Instead, there is only half the amount of calcium compared to carbon, while oxygen remained three times that of calcium. At the 15 at.% C iso-surface, however, the ideal stoichiometry of calcium carbonate is obtained, as see in the profile in Fig. 8 near 10 nm depth. The decay of carbon concentration from the iso-surface continued for about 9 nm into the clinker material, which may indicate a slight inter-reaction between the nanolimestone and the clinker.

4 Conclusions

Atom probe tomography is a powerful analytical microscopy tool that can be utilized for the visualization and analysis of the interaction of nanoparticles with cementitious materials. From the APT analysis shown, nanolimestone was found to react with clinker during hydration as seen by the amounts of calcium and carbon at the vicinity of the nanolimestone. There is a gradual change in concentration of elements in regions where clinker hydration occurs. Further tests need to be conducted to determine the interactions of nanolimestone with other phases of Portland cement, such as tricalcium silicate. The analysis of atomic structures will be part of future work.

Acknowledgement The authors would like to acknowledge the Oak Ridge Associated Universities (ORAU) – Tennessee Valley Authority (TVA) for sponsoring the present study (Grant No. 7–22976). The atom probe experiments were conducted at NUCAPT and tip preparation was conducted at NUANCE, both research facilities at Northwestern University, Evanston, Illinois.

References

1. Sancheza, F., & Sobolevb, K. (2010). Nanotechnology in concrete – a review. *Construction and Building Materials, 24*(11), 2060–2071.
2. Sobolev, K., & Shah, S. P. (Eds.). (2008). *Nanotechnology of concrete: Recent developments and future perspectives*. ACI Proceedings, Denver, ACI SP-254, p. 160.
3. Cerezo, A., Godfrey, T. J., & Smith, G. D. W. (1988). Application of a position-sensitive detector to atom probe microanalysis. *The Review of Scientific Instruments, 59*(6), 862–866.
4. Blavette, D., Deconihout, B., Bostel, A., Sarray, J. M., Bouet, M., & Menand, A. (1993). Review of scientific instruments. *American Institute of Physicis, 64*(10), 2911–2919.
5. Kelly, T. F., & Miller, M. K. (2007). Atom probe tomography. *Review of Scientific Instruments, 78*, 1–20.
6. Seidman, D. N., & STILLER, K. (2009). An atom-probe tomography primer. *MRS Bulletin, 34*(10), 717–724.
7. Miller, M. K., Cerezo, A., Hetherington, M. G., & Smith, G. D. W. (1996). *Atom-probe field-ion microscopy*. Oxford, UK: Clarendon.
8. Miller, M. K. (2000). *Atom-probe tomography – Analysis at the atomic scale*. New York: Kluwer.

9. Gault, B., Moody, M. P., Cairney, J. M., & Ringer, S. P. (2012). *Atom-probe microscopy*. New York: Springer Science + Business Media.
10. Kelly, T. F., & Larson, D. J. (2012). Atom probe tomography 2012. *Annual Review of Materials Research, 42*, 1–31.
11. Gordon, L. M., & Joester, D. (2011). Nanoscale chemical tomography of buried organic–inorganic interfaces in the chiton tooth. *Nature, 469*, 194–198.
12. Kawashima, S., Hou, P., Corr, D. J., & Shah, S. P. (2013). Modification of cement-based materials with nanoparticles. *Cement and Concrete Composites, 36*(1), 8–15.
13. Sato, T., & Beaudoin, J. (2011). Effect of nano-$CaCO_3$ on hydration of cement containing supplementary cementitious materials. *Advances in Cement Research, 23*(1), 33–43.
14. Larson, D. J., Prosa, T. J., Ulfig, R. M., Geiser, B. P., & Kelly, T. F. (2013). *Local-electrode atom-probe tomography*. New York: Springer Science + Business Media.

Nano- and Microstructural Characterization of Portland Limestone Cement Pastes

Elizabeth I. Nadelman, Dylan J. Freas, and Kimberly E. Kurtis

Abstract This research effort examines the rates of nano- and microstructural development in portland limestone cement pastes through Raman spectroscopy, specific surface area (SSA) analysis, and scanning electron microscopy (SEM). This paper considers the first of these techniques, evaluating chemical composition through *in situ* Raman spectroscopy measurements. Changes in the chemical composition of the hydrated cement paste is evaluated at various stages of hydration as a first step toward to relating compositional changes over time to rates of nano- and microstructural development. Results from this research effort will provide better insights into how changes in composition and fineness affect the rates of microstructural development in cement-based materials, which can ultimately be used to assess and predict their mechanical behavior and long-term durability.

Keywords Raman spectroscopy • Portland limestone cement • Hydration • Microstructural development

1 Introduction

Portland limestone cement compositions are becoming increasingly more popular as the construction industry looks for more sustainable and more durable materials to meet its long-term performance goals. Typically, limestone cements are formed by blending or intergrinding a limestone powder (10–15 % by mass in North America) with portland cement clinker, reducing the clinker fraction of the material. However, the changes to the cement's chemical composition and physical properties (e.g., fineness and particle size distribution) that result from the limestone addition will also cause changes to the cement's hydration behavior. Limestone additions have been shown to improve particle packing (filler effect), promote heterogeneous

E.I. Nadelman • K.E. Kurtis (✉)
School of Civil and Environmental Engineering, Georgia Institute of Technology, Atlanta, GA, USA
e-mail: elizabeth.nadelman@gatech.edu; kimberly.kurtis@ce.gatech.edu

D.J. Freas
Department of Chemistry, Williams College, Williamstown, MA, USA

K. Sobolev, S.P. Shah (eds.), *Nanotechnology in Construction*,
DOI 10.1007/978-3-319-17088-6_10

nucleation of hydration products (nucleation effect), improve the efficiency of hydration at low water-to-cement ratios (dilution effect), and interact with aluminates in the clinker to form additional carboaluminate phases [1–3]. Each of these effects influences the rate of nano- and microstructural development within the hydrated cement paste, which can be further related to changes in its permeability and ultimate durability. It is therefore important to understand how changes in cement composition and fineness will affect the rate of microstructural development within these cement-based materials.

Several techniques are traditionally used to study cement hydration, including isothermal calorimetry for the study of reaction kinetics, and thermogravimetric analysis (TGA) and X-ray diffraction (XRD) for determination of chemical composition. The morphology and structure of the hydrated cement paste are often investigated separately, using electron microscopy and porosimetry techniques; however, recent studies have suggested that it may be possible to predict structurally-relevant properties (e.g., setting time) from the chemical information obtained *in situ* using spectroscopic methods such as infrared (IR) absorption and Raman spectroscopy [4]. This research effort attempts to extend the recent studies in spectroscopic techniques to the prediction of nano- and microstructural development rates, using Raman spectroscopy in conjunction with specific surface area (SSA) analysis and scanning electron microscopy (SEM). Supporting calorimetric and TGA measurements will also be performed. It is anticipated that by correlating Raman spectroscopic signatures with the morphological information obtained by SEM and SSA, a comprehensive understanding of the nano- and microstructural development can be obtained.

2 Materials and Methods

Two commercially produced cements were used to prepare cement pastes at a water-to-cement ratio of 0.40: an ASTM C150 Type I/II ordinary portland cement, and a companion ASTM C595 Type IL portland limestone cement containing approximately 12 % limestone by mass. Both cements were produced from the same clinker so that the effect of the limestone addition on early-age hydration and microstructural development could be isolated. Chemical oxide analyses determined by X-ray fluorescence (XRF) for the two cements are provided in Table 1.

Isothermal calorimetry (TAM Air, TA Instruments) was performed on 7 g of paste at 25 °C for the first 72 h of hydration. Based on the heat evolution curves collected for each cement paste, it was determined that further characterization and

Table 1 Chemical oxide composition for Type I/II and Type IL cements obtained by XRF. LOI is loss on ignition at 1,000 °C

	SiO_2	Al_2O_3	Fe_2O_3	CaO	MgO	Na_2O	K_2O	TiO_2	P_2O_5	SO_3	LOI
Type I/II	19.18	4.54	3.02	62.82	3.61	0.09	0.6	0.26	0.08	3.07	2.57
Type IL	17.13	4.16	2.86	62.05	3.12	0.07	0.48	0.26	0.06	3.31	6.33

testing would be performed on companion samples after 1, 2, 6, 12, 24, 48, and 72 h of hydration.

Raman (Thermo Almega XR MicroRaman Spectrometer) spectra were collected on paste specimens using a 488 nm excitation, over the range of 200–1,200 cm^{-1}. Specimens weighing approximately 3 g were prepared on well slides and sealed under a borosilicate cover slip to prevent loss of moisture; the same specimen was used at all ages. Spectra were obtained using 50× magnification and an exposure time of 40 s; multiple spectra were collected and averaged at each age to reduce noise. Peak assignments were based upon a review of the literature [5–7].

Any remaining cement paste not used for Raman spectroscopy (~60 g) was stored in a separate sealed container. Small fragments of material totaling less than 5 g were removed at the appropriate ages and freeze-dried for 24 h at −48 °C and 0.2 mbar. Fragments used for TGA (Hitachi EXSTAR TG/DTA 7300) were further crushed into a fine powder, and measurements were carried out on approximately 20 mg of sample at a heating rate of 10 °C/min up to 900 °C. Calcium hydroxide ($Ca(OH)_2$) and calcium carbonate ($CaCO_3$) contents were calculated at each age by the weight loss between approximately 400–450 °C and 600–750 °C, respectively; both weight loss measurements were normalized by the sample weight at 105 °C to account for differences in initial moisture content. Three replicate samples were tested at each age and averaged.

Approximately 2 g of additional fragments measuring 1–2 mm in size were isolated for future specific surface area (SSA) analysis (Micromeritics ASAP 2020) using nitrogen BET theory. The results of the SSA and SEM analyses are not presented in this paper.

3 Results and Discussion

The heat evolution curves for the two cement paste mixtures (Fig. 1) indicate an onset of acceleration beginning at approximately 1 h for both mixtures. Maximum heat flow occurs at 6 h for the Type I/II mixture (5 mW/g) and at 5 h for the Type IL

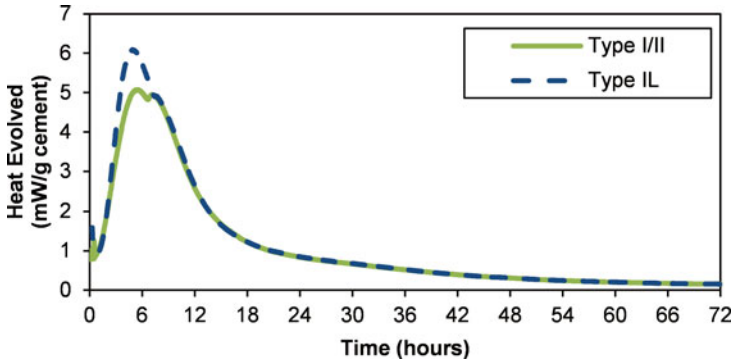

Fig. 1 Heat evolution of Type I/II (*solid line*) and Type IL (*dashed line*) cement pastes obtained by isothermal calorimetry at 25 °C

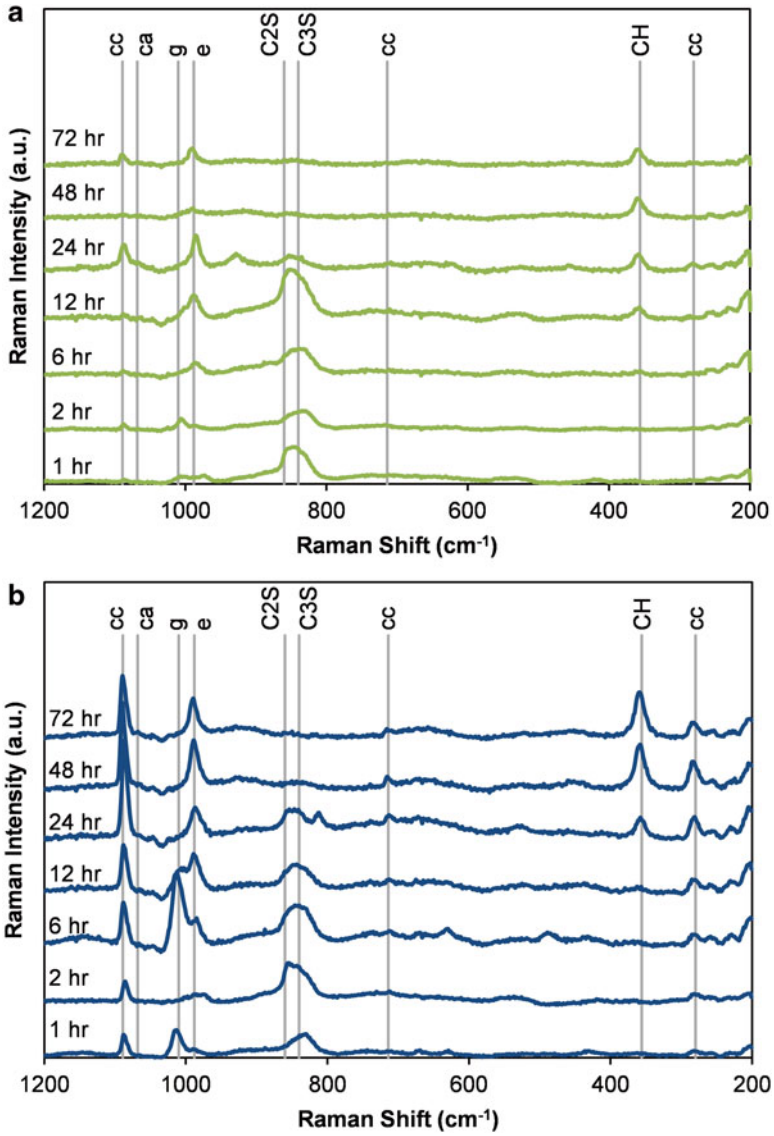

Fig. 2 Raman spectra for (**a**) Type I/II ordinary portland cement paste and (**b**) Type IL portland limestone cement paste. Raman shifts for $CaCO_3$ (*cc*), carboaluminates (*ca*), gypsum (*g*), ettringite (*e*), Ca_2SiO_4 (*C2S*), Ca_3SiO_5 (*C3S*), and $Ca(OH)_2$ (*CH*) are indicated

mixture (6 mW/g), showing an acceleration of the hydration reaction for the Type IL cement as well as an increase in heat flow. TGA results (Fig. 2) for the two pastes at 6 and 12 h reveal that this increased heat release is accompanied by a relative increase in $Ca(OH)_2$ content for the Type IL cement, leading to the conclusion that the acceleration can be attributed to the heterogeneous nucleation of hydration products on the surfaces of the limestone addition [1].

Table 2 Average calcium hydroxide and calcium carbonate contents measured by thermogravimetric mass loss for cement pastes at w/c = 0.4

	Raw (%)	6 h (%)	12 h (%)	24 h (%)	48 h (%)	72 h (%)
Type I/II – $Ca(OH)_2$	1.4	3.7	8.8	12.5	14.4	15.7
Type IL – $Ca(OH)_2$	1	4	9.6	12.4	14.2	15.6
Type I/II – $CaCO_3$	3.4	3.5	3.4	3.5	4.1	3.3
Type IL – $CaCO_3$	11.7	10.7	10.5	10.1	10.3	9.3

Little difference is observed in the heat evolution of the two cement pastes after about 8 h of hydration; however, TGA (Table 2) and Raman spectroscopy (Fig. 2) results still reveal different behaviors for the two cements after this time. It is therefore likely that after about 8 h, the nucleation effects causing an increase in hydration are offset by the dilution effects causing a decrease in hydration, producing no discernible differences between the heat evolutions, on the whole.

Changes in hydration behavior after about 8 h can be attributed primarily to the chemical interactions between the calcite ($CaCO_3$) in the limestone and the aluminate phases in the cement clinker. It can be seen from the TGA results in Table 2 that the concentration of calcite within the Type IL cement paste decreases gradually with time, from 11.7 % in the raw cement to only 9.3 % after 72 h of hydration; the calcite content of the Type I/II cement paste, meanwhile, remains nearly constant at about 3.5 %.

Accompanying this change in calcite content is the appearance of a small carboaluminate peak in the Raman spectra for the Type IL cement (Fig. 2b), beginning around 12 h of hydration and becoming more pronounced after 48 h. This peak is noticeably absent from the Raman spectra for the Type I/II cement paste (Fig. 2a), which instead shows a decrease in the intensity of the ettringite peak (~988 cm^{-1}) and a possible right-shift toward monosulfoaluminate (~982 cm^{-1}). The combined results of TGA and Raman spectroscopy, therefore, point to the conclusion that after 8 h of hydration, the influence of the limestone addition on cement hydration is primarily chemical in nature, with the $CaCO_3$ reacting with the aluminate phases in the clinker to form carboaluminate phases, rather than allowing the aluminate phases to react with the ettringite to form monosulfoaluminate [3]. Additional study of these cement paste systems through SEM and SSA analyses will yield further insights into the implications of these chemical changes as they relate to micro- and nano-structural development.

4 Conclusions

The research presented in this paper has been used to characterize the chemical evolution and hydration kinetics of ordinary and portland limestone cement pastes. Based on the results, it can be seen that fine limestone addition to ordinary portland cement accelerates hydration at early ages (<6 h) due to the increase in the surface area of the cement system and the heterogeneous nucleation of the

hydration products (especially $Ca(OH)_2$) on the surfaces of the limestone particles. Additionally, it was shown that a fraction of the calcium carbonate in the Type IL portland limestone cement is consumed during hydration, combining with the aluminate phases in the clinker to form carboaluminate hydration products after about 12 h of hydration. Finally, it was shown that Raman spectroscopy can be used for the *in situ* characterization of hydration in portland-like cement pastes, providing complementary chemical information to TGA and isothermal calorimetry.

Future work will focus on characterizing the morphological and structural changes that occur in these same cement pastes at the nano- and micro-scales, using the remaining freeze-dried cement paste specimens investigated in this work. It is anticipated that the chemical signatures obtained *in situ* using Raman spectroscopy can be related to the nano- and microstructural changes measured by specific surface area (SSA) analysis on each of the hydrating cement pastes, and that this technique can then be extended to the investigation of other cementitious binder systems.

Acknowledgements This work is based on research supported by the Georgia Department of Transportation, the National Nanotechnology Infrastructure Network, and the National Science Foundation. Any opinions, findings, and conclusions or recommendations expressed in the material are those of the authors and do not necessarily reflect the views of the supporting organizations.

References

1. Bonavetti, V., Donza, H., Menéndez, G., et al. (2003). Limestone filler cement in low w/c concrete: A rational use of energy. *Cement and Concrete Research, 33*, 865–871.
2. Bentz, D. P., & Peltz, M. A. (2008). Reducing thermal and autogenous shrinkage contributions to early-age cracking. *ACI Materials Journal, 105*(4), 414–420.
3. Lothenbach, B., Le Saout, G., Gallucci, E., & Scrivener, K. (2008). Influence of limestone on the hydration of Portland cements. *Cement and Concrete Research, 38*, 848–860.
4. Ylmén, R., Jäglid, U., Steenari, B.-M., & Panas, I. (2009). Early hydration and setting of Portland cement monitored by IR, SEM and Vicat techniques. *Cement and Concrete Research, 39*, 433–439.
5. Potgieter-Vermaak, S. S., Potgieter, J. H., & Van Grieken, R. (2006). The application of Raman spectrometry to investigate and characterize cement, part I: A review. *Cement and Concrete Research, 36*, 656–662.
6. Renaudin, G., Segni, R., Mentel, D., et al. (2007). A Raman study of the sulfated cement hydrates: Ettringite and monosulfoaluminate. *Journal of Advanced Concrete Technology, 5*, 299–312.
7. Torrens-Martin, D., Fernandez-Carrasco, L., Martinez-Ramirez, S., et al. (2013). Raman spectroscopy of anhydrous and hydrated calcium aluminates and sulfoaluminates. *Journal of the American Ceramic Society, 96*, 3589–3595.

Potential Application of Surface Enhanced Raman Spectroscopy as a Tool to Study Cementitious Materials

Chandni Balachandran, Jose F. Munoz, Terry Arnold, and Jack Youtcheff

Abstract Raman spectroscopy is a versatile tool for the study of cementitious materials due to its sensitivity to both amorphous as well as crystalline phases. However, this is not a well-established technique in cement chemistry due to fluorescence of these materials posing significant difficulties in the analysis. An alternative method to combat fluorescence, which has not yet been fully utilized in the Raman analysis of cementitious materials, is surface enhanced Raman spectroscopy (SERS). This technique involves the enhancement of the Raman signal by many orders of magnitude following the adsorption of analyte molecules on metal nanostructures. This paper discusses potential benefits of developing a technique based on SERS for concrete materials and also presents some preliminary results correlating Raman spectra with the aggregation of silver nanoparticles on samples.

Keywords Raman spectroscopy • Concrete • Surface enhanced raman scattering • Silver nanoparticles

1 Introduction

Raman spectroscopy, a versatile tool to characterize both amorphous and crystalline structures of the materials, was first applied to the characterization of cementitious materials by Bensted in 1976 [1]. Following this pioneering work, several studies exploring the use of Raman spectroscopy to characterize various anhydrous cement phases, hydration products as well as some secondary cementitious materials have been published [1, 2]. Unfortunately, the technique has been largely limited in analysis of grey cements due to the high background signal attributed to fluorescence,

C. Balachandran (✉) • J.F. Munoz
Chemistry Laboratory, SES Group & Associates LLC, Chesapeake City, MD, USA
e-mail: Chandni.balachandran.ctr@dot.gov; jose.munoz.ctr@dot.gov

T. Arnold • J. Youtcheff
Pavement and Materials Team, Turner-Fairbank Highway Research Center, McLean, VA, USA
e-mail: terry.arnold@dot.gov; jack.youtcheff@dot.gov

K. Sobolev, S.P. Shah (eds.), *Nanotechnology in Construction*,
DOI 10.1007/978-3-319-17088-6_11

which in turn obscures important spectral details [3]. This problem, coupled with the inherently poor Raman scattering of calcium silicate hydrate (C-S-H) gel, has led to Raman spectroscopy being labeled as a technique that might not be suitable for studying ordinary Portland cement (OPC) systems [3]. Previous attempts to reduce fluorescence, such as using a Raman microprobe or FT Raman with near-infrared (NIR) excitation have resulted in limited success [1, 4, 5]. Another method to combat fluorescence is surface enhanced Raman spectroscopy (SERS), an approach which has not been hitherto been fully explored when applied on cementitious materials [6].

The SERS phenomenon, first reported in 1974, involves the enhancement of Raman signal by many orders of magnitude following the adsorption of analyte molecules on plasmonic nanostructures. In SERS, the molecules of interest are in the vicinity of a nanostructured metal (Ag, Au and Cu), which results in an enhancement of their Raman signal. The enhancement produced by SERS is claimed to be due to a combination of an electromagnetic as well as a chemical interaction between the metal nanostructure and the target molecule [7].

This paper discusses the feasibility of applying SERS technique to combat fluorescence in the Raman analysis of cementitious materials. Preliminary data is provided showing the effect of aggregation of the Ag nanoparticles on the Raman spectra, resulting signal enhancement and interferences in the sample spectra.

2 Material and Methods

The silver colloid used to conduct the SERS measurements was prepared by reducing silver nitrate with sodium citrate as described by Lee and Meisel [8]. The Raman spectra were obtained using a Jasco NRS-3100 Laser Raman Spectrophotometer equipped with a 785 nm laser with power 135 mW, an Olympus BX100 microscope objective, and a CCD detector. The scanning electron microscopy (SEM) analysis was conducted using a FEI Quanta 650 microscope in secondary mode using an acceleration voltage of 5 kV. SERS measurements were obtained by depositing approximately 3 μL of the colloid on the fresh fracture surface of different cement paste samples and collecting the Raman spectra after the colloid has dried.

3 Results and Discussion

3.1 Characterization of Raman Fingerprint of Colloids

The SEM characterization of a drop of colloid deposited on an aluminum surface revealed that the Ag nanoparticles were approximately 50 nm in diameter with agglomerates of up to 100 nm in diameter. Raman measurements were conducted on the Ag colloid to clearly identify the peaks that may appear in the SERS spectra of samples which may be attributed to the colloid itself. The characteristic Raman

Table 1 Characteristic Raman bands and assignments of the silver colloid [9]

Band, cm^{-1}	532	617	691	817	937	1,059	1,330
Assignment	R	R	U	C	C/R	C	C

R rhodamine-like, *C* citrate, *U* unassigned

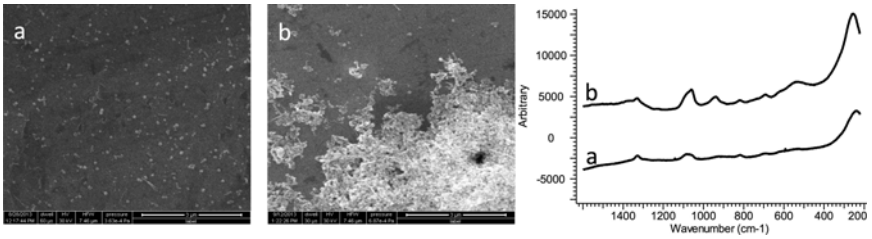

Fig. 1 Correlation between colloid deposition (SEM micrograph) and peaks in Raman spectrum of aluminum surface coated with: 2.1 g/L silver colloid and two coatings (**a**) and 8.4 g/L silver colloid and two coatings (**b**)

bands of an Ag colloid with 2.1 g/L concentration with the corresponding assignments are summarized in Table 1.

3.2 Influence of Nanoparticle Deposition in Raman Signal

The main advantage of using SERS-activated nanospheres for enhanced Raman characterization of cementitious materials resides in the simplicity of the synthesis process and possibility to produce size-controlled nanoparticles. The SERS effect is highly dependent on the size, shape and aggregation of the nanospheres. For this study, the nanospheres were obtained as colloids by the reduction of the metal salt with reducing and stabilizing agents. The SERS-active spots are normally localized in the interface between the metallic nanospheres. In this SERS hot spot, besides the sample of interest, reducing agents from the synthesis process can also be present. This fact, coupled with the difficulties of achieving the optimal aggregation when applying the colloids as films over solid samples, can lead to uncontrolled changes in the intensity of the SERS effect.

The following experiment was designed to study the aggregation effect in the SERS spectra. Colloids of variable concentrations were applied over an aluminum surface using a dip-coating approach. SEM micrographs along with Raman spectra were collected from the coated aluminum surfaces. The results are illustrated in Fig. 1. As the concentration of colloid increased, the level of aggregation of the silver nanoparticles as well as the intensity of a group of bands in the Raman spectra also increased. The observed bands are listed with relevant band assignments in Table 1. The results from this experiment clearly illustrate how deposition of excess of colloid during SERS application would bring up inherent peaks from the nanoparticles, which could potentially complicate the identification of peaks from the sample.

3.3 Application of SERS on Cementitious Materials: Preliminary Results and Challenges

A set of experiments was conducted to investigate the possibility of applying SERS on OPC paste samples, determine the nature of the peaks generated and highlight the potential overlap between bands from the Ag colloid as well as spectral regions of interest for C-S-H and other common OPC hydration products. The major observations from these experiments have been described in the following sections with the help of selected examples.

3.3.1 SERS Enhancement

The SERS spectra of the various samples indicated that that this technique did indeed appear to aid in combating the undesired fluorescence associated with the cementitious materials. Figure 2 shows the normal dispersive Raman spectrum (2a) as well as the SERS spectrum (2b) of a sample of OPC cement paste after 7 days of hydration. It is clearly evident from the SERS spectrum that the intensity of the Raman signal has been greatly enhanced, thus allowing more spectral detail to be visible over the broad fluorescent signal observed in the same region in the normal Raman spectrum. The regions R1, R2, R3, and R4 shown in Fig. 2b are the major spectral regions of interest for cement paste with the corresponding assignments summarized in Table 2. As is evident from Fig. 2b, the new peaks in the SERS spectrum of the cement paste appear, to a large extent, in expected positions.

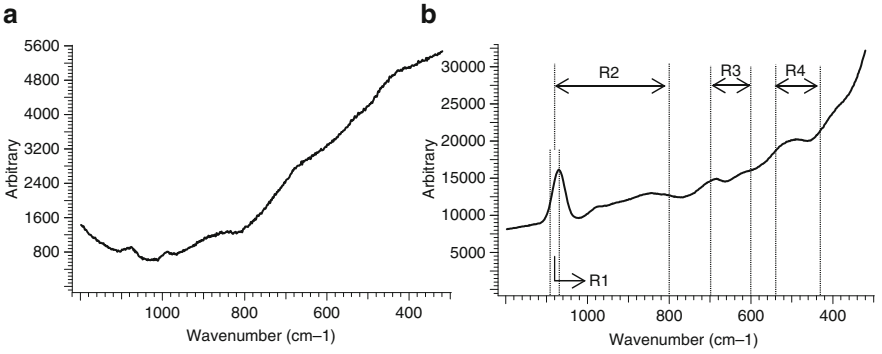

Fig. 2 Normal dispersive Raman spectrum of OPC (water to cement ratio = 0.45) after 7 days of hydration (**a**) and SERS spectrum after colloid application (Ag colloid-16.8 g/L concentration) (**b**)

Table 2 Characteristic Raman bands [10, 11]

Region, cm^{-1}	R1 (1090–1076)	R2 (1080–800)	R3 (600–700)	R4 (430–540)
Assignment	ν_1 CO_3	SS SiT/Si-O(H)/ ν_1 SO_4	SB Si-O-Si linkages	Internal deformations of SiT

SS symmetric stretching, *SB* symmetric bending, *SiT-SiO$_4$* tetrahedra

3.3.2 Verification of Raman Peaks

The spectra of various samples were collected at two different excitation wavelengths namely 785 nm and 532 nm. It was found that the laser wavelength did not affect the position of the bands in all of the samples tested thus ensuring that the peaks generated are entirely due to the Raman effect [5].

3.3.3 Spectral Interference of Colloids

While the SERS technique seems promising, it is essential that the SERS spectrum is interpreted with utmost care. The deposition of the Ag colloid on the sample may cause some spectral interference and may also induce some shifts in the actual peaks of the sample. Figure 3 shows the specific portion of the colloid spectrum, which may interfere with the sample spectra. Also displayed in Fig. 3 and described in Table 2 are the assignments for the spectral regions of interest where one might expect the vibrational bands of the cementitious systems to appear. It is evident from Fig. 3 that the Raman signal in the carbonate stretching vibration regions as well as the silicate stretching and bending vibration regions in R1, R2 and R3 respectively, in the sample spectra could have potential contributions from the Ag colloid. However, there are areas in the silicate stretching region between 1,000 and 970 cm^{-1} and 920–830 cm^{-1} which are devoid of any contribution from the colloid and Raman signal in these areas, if present, would easily be visible in the SERS spectra of the samples.

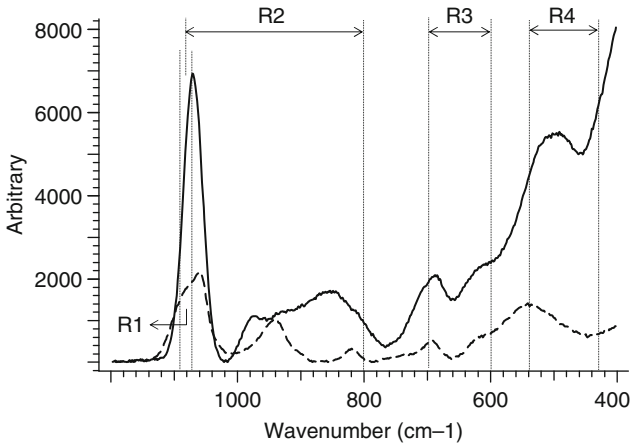

Fig. 3 Spectral interference from colloid (*dashed line*) on SERS spectrum of 7 days old hydrated cement paste (water to cement ratio = 0.45) with colloid. Ag colloid-16.8 g/L concentration

4 Conclusions

The application of SERS was found to successfully reduce fluorescence and increase intensity of Raman spectra of OPC samples. The enhanced peaks were confirmed to be true peaks, as was confirmed using two different laser wavelengths. The study revealed that certain areas in the carbonate stretching, silicate stretching and bending vibration regions of the spectra of cementitious materials had contribution from Ag nanoparticles. It appears that the peaks due to the colloid maybe related to the agglomeration of Ag nanoparticles on the sample surface. In conclusion, preliminary results suggest that, despite certain challenges, there is great potential for successfully developing a SERS technique for analyzing cementitious materials. If successful, this technique could be a powerful tool to understand the structure of the amorphous phases in cementitious materials.

References

1. Potgieter-Vermaak, S. S., Potgieter, J. H., & Van Grieken, R. (2006). The application of Raman spectrometry to investigate and characterize cement, part I: A review. *Cement and Concrete Research, 36*(4), 656–662.
2. Potgieter-Vermaak, S. S., Potgieter, J. H., Belleil, M., DeWeerdt, F., & Van Grieken, R. (2006). The application of Raman spectrometry to the investigation of cement: part II: A micro-Raman study of OPC, slag and fly ash. *Cement and Concrete Research, 36*(4), 663–670.
3. Richardson, I. G., Skibsted, J., Black, L., & Kirkpatrick, R. J. (2010). Characterisation of cement hydrate phases by TEM, NMR and Raman spectroscopy. *Advances in Cement Research, 22*(4), 233–248.
4. Conjeaud, M., & Boyer, H. (1980). Some possibilities of Raman microprobe in cement chemistry. *Cement and Concrete Research, 10*(1), 61–70.
5. Newman, S. P., Clifford, S. J., Coveney, P. V., Gupta, V., Blanchard, J. D., Serafin, F., Ben-Amotz, D., & Diamond, S. (2005). Anomalous fluorescence in near-infrared Raman spectroscopy of cementitious materials. *Cement and Concrete Research, 35*(8), 1620–1628.
6. Ebbert, C., Grundmeier, G., Buitkamp, N., Kroger, A., Messerschmidt, F., & Thissen, P. (2014). Towards a microscopic understanding of the calcium-silicate-hydrates/water interface. *Applied Surface Science, 290*, 207–214.
7. Kumar, G. P. (2012). Plasmonic nano-architectures for surface enhanced Raman scattering: a review. *Journal of Nanophotonics, 6*(1), 064503–1.
8. Lee, P. C., & Meisel, D. (1982). Adsorption and surface-enhanced Raman of dyes on silver and gold sols. *The Journal of Physical Chemistry, 86*(17), 3391–3395.
9. Sánchez-Cortés, S., & García-Ramos, J. V. (1998). Anomalous Raman bands appearing in surface-enhanced Raman spectra. *Journal of Raman Spectroscopy, 29*(5), 365–371.
10. Kirkpatrick, R. J., Yarger, J. L., McMillan, P. F., Ping, Y., & Cong, X. (1997). Raman spectroscopy of CSH, tobermorite, and jennite. *Advanced Cement Based Materials, 5*(3), 93–99.
11. Black, L., Breen, C., Yarwood, J., Garbev, K., Stemmermann, P., & Gasharova, B. (2007). Structural features of C–S–H (I) and its carbonation in air—A Raman spectroscopic study. Part II: carbonated phases. *Journal of the American Ceramic Society, 90*(3), 908–917.

Polymorphism and Its Implications on Structure-Property Correlation in Calcium-Silicate-Hydrates

Mohammad Javad Abdolhosseini Qomi, Mathieu Bauchy, Franz-Josef Ulm, and Roland Pellenq

Abstract Albeit concrete's ubiquitous presence in our built environment, our knowledge of elementary processes affecting its macroscopic properties is rather limited. To achieve deeper levels of understanding, it is imperative to uncover the true molecular structure of calcium-silicate-hydrates (C-S-H), the binding phase of cement paste responsible for its strength and durability properties. In this work, we discuss the co-existence of C-S-Hs of different molecular structures at a given stoichiometry from the viewpoints of the atomistic simulations. To this end, we propose a statistical physics-based approach to construct realistic models for C-S-H. Subsequently, we employ high-throughput combinatorial simulation framework to construct a database of realistic C-S-H models with calcium-to-silicon ratio (C/S) between 1.1 and 2.1. This finding has broad implications on the correlation between chemistry and physical properties of cementitious materials.

Keywords CSH nano texture • Molecular simulation • Free energy • Mechanical properties

M.J.A. Qomi
Department of Civil and Environmental Engineering, Massachusetts Institute of Technology, 77 Massachusetts Avenue, Cambridge, MA 02139, USA

M. Bauchy
<MSE>2 MIT-CNRS Joint Laboratory, Massachusetts Institute of Technology, 77 Massachusetts Avenue, Cambridge, MA 02139, USA

Department of Civil and Environmental Engineering, University of California, Los Angeles, CA 90095, USA

F.-J. Ulm
<MSE>2 MIT-CNRS Joint Laboratory, Massachusetts Institute of Technology, 77 Massachusetts Avenue, Cambridge, MA 02139, USA

R. Pellenq (✉)
<MSE>2 MIT-CNRS Joint Laboratory, Massachusetts Institute of Technology, 77 Massachusetts Avenue, Cambridge, MA 02139, USA

Centre Interdisciplinaire des Nanosciences de Marseille, CNRS and AIX-Marseille Université, Campus de Luminy, Marseille 13288, France
e-mail: pellenq@mit.edu

K. Sobolev, S.P. Shah (eds.), *Nanotechnology in Construction*,
DOI 10.1007/978-3-319-17088-6_12

1 Introduction

Concrete is the most used man-made material on Earth with an average consumption rate of one cubic meter per capita per annum and is solely responsible for 5–7 % of global CO_2 emissions. To cope with negative environmental impacts of concrete, myriad of multi-disciplinary research efforts have been carried out to optimize the chemistry of cement paste to achieve enhanced physical properties.

These studies investigate the effect of clinker chemistry modification [1] or the role of additives such as alkali-activated slag, fly ash, nano- and micro-silica on the physical properties and durability of hardened cement paste [2]. The routine approach is to embark on an expensive (both time consuming and capital intensive) and daunting laboratory experimental program to find the suitable material, its proper mass fractions and associated curing conditions. However, the main drawback of this approach is that it is subjected to significant degrees of uncertainty related to materials and testing conditions. This leads to contradictory observations for similar situations, which makes it quite challenging to reconcile these observations based on limited available data.

These complexities highlight the role of alternative approaches such as computational physical chemistry in providing a universal model for chemistry-property correlations in the broad family of cementitious binders [3]. The main concern then would be whether chemistry uniquely defines the state of a material. In fact, there are plenty of counter examples in nature that indicates chemistry is not solely enough to uniquely characterize a material. The most famous examples of which are silica glass and quartz or graphite and diamond. In physical chemistry, such group of materials with the same stoichiometry but different molecular structures is called “polymorph”. After many decades of research, the molecular structures of C-S-H are just recently coming to the picture [4–8]. Then, it would be imperative to explore the possibility of polymorphism in C-S-H. This motivates us to dedicate this work to the molecular origins of polymorphism in C-S-H via tools of computational physics. The paper is organized as follows. First, we present a systematic way to construct C-S-H models. Subsequently, we discuss the theoretical backgrounds for the calculation of elastic properties from the curvature of potential energy landscape and free energy content from the vibrational density of states. The next section discusses the evidences and consequences of polymorphism in C-S-H based on free energy arguments. Finally, our conclusive remarks close the paper.

2 Constructing Realistic C-S-H Models

The computational strategy exploited here aims at varying C/S systematically and explores resulting properties. This approach is combination of several classical atomistic simulation techniques. These techniques are deployed at different stages

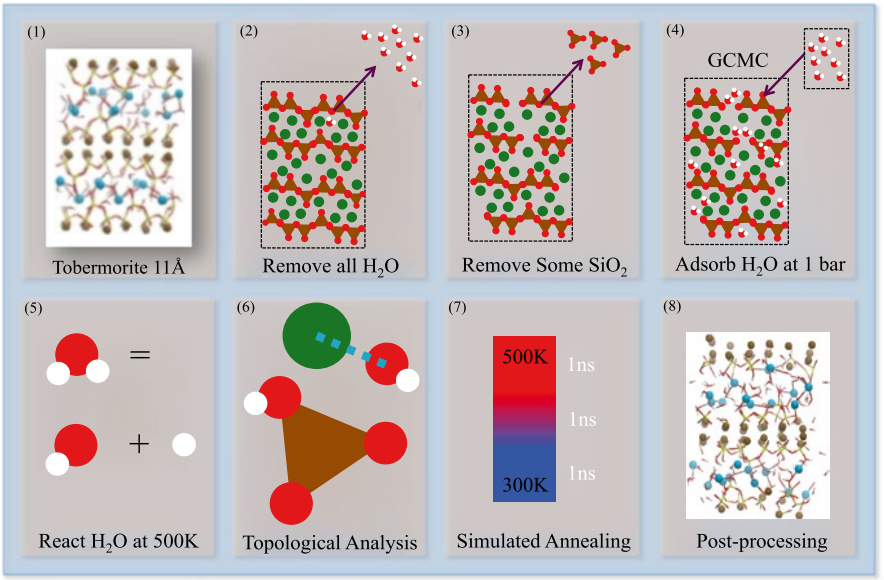

Fig. 1 The eight stages required to produce a database of realistic C-S-H models. A set of 150 C-S-H models is constructed with Ca/Si ratio ranging from 1.1 to 2.1

of model preparation. These atomistic simulation methods have classical nature and are performed using ReaxFF [9] and CSH-FF [10] potentials. As schematically presented in Fig. 1, there are eight explicit stages to construct a realistic molecular structure of C-S-H. To eliminate the finite size effect in computational modeling, we employ a 3*3*2 super-cell of the molecular structure of Tobermorite 11 Å Hamid [11]. The crystalline 11 Å Tobermorite has no hydroxyl groups and the length of its silica chains is infinite. In the second step, the entire water molecules are removed from the interlayer spacing. To increase C/S in the third stage, 150 numerical models are constructed by randomly cutting the silica chains (removing charge-neutral SiO_2 groups). This provides a wide range of C/S to investigate the effect of stoichiometry and polymorphism on physical properties of C-S-H. At this stage, first the interlayer calcium atoms and subsequently all the rest of atoms and cell dimensions are relaxed using energy minimization at 0 K. In the next stage, water molecules are adsorbed back to the interlayer spacing and nano-voids created by removing SiO_2 groups using the Grand Canonical Monte Carlo simulation. At this point, the interlayer water is reacted at 500 K with the defective calcium-silicate backbone of C-S-H using ReaxFF potential. In this stage, part of the interlayer water dissociates in to hydroxyl groups and proton [12]. Minor condensations of silica chains are also observed in some samples. In the sixth stage, a comprehensive topological analysis is performed to identify the local environment of each atom. This facilitates the transfer of model from reactive environments provided via ReaxFF potential to non-reactive environment in CSH-FF. In stage 7, a 3 ns

long simulated annealing is performed on each individual sample to reduce the temperature from 500 to 300 K at ambient pressure. Finally, the samples are relaxed and proper sampling of energy space is performed to measure elastic properties, hardness and free energy.

3 Elastic Properties of C-S-H at the Nanoscale

After the simulated annealing stage (stage 7 in Fig. 1), all models are further relaxed for 1 ns. Subsequently, 10 statistically independent frames are consecutively extracted from MD trajectories each 100 ps apart. This procedure is strictly followed to ensure proper unbiased statistics for each sample. Afterwards, all samples are relaxed via energy minimization at constant volume (CONV) with rational functional optimization (RFO) module for residuals less than 10^{-3} [13, 14]. This ensures that the Hessian matrix is positive definite to ensure convexity of the energy minima and to properly discard saddle points. We further relax all C-S-H models via energy minimization at constant pressure (CONP) with RFO option. We ensure that all available degrees of freedom, including atomic positions and unit cells, are properly relaxed. Afterward, the elastic properties are calculated for all models. The stiffness tensor, C_{ijkl} in tensor notation and C_{ij} in Voigt notation, is subsequently calculated from the analytical second derivative of the energy density via:

$$C_{ijkl} = \frac{1}{V}\left(\frac{\partial^2 E}{\partial \varepsilon_{ij} \partial \varepsilon_{kl}}\right) \tag{1}$$

where E and V are respectively internal energy and unit cell volume and ϵ_{ij} is the strain tensor. It should be noted that positive-definiteness of Hessian matrix entails positive-definiteness of the stiffness tensor. A wide range of elastic constants can be calculated from stiffness and compliance ($S = C^{-1}$) tensors. Two of the commonly used isotropic measures of the stiffness are bulk (K) and shear (G) moduli. The Voight-Reuss-Hill bounds of bulk and shear modulus are given in [7]. The Hill bounds or Voight-Reuss-Hill bounds are simply the average of Voigt and Reuss bounds [14]. These bounds are isotropic descriptions of a generally anisotropic medium. A wide range of materials in nature including clay [15] and Tobermorite minerals [2] exhibit anisotropic elastic properties. There are several approaches to quantify such anisotropy, the simplest of which is through the stiffness under uniaxial tension or the so-called Young's Modulus ($Y_i = d\sigma_{ii} / d\varepsilon_{ii}$). In anisotropic materials, the Young's Modulus depends on the direction of the applied strain field.

Figure 2 presents the change in elastic properties including bulk (Fig. 2a) and shear (Fig. 2b) moduli and Young's moduli parallel (Fig. 2c) and perpendicular (Fig. 2d) to the calcium-silicate lamellar sheets with respect to C/S ratio. Generally, these properties decrease with increasing C/S ratio. This decrease reflects the impact

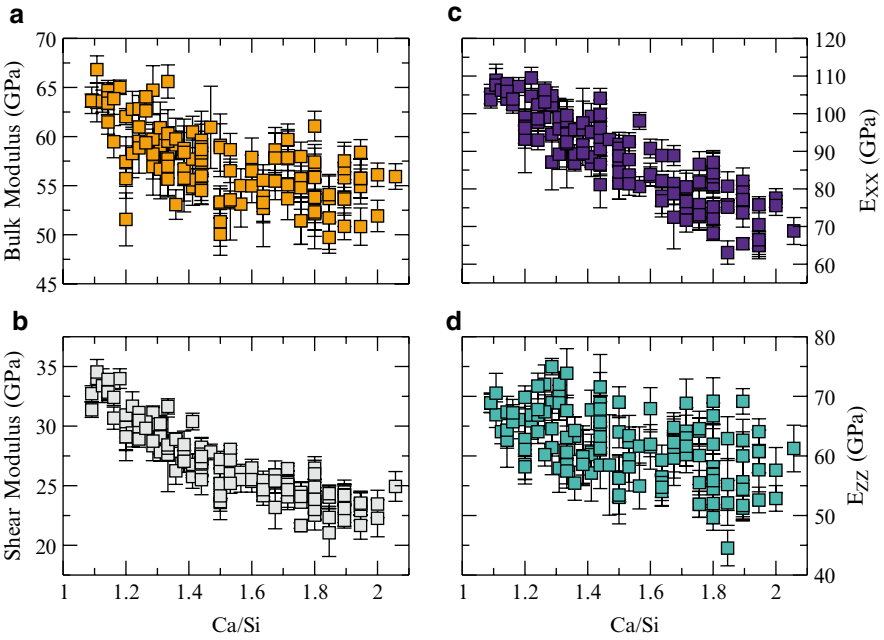

Fig. 2 Calculation of elastic properties in atomistic simulations by analytical calculation of the second derivative of energy landscape. This includes Voigt-Reuss-Hill bounds of (**a**) bulk and (**b**) Shear moduli and Young Moduli (**c**) parallel and (**d**) perpendicular to C-S-H's calcium-silicate sheets

of defects on the mechanical properties of CSH. In fact, accumulation of defects (SiO_2 vacancies) significantly reduces the rigidity of calcium-silicate sheets. This effect is well pronounced in bulk shear moduli and Young's moduli parallel to calcium-silicate layers. However, it is puzzling that Young's modulus perpendicular to layers is less affected by the presence of defects. This is in parts associated with the ionic nature of inter-plane interactions between adjacent calcium-silicate sheets. These ionic interactions depend on the electronegativity of calcium-silicate sheets characterized by their net charge per surface, which remains the same with increasing C/S. The interlayer water content also affects the inter-plane interactions by screening long-range Coulombic interactions. We recently demonstrated that the interlayer water content increases linearly with increasing C/S in agreement with elastic neutron scattering and drying experiments. This explains why increasing C/S entails a slight decrease in E_{ZZ}. The other perplexing nuance embedded in the variation of the elastic properties with C/S is that there is a range of possible properties for a given family of C-S-H models at a constant stoichiometry. This family of C-S-H model has the same C/S ratio but varies in the arrangement of SiO_2 vacancies within their calcium-silicate sheets. Therefore, our findings based on the results in Fig. 2 assert that the arrangement of defects within the molecular structure of C-S-H

affects its mechanical properties. Then, it would be imperative to investigate the impact of defect arrangement on the free energy content of C-S-H molecular structures. This would ultimately determine which molecular structure (defect arrangement) would be energetically more favorable.

4 Free Energy Calculations in Atomistic Simulations

Atoms in solids constantly oscillate around their equilibrium position at finite temperatures. At low temperatures, these oscillations can be decomposed to a linear superposition of vibrational modes known as '*phonons*'. In the case of infinite 3D solids, there are infinite numbers of phonons. The phonons are characterized by their values at a point in the reciprocal space, usually called k-point, within the first Brillouin zone. Hence, there are 3 N phonons per k-point where N is the number of atoms in the unit cell. Identification of phonons in a 3D periodic solid involves numerical calculation of the eigenvalues of dynamical matrix at each k-point:

$$D_{i\alpha j\beta} = \frac{1}{\sqrt{m_i m_j}} \sum_R \left(\frac{\partial^2 U}{\partial\alpha\,\partial\beta} \right) \exp\left(ik\left(r_{ij} + R \right) \right) \tag{2}$$

where m is the mass of atom, i and j indices denote two arbitrary atoms within the cut-off radius, α and β show the components in the real space, k is the reciprocal vector and R represents the sum over lattice vectors within the cut-off radius. Having phonons in hand, statistical mechanics can be employed as a powerful tool to bridge microscopic energy levels to macroscopic thermodynamical observables such as entropy, Helmholtz and Gibbs free energies and many others. The assumption in molecular physics is that all forms of the energy are independent and as a result the total energy can be decomposed to translational, rotational, vibrational and the contributions to the electronic state of the system. In the special case of solids at low temperatures (considerably below the melting point), the rotational and translational contributions can be neglected. In atomistic simulations, the electronic contribution is directly calculated via interatomic force field. Therefore, the challenge simplifies to the measurement of vibrational contributions. This is achieved via calculation of partition function, Z_{vib}, in the framework of lattice harmonic approximation. The vibrational energy level for a harmonic oscillator of the mth mode can be written as

$$U_{vib}^{m}\left(n,k \right) = \left(n + \frac{1}{2} \right) h\omega\left(m,k \right) \tag{3}$$

where n is the number of phonons occupying that particular energy level and h is Plank's constant. The number of phonons occupying an energy state is given by Bose-Einstein statistics:

$$n = \frac{1}{\exp\left(-\frac{h\omega}{k_B T}\right) - 1} \tag{4}$$

where T is the temperature and k_B is Boltzmann constant. The internal vibrational energy, U_{vib} can be written as the superposition of all the energy levels by considering that the energy at each state is the number of phonons occupying that state times the energy of each phonon:

$$U_{vib} = \sum_m \sum_k w_k \left(\frac{1}{2} h\omega + \frac{h\omega}{\exp\left(-\frac{h\omega}{k_B T}\right) - 1} \right) \tag{5}$$

where w_k represents the weight of a particular point in the Brillouin zone noting that the sum of the weights equal one. To calculate the internal energy, the summation should be over all oscillation modes, m, and reciprocal lattice vectors, k. The fist term in the internal energy is just due to zero point vibrational energy. The partition function in canonical ensemble can be written as:

$$Z_{vib} = \sum_m \sum_k w_k \frac{\exp\left(-\frac{h\omega}{k_B T}\right)}{\exp\left(-\frac{h\omega}{k_B T}\right) - 1} \tag{6}$$

It should be emphasized that the frequencies are explicit function of k and m, which are omitted from the above equation for brevity. The Helmholtz free energy, Ψ_{vib}, and Gibbs free energy, L_{vib}, are readily calculated using:

$$\Psi_{vib} = \sum_m \sum_k w_k \left(\frac{1}{2} h\omega + \ln\left(1 - \exp\left(-\frac{h\omega}{k_B T}\right)\right)\right) \tag{7}$$

$$L_{vib} = \Psi_{vib} + PV \tag{8}$$

where P and V are respectively the pressure and volume of the unit cell. In practice, the above double summation is reduced to integration over the phonon density of states (DOS). Generally, the integration involves a numerical scheme over a discrete set of points. Due to the lack of symmetry in C-S-H's molecular structures, the most general set of points in the first Brillouin zone known as Monkhorst-Pack scheme is used in this work. A set of 1,099 evenly spaced mesh of k-points, given by shrinking factors along each axis in reciprocal space, is adopted in all the simulations. Subsequently, the DOS is distributed over 60 equal bins and all the thermodynamic observables are calculated following the above-mentioned procedure.

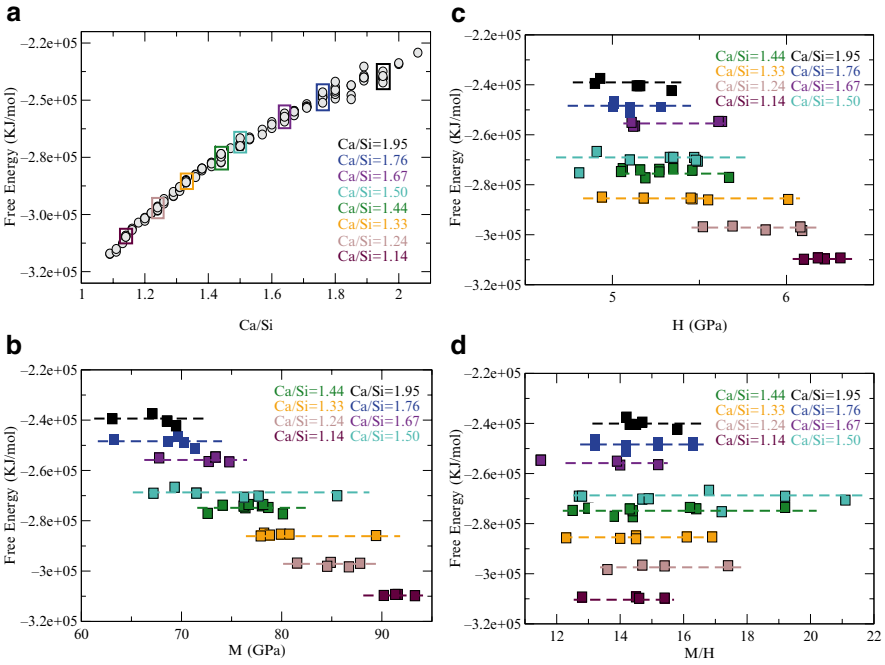

Fig. 3 The free energy content and its correlation with mechanical properties in C-S-H. (**a**) The free energy as a function of C/S. This can be expressed in terms of correlations between free energy and mechanical responses (**b**) M, (**c**) H and (**d**) M/H of C-S-H

5 Implications of Polymorphism in C-S-H

To rigorously study energetics of defect distributions, thermodynamics argument are required to assess the existence C-S-Hs of different molecular structure at equilibrium for a given stoichiometry. This is achieved via detailed analysis of free energy content in C-S-H models. Figure 3a presents the free energy content of C-S-H as a function of C/S. The free energy content is strongly correlated to and decreases with increasing C/S. Unlike the variations of free energy with respect to C/S, the free energy content of C-S-H models at a given C/S ratio is relatively constant. This mean that the free energy difference between two C-S-H configurations is smaller that k_BT, meaning these structures are rather energetically equi-probable. Therefore, C-S-H's of varying defect organization would coexist at equilibrium. A family of C-S-H molecular structures with identical stoichiometry and free energy content is called C-S-H polymorphs. Since C-S-H polymorphs are energetically competitive, then the only way to access different polymorphs are through kinetics (here being curing conditions for synthesis of cementitious materials).

Besides the above free energy arguments from this work, there are numerous compelling experimental results [7, 16, 17] suggesting that C-S-H at nano-scale can

have different molecular structures. NMR experiments of Chen et al. [17] suggest that C-S-H at a given stoichiometry could have different MCL. Elastic neutron scattering experiment of [16] implies that C-S-H at a known stoichiometry can have different water contents. Recently, we showed that coupled chemo-mechanical analysis via X-ray wavelength dispersive spectroscopy and nano-indentation indicates that the solid C-S-H phase at a given stoichiometry can have different mechanical properties [7]. Also as we discussed earlier, calculations of elastic and hardness properties point out that mechanical properties of C-S-H structures are not a single value for a given Ca/Si ratio. Rather, a range can exist at fixed chemical composition, so that it is expected for different studies of composition-dependent mechanical property investigations to reach different conclusions. As can be seen in Fig. 3b–d for indentation modulus, hardness and their ratios respectively, at a given free energy level, C-S-H polymorphs can have a range of mechanical properties. The hardness is calculated via bimodal deformation technique as extensively described in the following references [7, 18–20]. Therefore, polymorphism in C-S-H not only means structural differences in the molecular structure of C-S-H, but also entails statistically significant differences between their mechanical properties. Therefore, polymorphism implies that the pathway to obtain C-S-H structures with enhanced mechanical properties at a given C/S is through kinetics of reaction and precipitation.

6 Conclusions

In this work, we studied polymorphism in the molecular structure of C-S-H via tools of statistical mechanics. To this end, we introduced the notion of high-throughput combinatorial modeling to construct a realistic database of C-S-H models with varying C/S ratio. We used this database to study the effect of C/S ratio on physical properties of C-S-H including elastic constants and free energy contents. We provided strong thermodynamical arguments using free energy calculations to support the existence and stability of C-S-H of varying molecular structures at a given C/S ratio. It appears that the arrangement of SiO_2 vacancies in calcium-silicate sheets of C-S-H does not affect the free energy drastically. This means that families of C-S-H molecular structures are naturally energetically competitive meaning that they can coexist in nature. This finding has broad implications on structure-property correlation in cementitious materials.

References

1. Manzano, H., et al. (2011). Impact of chemical impurities on the crystalline cement clinker phases determined by atomistic simulations. *Crystal Growth and Design, 11*(7), 2964–2972.
2. Abdolhosseini Qomi, M. J., Ulm, F.-J., & Pellenq, R. J.-M. (2012). Evidence on the dual nature of aluminum in the calcium-silicate-hydrates based on atomistic simulations. *Journal of the American Ceramics Society, 95*(3), 1128–1137.

3. Bauchy, M., Abdolhosseini Qomi, M. J., Bichara, C., Ulm, F.-J., & Pellenq, R. J.-M. (2014). Nanoscale structure of cement: Viewpoint of rigidity theory. *The Journal of Physical Chemistry C, 118*(23), 12485–12493.
4. Richardson, I. G. (2008). The calcium silicate hydrates. *Cement and Concrete Research, 38*(2), 137–158.
5. Pellenq, R. J.-M., et al. (2009). A realistic molecular model of cement hydrates. *Proceedings of the National Academy of Sciences, 106*(38), 16102–16107.
6. Manzano, H., Dolado, J. S., & Ayuela, A. (2009). Elastic properties of the main species present in Portland cement pastes. *Acta Materialia, 57*(5), 1666–1674.
7. Abdolhosseini Qomi, M. J. et al. (2014) Combinatorial molecular optimization of cement hydrates. *Nature Communications, 5*, 4960. doi:10.1038/ncomms5960. Available at: http://www.nature.com/ncomms/2014/140924/ncomms5960/full/ncomms5960.html. Accessed 24 Sept 2014.
8. Bauchy, M., Qomi, M. J. A., Ulm, F.-J., & Pellenq, R. J.-M. (2014). Order and disorder in calcium–silicate–hydrate. *The Journal of Chemical Physics, 140*(21), 214503.
9. Manzano, H., Pellenq, R. J. M., Ulm, F.-J., Buehler, M. J., & van Duin, A. C. T. (2012). Hydration of calcium oxide surface predicted by reactive force field molecular dynamics. *Langmuir, 28*(9), 4187–4197.
10. Shahsavari, R., Pellenq, R. J.-M., & Ulm, F.-J. (2011). Empirical force fields for complex hydrated calcio-silicate layered materials. *Physical Chemistry Chemical Physics: PCCP, 13*(3), 1002–1011.
11. Hamid, S. (1981). The crystal-structure of the 11 A natural tobermorite $Ca_{2.25}[Si_3O_{7.5}(OH)_{1.5}].1H_2O$. *Zeitschrift für Kristallographie, 154*(3–4), 189–198.
12. Qomi, M. J. A., Bauchy, M., Ulm, F.-J., & Pellenq, R. J.-M. (2014). Anomalous composition-dependent dynamics of nanoconfined water in the interlayer of disordered calcium-silicates. *The Journal of Chemical Physics, 140*(5), 054515.
13. Gale, J. D. (1997). GULP: A computer program for the symmetry-adapted simulation of solids. *Journal of the Chemical Society, Faraday Transactions, 93*(4), 629–637.
14. Gale, J. D., & Rohl, A. L. (2003). The General Utility Lattice Program (GULP). *Molecular Simulation, 29*(5), 291–341.
15. Ebrahimi, D., Pellenq, R. J.-M., & Whittle, A. J. (2012). Nanoscale elastic properties of montmorillonite upon water adsorption. *Langmuir, 28*(49), 16855–16863.
16. Allen, A. J., Thomas, J. J., & Jennings, H. M. (2007). Composition and density of nanoscale calcium–silicate–hydrate in cement. *Nature Materials, 6*(4), 311–316.
17. Chen, J. J., Thomas, J. J., Taylor, H. F. W., & Jennings, H. M. (2004). Solubility and structure of calcium silicate hydrate. *Cement and Concrete Research, 34*(9), 1499–1519.
18. Aghaei, A., Abdolhosseini Qomi, M. J., Kazemi, M. T., & Khoei, A. R. (2009). Stability and size-dependency of Cauchy–Born hypothesis in three-dimensional applications. *International Journal of Solids and Structures, 46*(9), 1925–1936.
19. Khoei, A. R., Qomi, M. J. A., Kazemi, M. T., & Aghaei, A. (2009). An investigation on the validity of Cauchy–Born hypothesis using Sutton-Chen many-body potential. *Computational Materials Science, 44*(3), 999–1006.
20. Khoei, A. R., Ghahremani, P., Abdolhosseini Qomi, M. J., & Banihashemi, P. (2011). Stability and size-dependency of temperature-related Cauchy–Born hypothesis. *Computational Materials Science, 50*(5), 1731–1743.

Correlating Mechanical Properties and C-S-H Polymerization of Hardened Cement Paste Cured Under High Temperature and Pressure

Jung J. Kim, Kwang-Soo Youm, Kwang-Seok Chae, and Mahmoud Reda Taha

Abstract Cement paste specimens made from Type G oil well cement (OWC) and Type II ordinary Portland cement (OPC) are prepared using 0.45 water to cement ratio (w/c). The specimens were then hydrated under two curing conditions; room condition (20 °C with 0.1 MPa pressure) and an elevated condition (80 °C with 10 MPa pressure) for 28 days. The compressive strength of the hydrated cement pastes was measured using ϕ 30 mm diameter ×60 mm height cylinders. The calcium silicate hydrates (C-S-H) polymerization of the hydrated cement pastes was investigated using ^{29}Si MAS nuclear magnetic resonance (NMR) measurements. The correlation between the compressive strength of the cement paste and C-S-H polymerization was confirmed and discussed in light of basic C-S-H unit polymerization and the gel-space ratio.

Keywords Nanosilica • Cement polymerization • High temperature and pressure

1 Introduction

Compressive strength development with time is an important mechanical property of cementitious materials. The gel-space ratio concept, proposed by Powers and Brownyard [1], has been widely used to describe compressive strength development, where 'gel' includes all hydration products of cement and 'space' describes the voids in the hydrated cement. Calcium silicate hydrates (C-S-H) is known as the

J.J. Kim
Department of Civil Engineering, Kyungnam University, Changwon-si, South Korea

K.-S. Youm
GS E & C Infrastructure Team, Seoul, South Korea

K.-S. Chae
GS E & C Civil Offshore Research Team, Seoul, South Korea

M.R. Taha (✉)
Department of Civil Engineering, University of New Mexico, Albuquerque, NM, USA
e-mail: mrtaha@unm.edu

K. Sobolev, S.P. Shah (eds.), *Nanotechnology in Construction*,
DOI 10.1007/978-3-319-17088-6_13

major hydration product making up to 67 % of the hydration products of ordinary Portland cement (OPC) paste [2]. Therefore, C-S-H plays the most important role in developing the mechanical properties of hydrated cement. Moreover, most of the time-dependent mechanical properties of hydrated cement are believed to be controlled by C-S-H [3–5]. The structure of C-S-H was revealed as layered calcium silicate sheets bound by water molecules after Feldman-Sereda's model [6]. C-S-H structure was also interpreted as high density or low density structures of globules which consist of 'basic unit' having layered C-S-H [4]. In this study, an experimental investigation was conducted to correlate the compressive strength of cement pastes and C-S-H polymerization under elevated curing temperature and pressure. OPC and OWC pastes made with two curing conditions: room condition an elevated temperature and pressure condition. The compressive strength was determined and ^{29}Si nuclear magnetic resonance (NMR) measurements were performed to quantify C-S-H polymerization in the hydrated cement pastes.

2 Experimental Study

2.1 Materials and Curing Conditions

Type II OPC, known as low temperature and sulfate resistance cement [7], and Type G OWC [8] were used in the investigation. A w/c ratio of 0.45 was used for all specimens. Two types of cylinders: ϕ 10 mm × 10 mm height used for NMR measurements and ϕ 30 mm × 60 mm height specimens used for determining the compressive strength of cement paste. The two types of specimens were prepared for each type of cement and different curing conditions. The procedures for mixing hydraulic cement pastes followed the ASTM standards [9]. The specimens were molded in a tube for 1 day and then cured in the corresponding curing condition for 27 days. The rationale behind selecting these specific curing period and conditions was to simulate field conditions of OWC [10–12]. For room curing conditions, specimens were cured under tap water with a controlled temperature of 20 °C and pressures 0.1 MPa (1 atm). For elevated temperature and pressure curing conditions, a special set-up for producing elevated temperature of 80 °C and pressure of 10 MPa (98.7 atm) was prepared using 750 ml Parr® pressure vessel. 500 ml of tap water filled the vessel and specimens were cured in the water. The temperature was elevated and kept constant during curing time period and pressure was applied by injecting nitrogen gas at 10 MPa.

2.2 Testing Procedure

The compressive strength was determined using axial load test of the hardened cement pastes. ^{29}Si MAS NMR spectroscopy was performed in 7 mm cylinders spun at 4 kHz. A silicate tetrahedron having the number of n sharing oxygen atoms is expressed as Q_n where n is the number sharing oxygen atoms ranging from zero to

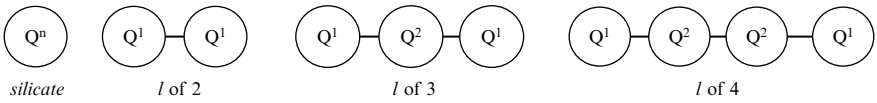

Fig. 1 Schematic representation of silica chain connections

four. The intensity of the silicate Q connections was determined using ^{29}Si MAS NMR technique. Using the intensity fractions of Q_{ns}, the degree of hydration D_h of a hydrated cement paste can be calculated after Bell et al. [13]

$$D_h = \mathrm{Q}^1 + \mathrm{Q}^2 + \mathrm{Q}^3 \tag{1}$$

The average degree of C-S-H connectivity D_c is calculated after Jupe et al. [10]

$$D_c = \frac{\mathrm{Q}^1 + 2\mathrm{Q}^2 + 3\mathrm{Q}^3}{\mathrm{Q}^1 + \mathrm{Q}^2 + \mathrm{Q}^3} \tag{2}$$

The C-S-H chain length is also calculated as

$$l = 2\left(1 + \mathrm{Q}^2 / \mathrm{Q}^1\right) \tag{3}$$

Considering that Q^1 and Q^2 represent the end-chain and the intermediate silicates respectively, l of 3 is the C-S-H silicate chain having three silicate connections. If the value of l is more than 3, it represents C-S-H silicate chain having three silicate connections as schematically shown in Fig. 1.

3 Results and Discussions

The compressive strength of OPC and OWC pastes cured under room and elevated curing conditions showed that OPC cured in room conditions (*OPC II-rm-28*) with compressive strength of 61.4 ± 5.1 MPa, OPC cured in elevated temperature and pressure conditions (*OPC II-elv-28*) with compressive strength 47.8 ± 4.4 MPa; OWC cured in room conditions (*OWC G-rm-28*) with compressive strength 56 ± 10.4 MPa, and OWC cured in elevated temperature and pressure conditions (*OWC G-elv-28*) with compressive strength of 43.8 ± 10.1 MPa. For both curing conditions, the compressive strength of the hardened OPC pastes is higher than that of the hardened OWC pastes. For the hardened cement pastes of OPC and OWC, the compressive strength of hardened cement pastes cured under room conditions is higher than hardened cement pastes cured under the elevated curing conditions. These results agree with other findings for the hardened cement cured under high temperature [14]. The observed ^{29}Si MAS NMR spectra were deconvoluted and presented in Fig. 2. The effects of different curing conditions on the degree of hydration in Eq. (1), the degree of C-S-H connectivity in Eq. (2) and the chain length in Eq. (3) were calculated and presented in Table 1. As expected, the degree of hydration of the hardened cement pastes cured under the elevated curing

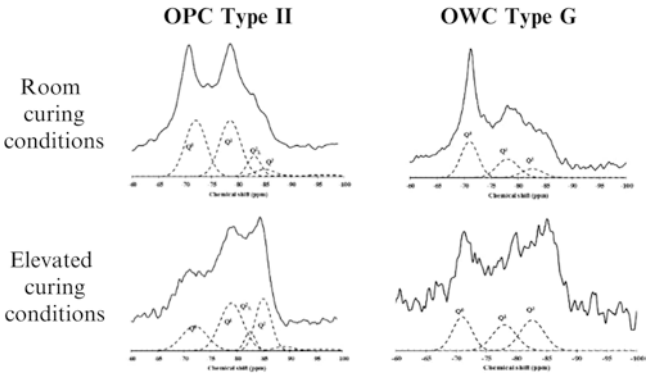

Fig. 2 Original and deconvoluted NMR spectra

Table 1 Integration of Q^n intensities by deconvolution of ^{29}Si MAS NMR

Specimens	Q^n (%)					D_h (%)	D_c	l
	Q^0	Q^1	Q^2	Q^3	Q^4			
OPC II-rm-28	41	40	19	–	–	59.0	1.322	2.950
OPC II-elv-28	22	38	40	–	–	78.0	1.513	4.105
OWC G-rm-28	51	33	16	–	–	49.0	1.327	2.970
OWC G-elv-28	32	31	37	–	–	68.0	1.544	4.387

D_h is degree of hydration: *Eq.* (*1*), *D_c is silicate chain connectivity*: *Eq.* (*2*), *l is silicate chain length*: *Eq.* (*3*), '*-rm*' *denotes room curing conditions*. '*-elv*' *denotes high temperature and pressure curing conditions*

conditions is higher than that of the hardened cement pastes cured under room conditions for both OPC and OWC. The degrees of hydration under the elevated curing conditions for OPC and OWC are 78 % and 68 % respectively. For the average degree of connectivity (*polymerization*), the highest degree of polymerization of 1.544 occurred with OWC paste specimens cured under elevated conditions.

The degree of connectivity under room curing conditions for OPC and OWC is similar as 1.322 and 1.327 respectively. For both OPC and OWC, the chain length of the hardened cement pastes cured under room conditions is less than 3.0, while that of the hardened cement pastes cured under the elevated conditions is over 4.0. This indicates that the '*basic C-S-H unit*' [4] in the hardened cement pastes cured under elevated temperature and pressure conditions is highly polymerized. To correlate strength and polymerization, Power's equation [1] is introduced

$$f_c = f_A X^n \tag{4}$$

where, f_c is the compressive strength of hardened cement pastes. f_A is the intrinsic compressive strength of hydration products, which represents the compressive strength of capillary pore-free cement paste. X is gel-space ratio at a time of hydration. n is a coefficient ranging between 2.6 and 3.0. Considering findings by others that the

compressive strength ratio of cement specimens with similar materials cured under different temperatures of 20 and 80 °C drops by a factor of 0.72 respectively [14], the gel-space ratio can be realized to drop by a factor of 0.885 using Eq. (4) with the assumption that f_A for both temperature conditions is the same. The above reduction factor of 0.885 is described here as a high temperature gel-space reduction factor. Now, considering our experimentally observed compressive strength of 61.4 MPa for OPC II-rm-28, the gel-space ratio can be calculated as 0.757 with f_A of 130 MPa and n of 2.7 [15]. The gel-space ratio of OPC II-elv-28 cured under high temperature and pressure can be estimated to drop to 0.67 from 0.757 given the 0.885 high temperature reduction ratio derived above. Using the observed compressive strength of 47.8 MPa for OPC II-elv-28, the intrinsic compressive strength f_A for the cement pastes cured under elevated curing conditions can be calculated as 140.8 MPa. Similarly for Type G OWC, the gel-space ratios of OWC G-rm-28 and OWC G-elv-28 are estimated as 0.73 and 0.65 respectively. The intrinsic compressive strength f_A for Type G OWC pastes cured under elevated curing conditions is then calculated as 141.6 MPa. The above calculation shows that the intrinsic compressive strength of the '*basic C-S-H unit*' might slightly increase under elevated curing conditions. However, the compressive strength of the hardened cement pastes decreases due to high temperature curing. We hypothesize that this contradiction is due to silicate polymerization and pressure. The basic C-S-H unit might have a higher strength under elevated curing condition due to silicate polymerization and C-S-H densification due to high pressure. On the other hand, volume change due to silicate polymerization and the effect of high pressure, would result in reducing the C-S-H volume and thus increase the capillary porosity resulting in reducing the cement paste strength. The above means that silicate polymerization and external pressure will help increasing the intrinsic compressive strength of the C-S-H unit f_A but will reduce the gel-space ratio, and thus cement paste compressive strength. Further investigations using BET measurements is necessary to confirm or negate the above hypothesis.

4 Conclusions

Compressive strength tests and ^{29}Si MAS NMR measurements were performed for OPC and OWC pastes hydrated under two curing conditions, 20 °C with 0.1 MPa pressure and 80 °C with 10 MPa pressure, for 28 days to correlate the compressive strength and silicate polymerization. The results showed that the compressive strength is higher under room curing conditions than under the elevated curing conditions. However, the mean degree of polymerization is higher under elevated curing conditions than under room curing conditions. Considering Power's equation, the observations can be interpreted as the compressive strength of 'basic C-S-H' increases under elevated curing conditions, however, silicate polymerization results in changing the gel-space ration to a level that overcomes the gains in the strength of basic C-S-H unit. Further research is warranted to confirm or negate the above hypothesis and analysis.

Acknowledgements This work was supported by "The development of CO_2 geological storage technologies through 1,000 t CO2-EOR pilot test" of the Korean Institute of Energy Technology Evaluation and Planning (KETEP) grant funded by the Ministry of Trade, Industry and Energy (MOTIE) (No. 2012 T100201728). The first author would like to acknowledge Foundation (NRF) Grant funded by the Korean government (MOE) (no. 2013R1A1A2062784).

References

1. Powers, T. C. (1960). *Physical properties of cement paste*. 4th international symposium on the Chemistry of Cement, Washington, DC, Vol. 1, pp. 577–609.
2. Diamond, S. (1976). Cement paste microstructure – An overview at several levels. In: *Hydraulic cement pastes; their structure and properties* (pp. 2–30). University of Sheffield, Sheffield: UK.
3. Larbi, J. A. (1993). Microstructure of the interfacial zone around aggregate particles in concrete. *Heron, 38*(1), 1–69.
4. Jennings, H. M., & Tennis, P. D. (1994). Model for the developing microstructure in portland cement pastes. *Journal of the American Ceramic Society, 77*(12), 3161–3172.
5. Foley, E., Kim, J. J., & Reda Taha, M. M. (2012). Synthesis and nano-mechanical characterization of calcium-silicate-hydrate (C-S-H) made with 1.5 CaO/SiO2 ratio. *Cement and Concrete Research, 42*, 1225–1232.
6. Feldman, R. F., & Sereda, P. J. (1968). A model for hydrated Portland cement paste as deduced from sorption-length change and mechanical properties. *Matériaux et Construction, 1*(6), 509–520.
7. ASTM-C150. (2009). *Standard specification for Portland cement*. West Conshohocken: ASTM.
8. API. (1990). *Specification for materials and testing for well cements* (API Specification 10). Washington, DC: API.
9. ASTM-C305. (1999). *Standard practice for mechanical mixing of hydraulic cement pastes and mortars of plastic consistency*. West Conshohocken: ASTM International.
10. Jupe, A. C., Wilkinson, A. P., Luke, K., & Funkhouser, G. P. (2005). Class H Oil well cement hydration at elevated temperature in the presence of retarding agents: An in situ high-Energy X-ray diffraction study. *Industrial Engineering Chemical Research, 44*, 5579–5584.
11. Scherer, G. W., Funkhouser, G. P., & Peethamparan, S. (2010). Effect of pressure on early hydration of Class H cement. *Cement and Concrete Research, 40*, 845–850.
12. Zhang, J., Weissinger, E. A., Peethamparan, S., & Scherer, G. W. (2010). Early hydration and setting of oil well cement. *Cement and Concrete Research, 40*, 1023–1033.
13. Bell, G. M. M., Benstedm, J., Glasser, F. P., Lachowski, E. E., Roberts, D. R., & Taylor, M. J. (1990). Study of calcium silicate hydrates by solid state high resolution 29Si nuclear magnetic resonance. *Advanced in Cement Research, 3*, 23–37.
14. Neville, A. M. (1995). *Properties of concrete*. Harlow: Pearsons/Prentice Hall.
15. Yajun, J., & Cahyadi, J. H. (2004). Simulation of silica fume blended cement hydration. *Materials and Structures, 34*, 397–404.

Part III
Biomimetics, Nano-assembly, Nano-production and Functionalization

Preparation and Application of Nanoscaled C-S-H as an Accelerator for Cement Hydration

Gerrit Land and Dietmar Stephan

Abstract In the present work an easy mechanochemical approach was used to prepare the C-S-H seeds out of simple commercial available materials. The preparation method was optimized with regard to achieve the highest acceleration by using statistical analysis of a factorial design of experiments setup (DoE). Isothermal heat flow calorimetry was used to quantify the efficiency of the seeds to accelerate the hydration of ordinary Portland cement (OPC). The setting and hardening behavior of cement pastes containing the seeds was studied by ultrasonic testing and Vicat needle penetration tests. The compressive strength after 12 h could be tripled by the addition of just 0.5 wt% in respect to the cement mass and a significant advance of strength remains for the following 3 days of hydration.

Keywords C-S-H seeding • Accelerator • Cement hydration

1 Introduction

The addition of nanoparticles to cementitious systems is one of the main topics of nanotechnology in construction materials and numerous materials have been tested in respect of different applications [1]. Many effects of the nanoparticles are related to the surface areas the particles provide. These surfaces may act as a site for the formation of crystal nuclei of hydration phases in the very early stage of cement hydration which will enhance the formation of hydration phases in the ongoing hydration [2]. This is especially worthwhile in the case of the C-S-H, because a faster C-S-H formation should result in a faster development of the mechanical properties of the cement paste. A surface which stimulates the development of C-S-H nuclei very effectively is the C-S-H itself. Therefore the addition of nanoscaled synthetic C-S-H to the cement paste, the so called C-S-H seeding, is a promising method to accelerate cement hydration for many applications.

G. Land • D. Stephan (✉)
Department of Civil Engineering, Building Materials and Construction Chemistry, Technische Universität Berlin, Berlin, Germany
e-mail: stephan@tu-berlin.de
http://www.baustoffe.tu-berlin.de

K. Sobolev, S.P. Shah (eds.), *Nanotechnology in Construction*,
DOI 10.1007/978-3-319-17088-6_14

The addition of relatively small amounts of C-S-H seeds to the cement causes a much higher heat flow in the dormant period of cement hydration. Additionally the acceleration period which is mainly allocated to the C_3S hydration can be observed much earlier and with a higher reaction rate due to the C-S-H addition [2, 3]. It is reported, that a minimum amount of C-S-H is necessary to achieve an acceleration by the seeds and that there is also an maximum threshold dose of C-S-H seeds above which additional C-S-H seeds do not result in further acceleration of the cement hydration [3]. Both effects depend on the cement composition, especially the alkali sulfate and the gypsum content. In addition the efficiency of the seeds depends on the C_3S surface area [3] and the structure of the synthetic C-S-H which can be controlled by polymers in the case of seeds synthesized by sol-gel methods [4]. There is also evidence that the lime to silica ratio of the C-S-H seeds have an influence on the chemical composition of the C-S-H which is formed by cement hydration so that a manipulation of the mechanical and durability properties of the hydrated cement paste might be possible [5].

2 Methods

The method which was used to prepare the C-S-H seeds for the following experiments is a mechanochemical approach. Hereby an amorphous siliceous material is ground in a jar mill in a saturated lime solution for a certain time. C-S-H phase is formed on the surface of the siliceous particles by pozzolanic reaction. By the simultaneous grinding process the C-S-H is sheared off the surface and fresh siliceous surface is created for further pozzolanic reaction.

2.1 Basic Preparation and Application of C-S-H Seeds

A defined amount of $CaCO_3$ was calcined at 1,000 °C to get CaO. After a cool down under Argon (Ar) the desired amount of deionized water was added to achieve lime water. The nanosilica sol (Köstrosol 0830, 1540 or 3550, CWK, Bad Köstritz, Germany) was added under constant dispersion with an ultra-turrax type disperser. A 500 mL PE jar was filled up to 1/3 of its volume with the dispersion. Another third of the jar was filled with grinding balls. The last third was flushed with Ar before it was closed and sealed to prevent carbonation. The PE jar was put into a ceramic jar of the jar mill which was additionally flushed with Ar and put onto the jar mill for the desired duration. The reaction process was followed by the determination of the $Ca(OH)_2$ content via thermogravimetric analysis on freeze-dried samples.

A CEM I 42.5 R type cement (Schwenk Zement, Bernburg, Germany) was used for all experiments with a water/cement ratio of 0.5. The fresh prepared seeds were

treated with ultrasound (Hielscher UP400S) directly before all experiments to ensure a thoroughly dispersion of the particles. For heat flow calorimetry (MC-CAL; C3 Prozess- und Analysentechnik, Haar, Germany) 10 g of cement were mixed with the desired dosage (wt% in respect to cement mass) of C-S-H seeds which were premixed with the required amount of DI water. The water content of the C-S-H dispersion was considered for the adjusting of the w/c-ratio. After 1 min of mixing on a vortex mixer the samples were placed in the calorimeter. The hydration heat was followed for 3 days at 20 °C. The results were ensured by double determination. For all other experiments a single batch of 1.5 kg cement and the accurate amount of C-S-H/mixing water-dispersion was mixed in a mortar mixer. Ultrasonic tests (IP-8, UltraTest, Achim, Germany) were performed for 3 days at 20 °C in double determination. The setting behavior of the cement pastes was followed by vicat-needle penetration test according to DIN EN 196-3. For compressive strength tests $2 \cdot 2 \cdot 2$ cm^3 cubes were prepared and stored at 20 °C. The cubes were demolded after 11.5 h and stored at 20 °C above water in a sealed container afterwards. First strength tests were performed 12 h after initial mixing. In the period from 12 to 24 h after mixing the tests were performed with an accuracy of ±5 min, afterwards within the limits according to DIN EN 196-1. To ensure the results 5 cubes were tested at each time.

2.2 Design of Experiments

In a series of pretests the CaO/SiO_2-ratio (C/S) of the C-S-H seeds (assuming a complete reaction of the reactants) was determined to be an important factor for the acceleration effectiveness of the C-S-H-seeds. Also the water/solid-ratio (w/s) of the dispersion, the duration of the grinding process and the particle diameters of the used nanosilica (manufacturer information) have an influence on the characteristics of the seeds. The factor levels for the DoE are shown in Table 1. The statistical model of the DoE assumes that the factors are polynomials of degree 2 and that there are no 3 factor interactions. The resulting Box-Behnken experimental plan (DoEasy Software, q-tec group, Lübeck, Germany) has 27 experiments.

For the response surface analysis the position of the heat flow maximum during the acceleration period of cement hydration was used as the response variable to be optimized. In a polyoptimization this target value was optimized to be as small as possible so that the heat flow maximum will occur as early as possible.

Table 1 Factor level of the DoE

Limits	C/S-ratio [–]	w/s-ratio [–]	Grinding duration [days]	Particle diameter [nm]
Lower Limit	0.4	4	1	8
Upper Limit	2	20	7	35

3 Results and Discussion

The response surface analysis which is shown in Fig. 1 shows that the C/S-ratio of the seed has a significant influence on the acceleration which can be achieved by adding 0.5 wt% of the seeds to an OPC. The results show that independently from the other three factors calcium-rich seeds have a better ability to accelerate the cement hydration than the low-calcium ones. This C/S-ratio of these seeds is close to the ratio of the average cementitious C-S-H, which is approx. 1.7. Thus a similar stoichiometry of the C-S-H seeds seems to be favorable to stimulate C-S-H nucleation on the surface of the seeds. Additionally the results indicate that at a given high C/S-ratio a large particle size of the siliceous particles is preferred over small particles. Pretests showed that the grinding time until a complete consumption of $Ca(OH)_2$ is reached increases with increasing particle size or rather that the reaction of the larger particle is slower. We assume that the reaction rate has an influence on the structure of the C-S-H gel which is formed and thereby also change its ability for nucleation reactions on its surface. The grinding time and the w/s-ratio have their optimum in the middle of their defined range, which most likely caused by changes in the rheological behavior of the mixture, when the water content is changed, which has a direct impact on the efficiency of the grinding.

By using the statistical model of the DoE the optimum for the response value, the position of the heat flow maximum t_{max}, was calculated. The result is that t_{max} should occur after 8.8 h after initial mixing (instead of 14.6 h in the reference) when 0.5 wt% of the optimized C-S-H (C/S-ratio = 2, w/s-ratio = 12.46, grinding duration = 3.93, particles size = 35 nm) are added to the cement paste.

In a series of confirmatory runs the statistical model was tested and was confirmed with an R^2 of 0.91. The results of the addition of 0.5 wt% of the optimized seeds are shown in Fig. 2. The heat flow maximum can be observed 8.9 h after initial mixing, which is almost the calculated value of 8.8 h, indicating that the statistical model is true.

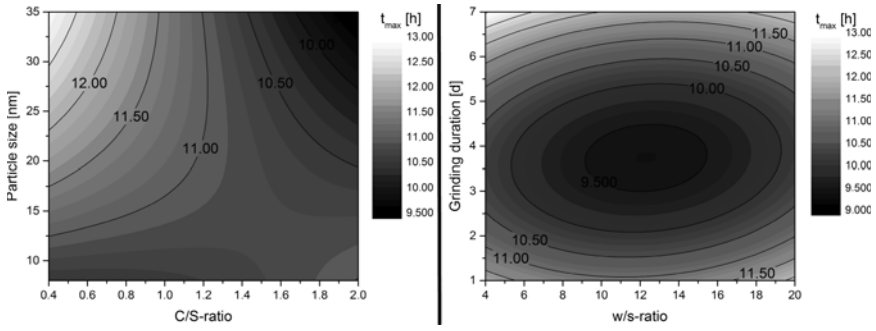

Fig. 1 Response surface analysis shows when the heat flow maximum (t_{max}) of the acceleration period occurs depending on the C/S-ratio and the particle size (*left*) and on the w/s-ratio and the grinding duration (*right*) of 0.5 wt% C-S-H added to the cement paste

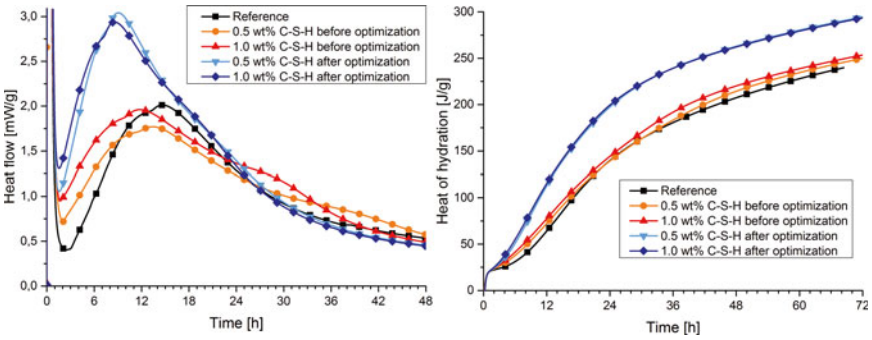

Fig. 2 Heat flow (*left*) and total heat of hydration (*right*) of an OPC with/without seeds

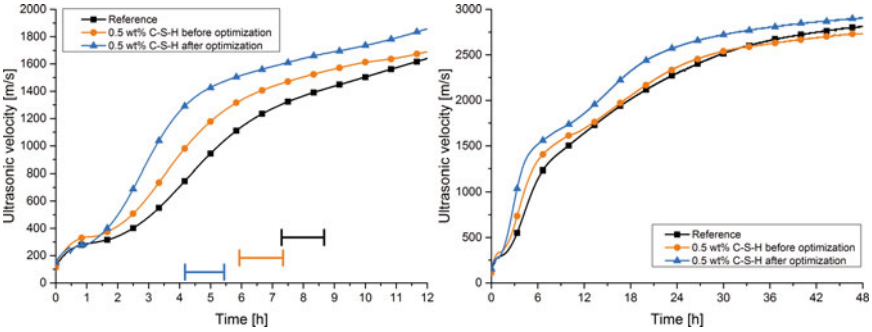

Fig. 3 Ultrasonic testing of an OPC during the first 12 h (*left*) and the first 2 days (*right*) after initial mixing. The duration of the setting of the cement is shown by bars (*left*)

When seeds are added to cement paste the acceleration usually shows a direct correlation with the concentration of the seeds. In the case of the optimized seeds an increase from 0.5 wt% to 1 wt% shows almost no effect. This indicates that the threshold limit of the concentration is already reached at 0.5 wt%.

The velocity of ultrasonic signals in cement paste increases with the formation of solid network structures and is a good evidence for the formation of the microstructure. When seeds are added this formation of solid structures starts earlier and at a much higher rate (Fig. 3). This effect is most pronounced between 2 and 6 h of hydration so we can conclude that the higher reaction rate in this period which was found on heat flow calorimetry directly causes a much denser and better connected microstructure. This is also confirmed by the results of the setting test, which are also shown in Fig. 3. The setting of the cement occurs earlier and the span between beginning and the end of setting gets shorter when C-S-H seeds are added.

The results of the ultrasonic test and the needle penetration test imply a faster development of strength in the paste when C-S-H seeds are added. The results of these tests are shown in Fig. 4. The compressive strength after 12 h is tripled when 0.5 wt% of seeds is added to the paste and an advance in compressive strength remains for the first days of hydration.

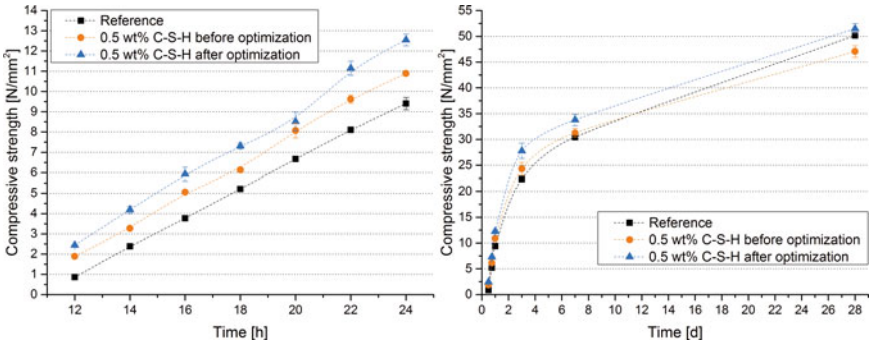

Fig. 4 Compressive strength of an OPC which contains C-S-H seeds during the first 24 h (*left*) and 28 days (*right*) after initial mixing

4 Conclusions

A mechanochemical preparation method for C-S-H seeds which is easy to handle and uses commercially available materials is presented. We could show that it is possible to enhance the acceleration behavior of C-S-H seeds which are prepared by this method by using experimental design and analysis. The C/S ratio has the highest relevance for the effectiveness of the seeds and lime-rich seeds could be determined to be the most effective. The addition of relatively small amounts of seeds to an OPC results in a significantly higher heat flow during the first 24 h of cement hydration and both the silicate and the aluminate clinker phases are affected by the seeds. The addition of the seed also improves the development of the microstructure of the hardening cement paste which results in an earlier and faster setting and multiplication of compressive strength.

References

1. Rashad, A. (2013). A synopsis about the effect of nano-Al_2O_3, nano-Fe_2O_3, nano-Fe_3O_4 and nano-clay on some properties of cementitious materials. *Materials and Design, 52*, 143–157.
2. Thomas, J. J., Jennings, H. M., & Chen, J. J. (2009). Influence of nucleation seeding on the hydration mechanisms of tricalcium silicate and cement. *Journal of Physical Chemistry C, 113*(11), 4327–4334.
3. Nicoleau, L. (2013). The acceleration of cement hydration by seeding: Influence of the cement mineralogy. *ZKG International, 1*, 40–49.
4. Nicoleau, L., Gädt, T., Chitu, L., et al. (2013). Oriented aggregation of calcium silicate hydrate platelets by the use of comb-like copolymers. *Soft Matter, 9*(19), 4864–4874.
5. Alizadeh, R., Raki, L., Makar, J. M., et al. (2009). Hydration of tricalcium silicate in the presence of synthetic calcium–silicate–hydrate. *Journal of Materials Chemistry, 19*(42), 7937–7946.

Effect of Heat Treatment on Phase Compositions of Clay Aluminosilicates

Mikhail Lebedev, Igor Zhernovsky, and Valeria Strokova

Abstract One of the methods of activation and modification to improve quality characteristics of raw materials is a thermal treatment that was used for property improvement of clay materials in this work. For this purpose the treatment thermal interval of 500–600 °C, allowing getting the material with stable properties when thermal treatment and high adsorptive activity was used.

The goal of this work is to study the mechanism of the processes occurring in these polymineral systems and contributing to positive changes in properties. According to X-ray and IR-spectroscopy analyses data for samples exposed to treatment at the temperature of 500 °C the transformation of the crystal structure of layered aluminosilicates, mainly kaolinite as 2D-nanoparticles into the frame aluminosilicates of zeolite group – 3D-nano-objects, in particularly, faujasite with size of crystallites about 80 nm (according to the X-ray analysis) is performed.

The change in the particles shape is observed: bonded clay minerals transfer to isometric formations, typical to minerals of zeolite group.

Keywords Clay aluminosilicates • Heat treatment • Zeolite • X-ray and IR-spectroscopy analysis • Microstructural analysis

1 Introduction

At the present stage of development of construction material science for improvement of composites characteristics, more popular becomes the application of different methods of activation and modification for quality improvement of raw materials. One of such methods is a thermal modification that was used for property improvement of clay materials in the frame of this work. For this purpose the

M. Lebedev (✉)
Center of High Technologies, Belgorod State Technological University Named After V.G. Shoukhov, Belgorod, Russia
e-mail: michaelL1987@yandex.ru

I. Zhernovsky • V. Strokova
Department of Materials Sciences and Technology of Materials, Belgorod State Technological University Named After V.G. Shoukhov, Belgorod, Russia
e-mail: zhernovsky.igor@mail.ru; vvstrokova@gmail.com

K. Sobolev, S.P. Shah (eds.), *Nanotechnology in Construction*,
DOI 10.1007/978-3-319-17088-6_15

temperature interval for treatment was determined as 500–600 °C, allowing getting the material with water-stable characteristics and high adsorptive activity [1, 2].

The research presented in this article focused on extension of assortment of raw materials for production of the filler of asphalt binder and asphalt concrete due to utilization of widely distributed raw materials such as sedimentary aluminosilicate rocks.

The objective of this work is to understand a mechanism of behavior in the polymineral systems that stimulating a favored changing in properties of the systems.

2 Experimental

2.1 Materials and Methods

In this research polymineral sedimentary rocks from South Ural were used. These materials include coal-bearing course of Korkino deposit, which are characterized by significant chemical and species composition associated with conditions and location of formation. For the purpose of generalization, the study was carried out with using one species of the rocks.

Qualitative evaluation of the phase composition for aluminosilicate raw was carried out with XRD analysis on the diffractometer DRON-4 (Russia) with using of CuAβ radiation. The full-width at half-maximum (FWHM) of these patterns was 0.05°. Interpretation of the diagrams and identification of the composing minerals were made with using of ICCD data base and Crystallographica Search-Match (Oxford Cryosystems) software. In this work also was used FTIR-spectroscopy (VERTEX 70, Bruker Optics, Germany). Microstructural analysis of the samples was carried out by SEM (Supra 50 VP, Germany) with analytical system INCA Energy + Oxford. SEM analysis of the samples was run without sputtering in the conditions of alternating pressure.

2.2 Samples Preparation

The main practical relevance of the research is in the study of thermal treatment influence on phase composition of clay materials used in this work. The thermal treatment presented by gradual heating up of initial material (bulk material) till required temperature, followed by thermal exposure for 2 h with gradual cooling down after that.

In order to estimate changing in composition and structure of the studied polymineral aluminosilicate rocks in dynamic, mineral composition, FTIR-spectroscopy and microstructure of the materials were investigated in an initial condition (previously, the specimens were milled in a ball mill for short time till the Blain specific surface of 430 m^2/kg) and after thermal treatment at 400, 500 and 600 °C (after thermal treatment the specimens were milled in a ball mill for short time till Blain specific surface of 600,610 m^2/kg).

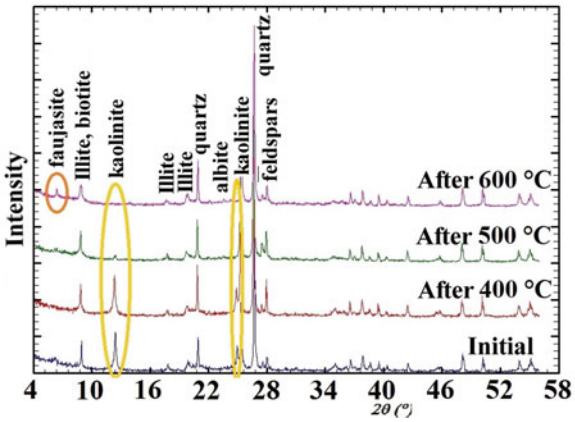

Fig. 1 X-ray diagram of aluminosilicates before and after treatment at 400 °C, 500 °C, 600 °C

3 Results and Discussions

3.1 XRD Analysis

According to XRD data, in the mineral composition of the initial specimens (Fig. 1), there are crystal phases of quartz, kaolinite clay, illite, biotite and feldspars. It should be noted, that some portion of rocks substance is X-ray amorphous including carbon-bearing impurities.

In compliance with obtained data, a thermal treatment of the initial materials induces changing in the mineral composition and, as a consequence, allowing getting the material with water-stable characteristics and high adsorptive activity [1, 2].

According to XRD data, after the thermal treatment at 500–600 °C, a transformation of crystal structure of layered silicates occurs. Mostly, the crystals of kaolitite clay with 2D-nanoparticles, according to traditional conception, get forming the minerals of zeolite type – 3D nanoobjects, mainly faujasite mineral (Fig. 1). That is confirmed by the factor, that with increasing of the temperature during thermal treatment, a significant reducing of reflections of kaolinite happens after 500 °C till full disappearing after 600 °C that can be seen on the X-ray diagrams for aluminosilicate (Fig. 1). A disappearing of kaolitite leads to formation of new, mainly, framework silicates. Mostly, they presented by high dispersed phases, which, because of their small size are invisible for X-ray diffraction. Thanks to certain conditions, it became possible for such X-ray amorphous minerals to get bigger, that induced the appearing of faujasite reflections. Based on XRD data, the size of crystallites of that zeolite was calculated that is about 80 nm.

It is necessary to mention, according to studies of the other researchers [3, 4], in the temperature interval of 500–600 °C aluminosilicate raw with similar composition may be synthesized to identical framework new formations.

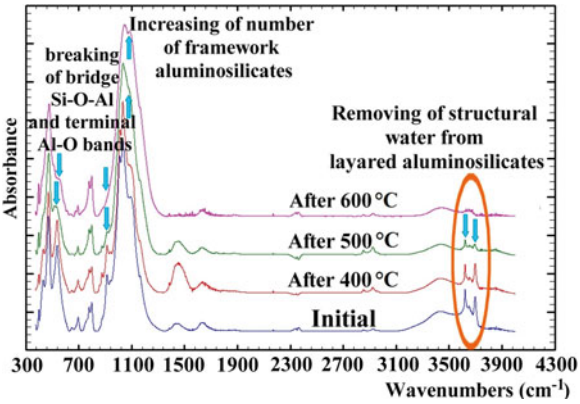

Fig. 2 FTIR-spectrum of the aluminosilicates with different Al_2O_3/SiO_2 ratio before and after treatment at 400 °C, 500 °C, 600 °C

3.2 FTIR-Spectroscopy Analysis

The mineral composition of the studied specimens is confirmed by IR-spectrums (Fig. 2). For the analyzed probe in initial condition the presence of aluminosilicate structural arrangements Q^3 typically prevails [5].

Thermal treatment of the material affects the structure with changing on molecular level. This is proved by IR-spectroscopy data of aluminosilicate materials after different thermal treatment (Fig. 2).

The analysis of the obtained IR-spectrum showed that increasing in temperature leads to changing of absorption band for aluminosilicate groups. Based on XRD data, after thermal treatment at 500 °C a transformation of crystal structure of layered silicates occurs followed by formation of zeolite type of minerals. To confirm this statement, it can be considered the shift of the absorption band of layered anions to the region with bigger wavenumbers from 1,035 to 1,053–1,067 cm^{-1}, which is evidence of increasing in polymerization degree of silicate system [6, 7] (Fig. 2). This is followed by a significant growth of absorption band intensity of framework structures Q^4 synchronous spreading of all "Si-O" profile in the region of 1,100–1,300 cm^{-1}.

Gradual decreasing of an intensity of the bands 915, 947 and 537 cm^{-1} can be explained by breaking of bridge-links Si–O–Al [8] as well as unbridge-links Al–O in the alumo-oxide octahedrons of kaolinite layered structures followed by dehydration, that can be confirmed by reducing of absorption bands intensity on the region of 3,600–3,700 cm^{-1} (Fig. 2). Herein, the transformation of Al from octahedron (AlO_6) coordination to tetrahedron (AlO_4) occurs. Appearing of the band at 556–560 cm^{-1} after thermal treatment at 600 °C can be explained by formation of double quaternate rings in the structure of zeolites with transformation of Al into tetrahedron orientation [9].

3.3 SEM Analysis of Microstructure

The effectiveness of the thermal modification on the studied aluminosilicate materials is justified by microstructural analysis.

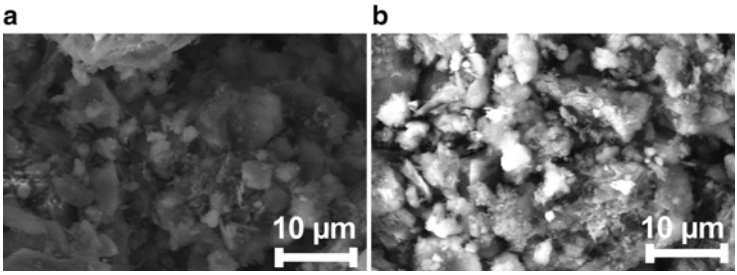

Fig. 3 Microstructure of the filler: (**a**) without thermal treatment; (**b**) with thermal treatment

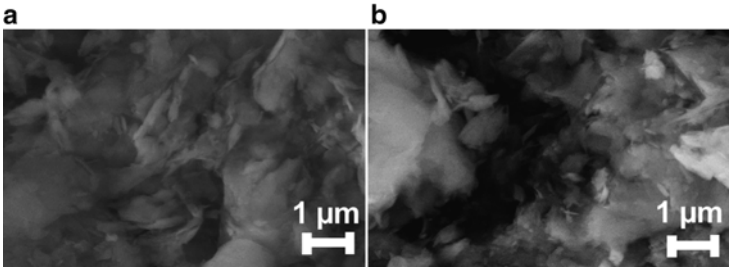

Fig. 4 High dispersed substance in the structure of aluminosilicate: (**a**) without thermal treatment; (**b**) with thermal treatment

To estimate the affect of thermal treatment on the raw a comparative analysis of microstructure of the filler at different conditions: after mechanical treatment and thermal modification of the initial materials followed by dispersion.

Mineral composition of the initial material, mainly, prevailing of clay minerals provides a high dispersity of obtaining filler (with Blain specific surface 430 m^2/kg) (Fig. 3). Analyzing the SEM pictures, it can be concluded of polyfractional particle distribution (Fig. 3a). As we can see, there are coarse particles with the size of 20–25 μm, but mostly the particles are presented with average size no more than 5 μm.

According to the obtained data, thermal treatment leads to increasing in specific surface and to growth of particle, related to synthesizing of new formations on the system and slight particle aggregation. That happens due to reducing of extra energy in the system induced by dehydration of layered aluminosilicates. The particle growth is proved by SEM data (Fig. 3b). The main portion of the system is presented by the particles with the size of 20–30 μm that have a high strength and because of it they can be appeared for building of a framework in bitumen-mineral compositions. The same morphology has a most part of the particles of modified mineral powder (Fig. 3b). Probably, a highly-developed surface can provide a high summary specific surface of the filler (with Blain specific surface of 610 m^2/kg).

When considering a highly-dispersed portion of the filler, it is necessary to note, that in the specimen without thermal treatment, particles with size of 200–300 nm are presented by clay phases on the form of thin flake-like pallets (Fig. 4a). Most likely, that X-ray amorphous substance can be a product of uncompleted mineral

formation stage. Because of the structure, it is highly reactive materials that may react to organic binder and water as well.

Thermal treatment gives a quality effect to fine phases. It was found, that after modification instead of thin pallets of the clay phases in the specimens appear isometric new formations (Fig. 4b), which may be attributed to zeolite type of minerals, the presence of with was confirmed with using XRD analysis. The size of those formations is slightly bigger than that of initial clay substance, where the size of a separate particle is about 1 μm (Fig. 4b). In accordance with composition and structure such type of material would be active components in the bitumen-mineral compositions.

4 Conclusions

Mineral powder based on aluminosilicate raw of clay composition is a highly-dispersed component in the bitumen-mineral compositions that provides its chemical activity to organic high-molecular compounds and to water. After water impaction, the characteristics of the composites get significantly worsen. But, at the same time, thermal activation of the compositions allows getting the material with water stable properties and high absorptive activity, that improves an adhesion between bitumen and particle surface and as consequence provides an advancing of physical and mechanical characteristics of asphalt binders and asphalt concretes. That happens due to changing in phase composition of mineral material, where a transformation of crystal structure of layered aluminosilicate takes place. Kaolinite transforms to framework aluminosilicates of zeolite type.

Therefore, understanding the mechanism of modification and activation of the materials, including non-conditioned materials, it is possible to improve the characteristics of the components of construction materials and composites their base.

Acknowledgements The research work is accomplished under the financial support from Ministry of Education and Science of Russian Federation in framework of State Assignment № 11.1550.2014 K; Russian Fond of Fundamental research, agreement № 14-41-08024.

References

1. Lebedev, M. S., Strokova, V. V., Zhernovsky, I. V., & Potapova, I. Y. (2012). Changing the properties of fillers of aluminosilicate raw materials under the influence of thermal modification. *Journal Building Materials, 9*, 68–70.
2. Strokova, V. V., Lebedev, M. S., Sobolev, K. G., & Potapova, I. Y. (2013). *New alumosilicate fillers based on sedimentary rocks for asphalt concrete*. XXII international materials research congress, Cancun.
3. Reyes, C. A. R., & Fiallo, L. Y. V. (2011). Application of illite- and kaolinite-rich clays in the synthesis of zeolites for wastewater treatment. *Earth and Environmental Sciences, 15*, 363–374.

4. Georgiev, D., Bogdanov, B., Angelova, K., Markovska, I., & Hristov, Y. (2009). *Synthetic zeolites – Structure, classification, current trends in zeolite synthesis. Review*. "Economics and Society development on the Base of Knowledge": Int. Sci. Conf. VII, Stara Zagora.
5. Lebedev, M. S., Zhernovsky, I. V., Strokova, V. V., Fomina, E. V., & Kozhukhova, N. I. (2014). Application of IR-spectroscopy for study of alumosilicate raw materials. *Applied Mechanics and Materials, 496–500*, 96–101.
6. Anfilogov, V. N., Bykov, V. N., & Osipov, A. A. (2005). *Silicate melts*. Moscow: "Science" Publishing House. 357 pp. (In Russian).
7. Vlasov, A. G., Pozubenkov, A. F., & Sevchenko, I. A. (1970). *Infrared spectra of alkaline silicates*. Leningrad: "Chemistry" Publishing House. 344 p. (In Russian).
8. Worrall, W. E. (1975). *Clays and ceramic raw materials*. London: Applied Science Publishers Ltd.
9. Rayalu, S. S., Udhoji, J. S., Meshram, S. U., Naidu, R. R., & Devotta, S. (2005). Estimation of crystallinity in fly ash-based zeolite-A using XRD and IR spectroscopy. *Current Science, 89*(12), 2147–2151.

Dispersed Inorganic or Organomodified Montmorillonite Clay Nanoparticles for Blended Portland Cement Pastes: Effects on Microstructure and Strength

Styliani Papatzani and Kevin Paine

Abstract Nanotechnology offers an opportunity to modify and observe cement at the nanolevel. In this research, the degree of dispersion of two aqueous suspensions of organomodified montmorillonite (OMMT) clay nanoparticles and one inorganic nanoclay (nC) dispersion was verified by TEM. The effect of the addition of each one of the three dispersions to a high limestone content (40 % by mass of binder) Portland limestone cement was investigated in terms of compressive strength, thermogravimetric (TG) analyses and morphological characteristics of the pastes. It was found that the upper limit of nC addition, in such pastes is 1 % nC solids by mass of binder and that intercalated OMMT cannot offer significant compressive strength improvement. However, there were strong indications that the pozzolanic reactions were promoted by the better dispersed OMMT and by the inorganic nC dispersion. The FESEM images captured, depicted the morphological characteristics of the nanomodified cement formulations. Furthermore, evidences suggest that the specific nanoclays can offer enhancement for flexural performance of blended cements with no degradation over time. Overall, the inorganic nC dispersion exhibited the highest pozzolanic activity, the highest flexural strength improvement and the most dense microstructure. The research reported was part of a much broader research project (FIBCEM) supported by the EU.

Keywords Inorganic nanoclays • OMMT • TEM • FESEM • TGA • Flexural & compressive strength

S. Papatzani (✉) • K. Paine
BRE Centre for Innovative Construction Materials, University of Bath, Bath, UK
e-mail: s.papatzani@bath.ac.uk; k.paine@bath.ac.uk
http://spapatzani.wix.com/stylianipapatzani; http://www.bath.ac.uk/ace/people/paine/

K. Sobolev, S.P. Shah (eds.), *Nanotechnology in Construction*,
DOI 10.1007/978-3-319-17088-6_16

1 Introduction

Recent researches have demonstrated that using nanoparticles, has a significant effect on the chemical reactions taking place during cement hydration and on the structural characteristics of the hydrates, with subsequent effects at the macro level; that is to say, mechanical characteristics and durability of the hardened cement paste [1]. The nanoparticles are more chemically reactive, since a greater surface area is available for reactions and/or they strengthen the nanostructure by minimizing the nanosized pores (0.5–5 nm wide) within the calcium silicate hydrates [2, 3]. A whole new range of hybrid nanocements can be produced with the addition of a variety of nanoparticles, such as nano-SiO_2 [4–7], nano-montmorillonite clay [8, 9] and others. In the current research, nanoparticles of montmorillonite clay were used.

Montmorillonite is a naturally occurring, hydrophilic mineral, belonging to the smectite family of clays. It has been used in many industrial applications because it exhibits a high specific surface area, high surface reactivity and high cation exchange capacity. It is a three layer mineral in which an octahedral aluminum layer is sandwiched between two tetrahedral silicon oxide layers [8]. They can only be considered to comprise of individual nanoparticles ready for reactions if the bonds bridging the layers are weakened to the extent of separation of the layers. This happens when a modifier, is introduced within the galleries, causing a change in the charge of the molecules and a subsequent separation of the layers. If the modifier is organic, the clay is said to be organomodified, becoming hydrophobic. The clays used in this research, were Viscogel XDB bentonites, supplied by Laviosa Chimica Mineraria S.p.A. They were organomodified with methylbenzyl dihydrogenated tallow ammonium salts by Lietuvos Energetikos Institutas (LEI) and dispersed with the use of surfactants (a non-ionic fatty alcohol and an anionic alkyl aryl sulphonate) by the UK Materials Research Institute (MaTRI). As an effect, two different organomodified nanoclay (nC) dispersions were prepared; nC1 and nC2, respectively. In addition, the inorganic, unmodified sodium montmorillonite nanoclay, commercially available as Dellite HPS was also supplied by Laviosa Chimica Mineraria, dispersed with an inorganic surfactant, by MaTRI, UK and used with the name nC3 in this research.

2 Experimental Procedure

2.1 Materials

The materials used were:

- Portland limestone cement CEMII/A-L42.5, with a limestone content of 14 %, conforming to EN 197–1.

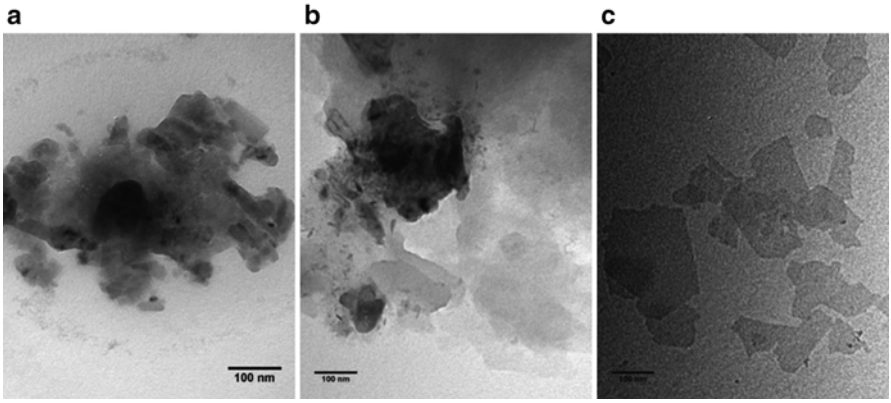

Fig. 1 TEM micrographs of: (**a**) nC1 at 150,000×, (**b**) nC2 at 120,000×, (**c**) nC3 at 120,000×

- Limestone (LS) (additional), conforming to EN 197–1.
- Organomodified nC1 and nC2 in an aqueous dispersion containing about 15 % by mass of nC particles.
- Unmodified inorganic sodium montmorillonite, nC3, in an aqueous dispersion containing about 15 % by mass of nC particles.
- PVA fibers, kuralon H-1, 4 mm – only for samples tested in flexure.
- Superplasticizer viscocrete 20HE – only for samples tested in flexure.

The nanoclays were characterized by Transmission Electron Microscopic (TEM) analyses (Fig. 1). Ten microliter of each nC dispersion was diluted in 100 ml of distilled water and small drops of the diluted solutions were dripped on copper mesh grids coated with a thin carbon film. Grids were dried at 25 °C prior to the insertion in the instrument. Samples were examined at a voltage of 120 kV and micrographs were acquired with GATAN Jeol view camera.

The nC1 dispersion is depicted in Fig. 1a, showing significant local conglomeration. The nC1 layers are intercalated and covered with organic matter, possibly coming from the organic modifier and are stacking on top of each other. This arrangement does not allow the reactive sides to be exposed, hence no seeding effect can be expected and additionally can cause localized shear failures in the materials. As an effect, cement pastes formulated with nC1 were predicted to have lower compressive strengths. Figure 1b shows nC2, exhibiting areas of agglomeration and still, excess of organic modifier. nC2, however, is more intercalated than nC1, expected, therefore, to perform better in terms of compressive strength when mixed in cement pastes. Figure 1c shows nC3, very well dispersed in which discrete platelets of nC can be identified, indicating that exfoliation has taken place, with some small agglomerates of impurities. Soft edges can be observed, lowering the possibilities of shear failure at the nanolevel.

2.2 Mix Design

Fifteen ternary cement combinations were generated by using Portland cement, limestone, and either of the two organomodified nC dispersions or the inorganic nC dispersion. PC60LS40, a non-pozzolanic blended cement mix, containing only Portland limestone cement (PC) and additional limestone (LS), was used as the reference to investigate whether the addition of nC has a pozzolanic effect. nC addition ranged from 0, 0.5, 1, 2, 4 to 5.5 % by mass of solids. The 5.5 % represented the upper limit of nanoclay addition in the cement paste. Water content in nC dispersions accounted for 85 %, which entered as part of the water content in the cement formulations to obtain water to binder ratio of 0.3. Therefore, the general formula of the matrix of the ternary nanomodified cement pastes was:

$$60PC + \left(40 - x\right)LS + xnC \tag{1}$$

Where x = % of nC solids at ranges from 0 to 5.5 %.

Dry constituents were pre-mixed for 60 s, then, the liquid phases, water and nC dispersion, were added and mixed with an automatic dual shaft mixer at 1,150 rpm for 3 min. The fresh paste was cast into cylindrical molds of 64 mm height and 32 mm diameter for compressive strength tests and samples of the pastes were also separately kept for compositional and microstructural analyses. Specimens were air cured in dry sealed conditions at 20 ± 2 °C for the first 24 h, then in water at 20 ± 2 °C, until the day of testing.

2.3 Analytical Testing

A suite of compressive and flexural (three point bending) strength tests was carried out on at least three samples of each formulation at each age. To characterize the pastes, arrest of hydration was performed following two different methodologies as described by Calabria-Holley et al. [5]. Secondary electron imaging of the coated with chromium pastes, was generated using a field emission electron microscope (FESEM) Jeol JSM 6,301 F. Thermogravimetric analysis (TGA) was carried out using Setaram TGA92. Each powder sample was placed in an alumina crucible and heated at a rate of 10 °C/min from 20 to 1,000 °C in nitrogen atmosphere.

3 Results and Discussion

A comparative study of the compressive strength on day 1, 7, 28, 56, 90 and 170 of pastes nanomodified with each of the three different nC dispersions was made (Figs. 2 and 3). An overall decrease in compressive strength for the nC pastes can

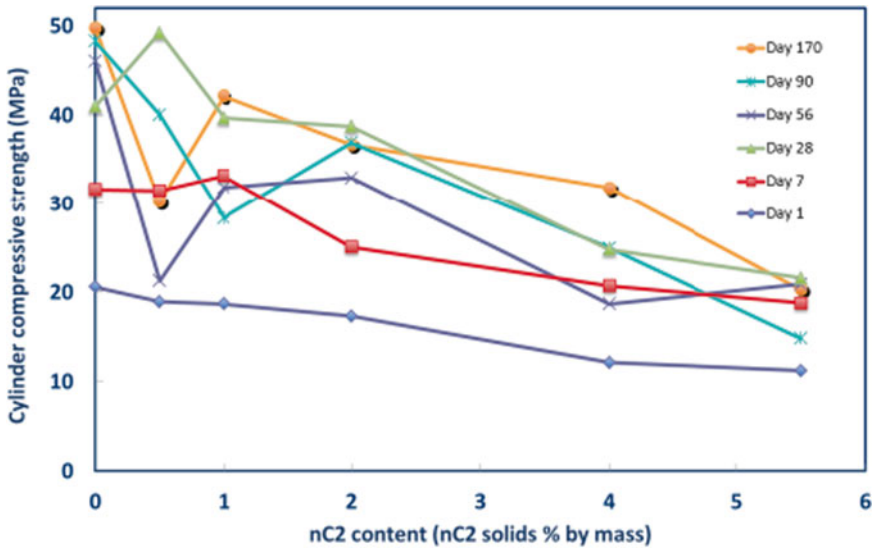

Fig. 2 Compressive strength of nC2 modified pastes

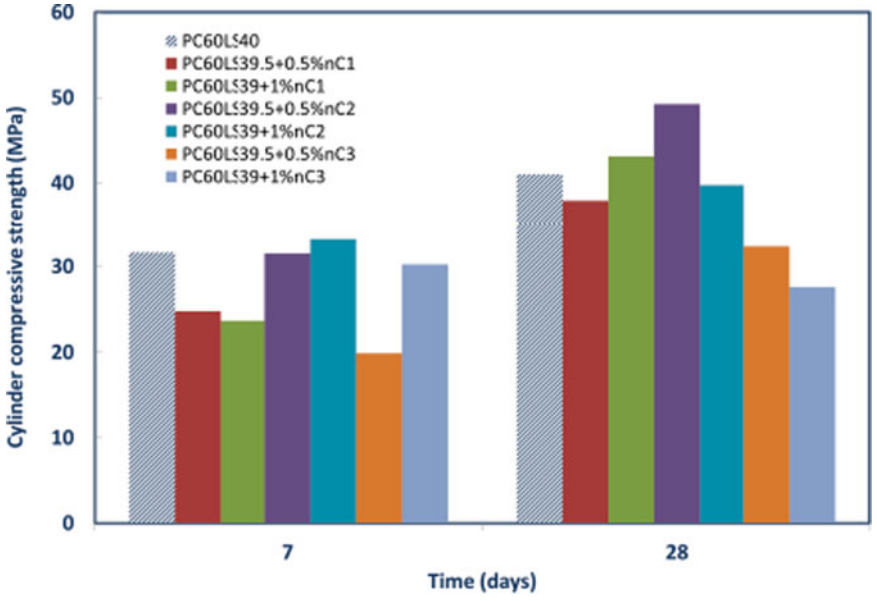

Fig. 3 Comparison of compressive strength of nC1, nC2 & nC3 modified pastes

be observed when compared to the reference paste, PC60LS40, especially after day 28. This phenomenon can be explained as follows:

- Intercalated organomodified dispersions exhibited excess of organomodifier and had low stability causing agglomeration of the nanoparticles, as observed by TEM analyses.
- Phase separation of nC2 was observed prior to mixing.
- nC2 and nC3 dispersions were very viscous and difficult to handle. Stirring the dispersion prior to mixing, may have not be enough to regain a homogeneous dispersion in turn agglomeration of the nanoparticles took place, inhibiting their potential for chemical reactions.

As can be observed indicatively in Figs. 2 and 3, marginal improvements were achieved with 0.5–1 % nC addition. Beyond this level no strength improvements were possible. Using these blended pastes as reference, three more fibre cement formulations were designed and specimens of 120×40×10 mm were created and tested in flexure containing: (a) 60 % PC, 40 % LS, 3 % PVA fibres and 2 % superplasticizer (SP) by mass of binder (F.PC60LS40PVA3SP2), (b) 60 % PC, 39 % LS, 3 % PVA, 2 % SP+1 % nC2 (F.PC60LS39PVA3SP2+ 1 % nC2) and (c) 60 % PC, 39 % LS, 3 % PVA, 2 % SP+1 % nC3 (F.PC60LS39PVA3SP2+1 % nC3). It can be seen in Fig. 4 that flexural strength can be enhanced by the nanoclay additions by 10–30 %, the results being more pronounced with nC3, which additionally exhibited smaller variations in terms of standard deviation (smaller than 1 MPa) and an almost stabilized strength after 28 days.

TG analyses showed that nC3 exhibited a greater pozzolanic activity as indicatively shown in Fig. 5, with the consumption of $Ca(OH)_2$ towards the production of

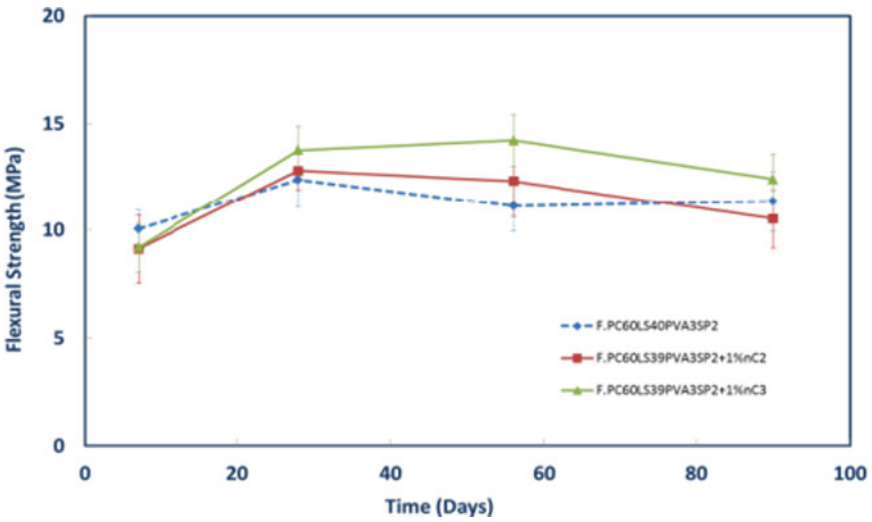

Fig. 4 Flexural strength of nC2 and nC3 modified pastes

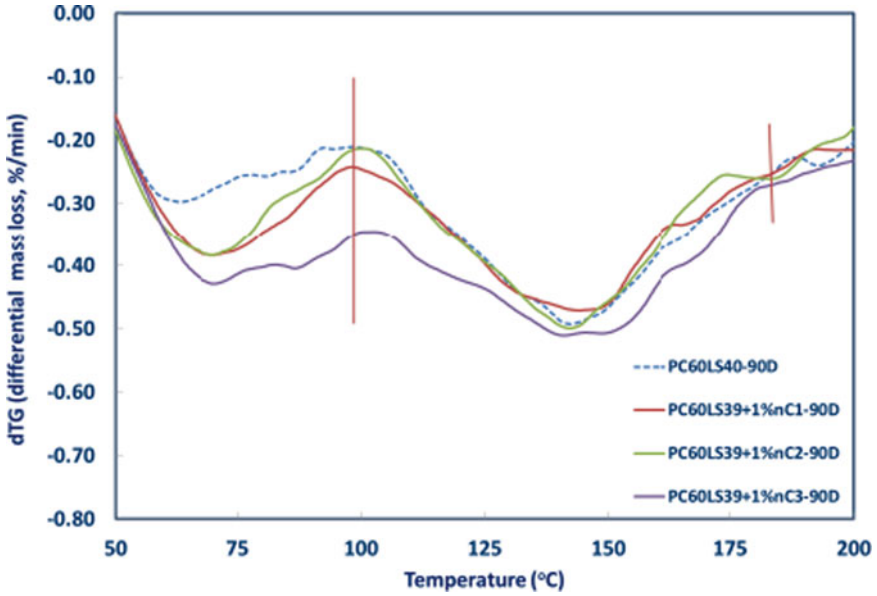

Fig. 5 Differential mass loss between 100 and 200 °C at day 90

additional C–S–H and ettringite [10]. Further analyses, not presented because of page limitations, suggested that given the time, nC2 can also engage in pozzolanic reactions.

Secondary image analyses at day 28 showed a porous structure as a result of the addition of nC1 (Fig. 6a) as well as with the addition of nC2 (Fig. 6b). However, the addition of nC3 (Fig. 6c) led to a visibly denser structure.

4 Conclusions

In this research, results on the effect of (i) inorganic nC dispersion and (ii) two different intercalated OMMT dispersions as additions in high limestone content Portland limestone cement were presented for the first time. It was acknowledged that improvements in performance were less pronounced than expected. The reason for this was that the nanomodified blended cement pastes were particularly sensitive to the initial level of dispersion of the nC and the content of organomodifier used for the OMMT. Improvements in flexural strength and pozzolanic activity were more distinct for the better dispersed nC particles, as shown by TEM analyses (Fig. 1c). However, one of the most important findings was that the inorganic nature of cement bore natural affinity with the inorganic dispersion, nC3, which delivered better results than the organically modified nC. The addition of superplasticizers can

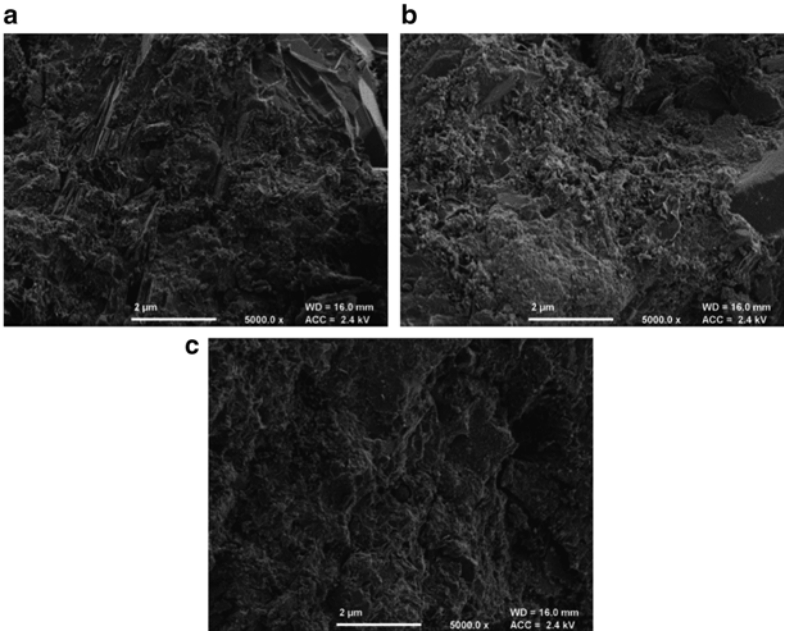

Fig. 6 FESEM micrographs of PC60LS39 + 1 % nC – day 28: (**a**) PC60LS39 + 1 % nC1 at 5,000×, (**b**) PC60LS39 + 1 % nC2 at 5000×, (**c**) PC60LS39 + 1 % nC3 at 5,000×

further improve the consistence of the pastes, rendering the nC more effective. Additional improvements in flexural strength can be expected even at later ages, whereas enhancement of compressive strength is less probable if superplasticizers are not added.

Acknowledgements The authors acknowledge European Commission funding (FIBCEM project, grant Number 262954) and all partners are thanked for their input and for the supply of materials. The authors would also like to acknowledge the Department of Chemical Engineering at the University of Bath for the use of the TG analyzer and Dr. J. Calabria-Holley for providing comments.

References

1. Papatzani, S. (2015). Effect of nanosilica and montmorillonite nanoclay particles on cement hydration and microstructure. Material Science and Technology, maneypublishing; (in press).
2. Sobolev, K., & Sanchez, F. (2012). *The application of nanoparticles to improve the performance of concrete*. NICOM 4: 4th international symposium on nanotechnology in construction, Agios Nikolaos, Crete.

3. Papatzani, S., Paine, K., & Calabria-Holley, J. (2015). A comprehensive review of the models on the nanostructure of calcium silicate hydrates. *Construction and Building Materials, 74*, 219–234.
4. Papatzani, S., Paine, K., & Calabria-Holley, J. (2014). *The effect of the addition of nanoparticles of silica on the strength and microstructure of blended Portland cement pastes*. 2014 international concrete sustainability conference, Boston.
5. Calabria-Holley, J., Paine, K., & Papatzani, S. (2014). Effects of nanosilica on the calcium silicate hydrates in Portland cement-fly ash systems. *Advances in Cement Research, 26*, 1–14.
6. Rashad, A. M. (2014). A comprehensive overview about the effect of nano-SiO2 on some properties of traditional cementitious materials and alkali-activated fly ash. *Construction and Building Materials, 52*, 437–464.
7. Папатзани С, Пэйн К, Калабрия-Холли Д. (2014). Прочность и микроструктура цементного камня с добавками коллоидного SiO_2 (Strength and microstructure of colloidal nanosilica enhanced cement pastes (In Russian)). Цемент и его применение (Cement and its Applications), *4*, 80–85.
8. Uddin, F. (2008). Clays, nanoclays, and montmorillonite minerals. *Metallurgical and Materials Transactions A, 39*, 2804–2814.
9. Chang, T. P., Shih, J. Y., Yang, K. M., & Hsiao, T. C. (2007). Material properties of Portland cement paste with nano-montmorillonite. *Journal of Materials Science, 42*, 7478–7487.
10. Ramachandran, V. S., & Beaudoin, J. J. (2001). *Handbook of analytical techniques in concrete science and technology, principles, techniques, and applications* (Building materials series). Norwich: William Andrew Publications.

Characterizing the Dispersion of Graphene Nanoplatelets in Water with Water Reducing Admixture

Erik Wotring, Paramita Mondal, and Charles Marsh

Abstract This research studied the effects of surfactant on graphene nanoplatelet (GNP) dispersion in water. Samples consisted of water, GNPs, and varied amounts of water reducing admixture (WRA). The GNPs were added at a fixed 0.2 % by weight of water while the amount of WRA used served as the independent variable. Sedimentation was qualitatively characterized by observing the rate at which GNPs settled out of suspension. Scanning Electron Microscopy (SEM) was used to obtain micrographs of the dried GNPs. The time evolution of light transmission through the supernatant region was measured with ultraviolet-visible spectroscopy (UV/Vis). Improved understanding and control of GNP dispersion in water has the potential to facilitate the beneficial use of this and similar materials in composites for resulting beneficial mechanical and electrical properties.

Key words Surfactant • Water reducing admixture • Grapheme • Nanoplatelet • SEM • UV/Vis • Dispersion • Composites

1 Introduction

Dispersion research to date involving graphene related compounds appears to mainly have focused on using oxide forms prepared in different ways along with various additions or modified solution environments. Graphene oxide, made by sonicating graphite oxide, can be prepared in a mixture of water, hydrazine, and ammonia [2]. By reducing graphite oxide nanoplatelets, one can create a stable dispersion of graphene in water [1]. The addition of alpha-zirconium phosphate nanoplatelets (ZrP) to graphene oxide leads to a stable dispersion in water [3].

E. Wotring (✉) • P. Mondal
Department of Civil and Environmental Engineering, University of Illinois at Urbana-Champaign, 205 N Mathews Ave., Urbana, IL 61801, USA
e-mail: ewotring@illinois.edu; pmondal@illinois.edu

C. Marsh
ERDC-CERL, US Army Construction Engineering Research Laboratory, 2902 Newmark Dr., Champaign, IL 61822, USA
e-mail: Charles.P.Marsh@usace.army.mil

K. Sobolev, S.P. Shah (eds.), *Nanotechnology in Construction*,
DOI 10.1007/978-3-319-17088-6_17

Electrostatic attraction and hydrogen bonding between the two constituents aided the overall dispersion, while ionization of oxygen constituents could lead to electrostatic repulsion of the graphene oxide particles [3]. Further, ionization of functional groups which contain oxygen could lead to electrostatic repulsion of the graphene oxide particles in the absence of the ZrP [3]. At the oil-water interface graphite oxide-based amphiphilic parrticles were thought to bond to water molecules at particle surface hydroxyl ligand sites [8]. As a result of this hydration, the graphite oxide particles repel one another or disperse [8].

Since covalent based surface modification may well weaken the structure of graphene nanoplatelets [6], it is suggested that study of unmodified GNP dispersion behavior may have advantage for later benefit in application, as well as for improved fundamental understanding. The use of anionic polymer poly(sodium 4-styrenesulfonate), or PSS, during reduction of graphite oxide nanoplatelets results in a stable suspension of PSS coated graphitic nanoplatelets that consist of many layers of graphene [7]. The addition of polyelectrolytes to GNPs was reported to result in a stable GNP suspension, which can be used to form self-assembled multilayers [4]. This method required extensive sonication, in addition to filtration [4]. This method of noncovalent functionalization preserves the mechanical and electrical properties better than covalent modification [4, 6]. Simply applying high-power sonication to GNPs in distilled water reportedly achieves dispersions that remain stable for 600 h [5].

The research on dispersion of GNPs in water without covalent surface modification is still limited. This paper reports a GNP dispersion method using surfactant as a dispersing aid. Specifically water reducing admixture (WRA), typically used for cementitious material, is used in this work as it is intended to ease the possible implementation of this dispersion into a cementitious composite. The dispersion method described here is simplified compared to other methods reported in literature [4]. The sonication time is relatively short and no additional stirring or filtration was used. Furthermore, the authors varied the dosage of the surfactant, the effect of which on GNP dispersion is still not well characterized. The authors hope to add to the characterization of these suspensions of dispersed GNPs in water.

2 Materials and Methods

The GNPs used in this work are xGnP-M-5 GNPs manufactured by XG Sciences, Lansing, MI. These GNPs are delivered as a dry powder of agglomerates that require dispersion. XG Science claims that their method of manufacture does not oxidize the GNPs, which separates these GNPs from the graphite, or graphene, oxide particles that other researchers have discussed. Non-oxidized GNPs have the advantage that none of the intrinsic structure is compromised, which preserves the mechanical properties of the GNPs. The dosage of GNPs was chosen to be a fixed 0.2 %, by weight of water. This value was chosen with an eye to apply this suspension to cementitious composites. With a water to cement ratio (w/c) of 0.5, this GNP dosage translates to 0.1 %, by weight of cement paste.

The WRA used in this study, AdvaCast 575, is a polycarboxylates based high range water reducing admixture manufactured by Grace Construction Products, Columbia, MD. The pH of this material is approximately 5.65. The WRA was dosed according to the ratio of the WRA weight to the GNP weight. As per the manufacturer, the maximum range of dosages spans from 130 to 650 ml per 100 kg of cementitious material. However, in practice the typical dosage range spans 200–390 ml per 100 kg of cementitious material. The authors took weight recommendations as basic guidelines. The manufacturer's recommended minimum dosage would fall at about a WRA to GNP ratio of 1.43.

The method of selecting WRA dosage was chosen because of the precedent in the literature pertaining to carbon nanotubes. Yu used a WRA to CNT ratio of 1.5 (2007). Metaxa used a WRA to CNT ratio of 4 (2012). Konsta-Gdoutos used WRA to CNT ratios of 0, 1.5, 4.0, 5.0, 6.25, and 8.0 (2010). GNPs have greater surface area per unit of mass than CNT [9]. The team imagines that the required range of WRA might be higher than was required for CNT. The morphological difference between CNTs and GNPs might lead to some error in estimating the dosage of WRA from CNT research. Only one of the two faces of the carbon lattice is exposed to the environment in CNTs; both faces are exposed in GNPs. The early experiments included a wider range of ratios. These experiments included the range of WRA to GNP ratios between zero and ten. This range was chosen to take a wide sample of data and to allow direction of subsequent experiments with narrower ranges of interest. The experiments in this paper focused on the range of WRA to GNP ratios between 0 and 4.

2.1 Sedimentation

Borosilicate glass scintillation vials were used for this experiment. The WRA, then the GNPs, were measured into each vial by weight. The team selected 0, 1, 2, and 4 as the weight ratios of WRA to GNP. Fifteen milliliter of water was dispensed into the vial with an Acura 825 pipettor, manufactured by Socorex, Écublens, VD, Switzerland. Finally, the suspension was sonicated with a CPX130PB sonicator, manufactured by Cole-Parmer, Vernon Hills, IL, with a ¼ inch probe for 5 min at 30 % amplitude. The total sonication energy was about 1,750 J. Sedimentation of GNPs in the vial were observed and recorded at regular intervals.

2.2 Scanning Electron Microscope (SEM)

The intent was to characterize the particle size and, if possible, the particle morphology. A holey carbon-coated copper TEM grid with thin deposit of GNP suspension was prepared and taped to SEM sample holder. To prepare the TEM grid, a drop of the GNP suspension was placed onto the TEM grid, and the capillary action of a Kimwipe was used to remove excess liquid. A 6060LV SEM, manufactured by JEOL, Tokyo, Japan, was used in high-vacuum mode for secondary electron

imaging. In this experiment, the authors studied ratios of WRA to GNP of 0, 1, and 2. These ratios were narrowed from the range used for sedimentation because the ratio of 4 showed visually similar behavior. Vials 0, 1, and 2 showed unique behavior to one another, so the authors focused on these ratios.

2.3 Ultraviolet–Visible Spectroscopy (UV–vis)

A Cary 50 UV–vis spectrophotometer, manufactured by Agilent, Santa Clara, CA, was used for these experiments. The instrument was used in a scanning absorbance mode and data collection was performed for 16 h. The transmittance was then calculated from this absorbance data. Because transmittance is inversely proportional to concentration by the Beer-Lambert law, the transmittance can serve as a measure of the stability of the suspension. The same sample preparation method as the one described in section 2.1 was used. For the reasons stated in the SEM section, the authors chose to focus this experiment on WRA to GNP ratios of 0, 1, and 2, to further characterize the differences between these uniquely behaving ratios.

3 Results and Discussion

3.1 Sedimentation

Figure 1 shows vials with ratios of WRA to GNP of 0, 1, 2, and 4, from left to right. The photographs were taken immediately after sonication and after 7 days of rest period without any agitation. After 7 days, at ratio 0, the GNPs settled into a thick layer, leaving a supernatant with no visible evidence of suspended GNPs. For ratio 1, the GNPs settled into a very thin layer, but some darkness remains in the supernatant. This darkness suggests that there remain some GNPs in suspension after 7 days. Ratios 2 and 4 had no visible layer of sediment at the bottom of the vial after 7 days. Most, or all, of the GNPs remained in suspension for ratios 2 and 4. Some gradation in the concentration of GNPs appeared near the top of the suspension for these highest two ratios.

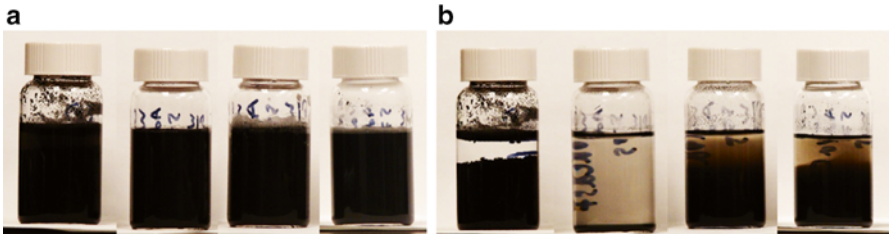

Fig. 1 Sedimentation vials after (**a**) 0 h, and (**b**) 7 days. *From left to right*, the vials have WRA to GNP weight ratios of 0, 1 2, and 4

As mentioned earlier, the particles in ratio 1 settled to a high degree in Fig. 1. The sediment in this vial occupied a smaller volume than the sediment in the vial with no WRA. It seems possible that the dispersant prevented the GNPs from reflocculating after dispersal, but was insufficient to keep the nanoparticles in suspension. This dosage falls below the manufacturer's recommended minimum dosage for cement dispersion and seemed to be insufficient for GNP dispersion as well.

Note the change in sedimentation behavior between ratios 1 and 2. This difference could be related to moving from below to above the recommended minimum dosage, which might correspond to full, or sufficient, coverage of nanoparticles by WRA in order to maintain stability of suspension. Further, a similar change does not occur when increasing the ratio from 2 to 4, which suggests that improvements in the stability of dispersion diminish with continued increase of WRA to GNP ratio. This behavior implies that, once the particles are fully coated with WRA, adding more WRA does not further improve the stability of the dispersion. This diminishing rate of return is what motivated the authors to only investigate ratios 0, 1, and 2 in subsequent experiments for this work.

3.2 Scanning Electron Microscope (SEM)

For sample without any WRA, large agglomerates of GNPs were observed which are not electron transparent (See Fig. 2). With addition of WRA, thin, electron transparent films of GNPs were observed as seen in Fig. 2b, c. The thin film appears to decrease in coverage as the WRA/GNP ratio increases from 1 to 2 and GNPs are observed more as individual small particles. This indicates effectiveness of WRA in GNP dispersion.

The authors also observed further subtle difference in behavior between GNP samples with different dosages of WRA. The diameter of the smallest GNP particle decreased with increasing dosage of WRA, as seen in Fig. 2. In the absence of WRA, the clumps of GNPs measured about 100–500 μm in length. For ratio 1, the particle

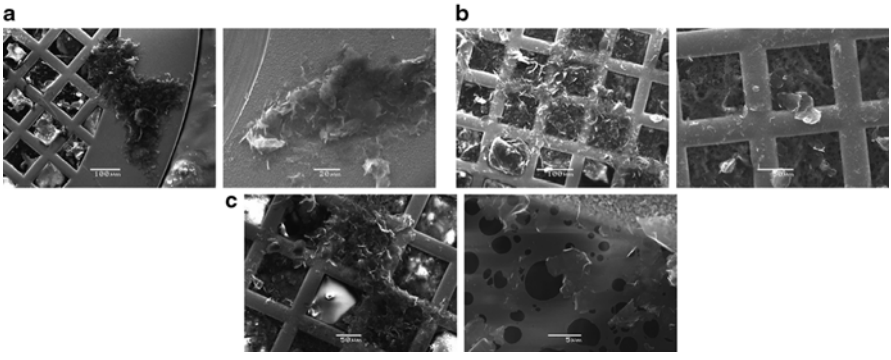

Fig. 2 WRA/GNP = (**a**) 0, (**b**) 1, and (**c**) 2. (**a**) *Left*: scale 100 μm; 180×. *Right*: scale 20 μm; 800×. (**b**) *Left*: scale 100 μm; 220×. *Right*: scale 50 μm; 430×. (**c**) *Left*: scale 50 μm; 300×. *Right*: scale 5 μm; 4,000×

size appeared to go down to about 10 μm in diameter. For ratio 2, the particle diameter measured about 5 μm. The particle size of dispersed GNPs corresponds to the effectiveness of dispersion as the larger particles are probably small agglomerates. The smaller the agglomerate, then, the more effective the dispersion. Therefore, the particle size can be taken as an indirect indicator of the quality of dispersion.

3.3 Ultraviolet–Visible Spectroscopy (UV–vis)

In Fig. 3, the solid line is the behavior that occurs in the absence of WRA. The transmittance does not change from about 2 %. This occurs because the GNPs rapidly agglomerated in the cuvette, and the height of the settled agglomerate exceeded the height at which the laser passed through the cuvette. This sediment, then, did not change in transmittance over the course of the experiment.

When comparing the ratios 0 and 1, the authors observed two main differences. Ratio 0 started at about 2 % transmittance, ratio 1 started at 0 % transmittance. This difference suggests that the GNPs had a relatively high concentration in suspension for ratio 1. The lack of agglomeration in ratio 1 also has a probable effect on the transmittance behavior. The lack of change in transmittance in ratio 0 is contrasted to the change in transmittance in ratio 1, which started after three hours. This change in transmittance suggests that the GNPs with ratio 1 had started to settle.

Another behavior is that, as the ratio of WRA to GNP moves from 1 to 2, there is a jump down in transmittance. In fact, in the 16 h of the experiment, the ratio 2 specimen

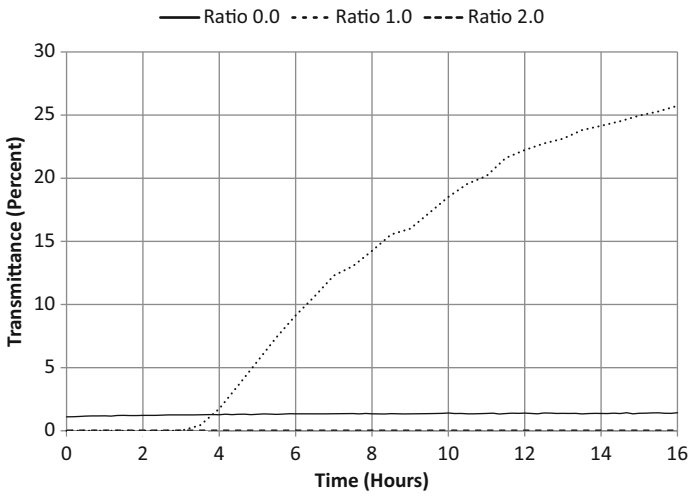

Fig. 3 Transmittance percentage versus time for several amounts of WRA

did not exceed zero percent transmittance. This indicates that the GNPs did not settle at all during the duration of the experiment. By comparison, the transmittance for ratio 1 started to change after three hours. After 16 h, ratio 1 had a transmittance of 25 %. This increase in transmittance indicates that ratio 1 had more GNP settlement than ratio 2. As with the sedimentation experiment, the change in behavior between ratios 1 and 2 is probably related to the surfactant more fully coating the GNPs.

4 Conclusion

The three experimental methods used in this study, taken together, suggest a few conclusions. With an increasing dosage of WRA for the concentration range tested, the GNPs remain in suspension more effectively. Additionally, the size of the agglomerates, according to SEM work, appears to decrease with increasing ratio of WRA to GNP. This decreased size of particles might mean that there is more total surface area available for interaction with a possible composite material.

Because of the significant change in behavior between the three dosages used in this paper, more detailed work is suggested, including more precise variation of WRA to determine the optimum dosages. The authors also plan to pursue additional analysis of this material system. They intend to study the effect of these nanoparticles, in a dispersed state, have on the performance of cementitious composites.

Acknowledgments This research is supported in part by the Section 219 authority of the U.S. Army Corps of Engineers Engineer Research and Development Center. Funding was also obtained from the U.S. Army Research, Development, Test, and Evaluation Program element AT41, “Military Facilities Engineering Technology”. The SEM images were obtained at the Frederick Seitz Materials Research Laboratory Central Facilities, University of Illinois, which is partially supported by the US Department of Energy under grants DE-FG02-07ER46453 and DE-FG02-07ER46471. The authors also acknowledge Sravanthi Puligilla, of the University of Illinois at Urbana-Champaign, who assisted with collection of SEM micrographs.

References

1. Geng, Y. (2009). Preparation of graphite nanoplatelets and graphene sheets. *Journal of Colloid and Interface Science, 336*(2), 592–598.
2. Li, D., Müller, M. B., Gilje, S., et al. (2008). Processable aqueous dispersions of graphene nanosheets. *Nature Nanotechnology, 3*(2), 101–105.
3. Li, P. (2014). Thermally stable and highly conductive free-standing hybrid films based on reduced graphene oxide. *Journal of Materials Science, 49*(1), 380–391.
4. Lu, J. (2010). Stable aqueous suspension and self-assembly of graphite nanoplatelets coated with various polyelectrolytes. *Journal of Nanomaterials*, 2010, 18648601–11.
5. Mehrali, M. (2014). Investigation of thermal conductivity and rheological properties of nanofluids containing graphene nanoplatelets. *Nanoscale Research Letters, 9*(15), 1–12.

6. Peyvandi, A. (2013). Surface-modified graphite nanomaterials for improved reinforcement efficiency in cementitious paste. *Carbon, 63*, 175–186.
7. Stankovich, S. (2006). Stable aqueous dispersions of graphitic nanoplatelets via the reduction of exfoliated graphite oxide in the presence of poly(sodium 4-styrenesulfonate). *Journal of Materials Chemistry, 16*(2), 155–158.
8. Yoon, K. Y. (2013). Graphene oxide nanoplatelet dispersions in concentrated NaCl and stabilization of oil/water emulsions. *Journal of Colloid and Interface Science, 403*, 1–6.
9. Zohhadi, N. Graphene nanoreinforcement for cement-based composites. Poster. American Ceramic Society Meeting. 8–10 July 2013.

Part IV
Nanoparticles

Studies on Hydration of Tricalcium Silicate Incorporating Silica Nano-particles

L.P. Singh, S.K. Bhattacharyya, S.P. Shah, and U. Sharma

Abstract The role of nano-silica during early stage hydration of tricalcium silicate (C_3S) has been investigated using w/b ratio 0.4 for the paste and 5.0 for aqueous phase studies. Results of ICP and XRD showed that the stage of supersaturation of Ca^{2+} is delayed by 30 min and formation of secondary/additional C-S-H starts at the early stages of C_3S hydration in the presence of nano silica. At later age of hydration (4–24 h), XRD results show the predominant nucleation effect of nano-silica upto 10 h. The crystalline peak of CH in nano-silica incorporated samples is more intense than the CH peak of pure C_3S samples, showing the acceleration in growth of hydrated products. While, at later age i.e. from 15 to 24 h, the intensity of CH peak decreases, due to the pozzolanic effect of nano-silica because in pure C_3S samples the intensity of CH peak regularly increase up to 24 h. XRD and FTIR results further reveal that, nano-silica accelerates the formation of crystalline calcium silicate hydrate (C-S-H).

Keywords Tricalcium silicate • Nano silica

1 Introduction

On contact with water, C_3S undergoes an intense, short-lived reaction, known as the pre-induction period. Oxygen ions from the surface of the C_3S lattice react with protons in the water and form hydroxide ions, which in turn combine with Ca^{2+} to form calcium hydroxide [1].

L.P. Singh (✉) • S.K. Bhattacharyya • U. Sharma
Environmental Science & Technology, CSIR-Central Building Research Institute, Roorkee, India
e-mail: lpsingh@cbri.res.in; director@cbrimail.com; purohitusa41@gmail.com

S.P. Shah
Civil and Environmental Engineering, Northwestern University, Evanston, Illinois, USA
e-mail: s-shah@northwestern.edu

K. Sobolev, S.P. Shah (eds.), *Nanotechnology in Construction*,
DOI 10.1007/978-3-319-17088-6_18

$$O^{2-}(\text{lattice}) + H^{+}(aq) \rightarrow OH^{-}(aq)$$
$$Ca^{2+}(\text{lattice}) + OH^{-} \rightarrow Ca(OH)_2$$

At the same time, silicate material from the 'C_3S' lattice surface enters into the liquid phase.

$$SiO_4^{4-}(\text{lattice}) + nH^{+}(aq) \rightarrow H_n SiO_4^{(4-n)-}(aq)$$

A complete reaction may be represented as:

$$C_3S + 3H_2O \xrightarrow{\text{Dissolution}} 3Ca^{2+} + H_2SiO_4^{2-} + OH^{-}$$
$$\downarrow \text{Precipitation}$$
$$C-S-H + Ca(OH)_2$$

The first stage of hydration called pre induction period starts, as C_3S grains comes in contact of water, where the dissolution of ions takes place rapidly. After a few minutes this reaction slows down and induction period start, this stage remains for 2–3 h. Reaction again accelerates after ending of induction period, when the concentration of ions reaches to the stage of super saturation [1, 2].

In recent years, applications of nano materials in construction have brought a new revolution by improving the performance of traditional building materials [3, 4]. Shah et al., 2010–2013 [5–7] have studied various engineering properties of cementitious systems using different kinds of nanomaterials such as colloidal nano-silica, nano-lime, carbon nanotubes etc. Singh et al., 2012 [8] have reported that addition of nano-silica into the cement paste refined the microstructure of the paste and calcium leaching is significantly reduced as nano-silica reacts with CH and forms additional C-S-H gel. The chemistry of hydration in the presence of nano-silica is an important issue from the point of research, especially during first 24 h of hydration. In the present studies, influence of nano-silica on hydration during first 24 h of C_3S was examined using XRD, and FTIR techniques.

2 Experiments

2.1 Tricalcium Silicate (C_3S)

C_3S was prepared by high-temperature solid-state reaction between calcium carbonate and silicic acid. Starting materials were mixed in the stoichiometric ratio (3:1) and then heated up to 1,000 °C with a rate of 10 °C/min and a curing of 5 h at this

Table 1 Characterization of C_3S

CaO	SiO_2	1–10 μ	10–30 μ	30–50 μ	Specific Surface Area (m^2/g)
74.2 %	24.9 %	41 %	55 %	4 %	3.01

Table 2 Characterization of synthesized n-SiO_2

Nano-silica	SSA (m^2g^{-1})	Particle size (nm)
n-SiO_2	116	30–70

temperature. The mixture was further heated to 1,500 °C with a rate of 5 °C/min and a curing of 12 h at the final temperature. The prolong heating at 1,500 °C is required to obtain a free lime content of ≤0.4 %. Prepared C_3S was grounded in a milling device using isopropanol as a dispersing agent to reduce the agglomeration and finally, the sample was dried at 40 °C after grinding. The properties of prepared C_3S are given in Table 1.

2.2 Nano-silica

Nano-silica synthesized from sol–gel method using water-glass as a precursor. The properties of synthesized nano-silica are given in Table 2.

2.3 Sample Preparation of Pure and Nano-silica Incorporated C_3S for Hydration Studies

For the study of hydration mechanism, in the presence of nano-silica in pure C_3S at early stage 10 % (w/w) laboratory synthesized powder n-SiO_2 added in powder form in the pure C_3S. Total w/c ratio kept 5.0 for pore solution analysis and 0.4 for paste study in all the samples. Hydration stopped at 2 min to 24 h which covers all the main stages of hydration.

2.4 Characteristics Techniques

In the present studies, influence of nano-silica on C_3S during first 24:00 h of hydration has been studied. The techniques, Inductive Couple Plasma (ICP) (model Prodigy XP, Teledyne Leeman lab, USA) for the determination of ionic concentration, Powder X-ray diffraction (model DMax-2200, Rigaku, Japan) was used for the study of different phases formed during the hydration at early stage. All the experiments were carried out at room temperature using copper radiation (Cu-Kα) at 40 kV/40 mA. Scanning was performed with a step width of 0.02° 2θ over an angular range from 5° to 80° with a scanning rate of 0.5°/min throughout the experiments. FTIR (model NEXUS (1100), Thermo Nicolet, FTIR, USA) used for the study of chemical bonding in hydrated phases

3 Result and Discussion

Hydration of the cementitious system is a complicated process and its complexity increases with the use of additives. Though the addition of nano-silica improves the early age strength, the precise chemistry behind the phenomenon is still not very clear. The concentration of Ca^{2+} in pore solution measured by ICP, show a sudden fall within first few minutes of hydration in the presence of nano-silica (Fig. 1). This attributes to the higher kinetics of nano-silica (due to its high specific surface area), which reacts with the Ca^{2+} released from C_3S grains and forms secondary C-S-H. XRD results also show the existence of additional C-S-H at early stages of hydration. In hydrated samples, characteristic peak of C_3S overlapped with the C-S-H peak at $2\theta = \sim 32$ [9]. The intensity of this peak gradually decreases upto 1 h in pure C_3S samples, showing the dissolution of C_3S (Fig. 2a). However, in the case of nano-silica incorporated C_3S, intensity of this peak increases upto 1 h (Fig. 2b) showing the formation of C-S-H. This new peak may be associated to the formation of secondary C-S-H, because this trend was absent in hydrated C_3S samples. The characteristics peak of C-S-H at $2\theta = 50.7$ gives the crystalline nature of C-S-H (jennite and tobermorite) [10]. In case of pure C_3S samples this peak appeared at 15 h and the intensity remains constant upto 24 h (Fig. 3a), while in the presence of nano-silica this peak appeared at 8 h and the intensity of this peak increases gradually upto 24 h (Fig. 3b). This indicates that in presence of nano-silica a well ordered crystalline C-S-H is formed.

Appearance of crystalline peak of CH at $2\theta = 18.2$ [9] in hydrated samples at early stage represents the stage of supersaturation of Ca^{2+} in the pore solution. In hydrated C_3S samples this peak appeared at 2:30 h of hydration (Fig. 4a(i)), while this stage comes 30 min later i.e. at 3 h in the presence of nano-silica (Fig. 4b(i)). These findings are also in consistent with the results obtained by ICP (Fig. 1). The concentration of Ca^{2+} falls at 2:30 h of hydration in case of pure C_3S samples

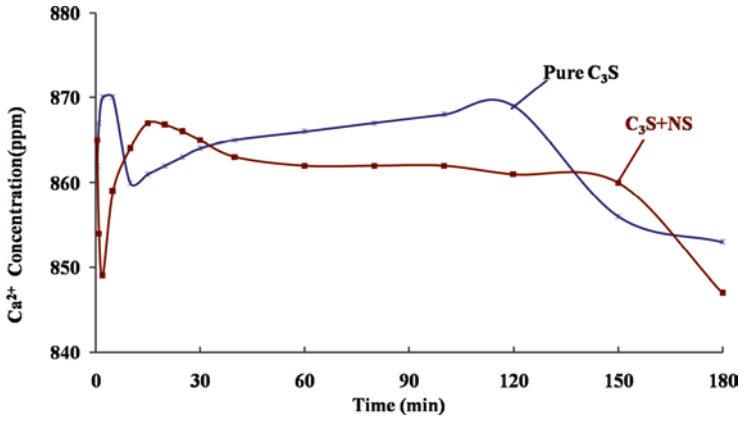

Fig. 1 Ca^{2+} concentration in pure and nano-silica incorporated C_3S

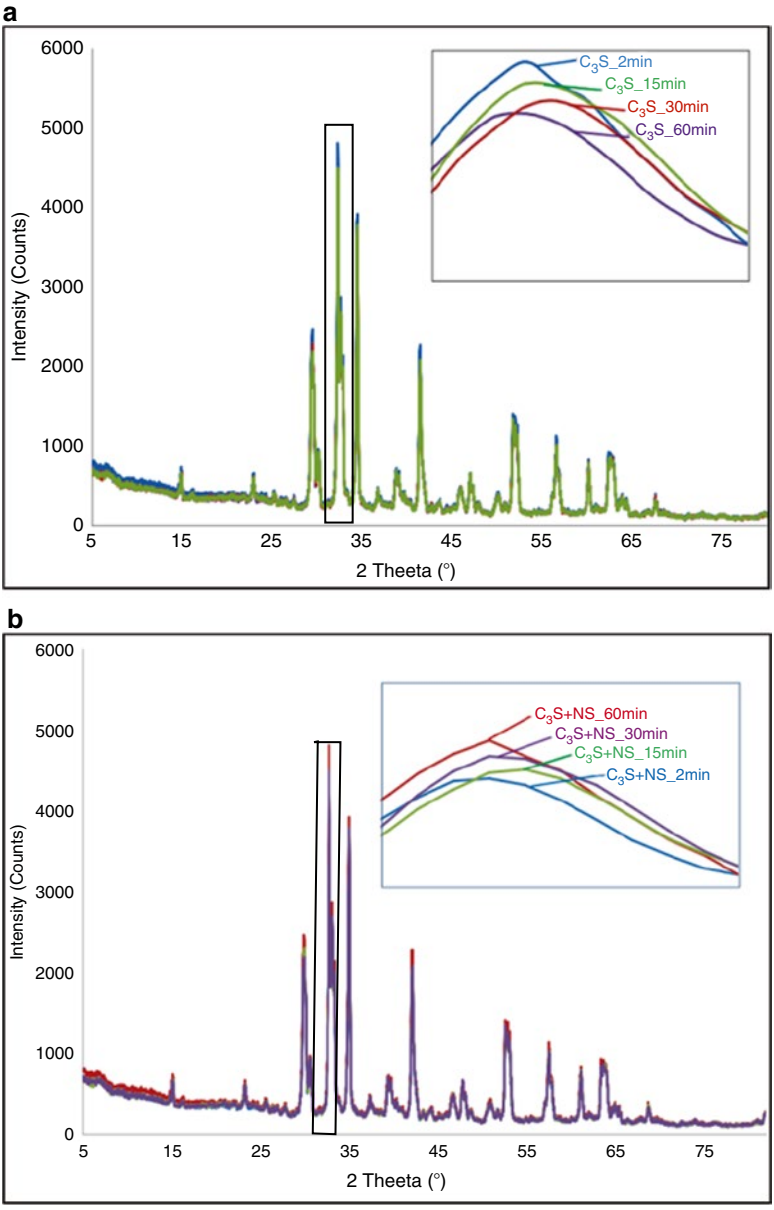

Fig. 2 XRD profile of hydrated pure C_3S (**a**) and nano-silica incorporated C_3S (**b**)

showing the stage of supersaturation when crystallization of CH takes place. This stage appeared at 3 h of hydration, i.e. 30 min later in the presence of nano-silica. This shift in the stage of super saturation occurs because, in the presence of nano-silica, Ca^{2+} are regularly consumed by the nano-silica and thus, forming secondary

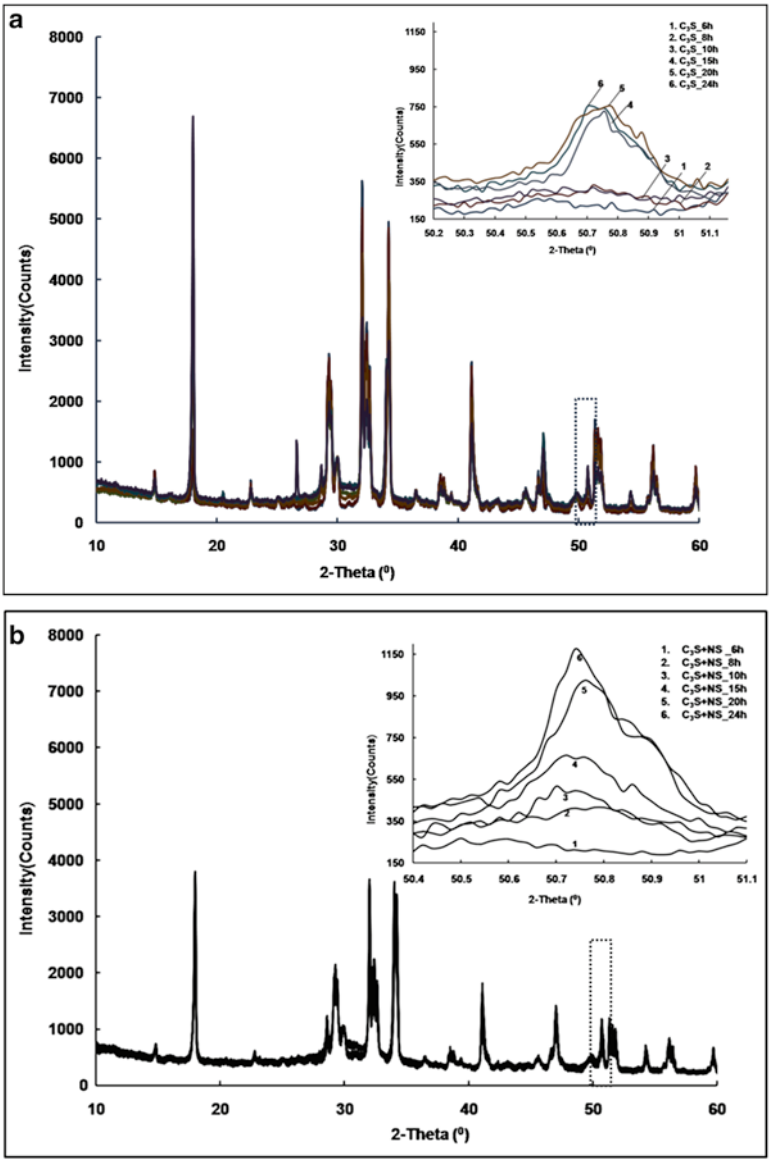

Fig. 3 Appearance of crystalline C-S-H peak in hydrated pure C_3S (**a**) and in nano-silica incorporated C_3S (**b**)

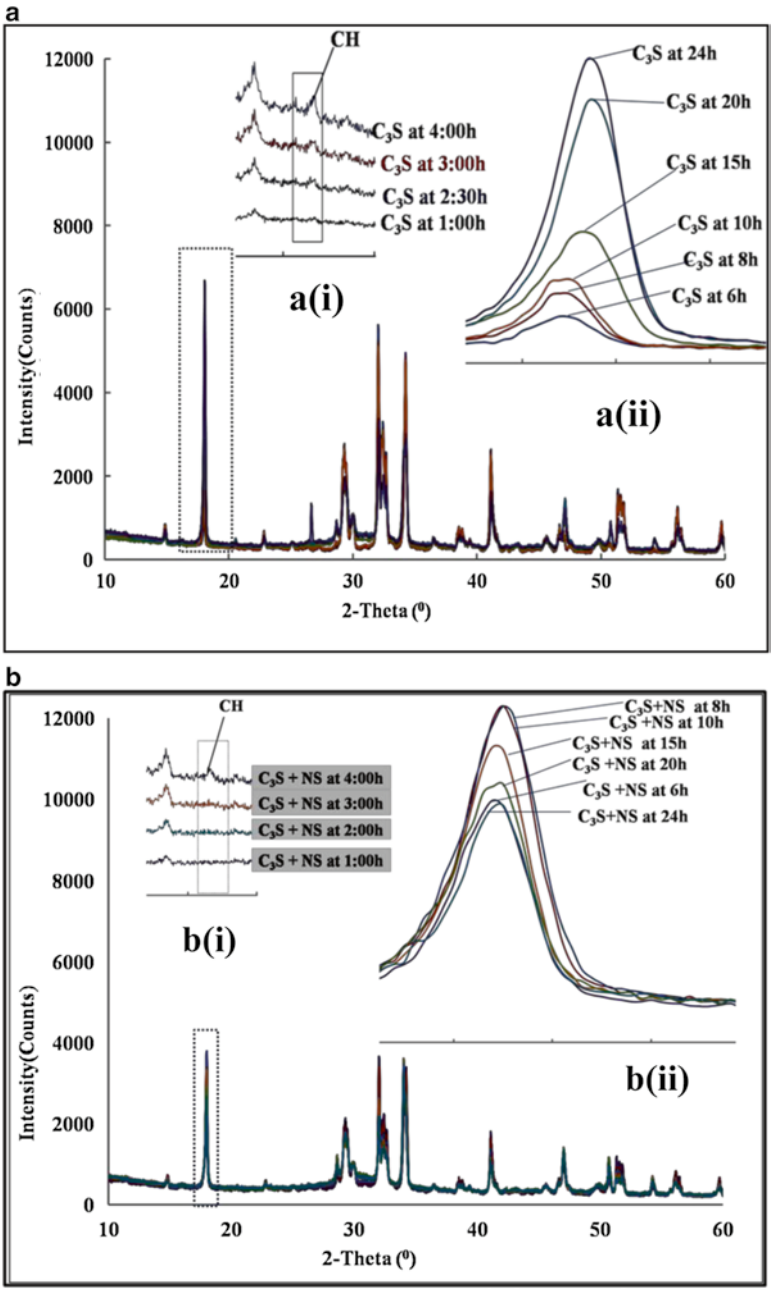

Fig. 4 Intense peak of CH in hydrated pure C_3S (**a**) and nano-silica incorporated C_3S (**b**)

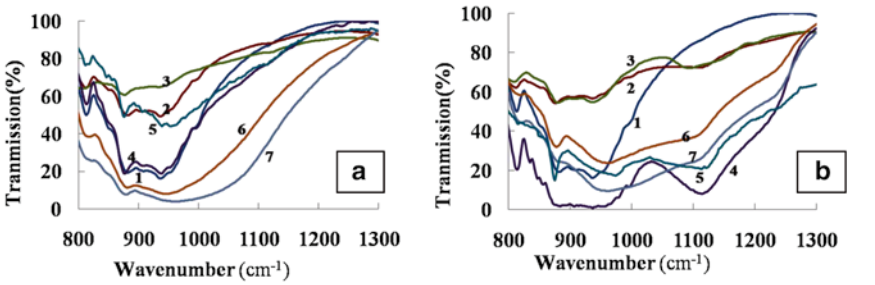

Fig. 5 FTIR of hydrated C_3S (**a**) and nano-silica incorporated C_3S (**b**) at different time intervals

C-S-H. Further, during acceleration period the intensity of CH peak in nano-silica incorporated C_3S samples increased upto 10 h (Fig. 4b(ii)) and have higher intensity than the CH peak of pure samples (Fig. 4a(ii)), indicates the nucleation effect of C-S-H seeds formed at early stage (upto 1 h) of hydration. While, at later age the intensity of this peak decreased upto 24 h (Fig. 4b(ii)) due to the pozzolanic effect of nano-silica, because, the intensity of CH peak in pure C_3S samples shows an increasing trend upto 24 h (Fig. 4b(ii)).

Further, in FTIR studies, a broad band at 850–930 cm^{-1} (characteristic peak of crystalline C_3S) [11] gradually decreases with the hydration (Fig. 5a, b) showing the consumption of C_3S during hydration. Depletion rate of this transmittance peak was higher in nano-silica incorporated C_3S than pure C_3S samples at early stages (upto 1 h) of hydration. This indicates that the dissolution process is accelerated in the presence of nano-silica. A shift in this peak towards higher region shows polymerization in silicate chain (Fig. 5a, b). This shift occurs at 18 h in pure hydrated samples (Fig. 5a) while, there was a quite intense Q^2 peak of silicate chain in nano-silica incorporated samples at 6 h (Fig. 5b). A slight hump of Q^3 peak is also observed at 18 and 24 h (Fig. 5b) shows higher polymerization in silicate chain and crystalline nature of C-S-H in the presence of nano-silica.

4 Conclusion

Nano-silica is being incorporated into the cement to give enhanced mechanical property, lower porosity and permeability, which are the crucial factors for increased durability. To understand the chemistry of hydration in the presence of nano-silica, C_3S was hydrated with a w/c ratio 0.4 for paste and 5.0 for aqueous phase studies. Hydration process was monitored for the first 24 h of hydration, which completely covered the all the main period of hydration and findings are as follows:

- XRD results show the presence of additional C-S-H at early stages of hydration as evident by new peak appearance and at later stage more crystalline phase of C-S-H observed in the presence of nano-silica.

- CH peak appeared 30 min later in nano-silica incorporated C_3S system, showing the shift in the stage of supersaturation of Ca^{2+} and at later age both the effects of nano-silica (i.e. nucleation and pozzolanic) are clearly visible.
- ICP results also show the existence of additional C-S-H and shift in the supersaturation stage of Ca^{2+} in the presence of nano-silica.
- FTIR results revealed that in the presence of nano-silica, dissolution of C_3S grain accelerates and polymerization in the silicate chain speeds up.

Acknowledgements The present work is supported by joint INDO-UK research programme under UKIERI scheme. Author (Usha Sharma) is grateful to University Grant Commission, New Delhi for grant of Senior Research Fellowship.

References

1. MacLaren, D. C., & White, M. A. (2003). Cement: Its chemistry and properties. *Journal of Chemical Education, 80*, 623–636.
2. Scrivener, K. L., & Nonat, A. (2011). Hydration of cementitious materials, present and future. *Cement and Concrete Research, 41*, 651–665.
3. Sobolev, K., & Gutierrez, M. F. (2005). How nanotechnology can change the concrete world: Part 1. *American Ceramic Society Bulletin, 84*(10), 14–17.
4. Sobolev, K., & Gutierrez, M. F. (2005). How nanotechnology can change the concrete world: Part 2. *American Ceramic Society Bulletin, 84*(11), 16–19.
5. Hou, P., Kawashima, S., Kong, D., David, J. C., Qian, J., & Shah, S. P. (2013). Modification effects of colloidal nano SiO_2 on cement hydration and its gel property. *Composites: Part B, 45*, 440–448.
6. Konsta-Gdoutos, M. S., Metaxa, Z. S., & Shah, S. P. (2010). Multi-scale mechanical and fracture characteristics and early-age strain capacity of high performance carbon nanotube/cement nanocomposites. *Cement and Concrete Research, 32*(2), 110–115.
7. Kong, D., Du, X., Wei, S., Zhang, H., Yang, Y., & Shah, S. P. (2012). Influence of nano-silica agglomeration on microstructure and properties of the hardened cement based materials. *Construction and Building Materials, 37*, 707–715.
8. Singh, L. P., Bhattacharyya, S. K., Mishra, G., & Ahalawat, S. (2012). Reduction of calcium leaching in cement hydration process using nanomaterials. *Materials and Technologies, 27*, 233–238.
9. Jadhav, R., & Debnath, N. C. (2011). Computation of X-ray powder diffractograms of cement components and its application to phase analysis and hydration performance of OPC cement. *Bulletin of Materials Science, 34*(5), 1137–1150.
10. Grangeon, S., Claret, F., Linard, Y., & Chiaberge, C. (2013). X-ray diffraction: A powerful tool to probe and understand the structure of nanocrystalline calcium silicate hydrates. *Acta Crystallographica, B69*, 465–473.
11. Bjornstrom, J., et al. (2004). Accelerating effects of colloidal nano-silica for beneficial calcium-silicate-hydrate formation in cement. *Chemical Physics Letters, 392*, 242–248.

Interaction of Amorphous Nano-aluminosilicates with Cement Pore Solution and the Effect on the Early Hydration Reaction of Portland Cement

J.F. Munoz, J.M.S. Silva, L. Perry, J. Youtcheff, and K. Sobolev

Abstract Amorphous nano-aluminosilicates are potentially seen as a new generation of nano-particle additives that can be used in cementitious materials. The primary objective of this research was to compare the effects of these novel nano-additives on the early hydration of Portland cement. The chemical and morphological changes undergone by the nano-particles as a result of exposure to cement pore solution were studied using Fourier transform infrared spectroscopy. The influence of the nano-particle solutions, or sols, on the cement hydration reaction was investigated using isothermal calorimetry. The results indicated a correlation between the arrangement of the aluminum within the silica framework and agglomeration of the nano-particles. Further, the effect of both these aspects on the hydration reaction of Portland cement is discussed.

Keywords Nanoaluminosiliates • C-A-S-H • Early hydration reaction and portland cement

J.F. Munoz (✉) • L. Perry
Chemistry Laboratory, SES Group & Associates LLC, Chesapeake City, MD, USA
e-mail: jose.munoz.ctr@dot.gov; lakesha.perry.ctr@dot.gov

J.M.S. Silva
National Research Council -Turner-Fairbank Highway Research Center,
Washington, DC, USA
e-mail: jmsanfil@gmail.com

J. Youtcheff
Pavement and Materials Team, Turner-Fairbank Highway Research Center,
McLean, VA, USA
e-mail: jack.youtcheff@dot.gov

K. Sobolev
Department of Civil and Environmental Engineering,
University of Wisconsin-Milwaukee, Milwaukee, WI, USA
e-mail: sobolev@uwm.edu

K. Sobolev, S.P. Shah (eds.), *Nanotechnology in Construction*,
DOI 10.1007/978-3-319-17088-6_19

1 Introduction

A new interest is currently growing in the use of nano-aluminosilicates as a novel type of additive in cement-based materials [1]. These nano-materials can be classified under non-calcinated nano-clays and amorphous nano-aluminosilicates based on the crystalline structure. Moderate quantities of clay minerals at nano-particle size range in cement-based materials can nucleate the formation of calcium silicate hydrate (C-S-H) [2], improve certain fresh state properties such as green strength [3], and decrease gas and water permeability of the hardened specimens [4].

Amorphous nano-aluminosilicates are potentially seen as a new generation of nano-particle additives that can be used in cementitious materials. The interest in these materials resides in their amorphous character, which may offer the possibility of nucleating alternative hydration products to C-S-H, such as calcium aluminate silicate hydrate (C-A-S-H), especially in systems where cement is a minor component, such as high volume fly ash mixtures.

The research work reported in this manuscript analyzes the effect of a group of amorphous nano-aluminosilicates on the early hydration of Portland cement paste. The data aids in identifying the mechanism undergone by these amorphous nano-aluminosilicates in the presence of cement pore solution and the effects on the early hydration reaction.

2 Material and Methodology

The following reagent grade chemicals were used in the preparation of the sols: tetra-ethyl orthosilicate (TEOS), aluminum-tri-sec-butoxide (ATSB), aluminum ethoxide (AE), sec-butyl alcohol ($C_4H_{10}O$), ethanol (C_2H_6O), nitric acid (HNO_3), sulfuric acid (H_2SO_4), hydrochloric acid (HCl), and deionized water (18.2 MΩ cm). The aluminosilicates sols were synthesized by mixing 1 mole of TEOS and 1.3 moles of the corresponding aluminum alkoxide, at a water to alkoxide molar ratio (r) of 194 and at mole of acid to mole of alkoxides ratios (A) of 0.22 or 0.13 depending of the nature of the aluminum alkoxide. The principal variables in the synthesis, summarized in Table 1.

The synthesis protocol used was a variation from the method described in Pozarnsky and McCormick, [5]. Following the synthesis, all sols were dialyzed [6]. A reactor was created to study the interaction between nano-particles and ions in the cement pore solution. A total of 167 g of cement and the corresponding 0.75 %

Table 1 Variables of the sol–gel synthesis process

Sample Id	AT-47	AT-57	AT-58	AE-48	AE-50	AE-52
Al Alkoxide	ATSB			AE		
Acid	HNO_3	H_2SO_4	HCl	HNO_3	H_2SO_4	HCl
A	0.22			0.13		
Particle size range (nm)	25–340	80–1,600	10–320	30–440	65–1,300	10–370

wt. replacement of nano-aluminosilicate were immersed in the reactor in two separated Spectrum Spectra/Por 3 RC dialysis membranes at a water to cementitious material ratio (w/c) of 3, purged with N_2 and stirred for 72 h. In order to simulate realistic cement pore solution conditions in the reactor, the membrane containing the nano-particle sol was immersed into the vessel once the reactor reached equivalent calcium concentration values as those in real cement paste samples [7]. After the 72 h period, the remaining nanoparticles were collected from the dialysis membrane and dried for analysis with the FTIR spectrometer.

An Empyrean Series 2 X-ray Diffraction System manufactured by Panalytical was used to examine the mineralogy of the nano-particles. The size range was determined with a Zeta Potential Analyzer ZETA PLUS manufactured by Brookhaven Instruments. Xerogels were analyzed using a Digilab Excalibur FTS 3000 Series Fourier transform infrared spectrometer. The spectra of KBr pellets with 0.3 % sample concentration were collected at 4 cm^{-1} resolution and co-adding 32 scans per spectrum. Isothermal calorimetry experiments were performed at 25 °C using a TAMair model TA instrument. Samples of cement paste containing 0.75 wt. % of nano-particles were prepared at water to cement ratio of 0.45.

3 Results and Discussion

3.1 Nanoparticle Characterization

The amorphous nature of the synthesized nano-aluminosilicates was revealed by the absence of sharp peaks and presence of humps in the XRD diffractograms. All the nano-aluminosilicates had the same diffractogram independent of the type of alkoxide and acid used during the synthesis, with humps at 7.4°, 26.5°, 39.8°, 65.2° and 68.1° 2θ. With the exception of the hump at 7.4° 2θ, which was associated with zeolite type mineral, the observed humps were linked to sillimanite mineral (Al_2SiO_5). The 26.5° 2θ is also a common hump in amorphous silicates [8].

The FTIR analysis of the samples displayed in Figure 1 provides additional information regarding the structure of the nano-particles. The tentative assignments of the principal bands in the 400–1,300 cm^{-1} region are summarized in Table 2. The FTIR spectrum showed typical characteristics of aluminosilicates. The Si-O-Si asymmetric stretching band in the samples was shifted toward a lower wavenumber (964 cm^{-1}) with respect to silica (1,082 cm^{-1}). This shift was caused by the incorporation of Al^{3+} into the Si^{4+} sites [9]. Additionally, the spectra showed a strong and broad vibration band between 493 and 690 cm^{-1}. This region was associated with the presence of bending and stretching bands of Si-O-Al and stretching of Al-O for condensed AlO_6 octahedral [9–11]. The FTIR spectrum did not show significant differences despite the type of alkoxide. Only the vibrational bands associated with the amorphous aluminosilicate backbone (1,010–1,250 cm^{-1}) showed differences due to the type of acid used in the synthesis. This is the case for the band at 1,064 cm^{-1} associated with vibrations of tetrahedral SiO_4 groups. Both samples, AT-57 and AE-50, synthesized in the presence of H_2SO_4, had a broader and more intense 1,064 cm^{-1} band than the

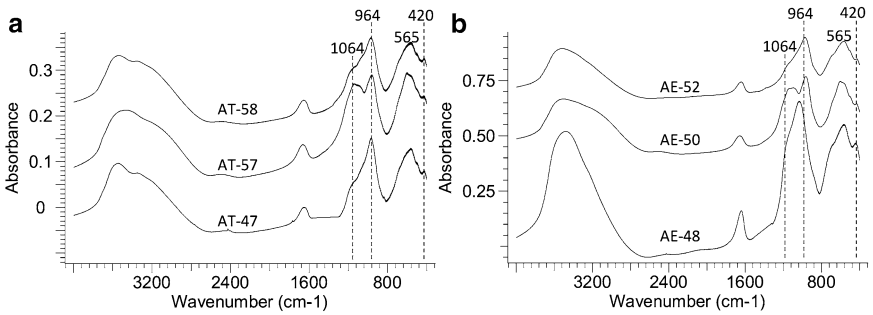

Fig. 1 FTIR spectra of the two nano-aluminosilicates synthesized series: ATSB (**a**) and AT (**b**)

Table 2 Characteristic bands and assignments of the nano-aluminosilicates before and after 3-days exposure to simulated pore solution

Band, cm^{-1}	Assignment	Reference
420	Si-O internal deformation of SiO_4 tetrahedral	[9]
497*	Bending of Si-O-Si and O-Si-O	[10]
530–620	Symmetric stretching of Si-O-T (T = Si or Al)	[10]
690*–710	Al-O stretching for condensed AlO_6 octahedral	[11]
867	Out of plane bending of CO_3^{-2}	[8]
960–990	Asymmetric stretching T-O-Si of (T = Si or Al)	[11]
1,064*	Vibrations of tetrahedral SiO_4 groups	[11]
1,110	Asymmetric stretching of Si-O	[10]
1,411–1,544	Asymmetric stretching (v3) of CO_3^{-2}	[10]

Note: * = shoulder

Table 3 Summary of the effect of nano-aluminosilicates on the early hydration of cement

Sample Id	Control	AT-47	AT-57	AT-58	AE-48	AE-50	AE-52
Max. C_3S Peak, hours	10.29	7.52	8.64	7.68	7.94	9.10	8.33
Max. Al-phase Peak, hours	14.04	10.15	11.91	10.40	10.84	12.24	12.71

other nano-aluminosilicates. These differences in the band can be attributed to the incorporation of sulfate ions by the nano-aluminosilicate [12].

3.2 Isothermal Calorimetry Data

In all the cases, the hydration of not only the tricalcium silicate (C_3S) peak but also the alumina-bearing phases was accelerated with respect to the control. The enhancement in the hydration of the alumina-bearing phases was caused by the strong capacity of this type of nano-particle to incorporate sulfates from the cement pore solution. Table 3 summarizes the magnitude of the acceleration effect in both

C_3S and alumina-bearing phases. The comparison based on alkoxide type revealed that the AE-based nano-aluminosilicates had less capacity to accelerate the hydration reaction then ATSB-based nano-aluminosilicates. Finally, a comparison based on the type of acid, indicated that AT-57 and AE-50 nano-particles synthesized in the presence of H_2SO_4 had less capacity to accelerate the hydration of both phases than the other two acids tested. One explanation for this behavior is the fact that these two nano-particles had the coarsest particle size distribution among all synthesized nano-aluminosilicates (see size distribution in Table 1). In addition, it is expected that the pre-existence of sulfate ions in the structure of these samples may mitigate the affinity for additional sulfate ion uptake from the pore solutions and therefore contribute less to the acceleration of the alumina-bearing phase.

3.3 Effect of Simulated Cement Paste Pore solution

As is summarized in Table 2, the broad band in the original samples located between 493 and 690 cm^{-1} evolved towards a more defined group of bands at 532, 617, 673, and 707 cm^{-1}. At the same time, the Si-O-T asymmetric stretching band shifted toward higher wavelength numbers and became better resolved. These changes indicated an increased polymerization and structured order of the nano-aluminosilicate caused by the incorporation of calcium from the simulated cement paste pore solution. This re-organization of the alumina-silica network was different depending on the nature of the nano-aluminosilicates. This difference is illustrated in Figure 2, where the spectrum before and after exposure are compared for two nano-particles, AT-58 and AE-52. Those nano-particles synthesized with AE alkoxide, such as AE-52 in Figure 2, developed an intense band at 1,110 cm^{-1}. This band was assigned to Si-O asymmetric stretching caused by a highly polymerized sheet and/or a framework structure [10], which indicated a higher propensity of AE-based nano-aluminosilicates to polymerize under cement pore solution conditions.

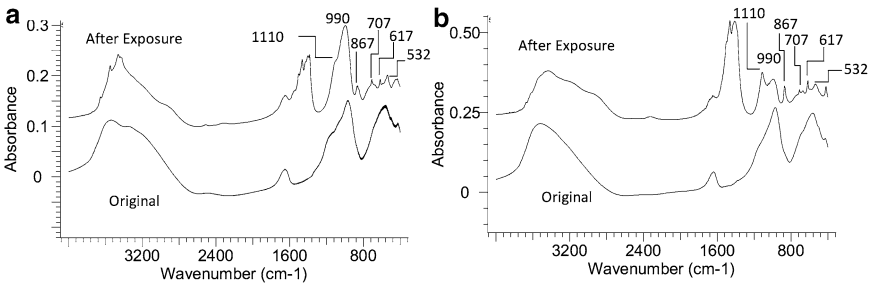

Fig. 2 Comparison of FTIR spectrum of nano-aluminosilicates before and after 3-days exposure to simulated pore solution. Sample AT-58 (**a**) and AE-52 (**b**)

4 Conclusion

Two series of nano-aluminosilicates were synthesized with different types of aluminum precursor in the presence of three acids. Both series were capable of accelerating the hydration of C_3S and alumina-bearing phases in Portland cement. However, those nano-particles synthesized using the ATSB showed higher acceleration capacity, most likely due to the higher content of aluminum in tetrahedral coordination. The higher degree of agglomeration and presence of sulfate ions in the nano-particle framework were identified as potential mechanisms to justify the lower acceleration in the hydration of cement in samples AT-57 and AE-50. The exposure to simulated pore solution triggered the incorporation of calcium into the alumina-silica framework causing an increase in the polymerization in all samples and more significantly in the AE-based nano-aluminosilicate.

References

1. Nehdi, M. L. (2014). Clay in cement-based materials: Critical overview of state-of-the-art. *Construction and Building Materials, 51*, 372–382.
2. Lindgreen, H., Geiker, M., Krøyer, H., Springer, N., & Skibsted, J. (2008). Microstructure engineering of Portland cement pastes and mortars through addition of ultrafine layer silicates. *Cement and Concrete Composites, 30*(8), 686–699.
3. Kawashima, S., Kim, J. H., Corr, D. J., & Shah, S. P. (2012). Study of the mechanisms underlying the fresh-state response of cementitious materials modified with nanoclays. *Construction and Building Materials, 36*, 749–757.
4. Farzadnia, N., Abang Ali, A. A., Demirboga, R., & Anwar, M. P. (2013). Effect of halloysite nanoclay on mechanical properties, thermal behavior and microstructure of cement mortars. *Cement and Concrete Research, 48*, 97–104.
5. Pozarnsky, G. A., & McCormick, A. V. (1995). Multinuclear NMR study of aluminosilicate sol–gel synthesis using the prehydrolysis method. *Journal of Non-Crystalline Solids, 190*(3), 212–225.
6. Muñoz, J. F., Yao, Y., Youtcheff, J., & Arnold, T. (2014). Mixtures of silicon and aluminum oxides to optimize the performance of nanoporous thin films in concrete. *Cement and Concrete Composites, 48*, 140–149.
7. Juilland, P., Gallucci, E., Flatt, R., & Scrivener, K. (2010). Dissolution theory applied to the induction period in alite hydration. *Cement and Concrete Research, 40*(6), 831–844.
8. Schneider, J. F., Hasparyk, N. P., Silva, D. A., & Monteiro, P. J. (2008). Effect of lithium nitrate on the alkali-silica reaction gel. *Journal of the American Ceramic Society, 91*(10), 3370–3374.
9. Jones, S. D., Pritchard, T. N., & Lander, D. F. (1994). Physical properties of sol–gel aluminosilicates. *Microporous Materials, 3*(4–5), 419–431.
10. Lee, W. K. W., & Van Deventer, J. S. J. (2003). Use of infrared spectroscopy to study geopolymerization of heterogeneous amorphous aluminosilicates. *Langmuir, 19*(21), 8726–8734.
11. Sinko, K., Mezei, R., Rohonczy, J., & Fratzl, P. (1999). Gel structures containing Al (III). *Langmuir, 15*(20), 6631–6636.
12. Peak, D., Ford, R. G., & Sparks, D. L. (1999). An in situ ATR-FTIR investigation of sulfate bonding mechanisms on goethite. *Journal of Colloid and Interface Science, 218*(1), 289–299.

The Effect of Nano-SiO_2 on Cement Hydration

Ismael Flores-Vivián and Konstantin Sobolev

Abstract The nanoparticles of SiO_2 with a size range of 5–20 nm were synthesized in acidic and basic medium from tetraethoxysilane (TEOS) using sol–gel method. The effect of agglomerated nanoparticles on the hydration of portland cement systems was analyzed by X-Ray Diffraction technique. Experimental results demonstrate that developed nano-SiO_2 produced in acidic medium accelerate the hydration by creating nuclei sites for the formation of C-S-H, whereas the nano-SiO_2 produced in basic medium reacted like a pozolanic material. Most of the portlandite was consumed and transformed into C-S-H due to a pozolanic reaction producing a dense microstructure characteristic for composites with both types of nanoparticles.

Keywords Cement • Hydration • Nanoparticles • SiO_2 • Tetraethoxysilane • TEOS • Sol–gel • Nuclei sites • C-S-H • Pozolanic • Portlandite • Microstructure

1 Introduction

For many years researches are trying to modify and improve the properties of portland cement systems at different levels. At a mesoscale (100 μm to 50 mm), researches deal with the optimization of aggregates to reduce the consumption of cementitious materials [1–5], as well as to improve the performance of concrete mixtures [6, 7]. Different compaction techniques [8] or addition of air entraining additive [9] have been used to enhance the durability against freeze-thaw damage. At a sub-micro-scale (100 nm to 1 μm) and micro-scale (1–100 μm), addition of supplementary cementitious materials was used to increase the mechanical performance and durability of portland cement based materials [10, 11]. At nanoscale (1–100 nm), nanoparticles such as SiO_2 and TiO_2, have been used in order to enhance

I. Flores-Vivián (✉)
Materials Development Manager, OVNIVER, Mexico
e-mail: ismaelfv1975@gmail.com

K. Sobolev
Department of Civil and Environmental Engineering,
University of Wisconsin-Milwaukee, Milwaukee, WI, USA
e-mail: sobolev@uwm.edu

K. Sobolev, S.P. Shah (eds.), *Nanotechnology in Construction*,
DOI 10.1007/978-3-319-17088-6_20

the reaction of supplementary cementitious materials, modify the rheological behavior as well as to improve the strength and durability of concrete [5].

At nanoscale, silica nanoparticles were used extensively to increase the mechanical performance and durability of concrete. Björnström et al., investigated the effects of colloidal silica and the hydration process of C_3S (alite, Ca_3SiO_5) [1] and β-C_2S (belite, β-Ca_2SiO_4) [2]. It was demonstrated that nanoparticles accelerate the formation of C-S-H gel in the first 24 h, especially, at higher dosage up to 5 %. Collepardi et al. [3], produced self-consolidated concrete with low-heat of hydration using 1 and 2 % of colloidal silica as a viscosity modifier. It was observed that nanoparticles enable production of a cohesive concrete with reduced segregation and bleeding. Qing et al., investigated the transformation of $Ca(OH)_2$ phase in pastes and concrete with silica fume and nanosilica [4]. The nanosilica increased the viscosity and reduced the setting time in pastes. In nanosilica concrete, the quantity of the $Ca(OH)_2$ crystals in the interface zone was smaller, and the mechanical performance at early age was better vs silica fume concrete. Flores et al. [5], studied the performance of synthesized nanosilica in portland cement mortars. The addition of superplasticizer and the effective nanoparticles dispersion technique were used to distribute the nano materials in the cementitious matrix enhancing the mechanical performance of mortars. Gaitero et al. [12], demonstrated that the addition of nano-SiO_2 (NS) in cementitious system can improve the mechanical performance by controlling the degradation of C-S-H under calcium leaching process. In spite of attractive performance, the application of nanoparticles is still limited, mainly because of high cost and limited supply.

In order to optimize the effect of nanomaterials in concrete, a better understanding of the effect associated with nanomaterials synthesis process is needed. There are different technologies that can produce nanomaterials and one of the most common is the synthesis using sol–gel. This technology allow to produce particles, films and fibers which depend on the molar ratio of the materials, type and amount of the catalyst, temperature, pH, amount of water, time of the process and the treatment applied after the synthesis [13]. These parameters can affect the overall behavior of the system when they interact with portland cement. The objectives of this work involves the production and characterization of nanoparticles of SiO_2 produced by the sol–gel process, and study of nanoSiO_2 effect on the hydration of portland cement systems using X-ray diffraction.

2 Materials and Test Procedures

Nanoparticles of SiO_2 were synthesized using the sol–gel method utilizing Tetraethoxysilane (98 % TEOS, supplied by Aldrich) as a precursor, ethanol (99.8 %, supplied by DEQ) as solvent, and deionized water (produced by a D4641 from Barnstead International). The reaction was realized in a basic (pH = 9) or acidic (pH = 2) reaction media by the addition of NH_4OH or HNO_3 (supplied by DEQ) with a concentration of 35 and 29 %, respectively. The reaction time and temperature were 3 h and 70 °C, respectively. The gel formation was achieved by the addition of ammonia as a catalyst. The specimens of nano-SiO_2 were obtained at a ethanol-to-TEOS molar ratio of 6 and water-to-TEOS ratio of 24, as presented in Table 1. The wet-gels were dried for 48 h at 70 °C to remove water and solvent. Fine particles

Table 1 Design and properties of nano-SiO_2

Specimen Type[a]	TEOS:Etanol:H_2O Molar ratio	Particle size (TEM), nm	Surface area (BET), m^2/kg
Basic	1: 6 : 24	15–20	133,000
Acidic	1: 6 : 24	<10, 17	337,100

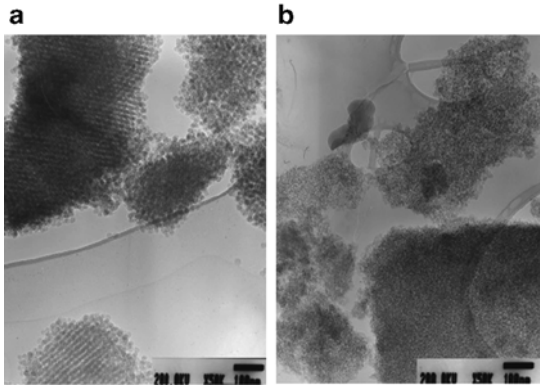

Fig. 1 Nano-SiO_2 produced using route: (**a**) Basic, and (**b**) Acidic

were obtained through 20 min of vibro-milling using a Sweco vibro-energy grinding mill at a weight ratio of the material and stainless steel balls of 1:10. The synthesized nano-SiO_2 particles were characterized by the Transmission Electron Microscopy (TEM, JEOL-2010) and Nitrogen Absorption (according to Brunauer-Emmett-Teller theory, BET; Quantachrome Nova E2000), as reported in Table 1. TEM was used to characterize the morphology and particle size distribution of nano-SiO_2 (Fig. 1). The obtained nano-SiO_2 particles are represented by highly agglomerated xerogel clusters with the size of 0.5–10 μm. The particles within the clusters are of the size of 5–20 nm and obtained xerogels had a surface area of 113,000 and 337,100 m^2/kg depending on the pH route used during the production. Portland cement (PC, conforming to ASTM Type I, supplied by CEMEX) was used in the experimental program. Commercially available polycarboxylate superplasticizer (SP, 31 % concentration, supplied by Handy Chemicals) was used as a modifying admixture. Prior to its application in pastes, SP was premixed with 18 % (by weight of SP) of tributyl-phosphate (99 % TBP, supplied by Aldrich) in order to compensate for air-entraining effect of the SP. Distilled water was used for the preparation of mortars.

The performance of nano-SiO_2 based pastes produced at a nano-SiO_2 dosage of 0.25 % by the weight of the binder (as a replacement of portland cement) and water-to-cement ratio (W/C) of 0.3 were compared with the properties of a reference mixture. All mixes had a SP dosage of 0.1 % (solid content) by weight of cementitious material. ASTM C305 standard was used for mixing. All specimens for the hydration study were cured according to ASTM C109 for 1, 28 and 90 days. At 1, 28 and 90 days of hydration, the specimens were milled in a ceramic mortar using ethanol to stop the hydration and obtain fine powder for the XRD analysis. The performance of the nanoparticles were evaluated by the X-ray diffraction technique (Bruker AXS D8), where the hydration of the portland cement pastes was monitored qualitatively by the intensity of the peaks of the crystal phases of portlandite and the presence of calcium silicates (C_3S and C_2S).

3 Experimental Results

The X-Ray diffraction results were used to identify the products of hydration at different curing times. The intensities of the minerals corresponding to non-hydrated cement and portlandite were used to qualify the hydration progress in the portland systems. At 1 day of hydration (Fig. 2a), the nanosilica synthesized in basic and acidic conditions slightly reduce the intensity of the portlandite and ettringite peaks against the reference paste (Ref.). The increment of the peaks of silicate phases

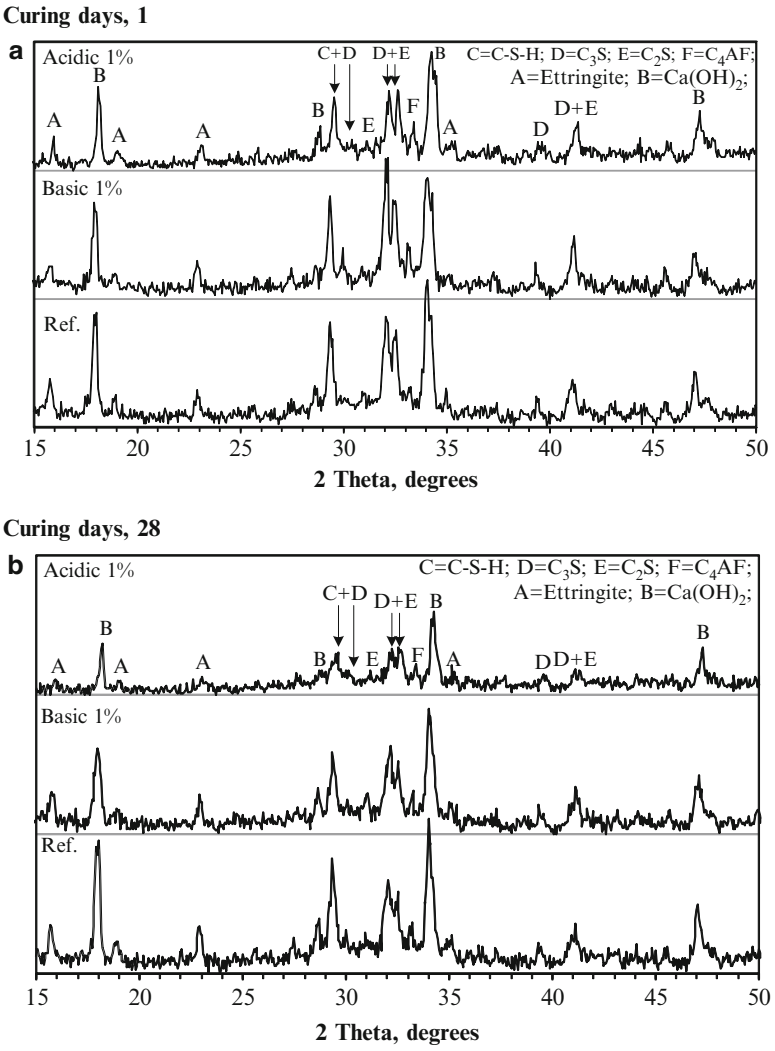

Fig. 2 X-ray diffractograms of hydrated portland cement systems hydrated at: (**a**) 1 day, (**b**) 28 days, and (**c**) 90 days

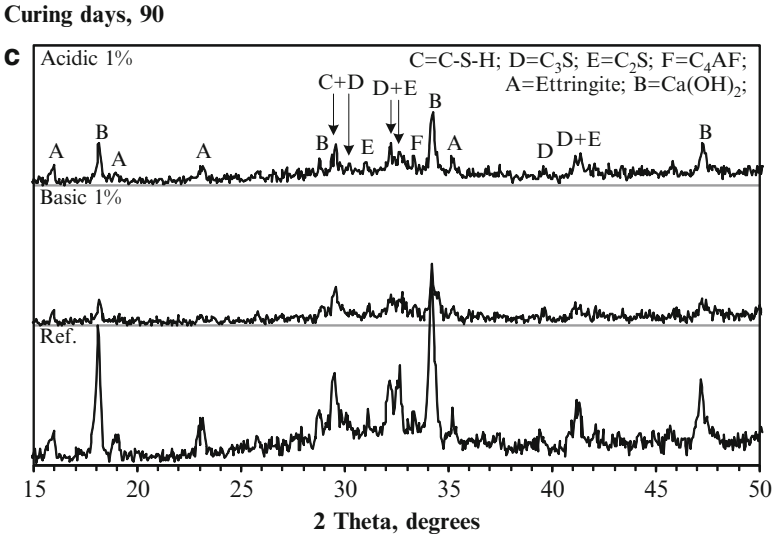

Fig. 2 (continued)

(D + E) in the specimens with the basic nanoparticles must be due to lower surface area and the coarseness of the agglomerated particles, reducing the ability to react at early ages. Acidic nanoparticles, with higher surface area and smaller particles, were able to react at early age, in spite of a certain degree of agglomeration. At 28 days of hydration (Fig. 2b), both nanosilica types reduced the intensity of the portlandite and ettringite peaks against the reference paste, where the reduction was more substantial for pastes with acidic nanoparticles. The reduction of the intensities was mainly due to a pozolanic reaction of the agglomerated nanoparticles, where the higher surface area of the acidic nanoparticles had the lower intensities. At 90 days of hydration (Fig. 2c), both nanosilica types reduced the intensity of the portlandite and ettringite peaks against the reference paste, where the change of the reduction was higher in basic nanoparticles. From 28 to 90 days of hydration, the intensities of the crystal peaks did not vary when the acidic nanoparticles were used. However, the intensities of the crystal peaks had a significant reduction when basic nanoparticles were utilized. The acidic nanoparticles seems to completely react at early ages (1–28 days), while agglomerated basic nanoparticles seems to react at later ages (28–90 days).

4 Conclusions

Agglomerated nanoparticles of SiO_2 were produced successfully by the sol–gel method under the parameters of the study. Nano-silica produced in acidic medium had a higher surface area and are more reactive in portland cement systems than the

material produced in basic medium. Nanoparticles of SiO_2 manufactured in acidic medium increased the reaction of portland cement at early ages, whereas the material produced in basic media, with lower surface area, performed more like a common pozonalic material, reacting with CH at later ages. In general, both types of nanosilica consumed significant quantities of CH densifying the C-S-H structure.

References

1. Björnström, J., Martinelli, A., et al. (2004). Accelerating effects of colloidal nano-silica for beneficial calcium-silicate-hydrate formation in cement. *Chemical Physics Letters, 392*, 242–248.
2. Björnström, J., & Panas, I. (2007). Antagonistic effect of superplasticizer and colloidal nano-silica in the hydration of Alite and Belite pastes. *Journal of Materials Science, 11*(42), 3901–3907.
3. Collepardi, M., et al. (2002). *Influence of amorphous colloidal silica on the properties of self-compacting concretes*. Dundee: Challenges in Concrete Construction.
4. Qing, Y., Zenan, Z., et al. (2007). Influence of nano-SiO2 addition on properties of hardened cement paste as compared with silica fume. *Construction and Building Materials, 21*, 539–545.
5. Flores, I., Sobolev, K., et al. (2010). Performance of cement systems with nano-SiO2 particles produced using sol–gel method. *Journal of the Transportation Research Board, 1*, 10–14.
6. "Global Climate Change," Geothermal Energy. (2013). www.epa.gov/climatestudents/solutions/technologies/geothermal
7. Kutepov, A., & Potapov, V. (2000). Movement and mass exchange of liquid drop in spinned flow of geothermal medium. *Teoreticheskie Osnovy Khimicheskoi Tekhnologii, 34*, 2.
8. American Society for Testing and Materials. (2007). Test method for flow of hydraulic cement mortar. *ASTM C*, *1437–07*, 611–612.
9. Muzenski, S., Flores-Vivian, I., & Sobolev, K. (2015). Hydrophobic engineered cementitious composites for highway applications. *Cement and Concrete Composites, 57*, 68–74.
10. Langan, B., Weng, K., & Ward, M. (2002). Effect of silica fume and fly ash on heat of hydration of Portland cement. *Cement and Concrete Research, 32*, 1045–1051.
11. Flores-Vivian, I., Pradoto, R., Moini, M., & Sobolev, K. (2013). The use of nanoparticles to improve the performance of concrete. *Nano Conference*, Brno.
12. Gaitero, J., Campillo, I., & Guerrero, A. (2008). Reduction of the calcium leaching rate of cement paste by addition of silica nanoparticles. *Cement and Concrete Research, 38*, 1112–1118.
13. Klein, L. (1985). Sol–gel processing of silicates. *Annual Review of Materials Science, 15*, 227–248.

Colloidal Nano-SiO_2 Migration in Hardened Mortars and Its Chemical Interaction with Cementitious Matrix

Ismael Diaz, Mercedes Sanchez Moreno, Ma Cruz Alonso, Rodrigo González, and Antonio Zaldivar

Abstract Concrete performance can be improved by using colloidal nano-SiO_2 (NS) by two different methods: direct addition at the fresh stage to improve mechanical and durability properties; and superficial application, such as sealing treatment to hinder further penetration of aggressive ions. Chemical interaction of NS with the hardened cement mortar (HCM) was analyzed in both situations. NS chemical reactivity was confirmed by SEM and TGA tests. Mortar specimens with nanosilica additions (up to 2.5 % cement weight) were prepared and cured for 7 days before characterization. A superficial treatment by migration of colloidal NS dispersion (30 % weight concentration) under a 12 V was applied on mortar samples after 7 days of curing. Reactivity of NS with the HCM was confirmed by energy dispersion spectroscopy analysis (EDS) coupled to scanning electron microscopy in backscattering (SEM-BS). The new silicon enriched C-S-H gels with C/S ratio around 1.0 were determined by TGA.

Keywords Nanosilica • Surface treatment • Migration

I. Diaz
Facultad de Ingeniería Mecánica y Eléctrica, Universidad Autónoma de Nuevo León, Pedro de Alba S/N, San Nicolás de los Garza, Nuevo León, Mexico
e-mail: diaz_1986@hotmail.es

M. Sanchez Moreno • M.C. Alonso
Instituto "Eduardo Torroja" de Ciencias de la Construcción (IETCC-CSIC), Serrano Galvache 4, 28033 Madrid, Spain

R. González (✉) • A. Zaldivar
Facultad de Ingeniería Civil, Universidad Autónoma de Nuevo León, Pedro de Alba S/N, San Nicolás de los Garza, Nuevo León, Mexico
e-mail: rhodio@hotmail.com

K. Sobolev, S.P. Shah (eds.), *Nanotechnology in Construction*,
DOI 10.1007/978-3-319-17088-6_21

1 Introduction

Nano-SiO_2 (NS) additions have shown a great capacity to improve some concrete properties such as reducing pore system, which is the medium through aggressive ions (e.g. Ca+, Cl– ions) come into the concrete and reach the steel rebar to promote corrosion [1]. The relation between corrosion mechanisms and the pore system is based on the principle that external ions move into the concrete matrix through the connectivity and water content of the pore system [2].

NS additions can work as a filler material, due to its dimensions and the feasibility to be clogged in the pore channels and create discontinuities in the pore connectivity. A second possible approach is pozzolanic activity, when it comes in contact with calcium hydroxide ($Ca(OH)_2$). The reaction of NS with byproducts of cement hydration produce new C-S-H gel which will increase matrix density [3, 4]. The conventional way of adding NS to the mix is during fresh concrete elaboration. NS are normally added along with mix water. Colloidal NS used in this work was slightly negative charged, whereby an electric field was set in order to migrate nanoparticles from the surface to the interior of the hardened mortar as a non-conventional way of adding NS [5, 6]. A cell was designed in order to perform the migration of NS through the HCM. This cell consisted of an acrylic container with two electrodes in both sides with an HCM sample assembled in the middle. Then, an electric field was applied through the cell.

An analysis was performed by scanning electron microscopy with an energy dispersive x-ray spectroscopy detector to compare HCM with NS addition in fresh state and a HCM after migration treatment. Microstructure and Ca/Si ratios measurements could indicate a reaction of NS with the HCM after migration, where lower values than common reported values show an enrichment of Si in the hydrated phases. Thus, it can be inferred that the movement of NS was effectively carried out under the presence of an electric field.

2 Materials and Methods

2.1 NS Addition

Samples production was performed using Ordinary Portland Cement (OPC, 42.5 R/SR sulphate resistant, with low tricalcium aluminate content of 3.8 % and low alkali content). In Fig. 1a a commercial colloidal NS aqueous dispersion (nano particle size around 7 nm) with an amorphous nature was mixed with water before mortar fabrication (water/cement: 0.5 and aggregate/cement 3:1) according to the ASTM C109 standard procedure. The colloidal NS was used as a replacement material at 2.5 % in weight, and an adjustment in the amount of water was made as well. Samples were cured in a moist curing room with a relative humidity of 95 ± 5 % and 22 ± 2 °C. Samples were eventually fractured in order to perform a future analysis according to the experimental schedule.

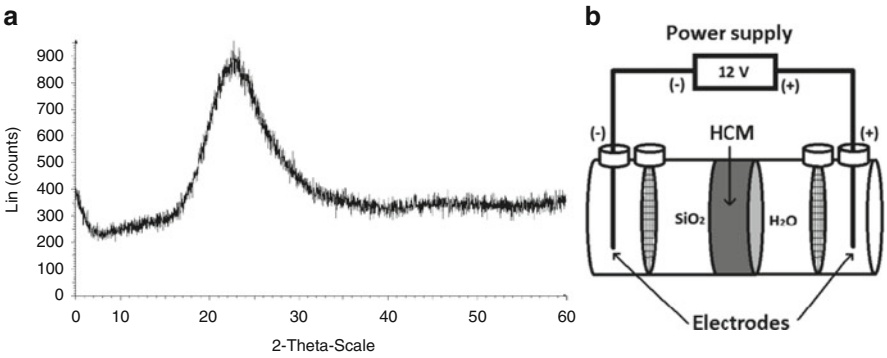

Fig. 1 Amorphous characteristic of NS (**a**) and general configuration of the electrical circuit of migration cells (**b**)

2.2 NS Migration

Cylindrical samples were produced (length 15 cm, diameter 7.5 cm) with a siliceous aggregate in a ratio of 3:1 with the cement and a water/cement ratio of 0.5. Samples were removed from the mold after a day of fabrication and they were stored for curing under controlled conditions in a room with a temperature of 22 ± 2 °C and a relative humidity of 95 ± 5 % for 56 days before testing. After curing, the top and the bottom sides of the samples were cut. From the remaining part, slices of 1.3 cm of thickness were obtained and conditioned for migration cells.

A day before the treatment with colloidal NS, the HCM samples were saturated in water under vacuum conditions. This process consisted in introducing the HCM samples in a container with a vacuum pressure of 133 Pa during 3 h. Then, water was poured into the container to cover the samples and the vacuum conditions were maintained for 1 more hour. Finally, the samples remained immersed in water for 18 h more to guarantee the total saturation of the mortar pores.

The assembly of the migration cells was performed according to electrical configuration from which was possible analyze if an ionic transport exist from the surface to the inside of a mortar sample (see Fig. 1b). This electrical circuit was determined from slightly negative charge of the NS. The main aim of this arrangement is only to study the ionic transport and its effect on the microstructure.

3 Results

3.1 Microstructure and Chemical Composition: Addition Versus Migration

It could be seen by SEM-EDS analysis that samples with NS by addition, presented a mostly conventional microstructure and chemical composition at early ages (2 and 7 days). Anhydride phases were mainly found, where EDS analysis indicated

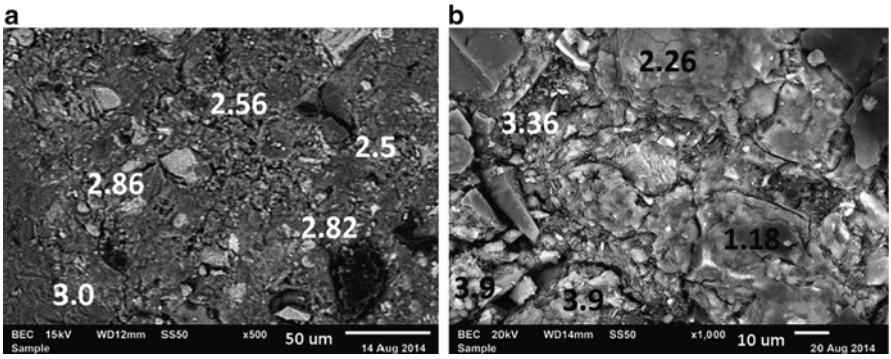

Fig. 2 Ca/Si values of cement mortar with 2.5 % NS addition; (**a**) 2 days and (**b**) 7 days

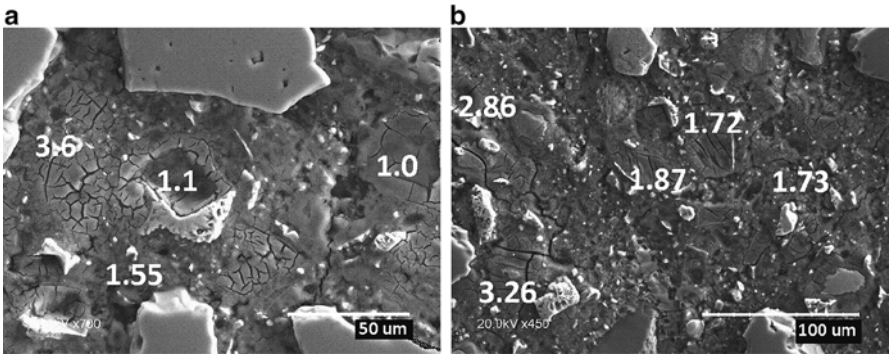

Fig. 3 Image of HCM after (**a**) and before (**b**) NS migration with Ca/Si values

the presence of Ca/Si values corresponding to C_3S and C_2S typical from cement particles. Figure 2 shows the sample with 2.5 % NS addition and indicates Ca/Si values of different areas. In Fig. 2a it can be seen that there are more similar values to those from a conventional cement paste fabricated under standard conditions, and due to its early age (2 days), hydrated products could not be easily detected. Figure 2b shows the sample at 7 days, and it indicates a value lower than reported C-S-H gel, this could be interpreted as NS agglomeration in the microstructure.

In the case of NS migration, images were taken from the surface in contact with the NS at the end of the 7 days of treatment. In some points (Fig. 3b), the sample showed values which are under those of conventional CSH gel (1.5–1.8) and other corresponding phases of a reference sample: C_3S: 3, C_2S: 2 (Fig. 3a) [7]. This lower values of Ca/Si showed in the microstructure, could be related to the transport of NS to the interior of the HCM. This transport of NS seems to result in a deposition of Si in the conventional phases and in a further enrichment of the matrix. This deposition could lead to a later reaction with sub products of the normal hydration process, like $Ca(OH)_2$, in a pozzolanic reaction or just acting as a filler or sealing

Table 1 Loss weight % by TGA of reference and NS treated sample

Range	Ref	NS
100–350	1.95	1.89
350–450	1.43	1.09

material. In any of these cases, it would be a process to densify the microstructure. From the surface in contact with the NS, a depth distance of these low Ca/Si values was measured up to 1.5 mm approximately.

3.2 Termogravimetric Analysis

Equipment of thermogravimetric and differential thermal analysis was used to determine the level of reactivity of NS in HCM. As reported by recent works, NS is well known to react and improve the hydration process, but its effect in HCM is not clear. In order to study this effect, an analysis of powered HCM after NS migration was carried out and it is shown in Table 1. The thermogravimetric analysis of the HCM sample was carried out with rate of 4 °C/min from 25 °C to 1,000 °C. In the results shown in Table 1 it can be seen that the weight loss in the range of temperature between 350 and 450 °C (which is related to the decomposition of $Ca(OH)_2$) in the sample after NS treatment is lower than the reference sample. It could be related to a reaction of the NS with the byproduct of hydration and a subsequent formation of new CSH gel. The difference between the weight loss in the range of C-S-H gel (100–350 °C) could be explained with the different composition of these gels; and also the effect of the electric field in HCM could be leading a leach of some phases.

4 Conclusions

The migration of NS through the HCM under an electric field has shown that it is possible to modify the chemical composition of an HCM with the increment of Si in the matrix. This increment could lead to the puzzolanic reaction of Si in the presence of calcium hydroxide and the posterior densification of the HCM. TGA analysis has provided results to infer the higher presence of C-S-H gel in samples after NS migration. Comparing the use of NS by addition in fresh stage, HCM samples have shown a tendency to behave as a conventional HCM at early age.

References

1. Hornbostel, K., Larsen, C. K., & Geiker, M. R. (2003). Relationship between concrete resistivity and corrosion rate – A literature review. *Cement and Concrete Composites, 39*, 60–72.
2. Rob, B. P., & Peelen, W. H. A. (2002). Characterization of chloride transport and reinforced corrosion in concrete under cyclic wetting and drying by electrical resistivity. *Cement and Concrete Composites, 24*, 427–435.

3. Byung, W. J., Chang-Hyun, K., Ghi-ho, T., & Jong-Bin, P. (2007). Characteristics of cement mortar with nano-SiO2 particles. *Construction and Building Materials, 21*, 1351–1355.
4. Haruehansapong, S., Pulngern, T., & Chucheepsakul, S. (2014). Effect of the particle size of nanosilica on the compressive strength and the optimum replacement content of cement mortar containing nano-SiO_2. *Construction and Building Materials, 50*, 471–477.
5. Cardenas, H., & Struble, L. (2006). Electrokinetic nanoparticle treatment of hardened cement paste for reduction of permeability. *Journal of Materials in Civil Engineering, 18*(4), 554–560.
6. Cardenas, H., Kupwade-Patil, K., & Eklud, S. (2011). Corrosion mitigation in mature reinforced concrete using nanoscale puzzolanic deposition. *Journal of Materials in Civil Engineering, 23*(6), 752–760.
7. Taylor, H. F. W. (1990). *Cement chemistry*. London: Academic.

Hydration Kinetics Study of Class G Oil-Well Cement and Olivine Nano-silica Mixtures at 20–60 °C

G. Quercia Bianchi, H.J.H. Brouwers, and K. Luke

Abstract In this study the heat evolution of standard density slurries (1.89 g/cm^3) of Class G oil-well cement and olivine nano-silica additions (0.5–2.0 % bwoc), cured under different temperatures (20–60 °C) and atmospheric pressure, were examined by isothermal calorimetry. Under isothermal and isobaric conditions, the dependency of cement hydration kinetics on curing temperature is related to the activation energy of the cementing slurry. The estimated apparent activation energy of the different slurries with olivine nano-silica varies from 38 to 44 KJ/mol using a dynamic method, at the temperature range of 20–60 °C. It is demonstrated that the addition of olivine nano-silica increases the rate and the heat of hydration of oil-well slurries. These effects are temperature dependent. Finally, comparable hydration degrees were obtained between slurries containing 0.5 % bwoc of olivine nano-silica and 10 % bwoc of oil-well grade micro-silica (mS).

Keywords Nano-silica • Olivine • Oil-Well • Cement • Hydration

1 Introduction

In oil and gas well construction, one of the most critical processes is that of primary well cementing. Primary well cementing is the process of placing cement in the annular space between the casing and the formation exposed to the drilled wellbore, with the major function to provide zonal isolation. Nano-materials, in particular colloidal silica, are known to improve on the properties of oil well cementing

G. Quercia Bianchi (✉)
Eindhoven University of Technology, Eindhoven, The Netherlands

Trican Well Service Ltd, Calgary R&D Centre, Calgary, AB, Canada
e-mail: g.quercia@tue.nl; gquercia@trican.ca
http://www.trican.ca; http://www.tue.nl

H.J.H. Brouwers
Eindhoven University of Technology, Eindhoven, The Netherlands

K. Luke
Trican Well Service Ltd, Calgary R&D Centre, Calgary, AB, Canada

K. Sobolev, S.P. Shah (eds.), *Nanotechnology in Construction*,
DOI 10.1007/978-3-319-17088-6_22

compositions [1]. Several methods are used to produce nano-silica, with the two most important commercial processes being neutralization of sodium silicate solutions with acid (colloidal silica) and flame hydrolysis (pyrogenic silica) [2]. These processes are expensive due to the price of the raw materials and the energy requirements involved. As a result of this a more economical method to produce nano-silica has been developed, based on dissolution of olivine (OnS) in acid. Published results [1] on the hydration kinetics and rheological tests of OPC cement pastes with OnS have shown its potential use as an additive to control the viscosity of the slurry, provide thixotropic behavior and possibility to enhance the early compressive strength. However, the effects of adding OnS to a Class G oil-well cement compared to a construction Type 1 cement as well as curing under conditions found typically in well cementing operations have not been studied to date. This paper reports on the use of isothermal calorimetry, as a first approach, to elucidate the effect of OnS on Class G cement slurries.

2 Materials and Experimental Methods

An OnS dispersion (synthesized at the pilot scale [1]) with 10.0 wt% solids, equivalent SiO_2 content of 99.1 wt% and a specific surface area measured by BET method of 399 m^2/g was used. The oil-well cement was a Class G HSR grade as classified by ISO 10426–1 [3]. Oil-well grade micro-silica (mS) with a 94.0 wt% of SiO_2, density of 2.3 g/cm^3 and BET specific surface area of 19 m^2/g was used for comparison with the OnS dispersion. Finally, a commercial dispersant based on modified polycarboxylate ether (PCE-type superplasticizer) with 35 % solids content and a density of 1.095 g/cm^3 was used for the calorimetric study. Distilled water was used in all experiments. A total of eight oil-well cement slurries with a normal density of 1.89 g/cm^3 (15.79 lbm/gal) were prepared according to the designs shown in Table 1. Slurry preparation consisted of adding dispersant and OnS or powder micro-silica to water in a high energy (600 W) hand blender (Philips HR 1363) at 20 s intervals. This was followed by addition of the cement over a 15 s period and then continuing mixing for an additional 1 min to obtain a homogeneous slurry. The formulated slurries were studied using an isothermal calorimeter (TAM® Air TA Instruments) at 20, 40 and 60 °C over a period of 48 h.

Table 1 Slurry designs used for hydration kinetic studies (density 1.89 g/cm^3)

Materials	Ref-1	CS-1	CS-2	CS-3	CS-4	CS-5	CS-6	CS-7
OnS-15 (% bwoc)[a]	0	0.5	1.0	1.5	2.0	0	0	0
Micro-silica (% bwoc)	0	0	0	0	0	1.0	2.0	10.0
Class G HSR (%)	100	100	100	100	100	100	100	100
Water (% bwoc)	44	44.1	44.3	44.4	44.6	43.7	43.5	41.3
Dispersant (gal/sk) × 100	6	6	6	6	6	6	6	6
w/b	0.44	0.44	0.44	0.44	0.45	0.44	0.44	0.41

[a]Equivalent SiO_2 content. Sk: 1 cement sack = 94 lbm (42.64 kg)

The progress of the hydration of the cement slurries was quantified by the hydration degree (α), which varies from 0 to 1. For this study, the hydration degree is estimated according to [4] as the ratio of heat evolved at time t to the total amount of heat available (Q_{max}). The value Q_{max} was calculated according to [5] using the cement composition and amount and type of silica. The maximum heat of olivine nano-silica or micro-silica was assumed to be equal from the amount of amorphous SiO_2 in both silica types (amount to 780 J/g according to [6]). The activation energy (Ea) was estimated using two different methods. The first method applied was considering a first order reaction rate (Arrhenius-type) expression as follows:

$$k = A \cdot e^{\frac{-Ea}{RT}} \tag{1}$$

where *R* equals the natural gas constant (8.314 J/mol/K), *T* equals the temperature in K at which reaction occurs, *k* equals the rate of heat flow evolution (*dH*/*dt*), *A* equals the proportionality constant (same units as k), and Ea equals the activation energy (J/mol). In the present study, *k* was calculated from the heat flow curves obtained for each slurry tested. It is derived as the slope of the best linear fit during the acceleration period. To quantify the apparent Ea, the methodology described by [7] was applied. The second method applied to determine the activation energy was the incremental reaction rate method. This method considers that the reaction rate is a function of the hydration degree (considering a differential first order rate approximation) [5]. In this method the reaction rate at each point where heat flow evolution was measured at a constant hydration degree. Thus, the activation energy is calculated from the heat rate results according to [8] as follows:

$$\mathrm{Ea}(\alpha) = R\left[\frac{\mathrm{T_1 T_2}}{\mathrm{T_1 - T_2}} \ln\left(\frac{\frac{d\alpha_1}{dt}}{\frac{d\alpha_2}{dt}}\right)\right] \tag{2}$$

in which R equals the natural gas constant, T_1 and T_2 are the curing temperatures (in K) and $d\alpha_1/dt$, $d\alpha_2/dt$ are the rate of hydration at T_1 and T_2, respectively. For the calculation of the activation energy using the incremental reaction rate method the data at 20–60 °C was considered.

3 Results and Discussion

From the heat flow curves (Fig. 1a) the hydration degree (α) of the different cement slurries studied was calculated (Fig. 1b). It is interesting that the final estimated α of 10 % mS slurry is the lowest in the tested range of temperatures (20–60 °C). The lowest hydration degree for 10 % mS is probably caused by the lower w/b ratio (0.41) compared to the others slurries tested (w/b = 0.44). The higher hydration degree obtained at all tested temperatures confirms again the acceleration effect

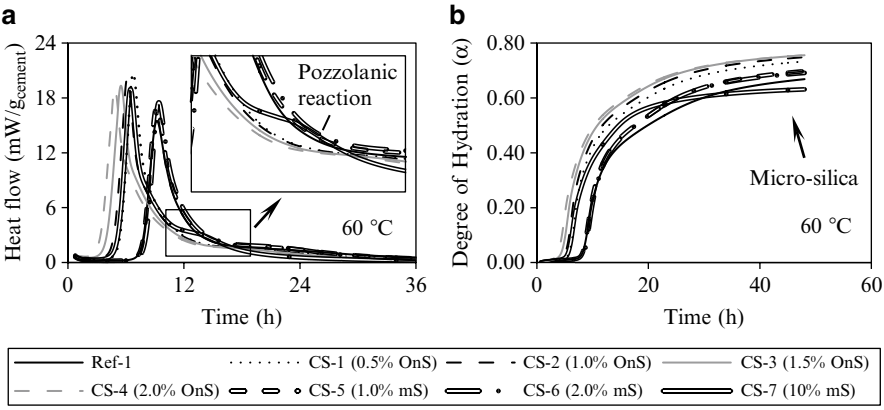

Fig. 1 Examples of obtained results at 60 °C of the different cement slurries (normal density 1.89 g/cm^3), (**a**) head flow curves and (**b**) estimated hydration degree curve

Table 2 Estimated hydration degree (α) for the different cement slurries (normal density 1.89 g/cm^3) tested at 20 °C, 40 °C and 60 °C, respectively

		20 °C			40 °C			60 °C	
Slurry	α (12 h)	α (24 h)	α (48 h)	α (12 h)	α (24 h)	α (48 h)	α (12 h)	α (24 h)	α (48 h)
Ref-1	0.023	0.22	0.44	0.27	0.47	0.59	0.35	0.55	0.65
CS-1	0.026	0.28	0.48	0.37	0.54	0.66	0.48	0.64	0.73
CS-2	0.031	0.30	0.49	0.39	0.54	0.66	0.51	0.67	0.75
CS-3	0.053	0.33	0.50	0.39	0.55	0.67	0.53	0.68	0.76
CS-4	0.089	0.35	0.50	0.39	0.55	0.67	0.54	0.68	0.76
CS-5	0.023	0.23	0.45	0.26	0.47	0.49	0.37	0.59	0.70
CS-6	0.022	0.23	0.45	0.29	0.49	0.61	0.36	0.59	0.69
CS-7	0.028	0.27	0.42	0.30	0.45	0.58	0.43	0.59	0.63

induced by the OnS additions. In general, the higher the temperature the higher the hydration degree for OnS slurries. Table 2 summarizes the calculated hydration degrees at 12, 24 and 48 h, for all the cement slurries tested. It is possible to observe from the data in this table that a small addition of OnS (0.5 % bwoc) has the same effect as 10 % bwoc of micro-silica. Higher α after 12 h results in cost reductions due to the decrease in waiting time to continue the drilling operations due to cementing operations. Also, operations performed can be easier due to the fact there is no need for additional blending steps of a high percentage of micro-silica.

In cement hydration, multiple reactions take place simultaneously, all of which are affected by temperature. The term apparent activation energy (Ea) is used to represent the average effect of temperature on the combined reactions. The estimated apparent activation energy results obtained for the first method (slope or linear approximation) and the second method (incremental calculation) are summarized

Table 3 Estimated average activation energy (Ea) of the different cement slurries (normal density 1.89 g/cm^3)

	Slope method (static)	Incremental method (dynamic)	Incremental method (dynamic)
Slurry	$Ea_{20–40–60}$ (kJ/mol)	$Ea_{20–40}$ (kJ/mol)	$Ea_{40–60}$ (kJ/mol)
Ref-1	63.57	38.18 ± 0.09 (39.57)	43.34 ± 0.05 (43.49)
CS-1	67.86	38.12 ± 0.11 (38.99)	43.37 ± 0.14 (41.40)
CS-2	64.52	38.20 ± 0.15 (39.24)	43.33 ± 0.06 (39.72)
CS-3	60.84	38.16 ± 0.05 (39.96)	43.35 ± 0.10 (40.48)
CS-4	58.34	38.14 ± 0.06 (37.89)	43.33 ± 0.07 (38.76)
CS-5	64.88	38.17 ± 0.11 (39.52)	43.29 ± 0.11 (41.92)
CS-6	67.65	38.14 ± 0.05 (38.41)	43.36 ± 0.04 (46.67)
CS-7	63.57	38.14 ± 0.07 (35.26)	43.32 ± 0.07 (43.40)

in Table 3. It is evident from the data presented in Table 3 that the Ea obtained by the slope method is different for all slurries. In the case of the OnS slurries, the Ea increases for 0.5 and 1.0 % bwoc OnS slurries (CS-1 and CS-2) compared to the reference, after that the Ea drops to a minimum of 58.34 kJ/mol for 2.0 % OnS (CS-4). Similar observation, but with lower extent, was made for the slurries with micro-silica (mS). Different interpretations can be made based on the obtained results. First, the drop in the activation energy, in general, confirms the acceleration effect induced by nano-silica particles.

Lower Ea means that the hydration reaction is enhanced or can occur easier. Also, according to [9], reactions with high Ea are very temperature-sensitive. On the contrary, reactions with low Ea are relatively temperature-sensitive. Based on this, it is possible to state that the addition of OnS and mS in concentrations lower than 2.0 % bwoc make the hydration reaction of Class G HSR more temperature-sensitive. The increase in the activation energy for small amounts of OnS and mS is not expected considering the observed acceleration effects. One explanation of this can be found in changes induced by the presence of nano-particles in the stoichiometry, kinetics and mechanism of cement hydration reaction [9]. Cement is composed of a number of different phases that react at different rates, so it is possible that the Ea may vary considerably as with the hydration degree [5]. Furthermore, hydration is initially reaction-rate-limited and becomes diffusion-limited as solid hydration products are formed [10]. For that reason an incremental calculation method was also applied to highlight how Ea is influenced by the progress of hydration (Table 3). The average Ea for slurries with OnS is slightly affected compared to the reference slurry. Nevertheless, considering the instantaneous Ea calculated at very early age ($\alpha = 0.01$) which is represented by the values in parenthesis in Table 3, it is possible to observe that the Ea is lower than the reference. This confirms again the role of OnS to decrease the Ea and thus, accelerating the slurry's setting. The same observation is valid for mS slurries which also decrease Ea. In Table 3 it is also possible to observe that the apparent activation energy varies with the temperature ($Ea2_{0–40} < Ea_{40–60}$). According to [8] this variation is not illogical insofar as the Arrhenius

relation has been established for simple reactions only. This energy represents a constant with chemical significance. In the case of the reaction of cement hydration, it concerns a macroscopic apparent activation energy, which translates to no chemical law at the microscopic level [6]. Further studies [5, 11] attributed the change of Ea with temperature rise. The fast initial hydration caused by high temperature leads to the formation of a thicker and more compact layer of hydration products (changes in microstructure level) around the cement grains that affects the hydration (increasing Ea).

4 Conclusions

In this study, the influence of olivine nano-silica (OnS) in the hydration behavior of oil-well Class G HSR cement has been addressed. Cementing mixes were tested using available calorimetric methods. Modifications in the cement degree of hydration and activation energy have been observed. The test results demonstrated that the temperature, specific surface area (concentration) and type of amorphous silica (OnS vs. mS) for the given w/b ratio are the controlling parameters. Based on these observations it is concluded that the OnS acts as an accelerating agent in well cementing slurries. Finally, comparable hydration degrees were obtained between slurries containing 0.5 % bwoc of OnS and 10 % bwoc of oil-well grade mS.

References

1. Quercia, G. (2014). *Application of nano-silica in concrete* (pp. 1–328). PhD dissertation, Eindhoven University of Technology, Eindhoven
2. Lazaro, A., Brouwers, H. J. H., Quercia, G., & Geus, J. W. (2012). The properties of amorphous nano-silica synthesized by the dissolution of olivine. *Chemical Engineering Journal, 211–212*, 112–121.
3. ISO 10426–1. (2009). *Petroleum and natural gas industries – Cements and materials for well cementing – Part 1: Specification* (pp. 1–38). ISO, Genève 20, CH-1211.
4. Van Breugel, K. (1991). *Simulation of hydration and formation of structure in hardening cement based materials* (pp. 1–295). PhD thesis, Delft University of Technology, Delft.
5. Poole, J. L., Riding, K. A., Folliard, K. J., Juenger, M. C., & Schindler, A. K. (2007). Methods for calculating activation energy for Portland cement. *American Concrete Institute (ACI) Materials Journal, 104*(1), 303–311.
6. Waller, V., de Larrard, F., & Roussel, P. (1996). *Modeling the temperature rise in massive HPC Structures*. Proceedings 4th international symposium on Utilization of High-strength/High-performance Concrete, Paris, pp. 415–421.
7. Glasstone, S., Laidler, K. J., & Eyring, H. (1941). *The theory of rate processes*. New York: McGraw-Hill.
8. Kada-Benameur, H., Wirquin, E., & Duthoit, B. (2000). Determination of apparent activation energy of concrete by isothermal calorimetry. *Cement and Concrete Research, 30*(2), 301–305.
9. Levenspiel, O. (1999). *Chemical reaction engineering* (3rd ed., pp. 1–684). New York: Wiley.

10. Bullard, J. W., Jennings, H. M., Livingston, R. A., Nonat, A., Scherer, G. W., Schweitzer, J. S., Scrivener, K. L., & Thomas, J. J. (2011). Mechanisms of cement hydration. *Cement and Concrete Research, 41*, 1208–1223.
11. Thomas, J. J. (2012). The instantaneous apparent activation energy of cement hydration measured using a novel calorimetry-based method. *Journal of the American Ceramic Society, 95*, 3291–3296.

Effect of Nano-silica on Fresh Properties and Rheology of Grouts

Mohammed Sonebi, Patrick Carr, and Y. Ammar

Abstract The effect of colloidal nano-silica on the fresh and rheological properties of cement-based grouts is investigated in this paper. These properties were evaluated by the mini-slump flow, marsh cone flow time, Lombardi plate cohesion meter, yield stress and plastic viscosity values. The key parameters investigated were the dosages of nano-silica and superplasticizer. Test results showed that the dosage of nano-silica had significant effect on the fluidity and rheological properties of grout. The increase in the dosage of nano-silica led to increasing the values of flow time, plate cohesion meter, yield stress and plastic viscosity, and reducing the mini-slump results. Conversely, the increase in the dosage of superplasticizer led to decreasing the values of flow time, plate cohesion meter, yield stress, and plastic viscosity, while increasing the mini-slump results.

Keywords Cohesion • Flow time • Mini-slump • Nano-silica • Yield stress • Viscosity

1 Introduction

There have been progressive developments in the field of nanotechnology, which enabled the manufacture of nano-scale materials (nano-silica (***nS***), carbon nanotubes, etc.) that can be incorporated in cement-based materials. Studies on the behaviour of cement-based materials incorporating nano-scale particles are necessary to develop better understanding of such composites. This can contribute to producing cementitious grouts with improved overall performance and durability. It has been stated that the behaviour of cement-based materials is dependent on nano-sized solid particles of calcium–silicate–hydrates (C–S–H), or nano-sized porosity

M. Sonebi (✉) • P. Carr
School on Planning, Architecture and Civil Engineering, Queen's University Belfast, Belfast, UK
e-mail: m.sonebi@qub.ac.uk

Y. Ammar
Department of Civil Engineering, Université de Sherbrooke, Sherbrooke J1K 2R, Canada
e-mail: Ammar.Yahia@USherbrooke.ca

K. Sobolev, S.P. Shah (eds.), *Nanotechnology in Construction*,
DOI 10.1007/978-3-319-17088-6_23

at the interfacial transition zone between cement and aggregates in the case of concrete [1, 2].

Previous studies [2–6] indicate that the inclusion of nS modifies fresh and hardened properties of cement-based materials compared to conventional mineral additions. For example, relative to silica fume, nano-silica shortened the setting time of mortar and reduced bleeding water and segregation, while improving the cohesiveness of the mixes in the fresh state [2, 5]. Typical properties affected by nano-sized particles include strength, durability, shrinkage and bonding with steel reinforcement [2]. This improvement is generally attributed to the fact that nano-particles of SiO_2 (nS) can fill the spaces between/within layers of C–S–H, acting as a nano-filler. Furthermore, the pozzolanic reaction of nS with calcium hydroxide produces more C–S–H, resulting in a higher densification of the matrix, which improves the strength and durability of the material [1, 2].

The objective of this study is to evaluate the effect of the various dosages of nS and SP ranging between 0.5–5 % and between 1.2–1.6 %, respectively, on the fresh properties measured with the mini-slump, Marsh cone (for saturation point), Lombardi Plate and the rheological properties of grouts (yield stress and plastic viscosity) determined by Vane rheometer.

2 Materials and Test Procedures

The grout mixtures were prepared with a fixed water-to-binder ratio (w/b) of 0.30. Ordinary portland cement CEM I 42.5 N [7] and colloidal nS were systematically used in all mixtures. nS has 50–60 nm of mean particle size and specific surface area (BET) was 80 m^2/g. The nS was in a colloidal form of an aqueous solution with SiO_2 content of 50 % by mass. Polycarboxylate polymer-based superplasticizer having solid content of 30 % and specific gravity of 1.10, was used. The water content in the mixes was adjusted to take amount of water contained in SP to maintain a fixed w/b.

The mixes were prepared in 2-L batches using a 5-L planar-action high-shear mixer. Tap water (16 ± 0.5 °C), colloidal nS, and SP were added together to the mixer and mixed for 1 min at low speed (140 rpm). CEM I was introduced within 2 min, at the end of which the mixer was stopped and any lumps of solids formed were crushed (1 min). Subsequently, the grout was mixed again for 2 min at high speed of 285 rpm and for 1 min at the low speed of 140 rpm.

For all tests, the timing is given from the first contact between cement and water (zero time). The mini-slump spread test was carried out immediately after the end of mixing (i.e. at 7 min). The transparent cone-shaped mould described elsewhere was used in this study in combination with a smooth Plexiglas plate. The test consists in filling the cone with grout, and gently lifts it during approximately 30 s after placement of the grout. When the flow stopped, the spread of the grout was measured in two perpendicular directions. The reported mini-slump values correspond to the mean values determined on two-perpendicular directions. Marsh cone test was car-

ried out using a metal cone with an orifice diameter of 10 mm. The test consisted in pouring 1 l of grout into the cone. After a waiting time of 15 s, the orifice was opened and the time taken for each 100 ml of grout to flow through the orifice was recorded, and the measurements were completed upon collecting 700 ml of grout.

The rheological measurements were carried out with a computer-controlled vane rheometer (Haake VT550). At 15 ± 1 min, approximately 800 ml of the sample was put into a plastic container where the vane was plunged. After 30 s rest, the test was started, and the data were automatically collected. After 30 s rest, the test was started, and the same testing parameters as above (velocities and their durations) were followed. The rheological parameters, yield stress (τ_0) and plastic viscosity (μ_p), were obtained from the descending curve using Herschel-Bulkley model to fit to the experimental data.

The cohesion of grout was determined at 30 ± 1 min with a Lombardi plate cohesion meter. A thin galvanized steel plate (100 × 100 × 1 mm) with known weight was immersed in the grout and hung on a stand placed on an electronic balance. The difference in weight values before and after immersion into the grout (dW) is determined. This test was followed by the fresh density measurement of the grout with a mud balancer and the thickness of the grout on the plate is then calculated as the ratio between dW and density of the grout with two sides of plate.

3 Results and Discussion

3.1 Fluidity

The variations of mini-slump and Marsh cone with SP for mixes prepared with different percentages of nS (0.5, 2, 3.5, and 5 %) are summarized in Fig. 1a, b. For 1.2 % SP dosage, only 2 % and 5 % of nS were tested. As expected, for mix without nS (only OPC), the increase in the dosage of SP from 1.2 to 1.6 % resulted in an improvement of fluidity and reduction of flow time, which is due to a better

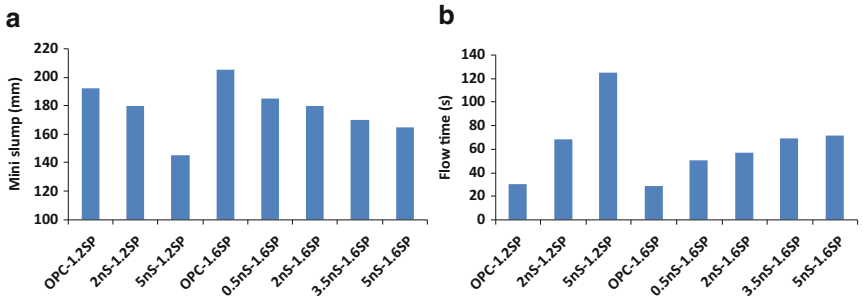

Fig. 1 (**a**) Variations of mini-slump and (**b**) flow time with percentages of SP and nS

dispersion of particles. The dosage of SP is shown to exhibit a significant effect on mini-slump due to steric and electrostatic repulsions among cement particles. The incorporation of SP disperses cement particles and this can therefore liberate some of water and increases the amount of free water otherwise entrapped within the flocculated system. This increase in free water can contribute in reducing the friction between particles, hence improves the flowability and deformability of the grout. For 1.6 % SP dosage, the increase of nS from 0.5 to 5 % led to a significant decrease (10 % reduction) in the fluidity and in case of 1.2 % SP, the reduction was 20 % when nS increased from 2 to 5 %. This may be due to the ultra fine nature of nS, which is likely to reduce the amount of SP per unit surface area. Hence, particle-particle van der Waals attractions may become increasingly important, which results in flocculated system.

The increase of nS led to an increase of flow time, especially in the case of mix made with lower SP dosage of 1.2 % (Fig. 1b). The increase in SP dosage to 1.6 % resulted in limited increase in flow time (Fig. 1b). For example, the use of 5 % nS resulted in increasing the flow time from 54 to 125 s (130 % increases) in the case of mix made with 1.2 % SP. In the case of mix made with 1.6 % SP, this increase was limited to 35 % (from 53 to 71 s). This is may be attributed to the beneficial effect of SP in dispersing the fine particles, thus liberating some of the free water otherwise entrapped within the flocculated system.

3.2 Plate Cohesion

The effect of increasing nS an SP contents on cohesion is shown in Fig. 2. As expected, adding SP in grouts without any nS resulted in a reduction in the cohesion. For any given dosage of SP, the increase in the percentage of nS increased the cohesion. This may be due to the ultra fine nature of nS, which is likely to reduce the amount of SP per unit surface area, and therefore increased the cohesiveness of grout.

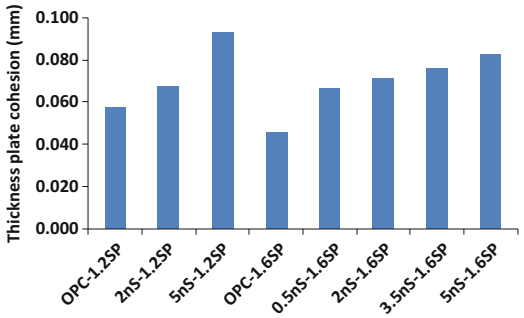

Fig. 2 Variations of plate cohesion with percentages of SP and nS

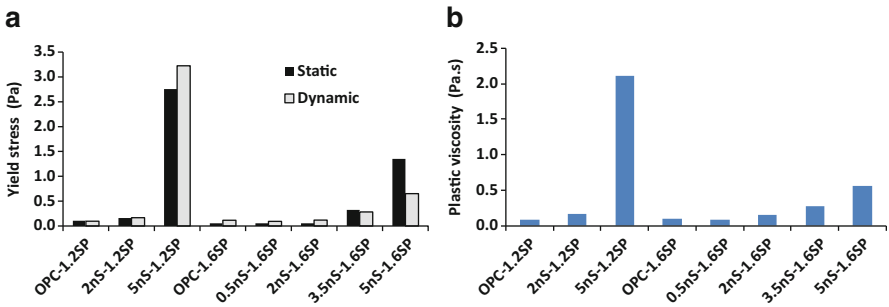

Fig. 3 (**a**) Variations of yield stress and (**b**) plastic viscosity with % nS, and SP

3.3 Yield Stress and Plastic Viscosity

Figure 3a presents the static and dynamic yield values of grout mixes made with various percentages of nS and two dosages of SP, corresponding to 1.2 and 1.6 %. For any given dosage of SP, the increase in the percentage of nS resulted in an increase of yield stress value. Similarly for mix made without nS, as expected the increase in dosage of SP led to a reduction in yield stress and improvement of fluidity. For a given percentage of nS, the increase of SP resulted in significant reduction in yield stress. Increasing the SP content produces a thicker adsorbed polymer layer and consequently weaker van der Waals attractions between the particles, therefore lower energy is needed to disperse the particles and secure lower yield stress [8].

The variations of the plastic viscosity with the dosage of SP and percentage of nS of all investigated grout mixes are presented in Fig. 3b. For mixes with nS, the plastic viscosity is affected by the dosage of SP. Similarly to the yield stress, for any given dosage of SP, the increase in the percentage of nS resulted in an increase of plastic viscosity. For example, for mix made with 1.2 %, the addition of 5 % nS resulted in an increase in plastic viscosity by 26 times. Comparatively, increasing the dosage of nS led to higher plastic viscosity, resulting in higher Marsh cone flow time values. As indicated earlier, this behavior is attributed to the very high surface area of nano-silica.

The replacement of cement by nano-silica led to an increase of the yield value and plastic viscosity for any given dosages of SP. When nS is incorporated into the grout in the fresh state it has a direct influence on the water demand required in the mixture to ensure a given fluidity level. This behaviour confirms the fact that additions of high surface area mineral particles to cement grout cause the need of higher amounts of water or SP in order to keep the workability of the mix. If the water content is kept constant, an increase of nS content will promote the packing of particles, decreasing the volume between them and decreased the free water in the system. Thus, there is a higher internal friction between solid particles, which contributes to increase the rheological parameters of the mixes. Therefore, the replacement of cement by nS at levels 0.5, 2, 3.5, and 5 % with superplasticized mixes significantly affect the flowability of the mixes (higher plastic viscosity and yield stress values).

4 Conclusions

Based on the results presented in this paper, the following conclusions can be pointed out:

- The percentage of nano-silica (nS) had a significant effect on mini-slump, plate cohesion meter, yield stress, and plastic viscosity.
- The increase in the dosage of nS in a well-dispersed form led to increasing the values of plate cohesion meter, yield stress and plastic viscosity, while reducing the mini-slump values. This is ascribed to the ultrafine nature of nS particles.
- The increase in the dosage of superplasticizer (SP) led to increasing the mini-slump values (fluidity), while reducing the values of yield stress, plastic viscosity, plate cohesion, and Marsh cone flow time of grout containing ultrafine particles. This is attributed to better deflocculation of particles at the fresh state and SP produces a thicker adsorbed polymer layer and consequently weaker van der Waals attraction between the particles.
- The used of nS resulted in higher yield stress and plastic viscosity values of grout, which may required higher water and SP demand to ensure a given deformability.

References

1. Li, H., Gang, H., Jie, X., Yuan, J., & Ou, J. (2004). Microstructure of cement mortar with nano particles. *Composites Part B: Engineering, 35*(2), 185–189.
2. Collepardi, S., Borsoi, A., Ogoumah Olagot, J. J., Troli, R., Collepardi, M., & Cursio, A. Q. (2005). *Influence of nano-sized mineral additions on performance of SCC*. In: Proceedings of the 6th international congress, Global Construction, Ultimate Concrete Opportunities, Dundee, pp. 5–7.
3. Jo, B. W., Kim, C. H., Tae, G. O., & Park, J. B. (2007). Characteristics of cement mortar with nano-SiO_2 particles. *Construction Building & Materials, 21*, 1351–1355.
4. Senff, L., Labrincha, J. A., Ferreira, V. M., Hotza, D., & Repette, W. L. (2009). Effect of nano-silica on rheology and fresh properties of cement pastes and mortars. *Construction Building & Materials, 23*, 2487–2491.
5. Qing, Y., Zenan, Z., Deyu, K., & Rongshen, C. (2007). Influence of nano-SiO_2 addition on properties of hardened cement paste as compared with silica fume. *Construction Building & Materials, 21*(3), 539–545.
6. Sonebi, M., Bassuoni, T. M., Kwasny, J., & Amanuddin, K. (2012). *Effect of nano-silica on fresh properties and rheolgy on cement-based materials*. Proceedings of 4th international symposium on Nanotechnology in Construction NINCOM4, Grete, 8 p.
7. BS EN 197–1 standards: 2000: *Cement: Composition, specification and conformity criteria for common cements*. British Standards Institution, UK, 2000, 50 p.
8. Lowke, D. (2009). *Interparticle forces and rheology of cement based suspensions*. Proceedings of the NICOM3 – Nanotechnology in Construction, Prague, pp. 295–301.

Effect of Olivine Nano-silica Additions on Cement Based Systems

G. Quercia Bianchi and H.J.H. Brouwers

Abstract In this study, the influence of olivine nano-silica (OnS) additions in cement based systems has been addressed. The obtained results demonstrate that the addition of OnS (1.5–3.8 % bwoc) increases the viscosity, yield point and hydration degree of the cementitious systems, mainly due to the increase of the total specific surface area of the mix. This holds also for the case when a fixed amount of SP is applied. Based on the performed analysis, it is concluded that the OnS acts as an accelerating and pozzolanic agent in concrete.

Keywords Nano-silica • Olivine • Cement • Mortar • Self-compacting concrete

1 Introduction

Olivine $(Mg,Fe)_2SiO_4$ is the fastest weathering silicate mineral dissolving easily in acids. During the dissolution in acid, the metallic ions (Mg^{2+},Fe^{2+}) are replaced by H^+, yielding $Si(OH)_4$ monomers and metallic ions in solution. After cleaning treatments an amorphous nano-silica is obtained [1]. The produced olivine nano-silica (OnS) has a specific surface area between 100 and 400 m^2/g, depending upon the dissolution and washing conditions. The size of the primary particles, which are agglomerated in clusters, ranges from 10 to 25 nm and the impurity content is below 5 % by weight. Literature related with the application of OnS in cement based materials is scarce, only one research work performed by Justnes and Ostnor is available [2], thus, the effect of adding OnS in cement based systems has not been studied. Based on this the present research aims to elucidate the effects of OnS in the fresh and hardened cement pastes, standard mortars and self-compacting concretes with low CO_2 footprint (eco-SCC).

G. Quercia Bianchi (✉)
Eindhoven University of Technology, Eindhoven, The Netherlands

Trican Well Service Ltd, Calgary R&D Centre, Calgary, AB, Canada
e-mail: g.quercia@tue.nl; gquercia@trican.ca
http://www.tue.nl; http://www.trican.ca

H.J.H. Brouwers
Eindhoven University of Technology, Eindhoven, The Netherlands

K. Sobolev, S.P. Shah (eds.), *Nanotechnology in Construction*,
DOI 10.1007/978-3-319-17088-6_24

2 Materials and Experimental Methods

Different olivine nano-silica cakes were used in dried or water dispersed form. The OnS used were prepared from different batches synthesized on pilot scale [3]. The cements used for the experiment were CEM I 52.5 N, CEM I 52.5 R, CEM III/B 42.5 N LH/HS as classified by CEN EN 197–1 (2000). For the mortar test, standard sand (0–2 mm) was used according to CEN EN 196–1 (2000). In addition, commercial superplasticizers (SP) based on modified polycarboxylic ether (PCE) and naphthalene lignosulfonate ether (NLS) were used for the paste, mortar and concrete experiment. For the self-compacting concrete (SCC) experiments, fluvial aggregates in the fractions 0–8 and 4–16 mm were used. In addition, fluvial sand in the fractions 0–4 mm was also used. Finally, a commercial fly ash was applied as supplementary cementitious material and filler. More details on the physicochemical characteristics of the materials used can be found in [3].

To study the effect of OnS and SP, rheological measurements and the mini spread-flow test were carried out to assess changes of the viscosity caused by the volumetric substitutions of cement (0.5, 1.5, 3.0, 4.5, 7.0 and 10 %). The rheological tests were complemented with isothermal calorimetric measurements (cement pastes with w/c of 0.5; and with or without SP). Afterwards, compressive and flexural strength of standard mortars following the procedure established in EN 196–1 (2000) were carried out. Finally, optimized eco-SCC mixes were designed and evaluated as recommended by [4]. The reference mix design was based on a commercial SCC formulation for sewage pipes (Table 1 and Fig. 1a). For the optimized eco-SCC mixes with OnS (Fig. 1b), the mix design concepts described by [5, 6] were used. In total, four mixes were tested at the pilot scale, considering a volume of 1 m^3. For this, two batches were cast with OnS cakes (DNOnS-14) produced from Norwegian olivine in The Netherlands and two batches with powder OnS produced from beneficiated dunites in Greece (PGOnS-1). One day before the pilot test, several water based dispersions with 10 wt% of OnS were prepared using both type (Dutch and Greek) nano-silica with an industrial rotor stator high energy mixer (3,000 rpm for 30 min).

Table 1 eco-SCC mix designs using olivine nano-silica as cement (CEM I 52.5R) replacement

Materials (kg/m^3)	SCC-$_{ref}$	SCC-$_{lab}$	SCC-$_{1D}$	SCC-$_{2D}$	SCC-$_{1G}$	SCC-$_{2G}$
DNOnS-14 (10 wt% solid)	–	122.0	122.0	122.0	–	–
PGOnS-1 (10 wt% solid)	–	–	–	–	122.0	122.0
CEM I 52.5 R	95.0	38.0	34.0	42.0	32.0	38.0
CEM III/B 42.5 N LH/LS	255.0	284.0	288.0	280.0	280.0	288.0
Fly-Ash	160.0	173.0	172.0	174.0	172.0	172.0
Fluvial gravel 0–8 mm	825.0	855.0	860.0	860.0	870.0	870.0
Fluvial gravel 4–16 mm	1091.0	845.0	860.0	860.0	870.0	860.0
Water	845.0	54.0	62.0	59.0	60.0	60
SP (% bwob)	3.5[a]	6.5[b]	5.0[c]	5.2[c]	4.0[c]	3.5[c]
w/b (measured after casting)	0.43	0.43	0.45	0.44	0.46	0.44

[a]SP2 NLS-type (Cugla® R11)
[b]SP3 PCE-type (Ha-Be Pantarhit® RC 100)
[c]SP5 PCE-type (Ha-Be Pantarhit® PC 150)

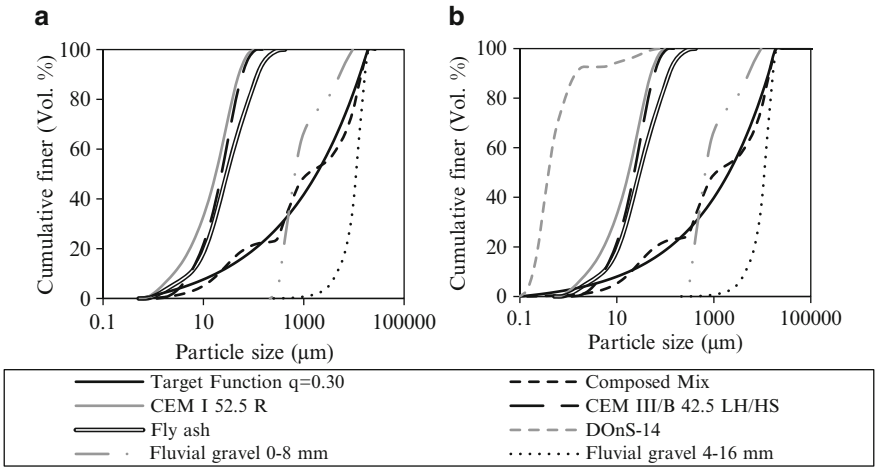

Fig. 1 PSD of the materials used, (**a**) reference eco-SCC with target function based on a q = 0.27 (D_{min} = 513 nm and D_{max} = 18.9 mm, (**b**) initial eco-SCC (OnS) with target function based on a q = 0.30 (D_{min} = 65 nm and D_{max} = 18.9 mm), *dashed lines* are the corresponding test mixes

3 Results and Discussion

3.1 Effects on Cement Paste

The obtained flow curves for all tested pastes are displayed in Fig. 2 the experimental data were fitted to the Herschel-Bulkley fluid model using the methodology recommended by [7]. This fluid model was selected as cement pastes show a shear thinning behavior.

The parameters determined by the rheological tests were compared with values obtained on mortar scale using the spread-flow test. It is demonstrated that the yield point of the paste is proportional to the spread flow and the total specific surface area [3]. The increase in the viscosity and in the yield point of the paste is a result of the increased specific surface are of the paste due to the addition of OnS. In this case it is demonstrated for a fix amount of SP that the workability of the cement paste decreased with increasing OnS content. In addition, it was found that the pastes presented a self-flowing characteristic when the cement paste possesses yield point values lower than 9 Pa.

The obtained heat flow and total heat curves for all tested pastes are displayed in Fig. 3.

For the first system studied, where no SP was added (Fig. 3a), the heat flow curves are close to the reference sample. The main difference observed was in the so called dormant period, which is clearly reduced with increasing volumetric substitution of cement by OnS. In addition, a slight increase in the main hydration peak (C_3S phase) was observed. This increase is produced by the higher reactivity of the OnS (pozzolanic behavior). In the second system studied (with SP) the retarding effect due to the addition of SP is still evident (Fig. 3b). Nevertheless, the accelerating

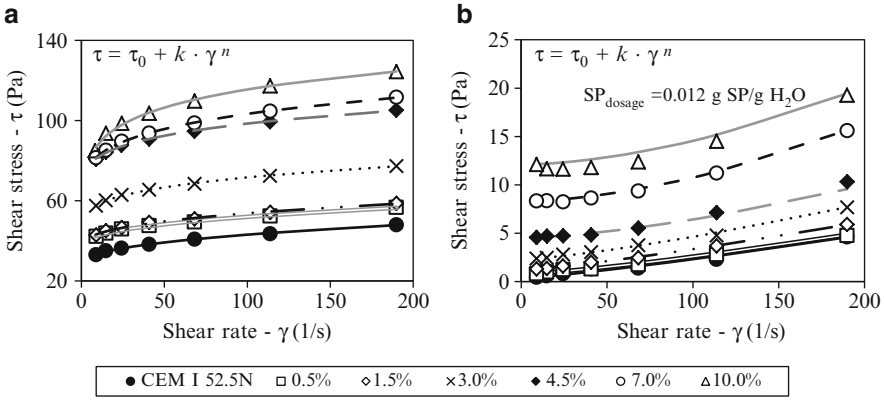

Fig. 2 Flow curves of the cement/OnS paste measured and adjusted to the Herschel-Bulkley fluid model: (**a**) without SP, (**b**) with fixed SP (0.6 % bwoc)

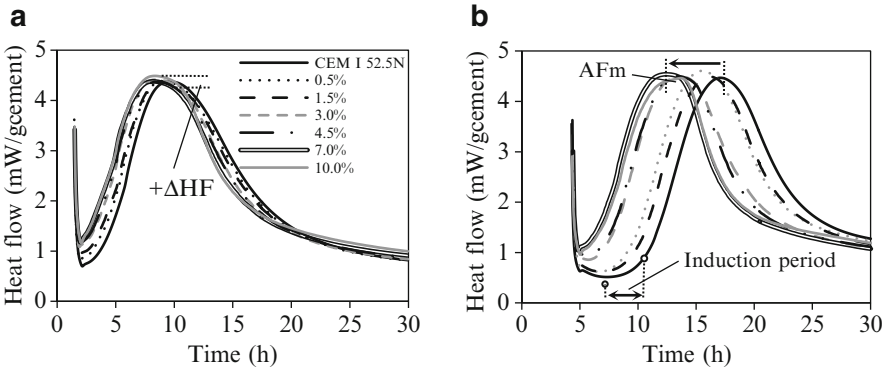

Fig. 3 Heat flow and total heat behaviour of cement/OnS paste: (**a**) without SP, (**b**) with fixed SP (0.6 % bwoc)

effect caused by the addition of OnS is also influential. In addition to this, an effect on the hydration of aluminates phases (secondary ettringite formation) is displayed for 10 vol% substitution level.

3.2 Effects on Standard Mortars

The mechanical properties of mortars with different OnS additions and a fixed SP content are shown in Fig. 4. In general, almost all flexural strength values dropped when OnS was added. This fact is caused by the high agglomerated state of the OnS, which produced a more porous interparticle transition zone (ITZ). On the contrary, it is possible to observe in Fig. 4b that the compressive strength increases until a maximum that depends on the age of the samples. Once the maximum is reached the compressive strength dropped in comparison to the reference. The highest value at 28-day was obtained with 1.5 vol% of cement replacement by OnS.

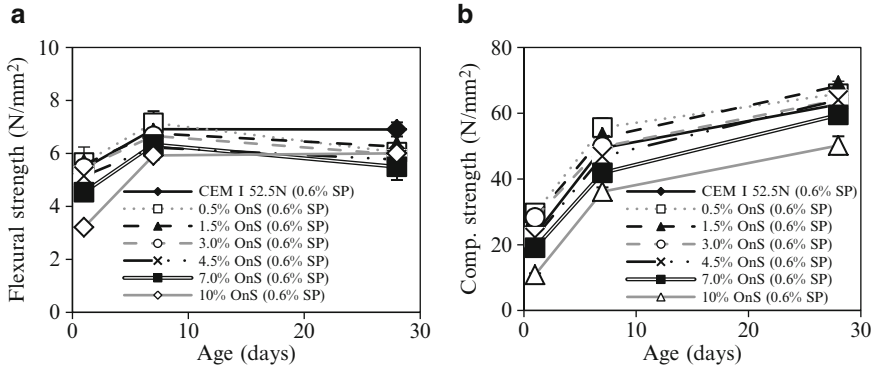

Fig. 4 Mechanical properties of mortars with different content of OnS (w/c = 0.5 and 0.6 % SP): (**a**) Flexural strength, (**b**) compressive strength

3.3 Ecological Self-Compacting Concrete (Pilot Test)

All resulting properties of the eco-SCC of the conducted pilot test tests are given in Table 2. As it can be seen in Table 2, only a lower slump-flow than the median value of 758 mm was obtained for the mix SCC-$_{2D}$.

The values of the others test are within the production specifications of the company. Based on this observation, it is possible to conclude that the SCC mixes met the required slump flow set by the company. On the other hand, high V-funnel times can be related to a low deformability due to high paste viscosity, a high interparticle friction or a blockage of the funnel. Directly linked to this observation are the long V-funnel values observed for SCC-$_{2G}$ mix. Also, the higher V-funnel time of mix SCC-$_{1G}$ is the result of a lower amount of SP and water use. In the case of the mechanical properties, several observations can be made. Both type of OnS tests show lower 16-h compressive strength than the required minimum (Table 2). Despite the lower 16-h strength of the mixes, the final cast products (garden pals) were de-molded without problems or failures. The lower 16-h compressive strength is the result of the lower total binder content of the mix compared to the reference (382 kg/m^3 vs. 369 kg/m^3). On the contrary, the 28-days compressive strength values were higher than the minimum value of the reference (55 N/mm^2) for both SCC types with OnS (Table 2). The higher 28-day strength is a consequence of the improved fly ash and slag reactivity induced by the OnS particles, as it was confirmed by [3]. Taking into account the fresh and hardened properties combined with the final product quality, the pilot testing was qualified as a success by the concrete producer.

As a further analysis, an estimation of the CO_2 foot-print of the resulted eco-SCC was performed using the equivalent CO_2 foot-print of each compound taken from [3]. The analysis demonstrated that CO_2 foot-print of an eco-SCC (151 kgCO_2/m^3) is 18 % lower than that the references SCC mix (184 kgCO_2/m^3). Not only was the equivalent CO_2 foot-print was reduced, it was also demonstrated that the use of 3.8 % bwoc of OnS and the mix design tool developed by [5] can enhance the use of other binders (slag and fly ash). Thus, the total binder content in the SCC was reduced from 382 to 369 kg/m^3 (13 kg less).

Table 2 Fresh and hardened properties of eco-SCC pilot test mixes

Mix	S(mm)	V-funnel time (s)	Stability time (s)	Blocking (mm)	16-hs C.S. (N/mm^2)	7-day C.S. (N/mm^2)	28-day C.S. (N/mm^2)
Reference	650–850	12–13	<3	<10	>8	N/S	>55
$SCC\text{-}_{1D}$	810–810	7.3–7.9	1.8	5.3	–	–	–
$SCC\text{-}_{2D}$	580–600	11.1–12.4	2.5	5.0	7.13	39.7	68.3
$SCC\text{-}_{1G}$	750–790	13.1–14.1	3.9	5.8	–	–	–
$SCC\text{-}_{2G}$	700–750	31.7–33.8	9.9	8.8	7.3	40.4	65.3

4 Conclusions

In this study, the influence of olivine nano-silica (OnS) additions in cement based systems has been addressed. The tests results demonstrated that the addition of OnS increases the viscosity and the yield point of the cement system. This holds also for the case in which commercial superplasticizers are applied. The increase in the viscosity and the yield point of the paste is the result of the increased specific surface area of the paste. Based on the isothermal calorimetric measurements and the analysis performed, it is possible to conclude that the OnS acts as an accelerating agent in concrete. The experiments also demonstrated that the possible optimum replacement level of OnS would be between 1.5 and 4.5 % by vol. to obtain a concrete with reduced CO_2 foot-print.

References

1. Lazaro, A., Brouwers, H. J. H., Quercia, G., & Geus, J. W. (2012). The properties of amorphous nano-silica synthesized by the dissolution of olivine. *Chemical Engineering Journal, 211–212*, 112–121.
2. Justnes, H., & Ostnor, T. (2001). Pozzolanic, amorphous silica produced from the mineral Olivine. In V. M. Malhotra (Eds.), *Proceedings of the 7th CANMET/ACI international conference on Fly ash, Silica fume, Slag, and Natural pozzolans in Concrete* (Vol. II), Chennai. American Concrete Institute (ACI) Special Publication 199, 769–781 (DOI 10.14359/10547).
3. Quercia, G. (2014). *Application of nano-silica in concrete* (pp. 1–328). PhD dissertation, Eindhoven University of Technology, Eindhoven.
4. EFNARC. (2005). *Specification and guidelines for Self Compacting Concrete-SCC*. Report, European Federation of Producers and Contractors of Specialist Products for Structures, Surrey.
5. Hüsken, G., & Brouwers, H. J. H. (2008). A new mix design concept for earth-moist concrete: A theoretical and experimental study. *Cement and Concrete Research, 38*, 1246–1259.
6. Hunger, M. (2010). *An integral design concept for ecological self-compacting concrete* (pp. 1–260). PhD thesis, Eindhoven University of Technology, Eindhoven.
7. Klotz, J. A., & Brigham, W. E. (1998). To determine Herschel-Bulkley coefficients. *Journal of Petroleum Technology, 50*, 80–81.

Use of a Nano Clay for Early Strength Enhancement of Portland Cement

Stefan Baueregger, Lei Lei, Margarita Perello, and Johann Plank

Abstract In this study it is reported that additions of kaolin, a natural and abundant clay mineral, can significantly increase the early strength of Portland cements. Its effectiveness greatly depends on the particle size which ideally should be less than 500 nm. For example, 5 % by weight of cement of nano-sized kaolin (d ~ 200 nm) increased the 16 h compressive and tensile strengths of a CEM I 42.5 R sample by 50 % and 60 % respectively. Strength enhancement occurs predominantly in slower reacting cements (CEM I 32.5, 42.5). Analysis via heat flow calorimetry and X-ray diffraction revealed that the nano clay in particular activates the hydration of the silicate phases C_3S and C_2S. Furthermore, rheological measurements evidenced an only minor effect on mortar viscosity. The results suggest that nano-sized kaolin represents an inexpensive additive which can boost the early strength of Portland cement without negatively affecting workability and other properties.

Keywords Cement • Nano kaolin • Strength enhancement

1 Introduction

Nanoparticles (e.g. nano silica) are known to increase the strength and durability of concrete or mortar. Capillary pores present in the cementitious matrix are filled with these nano particles resulting in an optimized packing density of the microstructure. Thus, strength of the hardened cement is enhanced and permeability is decreased by this filling effect. A typical application of micro and nano silica is ultra-high performance concrete (UHPC) where the interstitial spaces between cement and aggregates are filled completely with graded solids [1–5].

S. Baueregger • L. Lei • J. Plank (✉)
Construction Chemistry, Technische Universität München,
Lichtenbergstraße 4, 85747 Garching, Germany
e-mail: sekretariat@bauchemie.ch.tum.de

M. Perello
Dow Europe GmbH, Bachtobelstraße 3, 8810 Horgen, Switzerland
e-mail: mperello1@dow.com

K. Sobolev, S.P. Shah (eds.), *Nanotechnology in Construction*,
DOI 10.1007/978-3-319-17088-6_25

Furthermore, also nano C-S-H crystals (X-Seed®, BASF) prepared through templating with PCE superplasticizers were found to accelerate the silicate reaction of cement significantly and therefore enhance the early strength. The main advantage of this product compared to conventional accelerators is that the final strength is not negatively impacted which is the major drawback of e.g. calcium salts such as $CaCl_2$, $Ca(NO_3)_2$ or $Ca(HCOO)_2$. When dispersed in the cement pore solution these nano C-S-H particles initiate the crystallization of C-S-H by acting as seeding crystals. Owed to this homogeneous nucleation, the activation energy for C-S-H crystallization from cement is reduced, leading to accelerated formation of hydrate phases and early setting [6, 7].

Clay minerals which represent aluminosilicates are known to decrease the workability of concrete or mortar severely. Especially harmful is montmorillonite which can chemically sorb conventional polycarboxylate superplasticizers in its interlayer region [8]. Additionally, clay minerals decrease the final strength of concrete. Their layered structure and high surface area allow the incorporation and sorption of large quantities of water molecules, leading to a swelling of the clay particles. This way, workability is decreased by the significant water consumption and the microstructure is negatively impacted due to the presence of hydrated clay particles.

Upon calcination, the crystalline structure present in most clays is decomposed. Calcined clay minerals (e.g. metakaolinite) are amorphous pozzolanic materials which are known to boost the final strength of cement. These partially or non-crystalline aluminosilicates convert with calcium hydroxide in a pozzolanic reaction to C-S-H phases which contribute to the final strength. Supplementary cementitious materials (SCMs) such as fly ash or blast furnace slag which contain non-crystalline silica show a similar behavior. In composite cements (CEM II and III), these pozzolanic active SCMs are used to partially substitute cement clinker. Unfortunately, these materials possess a low reactivity only and therefore do not increase the early strength of cement [9–12].

Here, we present the possibility to enhance the early strength of Portland cement by adding crystalline nano-sized kaolin clay.

2 Materials and Methods

For investigation of the material properties of Portland cement in the presence of nano clays, two types of kaolin, namely K1 (KaMin HG90, KaMin LLC, Macon, US) and K2 (Chinafill 800, Amberger Kaolinwerke, Hirschau, Germany) were used. Their main difference is the particle size distribution, as is shown in Fig. 1a. Accordingly, the specific surface area and the anionic surface charge of K1 is higher compared to K2, due to the smaller particle size of K1. Table 1 summarizes these results.

The XRD pattern (Fig. 1b) of the kaolin powder samples revealed crystallinity for both K1 and K2. Sample K2 contains minor amounts of illite clay and quarz impurities. SEM analysis of the clay samples (Fig. 2) revealed the characteristic platelet shape of the kaolin particles.

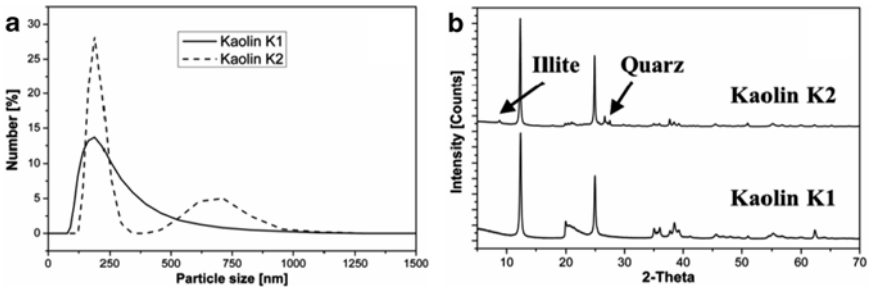

Fig. 1 (**a**) Particle size distribution, measured via dynamic light scattering (DLS), and (**b**) powder XRD pattern of the kaolinite samples K1 and K2

Table 1 pH-dependent anionic charge density and specific surface area (BET) of the kaolinite samples K1 and K2

Sample	Anionic charge amount [C/g]			Specific surface area, BET [m^2/g]
	pH 7	pH 12.5	SCPS	
Kaolin K1	−2.1	−5.9	−3.1	21
Kaolin K2	−1.0	−2.5	−1.6	10

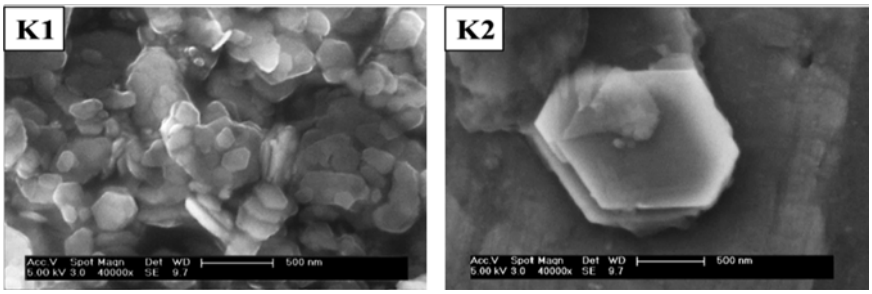

Fig. 2 Scanning electron microscope (SEM) images of dry kaolin samples K1 (*left*) and K2 (*right*)

The cement used in this study was a CEM I 52.5 N (d_{50} = 11.8 µm, HeidelbergCement, Geseke plant, Germany). For comparison, cement samples CEM I 42.5 R (d_{50} = 18.1 µm) and CEM I 52.5 R (d_{50} = 4.5 µm, Schwenk, Allmendingen plant, Germany) were used.

Compressive and tensile strength tests were carried out after 12, 16, 24 h and 28 d. Mortar specimens (nine prisms for each system, size: 160*40*40 mm) were prepared and tested according to DIN EN 196–1 at a w/c ratio of 0.5 for each system. The kaolin was added in two ways: (a) dry-blended together with cement and sand before addition of water and (b) dispersed in the mixing water via sonication.

For further characterization, hydration of OPC pastes in the presence and absence of kaolin was monitored via isothermal heat flow calorimetry at 20 °C and through in-situ XRD measurements. Ion contents present in cement pore solutions were analyzed via atomic absorption spectroscopy (AAS).

3 Results and Discussion

3.1 Compressive and Tensile Strength

The 16 h compressive and tensile strength of mortars prepared from CEM I 52.5 N with the addition of kaolin samples K1 and K2 at dosages of 1, 2 and 5 % bwoc are presented in Fig. 3. It was found that both, the 16 h compressive and tensile strength, were significantly increased when kaolin was present in the mortar.

The effect of strength enhancement depends on the dosage of the kaolin clay – the higher the dosage, the more pronounced is this effect. Additionally, this effect depends on the mode of kaolin addition, whether it is dry-blended together with cement and sand before mixing with water, or whether the clay is dispersed in the mixing water via sonication. The strongest enhancement of early strength can be achieved when kaolin is dispersed in the mixing water. For example, mortars prepared with 5 % of kaolin dispersed in the mixing water revealed a boost of compressive and tensile strength of around 30 % with CEM I 52.5 N.

Upon sonication, the kaolin agglomerates are decomposed and individual kaolin platelets are present in the mixing water. This confirms that the effect of kaolin on strength development much depends on the particle size of the clay mineral.

Table 2 presents the time-dependent results for the compressive and tensile strength of mortars prepared from CEM I 52.5 N and sample K2. Remarkably, by this kaolin strength is only enhanced at a curing time of 16 h. Another interesting effect is that the final strength (28 days) is not negatively influenced by nano kaolin.

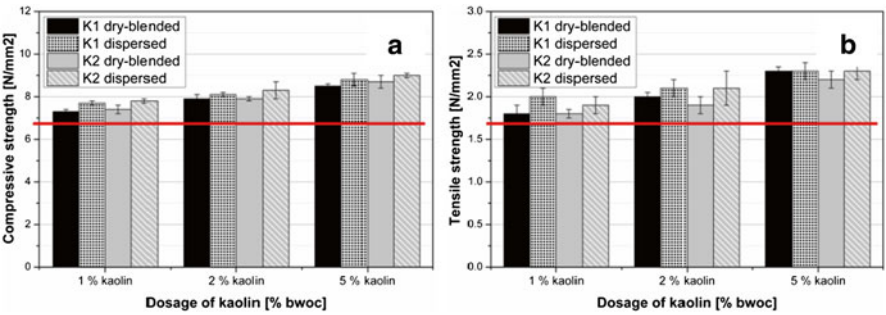

Fig. 3 Compressive (**a**) and tensile (**b**) strength after 16 h of mortar specimens prepared from CEM I 52.5 N containing 1, 2 or 5 % bwoc of kaolin sample K1 or K2. The red line represents the strength of the reference mortar without kaolin

Table 2 Compressive and tensile strength of CEM I 52.5 N after 12, 16, 24 h and 28 d in the presence and absence of 2 % bwoc kaolinite K2 (dispersed)

	Compressive/tensile strength [N/mm^2]			
	12 h	16 h	24 h	28 d
CEM I 52.5 N	3.0/0.9	7.1/1.7	14.2/3.5	73.1/8.3
CEM I 52.5 N + 2 % K2	3.0/0.9	8.3/2.1	14.6/3.5	73.4/8.3

Table 3 Sixteen hour compressive and tensile strengths of CEM I 42.5 R and CEM I 52.5 R in the presence and absence of 2 % bwoc of kaolin sample K2 (dispersed)

System	Compressive strength [N/mm^2]	Tensile strength [N/mm^2]
CEM I 42.5 R	4.5	1.2
CEM I 42.5 R + 1 % K 2	5.1	1.4
CEM I 42.5 R + 2 % K 2	5.9	1.6
CEM I 42.5 R + 5 % K 2	6.6	1.9
CEM I 52.5 R	26.2	5.5
CEM I 52.5 R + 2 % K 2	26.1	6.0
CEM I 52.5 R + 5 % K 2	26.7	5.7

For comparison, the effect of kaolin sample K2 on the 16 h early strength of CEM I 42.5 R and CEM I 52.5 R was tested. As is shown in Table 3, 5 % of K2 increase the compressive strength of CEM I 42.5 R by around 50 % and the tensile strength up to 60 %. For this slowly reacting cement a much stronger effect on the 16 h early strength is observed compared to previous CEM I 52.5 N (Table 2).

In contrast, no enhancing effect of kaolin on the strength of the much faster reacting CEM I 52.5 R can be seen. This result indicates that nano kaolin especially boosts the early strength of cements which exhibit a low reactivity. Here, the ion concentration in pore solution is lower compared to fast reacting cements, thus initiation of crystallization affects the overall hydration rate more.

3.2 Heat Calorimetry

Figure 4 shows the isothermal heat flow curves of cement pastes prepared from CEM I 52.5 N in the presence and absence of 1, 2 and 5 % bwoc of kaolin sample K1 which was dispersed in the mixing water via sonication. The result clearly demonstrates that the overall heat of hydration increases with increasing dosage of the kaolin clay whereas the time of the maximum heat flow is not affected. In the presence of kaolin, the slope in the cumulative heat of hydration curve particularly increases between 12 and 20 h. During this time period, cement hydration is promoted by kaolin K1. A similar trend was found for kaolin K2. These observations explain the results for the compressive and tensile strengths which in the presence of kaolin are especially increased around 16 h.

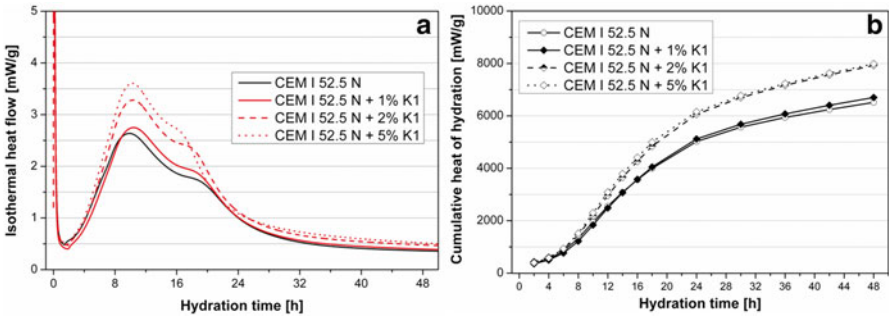

Fig. 4 (**a**) Isothermal heat flow and (**b**) cumulative heat of hydration of cement pastes (CEM I 52.5 N) modified with 1, 2 or 5 % bwoc of kaolin sample K1

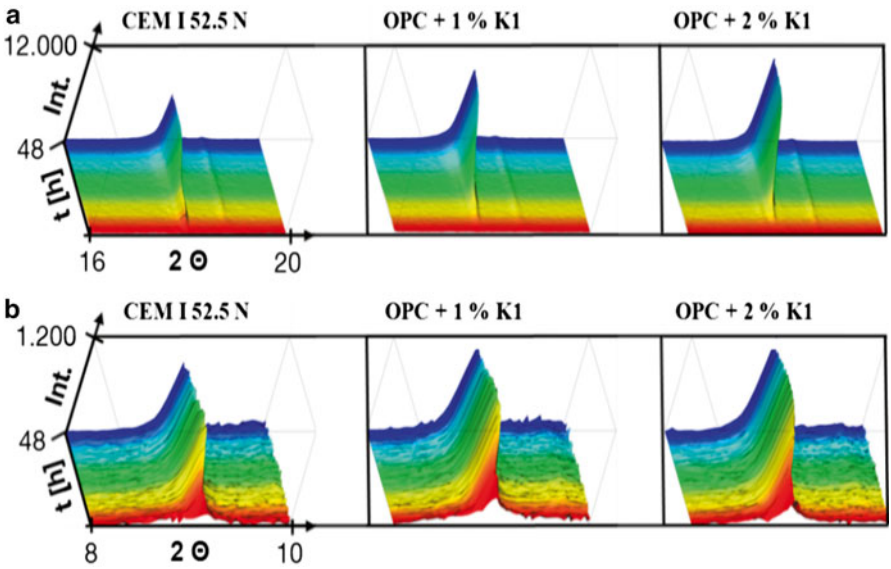

Fig. 5 Time-dependent evolution of (**a**) portlandite and (**b**) ettringite in cement pastes (CEM I 52.5 N) modified with 1 or 2 % bwoc of kaolin K1, measured via in-situ XRD

3.3 In-Situ X-ray Diffraction

Complementary to the calorimetric tests, the formation of crystalline hydrate phases during cement hydration was monitored for the first 48 h via in-situ XRD. Figure 5 presents the time-dependent evolution of the hydrate phases portlandite and ettringite. In the kaolin modified cement pastes, especially portlandite formation is significantly enhanced and ettringite formation is slightly increased. Thus, the XRD results confirm an enhanced silicate reaction which is responsible for strength development. Again, this effect is linked to the dosage of kaolin clay. The higher the

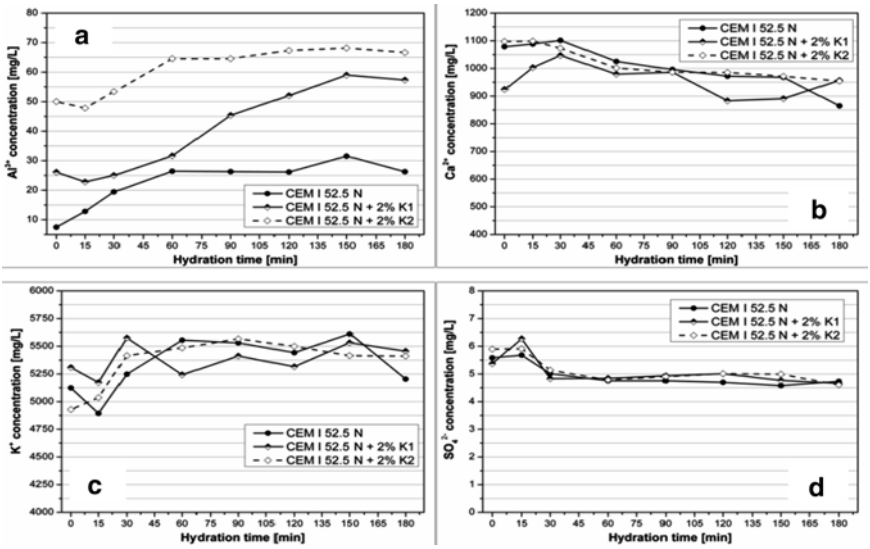

Fig. 6 Time-dependent concentrations of (**a**) Al^{3+}, (**b**) Ca^{2+}, (**c**) K^{+} and (**d**) SO_4^{2-} in cement pore solutions of CEM I 52.5 N in the presence and absence of 2 % bwoc of kaolin samples K1 and K2

dosage, the more pronounced is this effect. These results explain the increased heat flow observed for cement pastes containing kaolin, as presented above (Fig. 4).

3.4 Analysis of Cement Pore Solution

Analysis of the cement pore solution demonstrates that the concentration of Al^{3+} is increased in the presence of kaolin K1 and K2, whereas the concentrations of Ca^{2+}, K^{+} and SO_4^{2-} are not influenced. Obviously, aluminum is leached from the kaolin clay into the alkaline cement pore solution and forms tetra hydroxo aluminate $[Al(OH)_4]^{-}$. This result explains the acceleration of the aluminate reaction in the presence of kaolin (Fig. 6).

4 Conclusion

Our study demonstrates that nano kaolin clay can boost the early 10–24 h compressive and tensile strength of Portland cement without negatively impacting the final strength after 28 d. This effect is not caused by an optimized particle packing of the cementitious matrix (filler effect). Instead, such nano-sized kaolin clay increases the reactivity of the silicate and aluminate phases, as was evidenced via calorimetric and in-situ XRD measurements.

It was found that this effect is linked to the particle size and the mode of addition of the nano clay to mortar (dry-blended into cement or dispersed in the mixing water). A potential explanation for its performance is a seeding effect. Owed to heterogeneous nucleation, the activation energy for the crystallization of cement hydrates is reduced and thus early strength development is promoted. Additionally, aluminum is dissolved from kaolin into the cement pore solution, as was evidenced via AAS. This way, the crystallization of the aluminate hydrates is initiated.

References

1. Shaikh, F., Supit, S., & Sarker, P. (2014). A study on the effect of nano silica on compressive strength of high volume fly ash mortars and concretes. *Materials and Design, 60*, 433–442.
2. Biricik, H., & Sarier, N. (2014). Comparative study of the characteristics of nano silica-, silica fume- and fly ash-incorporated cement mortars. *Materials Research, 17*, 570–582.
3. Oltulu, M., & Sahin, R. (2014). Pore structure analysis of hardened cement mortars containing silica fume and different nano-powders. *Construction and Building Materials, 53*, 658–664.
4. Haruehansapong, S., Pulngern, T., & Chucheepsakul, S. (2014). Effect of the particle size of nanosilica on the compressive, strength and the optimum replacement content of cement mortar containing nano-SiO2. *Construction and Building Materials, 50*, 471–477.
5. Abd El Aleem, S., Heikal, M., & Morsi, W. M. (2014). Hydration characteristic, thermal expansion and microstructure of cement containing nano-silica. *Construction and Building Materials, 59*, 151–160.
6. Bräu, M., Ma-Hock, L., Hesse, C., Nicoleau, L., Strauss, V., Treumann, S., Wiench, K., Landsiedel, R., & Wohlleben, W. (2012). Nanostructured calcium silicate hydrate seeds accelerate concrete hardening: A combined assessment of benefits and risks. *Archives of Toxicology, 86*, 1077–1087.
7. Thomas, J., Jennings, H., & Chen, J. (2009). Influence of nucleation seeding on the hydration mechanisms of tricalcium silicate and cement. *Journal of Physical Chemistry, 113*, 4327–4334.
8. Lei, L., & Plank, J. (2014). A study on the impact of different clay minerals on the dispersing force of conventional and modified vinyl ether based polycarboxylate superplasticizers. *Cement and Concrete Research, 60*, 1–10.
9. Rashad, A. M. (2014). A comprehensive overview about the effect of nano-SiO_2 on some properties of traditional cementitious materials and alkali-activated fly ash. *Construction and Building Materials, 52*, 437–464.
10. Quercia, G., Spiesz, P., Husken, G., & Brouwers, H. (2014). SCC modification by use of amorphous nano-silica. *Cement and Concrete Composites, 45*, 69–81.
11. Morsy, M., Al-Salloum, Y., Almusallam, T., & Abbas, H. (2014). Effect of nano-metakaolin addition on the hydration characteristics of fly ash blended cement mortar. *Journal of Thermal Analysis and Calorimetry, 116*, 845–852.
12. Frias, M., & Martinez-Ramirez, S. (2009). Use of micro-Raman spectroscopy to study reaction kinetics in blended white cement pastes containing metakaolin. *Journal of Raman Spectroscopy, 40*, 2063–2068.

The Influence of Nano Silica Size and Surface Area on Phase Development, Chemical Shrinkage and Compressive Strength of Cement Composites

Jon S. Belkowitz, WhitneyLe B. Belkowitz, Robert D. Moser, Frank T. Fisher, and Charles A. Weiss Jr.

Abstract The changes in hydrated cement composition were measured as a means of quantifying the impact of nano silica size and surface area on cementitious properties. Nano silica dispersions were dosed to have an equal amount of exposed and reactive silica surface area, which contribute to pozzolanic reaction. The amount of calcium hydroxide was measured through thermogravimetric analysis to identify hydrate growth. The chemical shrinkage and compressive strength were also evaluated as a means to understand the impact that nano silica had on the early stages of hydration. Cement composites receiving the higher dosages of the larger nano silica particles exhibited higher levels of enhancement, showing decreased calcium hydroxide, decreased chemical shrinkage and increased compressive strength. The smaller nano silica particles exhibited enhancements at lower dosages, but at higher dosages an increase in calcium hydroxide, an increase in chemical shrinkage, and a decrease in compressive strength was recognized.

Keywords Cement • Nanosilica • Dispersion • Hydration • Pozzolanic • Calcium hydroxide • Chemical shrinkage • Compressive strength

J.S. Belkowitz (✉) • F.T. Fisher
Stevens Institute of Technology, Hoboken, NJ, USA
e-mail: JBelkowi@Stevens.edu; FFisher@Stevens.edu

W.B. Belkowitz
Intelligent Concrete, LLC, Broomfield, CO, USA
e-mail: Whitney@Intelligent-Concrete.com

R.D. Moser • C.A. Weiss Jr.
USACE Engineer Research & Development Center, Vicksburg, MS, USA
e-mail: Robert.D.Moser@USACE.Army.mil; Charles.A.Weiss@USACE.Army.mil

K. Sobolev, S.P. Shah (eds.), *Nanotechnology in Construction*,
DOI 10.1007/978-3-319-17088-6_26

1 Introduction

The composite nature of concrete is not restricted to the macroscopic domain, but encompasses the microscopic and nanoscopic realms [1–5]. Included in the hydrated cement composite are anastomosed networks of hydrated silicates (calcium-silicate-hydrates, C-S-H), as well as crystalline phases that may react with time (e.g., calcium hydroxide, CH) [6, 7]. The C-S-H network, although porous, is the principal material providing the strength and durability of the concrete. A common method to make concrete a stronger and a more durable material is by densification of C-S-H through pozzolanic reaction [3, 8, 9]. The pozzolanic compounds combine with CH to create more C-S-H. The use of nano silica in cementitious composites has become increasingly popular due to its ability to increase C-S-H production at extremely low dosages [12]. Despite the increased popularity a significant amount of research is still needed to understand the impact of nano silica size and surface area. The nano silica particles have a higher surface area in comparison to current pozzolanic materials. This higher surface creates a smaller surface potential, effectively reducing the stability of a particle in dispersion [10, 11, 13].

2 Materials and Methods

A Type I/II ordinary Portland cement (OPC) with a Blaine fineness of 0.345 m^2/g was used as the primary cementitious material for the experimentation. The chemical composition of OPC was: SiO_2, 19.9 %; CaO, 63.9 %; Al_2O_3, 4.8 %; Fe_2O_3, 3.2 %; C_3S, 57 %; C_2S, 13 %; and C_3A, 7 %. A Class F fly ash with a fineness of 0.420 m^2/g was used as a replacement pozzolanic material with a chemical composition of: SiO_2, 36 %; CaO, 13.7 %; Al_2O_3, 21 %; Fe_2O_3, 6.4 %; and Na_2O (total alkalis), 1.2 %. Three colloidal silica suspensions, with a silica purity of 99.9 %, and varying diameters and averaged surface areas (surface area, m^2/g) were used: 3–6 nm, 500 m^2/g (CS1); 15–17 nm, 190 m^2/g (CS2); and 45–47 nm, 80.0 m^2/g (CS3).

The dosages of nano silica, are listed in Table 1. The initial dosages were designed to have an equal amount of silica surface area supplied by a 20 % replacement of OPC by F Ash, assuming a total cementitious mass of 420 kg/m^3, for a total F Ash mass of 84 kg/m^3. The total free silica surface area brought by the F Ash was approximately 13,000 m^2 per cubic meter of concrete. This represents the initial

Table 1 Percent replacement of Portland cement with Nano Silica

	CS1 (%)	CS2 (%)	CS3 (%)	Class F fly ash equivalent (%)
DOS1	0.009	0.02	0.05	20
DOS2	0.09	0.23	0.55	200
DOS3	0.87	2.30	5.46	2,000
DOS4	1.75	4.60	10.92	4,000

dosage for the nano silica dispersions. Each successive dosage represented an increase by one order of magnitude of the silica surface area. The fourth dosage (DOS4) was for a free silica surface area of approximately 2,800,000 m^2/m^3.

The neat cement pastes for Thermogravimetric analysis (TGA) and nuclear magnetic resonance (NMR) were batched, mixed according to ASTM C 1608 [14] and placed in rubber molds measuring 25.4 mm by 12.7 mm by 6.3 mm the coupons were crushed to obtain particles not larger than a 0.044 mm. The crushed samples were placed in an acetone bath to quench the hydration. Thermal analysis of the specimens was performed using a Netzsch STA 449 Jupiter F1 simultaneous thermal analyzer up to 1,000 °C at a rate of 10 °C/min [15].

Description of the Si nuclei within the samples was conducted using a Bruker (Billerica, MA) Avance III (300 MHz) nuclear magnetic resonance (NMR) spectrometer equipped with a solid-state standard bore magic-angle spinning (MAS) probe. All samples were packed into 4 mm Zr rotors and spun at 5,000 Hz. The 29Si was analyzed using a cross-polarization (CP) MAS technique with a total suppression of sidebands (TOSS) sequenced to mathematically remove spinning sidebands [8, 16]. The CP-TOSS method was run for 2,000 scans and a 30-s recycle delay (referred to as d1) with liquid tetramethysilane (TMS) Chemical shrinkage ASTM C 1608 was used to prepare and measure the cement pastes [14]. The liquid levels in the pipettes were evaluated for 24 h. Measurements were taken every 60 min for 24 h. For the compressive the strength samples, the mixing procedure for the grout was followed per ASTM C 305 [12] and ASTM C 192 [17] into 50.8 mm diameter by 101.6 mm tall cylindrical non-absorbent plastic molds.

3 Experimental Results

To determine the total CH percentage, Table 2 from a composite, the loss of dehydroxylated water was compared to a ratio of water and CH molecular masses (4.11) and factored into Eq. (1) [15].

$$\text{Total CH } \% = \left(\text{H}_2\text{O Loss } \%_{DEHYDROX}\right) \times \left[\frac{MolWt_{\text{H}_2\text{O}}}{MolWt_{CH}}\right] \tag{1}$$

The values listed in Table 2 for the CS1 mixtures illustrate a reduction of CH content when compared to both of the reference sample sets. As the dosage of the CS1 (and CS2) increases there is a reduction in CH content. It should be noted that all the values from the CS1 and CS2 samples sets were lower than the CH content of the OPC sample. This was not the case when comparing the F Ash sample to CS1 and CS2. Where all the CS1 mixtures (as well as the lower two dosages of CS2) have a higher CH content then the F Ash.

For the CS3 there is a slight increase in CH content for DOS1 and DOS2 over the references and the other nano silica mixtures. This is presumably occurring due to the lower reactivity of the larger nano silica particles, lower degree of pozzolanic

Table 2 Values correlating to hydration over 24 h and at 28 days

Mixture ID	CH mass loss (%), 28 days	f'c, 24 h (MPa)	f'c, 28 days (MPa)	Chemical shrinkage (ml/g), 24 h	Deg. of Hyd., 28 days (%)
OPC	13.97	10.4 (±0.2)	41.0 (±0.6)	0.0474	78.11
F Ash	10.28	5.0 (±0.3)	43.4 (±0.5)	0.0299	77.52
CS1 – 1	13.28	19.0 (±0.3)	49.1 (±0.7)	0.0316	77.24
CS1 – 2	12.58	18.2 (±0.3)	47.1 (±0.7)	0.0275	62.92
CS1 – 3	12.00	16.2 (±0.2)	42.8 (±0.6)	0.0352	63.36
CS1 – 4	10.32	7.5 (±0.1)	35.3 (±0.9)	0.0402	76.03
CS2 – 1	13.60	15.2 (±0.3)	48.5 (±0.9)	0.0374	67.70
CS2 – 2	11.30	14.0 (±0.4)	47.1 (±0.7)	0.0370	63.53
CS2 – 3	10.15	12.9 (±0.1)	46.7 (±0.7)	0.0341	68.28
CS2 – 4	9.62	11.7 (±0.1)	42.6 (±0.1)	0.0237	77.16
CS3 – 1	15.25	11.2 (±0.3)	43.5 (±0.1)	0.0326	81.45
CS3 – 2	14.63	13.6 (±0.1)	47.4 (±0.4)	0.0316	74.73
CS3 – 3	10.03	17.1 (±0.3)	51.3 (±0.5)	0.0314	72.99
CS3 – 4	5.67	18.9 (±0.1)	51.3 (±0.5)	0.0289	76.62

reaction. The higher dosages of the CS3 (DOS3 and DOS4) generate a greater reduction in CH, with DOS4 generating the least amount of CH.

For NMR studies, the degree of hydration, α in Eq. (1), was defined by Al-Dulaijan et al., as a ratio of higher order silicon species (Q2 and Q3) to the total silicon species (Q1, Q2 and Q3) found in the hydrated cement composite [18]:

$$\propto = \left[\frac{(Q2 + Q3)}{(Q1 + Q2 + Q3)} \right] \times 100 \ \% \tag{2}$$

The degree of hydration showed that for the middle dosages of CS1 (DOS2 and DOS3) there is a decrease in degree of hydration. Despite this setback there is a significant increase in the degree of hydration for the highest and lowest dosage (DOS1 and DOS4). Furthermore, a moderate decrease in the degree of hydration is apparent for the highest dosages of CS2 (DOS4). For the lowest dosages of CS3 (DOS1), an increase in degree of hydration can be clearly observed. There is a small reduction in the degree of hydration for the higher dosages of CS3 (DOS2, DOS3 and DOS4).

The chemical shrinkage results in Table 2 for the CS1 mixtures illustrate a reduction at all dosages. Furthermore, the lower dosages of CS1 (DOS1 and DOS2) exhibit a lower chemical shrinkage than that of the F Ash mixture. As the dosages of the CS1 increases (DOS3 and DOS4), there is a greater amount of chemical shrinkage.

The data illustrated in Table 2 for the CS2 mixtures follows the same trend for the residual CH content. At the lower dosages of the CS2 there is an increase in the amount of chemical shrinkage when compared to the lower CS1 dosages. As the

amount of CS2 is increased there is a drastic reduction in chemical shrinkage when compared to the references. For the lower two dosages of CS3 (DOS1 and DOS2) there is a slight increase and slight decrease in the CH content presumably occurring due to the lower surface area of reactive silica of the larger nano silica particle and thus lower reactive surface area. The higher dosages of the CS3 (DOS3 and DOS4) generate the greatest reduction in chemical shrinkage for cement composites when compared to the references.

The compressive strength results listed in Table 2 show the lower dosages of CS1 and CS2 showed an increase in the compressive strength of the cement composites over the references. As the dosages of CS1 and CS2 are increased, there is still an increase in 24-h strengths but a reduction in compressive strength at 28 days. Conversely, the mixtures that had the lower dosages (DOS1 and DOS2) of the CS3 developed a lower compressive strength gain, for both 24-h and 28 day, than the higher dosages of CS3. There seemed to be a relationship between the effectiveness of the nano silica dispersion, surface area and nano silica replacement of cementitious.

4 Conclusions

Higher dosages of the largest nano silica dispersions seemed to have the greatest impact on reducing CH content. This phenomenon could be due to: (1) A reduction in the effectiveness of the smaller nano silica dispersion at higher dosages and (2) A higher effectiveness of the larger nano silica dispersion at higher dosages. While the stability of the nano silica dispersions was not a focal point of this research, the change in effectiveness could be a factor related to the stability of the nano silica dispersion in the fresh cementitious mixture. The NMR spectra showed lower dosages of the largest nano silica particle had a greater impact then the smaller nano silica particles at all dosages.

The chemical shrinkage data, illustrated that when the dosage of the smallest nano silica dispersion is increased there is an increase in chemical shrinkage. At the higher dosages of the larger nano silica dispersions there is a reduction in chemical shrinkage. While the higher dosages of the larger nano silica dispersion are still effective at enhancing the HCM; the smaller nano silica dispersions might have become ineffective. The greatest impact on compressive strength was from the smaller nano silica particles at lower dosages and larger nano silica particles at higher dosages had the greatest impact. While future research is needed to identify how an overabundance of nano silica will impact the HCM; the research conducted supports the use of nano silica enhance cement composites, grout and concrete.

Acknowledgement The authors would also like to thank Katie Bartojay of the Bureau of Reclamation for reviewing of the data, results and discussion of this research. The authors would also like to thank Steve Miller from Intelligent Concrete, LLC for reviewing, restructuring and editing drafts for final publication. The partial support of the National Science Foundation under Grant No. NSF DGE-0742462 and CMMI-0846937 is gratefully acknowledged. The authors

would like to express their gratitude to AkzoNobel, Inc for supplying the different Cembinder products for this research. The Army Corp of Engineers was gracious enough to conduct a multitude of experiments to complete the objectives of this research project.

References

1. Qiao, L., Guo, L., & Hong, J. (2010). Mechanical properties and microstructure characterization of calcium silicate hydrate (C-S-H) gel. *Materials Science Forum, 650*, 63–66.
2. Richardson, I. (2004). Tobermite/jennite and tobermite/calcium hydroxide-based models for the structure of C-S-H: Applicability to hardened pastes of tri-caclium silica, dicalcium-silicate, Portland cement and blends of Portland cement with blast-furnace slag, metakaolin or silica fume. *Cement and Concrete Research, 34*, 1733–1777.
3. Constantinides, G., & Ulm, F. (2007). The nanogranular nature of C-S-H. *Journal of the Mechanics and Physics of Solids, 55*, 64–90.
4. Manzano, H., Dolado, J., Guerrero, A., & Ayuela, A. (2007). Mechanical properties of crystalline calcium-silicate-hydrates: Comparison with cementitious C-S-H gels. *Physica Status Solidi (A), 204*, 1775–1780.
5. Richardson, I. G. (2007). The calcium silicate hydrates. *Cement and Concrete Research, 38*, 137–158.
6. Belkowitz, J., & Armentrout, D. (2010). An analysis on nano silica in the cement hydration process. *Concrete sustainability conference* (pp. 1–15). Albuquerque: National Ready-Mixed Concrete Association.
7. Thomas, J., Jennings, H., & Allen, A. (2010). Relationships between composition and density of tobermorite, jennite, and nanoscale CaO-SiO2-H2O. *The Journal of Physical Chemistry C, 114*, 7594–7601.
8. Taylor, H. (1997). *Cement chemistry*. New York: Thomas Telford Books.
9. Helmuth, R. (1987). *Fly ash in cement and concrete*. Skokie: PCA.
10. Wise, H., & Oudar, J. (1990). *Material and concepts in surface reactivity and catalysis*. Dover: Dover Publications.
11. Iijima, M., & Kamiya, H. (2009). Surface modification for improving the stability of nanoparticles in liquid media. *KONA Powder and Particle Journal, 27*, 119–129.
12. ASTM C 305–12. (2012). *Standard practice for mechanical mixing of hydraulic cement pastes and mortars of plastic consistency*. ASTM. www.astm.org.
13. Nazari, A., & Riahi, S. (2011). The effects of SiO2 nanoparticles on physical and mechanical properties of high strength compacting concrete. *Composites Part B: Engineering, 42*, 570–578.
14. ASTM C 1608–07. (2007). *Standard test method for chemical shrinkage of hydraulic cement paste*. West Conshohocken: ASTM International.
15. Midgely, M. (1979). The determination of calcium hydroxide in set portland cements. *Cement and Concrete Research, 9*, 77–82.
16. Cong, X., & Kirkpatrick, R. J. (1996). ^{29}Si and ^{170}NMR investigation of the structure of some crystalline calcium silicate hydrates. *Advanced Cement Based Materials, 3*, 133–143.
17. ASTM C 192–12. (2012). *Standard practice for making and curing concrete test specimens in the laboratory*. West Conshohocken: ASTM International.
18. Al-Dulaijan, S., Al-Tayyib, A., Al-Zahrani, M., Parry-Jones, G., & Al-Mana, A. (1995). Si MAS-NMR study of hydrated cement paste and mortar made with and without silica fume. *Journal of the American Ceramic Society, 78*, 342–346.

Electrochemical Injection of Nanoparticles into Existing Reinforced Concrete Structures

Jiří Němeček and Yunping Xi

Abstract This paper deals with the chloride extraction from concrete and shows possibilities of injection of selected nanoparticles and a hydrophobic agent into existing reinforced concrete structures by means of electromigration technique. Accelerated chloride penetration tests are employed to simulate natural chloride exposure. The developed chloride profile is then removed by electroextraction. Similarly, specimens are injected with different concentrations of colloidal nanosilica particles and a siliconate. It is shown in the paper that chlorides can be effectively extracted from the concrete using small voltage lasting for several days. Solutions of nanosilica and siliconate can be transported into concrete via the electric field. Once injected nanosilica can act as a microstructure densifier and further reduce chloride penetration due to the decreased diffusivity of the treated concrete. Siliconate acts on hydrohobization of the outer specimen layer.

Keywords Concrete • Chlorides • Electromigration • Electroextraction • Nanoparticles

1 Introduction

Nanoparticles added into mixtures of concrete can be utilized in many ways. Most of their applications is related to stiffness and strength development of newly cast concretes. Nanosilica can act both as hydration moderator and densification agent, e.g. [1, 2]. Nanoclays can significantly increase workability of the concrete in fresh state, e.g. [1]. Nanoparticles of TiO_2 can serve as self-cleaning admixture.

J. Němeček (✉)
Department of Mechanics, Faculty of Civil Engineering,
Czech Technical University in Prague, Prague, Czech Republic
e-mail: jiri.nemecek@fsv.cvut.cz
http://mech.fsv.cvut.cz/~nemecek

Y. Xi
Department of Civil, Environmental, and Architectural Engineering,
University of Colorado, Boulder, CO, USA
e-mail: yunping.xi@colorado.edu

K. Sobolev, S.P. Shah (eds.), *Nanotechnology in Construction*,
DOI 10.1007/978-3-319-17088-6_27

A lot of works have been also dedicated to the strengthening effect of carbon nanotubes in cement paste, e.g. [3]. Depending on the particular nanoparticle, the uses of additional treatments such as e.g. functionalization, surfactants, sonication, etc., the dispersion of particles in the material have been developed. On the other hand, transport of any species into the hardened concrete is a challenging task. Fortunately, concrete is a porous media whose microstructure contains considerable amount of pores which allows water with ionic species to be transported in or out of the material. The presence of water or moist air in pores may have both beneficial effects (strength development, drying shrinkage reduction, etc.) as well as negative effects (carbonation caused by dissolved CO_2, alkali-silica reaction, transport of e.g. chloride ions). Durability and service life of reinforced concrete structures is in a large extent determined by the concrete transport properties and state of the embedded reinforcing steel. Chlorides used in deicers have the most detrimental effect on the steel reinforcement. After reaching a critical chloride concentration [4, 5] corrosion of steel rebars starts.

In this study we use electrochemical chloride extraction method [6, 7] which allows for non-destructive treatment of chloride affected reinforced structures that are in risk of steel corrosion. As proposed by several researchers the electrochemical extraction can be combined with injection of corrosion inhibitors [8, 9]. Electromigration is used as a temporary treatment to decrease chloride concentration and to extend the service life of the structure. In this study we firstly show the effectiveness of the chloride extraction using electromigration technique and then we employ electromigration to inject nanoparticles into existing concrete to cover inner pore surfaces, densify the microstructure and block further ion (chloride) migration. The present method is conducted on laboratory specimens but could be applied on a larger scale structure.

2 Experimental Program

2.1 Samples and Testing Procedure

Normal strength concrete specimens were prepared from Portland cement ASTM C150 type I (Holcim), quartz sand, gravel and water in the ratio of 415/831/831/182 kg/m^3. Water to cement ratio was 0.44. No plasticizer or further admixture were added to the mixture. Samples were cast into cylindrical moulds having 100 mm in diameter and 200 mm in height. Resulting concrete density reached 2,360 kg/m^3. After 24 h the samples were demoulded, placed into water and cured until testing. Samples were tested at the age of 40–80 days. Fifty millimeter thick slices were prepared from the cylinders for testing in the electrochemical chamber.

Experiments were performed using an electromigration chamber (used for RCPT test; ASTM C1202) consisting of two compartments filled with electrolyte solutions and the sample placed in between them. Each compartment contained stainless steel mesh electrode attached to a DC source with constant electric potential of 20 V.

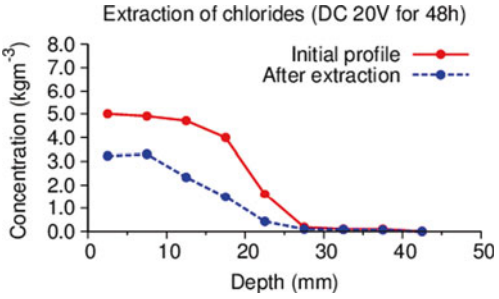

Fig. 1 Chloride profiles after accelerated chloride penetration test and after extraction (concentration given in Cl per cement content)

Table 1 Healing agent properties

Sample	Agent	Producer	Weight content (%)	Specific surface (m^2/g)	Particle size range (nm)	pH
NS1	Nanosilica	AkzoNobel	15[a] wt%	234[b]	5–50[b]	9–11
NS2	Nanosilica	Sigma-Aldrich	30[a] wt%	198–250[a]	Undeclared	8.6–9.3[a]
NS3	Nanosilica	AkzoNobel	50[a] wt%	50[b]	19–156[b]	9–11
SM1	Siliconate	Gelest	3 vol%	–	–	13
SM1	Siliconate	Gelest	10 vol%	–	–	13

[a]Data taken from product sheet
[b]Data taken from Quercia et al. [2]

Tests were conducted in the lab temperature of 25 °C. Three types of tests were conducted:

(i) Accelerated chloride penetration tests (ACP). ACP test was performed to rapidly (compared to natural diffusion of chloride) develop a chloride profile inside the concrete specimen (Fig. 1). The ACP test lasted for 48 h.
(ii) Chloride extraction (CE). To check the effectiveness of the extraction process, chlorides were extracted from ACP samples by reversing the polarity in the chamber. Again, the test lasted for 48 h.
(iii) Nanoparticle injection (NI). The third type of test involved injection of nanoparticles into concrete specimens using the electric field in the chamber. After injection, samples were dried for 24 h at 50 °C to allow bonding of nanoparticles on inner pore surfaces. Then, samples were vacuum saturated with deionized water. The effectiveness of the treatment was checked with subsequent ACP test.

For the chloride penetration test 3 % NaCl solution was used in upstream (injecting) compartment. For extraction, both compartments were filled with 0.3 N NaOH solution. In the third test type different nanoparticle solutions were placed in the upstream compartment and injected. Different weight concentrations (15–50 %) and particle size distributions were used in injection tests (Table 1). The nanosilica dispersions are produced as anionic stabilized with sodium cations (pH 9–11). It was assumed that nanosilica can be transported to inner pores and act both on the densification of the microstructure and to form additional C-S-H gel inside the pores.

Silanes and siloxanes are known to deliver water-repellent properties to concrete surface with the limited ability to penetrate inside the specimen. To further improve the hydrophobicity of the concrete, a previously selected water soluble siliconate was chosen for electromigration test. Water diluted sodium methylsiliconate with the chemical formula CH_5NaO_3Si was tested in two concentrations of 3 and 10 vol% (samples SM1 and SM2; Table 1).

2.2 Test Results

After each type of test, chloride concentration profile (acid soluble) was assessed. Samples were drilled by a hard metal drill-bit in perpendicular direction to the surface exposed to chlorides and the concrete powder collected in 5 mm depth interval. The chloride concentration was then measured with ion selective electrode in an acid leached concrete powder. The concentration was recalculated as a weight ratio per cement content. Resulting concentration profiles are presented in Figs. 1 and 2. Figure 1 shows concentration profile developed by ACP and used as initial chloride profile for extraction process. The accelerated profile was developed using electric field in 2 days which is roughly 90 times faster than in natural conditions. After extraction lasting for another 2 days 35 % drop in surface chloride concentration was reached. The concentration was lowered in the whole sample by a larger amount (Fig. 1) which shows effectiveness of the electromigration method.

Later, samples injected with nanoparticles were also subjected to ACP test. Figure 2 presents concentration profiles of chlorides after the test. Obviously, chloride concentrations are lower compared to untreated sample which show both nanosilica and siliconate can effectively block chloride ingress into the sample although the blocking mechanism can be slightly different. Nanosilica can form C-S-H gel on inner pore surface and in higher concentration can physically block smaller pores and act on local densification of the microstructure. Such densification leads to further slower diffusion and slower migration of ions in case of accelerated tests. The best performance was achieved on samples injected with 50 % nanosilica solution (NS3). The decrease in the surface concentration was 72 % compared to untreated samples. It is interesting to note that the best performance was also achieved with

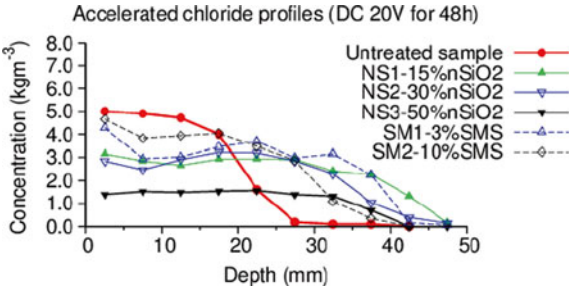

Fig. 2 Chloride profiles after accelerated penetration tests on differently treated samples (concentration given in Cl per cement content)

the largest dimensions of tested particles (19–156 nm) suggesting that the pore blocking mechanism is the primary one. About 40 % decrease was achieved on samples injected with 15–30 % nanosilica (NS1, NS2).

Despite the fact that the concentrations of chlorides developed after ACP test are lower on nanosilica treated samples than the untreated samples, the chlorides tend to affect deeper parts of the sample. Such behavior is still not fully understood. Possibly, it can be attributed to either vacuum treatment used in the procedure of sample resaturation or different mechanism of ion penetration takes place on samples exposed to dual electromigration procedure. This phenomenon needs further investigation.

Samples injected with sodium methylsiliconate (SMS) showed similar performance in terms of decreased chloride concentration after ACP test (Fig. 2). It is assumed that due to its smaller molecular size SMS can penetrate deeper to the sample by electromigration and bond to inner pore surfaces. Its chloride blocking effect is primarily based on the hydrophobization of the surfaces. Surface contact angle of a water droplet changed from 44° to 123° when 3 % SMS was used. However, the effect of chloride blocking was not as pronounced as in case of nanosilica for either of the tested SMS concentrations.

3 Conclusions

It was shown in the present study that how chlorides can be effectively extracted from concrete by means of electromigration technique. The concentration of chlorides was decreased to one half after application of low voltage (20 V) for 48 h. Extending the time or voltage would lead to further acceleration of the process. Our results support findings of previous researchers showing high efficiency of the technique that is applicable also on a large scale structure. For a real application, the same methodology can be used by connecting reinforcement as cathode and external metal or carbon meshes as anode.

Electromigration technique was further employed to inject selected nanoparticles into concrete. Two anionic solutions were tested. Nanosilica particles were driven into samples and were able to block subsequent chloride ingress. More than 70 % decrease in surface chloride concentration was achieved on samples treated with 50 % nanosilica solution. It is assumed that nanosilica acts mainly as local densifier of small capillary pores inside the specimen. Several issues still remain unclear, such as the exact penetration depth of nanosilica or siliconate and its influence on the chloride concentration in deeper part of concrete. Although most probable blocking mechanism have been proposed further investigation is desirable.

Since anionic solutions were used in this study, applications of the present technique to a real structure could be possible only on chloride free concrete. Otherwise, unwanted transport of negatively charged chlorides would endanger the reinforcement. Such situation could be avoided by using cationic nanoparticle solutions. Such studies will also be the future directions of the research.

Acknowledgement Financial support of the Czech Science Foundation (project 13-18652S) is gratefully acknowledged. Dr. Němeček would also like to thank for awarding him Fulbright-Masaryk scholarship which enabled the initiation of this work.

References

1. Kawashima, S., Hou, P., Corr, D. J., & Shah, S. P. (2013). Modification of cement-based materials with nanoparticles. *Cement and Concrete Composites, 36*, 8–15.
2. Quercia, G., Hüsken, G., & Brouwers, H. J. H. (2012). Water demand of amorphous nano silica and its impact on the workability of cement paste. *Cement and Concrete Research, 42*, 344–357.
3. Konsta-Gdoutos, M. S., Metaxa, Z. S., & Shah, S. P. (2010). Highly dispersed carbon nanotube reinforced cement based materials. *Cement and Concrete Research, 40*(7), 1052–1059.
4. Angst, U., & Vennesland, Ø. (2009). Critical chloride content in reinforced concrete – State of the art. In M. G. Alexander et al. (Eds.), *Concrete repair, rehabilitation and retrofitting II*. London: Taylor and Francis Group.
5. Ann, K. Y., & Song, H. W. (2007). Chloride threshold level for corrosion of steel in concrete. *Corrosion Science, 49*, 4113–4133.
6. Liu, Y., & Shi, X. (2009). Electrochemical chloride extraction and electrochemical injection of corrosion inhibitor in concrete: State of the knowledge. *Corrosion Reviews, 27*(1–2), 53–81.
7. Clemeña, G. G., & Jackson, D. R. (2000). *Trial application of electrochemical chloride extraction on concrete bridge components in Virginia* (Final Report FHWA/VTRC 00–R18) Charlottesville: Virginia Transportation Research Council.
8. Page, C. L., Ngala, V. T., & Page, M. M. (2000). Corrosion inhibitors in concrete repair systems. *Magazine of Concrete Research, 52*(1), 25–37.
9. Sawada, S., Page, C. L., & Page, M. M. (2005). Electrochemical injection of organic corrosion inhibitors into concrete. *Corrosion Science, 47*(8), 2063–2207.

On the Development of the Silicon Oxide Nanoparticle Thin Films to Reduce Building Energy Consumption

Somayeh Asadi

Abstract The growth of the cities is characterized by a great increase in built and paved areas, energy consumption, and heat generation. As a result, solar energy is absorbed by building and paved surfaces, causing the surface temperature of urban structures to become several degrees higher than ambient air temperatures. The phenomenon of urban warming is called heat island. High temperatures increase energy demand for air conditioning in buildings and photochemistry effects that increase atmospheric pollution, as well as increasing environmental impacts due to the demand of energy generation. Materials with high albedo and emittance attain lower temperatures when exposed to solar radiation, reducing the transfer of heat to the environmental air. Therefore, the objective of this study is to develop the Silicon Oxide (SiO_2) nanoparticle thin films as the solar reflective coating materials to be used either in the external façade of buildings, roof, and walls or for pavements and other urban structures. The prepared SiO_2 nanoparticle thin films were coated on different types of asphalt shingles. The near-infrared radiation (NIR) reflectance properties of the prepared samples were measured in the laboratory. In addition, the effect of the SiO_2 nanoparticle thin films on energy loads was quantified using EnergyPlus simulation program. It was found that the prepared asphalt shingles doped SiO_2 nanoparticle film coatings has the high solar reflectance index value (SRI) in comparison with the conventional asphalt shingles. Results indicated that asphalt shingle surfaces with high SRI represent a major contributing factor to the urban heat island effect.

Keywords Nanoparticle coatings • Asphalt shingle • Energy consumption • Reflective materials • Heat island effect

S. Asadi (✉)
Department of Architectural Engineering, Pennsylvania State University, State College, PA, USA
e-mail: asadi@engr.psu.edu

K. Sobolev, S.P. Shah (eds.), *Nanotechnology in Construction*,
DOI 10.1007/978-3-319-17088-6_28

1 Introduction

Roof surfaces are considered as a large fraction of the urban landscape. Accordingly, urban sustainability leaders are gradually looking for new roofing technologies to achieve a range of goals. These include electricity production, reducing building energy consumption, improving the urban heat island (UHI) effect and reducing storm-water runoff. Heat island intensity in hot climates may increase up to 10 °C which result in higher discomfort and pollution levels while it has a significant effect on the building cooling load. UHI phenomenon in combination to the global climatic change deteriorate the microclimatic conditions that are characterized by increased ambient temperatures, longer duration of hot spells, and more frequent heat waves. With trends of increasing urban sprawl, air pollution, heat related illness and mortality, water temperatures in streams, and greenhouse gas emissions, new mitigation methods are being developed to solve these issues. Various methods including usage of green spaces, application of highly reflective materials, decrease of the anthropogenic heat, solar control of open spaces, use of environmental heat sinks, and increase of the wind flow in the canopy layer have been utilized to reduce the heat island effect. Among them, highly reflective roofing systems have been analyzed over several decades to assess their ability to achieve sustainability goals, including reducing building energy consumption and mitigating the urban heat island. The performance of materials with high solar reflectance and infrared emittance values, known as cool materials, has been extensively studied [1–9]. In a study conducted by Akbari et al., building energy simulations were conducted and it was found that an increase in roof albedo of 0.4 resulted in peak cooling demand savings of 20–40 % in residences and 5–10 % in offices at the Los Angeles basin. Joudia et al. [10] studied the thermal behavior of small cabins with reflective coatings on both interior and exterior cladding, under different conditions and climates in order to clarify the potential energy saving by smart choices of clad coatings. They found that the effect of exterior and interior surface radiation properties under the different conditions on heating and cooling was significant in line with experimental results and readily explained by the concept inherent in the model. Having investigated the effect of cool roofs to mitigate heat island effect and reduce energy consumption, Eilert [11] found that the cooling benefit of a roof surface with high solar reflectance decreases with time as the surface accumulates dust and deposits.

Several experiments and numerical studies have been conducted to assess the efficiency of cool roofs in reducing building energy consumption as well as heat island mitigation [12–18]. In a study conducted in Hong Kong on the energy efficient envelope design for high-rise apartments, it was found that a 30 % reduction in solar absorptance can achieve 12 % saving in annual required cooling energy [19]. Investigated the impact of color on indoor temperatures in the hot and humid climates [20]. Their result showed that for lightweight construction, the maximum air temperature inside the black cell was higher by about 12 °C than that of the white cell. Moreover, the air temperature inside the white cell was only 2–3 °C higher than the outdoor. In a similar study, Zinzi and Fasano [21] quantified the impact of cool roofs in improving indoor thermal comfort in residential buildings in Italy.

The roof was covered by paint with a measured solar reflectance of 85.9 % and measurements were conducted before and after the application of the paint on the roof. The temperature of the room under the roof was higher than 27 °C for 99.8 % of the time, while in the room below it was 64 %. After the roof was coated, the percentage was, respectively, 58 % and 48 %. Shariah et al. conducted a numerical study [22] for the moderate climate of Amman and the hot climate of Aqaba, in Jordan in order to assess the effect of roof reflectivity on building energy consumption. Results showed that by increasing the external reflectance of the roof from 0 to 1, the energy load decreases by 32 % for a non-insulated building and 26 % for an insulated building in Amman. Higher energy savings were obtained for Aqaba.

In a parallel recent trend, researchers have begun to investigate the application of nanocrystalline as the cool materials since they possess interesting optical properties such as increased band gap and enhanced fluorescence intensity. Among the nanocrystalline materials, metal oxide nanoparticles belong to an interesting class of compounds. Metal oxide nanoparticles can be prepared in unique shapes and they exhibit remarkably different chemical properties compared to macrocrystals. The particle size of an oxide can affect its color that in turn can affect its reflectance properties. Moreover, metal oxide nanoparticles possess high surface areas making them useful for a variety of applications including coatings. Therefore, the objective of this study is to develop the Silicon Oxide (SiO_2) nanoparticle thin films as the solar reflective coating materials to be used either in the external façade of buildings, roof, and walls or for pavements and other urban structures. The prepared SiO_2 nanoparticle thin films were coated on different types of asphalt shingles. The near-infrared radiation (NIR) reflectance properties of the prepared samples were measured in the laboratory. In addition, the effect of the SiO_2 nanoparticle thin films on energy loads was quantified using EnergyPlus simulation program.

2 Methodology

2.1 Materials and Methods

The following materials were used to prepare solar reflective SiO_2 nanoparticle thin films: tetra-ethoxy-silane (TEOS) purchased from VWR. Hydrochloric Acid (HCL) was purchased from Sigma-Aldrich and SiO_2 with a size less than about 100 nm was purchased from Alfa Aesar.

2.2 Preparation Procedure

A single batch process was used in this study to develop SiO_2 nanoparticle thin film coatings. The matrix solution was prepared by first adding 8.57 ml of TEOS to 60 ml of HCL with concentration of 0.01 mol/L. In the next step, the mixture was

Table 1 Different preparation scenarios

Asphalt shingle color	Preparation procedure	
	A	1.0 mol HCL+TEOS; 1.0 gr SiO_2
Shasta white	B	0.01 mol HCL+TEOS; 1.0 gr SiO_2
Sierra gray	C	0.01 mol HCL+TEOS; 2.0 gr SiO_2
Weathered wood	D	1.0 mol HCL+TEOS; 2.0 gr SiO_2

Fig. 1 Prepared asphalt shingles

stirred for 1 h at 60 °C at an agitation rate of 500 rpm to form a micro-porous solution of silica. After cooling, the prepared solution was divided into 10 ml portions into which different amounts of nanoparticles were added. The matrix of the nanoparticles and mixture was then applied to the asphalt shingle with different colors. Four different procedures were used to prepare asphalt shingle samples with three different colors as can be seen in Table 1. In addition, Fig. 1 shows the prepared samples.

2.3 Solar Reflectivity Measurement

Figure 2 shows the sketch of the conventional and reflective roofs. During the daylight hours, a roof is constantly subjected to solar energy striking its surface. The term "Solar Reflectance" is a measure of the amount of that solar energy that is immediately reflected from the surface. It is not reflected heat, but reflected electromagnetic energy from the sun. The solar energy that is not reflected away from the

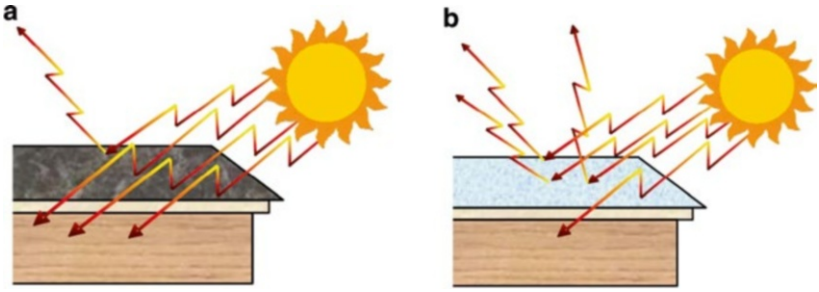

Fig. 2 Operation of conventional and reflective roofs. (**a**) Conventional roof. (**b**) Reflective roof

surface is absorbed into the outer surface of the roof product and is converted into heat. The heat can be removed by convection as air flows over the surface, or by conduction through the roof material into the sheathing below. A reflective roof with high solar reflectance and high thermal emittance would have a lower surface temperature as compared to a conventional roof. In the case of a reflective roof, a lower surface temperature translates into less heat gain into the attic space or living space below the roof. The result is a cooler living space and lower cooling/heating energy consumption.

The Solar Spectrum Reflectometer (SSR) was used to measure the percent total solar reflectance of the prepared asphalt shingles according to the ASTM C1549. The SSR measures total solar reflectance based on four filtered detectors and utilizes a tungsten filament light source. The SSR employs a diffuse tungsten halogen lamp to illuminate the coated flat surface, the reflected light of which is detected by four detectors, each of which is equipped with color filters targeted to identify four wavelengths in the solar spectrum: 380 nm (ultraviolet [UV]), 500 nm (blue), 650 nm (red), and 1,220 nm (infrared [IR]). The measurement spectrum is calculated by collecting the weighted sum of the response spectra from each detector.

2.4 Solar Reflectance Index (SRI)

The SRI incorporates both solar reflectance and emittance into a single value and is a measure of the constructed surface's ability to stay cool in the sun by reflecting solar radiation and emitting thermal radiation. It is defined such that a standard black surface (initial solar reflectance of 0.05, initial thermal emittance of 0.90) has an initial SRI of 0, and a standard white surface (initial solar reflectance of 0.80, initial thermal emittance of 0.90) has an initial SRI of 100. Materials with the highest SRI values are the coolest choices for roofing. To calculate the SRI of the prepared asphalt shingles with and without SiO_2 nanoparticle coating, their solar reflectance and thermal emittance were measured in the laboratory.

The SRI of the asphalt shingle with and without SiO_2 nanoparticle coating was calculated according to ASTM E 1980. The following formula was used to calculate the SRI:

$$SRI = 123.9 - 141.35\,X + 9.655X^2 \tag{1}$$

$$\mathrm{X} = \frac{(\alpha - 0.02\varepsilon 1)(8.797 + h_c)}{(9.5205\varepsilon + h_c)} \tag{2}$$

Where α is the solar absorptance and ϵ represent for the thermal emissivity of the prepared asphalt shingle samples. Table 2 shows the SRI of some of the conventional asphalt shingles [23]. In addition, Table 3 shows the SRI of the samples which were prepared in the laboratory. As it can be seen, the shasta white asphalt shingle coated with 1.0 mol of HCL plus TEOS and 2.0 gr of SiO_2 has the highest SRI (i.e. 41). On the other hand, weathered wood asphalt shingle coated with 1.0 mol of HCL plus TEOS and 1.0 gr of SiO_2 has the lowest SRI (i.e. 12) in comparison with other samples.

Table 2 Solar reflectance index of asphalt shingles

Type of the asphalt shingle	SRI	Type of the asphalt shingle	SRI
White	21	Black	1
Shasta white	27	Aspen grey	17
Gray	4	Weathered wood	4
Green	18	Dark brown	4
Antique silver	19	Beachwood sand	19

Table 3 Solar reflectance index of asphalt shingles

Asphalt shingle color	Preparation procedure	Solar reflectance index
Weathered wood	Control	2
	A	12
	B	19
	C	18
	D	21
Sierra gray	Control	6
	A	23
	B	27
	C	27
	D	31
Shasta white	Control	23
	A	32
	B	35
	C	35
	D	41

3 Results and Discussions

As mentioned, the SSR reflectance of the prepared samples was measured according to the ASTM C1549. Figure 3 shows the measured SSR reflectance of the weathered wood, sierra gray, and shasta white asphalt shingle samples which were coated with SiO_2 nanoparticle films. In order to understand the effect of preparation procedure on the thermal reflectance of the asphalt shingle, the SSR reflectance of each procedure was measured separately. Results showed that sample D which coated with 1.0 mol of HCL plus TEOS and 2.0 gr of SiO_2 has the highest SSR reflectance value in comparison with samples A, B, and C and similar trend is seen for all the asphalt shingle samples with different colors. On the other hand, sample A which coated with 1.0 mol of HCL plus TEOS and 1.0 gr of SiO_2 has the lowest SSR reflectance value in comparison with other samples. An important observation is that there is no substantial difference between sample B (i.e. 0.01 mol of HCL plus TEOS and 1.0 gr of SiO_2) and sample C (i.e. 0.01 mol of HCL plus TEOS and 2.0 gr of SiO_2) in asphalt shingles with different colors. This can be attributed to the significant effect of the HCL and TEOS solution on the SSR reflectance of the prepared asphalt shingles. Results showed that the SiO_2 nanoparticle films increase the SSR solar reflectance of the weathered wood asphalt shingle from 0.065 to 0.193. The same trend is seen in both sierra gray and shasta white asphalt shingle samples. The SSR reflectance of the sierra gray asphalt shingle increased from 0.161 to 0.287 and in shasta white asphalt shingle from 0.234 to 0.363.

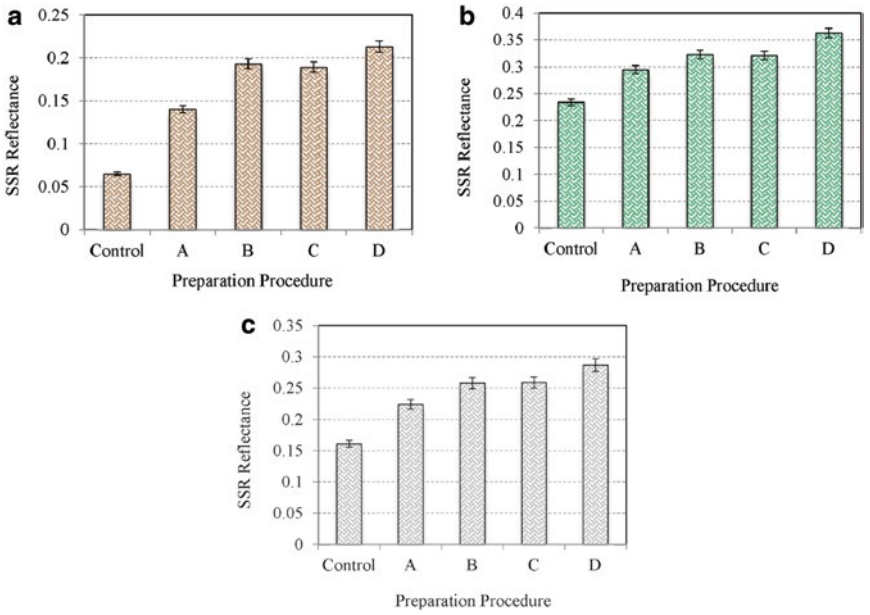

Fig. 3 Measured SSR reflectance. (**a**) Weather wood. (**b**) Sierra Gray. (**c**) Shasta White

4 Estimating the Impact of the SiO_2 Nanoparticle Thin Films on Energy Loads

EnergyPlus [24] which is a widely accepted simulation program for modeling annual building energy consumption was used to calculate the effect of the SiO_2 nanoparticle thin films on energy loads. EnergyPlus is commonly used to model heating, cooling, lighting, ventilation, and other energy flows within buildings. In this paper the design of a single-family residential building located in Tampa, Florida, USA, is considered as a case study. The total area of the building is 186 m^2 with a slab-on-grade foundation. The internal gains due to people, lighting and electric appliances are estimated according to annual values narrowed down by the ASHRAE [25] and taken into the calculations as a profile with monthly values. Heat pump air-to-air ventilation system is used, which provides the space cooling and heating. The indoor design temperature is 22 °C for space heating and 26.6 °C for space cooling. Calculation results of sensible cooling load from three types of roof surface materials are illustrated in Fig. 4. Asphalt shingle surfaces with minimal solar reflectance and large heat storage capacity represent a major contributing factor to the urban heat island effect. The monthly sensible cooling load for three types of asphalt shingle including shasta white, weathered wood, sierra gray is calculated. The results show that all asphalt shingles doped SiO_2 nanoparticle film coatings demonstrate lower cooling load than conventional asphalt shingle of the same color. Shasta white, weather wood, and sierra gray asphalt shingle coated with SiO_2 nanoparticle film provide 4.3, 3.2, and 2.9 % lower cooling load than the control sample. As expected, the monthly cost savings in shasta white asphalt shingle is higher than the sierra gray and weather wood in each month.

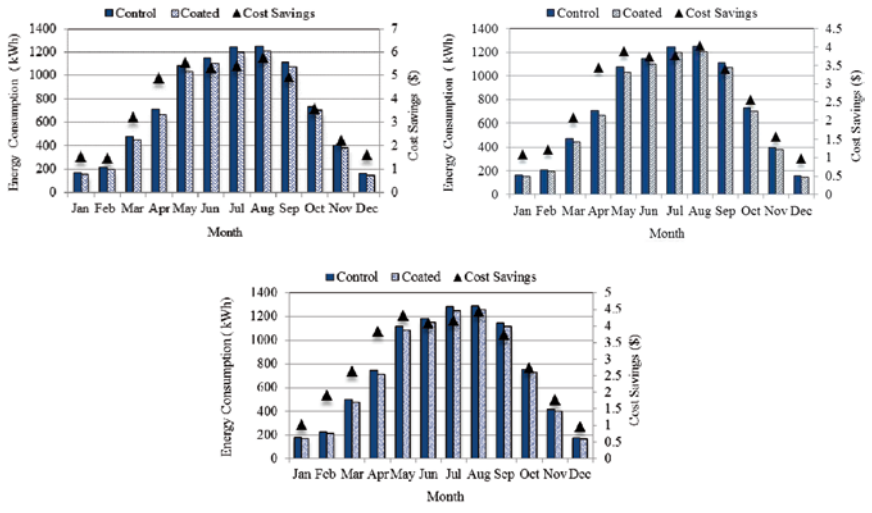

Fig. 4 Sensible cooling load

5 Conclusions

An increased environmental awareness in the United States has recently resulted in push for sustainable product and practices to reduce energy consumption, increase cost effectiveness, and to eliminate health and safety hazards. An experimental study was carried out to produce SiO_2 nanoparticle films as the reflective coatings for asphalt shingle materials. In addition, the effect of the SiO_2 nanoparticle thin films on energy loads was quantified using EnergyPlus simulation program. Based on the results of this analysis, the following conclusions may be drawn:

- The prepared asphalt shingles doped SiO_2 nanoparticle film coatings has the high SRI values in comparison with conventional asphalt shingles.
- Results showed that the shasta white asphalt shingle coated with 1.0 mol of HCL plus TEOS and 2.0 gr of SiO_2 has the highest SRI (i.e. 41). On the other hand, weathered wood asphalt shingle coated with 1.0 mol of HCL plus TEOS and 1.0 gr of SiO_2 has the lowest SRI (i.e. 12) in comparison with other samples.
- It was found that sample D which coated with 1.0 mol of HCL plus TEOS and 2.0 gr of SiO_2 has the highest SSR reflectance value and similar trend is seen for all the asphalt shingle samples. On the other hand, sample A which coated with 1.0 mol HCL plus TEOS and 1.0 gr of SiO_2 has the lowest SSR reflectance value in comparison with other samples.
- No substantial difference between sample B (i.e. 0.01 mol of HCL plus TEOS and 1.0 of gr SiO_2) and sample C (i.e. 0.01 mol of HCL plus TEOS and 2.0 gr of SiO_2) was seen in different types of asphalt shingles.
- Results indicated that asphalt shingle surfaces with high SRI represent a major contributing factor to the urban heat island effect.
- The results show that all asphalt shingles doped SiO_2 nanoparticle film coatings demonstrate lower cooling load than conventional asphalt shingle of the same color. Shasta white, weather wood, and sierra gray asphalt shingle coated with SiO_2 nanoparticle film provide 4.3, 3.2, and 2.9 % lower cooling load than the control sample.
- The monthly cost savings in shasta white asphalt shingle is higher than the sierra gray and weather wood in each month.

References

1. Berdahl, P., & Bretz, S. (1997). Preliminary survey of the solar reflectance of cool roofing materials. *Journal of Energy and Buildings, 25*, 149–158.
2. Berdahl, P., Akbari, H., Levinson, R., & Miller, W. (2008). Weathering of roofing materials – An overview. *Journal of Construction and Building Materials, 22*(4), 423–433.
3. Synnefa, A., Dandou, A., Santamouris, M., & Tombrou, M. (2007a). *An energy efficient solution to mitigate heat islands and reduce cooling energy loads*. Proceedings of the international conference of Sustainable Buildings 2007. , Lisbon.
4. Synnefa, A., Santamouris, M., & Akbari, H. (2007). Estimating the effect of using cool coatings on energy loads and thermal comfort in residential buildings in various climatic conditions. *Journal of Energy and Buildings, 39*, 1167–1174.

5. Prado, R. T. A., & Ferreira, F. L. (2005). Measurement of albedo and analysis of its influence the surface temperature of building roof materials. *Journal of Energy and Buildings, 37*, 295–300.
6. Karlessi, T., Santamouris, M., Apostolakis, K., Synnefa, A., & Livada, I. (2009). Development and testing of thermochromic coatings for buildings and urban structures. *Solar Energy, 83*, 538–551.
7. Karlessi, T., Santamouris, M., Synnefa, A., Assimakopoulos, D., Didaskalopoulos, P., & Apostolakis, K. (2011). Development and testing of PCM doped cool colored coatings to mitigate urban heat island and cool buildings. *Building and Environment, 46*, 570–576.
8. Synnefa, A., Santamouris, M., & Livada, I. (2006). A study of the thermal performance of reflective coatings for the urban environment. *Solar Energy, 80*(8), 968–981.
9. Hui Shen, H. T., & Tzempelikos, A. (2011). The effect of reflective coatings on building surface temperatures, indoor environment and energy consumption—An experimental study. *Energy and Buildings, 43*, 573–580.
10. Ali Joudia, H. S., Cehlin, M., & Rönnelid, M. (2013). Reflective coatings for interior and exterior of buildings and improving thermal performance. *Applied Energy, 103*, 562–570.
11. Eilert, P. (2000). *High albedo (cool) roofs: Codes and standards enhancement (CASE) study*. San Francisco: Pacific Gas and Electric Company.
12. Doulos, L., Santamouris, M., & Livada, I. (2004). Passive cooling of outdoor urban spaces: The role of materials. *Solar Energy, 77*, 231–249.
13. Santamouris, M., Synnefa, A., Kolokotsa, D., Dimitriou, V., & Apostolakis, K. (2008). Passive cooling of the built environment—Use of innovative reflective materials to fight heat island and decrease cooling needs. *International Journal of Low Carbon Technologies, 3*, 71–82.
14. Dionysia Kolokotsa, C. D., Papantoniou, S., & Vlissidis, A. (2012). Numerical and experimental analysis of cool roofs application on a laboratory building in Iraklion, Crete, Greece. *Energy and Buildings, 55*, 85–93.
15. Stathopouloua, M., Synnefaa, A., Cartalisa, C., Santamourisa, M., Karlessia, T., & Akbarib, H. (2009). A surface heat island study of Athens using high-resolution satellite imagery and measurements of the optical and thermal properties of commonly used building and paving materials. *Sustainable Energy, 28*, 59–76.
16. Kolokotronia, M., Gowreesunker, B. L., & Giridharan, R. (2013). Cool roof technology in London: An experimental and modelling study. *Energy and Buildings, 67*, 658–667.
17. Jo, J. H., Carlson, J. D., Golden, J. S., & Bryan, H. (2010). An integrated empirical and modeling methodology for analyzing solar reflective roof technologies on commercial buildings. *Building and Environment, 45*, 453–460.
18. Zhiyang Shi, & Xiong Zhang. (2011). Analyzing the effect of the longwave emissivity and solar reflectance of building envelopes on energy-saving in buildings in various climates. *Solar Energy, 85*(1), 28–37.
19. Cheung, C. K., Fuller, R. J., & Luther, M. B. (2005). Energy efficient envelope design for high rise apartments. *Energy and Buildings, 37*(1), 37–48.
20. Cheng, V., & Givoni, B. (2005). Effect of envelope color and thermal mass on indoor temperatures in hot humid climate. *Solar Energy, 78*, 528–534.
21. Zinzi, M., & Fasano, G. (2009). Properties and performance of advanced reflective paints to reduce the cooling loads in buildings and mitigate the heat island effect in urban areas. *International Journal of Sustainable Energy, 28*(1–3), 123–139.
22. Shariah, A., Shalabi, B., Rousan, A., & Tashtoush, B. (1998). Effects of absorptance of external surfaces on heating and cooling loads of residential buildings in Jordan. *Energy Conversion and Management, 39*(3/4), 273–284.
23. EETD, E.E.T.D. (2014). *Solar Reflectance Index of Asphalt shingles*. http://energy.lbl.gov/coolroof/asshingl.htm
24. Crawley, D., Lawrie, L. K., Pedersen, C. O., & Winkelmann, F. C. (2000). Energy plus: Energy simulation program. *ASHRAE, 42*, 49–56.
25. ASHRAE (2002) *ASHRAE guideline 14–2002: Measurement of energy and demand Savings 2002*. American Society of Heating, Refrigerating and Air-Conditioning Engineers (ASHRAE), Atlanta GA.

Part V
Carbon Nanomaterials

Cement Reinforcement by Nanotubes

Roey Nadiv, Michael Shtein, Alva Peled, and Oren Regev

Abstract Loading a matrix with nano-sized particles such as nanotubes (carbon or tungsten di-sulfide) is expected to improve the mechanical properties of composite materials better than traditional (macroscopic) fillers due to extra-ordinary mechanical properties accompanied by high surface area. One of the major challenges towards achieving this goal is an effective dispersion of the as-produced aggregated nanotubes. In this work we demonstrate a novel dispersion method, facilitating the integration of individual nanotubes in cement paste matrix. We demonstrate the effectiveness of our nanotubes dispersion method by enhancing both flexural strength and compressive strength of cement paste using carbon and tungsten di-sulfide nanotubes. Finally, a comprehensive fractography study indicates that both types of nanotubes fail via pull-out mechanism with an intermediate state of bridging mechanism.

Key words Nanotubes • Composite • Dispersion • Cement • Matrix

R. Nadiv (✉)
Department of Chemical Engineering, Ben-Gurion University of the Negev, Beer-Sheva 84105, Israel
e-mail: roeynadiv@gmail.com

M. Shtein • O. Regev
Ilse Katz Institute for Nanoscale Science and Technology, Ben-Gurion University of the Negev, Beer-Sheva 84105, Israel

Department of Chemical Engineering, Ben-Gurion University of the Negev, Beer-Sheva 84105, Israel

A. Peled
Department of Structural Engineering, Ben-Gurion University of the Negev, Beer-Sheva 84105, Israel

K. Sobolev, S.P. Shah (eds.), *Nanotechnology in Construction*,
DOI 10.1007/978-3-319-17088-6_29

Abbreviations

CNT	Carbon nanotube
NT	Nanotube
PC	Plain cement paste
SEM	Scanning electron microscope
TEM	Transmission electron microscope
WS_2NT	Tungsten di-sulfide nanotube

1 Introduction

Cement, is characterized by a high compressive strength on one hand and a low tensile and flexural properties on the other [1, 2]. The latter properties are expected to be improved by loading nanofiller into the cement paste matrix. For cement nanocomposite (**CNC**) reinforcement purposes, carbon nanotube (**CNT**) is the most widely used nanofiller because of its extra-ordinary mechanical properties [3] and high surface area (~100–700 m^2/g) [4]. Tungsten di-sulfide nanotube (**WS_2NT**) is also a promising cement nanofiller [5], characterized by high aspect ratio (e.g., high surface area) along with attractive mechanical properties [6, 7], as manifested in epoxy composites [8].

The utilization of nanotubes (**NT**) (both CNT and WS_2NT) in composite materials is often hindered by the NT's tendency to form aggregates. NT aggregates due to strong interfacial van der Waals interactions, hence reducing their effective surface area, which consequently leads to a decrease in the stress transfer between the matrix and the filler. Furthermore, NT aggregates act as stress concentrator and could initiate crack propagation. Therefore, developing a method to effectively disperse NTs is essential.

In this study, we demonstrate a novel dispersion method of NTs in cement paste matrix. The research aims at reinforcing plain cement paste (**PC**) by individually dispersed NTs in order to enhance the flexural properties; while preserving or even improving other mechanical properties (e.g., compressive strength). A fractographic study reveals the reinforcing and failure mechanisms of NTs in CNC.

2 Experimental

Multi-wall CNT (diameter = 10–20 nm, length = 10–30 μm, Cheaptubes), WS_2NT (diameter = 30–100 nm, length = 1–10 μm, NanoMaterials), β-Lactoglobulin (CAS 9045-23-2, Sigma–Aldrich) and Pluronic F-127 (CAS 9003-11-6, Sigma–Aldrich) were used as received.

NT dispersions in aqueous solution are prepared by sonication in the presence of dispersants (Table 1).

Table 1 NT dispersion parameters

NT	Dispersant	Dispersant concentration (mg/mL)	NT concentration (mg/mL)	Sonication (energy) (J)
CNT	Pluronic F-127	1.5	2.0	Tip sonication (5,040)
WS_2NT	β-Lactoglobulin	2.0	6.0	Bath sonication (540)

Two sonication methods are used: Bath sonication (30 W, 32 kHz, Elma sonic model S10, Elma) and Tip sonication (500 W – 20 kHz, 20 % amplitude μtip, Q500, Qsonica) for CNT and WS_2NT, respectively. Temperature is kept at 0 °C.

Following sonication, to allow the precipitation of large aggregates, a phase separation by decantation is conducted and the NT's concentration in the supernatant is calculated [9]. The supernatant (exfoliated NTs) is freeze-dried (Lobanco Freezone 2.5) yielding a cotton-like powder of NTs wrapped with dispersant. The freeze-dried NTs are then mixed in water (water:cement ratio of 0.4) and bath-sonicated for 2 min. The cement (Portland cement CEM I 52.5 R, Nesher Israel cement enterprises) is gradually added and mechanically mixed for 4 min. The mixture is then casted and placed for 4 min inside a vibration machine to allow degassing. The CNC specimens are de-molded 24 h after casting and cured by immersion in water vessel at room temperature for 14 d.

The NT dispersion quality is examined by Transmission electron microscope (**TEM**) (FEI Tecnai 12 G2 TWIN TEM). The flexural strength is determined by three point bending test (ASTM D790), using a prism-shaped specimens with dimensions of $8 \times 8 \times 60$ mm^3. The measurements are performed by LRX, LLOYD (capacity of 5 kN) using a constant extension rate of 0.5 mm/min. The compressive strength is determined by ASTM C109, using a 12 mm cube specimens. The measurements are performed by Instron 5982 (capacity of 100kN) using a constant extension rate of 2 mm/min. Finally, the fractographic study is conducted on the specimen's fractured surfaces using a high resolution scanning electron microscopy (**SEM**) (JEOL, JSM-7400 F).

3 Results and Discussion

3.1 Dispersion Method

Achieving maximal mechanical properties enhancement depends on the dispersion quality of the as-received NT aggregates. Therefore, liquid dispersions of exfoliated NTs in water by sonication are stabilized by dispersants, which sterically prevents NT re-aggregation. Electron microscopy was used to monitor the dispersion quality throughout the preparation. The as-received NTs (Fig. 1a, b) are clearly aggregated. Following sonication and decantation, the supernatant phase contains individual NTs (Fig. 1c, d). Finally, their integration in the cement results in a uniformly dispersed NTs in the CNC (Fig. 1d, f).

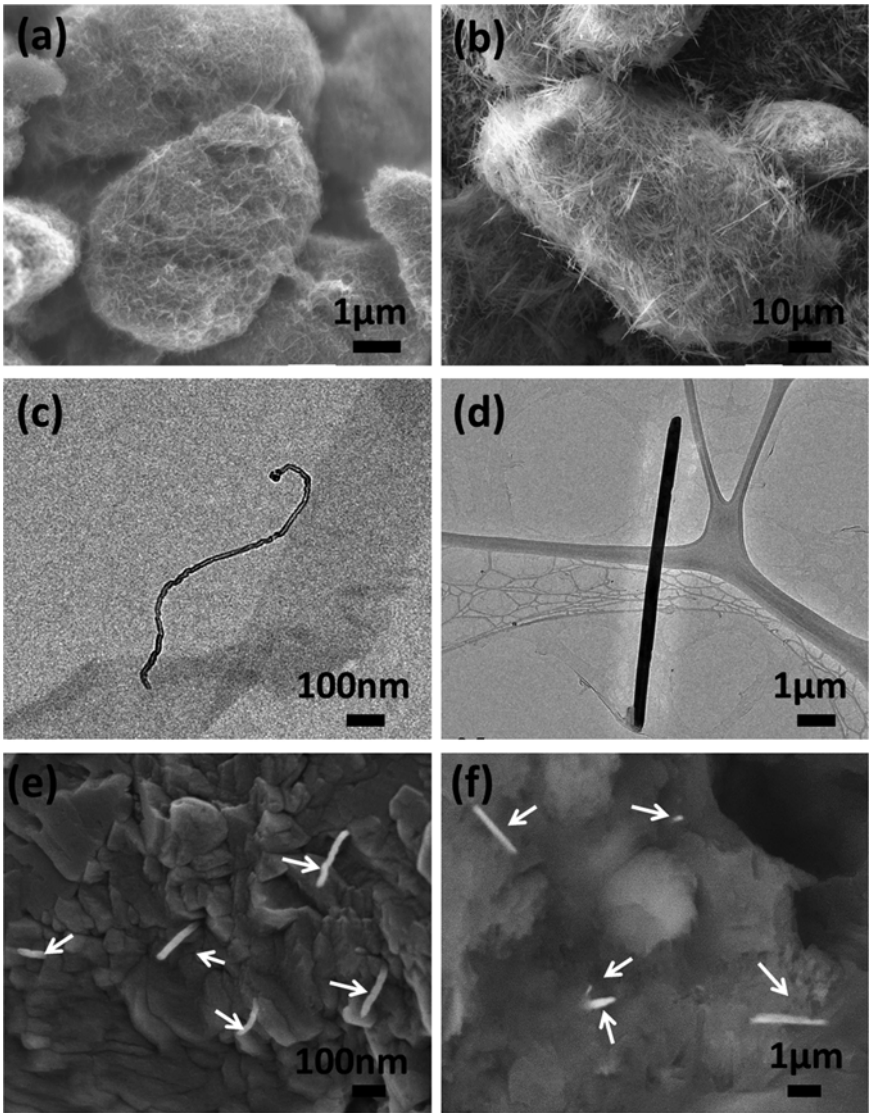

Fig. 1 SEM images of as-received aggregated (**a**) CNT and (**b**) WS_2NT; TEM images of individually dispersed (**c**) CNT and (**d**) WS_2NT following sonication and decantation (see text); SEM image of (**e**) 0.15 vol% CNT-based CNC and (**f**) 0.063 vol% WS_2NT-based CNC fractured specimens, indicating well dispersed NTs (*white arrows*)

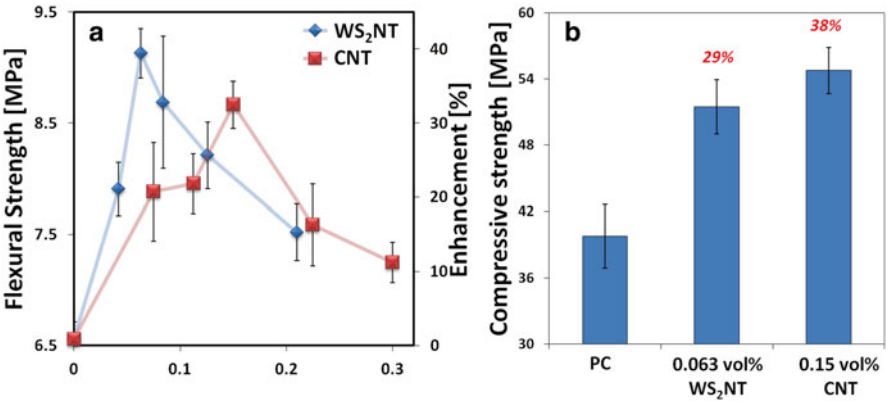

Fig. 2 (**a**) Flexural strength and its enhancements (over PC) of CNC following 14 d curing as a function of NT concentration. The connecting *lines* are only guidance to the eyes. (**b**) Compressive strength of PC, 0.063 vol% WS_2NT and 0.15 vol% CNT-based CNCs (enhancement over PC is indicated (*red*) for each CNC)

3.2 *Mechanical Properties*

The efficiency of NT reinforcement is also affected by the filler content. Previous studies indicate that the performance of composite materials is strongly affected by NT concentration [8, 10]. Therefore, we prepared CNCs with various NT vol% (CNT or WS_2NT) and tested their flexural strength (Fig. 2a). At low NT vol%, the flexural strength enhancement is relatively mild, and the flexural strength increases with increasing NT vol% until it reaches the optimal concentration (0.15 and 0.063 %, for the CNT and WS_2NT, respectively). At the optimal concentration, a significant flexural strength enhancement of 85 and 70 % is obtained for WS_2NT and CNT, respectively. At these concentrations the compressive strength is also improved by 23 and 38 % for WS_2NT and the CNT, respectively (Fig. 2b).

These high mechanical properties enhancements are attributed to the efficiency of dispersion method yielding individually dispersed NT (Fig. 1e, f).

3.3 *Fractographic Study*

The NTs in the composite materials serve as crack propagation inhibitors (*Bridging* mechanism) [8, 11]. However, when the CNC experiences failure, the NT could fails either via its *pull-out* from the matrix or through its *fracture*. The former generally occurs in the case of relatively weak NT-matrix interfacial adhesion and the latter in the case of strong one [12]. By observing the CNC's fractured surfaces, we indicate that the NTs indeed reinforce the CNC by bridging mechanism (Fig. 3a, b).

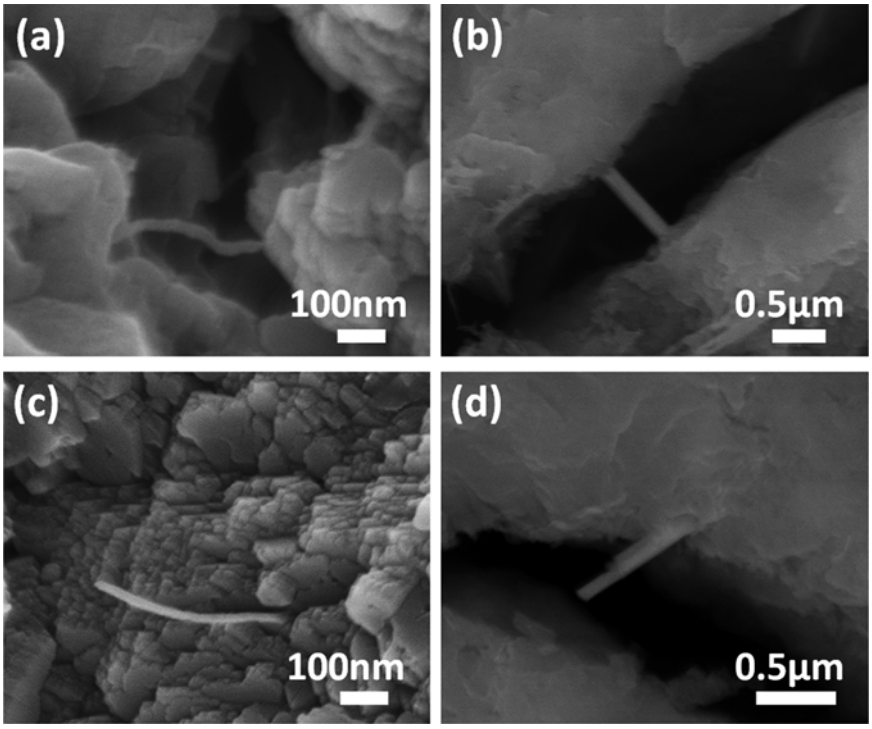

Fig. 3 SEM images of NT-based CNC fractured surfaces at optimal NT concentration, indicating bridging mechanism of (**a**) CNT and (**b**) WS_2NT; pull-out mechanism of (**c**) CNT and (**d**) WS_2NT

Finally, at complete failure, the NTs undergo pullout mechanism, manifested by a substantial part of the NT protruding from the specimen surface (Fig. 3c, d). The pullout mechanism is expected considering the porous structure of cement paste, i.e., low interfacial area and hence weak interfacial bonding.

Given these results and based on prior knowledge regarding NTs failure mechanism [8, 12], it is clear that in order to further increase the flexural strength it is vital to increase the NT-cement interfacial adhesion.

4 Conclusions

We efficiently disperse two types NTs, namely, CNT and WS_2NT. The effective dispersion method yields substantial flexural strength enhancement following 14 d. The compressive strength is also enhanced by the NT loading. Our results show that loading cement by CNTs offer higher compressive strength while WS_2NT loading provides better flexural strength. An in-depth SEM fractography study indicates that the NTs reinforce the matrix by inhibiting crack propagation via bridging, and fail via pullout mechanism.

References

1. Taylor, H. F. (1997). *Cement chemistry*. London: Thomas Telford.
2. Bye, G. C. (1999). *Portland cement: Composition, production and properties*. London: Thomas Telford.
3. Yu, M. F., Lourie, O., Dyer, M. J., Moloni, K., Kelly, T. F., & Ruoff, R. S. (2000). Strength and breaking mechanism of multiwalled carbon nanotubes under tensile load. *Science, 287*, 637.
4. Peigney, A., Laurent, C., Flahaut, E., Bacsa, R. R., & Rousset, A. (2001). Specific surface area of carbon nanotubes and bundles of carbon nanotubes. *Carbon, 39*(4), 507–514.
5. Tenne, R., Margulis, L., Genut, M., & Hodes, G. (1992). Polyhedral and cylindrical structures of tungsten disulphide. *Nature, 360*(6403), 444–446.
6. Kaplan-Ashiri, I., Cohen, S. R., Gartsman, K., Ivanovskaya, V., Heine, T., Seifert, G., Wiesel, I., Wagner, H. D., & Tenne, R. (2006). On the mechanical behavior of WS2 nanotubes under axial tension and compression. *Proceedings of the National Academy of Sciences of the United States of America, 103*(3), 523–528.
7. Tang, D.-M., Wei, X., Wang, M.-S., Kawamoto, N., Bando, Y., Zhi, C., Mitome, M., Zak, A., Tenne, R., & Golberg, D. (2013). Revealing the anomalous tensile properties of WS2 nanotubes by in situ transmission electron microscopy. *Nano Letters, 13*(3), 1034–1040.
8. Shtein, M., Nadiv, R., Lachman, N., Daniel Wagner, H., & Regev, O. (2013). Fracture behavior of nanotube–polymer composites: Insights on surface roughness and failure mechanism. *Composites Science and Technology, 87*, 157–163.
9. Shtein, M., Pri-bar, I., & Regev, O. (2013). A simple solution for the determination of pristine carbon nanotube concentration. *Analyst, 138*(5), 1490–1496.
10. Konsta-Gdoutos, M. S., Metaxa, Z. S., & Shah, S. P. (2010). Multi-scale mechanical and fracture characteristics and early-age strain capacity of high performance carbon nanotube/cement nanocomposites. *Cement and Concrete Composites, 32*(2), 110–115.
11. Makar, J. M., Margeson, J., & Luh, J. (2005). *Carbon nanotube/cement composite – Early results and potential applications*. 3rd International conference on Construction Materials: Performance, Innovation and Structural Implications, pp. 1–10.
12. Hull, D., & Clyne, T. (1996). *An introduction to composite materials*. Cambridge: Cambridge University Press.

Surface Properties of Carbon Nanotubes and Their Role in Interactions with Silica

Anastasia Sobolkina, Viktor Mechtcherine, Cornelia Bellmann, Benjamin Schur, and Albrecht Leonhardt

Abstract Different approaches, including determination of the surface tension via capillary penetration measurements and characterization of the surface chemical composition by means of X-ray photoelectron spectroscopy (XPS), were applied to reveal the surface properties of various CNT types produced from acetonitrile (CH_3CN), cyclohexane (C_6H_{12}) and methane (CH_4). Significant differences were found in the polarity of the CNT surfaces depending on the used precursors. The surface tension of the CNTs increases by utilization of carbon sources in the following order: cyclohexane, methane, acetonitrile. Using XPS analysis a comparatively high contents of nitrogen and oxygen atoms were detected on the surface of the CH_3CN-CNTs. Based on the results of the mass spectrometry, the strong hydrophobic character observed for the C_6H_{12}-CNTs is assumed to originate from polycyclic aromatic hydrocarbons deposited on the nanotubes' surface during synthesis. The investigation of the deposition of silica on the CNTs by a sol-gel method showed that the polar surface of the CH_3CN-CNTs provided the most favorable condition for the heterogeneous precipitation of silica. In contrast, no precipitation of silica was observed on the hydrophobic C_6H_{12}-CNTs.

Keywords Carbon nanotubes • Surface tension • Surface chemistry • Silica • Adsorption

A. Sobolkina (✉) • V. Mechtcherine
Institute of Construction Materials, Technische Universität Dresden,
D-01062 Dresden, Germany
e-mail: Anastasia.Sobolkina@tu-dresden.de; mechtcherine@tu-dresden.de

C. Bellmann • B. Schur
Leibniz Institute of Polymer Research Dresden, D-01069 Dresden, Germany
e-mail: bellmann@ipfdd.de; schur@ipfdd.de

A. Leonhardt
Leibniz Institute for Solid State and Material Research, D-01069 Dresden, Germany
e-mail: A.Leonhardt@ifw-dresden.de

K. Sobolev, S.P. Shah (eds.), *Nanotechnology in Construction*,
DOI 10.1007/978-3-319-17088-6_30

1 Introduction

In order to understand phenomena occurring at the CNT/matrix interface, it is required to look into physicochemical properties of the nanotube surface. This study aims to investigate the surface properties of various CNTs with respect to precursors and methods used for their synthesis. Another focus is on the exploring the interaction mechanism between the CNTs and silica being precipitated from an aqueous solution containing tetraethyl orthosilicate as silica source.

2 Material and Methods

Three types of CNTs varied with respect to the precursors, synthesis methods, and tube dimensions were used for this study; see Table 1.

The surface tension of the CNTs was indirectly determined by means of the capillary penetration method described in the previous studies [1, 2]. Particularly, a CNT powder packed homogeneously in a glass tube was brought into contact with ethanol-water mixtures with different surface tensions γ_{lv}. The penetration velocity was determined by measuring the weight change as function of time. According to Grundke et al. [1], the wetting tension $\gamma_{lv}\cos\theta$ can be calculated as follows:

$$\gamma_{lv}\cos\theta = \left(\frac{2}{A^2 r}\right)\left(\frac{\eta}{\rho^2}\right)\left(\frac{M^2}{t}\right), \tag{1}$$

where $(2/A^2r)$ represents the geometry of the capillary, (η/ρ^2) reflects the properties of the liquid and (M^2/t) is obtained from the experimental data. Since the geometry of the capillary system in the case of a powder packing is unknown, the term $(2/A^2r)$ can be replaced in Eq. (1) by an unknown factor $1/K$:

$$K\gamma_{lv}\cos\theta = \left(\frac{\eta}{\rho^2}\right)\left(\frac{M^2}{t}\right). \tag{2}$$

The term (M^2/t) in Eq. (1) can be determined experimentally as the slope of the linear part of the plot of M^2 versus t. As shown by Grundke et al. [1], the plot of $K\gamma_{lv}\cos\theta$ versus the surface tension γ_{lv} of the test liquids reaches a maximum, when the solid

Table 1 Selected properties of the carbon nanotubes under investigation

Labeling	CH_3CN-CNTs	CH_4-CNTs	C_6H_{12}-CNTs
Synthesis method	Aerosol-assisted CVD	Fixed-bed CVD	Aerosol-assisted CVD
Precursor	Acetonitrile	Methane	Cyclohexane
Type of CNTs	Multi-walled	Few-walled	Multi-walled
Diameter d, nm	70 ± 20	1…15	90 ± 20
Length l, µm	100…300	Approx. 10	200…400
Specific surface area, m^2/g	77	354	29

and liquid surface tensions are equal. Thus, the surface tension of a powder can be determined by finding the maximum $K\gamma_{lv}\cos\theta$ value in the $K\gamma_{lv}\cos\theta$ vs. γ_{lv} plot.

The surface chemistry of the CNTs was characterised by X-ray photoelectron spectroscopy (XPS). Photoelectrons in XPS measurements were excited with Mg Kα (1,253.6 eV) radiation and analyzed with constant pass energy of 15 eV.

The deposition of silica on the as-grown CNTs was performed as follows: CNTs were first dispersed in distilled water in a concentration of 0.5 wt% without using any surfactant. As a silica precursor, tetraethyl orthosilicate (TEOS, >98 %) from Merck was utilized. Ethanol (98 %) was used as a co-solvent. The hydrolysis and condensation of TEOS occurred without addition of a catalyst under neutral pH conditions. The aqueous dispersion of CNTs, ethanol, and TEOS utilized in a weight ratio of 20:6:1, respectively, was mixed in a vessel mounted onto the reflux cooler and subsequently heated to 70 °C with continuous stirring for 30 min in order to accelerate the sol-gel reaction. Thereafter, the reaction proceeded at room temperature for 10 h. To remove the residual colloidal solution, the CNTs were filtered by washing with a water-ethanol mixture and subsequently dried at 110 °C.

3 Results and Discussion

Figure 1 represents the experimental results of the capillary penetration measurements performed for the CH_3CN-CNTs, CH_4-CNTs and C_6H_{12}-CNTs using ethanol-water mixtures with different ratios as test liquids. As can be seen, the curves obtained for the C_6H_{12}-CNTs and CH_4-CNTs show the maximum $K\gamma_{lv}\cos\theta$ value at a liquid surface tension γ_{lv} of approximately 31 and 55 mJ/m^2 and the surface tensions γ_{sv} of the CNTs correspond to the respective surface tensions of the ethanol-water mixtures in the maximum of the curve. In the case of the CH_3CN-CNTs, the

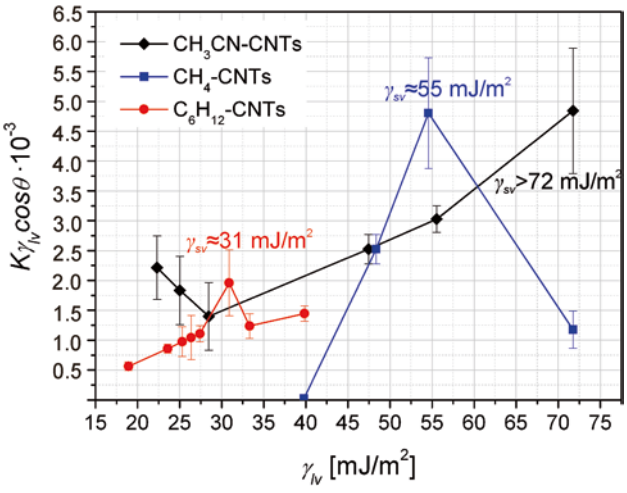

Fig. 1 Results of capillary penetration measurements for different CNT types

Table 2 Atomic concentration of elements detected on the surfaces of the CNTs

	Total element content, at.%				
Sample	C 1s	O 1s	N 1s	C/N	C/O
CH_3CN-CNTs	95.9	1.6	2.4	39.9	59.9
CH_4-CNTs	98.6	1.0	0.4	246.5	98.6
C_6H_{12}-CNTs	98.6	1.4	–	–	70.4

maximum has not yet been achieved in the measuring range (water with approximately 72 mJ/m^2 is the liquid with the highest surface tension). This implies that the surface tension γ_{sv} value of CH_3CN-CNTs must be higher than the surface tension of water. Hence, the CH_3CN-CNTs exhibited the greatest surface hydrophilicity compared to CH_4-CNTs and C_6H_{12}-CNTs.

In order to explain such large differences in the hydrophilic-hydrophobic surface properties observed, the CNTs were subjected to XPS analysis for characterization of the chemical composition of their surfaces. Table 2 shows the atomic concentrations of elements detected on the CNT surfaces. As can be seen, along with expected carbon atoms, the XPS detected the presence of heteroatoms, such as nitrogen and/or oxygen, on the CNT surfaces. This indicates that the CNTs are modified with different surface functionalities acting as active centres on their surfaces [3]. The highest concentration of the heteroatoms was detected on the CH_3CN-CNT surface, which clarifies its high polarity observed in the capillary penetration experiments.

It is assumed that the strong hydrophobic character of the C_6H_{12}-CNTs originates from a deposition of carbon species formed during cyclohexane pyrolysis on the surface of the nanotubes. In order to identify the molecular species adsorbed on the CNT surfaces, the mass spectrometry experiments were carried out. Figure 2 shows the positive-ion mass spectra obtained for the C_6H_{12}-CNTs, CH_4-CNTs and CH_3CN-CNTs by their heating up to 360 °C within 5 min. As can be seen, the spectra of all CNT types contain low-mass hydrocarbon ions of series $[C_nH_{2n\pm1}]^+$ (m/z 57, 69, 83, 97, 111, 125) and $[C_nH_{2n-3}]^+$ (m/z 137, 151, 165, 179, 193) originated from the alkyl, cycloalkyl moieties and dienes, alkynes or cycloalkenes, respectively [4]. Among the ions of aliphatic hydrocarbons, family peaks at m/z 178, 202, 228, and 252 attributed to polycyclic aromatic hydrocarbons (PACs) with different molecular formulas, such as $C_{14}H_{10}$, $C_{16}H_{10}$, $C_{18}H_{12}$, $C_{20}H_{12}$, were found in the spectrum of the C_6H_{12}-CNTs. It is common knowledge that PACs are nonpolar and hydrophobic in nature. It is presumed that the adsorption of such PACs as non-volatile substances on the tube walls is responsible for the low surface tension determined for the C_6H_{12}-CNTs.

In the next stage, the deposition of silica on the CNTs using the sol-gel method was investigated. As can be seen from the TEM images, the precipitation of silica was most successful on the hydrophilic surface of the CH_3CN-CNTs, see Fig. 3. This was obviously caused due to non-covalent interactions taking place between surface functionalities of the CH_3CN-CNTs and the silanol groups of the silica species presented in the aqueous solution. In contrast, no direct precipitation of silica was observed on the hydrophobic surface of the C_6H_{12}-CNTs. In case of the CH_4-CNTs with a comparatively very small diameter, their strong entanglement – even if they were pre-dispersed – prevented a uniform deposition of silica on the nanotubes.

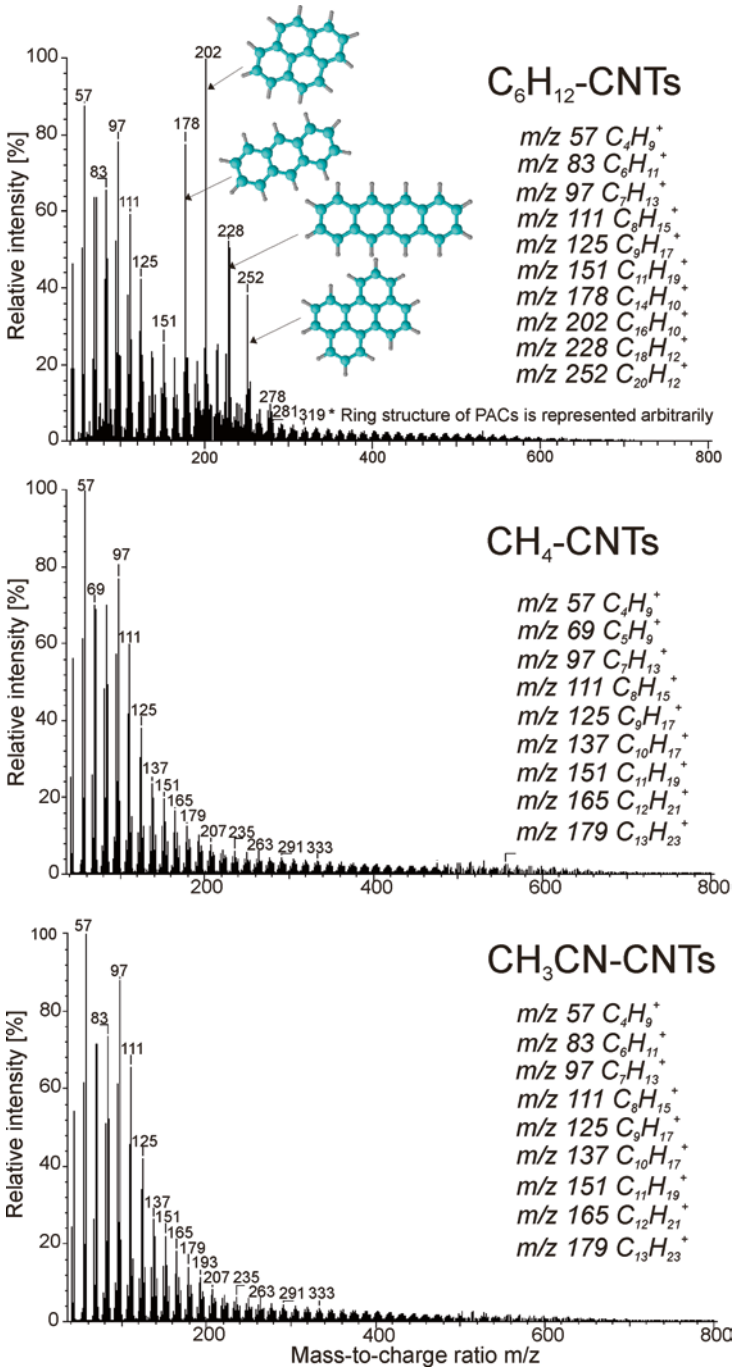

Fig. 2 Positive-ion mass spectra recorded over a range m/z 40–800 for the CNTs on a Finnigan MAT 95 mass spectrometer using electron impact ionization at 70 eV

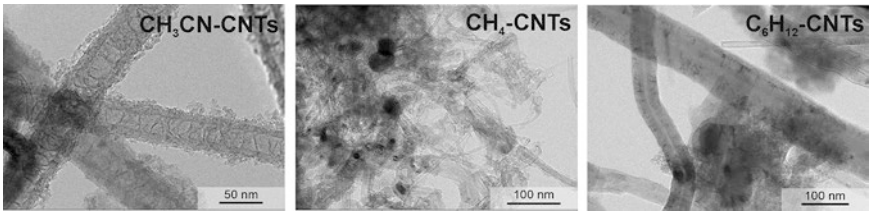

Fig. 3 TEM images of the CNTs after sol-gel dip coating with silica

4 Conclusions

In summary, it can be concluded that the surface properties of CNTs can be significantly affected by the precursors as well as by the chosen synthesis methods. The abundance of the heteroatoms (i.e. nitrogen, oxygen) on the CNT surface, such in the case of the CH_3CN-CNTs, leads to an increase in the surface tension and thus enhanced hydrophilicity of the nanotubes' surface. Using cyclohexane as carbon source, CNTs with a very low surface tension of approximately 31 mJ/m^2 have been produced. This was evidently caused by the deposition from the gaseous phase some pyrolytic products of cyclohexane, such as PACs, from the gaseous phase on the growing CNTs. Another important finding is that increasing surface tension of the CNTs supplies favourable conditions for the precipitation of silica on them.

References

1. Grundke, K., Bogumil, T., Gietzelt, T., et al. (1996). Wetting measurements on smooth, rough and porous solid surfaces. *Progress in Colloid and Polymer Science, 101*, 58–68.
2. Bellmann, C., Caspari, A., & Grundke, K. (2009). Controlling of surface parameters of particles used for electrocodeposition. *Key Engineering Materials, 412*, 273–278.
3. Sobolkina, A., Mechtcherine, V., Bellmann, C., et al. (2014). Surface properties of CNTs and their interaction with silica. *Journal of Colloid and Interface Science, 413*, 43–53.
4. McLafferty, F. W., & Tureček, F. (1999). *Interpretation of mass spectra* (4th ed.). Sausalito: University Science.

The Effect of Functionalized Carbon Nanotubes on Phase Composition and Strength of Composites

Sergey Petrunin, Viktor Vaganov, and Konstantin Sobolev

Abstract This paper reports on the influence of carbon nanotubes (CNTs) surface functionalization on structure and composition of cementitious phase. Phase composition was determined by X-Ray analysis according to the Rietveld method. It was found that the presence of oxygen-containing functional groups on CNTs surface' leads to intensification of the hydration process and an increase in concentration of C-S-H gel from 65.9 to 74.4 %. Based on the experimental results the hypothesis of formation of cement composite structure for different CNTs' surface functionalizations is described.

Keywords Cement composite • Carbon nanotubes (CNTs) • Functionalization • X-Ray • Structure • Strength

1 Introduction

Recently, scientists have paid special attention to investigation of the allotropic forms of carbon such as carbon nanotubes (CNTs). CNTs have extended cylindrical hollow structure formed by carbon sheets curtailed into a solid drown tube of graphene [1]. Considerable interest in CNTs is caused by unique electronic, thermal, electric, optical, chemical and mechanical properties of this material [2, 3]. The field of CNTs application is rather wide and includes two main focus areas: in the form of the elements of individual system and as reinforcing fibers in composite materials with various matrixes [4].

S. Petrunin (✉)
Department of Construction Production, Vladimir State University, Vladimir, Russia
e-mail: ser-petru@yandex.ru

V. Vaganov
Department of Applied Mathematics and Physics, Vladimir State University, Vladimir, Russia

K. Sobolev
Department of Civil Engineering and Mechanics, University of Wisconsin-Milwaukee, Milwaukee, WI, USA

K. Sobolev, S.P. Shah (eds.), *Nanotechnology in Construction*,
DOI 10.1007/978-3-319-17088-6_31

There are many publications related to CNTs' application in cement systems [5–7]. The properties of nanomodified concrete depend on the CNTs aspect ratio and surface functionalization. Having studied the influence of the CNTs' aspect ratio on concrete properties, authors established that by introducing twice as few long-length nanotubes as short ones, an almost identical increase of cement composite mechanical properties was observed [8]. In this case, CNTs act as reinforcing elements of the structure leading to the reduction of internal defects and an increase in crack resistance of the material. The improvement of concrete strength is explained by the formation of spatial grids of CNTs, which leads to pockets filling and C-S-H crystals binding [9]. In this way longer CNTs can unite the crystals located at a greater distance from each other. On the other hand, increasing the length increases the CNTs' tendency to entangling and formation of agglomerates. In some cases, this process worsens the uniformity of distribution and complicates the process of CNTs' introduction in a volume of composite. As mentioned above, the properties of nano-modified concrete depend not only on the aspect ratio, but also on the CNTs surface functionalization. According to Li et al., modification of cement system with functionalized CNTs contributes to a substantial increase in concrete strength compared with pure CNTs [10]. Microstructural investigation demonstrated the existence of functionalized CNTs covered with hydration products, whereas hydration products on the surface of pure CNTs are absent. Functionalized CNTs can interact with hydration products of cement, leading to a decrease in porosity and, as a result, to an increase in composite strength.

In most cases, researchers explain the improvement of composite strength by the CNTs' reinforcing effect without consideration of the CNTs' influence on the phase transformations in hardening cement paste. Thus, CNTs are considered as binding elements uniting the separate hydrate grains playing a bridging role and promoting stress distribution through microcracks. On this basis, the purpose of the given research is to study the structure and phase composition of concrete with pure and functionalized CNTs.

2 Experimental Program

2.1 Materials

Portland cement CEM I 42.5B supplied by JSC "Mordovcement," standard quartz sand with a fineness modulus of 1.5 and multi-walled carbon nanotubes produced by CVD technology at Vladimir State University (Russia) were used in this research. The CNTs' concentration in the composite was 0.05 % of the cement mass. Polycarboxylate (PCE) superplasticizer P-11 supplied by JSC "Macromer" was used to reduce the sedimentation and facilitate the dispersion of CNTs in water.

2.2 Preparation of Concrete Samples

All cement composites had the component ratio of 0.3:1:1 for water, cement, and sand, respectively. The CNTs were mixed with water and the polycarboxylate superplasticizer and sonicated at 20 kHz using the ultrasound processor (IL100-6/1-1) at maximal power (700 W) for 60 min. Cement and sand were added into a planetary mixer. Then the required amount of water with superplasticizer and carbon nanotubes was added into the mixer. The entire mixture was stirred for 7 min. After this procedure, the composite mixture was placed into the metal molds with dimensions of 40 × 40 × 160 mm and compacted by vibration. The composite specimens were demolded after 24 h of initial hardening and were stored in lime water until the testing age.

2.3 CNTs' Functionalization

CNTs' functionalization by oxygen groups was carried out to improve the hydrophilic properties and the interaction between the surface of CNTs and the material matrix. The functionalization was carried out as follows: CNTs were placed in a flask and backed up with the mix of concentrated HNO_3 and H_2SO_4 at a ratio of one-to-five. The mix was heated to 70 °C at continuous hashing for 3 h. During this process, the nickel catalyst particles left from the synthesis were oxidized with gas liberation. The solution was then cooled, diluted with distilled water and filtered. The filtered CNTs were washed out and dried. The assessment of functionalized groups occurring on the CNTs' surface was made with the help of infrared spectroscopy.

The initial MWCNTs were in the form of filaments with a diameter 30–60 nm and a length from 100 nm to several microns. Figure 1 shows the SEM and TEM images of carbon nanotubes after synthesis and functionalization.

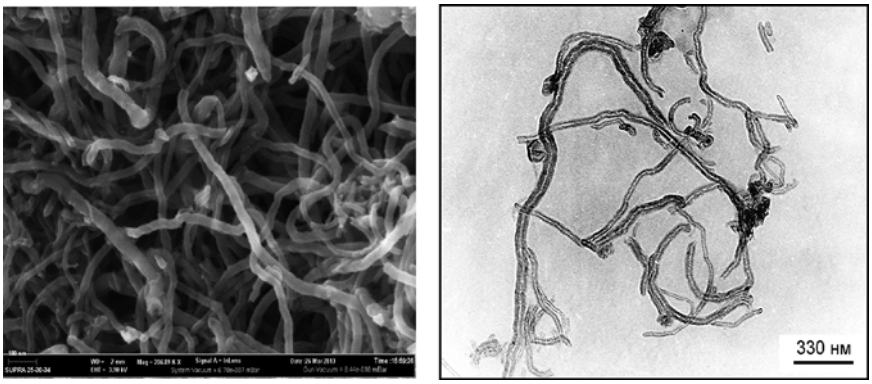

Fig. 1 The SEM image (*left*) and TEM (*right*) of functionalized CNTs

Coagulation resistance of CNT dispersions depends on the character of charge distribution on nanotubes surface formed by the absorption of ions from the solution and the dissociation of the CNTs surface. Inoculating of oxygen-containing groups promotes the redistribution of surface charges and improves the hydrophilic properties of CNTs. Thus, the functionalization leads to improved distribution of CNTs

2.4 Research Methods

Mortar specimens were tested for compressive and tensile strength at the age of 1-, 7- and 28-days. The phase composition was defined on the Brucker D8 Advance diffractometer using the Rietveld method.

3 Results and Discussion

3.1 Mechanical Properties

The mean values of compressive and tensile strength of reference and modified cement composites are listed in Table 1. For each test, five specimens were tested. The deviation of the measured values from their means were not more than 5 %, indicating that the obtained results are statistically significant. The reference composites contained the same dosage of PCE superplasticizer as CNT composites. The 1-day and 7-day compressive strength of composites with functionalized CNTs was higher than the strength of concrete with pure CNTs. Nevertheless, at the age of 28 days, the composite with non-modified CNTs possessed the greatest strength. In tensile strength tests, composite with non-functionalized CNTs had the best results irrespective of curing time (Table 1).

The presence of functional groups accelerates the process of cement hydration and strength development. The greatest increase in the tensile strength of concrete with the addition of raw CNTs is explained by the fact that functionalized CNTs have a large number of structural defects. Therefore, a greater reinforcement effect resulting from the modification of the concrete matrix is observed under the addition of less defective reference CNTs.

Table 1 Strengths of different mixes

	Compressive strength (MPa) at the age of			Tensile strength (MPa) at the age of	
Mix	1 day	7 days	28 days	7 days	28 days
Reference	22.0±4.1 %	47.0±3.6 %	51.0±4.3 %	5.6±3.1 %	7.0±2.9 %
CNTs	27.0±4.4 %	50.0±4.1 %	62.0±4.1 %	7.0±2.9 %	7.7±3.1 %
Functionalized CNTs	28.5±4.7 %	52.0±3.9 %	57.0±4.7 %	6.1±2.7 %	7.5±3.1 %

Table 2 Phase composition

Minerals	Reference (%)	CNTs (%)	Functionalized CNTs (%)
C_3S	8.9	8.1	6.5
C_2S	4.4	4.1	3.7
C_4AF	3.2	2.8	2.6
$Ca(OH)_2$	9.2	7.3	7.7
$CaCO_3$	6.7	5.6	4.9
Ettringite	0.3	0.3	0.2
C-S-H	65.9	71.9	74.4

3.2 X-ray Analysis of Hydrates

The changes of C-S-H due to the introduction of CNTs are identified. The resulting changes in phase composition of composites are demonstrated in Table 2. The increase in the amorphous phase corresponds to the increase of cement hydration, promoting the acceleration of hydration and an increase in the strength of a material.

The amorphous phase in a reference specimen is 65.9 %. The increase of the amorphous phase to 74.4 % was recorded for the composite with functionalized CNTs. The character of the amorphous phase development corresponds to a tendency of compressive change at the age of 1 day. The results show that composite with functionalized CNTs contained the greatest volume of C-S-H gel and possesses higher strength, whereas composites modified by pure CNTs have lower C-S-H gel concentration and weaker strength characteristics.

3.3 Hypothesis Related to Composite Structure Formation

In the process of cement hydration, the OH^-, Ca^{2+}, $CaOH^-$ and $H_2SiO_4^{2-}$ ions are deposited on the surface of the cement grains and form a layer consisting of C-S-H gel with embedded $Ca(OH)_2$ crystals (Fig. 2a). With time, the thickness of this layer increases and its ionic permeability decreases. The formation of C-S-H gel and $Ca(OH)_2$ takes place when Ca^{2+} concentration exceeds the saturation limit by factor of 1.5–2.

The intensification of hydration in the system with CNTs is due to an additional sorption of Ca^{2+} ions on the surface of the CNTs. In this case, the hydration is accelerated, since the formation of C-S-H and $Ca(OH)_2$ crystals occurs in the zones supersaturated by Ca^{2+} ions. The fragmentary formation of hydration products on the CNTs surfaces contributes to the improvement of ion exchange between the solid and liquid phases and results in an acceleration of new phase formation (Fig. 2b). The presence of oxygen-containing groups on the surfaces of the CNTs leads to a more active sorption of Ca^{2+} ions and higher rates of hardening when functionalized CNTs are used (Fig. 2c). According to this hypothesis, the CNTs act

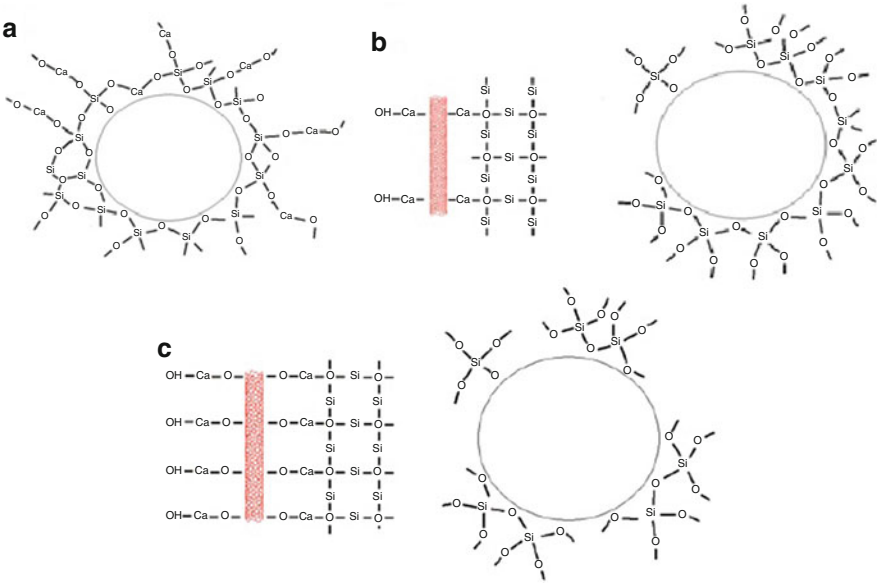

Fig. 2 The hydration process: (**a**) without CNTs, (**b**) with pure CNTs, (**c**) with functionalized CNTs

as the centers of crystallization for hydration products contributing to the acceleration of hydration, increase of the concentration of C-S-H gel and strength improvement of CNTs based composites.

4 Conclusions

The introduction of CNTs affects the composition of hydrated cementitious composites due to creation of additional crystallization centers accelerating the hydration processes. It is established that the formation of oxygen-containing functional groups on the surface of CNTs leads to an increase in early strength compared with the composite containing pure CNTs. However, at the age of 28 days, composite with non-modified CNTs had the best strength characteristics.

References

1. Ivanovskaya, V. V., & Ivanovskiy, I. L. (2011). Atom-modified nanotubes. *Russian Chemical Reviews, 80*, 761–783.
2. Salvetat, J. P., Bonard, J. M., Thomson, N. H., Kulik, A. J., Forro, L., & Benoit, W. (1999). Mechanical properties of carbon nanotubes. *Applied Physics, 65*, 255–260.
3. Rakov, E. G. (2006). *Nanotubes and fullerenes*. Moscow: Logos.

4. Rakov, E. G. (2001). Chemistry and application of carbon nanotubes. *Russian Chemical Reviews, 70*, 934–937.
5. Sobolev, K., & Ferrada-Gutiérrez, M. (2005). How nanotechnology can change the concrete world: Part 1. *American Ceramic Society Bulletin, 10*, 14–17.
6. Sanchez, F., & Sobolev, K. (2010). Nanotechnology in concrete – A review. *Construction and Building Materials, 24*, 2060–2071.
7. Makar, J., Margeson, J., & Luh, J. (2005, August 22–24). *Carbon nanotube/cement composites – Early results and potential applications*. Proceedings of the 3rd international conference on Construction Materials: Performance, Innovations and Structural Implications, Vancouver.
8. Konsta-Gdoutos, M. S., Metaxa, Z. S., & Shah, S. P. (2010). Muli-scale mechanical and fracture characteristics and early-age strain capacity of high performance carbon nanotube/cement nanocomposites. *Cement and Concrete Composites, 32*, 110–115.
9. Sobolkina, A., Mechtcherine, V., Khavrus, V., Maier, D., Mende, M., Ritschel, M., & Leonhardt, A. (2012). Dispersion of carbon nanotubes and its influence on the mechanical properties of the cement matrix. *Cement and Concrete Composites, 34*, 1104–1113.
10. Li, G. Y., Wang, P. M., & Zhao, X. (2005). Mechanical behavior and microstructure of cement composites incorporating surface-treated multi-walled carbon nanotubes. *Carbon, 43*, 1239–1245.

Surface Modified Carbon Nanotubes for an Enhanced Interaction with Cement Based Binders

Volker Butters, Torsten Kowald, Majid Mahjoori, and Reinhard Trettin

Abstract Carbon nanotubes are often used to enhance mechanical performance or to change electrical or heat conductivity properties of concrete. In many cases the benefits arising from a modification of concretes by carbon nanotubes are limited due to an insufficient linkage of the nanoparticles to the matrix. Additionally, the hydrophobic nature of the material hinders an efficient incorporation and thus homogeneous distribution in the cementitious matrix. To improve interaction of carbon nanotubes with cement-based binders the nanoparticles were coated with highly reactive SiO_2. The modification was done by an adapted sol-gel process to achieve a coating thickness of 10–20 nm. The nanotubes were characterized in terms of morphology, SiO_2 content and specific surface area. As a first step the interaction of the modified nanoparticles with a hydrating tricalcium silicate was investigated and showed high pozzolanic reactivity, strong acceleration of hydration as well as changes of the calcium silicate hydrate morphology.

Keywords Carbon nanotubes • Silica coating • Pozzolanic reactivity • Tricalcium silicate

1 Introduction

Carbon nanotubes (CNTs) were applied to cementitious materials due to the outstanding properties like very good tensile strength, electrical and heat conductivity. Main targets were for example to improve mechanical properties, microstructure, electrical and heat conductivity. The enhancements could be used to design construction materials with thinner cross sections, higher durability or even monitoring capabilities [1–5]. A challenging property of as-received CNTs is the hydrophobicity which impedes a good linkage to hydration products of the concrete matrix. To overcome this problem CNTs are often chemically surface modified e.g. by oxidation [4, 5]. During treatment by nitric or sulfuric acid structural defects, hydroxyl and carboxyl groups are formed. Therefore CNTs become more hydrophilic which

V. Butters • T. Kowald (✉) • M. Mahjoori • R. Trettin
Institut für Bau-und Werkstoffchemie, Universität Siegen, Siegen, Germany
e-mail: kowald@chemie.uni-siegen.de

K. Sobolev, S.P. Shah (eds.), *Nanotechnology in Construction*,
DOI 10.1007/978-3-319-17088-6_32

provides an improved dispersibility in water and bonding to hydration products. Further the functionalization improves interaction of CNTs and hydration products. In former studies influences on calcium hydroxide (CH) and calcium silicate hydrates (C-S-H) were found [2, 3]. The results point to a heterogeneous nucleation of CH and C-S-H on the CNTs. For further improvement of dispersibility and interaction with C-S-H a coating of CNTs by SiO_2 via a sol-gel process [6] seems promising. Improved dispersion quality and better workability was found by Stynoski et al. when SiO_2 coated CNTs were used [7]. By adjusting the coating process such that a SiO_2 with high reactivity is achieved, a pozzolanic reaction similar to other nanostructured SiO_2 [8] could improve bonding to C-S-H.

Within this study SiO_2 modified CNTs (SiO_2CNTs) were tested for stability of the coating during dispersion process, pozzolanic reactivity, influence on the hydration of tricalcium silicate (C_3S) and influence on the morphology of C-S-H.

2 Results and Discussion

2.1 Coating and Characterization of CNTs

The coating process was done by a sol-gel method using tetraethyl orthosilicate (TEOS) [6]. Homogeneity and thickness of the coating were investigated by scanning electron microscopy (SEM) and transmission electron microscopy (TEM). The CNTs were homogeneously pearl necklace like covered by SiO_2 and showed a better separation of the tubes compared to the as-received material (Fig. 1).

The investigation by TEM underlines the good connection of the coating to the CNTs. From the ChemiSTEM analysis and the distribution of silicon a homogeneous coating with a thickness of 10–20 nm around the CNT was proven (Fig. 2).

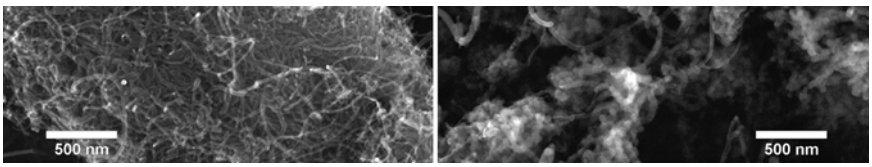

Fig. 1 Oxidized multi-walled CNTs (length <10 µm, diameter ~20–30 nm, specific surface area = 220 m^2/g) before (*left*) and after coating with SiO_2 (*right*), SEM

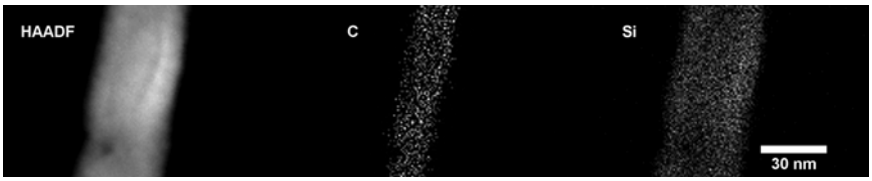

Fig. 2 Investigation of the coating of the SiO_2CNTs, high angle annular dark field image (*left*), carbon distribution (*middle*) and silicon distribution (*right*)

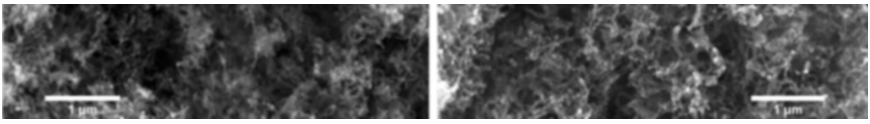

Fig. 3 Dried sample of SiO_2CNT after 45 min ultrasonic treatment, in demineralized water saturated with SiO_2 (*left*), in pure demineralized water (*right*), SEM

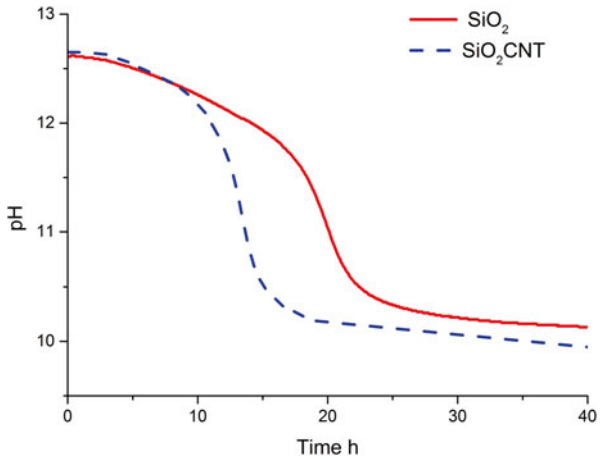

Fig. 4 Investigation of the pozzolanic reactivity of SiO_2CNTs in a saturated calcium hydroxide solution compared to a nanostructured silica with a similar SiO_2 concentration of 0.5 % w/w

The specific surface area as determined by nitrogen sorption using the BET method was 110 m^2/g. A carbon content of 15 % w/w was determined by oxidation of the CNTs in air and measuring the mass loss by thermogravimetric analysis.

SiO_2CNTs can be easily dispersed in water whereby for reaching a good dispersion quality the use of an additive is advisable. Even after 45 min ultrasonic treatment the coating was not destroyed in case of using demineralized water saturated with SiO_2 (Fig. 3, left). Tests showed a partly or even complete dissolution of the coating if pure demineralized water was used (Fig. 3, right).

2.2 Pozzolanic Reactivity

The pozzolanic reactivity of the coating was investigated by measuring pH values of a saturated $Ca(OH)_2$ solution containing SiO_2CNTs or a nanostructured SiO_2 with a similar specific surface area of 90 m^2/g. Concentrations of 0.5 % w/w SiO_2 (0.59 % w/w SiO_2CNT) were used for both measurements. Both materials showed a high pozzolanic reactivity that can be seen in the decreasing pH value. Compared to a nanostructured SiO_2 the coating of the SiO_2CNTs showed a faster reaction (Fig. 4).

2.3 Influence on the Hydration of C_3S

The influence of the SiO_2CNTs on the hydration of C_3S was analyzed by isothermal heat flow calorimetry (DCA). According to a CNT content of 0.0 % w/w of 0.1 % w/w and 1.0 % w/w, samples with concentrations of 0.0 % w/w, 0.67 % w/w and 6.67 % w/w SiO_2CNTs related to C_3S were prepared and investigated. For comparison a sample with 5.67 % w/w nanostructured SiO_2 was measured. Nanomaterials were dispersed within demineralized water which was saturated with SiO_2 for 15 min by ultrasonic treatment (sonotrode 2.5 mm, amplitude 0.9, cycle 0.5) using a Hielscher UP200S.

All measurements containing nanomaterials showed a shortening of the induction period compared to the pure C_3S sample. The acceleration period started after 4.9 h in case of the pure C_3S and after 4.6 h when 0.67 % w/w SiO_2CNT was used. For the two samples containing 5.67 % SiO_2 or 6.67 % w/w SiO_2CNT the acceleration period began after 2 h (Fig. 5, left). The cumulative heat after 20 h of hydration was higher for the nanomaterial containing samples. Again 5.67 % w/w SiO_2 and 6.67 % w/w SiO_2CNT showed similar results and the strongest effect (Fig. 5, right). The coating and the nanostructured SiO_2 showed similar reactivity with C_3S.

2.4 Influence on the Degree of Hydration of C_3S and on the Morphology of C-S-H

Hydration of C_3S samples containing 0.0, 0.67 and 6.67 % w/w SiO_2CNTs was stopped after 4 h or 8 h by vacuum drying. The samples were investigated for influences on hydration products by SEM. Based on results determined by quantitative X-ray powder diffraction (XRD) and thermogravimetry (TG) the degree of hydration of C_3S was calculated. Surface area and mesoporosity were measured by nitrogen adsorption using the BET and BJH method.

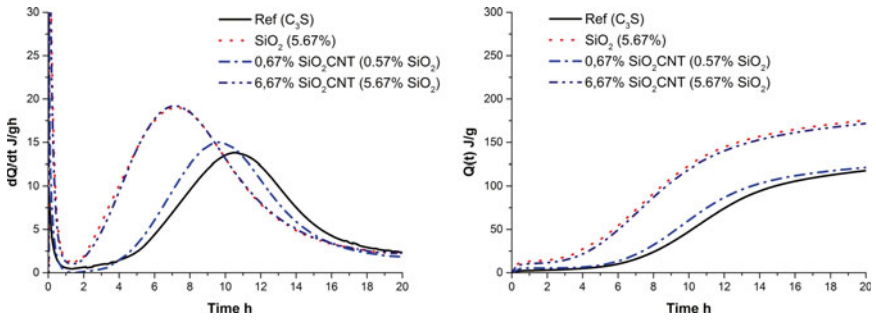

Fig. 5 Investigation of the influence of SiO_2CNTs on the hydration of C_3S by isothermal heat flow calorimetry

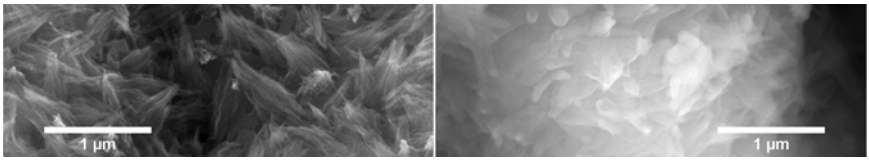

Fig. 6 C_3S without (*left*) and with SiO_2CNTs (*right*) at a hydration time of 8 h

Table 1 Influence of SiO_2CNTs on the specific surface area and pore volume after 8 h

SiO_2CNT content (% w/w)	Specific surface area (m^2/g)		Pore volume 4–200 nm (cm^3/g)	
	Measured	Normalized	Measured	Normalized
0.00	3.0	13.7	0.0230	0.1050
0.67	5.8	27.0	0.0360	0.1671
6.67	14.6	24.0	0.1320	0.2165

In contrast to the reference sample which was still liquid after 4 h the sample with 6.67 % w/w SiO_2CNTs was hardened. The SEM images of the pastes showed already after 4 h of hydration that all SiO_2CNTs were completely covered by reaction products. After 8 h a denser microstructure of C-S-H in case of the SiO_2CNT containing sample was found (Fig. 6).

The SEM images indicated an influence on the structure of the C-S-H phases and an acceleration of hydration. The acceleration was proven by advanced degrees of hydration of C_3S as determined by XRD and TG. The reference showed degrees of hydration of 2 % after 4 h and 22 % after 8 h and the sample with 6.67 % w/w SiO_2CNTs 8 and 61 %.

To approve the assumption that the sample with SiO_2CNTs shows a different morphology of C-S-H, surface area and porosity were analyzed. Due to the high specific surface area of C-S-H and the accelerated hydration samples with SiO_2CNTs should also show higher values for the specific surface areas of hydrated samples. To take into account the surface area of SiO_2CNT, the maximum contribution to the sample was calculated. Based on the value of 110 m^2/g the maximum contribution with 6.67 % w/w is 7.4 m^2/g. But specific surface areas are mainly governed by C-S-H because SiO_2CNTs showed a complete coverage with hydration products already after 4 h of hydration. To take the different degrees of hydration into account surface area was normalized to a theoretical value of 100 %. The normalized surface area was nearly two times the value for the pure C_3S in case of the two samples with SiO_2CNTs (Table 1). The results indicate that by the advanced hydration and/or the pozzolanic reaction of SiO_2CNTs the morphology of the hydration products is influenced. The higher specific surface areas correspond to the denser structure of the C-S-H phases which was observed during the SEM studies. Because the hydration products grow into bigger pores the amount of pores within the measurement range was increased. This leads to a higher pore volume for pores smaller than 200 nm.

3 Summary and Conclusions

In this work SiO_2 coated CNTs with a high pozzolanic reactivity were produced. Experiments showed that thickness of the coating is only preserved if SiO_2 saturated water during preparation of dispersions is used. Otherwise the coating is partly or even complete removed and the desired pozzolanic reaction during hydration and the preferred formation of C-S-H around the CNTs cannot be achieved.

SiO_2CNT showed a strong influence on the hydration of C_3S which can be explained by an early formation of C-S-H by pozzolanic reaction. The SiO_2CNTs act as seeds for nucleation which accelerates hydration with a shortened induction period of C_3S. It was shown that especially early hydration of C_3S was influenced by SiO_2CNTs and that denser C-S-H was formed. Finally, the results show that the coating can improve the incorporation of the CNTs.

Acknowledgments This research was performed in the frame of CarboBau, a subproject of Inno.CNT, which is an interdisciplinary innovation alliance, funded by the German Federal Ministry of Education and Research.

References

1. Campillo, I., Dolado, J. S., & Porro, A. (2004). High-performance nanostructured materials for construction. In P. J. M. Bartos, J. J. Hughes, P. Trtik, & W. Zhu (Eds.), *Proceedings of the first international symposium on Nanotechnology and Construction* (pp. 215–225). Cambridge: Royal Society of Chemistry.
2. Sáez de Ibarra, Y., Gaitero, J. J., Erkizia, E., & Campillo, I. (2006). Atomic force microscopy and nanoindentation of cement pastes with nanotube dispersions. *Physica Status Solidi (A)*. doi:10.1002/pssa.200566166
3. Han, B., Yu, X., & Kwon, E. (2009). A self-sensing carbon nanotube/cement composite for traffic monitoring. *Nanotechnology*. doi:10.1088/0957-4484/20/44/445501
4. Kowald, T., & Trettin, R. (2009). Improvement of cementitious binders by multi-walled carbon nanotubes. In Z. Bittnar (Ed.), *Proceedings of the 3rd international symposium on Nanotechnology in Construction*. Heidelberg: Springer. doi:10.1007/978-3-642-00980-8_34
5. Li, G. Y., Wang, P. M., & Zhao, X. (2005). Mechanical behavior and microstructure of cement composites incorporating surface-treated multi-walled carbon nanotubes. *Carbon*. doi:10.1016/j.carbon.2004.12.017
6. Li, H., Ha, C. S., & Kim, I. (2009). Fabrication of carbon nanotube/SiO2 and carbon nanotube/SiO2/Ag nanoparticles hybrids by using plasma treatment. *Nanoscale Research Letters*. doi:10.1007/s11671-009-9409-4
7. Stynoski, P., Mondal, P., & Marsh, C. (2012). Novel processes to improve CNT utility in cement. In M. S. Konsta-Gdoutos (Ed.), The proceedings of the NICOM4 were distributed on CD by Maria S. Konsta-Gdoutos and Stavros N. Shiaeles. Agios Nikolaos
8. Butters, V., Kowald, T., & Trettin, R. (2013). Coating of CNTs by SiO2 and their influence on hydrating tricalcium silicate. In D. Stephan, H. Daake, V. Märkl, & G. Land (Eds.), *1st International conference on the Chemistry of Construction Materials* (pp. 377–380). Frankfurt: GDCh. ISBN 978-3-936028-75-1.

Characterization of Cement-Based Materials Modified with Graphene-Oxide

Ye Qian, Maika Yzabelle Abdallah, and Shiho Kawashima

Abstract For applications in cement and concrete, studies on carbon-based nanomaterials have been almost exclusively on carbon nanotubes, even constituting a large portion of studies on nanomaterials of any type. Although a promising approach, economic and dispersion issues continue to limit industry acceptance. Graphene oxide (GO), derived cost-effectively from graphite, shows good dispersion in water. In this paper, preliminary results showing the beneficial effects of graphene oxide on the hardening and mechanical properties of cement-based materials are presented.

Keywords Graphene-oxide • Nanomaterials • Cement

1 Introduction

The potential of the use of carbon nanotubes/nanofibers (CNTs/CNFs) to enhance the mechanical properties of cement-based materials has been demonstrated in a number of studies [1–4]. However, as is the case when incorporating any additive or fiber in a cement matrix, achieving effective dispersion is a challenge [5]. And the difficulty increases with decrease in size, where specific surface area increases exponentially as dimensions fall below 100 nm. The use of graphene oxide in cement-based materials has not been widely explored [6–8]. Graphene, the 2D counterpart to CNT, and its oxidized form graphene oxide, has superior elastic modulus and tensile strength. Compared with graphene and CNT, graphene oxide (GO) is readily dispersible in water, requiring only moderate sonication [9–11]. Due to its high specific surface area and 2D feature, it exhibits a very low percolation threshold, which can significantly limit the addition level required.

In this paper, the preliminary results of a study on graphene oxide-reinforced cement paste and mortar are presented. The influence of very small amounts (less than 0.05 % by mass of cement) of GO on rate of hydration heat of cement paste and flexural strength and modulus of mortar are presented.

Y. Qian (✉) • M.Y. Abdallah • S. Kawashima
Department of Civil Engineering and Engineering Mechanics, Columbia University, New York, NY, USA
e-mail: yq2157@columbia.edu; mya2109@columbia.edu; sk2294@columbia.edu
http://www.columbia.edu/~sk2294

K. Sobolev, S.P. Shah (eds.), *Nanotechnology in Construction*,
DOI 10.1007/978-3-319-17088-6_33

2 Experimental Methods and Procedures

2.1 Materials

Graphene oxide is in aqueous suspension form in deionized water with a concentration of 2 mg/mL. No superplasticizer is added. The stability of the suspension is evaluated through absorbance spectra. Suspensions are diluted with deionized water by a factor of 5 by volume, then centrifuged at 5,000 rpm for 5 min. The absorbance spectra (190–1,100 nm) of the supernatant of samples before and after centrifugation are measured with a spectrophotometer. The absorbance values at 550 nm are 0.98 and 0.96 before and after centrifugation, respectively. This indicates 98.3 % is retained in suspension, therefore highly stable.

Type I Portland cement and deionized water are used in all mixtures. And oven-dried sand passing through sieve #16 (diameter smaller than 1.19 mm) is used in all mortar mixtures. All mixtures have a water-to-cement ratio (W/C) of 0.43 by mass. Mortar has a sand-to-cement ratio (S/C) of 2:1 by mass.

Graphene oxide is added at levels of 0, 0.01, 0.03 and 0.05 % by mass of cement in paste and mortar mixtures. Cement paste samples are denoted as CP, GO.01, GO.03 and GO.05, respectively. Mortar samples are denoted as M, MG1, MG3 and MG5, respectively. The water in the GO suspension and sand absorption are considered when proportioning to achieve the desired W/C.

2.2 Methods

The rate of heat of hydration of cement pastes is measured using a TAM Air isothermal calorimeter. The temperature is set at 25 °C and the heat of hydration is recorded up to 80 h. Cement paste samples are prepared by hand-stirring for 4 min.

Mortar samples are tested for flexural strength. After 10 min mixing of cement, water, sand and GO suspension, the mortar is cast in 25.4 × 25.4 × 304.8 mm prism molds in two layers, consolidating on a vibration table in between. They are demolded after 1 day and cured in water at room temperature for 7 and 28 days. Prisms are cut into 25.4 × 25.4 × 76.2 mm samples. Four point bending test are performed on an Instron 5984 Universal Testing Machine with a 151 kN capacity. Loading is force controlled at a rate of 1.1 MPa/min.

3 Results

3.1 Rate of Hydration

The normalized heat flow and normalized heat of hydration curves for pastes with 0, 0.01, 0.03 and 0.05 % GO addition are shown in Fig. 1. From Fig. 1a, all curves exhibit two shoulders – the first is due to silicate reaction and the second is due to

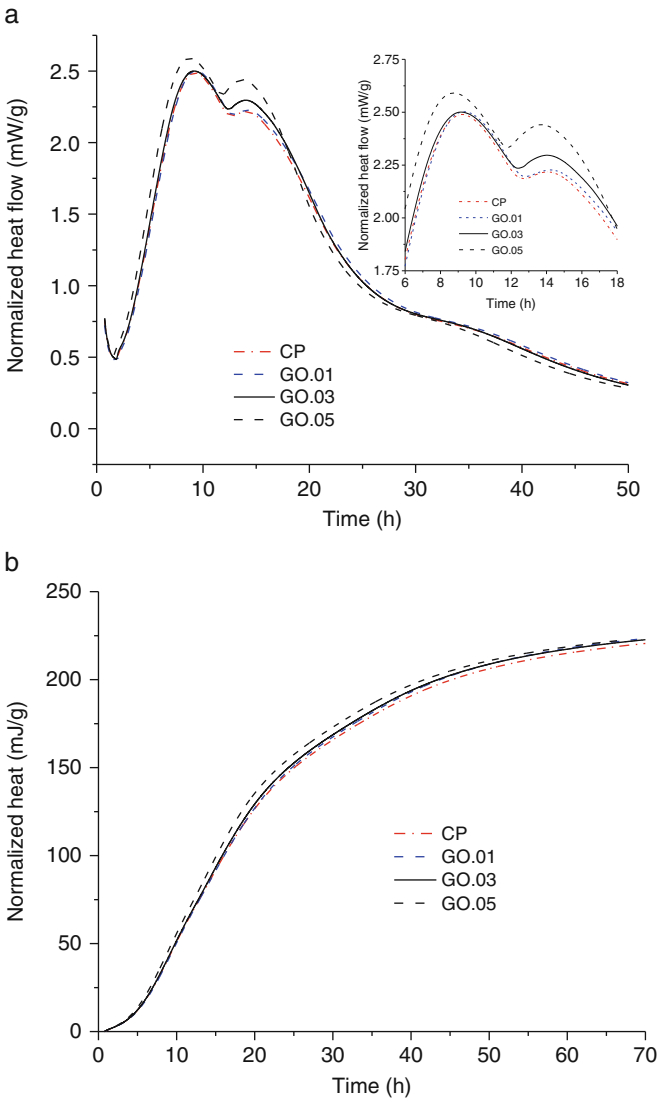

Fig. 1 Normalized (**a**) heat flow and (**b**) cumulative heat generated of cement pastes with 0, 0.01, 0.03 and 0.05 % graphene oxide addition

aluminate reaction. Graphene oxide has a slight accelerating effect on both, where the peaks are shifted up and to the left. Compared with CP, the first and second peak of GO.05 increases 3.6 % and 9.6 %, respectively. This may be attributed to the seeding effect that is often observed in cementitious systems with nanomaterials [12, 13]. While at the deceleration period, GO.05 shows smaller heat flow, rendering almost the same total normalized heat for all samples at 70 h after mixing, as shown in Fig. 1b.

3.2 Four Point Bending Test

The results of the four point bending test are shown in Figs. 2 and 3. Figure 2 shows the relationship between flexural strength of mortar and GO addition at 7 days and 28 days. Even at small additions of graphene oxide, there is an apparent increase in strength. Compared to the neat cement paste, at 0.03 %, graphene oxide increases the flexural strength of mortar by 18.7 % and 13.7 % at 7 days and 28 days, respectively.

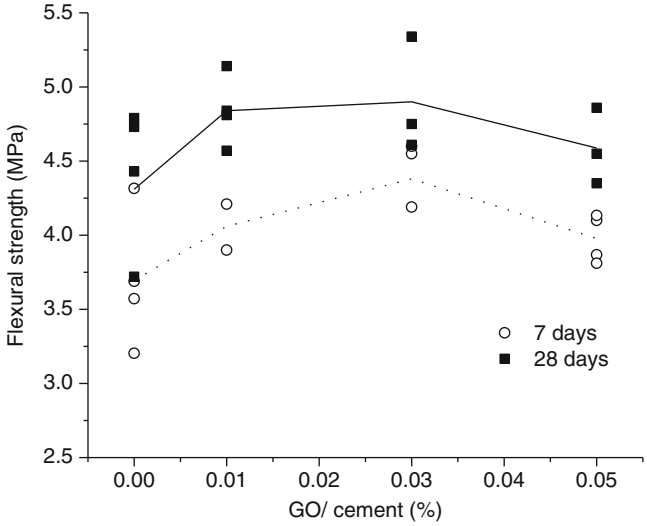

Fig. 2 Flexural strength of mortar with GO addition

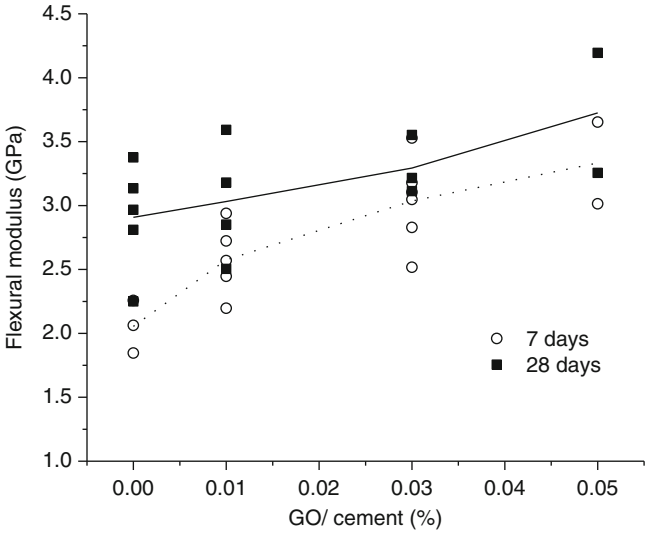

Fig. 3 Flexural modulus of mortar with GO addition

As summarized in Fig. 3, the flexural modulus of mortar samples at 7 and 28 days, with increasing GO addition, the flexural modulus increases. Especially at 7 days, the flexural modulus of GO.05 increases 61.7 % compared to CP. It could be due to bridging and strengthening effect of graphene oxide in the cement matrix, or refined pore structures [3, 14].

4 Conclusions

The preliminary results of a study on graphene oxide-reinforced cement pastes and mortar are presented. Results indicate that at relatively low additions (below 0.05 % by mass of cement), graphene oxide can enhance flexural strength. Work is ongoing on later-age properties, i.e. strength gain and permeability, and microstructural characterization.

Acknowledgements The authors gratefully acknowledge the support by the staff of the Carleton Laboratory.

References

1. Cwirzen, A., Habermehl-Cwirzen, K., & Penttala, V. (2008). Surface decoration of carbon nanotubes and mechanical properties of cement/carbon nanotube composites. *Advances in Cement Research, 20*, 65–73.
2. Sanchez, F., & Ince, C. (2009). Microstructure and macroscopic properties of hybrid carbon nanofiber/silica fume cement composites. *Composites Science and Technology, 69*, 1310–1318.
3. Konsta-Gdoutos, M. S., Metaxa, Z. S., & Shah, S. P. (2010). Highly dispersed carbon nanotube reinforced cement based materials. *Cement and Concrete Research, 40*, 1052–1059.
4. Konsta-Gdoutos, M. S., Metaxa, Z. S., & Shah, S. P. (2010). Multi-scale mechanical and fracture characteristics and early-age strain capacity of high performance carbon nanotube/cement nanocomposites. *Cement and Concrete Composites, 32*, 110–115.
5. Vaisman, L., Wagner, H. D., & Marom, G. (2006). The role of surfactants in dispersion of carbon nanotubes. *Advances in Colloid and Interface Science, 128*, 37–46.
6. Lv, S., Ma, Y., Qiu, C., Sun, T., Liu, J., & Zhou, Q. (2013). Effect of graphene oxide nanosheets of microstructure and mechanical properties of cement composites. *Construction and Building Materials, 49*, 121–127.
7. Peyvandi, A., Soroushian, P., Balachandra, A. M., & Sobolev, K. (2013). Enhancement of the durability characteristics of concrete nanocomposite pipes with modified graphite nanoplatelets. *Construction and Building Materials, 47*, 111–117.
8. Le, J.-L., Du, H., & Dai Pang, S. (2014). Use of 2D Graphene Nanoplatelets (GNP) in cement composites for structural health evaluation. *Composites Part B: Engineering, 67*, 555–563.
9. Paredes, J. I., Villar-Rodil, S., Martinez-Alonso, A., & Tascon, J. M. D. (2008). Graphene oxide dispersions in organic solvents. *Langmuir, 24*, 10560–10564.
10. Wajid, A. S., Das, S., Irin, F., Ahmed, H., Shelburne, J. L., Parviz, D., Fullerton, R. J., Jankowski, A. F., Hedden, R. C., & Green, M. J. (2012). Polymer-stabilized graphene dispersions at high concentrations in organic solvents for composite production. *Carbon, 50*, 526–534.

11. Zhu, Y., Murali, S., Cai, W., Li, X., Suk, J. W., Potts, J. R., & Ruoff, R. S. (2010). Graphene and graphene oxide: Synthesis, properties, and applications. *Advanced Materials, 22*, 3906–3924.
12. Sanchez, F., & Sobolev, K. (2010). Nanotechnology in concrete – A review. *Construction and Building Materials, 24*, 2060–2071.
13. Ridi, F., Fratini, E., & Baglioni, P. (2011). Cement: A two thousand year old nano-colloid. *Journal of Colloid and Interface Science, 357*, 255–264.
14. Li, G. Y., Wang, P. M., & Zhao, X. (2005). Mechanical behavior and microstructure of cement composites incorporating surface-treated multi-walled carbon nanotubes. *Carbon, 43*, 1239–1245.

Graphene Nanoreinforcement for Cement Composites

Nima Zohhadi, Nirupam Aich, Fabio Matta, Navid B. Saleh, and Paul Ziehl

Abstract This paper reports on research aimed at investigating the reinforcing effects of graphene nanoplatelets (GNPs) in cement composites. Nanoreinforced cement mortar cubes were prepared using surfactant-coated GNPs. The dispersion and embedment of GNPs in the cement matrix were verified based on evidence from compression strength tests and scanning electron microscopic imaging. Results from fracture mechanics tests on notched beams were then used to evaluate the effect of incorporating well-dispersed, surfactant-coated GNPs on the flexural strength and stiffness of cement paste. 3D digital image correlation measurements were used to study the morphology and evolution of the fracture process zone in plain and GNP-reinforced cement paste.

Key words Graphene • Nanoplatelets • Cement • Composites • Surfactant • Strength • Stiffness • Fracture

1 Introduction

Compelling mechanical properties, such as elastic modulus of ~1 TPa and tensile strength of ~100 GPa [1], make graphene nanoplatelets (GNPs) attractive as nanoreinforcements for cement composites [2]. In particular, the larger ratio of exterior surface area to weight compared with multiwalled carbon nanotubes may facilitate interaction with cement hydrates. Due to their small size (e.g., thickness of ~10 nm, side length of ~10^2 nm) GNPs can also act as 'fillers', reducing the porosity of cement matrices. Alkhateb et al. [3] reported that the incorporation of 0.5 % (i.e., by weight of cement) of oxidized GNPs resulted in an average increase in the

N. Zohhadi • F. Matta (✉) • P. Ziehl
Department of Civil and Environmental Engineering,
University of South Carolina, Columbia, SC, USA
e-mail: fmatta@sc.edu

N. Aich • N.B. Saleh
Department of Civil, Architectural and Environmental Engineering,
University of Texas at Austin, Austin, TX, USA

K. Sobolev, S.P. Shah (eds.), *Nanotechnology in Construction*,
DOI 10.1007/978-3-319-17088-6_34

longitudinal and shear modulus of cement paste of 23 % and 37 %, respectively. Lv et al. [4] reported an average 79 % and 61 % increase in the tensile and flexural strength of cement mortar, respectively, using 0.03 % of oxidized GNPs.

This paper reports on research on the reinforcing effect of GNPs in cement composites. GNPs were dispersed in cement mortar after functionalization by means of surfactant-coating (e.g., [5]). Compressive strength characterization and scanning electron microscopy (SEM) imaging were used to verify dispersion and embedment in the composite matrix. Then, the effects of well-dispersed and chemically affine GNPs on the flexural strength, stiffness and damage tolerance of cement paste were studied based on evidence obtained from three-point bending tests on single-edge notched beam specimens. 3D digital image correlation (DIC) measurements were performed to yield full-field strain maps to study the morphology and evolution of the fracture process zone (FPZ). The results presented herein offer new evidence on the strengthening, stiffening and fracture-toughening effects of incorporating GNPs in cement composites.

2 Materials and Methods

Type I ordinary Portland cement and silica sand were used to manufacture mortar cubes and cement paste beams. GNPs (Graphene Laboratories Inc., cat# SKU-NP-FL2, Calverton, NY) with manufacturer-specified average thickness and particle size of 8 and 550 nm, respectively, were used. The surfactant used for functionalization purposes was sodium deoxycholate, NaDC (Sigma Aldrich, cat#D6750, St. Louis, MO). NaDC was dissolved in water by magnetic stirring at 1,200 rpm. GNPs were then added to the aqueous solution using a surfactant-to-GNP weigh ratio of 7:1, and the resulting suspensions were sonicated for additional 20 min. Specimens and test methods are presented below.

Compressive Strength Characterization Compression tests were performed on 2-in. (50-mm) cube specimens having cement:sand:water weight proportions of 1:2.75:0.5. Two GNP concentrations, 0.05 and 0.5 %, were used. Three specimens per group were cast and moist-cured for 24 h, demolded, and cured in saturated lime water for additional 27 days. The compression tests were performed using a test frame (MTS 810, MTS Systems Corp., Eden Prairie, MN) at a constant displacement rate of 0.625 mm/min.

Fracture Mechanics Tests Three-point bending tests were performed on 20×20×80 mm single-edge notched beam specimens made of cement paste with water-to-cement (*w/c*) ratio of 0.5 (Fig. 1a). Three specimens per group (plain and 0.05 %-GNP reinforced cement paste) were moist-cured for 24 h, demolded, and cured in saturated lime water for additional 27 days. A water-cooled diamond saw was used to cut 6-mm long and 2-mm wide notches at the mid-span section of each specimen (Fig. 1b). A clip gage was used to measure the crack-mouth opening displacement (CMOD). The bending tests were performed using a test frame (MTS 810, MTS Systems Corp., Eden Prairie, MN) at a constant displacement rate of 0.01 mm/min.

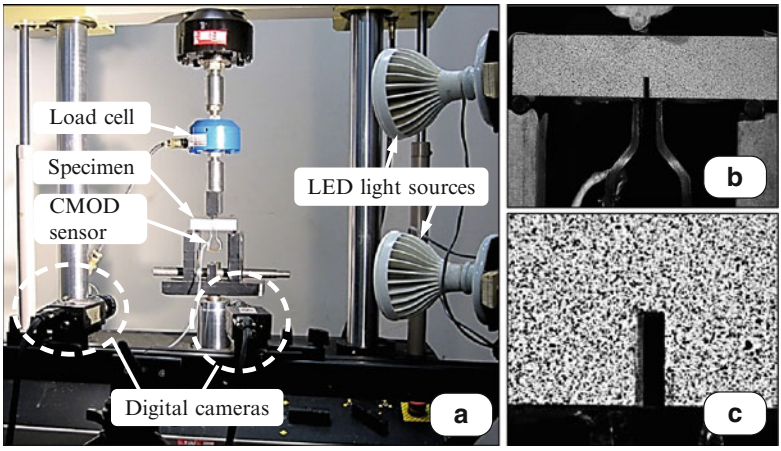

Fig. 1 Fracture mechanics and DIC experiments: (**a**) test setup; (**b**) close-up photograph of notched beam specimen; and (**c**) close-up view of speckle pattern around 2×6 mm notch

Scanning Electron Microscopy Imaging SEM imaging was performed on mortar and cement paste samples extracted from fracture surfaces, using a Zeiss Ultra Plus Field Emission Scanning Electron Microscope. All samples were oven-dried for 24 h at 60 °C and gold-sputtered prior to being examined under the scope.

Digital Image Correlation Measurements A thin layer of white wash was applied on the surface of the specimens and a dark speckle pattern was spray-painted on the white-washed background (Fig. 1c). Two 5-MP cameras (Grasshopper GRAS-50S5M-C, Point Grey, Richmond, Canada) equipped with 35-mm lenses were used to acquire images at a rate of 5 frames per second (Fig. 1a). The 3D-DIC analysis was performed using the software Vic-3D (v7, Correlated Solutions Inc., Columbia, SC) using a subset size of 49×49 pixels and step of 15 pixels [6].

3 Results and Discussion

3.1 Compressive Strength

The average compressive strength values of mortar cubes are reported in Table 1. Standard deviation values are also provided as a measure of consistency (i.e., comparing the results of plain and nanoreinforced mortar). Cubes reinforced with 0.05 % of surfactant-coated GNPs exhibited consistent increase in compressive strength, which was on average 28 % greater than that of plain mortar cubes. However, further increasing the GNP concentration to 0.5 % resulted in an average 37 % decrease in strength. The SEM micrographs in Fig. 2 illustrate the representative microstructure of GNP-reinforced mortar. Debundled GNPs were typically found indicating

Table 1 Mortar compressive strength test results

Specimen group	Compressive strength (MPa)
Control (plain mortar)	23.3 ± 3.76
0.05 % surfactant-coated GNPs	29.9 ± 3.55
0.5 % surfactant-coated GNPs	14.7 ± 4.23

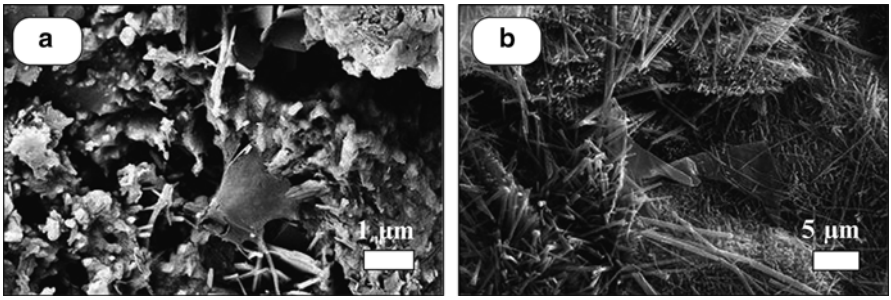

Fig. 2 SEM micrographs illustrating dispersion of surfactant-coated GNPs in cement mortar: (**a**) 0.05 % concentration; and (**b**) 0.5 % concentration

that a good dispersion was achieved (Fig. 2a). However, SEM micrographs of fracture surfaces from samples reinforced with 0.5 % of GNPs revealed the presence of diffused surfactant by-products in the form of needle-like structures in the vicinity of GNPs (Fig. 2b), seemingly hindering the effective embedment of and contact between GNPs and cement matrix, and creating discontinuities (defects) in the matrix. During fabrication, it was also noted that increasing the GNP concentration (i.e., the absolute amount of surfactant) negatively affected workability.

Based on this preliminary evidence, the decrease in strength for mortar reinforced with 0.5 % of GNPs was attributed to the presence of diffused surfactant by-products and reduced workability, facilitating the formation of defect sites.

3.2 Flexural Strength and Stiffness

The flexural strength and elastic stiffness results from the notched cement paste beam tests are reported in Table 2. Representative load-CMOD curves for plain and GNP-reinforced beams are shown in Fig. 3. The incorporation of 0.05 % of surfactant-coated GNPs led to an increase in average flexural strength and elastic stiffness by 39 % and 109 %, respectively, thus corroborating the results obtained for mortar (Table 2). These enhancements can be attributed to different effects including composite action, decrease in porosity, and crack-bridging provided by well-dispersed and embedded GNPs [6]. In particular, GNPs can fill in meso-pores (2–50 nm) as well as micropores (e.g., Fig. 2a), resulting in reduced as well as refined porosity, and thus higher density, stiffness, and crack-arrest capabilities. Porosity reduction and refinement has been previously reported for the case of MWCNTs embedded in cement paste [7].

Table 2 Cement paste bending test results

Specimen group	Peak load (N)	Elastic stiffness (N/mm)
Control (plain cement paste)	110.9 ± 3.34	5,476 ± 561
0.05 % surfactant-coated GNPs	153.8 ± 12.59	11,454 ± 2,529

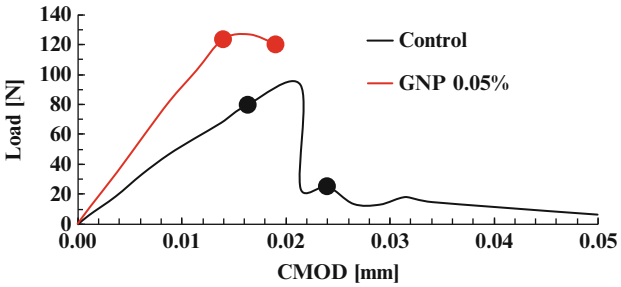

Fig. 3 Representative load-CMOD curves from cement paste notch beam tests. Markers indicate load-CMOD coordinates for DIC strain maps in Fig. 4

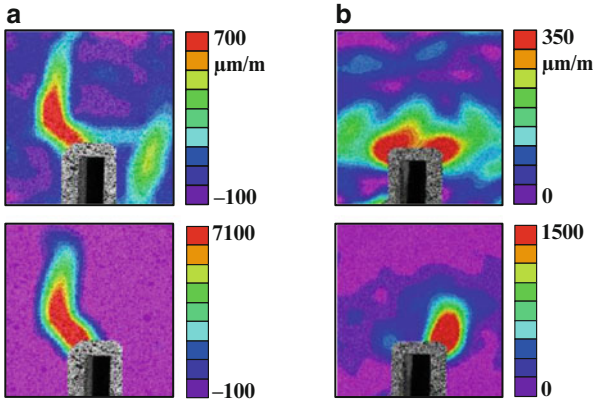

Fig. 4 Representative 3D-DIC principal tensile strain maps (in μm/m) at load-CMOD coordinates marked in Fig. 3: (**a**) plain cement paste; and (**b**) 0.05 % GNPs

3.3 Fracture Process Zone

Representative 3D-DIC principal tensile strain maps illustrating the morphology and evolution of the FPZ before and after reaching the peak load (referring to the markers in Fig. 3) are shown in Fig. 4. In plain cement paste, the FPZ developed in a well-defined and narrow area around the crack tip (Fig. 4a). In GNP-reinforced cement paste, in the non-linear pre-peak loading stage (i.e., as internal damage develops prior to reaching the peak load), the strain contours show that the FPZ developed in a larger area of more distributed damage. In fact, the strain contours show a smoother transition between more and less damaged areas for GNP-reinforced paste (Fig. 4b), supporting the hypothesis that well-dispersed and embedded GNPs contribute to radically improving damage tolerance.

4 Conclusions

Based on the experimental evidence presented herein, the following salient conclusions are drawn.

- Surfactant-coating of GNPs in a 0.05 % concentration led to good dispersion and embedment in cement mortar and paste. In fact, the incorporation of 0.05 % of GNPs resulted in an average increase in compressive strength of mortar, and flexural strength and elastic stiffness of cement paste, of 28 %, 39 %, and 109 %, respectively.
- The fracture process zone in GNP-reinforced cement paste consisted of significantly larger areas of distributed damage with a smoother transition between more and less damaged areas, supporting the hypothesis that well-dispersed and embedded GNPs contribute to a radical enhancement of damage tolerance.

Acknowledgements The support of the University of South Carolina through a Promising Investigator Research Award (PIRA) is gratefully acknowledged. Special thanks are extended to: Prof. A. Reynolds and Mr. D. Wilhelm (Department of Mechanical Engineering), and Ms. English Player (formerly undergraduate student and Magellan Mini-grantee), for assistance in the preparation and testing of cement composite samples; Prof. M. Sutton (SC Center for Mechanics, Materials and Non-Destructive Evaluation) for lending the 3D-DIC equipment; and Correlated Solutions, Inc., for donating the software Vic-3D.

References

1. Lee, C., Wei, X., Kysar, J. W., et al. (2008). Measurement of the elastic properties and intrinsic strength of monolayer graphene. *Science, 321*, 385–388.
2. Zohhadi, N., Aich, N., Khan, I. A., Matta, F., Saleh, N. B., & Ziehl, P. (2012). Graphene nanoreinforcement for cement-based composites. In M. S. Konsta-Gdoutos (Ed.) *Proceedings of 4th international symposium on Nanotechnology in Construction (NICOM-4)*, Paper 178, 7 p.
3. Alkhateb, H., Al-Ostaz, A., Cheng, A. H. D., et al. (2013). Materials genome for graphene-cement nanocomposites. *Journal of Nanomechanics and Micromechanics, 3*(3), 67–77.
4. Lv, S., Ma, Y., Qiu, C., et al. (2013). Effect of graphene oxide nanosheets of microstructure and mechanical properties of cement composites. *Construction and Building Materials, 49*, 121–127.
5. Luo, J., Duan, Z., & Li, H. (2009). The influence of surfactants on the processing of multi-walled carbon MWCNTs in reinforced cement matrix composites. *Physica Status Solidi A: Applications and Material Science, 206*(12), 2783–2790.
6. Zohhadi, N. (2014). *Functionalized graphitic nanoreinforcement for cement composites*. PhD dissertation, University of South Carolina.
7. Nochaiya, T., & Chaipanich, A. (2011). Behavior of multi-walled carbon nanotubes on the porosity and microstructure of cement-based materials. *Applied Surface Science, 257*(6), 1941–1945.

Measurement and Modeling of the Elastic Modulus of Advanced Cement Based Nanocomposites

Maria G. Falara, Chrysoula A. Aza, Panagiotis A. Danoglidis, Maria S. Konsta-Gdoutos, and Emmanuel E. Gdoutos

Abstract Carbon nanotubes and carbon nanofibers exhibit several distinct advantages as a reinforcing material for cementitious composites, as compared to more traditional fibers. They exhibit significant greater strength and stiffness, which greatly improve the composites' mechanical behavior. In this research, an experimental study of the mechanical characterization of cement based nanocomposite materials reinforced with carbon nanotubes is presented. The classic micromechanical approach for fiber reinforced composites was employed to develop predictive models for the modulus of elasticity of the nanocomposites. Results reveal a good agreement between the experimental and predicted values, when using the Benveniste model with disk like inclusions.

Keywords Carbon nanotubes • Mortar nanocomposites • Modulus of elasticity • Micromechanics models • Benveniste

1 Introduction

The utilization of multi-walled carbon nanotubes (MWCNTs) in cement based composites has shown to improve their mechanical properties due to the distinct advantages that nanotubes exhibit [1–4]. Specifically, Konsta-Gdoutos et al. [3] recent research on the reinforcing effect of MWCNTs in cement matrix (w/c = 0.485) indicated that small amounts of effectively dispersed MWCNTs can strongly reinforce the cement paste matrix by increasing the flexural strength and the Young's modulus of plain cement paste by 25 % and 50 %, respectively. Nanoidentation results by Konsta-Gdoutos et al. [4] suggest that MWCNTs can strongly modify and reinforce the nanostructure of the cementitious matrix. Compared to plain cement matrix, the nanocomposites appear to have higher amount of high stiffness C-S-H

M.G. Falara (✉) • C.A. Aza • P.A. Danoglidis • M.S. Konsta-Gdoutos • E.E. Gdoutos
Department of Civil Engineering, Democritus University of Thrace,
Vas. Sofias 12, Xanthi 67100, Greece
e-mail: mfalara@civil.duth.gr; azachrysoula@gmail.com;
pdanogli@civil.duth.gr; mkonsta@civil.duth.gr; egdoutos@civil.duth.gr

K. Sobolev, S.P. Shah (eds.), *Nanotechnology in Construction*,
DOI 10.1007/978-3-319-17088-6_35

and reduced nanoporosity that implies to the development of high-performance cementitious nanocomposites. In this research a classic micromechanical approach was used to develop predictive models for theoretical evaluation of modulus of elasticity of the nanocomposites reinforced with 0.048, 0.08 and 0.1 wt% of cement. Fracture mechanics tests were also performed to evaluate the modulus of elasticity of these nanocomposites. A comparison between Voigt, Reuss, Benveniste predicted values and experimental results is carried out.

2 Predictive Models for the Modulus of Elasticity

To determine the modulus of elasticity of a composite it is necessary to know the volume fraction of the phases of the material (matrix and reinforcement), the modulus of the different phases of the material, and finally the geometric details regarding the phases of the material. For each possible volume fraction of reinforcing phase material, the modulus of elasticity of the composite material is located between an upper and a lower bound and the value depends on the configuration of the inclusion within the matrix. The models used to determine these limits are proposed by Voigt and Reuss, respectively.

Mori-Tanaka [5] proposed a model that originally concerned the determination of the average internal stress in the matrix of a composite with misfitted inclusions which were considered to be ellipsoidal. Benveniste [6], based on Mori-Tanaka's theory, developed a simple form expression for the determination of modulus of elasticity of composite materials. This method limits to two-phase composites retaining the generality of anisotropic elastic constituents with the inclusion phase, consisting of ellipsoidal particles which can be aligned or randomly oriented.

3 Experimental Program

3.1 Materials and Specimen Preparation

Specimens 20×20×80 mm were prepared by adding multiwall carbon nanotubes (MWCNTs) of 20–40 nm diameter and length >10 μm. Cement paste samples were prepared using ordinary Portland cement at a water to cement ratio (w/c) 0.3 and 0.485. Also mortar samples were prepared at a water to cement ratio 0.485 and adding fine aggregate sand at a sand to cement ratio (s/c) 2.75. To achieve homogeneous dispersion of MWCNTs, suspensions were prepared by adding the MWCNTs in an aqueous surfactant solution and applying ultrasonic energy at room temperature following the method described in [3]. The materials were mixed according to ASTM C305. The samples were cured in lime-saturated water after 24 h of moist curing.

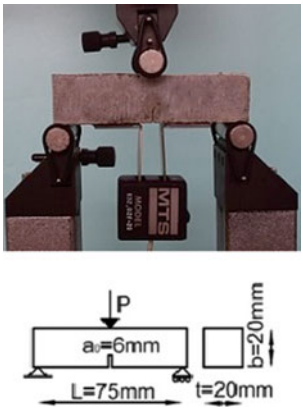

Fig. 1 Three-point bending experimental configuration and set-up

3.2 Young's Modulus Experimental Determination

Young's modulus was measured by fracture mechanics tests, using the two-parameter model by Jenq and Shah [7]. Tests were conducted on notched specimens of 20×20×80 mm at the age of 28 days, using a closed-loop MTS servohydraulic testing machine with a 25 kN capacity (Fig. 1). The crack mouth opening displacement (CMOD) at the notch, set at a rate of 0.012 mm/min and 0.009 mm/min for w/c 0.485 and 0.3 respectively, was used as the feedback control signal for running the test. The ASTM C348 was followed to determine the average values of the Young's modulus.

3.3 Young's Modulus Prediction

To determine the Young's modulus of the MWCNT nanocomposites, the volume fractions of the CNTs and the matrix was initially estimated using the densities of all materials (cement, water, sand, surfactant and CNTs). The volume fraction of MWCNTs was calculated using the bulk density which is 0.18 g/cm^3 according to the manufacturer. Bulk density is essentially the volume occupied by CNTs in the matrix and was used for the theoretical calculations. Young's modulus of matrix (plain cement paste/mortar) is the 28-day experimental value investigated by fracture mechanics tests and CNTs' Young's modulus is 1 TPa. Calculations were performed for cement pastes reinforced with 0.048 and 0.08 wt% MWCNTs and cement mortars reinforced with 0.08 and 0.1 wt% MWCNTs.

4 Results and Discussion

The results of the average Young's modulus (E) of cement paste (CP) and mortar (M) nanocomposites are presented in Fig. 2. All nanocomposites exhibited a higher elastic modulus than that of the neat cement paste and mortar. Cement pastes reinforced with 0.048 and 0.08 wt% MWCNTs exhibited an increased Young's modulus, calculated to 28.4 % and 47.8 % respectively. Interestingly, although the mortar matrix stiffness is a little higher than the cement paste's, the elastic modulus of the 0.08 and 0.1 wt% mortar MWCNTs nanocomposites is significantly increased by 75.14 % and 92.3 % respectively.

The results suggest that load transfer is far more effectively accomplished by the MWCNT reinforcement in the mortar matrix than in the paste. It is important to note here that when comparing the mechanical performance of paste and mortar nanocomposites, with the same per weight of cement content of CNTs, the amount of MWCNTs in the mortar mixes is half the amount of the one in the paste nanocomposites. As shown in Table 1, a meaningful comparison will account for a similar quantity of MWCNTs in the mix (MWCNT count). In this context, the Young's modulus of the 0.1 wt% mortar nanocomposite is measured 27.4 GPa, which is more than two times higher than that of the 0.048 wt% paste nanocomposite.

The experimental results of the Young's modulus of cement pastes of w/c = 0.3, reinforced with 0.048 and 0.08 wt% MWCNTs, are compared to the values predicted by the Voigt, Benveniste-Mori Tanaka and Reuss models in Fig. 3. It is observed that the Young's modulus of the paste nanocomposites approaches the Benveniste predicted values.

Experimental values and predicted values according to the Benveniste-Mori Tanaka model for the paste nanocomposites at w/c = 0.485 and w/c = 0.3 are in good agreement, as shown in Fig. 4. However, as it is depicted from Fig. 5, neither the Benveniste, nor the upper bound model agree well with the experimental values of the mortar nanocomposites.

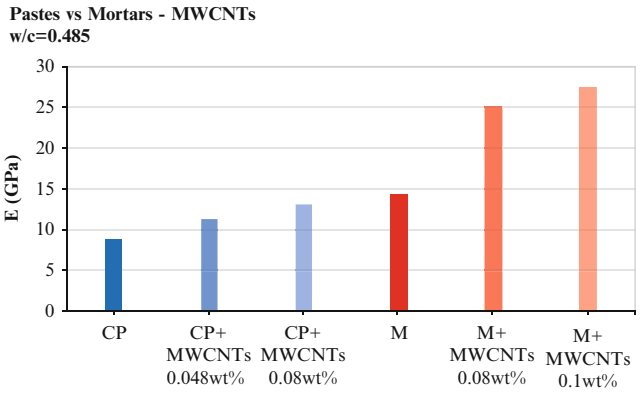

Fig. 2 Young's modulus of cement pastes and mortars reinforced with MWCNTs

Table 1 Amount of MWCNTs for both cement paste and cement mortar matrices

Samples	MWCNTs count
CP + MWCNTs 0.048 wt%	4.71×10^{11}
M + MWCNTs 0.1 wt%	3.61×10^{11}

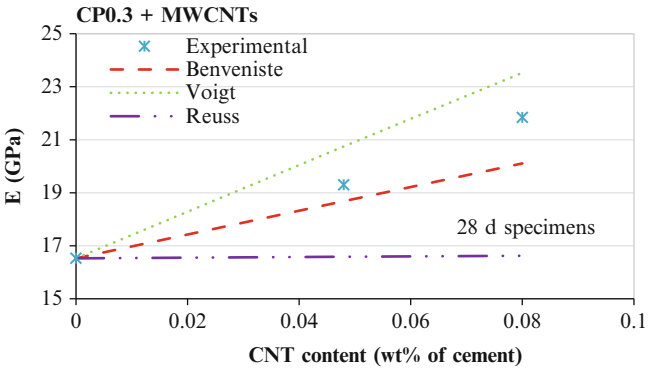

Fig. 3 Experimental Young's modulus of cement paste reinforced with MWCNTs compared to predictive models

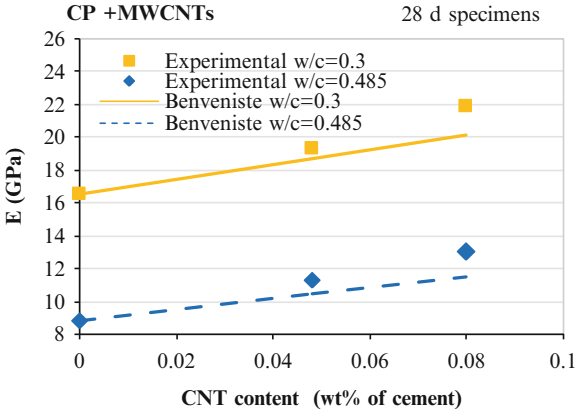

Fig. 4 Experimental Young's modulus and Benveniste predicted values of cement pastes (w/c = 0.3, 0.485) with MWCNTs

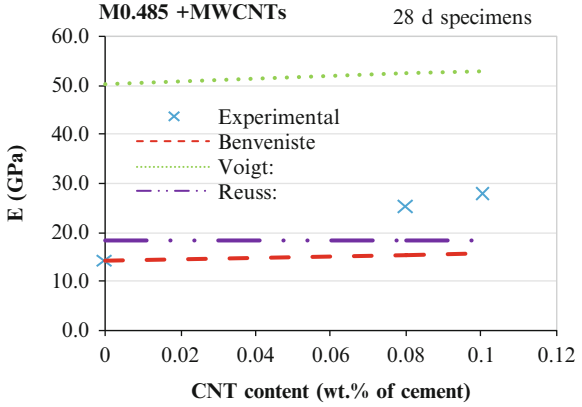

Fig. 5 Experimental Young's modulus of cement mortars with MWCNTs compared to predictive models

5 Conclusions

The modulus of elasticity of cement pastes and mortars reinforced with well dispersed MWCNTs were investigated. Three-point bending test results confirm that the Young's modulus of all MWCNT nanocomposites is significantly improved. The increase in Young's modulus of mortar nanocomposites was higher compared to cement paste for the same amount of CNTs in the matrix suggesting that load transfer is far more effectively accomplished by the MWCNT reinforcement in the mortar matrix than in the paste. To develop predictive models for the modulus of elasticity of the nanocomposites, the experimental Young's modulus results of cement paste and mortar nanocomposites were compared to the predicted values by the Voigt, Benveniste-Mori Tanaka and Reuss models. Results of cement paste nanocomposites reveal a good agreement between the experimental and the predicted values by the Benveniste-Mori Tanaka model. Instead, the experimental values of the mortar nanocomposites approach the lower bound, as defined by the Reuss model.

Acknowledgements The authors would like to acknowledge the financial support of the National Strategic Reference Framework (NSRF) – Research Funding Program "SYNERGASIA 2011 – Nano-Modified Smart Concrete (NSC) (11SYN_5_1430)", Partnerships of Production and Research Institutions in Focused Research and Technology Sectors, funded by the European Union (European Social Fund – ESF) and Greek national funds through the Operational Program "Competitiveness and Entrepreneurship and Regions in Transition (EPAN II)". Sika Hellas Inc and Glonatech Inc are kindly acknowledged for supplying the superplasticizer and the carbon nanotubes respectively.

References

1. Konsta-Gdoutos, M. S., Metaxa, Z. S., & Shah, S. P. (2010). Highly dispersed carbon nanotubes reinforced cement based materials. *Cement and Concrete Research, 40*, 1052–1059.
2. Konsta-Gdoutos, M. S., Metaxa, Z. S., & Shah, S. P. (2010). Multi-scale mechanical and fracture characteristics and early-age strain capacity of high performance carbon nanotube/cement nanocomposites. *Cement and Concrete Composites, 32*, 110–115.
3. Metaxa, Z. S., Seo, J. W. T., Konsta-Gdoutos, M. S., Hersam, M. C., & Shah, S. P. (2012). Highly concentrated carbon nanotube admixture for nano-fiber reinforced cementitious materials. *Cement and Concrete Composites, 34*, 612–617.
4. Metaxa, Z. S., Konsta-Gdoutos, M. S., & Shah, S. P. (2009). Carbon nanotube reinforced concrete. *ACI Special Publication, 267*, 11–20.
5. Mori, T., & Tanaka, K. (1973). Average stress in matrix and average elastic energy of materials with misfitting inclusions. *Acta Metallurgica, 21*, 571–574.
6. Benveniste, Y. (1987). A new approach to the application of Mori – Tanaka's theory in composite materials. *Mechanics of Materials, 6*, 147–157.
7. Shah, S. P., Swartz, S. E., & Ouyang, C. (1995). *Fracture mechanics of concrete: Application of fracture mechanics to concrete, rock and other quasi-brittle materials*. New York: Willey.

The Effect of Carbon Nanofibers on the Strength of Concrete with Natural and Recycled Aggregates

Ardavan Yazdanbakhsh and Calvin Chu

Abstract This work reports on an experimental investigation about the effect of carbon nanofibers (CNFs) on the compressive strength of: (1) hardened portland cement paste and (2) two types of concrete; with natural and recycled coarse aggregates. It was observed that the incorporation of nanofibers caused a slight increase in the compressive strength of cement paste. However, for each type of aggregate, the strength of CNF-incorporated concrete was lower than that of control plain concrete. Based on the SEM studies and visual observations of the hardened paste specimens, the reason for these different behaviors was found to be the different dominating mechanisms by which bleeding is controlled in paste and concrete mixes; in paste CNF clumps partially block the pores and bleed water channels, while in concrete a portion of free water is adsorbed on the surfaces introduced by aggregates.

Keywords Carbon nanofibers • Recycled aggregate • Strength • Shrinkage

1 Introduction

The use of carbon nanofilaments (either carbon nanotubes (CNTs) or carbon nanofibers (CNFs)) in cement-based materials has been researched for the past few decades. Some of the investigations have shown improvements (typically minimal) on the mechanical and durability-related properties of cement-based materials (the readers are referred to [1–6] for a review of some of those studies). It will be a significant achievement, if CNT/Fs can be used as a more economical and environmental-friendly alternative to other additives and methods used for enhancing the properties of concrete. However, there are important barriers to achieving that goal; (1) CNT/Fs are expensive, (2) It is very difficult to uniformly disperse CNT/Fs in cementitious matrices, and (3) There are social barriers against using them. In addition, there is a wide range of types of carbon nanofilaments. Tyson et al. [1] showed that different types of CNT/Fs with different surface treatments

A. Yazdanbakhsh (✉) • C. Chu
Civil Engineering Department, City College of New York, New York, NY, USA
e-mail: ayazdanbakhsh@ccny.cuny.edu; cchu04@citymail.cuny.edu
http://www.ccny.cuny.edu/profiles/Ardavan-Yazdanbakhsh.cfm

K. Sobolev, S.P. Shah (eds.), *Nanotechnology in Construction*,
DOI 10.1007/978-3-319-17088-6_36

can affect the mechanical properties of hardened cement paste very differently. To date, no standard framework has been developed for characterizing the properties of CNT/Fs.

Poor dispersibility of CNT/Fs remains a major barrier against using them in cement-based composites. Yazdanbakhsh and Grasley [7] showed that although certain types of carbon nanofilaments (such as ball-milled CNFs, which are in part damaged and broken) can be dispersed in water by the traditional method of using superplastcizers and ultrasonic processing, when the water-CNF suspension is mixed with cement, the CNF particles start to reagglomerate. Therefore, it may prove valuable to know whether incorporating poorly dispersed CNT/Fs in cement-based composites can cause any improvements in mechanical performance and durability. Many of the past investigations have been performed on the properties of CNT/F-incorporated cement paste rather than mortars and concrete. The goal of the presented work is to investigate if the properties of hardened cement paste incorporating poorly dispersed CNT/Fs reflect the properties of concrete incorporating the same paste as binder.

2 Materials and Methods

The CNFs were provided by Applied Sciences Inc. under the commercial name Pyrograph PR-24-XT-PS. Commercially available Type I portland cement, high-range polycarboxylate-based superplasticizer and washed sea sand were used. The natural coarse aggregates (NA) was crushed granite within ASTM No. 7 (1/2 in maximum size) gradation range. The recycled aggregate (RCA) was produced with the same gradation range by a local recycling plant through crushing concrete demolition rubbles. ACI 211.1 volume method was used to develop proportions for normal-strength concrete (targeted at 4,000 psi) incorporating RCA (Table 1). The same volumetric proportions were used to produce NA concrete and cement paste. For CNF-incorporated mixes, CNFs were first added to the water-superplasticizer solution and then sonicated with a probe ultrasonic processing device for 5 min to produce a CNF suspension. The suspension was then mixed with other ingredients in a small laboratory drum mixer. Paste and concrete mixes were poured into 4 in.×8 in. cylinder molds and covered with plastic sheets. Two specimen were

Table 1 Mix proportions of paste and concrete batches

Mix	w/c Wt. ratio	CNF/c Wt. ratio	Agg. content Vol. cont., %	Fine/coarse Vol. ratio
Plain paste	0.525	0.00	0	NA
CNF paste	0.525	0.01	0	NA
Plain NA concrete	0.525	0.00	68	0.79
CNF NA concrete	0.525	0.01	68	0.79
Plain RCA concrete	0.525	0.00	68	0.79
CNF RCA concrete	0.525	0.01	68	0.79

produced for each mix. Concrete and paste specimens were demolded 24 h and 72 h after casting respectively and transferred to a humidity chamber (RH ≈ 100 %). All the specimens were tested after 28 days for compressive strength according to ASTM C39. The fractured surface of one of the CNF-paste specimens was studied using scanning electron microscopy (SEM).

3 Results and Discussion

The average compressive strength values of the paste and concrete specimens are presented in Table 2. The results show the dependency of the strength of concrete on the type of aggregates; for each type of material (either plain or CNF-incorporated), the paste is weaker than the NA concrete and stronger than RCA concrete. As expected, based on the previous study of Yazdanbakhsh et al. [2], CNFs increase the strength of cement paste. However, CNF-incorporated concrete specimens are weaker than their plain counterparts. The investigators hypothesize that the reason for this contradiction, as will be explained in this section, is the mechanism by which CNFs can maintain some degree of macro-scale homogeneity in paste.

Figure 1 shows plain and CNF paste samples three days after casting. It can be clearly seen that the plain paste has shrunk significantly more than the CNF paste. It was also observed that there was a higher amount of bleed water at the top of the plain paste one day after casting. CNFs move with bleed water but due to their shape and high aspect ratio they entangle and partially block many of the pores and channels through which water is transported. In addition, many of the fibers are already clumped and are more effective in blocking the pores. Figure 2 is the SEM image of the fractured surface of a CNF paste specimens. The image shows a pore that is filled with CNFs. A thorough SEM scanning of the surface of hydrated CNF paste showed that most of CNFs are accumulated in voids and porous zones of the paste. Only a very small portion of the CNFs or CNF clumps were tightly embedded in hydration products, as in Fig. 3. It seems that the CNFs are more likely to remain in the pore water rather than integrating with the hydration products. Figure 4 supports this hypothesis. There is a dark spongy layer at the top of the CNF paste specimens, which mostly consists of the CNFs that could make it out of the specimen with bleed water.

Table 2 Compressive strength of paste and concrete specimens

	Comp. strength	Incr/decr. in comp. strength
Mix	Psi	Relative to plain, %
Plain paste	4,830	N.A.
CNF paste	5,220	8
Plain NA concrete	6,890	N.A.
CNF NA concrete	5,600	−19
Plain RCA concrete	4,350	N.A.
CNF RCA concrete	4,120	−5

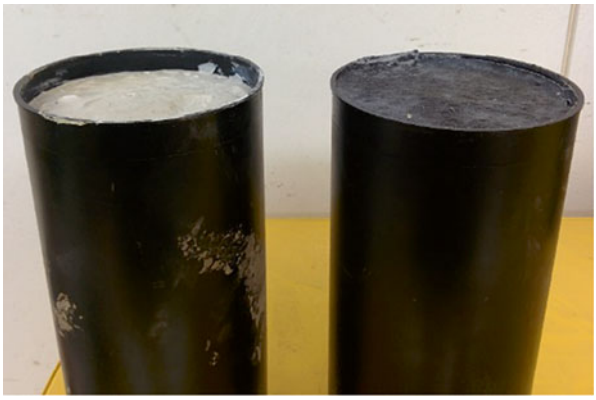

Fig. 1 Plain paste (*left*) and CNF paste (*right*) prior to demolding

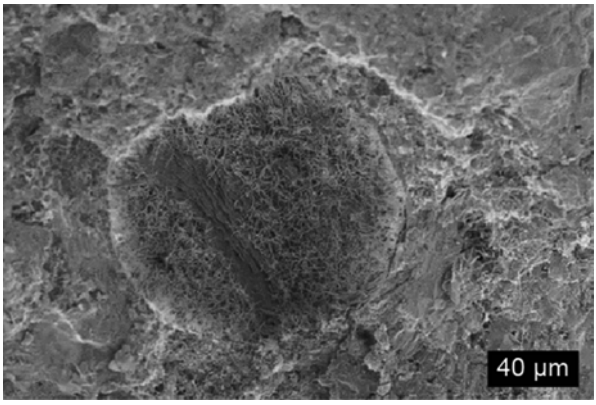

Fig. 2 A large void in hydrated cement paste

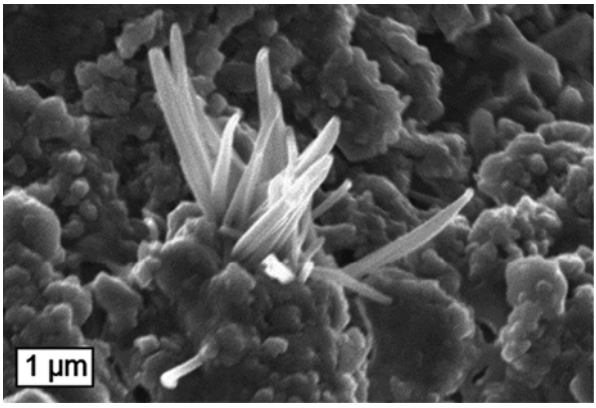

Fig. 3 A clump of tightly packed CNFs surrounded with and bonded to hydrated cement

Fig. 4 Cylinders of plain paste (*left*) and CNF paste (*right*) after demolding

Figure 4 shows the top surface of both plain and CNF paste specimens. There is a relatively thick light-colored layer at the top of the plain specimen. The layer was scratched using a nail tip and found to be very weak. When the plain cement paste is fresh, the cement particles subside due to their high SG and as a result the mixing water moves up (bleeding), therefore, the top part and particularly the light-colored layer has a less content of cement and eventually less hydration products. This weak zone may facilitate the failure of the specimen under axial compressive load. On the other hand, in the CNF paste specimens the dark layer is relatively thin and appearance of the hardened paste under this layer is relatively uniform. The specimen has shrunk less since the downward movement of solid cement particles in fresh paste requires the upward movement of water, which is hindered by CNF agglomerations in the pores and bleed water channels.

As mentioned earlier, the plain concrete specimens were stronger than those incorporating CNFs. After casting, it was observed that bleeding was insignificant in the concrete specimens and, therefore, was not a main parameter affecting strength; hardly any bleed water was observed on the surface of concrete specimens during the period of 24 h after casting. In addition, no visible shrinkage was observed in any of the concrete specimens. Aggregates, in particular fine aggregates, form most of the volume of concrete and therefore introduce additional surface to the cementing matrix. In other words, the water to cement-surface ratio in both paste and concrete mixes is the same, while in the concrete mixes a significant amount of additional surface is introduced by aggregates on which the mixing water is adsorbed. This could be clearly observed during mixing and casting; while concrete mixes were hardly flowable, paste mixes (both plain and CNF-incorporated) flowed like low-viscosity liquids.

It has been noted that the weak zones caused by CNF agglomerations can negatively affect the mechanical performance of cement based matrices [7]. Figure 5 shows an entangled clump of CNFs that has created a weak zone in the cementitious matrix; inside the clump the CNFs are neither bonded to the matrix nor to each other. These agglomerations are different from those formed in the spherical large void shown in Fig. 2; such large voids form in cement paste, typically due to the

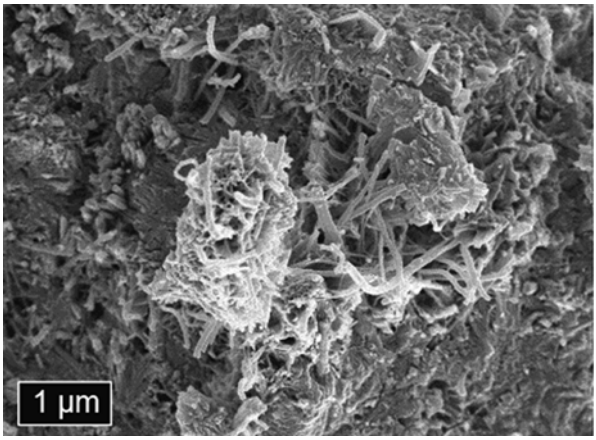

Fig. 5 CNF agglomerations generating weak zones in hydrated cement paste

presence of air, regardless of the presence of CNFs. The amount of weak zones depends on the amount of CNFs introduced to the paste. In this study, the dosage of CNFs was 1.0 % of the weight of cement, which is much higher than the maximum limit, found by other investigators, resulting in a reasonably uniform dispersion in cement paste. From the above arguments it can be inferred that, for the mixes investigated in this study, the dominating factors that negatively affect compressive strength are bleeding in paste specimens and weak zones caused by CNF-agglomeration in concrete specimens. More investigations must be performed to find out why the drop in strength due to the incorporation of CNFs in RCA concrete was less than that in plain concrete; is it only of an statistical nature due to the small number of specimens tested or possibly different transport and agglomeration mechanisms in the two types of concrete?

4 Concluding Remarks

The findings from the presented study leads to the following conclusions:

- CNFs can affect the properties of hydrated cement paste and concrete very differently due to the differences in the mechanism of moisture transport within fresh paste and fresh concrete.
- Agglomerated CNFs, and CNFs that reagglomerate in the fresh paste can effectively control bleeding in cementitious matrices by partially clogging the channels and voids through which bleeding water is transported.
- Due to the lower bleeding in CNF paste specimens, they underwent less shrinkage and were stronger than plain paste specimens.
- The incorporation of CNFs resulted in a lower reduction in compressive strength in RCA concrete than in plain concrete (5 % vs. 19 %). This finding must be confirmed by testing larger numbers of specimens, and further studied through SEM investigation of the aggregates embedded in RCA concrete.

Acknowledgment The authors wish to thank the support of Con-Strux Company for providing the project with recycled construction and demolition waste. This project was partly supported, by the NSF, Emerging Frontiers in Research and Innovation (EFRI), Award No. 1345379.

References

1. Tyson, B., Al-Rub, R. A., Yazdanbakhsh, A., & Grasley, Z. (2011). Carbon nanotubes and carbon nanofibers for enhancing the mechanical properties of nanocomposite cementitious materials. *Journal of Materials in Civil Engineering, 23*(7), 1028–1035.
2. Yazdanbakhsh, A., Grasley, Z., Tyson, B., & Abu Al-Rub, R. (2012). Challenges and benefits of utilizing carbon nanofilaments in cementitious materials. *Journal of Nanomaterials, 2012*, 8.
3. Yazdanbakhsh, A., Grasley, Z., Tyson, B., & Abu Al-Rub, R. (2009). Carbon nanofibers and nanotubes in cementitious materials: Some issues on dispersion and interfacial bond. *ACI Special Publication. SP 267–3*, 21–34.
4. Yazdanbakhsh, A., Grasley, Z., Tyson, B., & Abu Al-Rub, R. (2010). Distribution of carbon nanofibers and nanotubes in cementitious composites. *Transportation Research Record: Journal of the Transportation Research Board, 2142*(2), 89–95.
5. Stynoski, P., Mondal, P., Wotring, E., & Marsh, C. (2013). Characterization of silica-functionalized carbon nanotubes dispersed in water. *Journal of Nanoparticle Research, 15*(1), 1–10.
6. Konsta-Gdoutos, M. S., Metaxa, Z. S., & Shah, S. P. (2010). Highly dispersed carbon nanotube reinforced cement based materials. *Cement and Concrete Research, 40*(7), 1052–1059.
7. Yazdanbakhsh, A., & Grasley, Z. (2014). Utilization of silica fume to stabilize the dispersion of carbon nanofilaments in cement paste. *Journal of Materials in Civil Engineering, 26*(7), 06014010.

A New Class of Carbon Nanotube: Polymer Concrete with Improved Fatigue Strength

Sherif M. Daghash, Rafi Tarefder, and Mahmoud M. Reda Taha

Abstract Polymer concrete (PC) has been used successfully as bridge deck overlays and in machine foundations. In such applications, PC is subjected to cyclic loading and thus is prone to fatigue failure. In this paper, we introduce a new method for improving the fatigue strength of PC using carbon nanotubes. To overcome the challenge of fatigue testing of concrete, a four point flexural displacement control test borrowed from Asphalt standards in AASHTO was used. In this test the displacement was ramped up from zero to 1.2 mm then the PC specimen ($25 \times 25 \times 200$ mm) was cycled between zero and 1.2 mm using a sinusoidal signal with a frequency of 0.5 Hz. Guided by AASHTO specifications, failure is defined as 50 % reduction in stiffness. Four PC mixes were tested. These mixes incorporated neat epoxy, and epoxy including 0.5, 1.0 and 1.5 % multi-walled carbon nanotubes (MWCNTs) by weight of epoxy resin. Damage in PC due to fatigue was evaluated with time. The experiments showed the ability of MWCNTs to improve fatigue strength by 61 and 100 % for PC incorporating 0.5 and 1.0 % MWCNTs respectively. PC incorporating 1.5 % MWCNTs reached 50,000 cycles without experiencing fatigue failure showing improvement above 520 %. Microstructural analysis of PC was conducted using scanning electron microscope (SEM) to explain the ability of MWCNTs to significantly improve fatigue strength of PC.

Keywords Polymer • Concrete • Bridge • Overlays • Cyclic loading • Fatigue • Strength • Carbon nanotubes • Multi-wall • Microstructure

S.M. Daghash
Department of Civil Engineering, University of Virginia, Charlottesville, VA, USA

R. Tarefder • M.M.R. Taha (✉)
Department of Civil Engineering, University of New Mexico, Albuquerque, NM, USA
e-mail: mrtaha@unm.edu

K. Sobolev, S.P. Shah (eds.), *Nanotechnology in Construction*,
DOI 10.1007/978-3-319-17088-6_37

1 Introduction

Polymer concrete (PC) is defined as a hardened composite produced by mixing a polymer resin or a monomer with aggregate without adding any Portland cement. In the 1950s, PC was first commercially used in the United Stated in order to produce synthetic marble and to manufacture architectural façade panels. It was then developed through the 1970s and the 1980s. This development significantly improved PC and made it available for commercial production. Over the last 20 years, PC has gained remarkable acceptance in infrastructure applications due to its enhanced mechanical and chemical properties compared with conventional concrete. PC has also advantages of easy placement, fast curing, and rapid setting time [1]. PC has been used in many transportation applications [2, 3] and as overlays made of polymer binder system and filler powder without coarse aggregate. Aggregate might be broadcast on top of PC overlay to increase the overlay friction necessary for traffic. PC bridge overlays experience millions of loading and unloading cycles due to traffic. These cycles cause fatigue which is observed in stiffness degradation over time followed by cracking and potentially fracture. In PC overlays, cracks would initiate between the overlay and the substrate due to debonding between the two materials. This cracking might also initiate due to temperature effects. Under continuous cyclic loading, such debonding cracks propagate horizontally resulting in complete debonding between the overlay and the substrate. Moreover, such cracks can propagate vertically through the overlay causing overlay deterioration.

Fatigue life of PC decreases with increasing the maximum stress or/and the stress range [4]. Wheat et al. [5] investigated fatigue behavior of Portland cement concrete beams overlaid by epoxy PC. The composite beams survived 2 million load cycles without significant loss of stiffness or delamination. Nano particles such as nanoclay, carbon nanotubes, and carbon nanofibers have been recently examined to improve polymer materials. Furthermore, the mechanical properties including tensile strength and strain of latex modified concrete were reported to be significantly improved at low Carbon Nanotubes (CNTs) content [6]. CNTs are tabular structure made from concentrically rolled single or multiple graphite sheets. CNTs were first introduced as single-walled carbon nanotubes (SWCNTs) and proved to have superior mechanical properties, but SWCNTs showed to be significantly expensive. High-purity SWCNTs are synthesized and grown using thermal Chemical vapor deposition (CVD) at a growth temperature of and above 700 °C [7]. Multi-walled carbon nanotubes (MWCNTs) appeared later as a cheaper alternative form of CNTs. Using the chemical vapor deposition (CVD), MWCNTs are synthesized at a relatively low temperature of 450 °C compared to 700 °C for SWCNTs [8]. To improve the chemical bond between CNTs and polymer matrix, CNTs need to be functionalized to react with the polymer matrix. Swain et al. [9] showed that allylester or silane functionalized MWCNTs improved polymer nanocomposites.

In this paper, we present a new class of PC with significantly improved fatigue strength. The new PC class is produced by incorporating Multi-Walled Carbon Nano Tubes (MWCNTs) in the polymer mix binder prior to concrete mixing. The mixes are made of low modulus polysulfide epoxy typically used to produce polymer concrete overlays for bridge decks. In order to ensure the chemical bond between MWCNTs

and epoxy, MWCNTs functionalized with COOH groups were used. The epoxy resin contains reactive epoxy groups (C-O-C) at the two ends of the polymer chain. Similarly, the hardener typically contains amino groups (NH_2). The proposed functionalized MWCNTs contain carboxyl groups (COOH) which reacts with the epoxy groups in the resin and become part of the chemical structure of the epoxy polymer system.

2 Methods

The epoxy used in this research consisted of two components, Bisphenol A/ Epichlorohydrin epoxy resin, and Phenol based epoxy hardener. Epoxy resin and epoxy hardener were mixed by a ratio of 2:1. Neat epoxy was reported to have density of 1,054 kg/m^3 and pot life of 15–30 min at 21 °C. The epoxy was then mixed with a filling powder of crystalline silica (quartz), and ceramic microspheres. The epoxy was used as supplied to produce neat PC overlay or mixed with MWCNTs supplied by Cheap Tubes, Inc. The MWCNTs were functionalized with carboxyl (COOH) groups and were produced using Catalysed Chemical Vapour Deposition (CCVD) technique with purity greater than 95 % by weight. The MWCNTs used have a 20–30 nm outer diameter and 5–10 nm inner diameter with an aspect ratio of 1,000.

Four mixes were prepared and examined in this research. The mixes were neat polymer concrete (PC) overlay without MWCNTs; and three other PC overlay mixes incorporating 0.5, 1.0, and 1.5 % MWCNTs by weight of the epoxy resin incorporating 1.44, 2.88, and 4.32 (kg/m^3), respectively. The PC mix included resin: 288 (kg/m^3), hardener: 128 (kg/m^3) and powder of 1,570 (kg/m^3). For the neat PC mix, the required amount of resin and hardener were mixed together for 2–3 min using a low speed mixer following ASTM C881 [10], after which silica filling powder was added. Mixing continued using standard concrete mixer for 2–3 min until the mixture was uniform. For the three other mixes, MWCNTs were added to the required amount of the resin, the mix was stirred for 2 h at 110 °C using magnetic stirring. This relatively high mixing temperature was used to reduce the resin viscosity to improve the dispersion of MWCNTs. The mix was then sonicated for 2 additional hours at 65 °C. The MWCNTs-epoxy resin nanocomposite was left to reach room temperature and then mixed with the hardener for 2–3 min. The required powder was added and mixing continued for 2–3 additional minutes until the PC mixture was uniform. All PC specimens were left to cure at 22 °C and 50 % relative humidity for 7 days as recommended by ACI committee 548 [1].

The fatigue test was four-point bending fatigue test performed following the guidelines of determining the fatigue life of compacted hot-mix asphalt subjected to flexural stresses as reported by AASHTO standards T321-07 [11]. Displacement was ramped up from zero to 1.2 mm in 2 min then test specimens were cycled between 0.0 and 1.2 mm using a sinusoidal waveform with a frequency of 0.5 Hz. From each mix, five prisms with dimensions of $25 \times 25 \times 200$ mm were prepared in order to be tested. The test set-up was designed to hold two LVDTs at the centre line of the tested specimen in order to record the displacement. Through the test, time, load, and displacement were recorded using standard data acquisition system with sampling rate of 10 Hz for all tests. In each test, the specimen flexural rigidity and

fatigue damage defined as the ratio between the losses in flexural rigidity at any cycle to the initial flexural rigidity were calculated using the following equations for four-point bending setup:

$$EI(i) = \left(\frac{5}{288}\right) \times \frac{\Delta P(i) \times L^3}{\Delta \delta(i)} \tag{1}$$

$$D(i) = 1 - \frac{EI(i)}{EI(0)} \tag{2}$$

where *EI(i)* is the specimen flexural rigidity at the ith cycle, *E* is the modulus of elasticity, *I* is the cross sectional second moment of inertia, $\Delta P(i)$ is the difference between maximum and minimum loads at the ith cycle, $\Delta\delta(i)$ is the corresponding difference between displacements, *L* is the span length of 175 mm, *D(i)* is the fatigue damage in %, and *EI(0)* is the initial flexural rigidity at the 50th load cycle according to AASHTO standard [11]. Failure was considered to occur when the specimen experienced 50 % reduction in its initial flexural rigidity.

3 Results and Discussion

As mentioned earlier, force and mid-span displacement were recorded. Failure time is defined as the time where PC stiffness reached 50 % of its initial stiffness. Figure 1a shows the variation of the number of cycles to failure for the four mixes. While the mean failure of neat specimens occurred at 8,064 cycles, the 0.5 and 1.0 % MWCNTs specimens recorded mean failure at 12,985 and 16,129 cycles with increase of 61 and 100 %, respectively. The 1.5 % MWCNTs specimens reached 50,000 cycles without failure recording mean increase in fatigue number of cycles to failure in excess of 520 %. Statistical analysis using student *t-test* proved all the improvement of PC fatigue to be significantly different.

We define damage here as the onset of loss of stiffness that takes place prior to crack initiation. From Fig. 1b, damage evolution can be divided into three distinct stages. The first stage is the primary damage stage characterized by a linear (or logarithmic) relationship with high slope. The second stage is the secondary or steady state damage with a relatively low slope compared with the primary damage slope

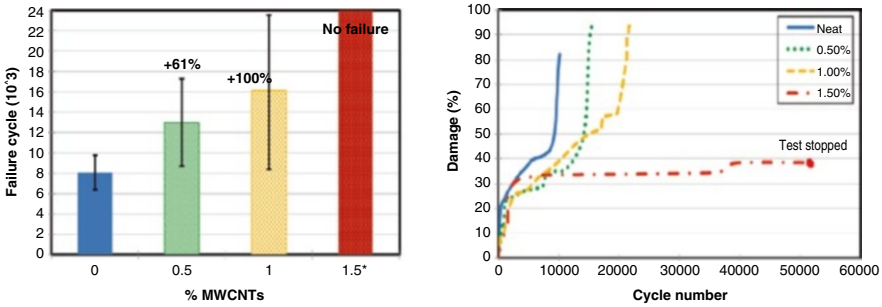

Fig. 1 Effect of MWCNTs on (**a**) fatigue strength (**b**) damage in PC

and the third stage is the tertiary damage with significantly high slope leading to fracture. It can be observed that the primary damage extended to approximately 23, 25, and 32 % in PCs incorporating 0.5, 1.0, and 1.5 % MWCNTs respectively compared with 20 % for neat PC specimens. Moreover, the steady state damage extended to approximately 13,000 and 20,000 cycles in the case of 0.5 and 1.0 % MWCNTs, respectively compared with approximately 10,000 cycles for the neat PC specimens. Furthermore, higher level of final damage, 95 % in the case of 0.5 and 1.0 % MWCNTs, was observed compared with 82 % damage in neat specimens. While this final damage took place after 10,000 cycles for neat specimens, it occurred after 15,000 and 23,000 cycles with 0.5 and 1.0 % MWCNTs, respectively. In the case of 1.5 % MWCNTs, the total damage was limited to approximately 35 % up to 38,000 cycles and to approximately 40 % up to 50,000 cycles. It is important to state that no tertiary damage was experienced and no failure was observed up to 50,000 cycles for PC incorporating 1.5 % MWCNTs. It is obvious from the fatigue test results that incorporating MWCNTs significantly improved damage resistance of PC overlays under cyclic loading.

Fatigue damage evolution in PC specimens can be related to two factors; the ability of PC to resist crack initiation and the ability of PC to resist cracks propagation. Under cyclic loading, damage would accumulate in the specimen through primary and steady state damage zones. At the end of the steady state damage, micro-cracks would be initiated. In the tertiary damage zone, these cracks would propagate inside the overlay resulting in fracture of the overlay as in Fig. 1b.

4 Microstructural of Epoxy-MWCNTs Nanocomposite

Fracture surfaces of epoxy-MWCNTs specimens incorporating 1.0 % MWCNTs were investigated by Scanning Electron Microscope (SEM). A Hitachi S-5200 Nano SEM was used. The SEM apparatus has magnification rate ranging from 100× to 2,000,000× with a guaranteed resolution of 1.7 nm at 1 Kv and 0.5 nm at 30 Kv. Figure 2 shows SEM images of MWCNTs (indicated by yellow arrows) as longitudinal tubular particles observed at the fracture surface of PC.

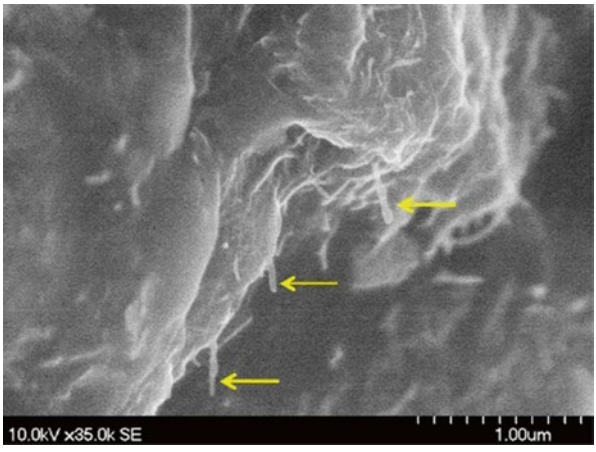

Fig. 2 SEM images of showing MWCNTs at PC crack surfaces

5 Conclusions

A new generation of polymer concrete was produced by incorporating MWCNTs in low modulus polysulfide epoxy with fine aggregate to produce PC overlays. Incorporating MWCNTs significantly improved PC overlay resistance to damage propagation under cyclic loading. Moreover, PC specimens with MWCNTs failed at higher total number of fatigue cycles compared with neat PC specimens. The increase in PC fatigue strength (defined as the numbers of cycles corresponding to 50 % loss in stiffness) was significant and exceeded 520 % for PC specimens incorporating 1.5 % MWCNTs compared neat PC specimens. Furthermore, the number of cycles to fracture was also significantly improved. No failure was observed in PC incorporating 1.5 % MWCNTs. SEM images showed the MWCNTs bridging the microcracks which allowed PC to continue carrying loads. It is evident that MWCNTs can significantly improve fatigue strength of PC overlays.

Acknowledgements This work was supported by Southern Plains Transportation Center (SPTC). The authors greatly acknowledge this support.

References

1. ACI Committee 548 (1996) *548.6R-96: Polymer concrete-structural applications state-of-the-art-report* (reported by ACI 548 Polymers and Adhesives for Concrete). Farmington Hills: American Concrete Institute.
2. Zhao, L., Karbhari, V. M., Hegemier, G. A., & Seible, F. (2004). Connection of concrete barrier rails to FRP bridge decks. *Composites: Part B, 35*(4), 269–278.
3. Lopez-Anido, R., Gangarao, H. V. S., Pauer, R. J., & Vedam, V. R. (1998). *Evaluation of polymer concrete overlay for FRP composite bridge deck*. Proceedings of the Marketing/Technical/Regulatory Sessions. EXPO '98, Composites Institute, New York, 13-F/1-6.
4. Dowling, N. E. (2007). *Mechanical behavior of materials: Engineering methods for deformation, fracture, and fatigue* (3rd ed.). Upper Saddle River: Prentice-Hall.
5. Wheat, D. L., Fowler, D. W., & Al-Negheimish, A. I. (1993). Thermal and fatigue behavior of polymer concrete overlaid beams. *Journal of Materials in Civil Engineering, 5*(4), 460–477.
6. Soliman, E., Kandil, U. F., & Reda Taha, M. M. (2012). The significance of carbon nanotubes on styrene butadiene rubber (SBR) and SBR modified mortar. *Materials and Structures, 45*, 803–816.
7. Sharmaa, R., & Iqbal, Z. (2004). In situ observations of carbon nanotube formation using environmental transmission electron microscopy. *Applied Physics Letters, 84*(6), 990–992.
8. Ting, J. H., Lyu, J. Y., Huang, F. Y., Li, T. L., Hsu, C. L., & Liu, C. W. (2008, July 13–16). *Synthesis of single-wall carbon nanotubes by atmospheric thermal CVD* (pp. 157–160). The University/Government/Industry Micro/Nanotechnology (UGIM) Symposium. Louisville: University of Louisville. http://louisville.edu/ugim.
9. Swain, S., Sharma, R. A., Patil, S., Bhattacharya, S., Gadiyaram, S. P., & Chaudhari, L. (2012). Effect of allyl modified/silane modified multiwalled carbon nano tubes on the electrical properties of unsaturated polyester resin composites. *Transactions on Electrical and Electronic Materials, 13*(6), 267–272.
10. ASTM C881–13 (2014) *ASTM C881/C881M – 14 standard specification for epoxy-resin-base bonding systems for concrete active standard ASTM C881/C881M* (Vol. 04.02). Developed by Subcommittee: C09.25. West Conshohocken: ASTM International.
11. AASHTO T 321–07 (2007) *Standard method of test for determining the fatigue life of compacted hot-mix asphalt (HMA) subjected to repeated flexural bending*. Washington, DC: American Association of State and Highway Transportation Officials.

Part VI
Modeling and Simulation

Atomistic Study of the Mechanism of Carbonation

Andreas Funk and Reinhard Trettin

Abstract Calcium-rich clinker forms CSH-phases and domains of portlandite, which protect reinforcement as well as the cement itself from acidic attacks because of the increased pH value of these hydroxide-rich regions. Carbonation of portlandite reduces the pH value and thus weakens this protective effect. The mechanisms of carbonation are not fully understood yet. For a true mechanistic understanding it is necessary to understand the atomistic processes occurring during carbonation. This process is of great importance for construction chemistry, energy storage and even in astrochemistry. Based upon atomistic simulations we show and explain the reaction mechanisms of the carbonation of portlandite including all intermediate structures and transition states.

Keywords Carbonation • Simulation • Surface reactions • Reaction mechanisms • Density functional theory

1 Introduction

Carbonation of calcium hydroxide is a process of great technical importance. It leads to hardening of lime-based inorganic binders (Eq. 1), i.e., lime mortars, which gives the chemical and physical properties necessary for the application as building material [1].

$$\mathrm{Ca(OH)_2 + CO_2 \rightarrow CaCO_3 + H_2O} \tag{1}$$

Cement-based building materials, i.e., concrete, are influenced by carbonation in different ways. Most important for the sustainability of concrete is a reduction of the pH value within the pore solution, a result of the formation of carbonate which leads

A. Funk (✉)
Institut für Bau- und Werkstoffchemie, Universität Siegen, Siegen, Germany

Institut für Konstruktiven Ingenieurbau, Universität Kassel, Kassel, Germany
e-mail: andreas.funk@uni-kassel.de

R. Trettin
Institut für Bau- und Werkstoffchemie, Universität Siegen, Siegen, Germany

K. Sobolev, S.P. Shah (eds.), *Nanotechnology in Construction*,
DOI 10.1007/978-3-319-17088-6_38

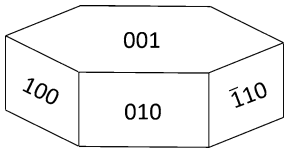

Fig. 1 Crystal surfaces of portlandite

Table 1 DFT settings

Functional	Approach	PW cutoff	Pseudo-potentials	Gaussian basis	Dispersion	SCF convergence
revPBE	Gaussian and plane waves (GPW)	500 Ry	Norm-conserving	double-ζ (DZVP)	Grimme D3	10^{-8} E_h
[3, 4]	[5]		[6–8]	[9]	[10]	

Table 2 Parameters of the orthogonal simulation cells

Surface	Periodic dimensions	Length in x	Length in y	Length in z	Surface groups	Crystal layers
(001)	x, y	14.3560 Å	12.4327 Å	55.0000 Å	4×4	6
(100)	y, z	55.0000 Å	18.6490 Å	19.6440 Å	4×4	6

Table 3 Minimal accuracy of the optimizations

Optimization	Method	RMS gradient	RMS displ.	Maximum gradient	Maximum displ.	Energy
Minimum	BFGS	0.30 mE_h/a_0	0.0015 a_0	0.45 mE_h/a_0	0.0030 a_0	0.1 kcal/mol
TS	NEB	0.30 mE_h/a_0	0.0015 a_0	–	–	1 kcal/mol

to dissolution of passivating oxide layers. This renders the passivation insufficient to prevent oxidation of the reinforcement in concrete and leads to a reduction of the service life time of concrete [1, 2].

The reaction mechanism of carbonation with atomistic proof has not been carried out yet. Especially a model for the factors influencing this reaction at atomistic scale is missing. In this study we present simulations of the carbonation of portlandite at atomic scale using density functional theory (DFT). The results include the carbonation of two different crystal surfaces, the basal (001) surface and the (100) surface as representative for the manifold of six prism faces (cf. Fig. 1).

2 Details of the Computations

As reactants we have used a single carbon dioxide molecule, a cluster of a single carbon dioxide molecule accompanied by four water molecules, and a cluster of carbonic acid accompanied by three water molecules, respectively. DFT settings are given in Table 1 and the parameters of the simulation cell are given in Tables 2 and 3.

All minima on the potential-energy surface were optimized by a quasi-Newton approach and transition states (TS) were optimized using nudged elastic band (NEB) methods [11–13].

3 Results and Discussion

Several structures and reaction paths were computed, presented in this section in figures including the energetics of the reaction paths. Activation enthalpies ΔH_a are given underneath the arrows of the equations, enthalpies of adsorption ΔH_{ad} are relative to the free reacting cluster, and enthalpies of formation ΔH_r are given with respect to the previous structure, i.e., the last stable intermediate reacting to the respective product.

The two crystal surfaces were obtained by cutting an ideal crystal structure properly and subsequent optimization. Both surfaces show different behavior under optimization. The (001) surface shows no significant structural changes, while the (100) surface gets the hydroxide groups re-ordered so that they point outwards the crystal.

In absence of water the reaction occurs *via* direct collision between carbon dioxide and hydroxide. With four water molecules per carbon dioxide molecule it is possible to form a small cluster of four water molecules [14] or a cluster of carbonic acid with three water molecules [14]. The first one reacts similar to the case in absence of water, whereas the second one reacts by two subsequent proton transfers. The structural differences between the (001) surface (cf. Fig. 2) and the (100) surface (cf. Fig. 3) become obvious. Especially the strong barrier for bicarbonate formation in the (001) surface is completely reduced in the (100) surface. The reason is in the arrangement of the hydroxide ions in the surface. In the basal surface, the hydroxides are in parallel arrangement and have to be rotated to allow for a collision with carbon dioxide. This is electrostatically unfavorable. In contrast, hydroxide is already in an optimal position for collision in the prism surface.

Water has a similar effect onto carbonation in both surfaces. The catalytic water molecules form a supporting hydrogen bond network with surface and reactants, hence stabilizing both, products and transition states. This can be seen clearly in Figs. 2 and 3. At the same time, if water adsorbs in between reactant and surface it adds to the reaction barrier as carbon dioxide has to pass through the water layer. Although this gives only additional 6–8 kcal/mol it may put the picture in favor of carbonic acid as reactant if the entire surface is covered by water layers. In such a case, carbonic acid can easily react upon adsorption in a barrierless way by a fast proton transfer reaction, neutralizing a hydroxide ion and forming bicarbonate, followed by a second proton transfer to form carbonate.

Table 4 Colors for different species in the figures

Ca	O	H	C	Catalytic H_2O	Non-reactive atoms	H-bonds
Blue	Red	White	Dark gray	Green	Gray shadows	Light blue

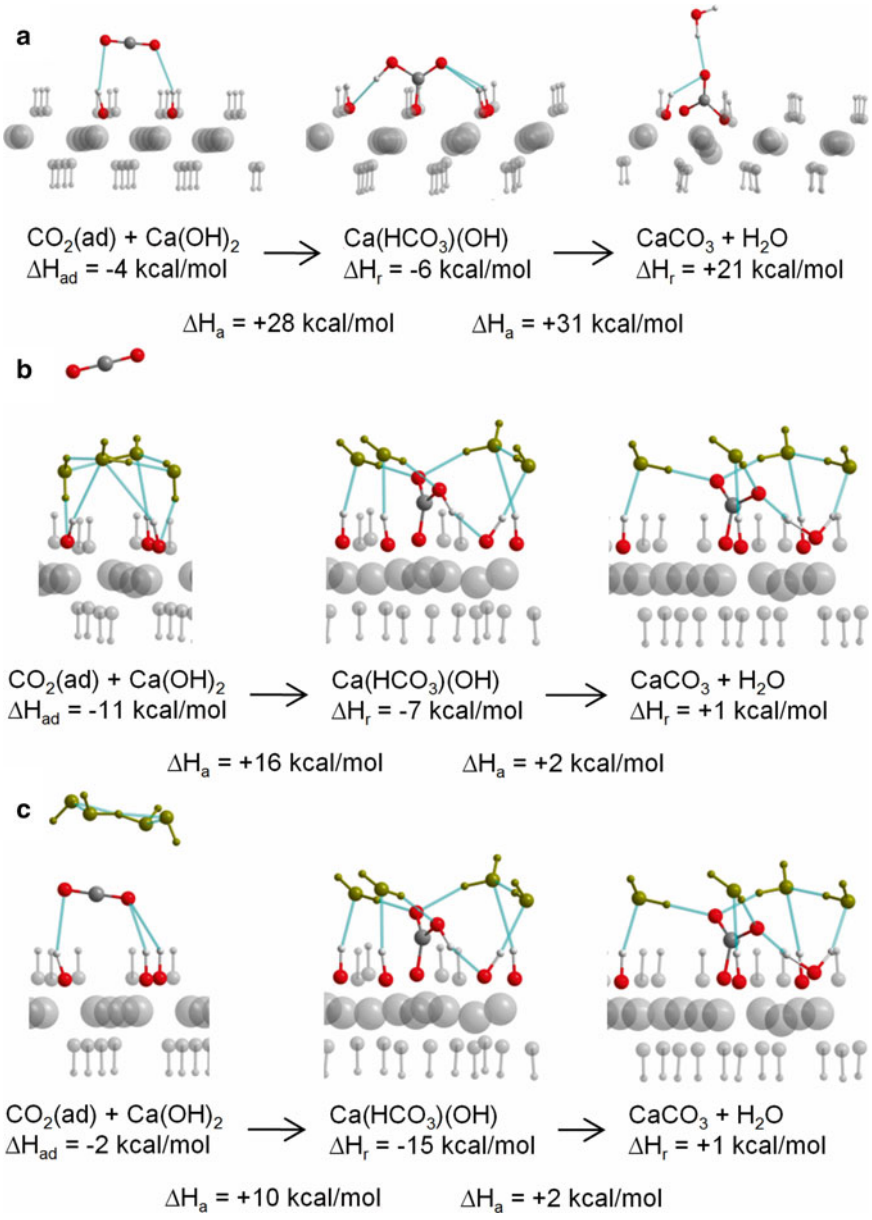

Fig. 2 Structures and reaction path from adsorbed carbon dioxide to calcium carbonate in the (001) surface of portlandite (**a**) in absence of water, (**b**) with four catalytic water molecules per CO_2 molecule in between reactant and surface, and (**c**) with four catalytic water molecules per CO_2 molecule above the reactant

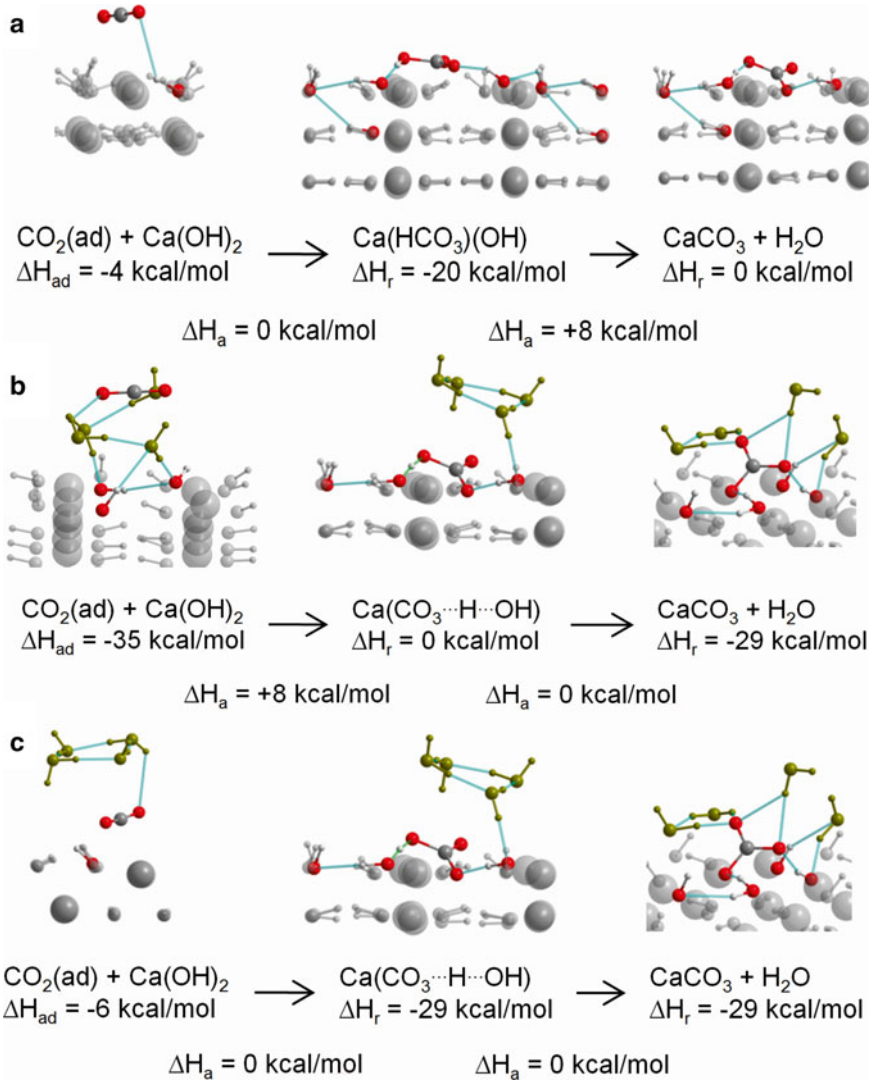

Fig. 3 Structures and reaction path from adsorbed carbon dioxide to calcium carbonate in the (100) surface of portlandite (**a**) in absence of water, (**b**) with four catalytic water molecules per CO_2 molecule in between reactant and surface, and (**c**) with four catalytic water molecules per CO_2 molecule above the reactant

4 Summary and Conclusion

The carbonation of portlandite has been studied in detail using DFT with dispersion corrections. In agreement with experimental findings it has been found that the (100) surface as representative of the prism faces of portlandite crystals is more susceptible to carbonation than the basal (001) surfaces. The reason for this different reactivity is in the different arrangement of hydroxide ions in the surface and the resulting higher surface energy of the prism faces.

Furthermore, it has been proven by our simulations that water acts as catalyst for carbonation. The reason for the catalytic activity is, like in the catalytic activity in carbonic acid formation, the provision of a stabilizing network of hydrogen bonds. This stabilizes both, the products and the transition states. In general it can be stated that carbonation does not necessarily require carbonic acid, but water is necessary at least to form carbonate. In case of too low amounts of water the reaction may stop at bicarbonate formation, which can lead to increased solubility when more water is added subsequently. Furthermore, carbonic acid will probably be the more favorable reactant when portlandite is covered with water, as water layers may prevent carbon dioxide to penetrate into the surface.

References

1. Hewlett, P. C. (2004). *Lea's chemistry of cement and concrete* (4th ed.). Oxford: Elsevier Butterworth-Heinmann.
2. Parrott, L. J. (1994). A study of carbonation-induced corrosion. *Magazine of Concrete Research, 46*(166), 23–28. doi:10.1680/macr.1994.46.166.23.
3. Perdew, J. P., Burke, K., & Ernzerhof, M. (1996). Generalized gradient approximation made simple. *Physical Review Letters, 77*(18), 3865–3868. doi:10.1103/PhysRevLett.77.3865.
4. Zhang, Y., & Yang, W. (1998). Comment on "generalized gradient approximation made simple". *Physical Review Letters, 80*(4), 890. doi:10.1103/PhysRevLett.80.890.
5. Lippert, G., Hutter, J., & Parrinello, M. (1997). A hybrid Gaussian and plane wave density functional scheme. *Molecular Physics, 92*(3), 477–488. doi:10.1080/002689797170220.
6. Goedecker, S., Teter, M., & Hutter, J. (1996). Separable dual-space Gaussian pseudopotentials. *Physical Review B, 54*(3), 1703–1710. doi:10.1103/PhysRevB.54.1703.
7. Hartwigsen, C., Goedecker, S., & Hutter, J. (1998). Relativistic separable dual-space Gaussian pseudopotentials from H to Rn. *Physical Review B, 58*(7), 3641–3662. doi:10.1103/PhysRevB.58.3641.
8. Krack, M. (2005). Pseudopotentials for H to Kr optimized for gradient-corrected exchange-correlation functionals. *Theoretical Chemistry Accounts, 114*(1–3), 145–152. doi:10.1007/s00214-005-0655-y.
9. VandeVondele, J., & Hutter, J. (2007). Gaussian basis sets for accurate calculations on molecular systems in gas and condensed phases. *Journal of Chemical Physics, 127*(11), 114105. doi:10.1063/1.2770708.
10. Grimme, S., Antony, J., Ehrlich, S., et al. (2010). A consistent and accurate ab initio parametrization of density functional dispersion correction (DFT-D) for the 94 elements H-Pu. *Journal of Chemical Physics, 132*(15), 154104. doi:10.1063/1.3382344.

11. Henkelman, G., & Jónsson, H. (2000). Improved tangent estimate in the nudged elastic band method for finding minimum energy paths and saddle points. *Journal of Chemical Physics, 113*(22), 9978. doi:10.1063/1.1323224.
12. Henkelman, G., Uberuaga, B. P., & Jónsson, H. (2000). A climbing image nudged elastic band method for finding saddle points and minimum energy paths. *Journal of Chemical Physics, 113*(22), 9901. doi:10.1063/1.1329672.
13. Trygubenko, S. A., & Wales, D. J. (2004). A doubly nudged elastic band method for finding transition states. *Journal of Chemical Physics, 120*(5), 2082. doi:10.1063/1.1636455.
14. Nguyen, M. T., Matus, M. H., Jackson, V. E., et al. (2008). Mechanism of the hydration of carbon dioxide: Direct participation of H2O versus microsolvation. *Journal of Physical Chemistry A, 112*(41), 10386–10398. doi:10.1021/jp804715j.

A Real Microstructural Model for Cement Concrete Modeling

Yang Lu, Stephen Thomas, and Edward J. Garboczi

Abstract A real multiphase microstructure, Anm model, with irregular shape particles has been proposed. The Anm model places multiple irregular shape particles into a pre-defined empty box according to the real parking density to build up particles embedded in matrix material model in all scales from nano to macro. However, the packing accuracy and efficiency need to be improved, since the original Anm model's algorithms has limited function and relative low parking efficiency. Furthermore, it cannot control the inter-particle distance. In this paper, we upgraded the initial algorithms by the following innovations: (1) integrated a new contact function, extending overlap box (EOB) to make the contact detection more accurately and efficiently; (2) the particle parking algorithm has been implemented to associate multiple aggregate shape database with each size bin; (3) an uniform thickness shell has been put around each parking particle, which can make the inter-particle distance customizable when we park nano-scale particles considering possible charge interactions between individual nano-particles.

Keywords Irregular shape nano-particles • Anm model • Extending overlap box • Uniform thickness shell

Y. Lu (✉)
Civil Engineering Department, Boise State University, Boise, ID 83725-2060, USA
e-mail: yanglufrank@boisestate.edu

S. Thomas
Material Science & Engineering Department, Boise State University,
Boise, ID 83725-2090, USA
e-mail: stephenthomas1@u.boisestate.edu

E.J. Garboczi
Applied Chemicals and Materials Division, National Institute of Standards and Technology,
Boulder, CO 80305-647, USA
e-mail: edward.garboczi@nist.gov

K. Sobolev, S.P. Shah (eds.), *Nanotechnology in Construction*,
DOI 10.1007/978-3-319-17088-6_39

1 Introduction

Concrete is primarily composed of coarse aggregates, fine aggregates (sand) and cement paste. Aggregate characteristics such as density and uniformity of aggregate packing and the corresponding particle size distribution have been found to play a paramount role in strength and behavior of these concretes [1]. The proper selection of aggregates can minimize the water and cementitous materials contents needed to ensure adequate workability. Dense particle packing reduces paste consumption, thereby also providing significant cost savings [2]. Models for predicting concrete compressive strength also base their validation on producing concrete mixtures of optimum packing density [3]. An in-depth understanding of the packing of aggregates in concrete is essential in optimizing the mix composition.

Existing concrete microstructural models of particles embedded in matrix materials are only represented by regular shape particles like spheres, ellipsoids, or multi-faceted polyhedrons. However, the real particle shapes are more complex and sometimes play an essential role of macroscale properties. Spherical Harmonics has been employed to characterize the irregular shape of particles from nano to continuum scale numerically. Preceding research proposed a virtual concrete and mortar mesostructure model, entitled Anm model [4], using the idea of representing actual shapes of aggregate particles by spherical harmonic series characterized from X-ray CT scanned digital images. In this model, the irregular shaped particles are randomly arranged in a cubic box where the packing algorithm is driven by particle size distribution (PSD) and packing density (PD). The PD is defined as the volume fraction of the aggregates within the simulation box. The particles are parked one at a time in decreasing order of size. Each particle is first assigned a random location within the container and checked for contact with any already parked particles. If an overlap is detected, a new location is attempted. If the particle could not be parked using a maximum number of locations, the particle shape is then randomly rotated for a predefined maximum number of attempts to find a location without overlap with other particles. If rotating the particle did not result in successful parking, it is rescaled within the current sieve size range. If the rescaling did not result in successful parking, a predefined number of alternate shapes are used to try and achieve successful parking. If none of these attempts were successful in parking the particle from the current sieve, the next sieve is selected and this process is repeated.

Recently, nanotechnology application in construction has been focusing on the investigation of the structure of cement based materials, and their binding and fracture mechanisms. Experimental results demonstrate nanoparticles (nanosilica and nano-SiO_2) to be very effective additives to for improving concrete strength, crack-resistance, and durability. The formed composite nanostructure leads to very high strength and toughness of the shell due to interlocking of nano-blocks of calcium carbonate responsible for the crack arrest and dissipation of energy. The relatively small quantities of nanosized materials are sufficient to improve the performance of nanocomposites. Well-dispersed nanoparticles improve the segregation resistance and workability of the system. However, well-graded nanoparticles' irregular size, shape, and gradation cannot be characterized and designed by experimental

Fig. 1 Packing star shaped particles to model material mesostructure of mortar or concrete

alone, because of the agglomeration effect in nano-scale. The proposed Anm model provides an alternative to simulate, design, and predict the microstructure formed by nanoparticles from real size and shape. The particle shapes included in the Anm database are dimensionless, which makes it customizable to nano or micro for modeling objectives. Anm model can be employed to generate microstructure for optimizing the nanoscale mechanical, chemical, and physical behaviors, such as (1) nano-particles fill the voids between cement grains; (2) well-dispersed nano-particles act as centers of crystallization of cement hydrates; (3) improving the structure of the aggregates' contact zone, resulting in a better bond between aggregates and cement paste.

The Anm model can use any arbitrary particle size distribution, described as a sieve analysis or sieve range. A certain volume fraction of the particles to be placed is located in each sieve size (e.g., 1–2 mm). Each sieve size is assigned a fraction of the total particle size distribution, such that the sum of volumes assigned to all the sieve ranges add up to the total particle size distribution. In the Anm model, each sieve range volume must be occupied before placing particles from the next sieve range, starting from the largest sieve range. Figure 1 is the visualization of the progress of particle packing in the container. In this illustration, three sieve ranges are assigned in the order from coarse to fine.

In this paper, we developed two algorithms to improve the Anm model. (1), integrating a new, faster, and more accurate particle contact algorithm, titled extent overlap box (EOB). Note that EOB algorithm is used to check the overlap between two particles more accurately and efficiently than the initial contact function. (2), An algorithm that can coat a star-shaped particle with a uniform-thickness shell [5] has been integrated in the virtual concrete model. The space between the two spheres has a uniform thickness t. For irregular shapes, making the coating of uniform thickness at all points of the particle surface is not easy. This mathematical problem has been solved for star-shaped particles with a spherical harmonic series representation. Henceforth, this uniform-thickness shell shall simply be referred to as "shell" in this paper. In addition, the ability to place shells around each particle means that the Euclidean distance from each particle's surface at every point of the surface can be known, so that processes which are a function of distance from a particle surface can be more easily simulated. The rest of this paper will address the effects of using the new particle contact method and shell in the concrete microstructure model.

In Sect. 2 we discuss integration of the new contact function algorithm into the Anm model and adding a shell to the irregular shaped particles. Section 3 illustrates some results obtained with the improved Anm model from multi-sieve ranges. Section 4 concludes the discussions.

2 Methodologies Development

2.1 Integration of New Contact Search Algorithm

During the particle parking process, the critical step is to check if the new particle has contact with the already parked particles. Two spherical objects cannot overlap if the distance between their center points is more than the sum of their radii. In the case of irregularly shaped particles, the method for detecting contact is more complex. Previously, an analytical method, which solved nonlinear equations using the Newton Raphson (NR) iteration method, was employed to detect contact between two spherical harmonic particles [4]. The NR method was time consuming due to its iterative approach and if the searching tolerance was set too high, small overlaps could occur for some irregular shape particles even when the algorithm indicated that they were not overlapping.

The new method that has been added to the Anm model is called the Extent Overlap Box (EOB) search algorithm [5]. A three-step process is followed in this algorithm with increasing level of rigor to search for a contact between the two particles. The goal is to limit the most rigorous contact search algorithm to particles with very minimal overlap. In the first step, the EOB algorithm attempts to search for an overlap along the line that connects the center point of the two particles. For two irregular particle shapes, we calculate the radius of the particles along the direction given by the line joining the two center points. If the sum of the radii is more than the length of this line, the particles are marked as overlapping. If they do not overlap along the line of centers, the extent box for both the particles are computed and an overlap in the extent boxes is identified, if any exists. It is noted that each particle has an extent box. The extent box is defined as a rectangular box surrounding the particle and touching it right at the surface. It is the minimum size box that can hold the particle.

If the extent boxes of two particles do not overlap each other, there is zero probability that the particles can overlap. But, if the two extent boxes do overlap, then the particles themselves can overlap only within the intersection of the extent boxes, which is itself a rectangular box called the extent overlap box (EOB). The EOB is the only volume that needs to be considered further to determine overlap or non-overlap. The EOB contact algorithm [5] is faster than the Newton Raphson method [4] owing to the fact that only the surface points on one particle that are also inside the EOB are checked for contact with the other particle. It is more accurate than the Newton Raphson method because false negatives were not seen in an extensive series of visual checks.

2.2 Integration of the Uniform-Thickness Shell Algorithm into Anm

The uniform-thickness shell can be used to simulate the interfacial transition zone (ITZ) around aggregate particles in mortar and concrete. Usually, crack development within normal portland cement concrete takes place inside the ITZs [6]. Results from [7] showed that the ITZ was found to be quite heterogeneous, because higher concentration of large voids and cracks in the ITZ was observed. It was noted that the connectivity of the weaker areas such as large voids and cracks along the interface governs failure.

A shell of thickness t added to a sphere with radius R has a radius R' = R + t because the surface normal of a point on the sphere surface is parallel to its radius vector. In a star shaped particle, a shell can be added by extending the radius vector for each value of θ and $\varnothing$, such that the distance between the original surface and the new shell, measured along a surface normal vector originating from the same point on the original surface, is of length $\left|\vec{t}\right|$ [5]. Figure 2 shows a visualization of a shell around a single particle. The wired surface shows the shell, while the solid surface shows the original surface of the original irregularly-shaped particle.

The shell model, along with the Anm model, has the potential to serve as a microstructural modelling tool in several areas of research that are difficult to do experimentally either due to the scale or due to the complexity of the materials. Two interesting studies that can benefit from this are the effects of ITZ on the electrical conductivity of mortar [8], and interfacial structures that have been found to have a significant effect on thermal conductivity of nanoparticle-fluid mixtures [9]. More recently, the effect of ITZ on the diffusivity of chlorine in cementitious materials were also studied [10]. In the chlorine diffusion research, the Anm model was employed to build a virtual mortar microstructure and a small surface crack was created on top of it to study the influence of crack on chlorine transport. It is noteworthy that the 3D multiphase microstructure meshing method [11] was used to create 3D tetrahedral elements. The created 3D mesh was included in finite element analysis for chlorine diffusion simulation.

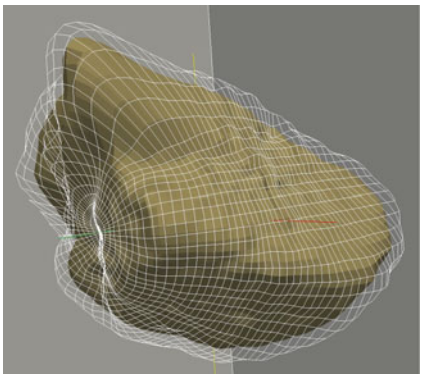

Fig. 2 Irregular shape particle with uniform thickness shell of thickness t = 0.2 % of particle length

3 Results and Discussion

3.1 Particle-Particle Contact Function

The EOB method has been found to be more efficient when compared to the old Newton-Raphson (NR) method. The EOB method is faster than the NR method even without parallelization by about 19 %. The EOB method with parallelization (with 8 processors) was found to be about 82 % faster than the NR method (single processor). 139 particle pairs of different sizes were used for this comparison. A software timer was used to measure the time taken exclusively by the inter-particle contact functions and the values were saved on a file by the program for analysis. The standard deviation of the execution time for the EOB method and NR method were found to be 909 and 5,487 ms, respectively. The average execution times were 775 and 4,354 ms, respectively.

3.2 Uniform-Thickness Shell

An interesting question discussed earlier [5] was if there was any difference in creating a single shell of thickness $5t$ or five shells of thickness t. Shells were added to a particle, first as a single shell of 0.1 % thickness, then 10 shells with 0.01 % thickness each, and finally 100 shells with 0.001 % thickness relative to the particle length. We observed that the volume of the new particle remains the same. The overall time taken to create the uniform thickness increased approximately linearly, since a similar shell generation algorithm is repeated more times for the larger number of shells.

Another interesting point is how the particle density of the Anm model is affected by different values of the uniform shell thickness used during the parking when the shells are not allowed to overlap. We simulated a cubic container with an edge length of 66 mm and parked particles from a coarse aggregate shape database with sizes ranging from 7 to 11 mm. The gradation was defined by four sieves: Sieve 1 (particle width ranging from 10 to 11 mm), Sieve 2 (9–10 mm), Sieve 3 (8–9 mm) and Sieve 4 (7–8 mm). The suggested fraction (volume fraction of total volume) of particles to be parked from each sieve is 0.25 and the suggested total packing density PD of the simulation box is 0.25. The maximum number of random locations attempted with each sieve range is set to 2,000, whereas the number of random shape, orientation and size attempts are all set to 1. The shell size was gradually increased from 0 to 2 % of the particle length and its effect on the resulting simulation box was observed.

Table 1 describes the actual particle size distribution and individual PD achieved by each sieve. Generally, the PD is expected to reduce as the shell thickness increases, because the particles with shell have a larger volume compared to particles without the shell. Due to this reason, the volume of particles that can be accommodated in

Table 1 Particle size distribution and achieved volume fraction by particles from individual sieves

Shell thickness (%)	Sieve 1 (10–11 mm)	Sieve 2 (9–10 mm)	Sieve 3 (8–9 mm)	Sieve 4 (7–8 mm)	Total PD
0	0.2569	0.2540	0.2519	0.2524	0.2632
0.4	0.2569	0.2523	0.2511	0.2514	0.2623
0.8	0.2575	0.2538	0.2523	0.2416	0.2607
1.2	0.2503	0.2507	0.2526	0.2473	0.2595
1.6	0.2503	0.2521	0.2521	0.2081	0.2496
2	0.2501	0.2520	0.2514	0.1952	0.2460

the fixed volume box is reduced. This lack of available space is first experienced by the particles parked last. We can see that Sieve 4, the smallest sieve, experiences a decreasing trend in PD. It is reasonable to assume that if the shell thickness is further increased this effect will be noticed on Sieve 3, Sieve 2 and so forth.

It is important to note that, in this simulation, there are other factors influencing the packing of the particles. The random packing does not result in a reliable dense packing where all the particles are almost touching their neighbors. Without the shell, many particles are already parked separately by a distance larger than the thin shell. Therefore, only a fraction of the particles which are almost touching its neighbor is influenced by the shell and contribute to a reducing PD. Sometimes, such particles which fail to park in a particular location due to the presence of the shell, may favorably alter the random packing sequence resulting in a slight increase in the number of particles parked. This effect is noticed in Table 1, in Sieve 4, for shell thickness of 1.2 and 1.6 %.

4 Conclusion

The Anm model provides an effective method to simulate the proportioning of the aggregates considering real particle shape effects. It has been improved and enhanced with a faster and more accurate particle contact function and an algorithm that can place a shell around any particle. This shell can simulate any kind of interfacial zone between aggregate particles and cement paste matrix, like the interfacial transition zone in mortar and concrete. The following conclusions are made based on the results presented here:

1. The EOB method is proposed to be a more efficient and accurate method of detection of inter-particle contact when compared to the NR method used by the first version of the Anm model.
2. The uniform-thickness shell provides a customizable tool to control the minimum inter-surface distance of particles during parking process. The shell provides a valuable method to simulate the highly heterogeneous properties of an interfacial transition zone around the particles.

Acknowledgement We thank the National Institute of Standards and Technology Project: Innovative Measurement Science - Shape Metrology, for partial support of this work. We also acknowledge the support of the Boise State University's R1 supercomputing facilities in performing the numerical simulations.

References

1. Neville, A. M. (2011). *Properties of concrete* (5th ed., p. 846). Harlow/New York: Pearson.
2. Kwan, A. K. H., & Fung, W. W. S. (2009). Packing density measurement and modelling of fine aggregate and mortar. *Cement and Concrete Composites, 31*(6), 349–357.
3. Lecomte, A., de Larrard, F., & Mechling, J. M. (2005). Predicting the compressive strength of concrete: The effect of bleeding. *Magazine of Concrete Research, 57*(2), 73–86.
4. Qian, Z. (2012). *Multiscale modeling of fracture processes in cementitious materials*. Ph.D. thesis, Delft University of Technology, Delft.
5. Garboczi, E. J., & Bullard, J. W. (2013). Contact function, uniform-thickness shell volume, and convexity measure for 3D star-shaped random particles. *Powder Technology, 237*, 191–201.
6. Bentur, A., Alexander, M. G., & Comm, R. T. (2000). A review of the work of the RILEM TC 159-ETC: Engineering of the interfacial transition zone in cementitious composites. *Materials and Structures, 33*(226), 82–87.
7. Mondal, P., Shah, S. P., & Marks, L. D. (2009). Nanomechanical properties of interfacial transition zone in concrete. In Z. Bittnar (Ed.), *Nanotechnology in construction 3* (pp. 315–320). Berlin/Heidelberg: Springer.
8. Shane, J. D., et al. (2000). Effect of the interfacial transition zone on the conductivity of portland cement mortars. *Journal of the American Ceramic Society, 83*(5), 1137–1144.
9. Xie, H. Q., Fujii, M., & Zhang, X. (2005). Effect of interfacial nanolayer on the effective thermal conductivity of nanoparticle-fluid mixture. *International Journal of Heat and Mass Transfer, 48*(14), 2926–2932.
10. Lu, Y., et al. (2012). *Modeling of chloride transport in cracked concrete: A 3-D image–based microstructure simulation*. Proceedings of the COMSOL conference 2012, Boston.
11. Lu, Y., & Garboczi, E. (2014). Bridging the gap between random microstructure and 3D meshing. *Journal of Computing in Civil Engineering, 28*(3), 04014007.

Part VII
High-Performance Materials

Understanding the Dispersion Mechanisms of Nanosilica in Ultra High Performance Concrete

Aileen Vandenberg and Kay Wille

Abstract One of the current challenges to nanoengineering cementitious composite materials is obtaining proper dispersion of nano-sized particles in the cementitious composite matrix. Proper dispersion of particles can lead to improved particle packing density, a key parameter in improving the mechanical, chemical, and sustainable properties of the cementitious composite. Current advances in optimizing particle packing density have led to the development of higher strength, higher durable cementitious composite materials, such as ultra-high performance concrete (UHPC). Further advancement of UHPC can be achieved by the addition of properly dispersed nano-sized particles which will assist in broadening the particle size distribution for further optimization of the particle packing density. Among the vast variety of potential nano-particles, nanosilica is the most studied to date. Nanosilica has been shown to improve macroscopic properties such as mechanical strength, durability, and chemical resistivity of cementitious materials. However, as the average particle diameter size decreases the water demand increases and challenges a balanced mix design. More fundamental work needs to be done in order to understand how nanosilica disperses inside the hydrating matrix. Our research investigations will focus on the interfacial interactions between nanosilica and the hydration products, the ions of the pore solution, and the polymers of admixtures.

Keywords One nanoengineering • Cement • Composite • Nanoparticles • Hydration • Pore solution • Admixtures • Packing density • Strength • Ultra-high performance concrete • UHPC

1 Introduction

Four decades ago high range water reducing polymers revolutionized concrete material design through enhancing the dispersion of cement particles. Additionally, improved particle packing models were applied to cementitious materials to

A. Vandenberg (✉) • K. Wille
Civil and Environmental Engineering Department, University of Connecticut, Mansfield, CT, USA
e-mail: aileen.vandenberg@uconn.edu; kwille@engr.uconn.edu

K. Sobolev, S.P. Shah (eds.), *Nanotechnology in Construction*,
DOI 10.1007/978-3-319-17088-6_40

optimize the particle packing density. These two improvements led to a breakthrough in concrete technology of ultra-high performance concrete (UHPC). UHPC is characterized by a very low water-to-binder (w/b) ratio (generally less than 0.2) that has a compressive strength in excess of 150 MPa, superior durability properties, and a particle size distribution typically between 100 nm and 5 mm [1]. UHPC can be further improved by increasing the particle size distribution to include nano-sized particles, defined as particles with an average diameter of less than 100 nm. Yet, introducing such small particles into UHPC brings up the question how to control self-assembly. Particles below 100 nm are completely dominated by particle-particle interactions [2]. These nano-sized particles have a large surface-to-volume ratio and high surface energy, and thus are controlled by surface forces (e.g., van der Waals) rather than volume forces (e.g., gravity). Understanding surface characteristics leads to understanding particle interactions which then leads to macroscopic properties (mechanical strength, durability, heat resistance). Macroscopic product properties are a function of particle properties (particle shape, size distribution, morphology, interfacial characteristics, chemical composition) and process properties (production method, material source, temperature, pressure, etc.). Dispersity is characterized by particle size distribution, shape and morphology, and interfacial properties [3].

The most commonly studied nano-sized particle used in cement and concrete is nanosilica [4]. It has shown to improve concrete macroscopic properties, such as compressive strength and durability [5]. In order to exploit all of the beneficial properties of nanosilica, further research needs to be done on its dispersion and stability in a cementitious hydrating environment. Therefore, more ways to control process methods and particle properties should be investigated. The following paragraphs will highlight some of these concepts.

2 Discussion

2.1 Silica Process Methods and Silica Particle Properties

When considering the different process methods for nanosilica, it is important to consider silica fume. While silica fume is considered a micro-sized particle, nano-sized particles (smaller than 100 nm) do exist in the particle size distribution. The process route of silica fume, a by-product of the silicon and ferro-silicon alloy industries, starts with reducing quartz at high temperatures (2,000 °C) in an electric arc furnace. The quartz oxidizes and condenses into small amorphous silica spheres [6]. Another high heat process method is that of fumed silica or pyrogenic silica. Pyrogenic silica is produced from the flame hydrolysis of silicon tetrachloride ($SiCl_4$) at around 1,800 °C [7]. This process produces an amorphous powder in the submicron particle range.

Additionally, there are process methods that do not require such high heat. One such process is the precipitation method first developed by Iler [8]. In this method a sodium silicate precursor is acidified at temperatures between 50 and 100 °C resulting

in nanosilica precipitating out. This method has also been used with rice husk ash as a precursor [9]. Another process method is the sol-gel process, also known as colloidal nanosilica. At room temperature the pH of an organosilicon solvent (e.g., tetraethyl orthosilicate-TEOS) is adjusted to the gelling point of silica. The gel is then filtered and either dried or dispersed in solution [10]. A special method developed by Stöber falls under this process method [11]. Finally, alternative process biological methods of nanosilica do exist such as the olivine and sulfuric method [12].

The reactive sites on a silica particle surface are silanol groups (Si–O–H). Three types of silanol groups can exist on the surface- isolated (Si-OH), germinal (Si-OH2), and etherial (Si–O–Si) [2]. The frequency and density of these groups depend on the synthesis method. Pyrogenic silicas and silica fume have less silanol groups than colloidal silica and precipitated silica due to condensation that occurs during synthesis [13]. Silanol groups form hydrogen bonds with ions and other polar molecules very easily. Therefore, nanosilica can be well dispersed in water with a basic pH value of 7–9 [8, 14–17]. This is due to hydrogen bonding between the deprotonated surface silanol groups and the water molecules, leading to a formation of a water layer around the particle. However, as the pH value rises above 10 dissolution of silica leads to ion-exchange mechanisms displacing the protons of the silanol groups [8, 14, 18]. This prevents water from forming a hydrogen bond with the silanol group impeding the particle dispersion. In high pH silica bonding can occur, if one silica particle contains a dissociated silanol and another silica particle contains an associated group. They link together through an acid-base interaction. Beyond pH of 12 it is postulated that silanol groups will fully disassociate, leading to destabilization and aggregation of silica particles [15, 18]. Thus, in a cementitious pore environment well-dispersed nanosilica hydrosols will most likely experience a degree of re-agglomeration. This degree is still unkown and may depend on the initial hydrosol stabilizer, the specific surface area, surface reactivity, primary particles size, and porosity of the nanosilica particle. Further investigations will need be undertaken to examine this degree of re-agglomeration and how detrimental the re-agglomeration is.

2.2 Silica Particle in Hydrating Cementitious Matrix

The process method chosen will greatly influence the particle dispersity. Dispersity is a function of particle shape, size, size distribution, morphology, surface-to-volume ratio, porosity, and chemical characteristics [3]. In order to understand the dispersity of silica in a cementitious matrix these property parameters need to be taken into consideration. In a recent study Quercia et al. [10] compared how different process methods change the morphological and textural characteristics of different amorphous nanosilicas. Particle parameters such as specific surface area (SSA), particle size, pore size distribution, porosity, and shape were compared to see how slump-flow properties of normal concrete mortar were affected. Their study demonstrated that SSA, porosity, and average primary particle size are the parameters with

the largest influence on slump. In a related study, Quercia et al. [19] studied the water demand of these different nanosilicas. They noticed that the pH of the pore fluid differed depending on the process route of the silica used. Additionally, they found that colloidal silica had less relative pozzolanic index compared to other production methods. They postulated that surface area determines the agglomeration state which in turn determines the relative pozzolanic reactivity. While these studies show that textural and morphological parameters have a large influence on the water demand and on the agglomeration state of the silica particles in normal concrete environments, considerations of the chemical reactivity of the silica surface, the superplasticizer-silica particle interactions, and lower water-to-cement (w/c) ratios were not investigated.

Recently, Oertel et al. [7, 13, 20] attempt to address some of these issues. In their investigations they compared conventional silica fume, pyrogenic silica, and Stöber synthesized nanosilica particles comparing the specific surface area, silanol group densities, and solubility in alkaline suspensions. Oertel proposed two reaction paths for silica: (i) pozzolanic reaction or (ii) nucleation seeding effect. Interestingly though, the authors found that the Stöber particles did not appear to follow either path. Instead they found that silicate ions, formed from the dissolution of silica, interacted with alkali ions (Na^+ and K^+) that were immediately released upon hydration of cement clinker. These alkali cations react with silicate ions and form alkali silicate oligomers. Additionally, Ca^{2+} ions that are released from the dissolution of cement clinker interact with silicate ions to form calcium silicate oligomers and in some cases calcium alkali silicate oligomers. This oligomerization may lead to a calcium rich silicate gel layer that surrounds the silica particles. This gel layer may prevent the silica particles from acting as nucleation seeding sites for calcium-silicate-hydrate (C-S-H) or taking part in a pozzolanic reaction with calcium hydroxide (CH). Furthermore, the UHPC mix with Stöber particles did not show increased early day strength or accelerated heat curves like the pyrogenic silica and silica fume UHPC mixes. However, the Stöber particle mixes did show that the 28 day compressive strength was comparable and even a little higher than the other forms of silica. While, the authors' findings show that surface reactivity of silica is an important parameter to consider in understanding dispersion mechanisms, their investigations focused on particle sizes larger than 100 nm. Additionally, consideration of the superplasticizer-silica interactions were not addressed.

Nanosilica not only has potential to interact with the cement hydration products, but also to interact with high range water reducing polymers in the matrix. It has been shown that current commercially available superplasticizer polymers exhibit incompatibilities with nanosilica [21]. Glotzbach et al. [22] used AFM to study silica-silica particle interactions in a closed fluid cell. The fluid cell was injected with a fluid environment similar to the pore environment of a cement paste. Four different plasticizer polymers were injected at separate times into the fluid cell to observe the interaction forces between silica particles in the presence of plasticizer. In this study a commercially available PCE with a high molecular weight, and three custom-made polymers were used. Shear and force measurements showed that the

commercial polymer was most incompatible with silica particles. Its large backbone and long side chains might lead to particle bridging. The smaller polymers with shorter side chains and different functionalities were more compatible. The study by Glotzbach demonstrated that better dispersing polymers are needed for nanosilica. One possible route is functionalization of nanosilica surface with organic molecules similar to current dispersing polymers used for cement and silica fume. Shin et al. [23] functionalized nanosilica particles with poly(ethylene glycol) methacrylate (PEGMA) by treating Stöber silica particles with triethoxyvinylsilane (VTES) before grafting PEGMA via UV-photopolymerization on them. While, the research intentions were not for cement this could be a possible route to take in finding more compatible dispersing polymers for nanosilica.

3 Conclusion

This paper has attempted to address important parameters to consider for understanding dispersion mechanisms of nanosilica. Dispersity mechanisms are influenced by synthesis methods, particle surface properties, and particle size properties. Incompatibilities of superplasticizers with nanosilica show that better admixtures need to be developed. One possible route to this is surface functionalization. Additionally, some degree of agglomeration will take place. Understanding this degree of agglomeration and how detrimental its effects are to the hydrating cementitious matrix needs further investigation.

References

1. Wille, K., Naaman, A. E., & Parra-Montesinos, G. J. (2011). Ultra high performance concrete with compressive strength exceeding 150 MPa (22 ksi): A simpler way. *ACI Structural and Materials Journal, 108*, 46–54.
2. Parida, S. K., Dash, S., Patel, S., & Mishra, B. K. (2006). Adsorption of organic molecules on silica surface. *Advances in Colloid and Interface Science, 121*, 77–110.
3. Peukert, W., Schwarzer, H., Götzinger, M., Günther, L., & Stenger, F. (2003). Control of particle interfaces — the critical issue in nanoparticle technology. *Advanced Powder Technology, 14*, 411–426.
4. Singh, L. P., Karade, S. R., Bhattacharyya, S. K., Yousuf, M. M., & Ahalawat, S. (2013). Beneficial role of nanosilica in cement based materials – A review. *Construction and Building Materials, 47*, 1069–1077.
5. Sobolev, K., Flores, I., Hermosillo, Torres-Martinez L, Valdez, P. L., Zarazua, E., & Cuellar, E. L. (2009). *Engineering of SiO2 nanoparticles for optimal performance in nano cement-based materials*. In Z. Bittnar, P. J. M. Bartos, J. Nemecek, V. Smilauer, & J. Zeman (Eds.), *Nanotechnology in Construction Proceedings of the NICOM3* (pp. 139–148). Prague/Berlin/Heidelberg: Czech Republic/Springer, doi:10.1007/978-3-642-00980-8.
6. Snellings, R., Mertens, G., & Elsen, J. (2012). Supplementary cementitious materials. *Reviews in Mineralogy and Geochemistry, 74*, 211–278.

7. Oertel, T., Hutter, F., Helbig, U., & Sextl, G. (2014). Amorphous silica in ultra-high performance concrete: First hour of hydration. *Cement and Concrete Research, 58*, 131–142.
8. Iler, R. K. (1979). Chemistry of silica – Solubility, polymerization, colloid and surface Properties and biochemistry, 896, Wiley, New York.
9. Thuadaj, N., & Nuntiya, A. (2008). Preparation of nanosilica powder from ride husk ash by Precipitation Method. *Chiang Mai Journal of Science, 35*, 206–211.
10. Quercia, G., Lazaro, A., Geus, J. W., & Brouwers, H. J. H. (2013). Characterization of morphology and texture of several amorphous nano-silica particles used in concrete. *Cement and Concrete Composites, 44*, 77–92.
11. Stöber, W., Fink, A., & Bohn, E. (1968). Controlled growth of monodisperse silica spheres in the micron size range. *Journal of Colloid and Interface Science, 26*, 62–69.
12. Lazaro, A., & Brouwers, H. J. H. (2010). *Nano-silica production by a sustainable process; Application in building materials*. 8th fib PhD symposium in Kgs Lyngby, Denmark.
13. Oertel, T., Hutter, F., Tänzer, R., Helbig, U., & Sextl, G. (2013). Primary particle size and agglomerate size effects of amorphous silica in ultra-high performance concrete. *Cement and Concrete Composites, 37*, 61–67.
14. Amiri, A., Øye, G., & Sjöblom, J. (2009). Influence of pH, high salinity and particle concentration on stability and rheological properties of aqueous suspensions of fumed silica. *Colloids and Surfaces A: Physicochemical and Engineering Aspects, 349*, 43–54.
15. Chen, S., Øye, G., & Sjöblom, J. (2007). Effect of pH and salt on rheological properties of aerosil suspensions. *Journal of Dispersion Science and Technology, 28*, 845–853.
16. Ding, P., & Pacek, A. W. (2008). De-agglomeration of silica nanoparticles in the presence of surfactants. *Journal of Dispersion Science and Technology, 29*, 593–599.
17. Pacek, A. W., Ding, P., & Utomo, A. T. (2007). Effect of energy density, pH and temperature on de-aggregation in nano-particles/water suspensions in high shear mixer. *Powder Technology, 173*, 203–210.
18. Depasse, J. (1999). Simple experiments to emphasize the main characteristics of the coagulation of silica hydrosols by alkaline cations: Application to the analysis of the model of Colic et al. *Journal of Colloid and Interface Science, 220*, 174–176.
19. Quercia, G., Huesken, G., & Brouwers, H. J. H. (2012). Water demand of amorphous nano silica and its impact on the workability of cement paste. *Cement and Concrete Research, 42*, 344–357.
20. Oertel, T., Helbig, U., Hutter, F., Kletti, H., & Sextl, G. (2014). Influence of amorphous silica on the hydration in ultra-high performance concrete. *Cement and Concrete Research, 58*, 121–130.
21. Fernández, J. M., Duran, A., Navarro-Blasco, I., Lanas, J., Sirera, R., & Alvarez, J. I. (2013). Influence of nanosilica and a polycarboxylate ether superplasticizer on the performance of lime mortars. *Cement and Concrete Research, 43*, 12–24.
22. Glotzbach, C., Stephan, D., & Schmidt, M. (2013). Measuring interparticle forces: Evaluation of superplasticizers for microsilica via colloidal probe technique. *Cement and Concrete Composites, 36*, 42–47.
23. Shin, Y., Lee, D., Lee, K., Ahn, K. H., & Kim, B. (2008). Surface properties of silica nanoparticles modified with polymers for polymer nanocomposite applications. *Journal of Industrial and Engineering Chemistry, 14*, 515–519.

Acid Resistance of Ultra High-Performance Concrete (UHPC)

Andreas Koenig and Frank Dehn

Abstract Based on the knowledge of the deterioration mechanisms of different acid solutions the performance of UHPC – amongst others – in different acid environments was comparatively tested. The interconnection between the acid solutions and UHPC was examined by pH-value measurements, light microscopy (LM), scanning electron microscopy with energy dispersive X-ray analyzer (SEM+EDX), X-ray diffraction (XRD) and thermal analysis (DTA/TG). To achieve a consistent accelerated and reproducible ageing the acid solution has to be constantly homogenized, the pH-value and the saturation of the solution has to be controlled as well as adjusted. The results show that concretes with very high strength (such as UHPC) have not automatically an excellent resistance against acid solutions. A very high acid resistance can only be achieved by a very low capillary porosity and a very low reactivity against the acid solution.

Keywords Acid resistance • Ultra High-Performance Concrete (UHPC)

1 Introduction

In many cases constructions interact with different kinds of acid solutions. If the acid resistance of the construction material is too low, normally a coating system with a sufficient resistance is used to enable a permanent protection of the constructions. In practice, the functionality of coating systems is unexpectedly disturbed because of complex boundary conditions, insufficient surface preparation and defects in form of joints and connection points. In recent years, concretes with low binder content and a high acid resistance were developed and applied in Germany [1]. New experiences with UHPC with very high binder contents show also a very good performance under acid conditions [2–5]. The aim of this paper is to summarize an experimental study in which different types of concrete have been exposed to demanded with different acids and the depth of degradation (DD) was measured. Additionally, the mechanisms of the acid attack were analyzed using different methods.

A. Koenig (✉) • F. Dehn
Professorship for Multifunctional Construction Materials, Leipzig University,
Scharnhorststrasse 20, 04275 Leipzig, Germany
e-mail: akoenig@uni-leipzig.de; fdehn@uni-leipzig.de
http://www.mfkw-leipzig.de

K. Sobolev, S.P. Shah (eds.), *Nanotechnology in Construction*,
DOI 10.1007/978-3-319-17088-6_41

2 Materials and Methods

2.1 Materials

The study was conducted on hardened cement pastes and different types of concretes (normal-strength concrete = N1, high-strength concrete = H1, UHPC = U1–U4) made with different binder types (see Table 1). The used cements are designated in the European standard EN 197-1:2011-11. Optional, blast-furnace slag (BFS), silica fume (SF) with different particle sizes (SF1 = micro particles, SF2 = nano particles) and quartz powder (QP) were added. Hardened cement past samples were produced, were stressed and characterized to determine the effects in the concretes. In addition to the concrete mixes, hardened cement paste samples with the aforementioned types of cement and constant water to binder ratio (w/b-ratio) of 0.45 were produced. The composition of the concretes mixtures are listed in Table 1. The test specimens were stored in a curing room at a temperature of 20 °C and a relative humidity of 65 % until the time of testing (56 days).

2.2 Analytic Methods

DTA/TG investigations were performed to determine the $Ca(OH)_2$-content and the mineralogical phase composition in hardened cement pastes were determined before and after the acid attack by using XRD. After the acid-exposure, the LM was used to quantify the damage depth and the SEM + EDX was used to analyze the distribution of the chemical elements on polished sections.

Table 1 Composition (kg/m^3) of the tested concretes

Components	N1	H1	U1	U2	U3	U4
Cements						
CEM I 42,5 R-SR	360	–	–	–	–	–
CEM I 52.5 R	–	–	665	665	832	222
CEM II/B-M (S-D) 52.5 N	–	380	–	–	–	–
Additives						
BFS	–	–	–	–	–	584
SF1	–	42	120	93		320
SF2	–	–	–	27	–	–
QP	–	–	299	299	197	214
Water	162	127	182	220	208	189
Superplasticizer	3.6	18.2	29.3	29.3	46.6	51.1
Aggregates						
Sand 0–0.8 (quartzite)	–	–	1,112	1,008	973	970
Sand 0–2 (quartzite)	704	902	–	–	–	–
Gravel 2–8 (basaltic)	392	1,087	–	–	–	–
Gravel 8–16 (basaltic)	899	–	–	–	–	–

3 Test Procedure

The foreseen concrete samples for the acid attack were cut from the middle of a cube after 56 days. In addition to the concrete samples, hardened cement paste samples were similarly stored to identify the reaction products. In order to realize a constantly stress, the pH-value was permanently controlled by an automatic titration unit and the solution was constantly mixed. In order to prevent saturation, the *Ca-concentration* was measured and based on the results the solution was changed. Sulphuric acid with a pH-value of 2 and an organic acid mix (1.5 % acetic acid, 0.5 % propionic acid, 3.0 % lactic acid) with a pH-value of 3 were used. A complete description of the test procedure is published in [6–7].

4 Results and Discussion

Based on the polished sections the UHPC show a lower depth of degradation (DD) than the reference concretes N1 and H1. The mass losses of the UHPC-samples are similar to the reference systems with the higher DD. Despite the higher pH-value, the DD is bigger for the organic acid mix (pH = 3) than for the sulphuric acid (pH = 2) (see Table 2).

4.1 Dependency on Concrete

The low DD of UHPC is due to a very high packing density and results from its low capillary porosity (positive effect). The porosity influences the transport mechanisms (especially diffusion) and the specific area of potential reaction partners. On the other hand, the high binder content of UHPC means a higher content of reaction partners (hardened cement paste) and a lower content of inactive components (aggregates). At a constant chemical attack (const. pH-value, no saturation) more hardened cement

Table 2 Results after 12 weeks in different acid solutions

Damage	Unit	N1	H1	U1	U2	U3	U4
Sulphuric acid (pH = 2)							
Depth of erosion (DE)	mm	0.24	0.00	0.00	0.00	0.41	0.00
Depth of reaction (DR)	mm	2.09	2.18	1.96	2.17	1.48	2.22
Depth of degradation (DD)	mm	2.33	2.18	1.96	2.17	1.89	2.22
Mass loss	M.-%	6.30	3.60	3.00	3.80	8.20	4.60
Organic acid mix (pH = 3)							
Depth of erosion (DE)	mm	0.34	0.09	0.00	0.00	0.27	0.17
Depth of reaction (DR)	mm	7.32	5.38	4.45	4.90	4.65	3.99
Depth of degradation (DD)	mm	7.66	5.47	4.45	4.90	4.92	4.16
Mass loss	M.-%	6.22	3.96	5.06	5.70	7.67	4.65

paste is dissolved. In contrast to other durability properties (for example carbonation and chloride diffusion) the performance of the concrete depends not only on its porosity. The acid resistance of UHPC is not much better than for normal- or high-strength concretes. The remarkable high mass losses of UHPC result from the reduced aggregate size and the high binder content. With an increasing ratio of aggregate size in contrast to the depth of erosion (DE), the amount of soluble particles increases as well. The comparison of the acid resistance of U1 or U2 with U3 demonstrates that the acid resistance can only be improved by optimizing the binder system. The mineral phase of the hardened cement paste with the highest solubility is portlandite ($Ca(OH)_2$). By addition of pozzolanic powder and/or by reduction the clinker content (use blast-furnace slag), the $Ca(OH)_2$ amount can be reduced. The particle sizes of silica fume had no a clearly effect on the acid resistance of UHPC. DTA/TG results show the influence of these components of the development of the $Ca(OH)_2$ amount (see Fig. 1). At the same time, C-S-H-phases are formed with a lower C/S ratio (CaO/SiO_2) when these clinker hydrate. These mineral phases have probably a higher acid resistance because of the lower *Ca*-content.

4.2 Dependency on Acid Solution

If the pH-value is constant, the organic acid mix has a higher damage potential than sulphuric acid. The resulting depth of degradation (DD) as a sum of the depth of erosion (DE) and reaction (DR) is bigger for an organic acids attack regardless the concrete composition (see Table 2). The increasing damage potential of organic acids results from incomplete dissociation, faster local dissociation (buffer effect) and higher solubility of the acid specific salts. Generally, the DE is smaller and the DR is

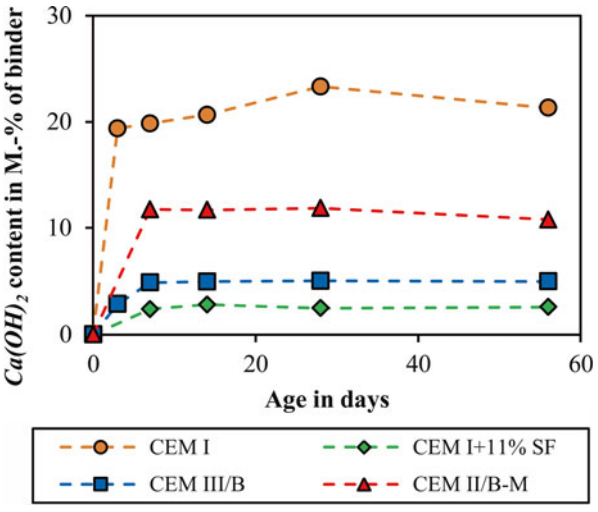

Fig. 1 Development of $Ca(OH)_2$-content in hardened cement pastes of different composition (cement types) based on DTA/TG-results

bigger when concrete is exposed to organic acids. That is the reason why the mass loss does not change although a higher DD is obvious. The acid specific zonation is very important for the apparent evaluation of the DD. At the DR, the *Ca-content* decreases and the *Al-* and *Fe*-concentration increases automatically (see Fig. 3). The reaction products are X-ray amorphous. In detail, when sulphuric acids react, the sulphur content increases significantly in the transition zone (TZ) between matrix and aggregates. The sulphur reacts with $Ca(OH)_2$, particular in the TZ and gypsum (see Fig. 3) precipitates from the acid solution (see Fig. 4).

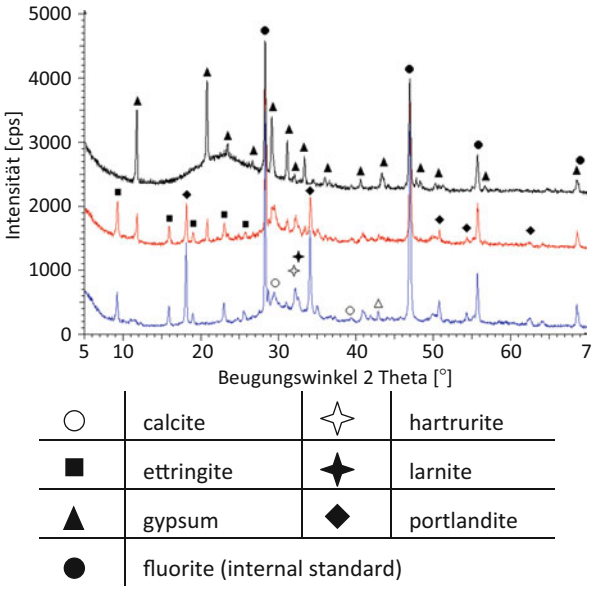

Fig. 2 Mineral phases in hardened cement pastes (CEM II/B-M) before (*blue-down*) and after exposure in sulphuric acid (*red-middle* = volume, *black-up* = surface)

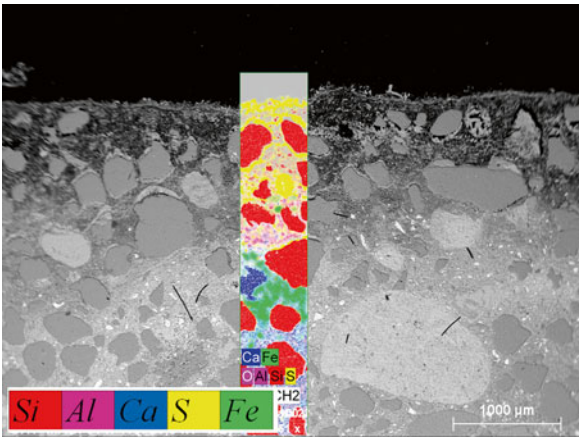

Fig. 3 Cross-section of N1 after 12 weeks of storage in sulphuric acid (pH = 2.0)

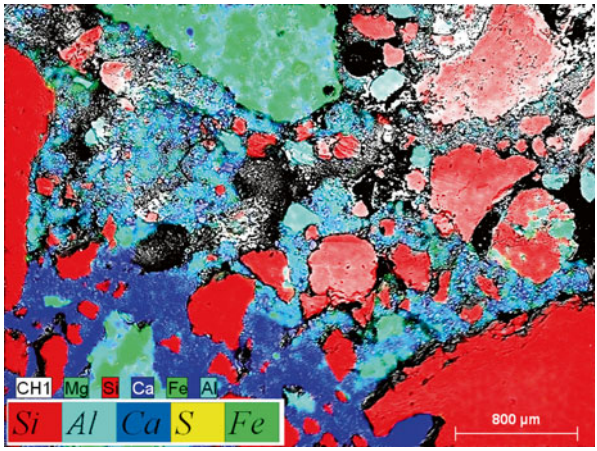

Fig. 4 Cross-section of N1 after 12 weeks of storage in an organic acid mix (pH = 3.0)

5 Conclusions

Four UHPC (U1–U4), a normal-strength (N1) and one high-strength concrete (H1) were stressed by an organic acid mix and a sulphuric acid for 12 weeks in an acid testing device. The most important findings of the study are:

1. UHPC had a lower DD as normal- or high-strength concretes without reference to the acid and the composition of the concretes. However, the difference in the performance is not so big in comparison with other durability properties. The mineral phases of the hardened cement paste are thermodynamically unstable and the content increased with increasing binder content (negative influence). On the other hand, the increasing binder content and the lower w/b-ratio resulted in a lower porosity.
2. The mass loss depends on the depth of degradation and the size of the concrete components (binder, aggregates). The mass loss is not a direct indicator to quantify the degree of degradation.
3. The depth of degradation could be minimized by reducing the $Ca(OH)_2$-content by using pozzolanic or latent hydraulic granulated blast-furnace slag.
4. The organic acid mix had a bigger damaging potential than for example sulphuric acid. The reasons are the high concentration comparing high pH-values (incomplete dissociation), the quicker local dissociation (buffer effect) and the higher solubility of the acid-specific salts.

References

1. Huettl, R., & Hillemeier, B. (2000). Hochleistungsbeton – Beispiel Säureresistenz. *Beton- und Fertigteiltechnik (BFT) International, 1*, 52–60 (in German).
2. Müller, H. S., & Scheydt, J. (2011). Dauerhaftigkeit und Nachhaltigkeit von ultrahochfesten Beton. *Beton,* 60:336–343 (in German).
3. Mueller, C., Palecki, S., Möser, B., & Frank, L. (2010, May/June). *Durability of Ultra-High Performance Concrete (UHPC).* Proceedings of the 3rd International *fib* Congress incorporating the PCI annual Convention and Bridge conference, Washington, DC.
4. Franke, L., Schmidt, H., & Schmidt-Doehl, F. (2010). Prüfung der Beständigkeit von Mörtelprodukten gegenüber saurem Angriff bis XA3. *Beton,* 59:20–31 (in German).
5. Franke, L., Deckelmann, G., & Schmidt, H. (2008, March). *Behaviour of ultra high-performance concrete with respect to chemical attack*. Proceedings of the 2rd International Symposium on Ultra High-Performance Concrete, Kassel.
6. Koenig, A., & Dehn, F. (2015). Test method to determine the acid resistance of conretes. *Beton- und Stahlbetonbau 110, 1*, 34–40 (in German).
7. König, A.; Dehn, F.: Main considerations for the determination and evaluation of the acid resistance of cementitious materials. Materials and Structures, 26.03.2015, doi:10.1617/s11527-015-0605-7.

Effect of Cellulose Nanopulp on Autogenous and Drying Shrinkage of Cement Based Composites

Liberato Ferrara, Saulo Rocha Ferreira, Marco della Torre, Visar Krelani, Flávio Andrade de Silva, and Romildo Dias Toledo Filho

Abstract Cellulose based materials, such as natural fibres, when added into a cement based matrix, can greatly affect the properties of the composite in its fresh state, early age and hardened state, including self healing capacity. This is due to their porous structure, hydrophilic character and water retention capability, which are likely to create additional moisture paths inside cement matrices. This paper focuses on the effect of nanoscale addition on the autogeneous and drying shrinkage of cement mortars formulated from HPFRCC mixes. Two other different kinds of cellulose based additions were also studied for comparison, respectively eucalyptus micro fibers and natural sisal fibers, together with "conventional" steel fibres. This study is a part of a larger investigation undertaken by the authors in the framework of the EU-FP7 research project EnCoRe (www.encore-fp7.unisa.it) aimed at assessing the possibility of using cellulose based materials and natural fibers as promoters of self healing processes in advanced cementitious composites.

Keywords Nanocellulose • HPFRCC • Shrinkage • Natural fibers

L. Ferrara (✉) • M. della Torre • V. Krelani
Department of Civil and Environmental Engineering,
Politecnico di Milano, Milan, Italy
e-mail: liberato.ferrara@polimi.it

S.R. Ferreira • R.D.T. Filho
Civil Engineering Department, COPPE, Universidade Federal do Rio de Janeiro,
Rio de Janeiro, Brazil

F.A. de Silva
Department of Civil Engineering, Pontifícia Universidade Católica do
Rio de Janeiro (PUC-Rio), Rio de Janeiro, Brazil

K. Sobolev, S.P. Shah (eds.), *Nanotechnology in Construction*,
DOI 10.1007/978-3-319-17088-6_42

1 Introduction

In the line of development of construction materials reinforced with natural fibers, many researches have been carried out on cementitious and polymeric matrix composites and promising results have been achieved, showing an improvement in durability, strength and ductility [1–8]. The decision to use natural fibers as reinforcement is beneficial from several points of view, including local availability, low cost and low energy consumption, and is thus likely to greatly contribute towards the overall sustainability of the intended applications. In view of this, cementitious composites reinforced with natural fibers have the great potentiality to become the ultimate green material option, minimizing the use of natural resources and the overall lifetime impact of construction materials and products.

Natural fibers have been traditionally used as a substitute of asbestos in the form of chopped, short, and/or in a pulp form for the production of thin elements for roofing and cladding. So far, cement based composites have been mainly reinforced by short or pulp cellulose fibers. More recently, studies have also focused on the mechanical behavior of sisal and other natural fibers and some investigations have also focused on the possibility of obtaining high performance and multiple cracking behavior employing natural fibers in cementitious matrices [3–8].

The use of natural fibers in developing high performance cementitious composites and products requires, first of all, a deep and thorough understanding of the mechanical behavior of the fibers themselves. As from a dedicated literature review, there is a large discrepancy in reported tensile strength and Young's modulus of natural fibers. This may be due, on the one hand, in part to uncertainties in the measurement of the fiber cross section area (due to the non-circular cross-section), and, on the other hand, to the limited resolution of the employed load and displacement measurement techniques. Anyway it has been shown, for example, that long randomly dispersed sisal fibers in thin cement based materials products were able to induce a multiple cracking process with a hardening behavior both in tension (strain-hardening) and bending (deflection hardening) [3–8].

Recently a further value to the addition of natural fibers in high performance cement based composites, besides the contribution to toughening of the brittle matrix, has been recognized. As a matter of fact, because of their highly hydrophilic nature and porous microstructures, natural fibers, either even simply during the mixing process or through dedicated pre-saturation, can absorb water. This water, through the porous network consisting of the same dispersed natural fiber reinforcement, can be released "on demand" at selected cracked or damaged locations and activate the delayed hydration reactions which are responsible of the healing processes of damage and cracks.

In the framework of project EnCoRe this problem is going to be largely investigated and, in this paper, with the aim of continuously promoting the development of sustainable cement based construction materials and products, the scale effect of cellulose-based reinforcement ranging from macro- to micro to nanoscopic scale will be investigated on the autogeneous and drying shrinkage of cement mortars formulated from typical composition of a High Performance Fiber Reinforced Cementitious Composites (HPFRCC) [9].

2 Materials, Experimental Tests and Preliminary Results

This paper aims at investigating the effect of cellulose nanopulps, and, comparatively, of other different scale natural fibre reinforcement on the autogenous and drying shrinkage of cement pastes formulated from typical HPFRCC composition. Together with nanopulp, micro fiber of eucalyptus and natural sisal fibers were investigated, besides a "conventional" high carbon steel fibre reinforcement. The main characteristics of the employed fibres are summarized in Table 1.

The nanopulp is produced through fibrillation of cellulose fibers. Nanofibrils, which are highly crystalline and hence likely to feature extremely high mechanical properties, have diameters of roughly less than 100 nm, lengths of several micrometers and have thus a large aspect ratio. Because of this, as well as of their large specific surface area with reactive OH^-groups, nanofibrils are an interesting material for several applications, like, rheology and emulsion stabilizers in food, paints and cosmetics, strength enhancers in paper and composite materials as well as for barrier applications in novel packaging concepts.

The cellulose nanopulp and the eucalyptus micro fibers used in this study were manufactured by SUZANO-Brazil. Accordingly, the nanopulp fibers have a nominal diameter between 20 and 50 nm and a density of 1.4 kg/dm^3. The concentration of solids is 1.5 % per liter, (15 g of nano fibers per liter of suspension – Fig. 1). Regardless of the source, in an aqueous environment, the rheological properties of the nanopulp suspension can be described in terms of pseudoplasticity and shear thinning behavior. The eucalyptus micro fibers were extracted by kraft pulping method and bleached treatment. The length of the fibers, according to the company,

Table 1 Characterization of natural fibers

Fiber type	Density (kg/dm^3)	Cellulose (%)	Hemicellulose (%)	Lignin (%)
Nanopulp	1.4	96.5	–	–
Eucalyptus	1.68	77.1	18.9	3.8
Sisal	1.04	60.5	25.7	12.1

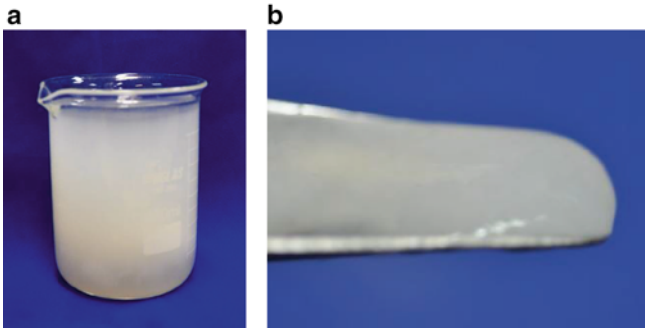

Fig. 1 (**a**) Nano cellulose pulp suspensions: concentration of 1.5 %. (**b**) The fibrils are randomly arranged and show a dense structure

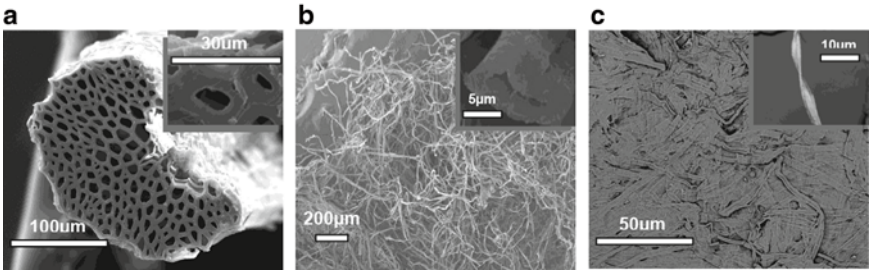

Fig. 2 SEM image of morphology of sisal fiber (**a**) The fiber cell structure showing the lumen void responsible for the water absorption; eucalyptus micro fibers (**b**) with a similar structure; and dried nano cellulose pulp () Nanofibrillated cellulose network structure when dryed on air, forming large nanofibrills (aglomerations)

Table 2 Mix composition of investigated cement composites

Constituent	Dosage (g/dm^3)				
Mix type	REF	Nanopulp	Eucalyptus	Sisal	Steel
Cement type I 52.5	600	600	600	600	600
Slag	500	500	500	500	500
Sand 0–2 mm	983	983	983	983	983
Water	200	187	200	200	200
Superplasticizer	33	33	33	33	33
Nanopulp	–	14	–	–	–
Eucalyptus	–	–	0.8	–	–
Sisal	–	–	–	14	–
Steel	–	–	–	–	100

was 0.8 mm. In Fig. 2, we can observe the cross section of the eucalyptus fiber. The eucalyptus fiber has tubular shape with a hollow internal cavity, i.e. the lumen, a typical feature of plant fibers, oval cross section and thick wall. Sisal fibers were obtained from sisal plants cultivated in farms located in the Bahia state, Brazil. They were extracted from the sisal plant leaves in the form of long fiber bundles. The fiber extraction from the leaf was done by semi-automatic crushers. From 10 kg of sisal leaves about 1.35 kg extractable fiber could be obtained. These fibers were characterized mechanically in [3, 4]. Sisal fiber microstructure is formed by numerous individual fiber-cells, which are about 6–30 µm in diameter, linked together by means of the middle lamella (Fig. 2).

High carbon straight brass coated steel fibers, 13 mm long and 0.16 mm in diameter, and with a tensile strength ≥2,000 MPa were employed (Beakert OL 13/0.16).

The cellulose nanopulps and different types of natural and steel fibres were employed to cast fibre reinforced cement mortars, formulated from the composition of a typical HPFRCC [7] (Table 2). The reference mortar consisted Portland Cement 52.5 typeR, blast furnace slag, water and super-plasticiser (Glenium ACE 300 ®) with a solid content of 31 %. The mixtures were produced in a room with controlled

temperature (21 ± 1 °C) using a 2 l mixer and following the mixing protocol detailed in [7]. Starting from a reference steel fibre dosage equal to 100 kg/m^3, dosage of sisal and eucalyptus microfibers was calculated for the same fibre volume fraction (V_f = 1.28 %) whereas for cellulose nanopulps a dosage of 0.2 % by volume was employed, also to guarantee target workability requirements.

For sisal fibers, the effect of a presaturation was also checked, soaking them in water for 1 hour and then wiping on absorbent paper before adding into the mix.

Six 160×40×40 mm specimens were cast with each for drying and autogeneous shrinkage tests. The environment where storing and testing was done was held at a temperature of 20 ± 1 °C and relative humidity of 50 ± 5 %. During production all samples were embedded with 25 mm steel pins in the middle of the two 40×40 mm faces that protruded the faces by approximately 5 mm. The specimens were demoulded 24 h after casting and, for autogenous shrinkage tests they were sealed by four layers of plastic film and a layer of aluminum tape. During the first 4 days, measures were taken twice per hour, and then the measuring interval was progressively relaxed up to two measures per days taken from 7 days onward. The mass change of the samples was also daily measured in a balance scale of 0.01 g accuracy. Thus it was possible to verify the efficacy in sealing performed and if there was any portion of the retraction as referring to shrinkage, assuming that the perfect seal occurs when the mass loss of the specimen with respect to their water mass reaches the maximum value of 0.5 %.

In Fig. 3, the results of the measured total and autogeneous shrinkage strains are shown. All types of natural fibres were able to affect the total and autogeneous shrinkage strain development. As a matter of fact a reduction in the autogeneous shrinkage was generally observed, because of the extra amount of internal (curing) water that natural fibres could absorb because of their hydrophilic nature, accompanied by a complementary increase in the total shrinkage, because of the additional porous path for moisture escape that the porous structure of natural fibres. The cellulose nanopulp, in the employed quantity, is likely to provide a slight reduction to the autogeneous shrinkage, which could be beneficial when used in synergy with other kinds of natural and artificial fibre reinforcement in HPFRCCs.

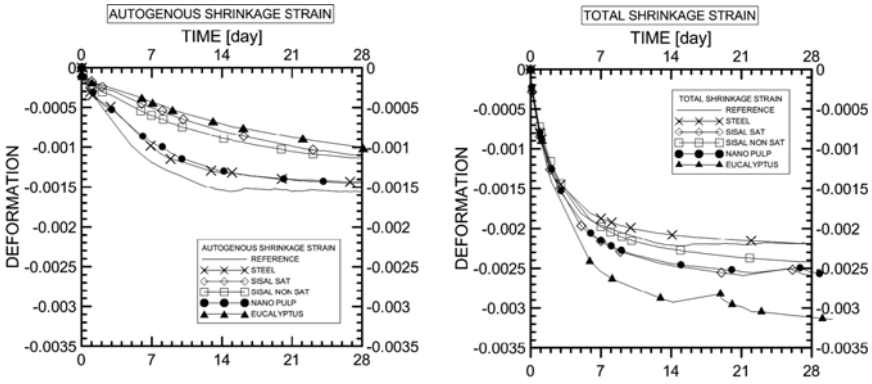

Fig. 3 Autogeneous and total shrinkage strain for different investigated HPFRCC mixes

3 Conclusions

In this paper the effects of cellulose nanopulps on autogeneous and total shrinkage of cement based composites has been investigated, and compared to other types of natural and industrial fibres. For the investigated volume percentage, the cellulose nanopulps slightly decreased autogeneous shrinkage whereas slightly increasing the total skrinkage strain. Coherently, the eucalyptus microfibers, which provided the highest benefit in terms of autogeneous shrinkage reduction, also resulted in the highest increase in total shrinkage. This study has to be meant as preliminary to a wider investigation on the use of different scale natural fibres as promoters of self healing processes in cementitious composites, thanks to the hydrofillic features and the porous network they are able to create inside the matrix.

References

1. Kim, J. K., & Mai, Y. W. (1998). *Engineered interfaces in fiber reinforced composites*. Amsterdam: Elsevier.
2. Sreekumar, P. A., Thomas, S. P., Saiter, J. M., et al. (2009). Effect of fiber surface modification on the mechanical and water absorption characteristics of sisal/polyester composites fabricated by resin transfer molding. *Composites Part A: Applied Science and Manufacturing, 40*, 1777.
3. Silva, F. A., Chawla, N., & Toledo Filho, R. D. (2008). Tensile behavior of high performance natural (sisal) fibers. *Composites Science and Technology, 68*, 3438–3443.
4. Silva, F. A., Chawla, N., & Toledo Filho, R. D. (2009). An experimental investigation on the fatigue behavior of sisal fibers. *Materials Science and Engineering A, 516*, 90–95.
5. Silva, F. A., Mobasher, B., & Toledo Filho, R. D. (2009). Cracking mechanisms in durable sisal reinforced cement composites. *Cement and Concrete Composites, 31*, 721–730.
6. Silva, F. A., Chawla, N., & Toledo Filho, R. D. (2010). Mechanical behavior of natural sisal fibers. *Journal of Biobased Materials and Bioenergy, 4*, 106–113.
7. Silva, F. A., Toledo Filho, R. D., Melo Filho, F. A., et al. (2010). Physical and mechanical properties of durable sisal fiber cement composites. *Construction and Building Materials, 24*, 777–785.
8. Melo Filho, J. A., Silva, F. A., & Toledo Filho, R. D. (2013). Degradation kinetics and aging mechanisms on sisal fiber cement composite systems. *Cement and Concrete Composites, 40*, 30–39.
9. Ferrara, L., Ferreira, S. R., Krelani, V., Silva, F., & Toledo Filho, R. D. (2014, November 3–5). *Effect of natural fibres on the self healing capacity of high performance fibre reinforced cementitious composites*. In E. Schlangen, et al., (Eds.), Proceedings SHCC3, 3rd international RILEM conference on strain hardening cementitious composites (pp. 9–16). Dordrecht.

Part VIII
Photocatalysis

Effect of Cement Types on Photocatalytic NO_x Removal and Its Underlying Mechanisms

Chi Sun Poon and Ming Zhi Guo

Abstract This paper revealed an interesting phenomenon. The photo-catalytic activity in terms of NO_x removal of cement pastes prepared with white cement (WC) and nano-TiO_2 (P25) was found to be superior to those prepared with ordinary Portland cement (OPC) and P25. Even by simply mixing P25 with anhydrous WC and OPC (without hydration), the same performance was observed. The UV-Vis diffuse reflectance spectra (DRS) of WC and OPC clearly showed that OPC was able to absorb much higher amounts of light within the range of 200–800 nm compared with WC. Also, the electrochemical impedance spectroscopy analysis pointed to a higher charge transfer resistance on the surface of OPC/P25 dry mixtures. Furthermore, the OPC/P25 dry mixtures displayed a much lower photoluminescence (PL) intensity. All the results suggest that the higher photocatalytic NO_x removal ability harboured by the WC/P25 mixtures is due to both the lower light absorption capacity and the lower charge transfer resistance of WC.

Keywords Titanium dioxide • White cement • Ordinary Portland cement • Photocatalytic NOx removal

1 Introduction

The advent of nanotechnology has greatly improved the performance of construction materials. Recently, the use of nano-TiO_2 in cementitious materials has garnered increasing attention [1]. The fine particle size of nano-TiO_2 can favourably enhance the mechanical properties of cementitious materials, such as compressive strength [2]. More importantly, this combination of nano-TiO_2 and cementitious materials brings a variety of value-added functions to the end products. Under UV light irradiation, these nano-TiO_2 containing products readily display self-cleaning, antimicrobial and air purification activities [3–5].

C.S. Poon (✉) • M.Z. Guo
Department of Civil and Environmental Engineering, The Hong Kong Polytechnic University, Hung Hom, Kowloon, Hong Kong
e-mail: cecspoon@polyu.edu.hk

K. Sobolev, S.P. Shah (eds.), *Nanotechnology in Construction*,
DOI 10.1007/978-3-319-17088-6_43

Using white cement (WC) to replace Ordinary Portland cement (OPC) for fabrication of self-compacting architectural mortar is a promising approach to enable the resultant products more aesthetically pleasing [6]. Besides, compared with OPC, WC was found to be able to enhance the photocatalytic NO_x removal efficiency of TiO_2 containing cement pastes [7]. But the reason underlying this finding had not been discussed. Another interesting finding was that adding different coloured pigments to the photocatalytic concrete surface layers gave rise to varied photocatalytic NO removal performance, with dark coloured pigments leading to the lowest efficiency [8]. This naturally raises research questions of whether the higher photocatalytic efficiency of WC pastes is a result of the less light absorption ability of the WC. Also, whether the presence of more transition metals, which give the OPC a grey colour, would adversely affect the electron-hole separation process. In this paper, the results of the attempts made to find out the underlying mechanism behind this intriguing phenomenon are presented.

2 Experimental

2.1 Materials

In this study, ASTM Type I Ordinary Portland cement (OPC, Green Island Cement Limited, Hong Kong) and white cement (WC, TAIHEIYO Cement Corp., Japan) were used to prepare the cement paste samples. A commercially available nano-TiO_2 powder (P25, Degussa) was used as the photocatalyst. The particle size of the TiO_2 was 20–50 nm, with a specific BET surface area of 50 ± 15 m^2 g^{-1}.

2.2 Mix Proportions and Sample Preparation

All the cement paste samples were prepared with a constant water-to-cement ratio of 0.4. Two different dosages of nano-TiO_2 (2 and 5 % by cement weight) as an addition to the cement/water mixture were used. Blank samples without TiO_2 addition were also made for comparison. All the proportioned powder materials were first mixed uniformly for about 5 min using a mechanical mixer. After that, water was added. A smooth and well blended paste was produced by further mixing for another 5 min. The paste was then cast into Petri dishes (7.5 cm Ø × 2.0 cm). The Petri dishes were vibrated by a vibrating table to ensure thorough compaction. The samples were then allowed to cure in an environmental chamber at 25 °C and 95 % RH for 24 h. After that, the hardened pastes were removed from the Petri dishes and placed back into the same chamber at the same conditions until the time of testing.

Dry mixtures of nano-TiO_2 (2 and 5 % by cement weight) particles and anhydrous cement (without the addition of water) were also prepared. The uniformly blended dry mixtures were put into Petri dishes for the photocatalytic NO_x removal experiment. For the other characterization experiment, the dry mixtures were also used.

2.3 Photocatalytic NO_x Removal

The reactor used in this study had been described in detail in our previous studies [3]. The NO_x removal performance of the hardened cement pastes was tested after 1 day of curing. The testing samples were put at the centre of the reactor. $1{,}000 \pm 50$ ppb inlet NO gas was allowed to flow at a rate of 3 L min^{-1} through the chamber. The relative humidity was maintained at about 30 %. Two UV-A fluorescent lamps ($2 \times$F8T5 BLB, HRK) were positioned parallel to each other on the glass cover of the reactor to provide the UV radiation. The UV-A intensity was maintained at 2 W m^{-2}, measured by a UV light meter (LT Lutron, Digital Instruments) calibrated at 340 nm, at the centre of the reactor. When the concentration of the NO gas reached equilibrium in the reactor, the lamps were turned on and the photocatalytic degradation was allowed to go on for 30 min. The details of the calculation of the amount of NO_x removal had been described previously [3].

2.4 Diffuse Reflectance UV-Vis Spectroscopy Analysis

To assess the light absorption capacity of the WC and OPC blended samples, diffuse reflectance UV-Vis spectroscopy analysis was carried out. The UV-Vis diffuse reflectance spectra were recorded on a Varian Cary 100 Scan UV-Vis system equipped with a Labsphere diffuse reflectance accessory to obtain the reflectance spectra of the testing samples over a range of 200–800 nm. $BaSO_4$ (Labsphere USRS-99-010) was employed as a reflectance standard. The spectra were converted from reflection to absorbance by the Kubelka-Munk method.

2.5 Electrochemical Impedance Spectroscopy (EIS)

To evaluate the efficiency of the charge separation and transportation of the WC and OPC blended samples, EIS was measured to give a direct indication of the charge transfer resistance on the surface of the tested samples. The EIS measurements

were conducted using an electrochemical workstation (Autolab PGSTAT302, Netherlands). Under open circuit condition, a three-electrode system was adopted. The resultant electrode served as the working electrode, with a platinum wire as the counter electrode and a Ag/AgCl (saturated KCl) electrode as the reference electrodes, which was performed in the presence of a 2.5 mM $K_3[Fe(CN)_6]/K_4[Fe(CN)_6]$ (1:1) mixture as a redox probe in 0.1 M KCl solution. The frequency range was from 100 kHz to 10 MHz. The EIS data was simulated and fitted by Nova Version 1.7 (AutoLab, Netherlands).

2.6 Photoluminescence Spectra

To investigate the amount of electron-hole pairs that can be excited and separated by photons, the photoluminescence (PL) spectra were recorded. The PL intensity at 420 nm indirectly reflects the number of photo-excited and separated electron-hole pairs because the separated pairs will recombine to emit radiative light, which was collected and analysed by the spectrophotometer. The photoluminescence (PL) spectra were measured at room temperature using an Edinburgh FLSP920 spectrophotometer.

3 Results and Discussion

3.1 Effect of Cement Types on NO_x Conversion

Figure 1a clearly shows that the paste samples prepared with WC displayed a significantly higher photocatalytic NO_x removal rate compared with those prepared with OPC. A similar trend was observed on the dry mixtures containing only dry cement and TiO_2 particles without the addition of water (Fig. 1b), suggesting that the occurrence of hydration is not the root cause of the observed difference in NO_x removal.

3.2 UV-Vis Diffuse Reflectance Spectra

The UV-Vis diffuse reflectance spectra (DRS) of the samples are shown in Fig. 2. From the absorption spectra between 200 and 800 nm, the OPC pastes had higher light absorption ability than WC pastes. The dry OPC itself also exhibited a much higher light absorption value compared with WC. Therefore, compared with OPC, WC can reflect more incident lights to the surrounding TiO_2 particles, resulting in a higher photocatalytic activity. And these results corresponded well with the photocatalytic NO_x removal activities.

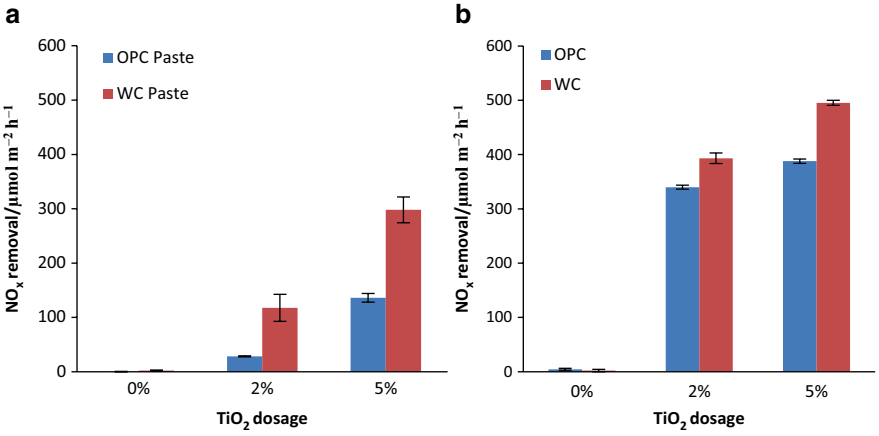

Fig. 1 Photocatalytic NO_x removal performance of TiO_2 incorporated cement pastes (**a**) and dry mixtures (**b**)

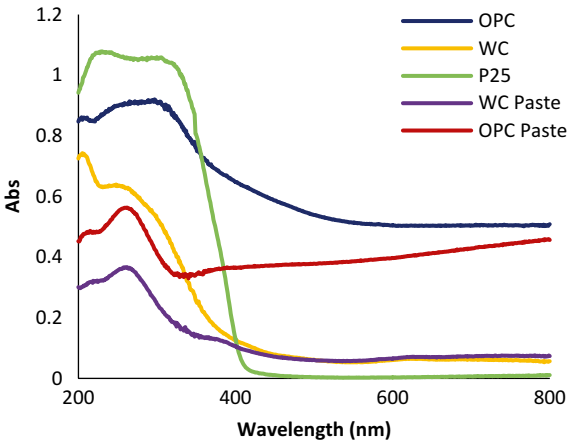

Fig. 2 UV-Vis diffuse reflectance spectra of the samples

3.3 Electrochemical Impedance Spectroscopy Analysis

The EIS measurements provide information on the efficiency of electron-hole separation on the surface of the tested samples. The size of the semicircle positively corresponds to the resistance of the sample's surface to the charge transfer. As shown in Fig. 3, the dry mixtures containing WC and P25 (5 % by cement weight) had a much shorter semicircle, which reflected a lower charge transfer resistance on the inter-surface [9]. In contrast, there was an obvious increase in the solid state interface

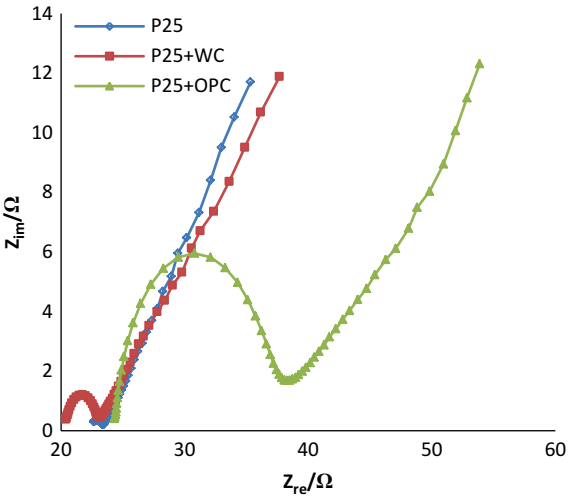

Fig. 3 EIS changes of the samples

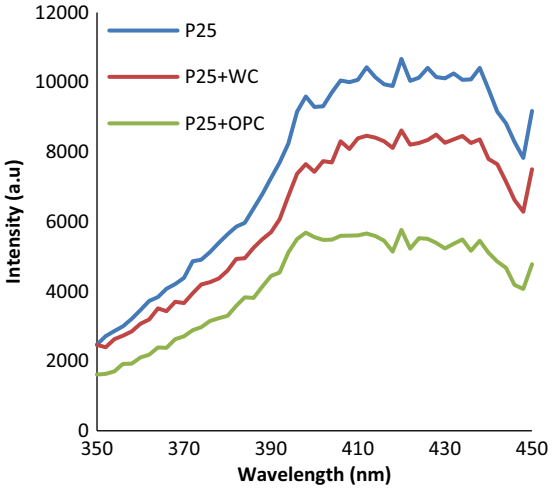

Fig. 4 Room temperature PL spectra of the samples under excitation wavelength 260 nm

layer resistance (as reflected by a bigger semicircle) for the OPC and P25 mixtures. Overall, for the WC/P25 mixtures, the electron-hole pairs could be easily transported, and thus an effective charge separation was expected to be accomplished.

3.4 Photoluminescence Spectra

Figure 4 shows the PL spectra of the samples under an excitation wavelength of 260 nm at room temperature. The PL emission intensity at 420 nm is an indicator of the radiative recombination of photon-excited electrons and holes [10].

Under our experimental conditions where no oxygen or water molecules were provided (the testing holder was sealed), a higher PL intensity meant a larger amount of electron-hole pairs can be excited and separated, and thus a higher photocatalytic activity. It is evident that the P25/OPC (1:1) had the lowest PL intensity, while P25/WC (1:1) displayed a higher one. These results further supported the observed photocatalytic NO_x removal activities of the dry mixtures containing OPC and WC.

4 Conclusions

In this study, samples prepared with WC and P25 were found to have a higher photocatalytic NO_x removal ability compared to OPC and P25 mixtures. Taking consideration all the results, it seems that a less light absorption capacity and a lower charge transfer resistance on the surface of WC are responsible for imparting the high NO_x removal property to the resultant products. As WC based architectural construction materials are being increasingly used worldwide, this study may bring added values to their broader applications in the foreseeable future.

Acknowledgment The authors wish to thank the Environment and Conservation Fund, the Woo Wheelock Green Fund and The Hong Kong Polytechnic University for funding support.

References

1. Poon, C. S., & Cheung, E. (2007). NO removal efficiency of photocatalytic paving blocks prepared with recycled materials. *Construction and Building Materials, 21*, 1746–1753.
2. Guo, M. Z., Ling, T. C., & Poon, C. S. (2012). TiO_2-based self-compacting glass mortar: Comparison of photocatalytic nitrogen oxide removal and bacteria inactivation. *Building and Environment, 53*, 1–6.
3. Chen, J., Kou, S. C., & Poon, C. S. (2011). Photocatalytic cement-based materials: Comparison of nitrogen oxides and toluene removal potentials and evaluation of self-cleaning performance. *Building and Environment, 46*, 1827–1833.
4. Guo, M. Z., Ling, T. C., & Poon, C. S. (2013). Nano-TiO_2-based architectural mortar for NO removal and bacteria inactivation: Influence of coating and weathering conditions. *Cement and Concrete Composites, 36*, 101–108.
5. Ballari, M. M., Hunger, M., Hüsken, G., & Brouwers, H. J. H. (2010). NO_x photocatalytic degradation employing concrete pavement containing titanium dioxide. *Applied Catalysis B: Environmental, 95*, 245–254.
6. Ling, T. C., & Poon, C. S. (2011). Properties of architectural mortar prepared with recycled glass with different particle sizes. *Materials and Design, 32*, 2675–2684.
7. Chen, J., & Poon, C. S. (2009). Photocatalytic cemetitious materials: Influence of the microstruture of cement paste on photocatalytic pollution degradation. *Environmental Science and Technology, 43*, 8948–8952.

8. Guo, M. Z., & Poon, C. S. (2013). Photocatalytic NO removal of concrete surface layers intermixed with TiO_2. *Building and Environment, 70*, 102–109.
9. Zhang, H., Lv, X. J., Li, Y. M., Wang, Y., & Li, J. H. (2010). P25-graphene composite as a high performance photocatalyst. *ACS Nano, 4*, 380–386.
10. Pei, C. C., & Leung, W. W. F. (2013). Enhanced photocatalytic activity of electrospun TiO_2/ZnO nanofibers with optimal anatase/rutile ratio. *Catalysis Communications, 37*, 100–104.

A Lavoisier Mass Balance Model for Photooxidation of NO by Nano TiO_2 in Roadway Microenvironments

Heather Dylla and Marwa Hassan

Abstract Increasing number of research has demonstrated that photocatalytic pavements are a promising solution for air pollution remediation of automobile sources. Due to the complexity of quantifying and understanding the photocatalytic reductions of pollutants in real world settings, models have been suggested as a methodology to understand the pollution reduction under the various environmental conditions. The objective of this paper was to create a model for the photooxidation of NO to be used in a Lavoisier mass balance model for roadway microenvironments. Using results from a previous kinetic study, a multiple linear regression model was created for both the Langmuir-Hinshelwood model constants as a function of intensity and relativity humidity. The models for k and Kd were then incorporated into the Langmuir-Hinshelwood apparent reaction rate model allowing for determination of the photocatalytic oxidation of NO at different environmental conditions. The resulting model was validated by additional laboratory runs not used to create the model determining that 87 % of model explains the data variability.

Keywords Kinetic modeling • Photocatalytic pavement • Lavoisier mass balance model

1 Introduction

Recently, due to growing concern of urban air pollution problems from traffic sources, significant interest has been given to photocatalytic pavements [1–3, 5, 8, 9]. Several laboratory studies have investigated efficiencies of photocatalytic pavements using various photocatalytic pavement mix designs under various

H. Dylla
Director of Sustainable Engineering at National Asphalt Pavement Association,
National Asphalt Pavement Association, Lanham, MD, USA
e-mail: hdylla@asphaltpavement.org

M. Hassan (✉)
CETF Associate Professor, Department of Construction Management College of Engineering,
Louisiana State University, Baton Rouge, LA, USA
e-mail: marwa@lsu.edu
https://www.cm.lsu.edu/people/faculty/facstaff/marwa.hassan

K. Sobolev, S.P. Shah (eds.), *Nanotechnology in Construction*,
DOI 10.1007/978-3-319-17088-6_44

environmental conditions demonstrating its potential [5, 6, 8, 9]. Yet, translating laboratory results to the field and understanding the efficacies in real world environments remains a challenge [3]. A promising approach to understanding photocatalytic pavements in real world conditions is through air pollution modeling approaches, which incorporates photocatalytic reaction kinetics.

2 Background

The NO reduction can be either diffusion mass-transfer controlled or reaction mass-transfer controlled, determined by whichever process is slowest. In a previous study by the authors, it was determined that the reaction kinetics were indeed reaction mass-transfer controlled and could be adequately described by the Langmuir-Hinshelwood (L-H) model for heterogeneous reactions [7]. Using this model, the NO photooxidation reaction rate is described as follows:

$$r_{NO} = \frac{k \times KC_{NO}}{1 + KC_{NO}} \tag{1}$$

where,

r_{NO} = NO photooxidation rate (mg/m^{3}s);
k = L-H reaction rate constant (mg/m^{3}s);
Kd = the L-H adsorption equilibrium constant (m^3/mg); and
C_{NO} = the concentration of NO in atmosphere (mg/m^3).

Since the reaction rate controls, diffusion is instantaneous. Thus, for a single pass experimental setup as described in the previous study by the authors, plug flow is assumed and the mass balance can be written as follows:

$$r_{NO} = -v_{air} \times \frac{dC_{NO}}{dx} = \frac{k \times KdC_{NO}}{1 + KdC_{NO}} \tag{2}$$

where,

$-v_{air}$ = velocity of air (m/s); and

$\frac{dC_{NO}}{dx}$ = rate of change of concentration per horizontal distance (mg/m^2).

In addition, the previous study also investigated the reaction kinetics under various environmental conditions by varying the relative humidity between 27 and 81 % and the irradiance between 0.52 and 3.52 W/m^2. This allowed for the calculation of the L-H constants (k and Kd) for each scenario tested. The results of the parametric study identified that relative humidity and light intensity both had a significant impact on the L-H constants [7].

Building from this, the objective of this study was to develop a model for the L-H constants as a function of relative humidity and light intensity. Then substituting these equations into the Eq. 1 the photocatalytic oxidation reaction rate of NO under

different environmental conditions can be predicted. The resulting model is an important input into Lavoisier mass balance models for roadway microenvironments, which can be used to better understand the significance of the photocatalytic reduction of NO in outdoor environments and how photocatalytic degradation compares to other mass transfer mechanisms.

3 Model Development

Using multiple linear regression a model was created for the both the L-H equilibrium adsorption constant, Kd, and the L-H reaction rate constant, k, using the 25 data points from a previous study [7]. A simple transformation was performed on the response variable to make linearity more appropriate. The square root transformation was used for both the Kd and the k response variables. Since the graphs above indicated that the effects of each predictor were not additive, interaction between the relative humidity variable and irradiance variable was investigated. As a result, the addition of a third variable, the product of the humidity and irradiance, was introduced into the models to account for possible interaction (Eqs. 3 and 4). Using SAS, stepwise regression was the procedure used to determine the independent variables included into the model with the significance level for entering of 0.15 and the significance level for staying of 0.05. The developed models are as follows:

$$\mathrm{Kd}(\mathrm{H,I}) = \left(0.01415 \times \mathrm{H} - 0.00176 \times \mathrm{H} \times \mathrm{I} + 0.45672\right)^2 \tag{3}$$

$$\mathrm{k}(\mathrm{H,I}) = \left(-0.007 \times \mathrm{H} \times \mathrm{I} + 0.69536 \times \mathrm{I} + 1.19801\right)^2 \tag{4}$$

where,

H = Humidity (%); and
I = Irradiance (W/m^2).

It is noted that the developed Kd and k models are only acceptable for the relative humidity and irradiance levels within the range of variation used to create the model as shown in Table 1.

By substituting the models created for Kd and k into Eq. 1, the apparent reaction rate model for the photooxidation of NO becomes a function of humidity and irradiance (Eq. 5).

$$\mathrm{r_{NO}} = \frac{\mathrm{k}(\mathrm{H,I}) \times \mathrm{Kd}(\mathrm{H,I}) \mathrm{C_{NO}}}{1 + \mathrm{Kd}(\mathrm{H,I}) \mathrm{C_{NO}}} \tag{5}$$

Table 1 Parameters investigated for model and the valid input ranges

	Range of variation	
Parameters	Low level	High level
Humidity (%)	27	81
UV Irradiance (W/m^2)	0.52	3.52
Humidity × UV Irradiance	14	285

3.1 Model Validation

The goodness of the fit of the Kd and k models was assessed through the coefficient of determination (R^2), the adjusted coefficient of determination (Adj R^2), which has been adjusted for the degrees of freedom and sample size, and the root mean square error (RMSE). These descriptive statistics for the developed Kd and k models are presented in Table 2. Furthermore, Fig. 1 compares the predicted k and Kd values to the experimental calculated k and Kd values. Since the coefficient of determination for both models is less than one, other variables not included in the model still may exist. One such variable is the impact of intermediates created from the photodegradation process, which in this case would be the creation of NO_2. Another part of the error could be explained by the higher error present at higher humidity levels when calculating the L-H constants, exhibited in previous study [7]. This could suggest that the L-H model may not be adequate at the higher humidity levels (>70 %) and other models need to be explored.

Table 2 Descriptive statistic of the developed models

Statistical parameters	Kd	K
Coefficient of determination (R^2)	0.784	0.8573
Adjusted coefficient of determination (Adj. R^2)	0.7644	0.8443
Root Mean Square Error (RMSE)	0.26	0.15

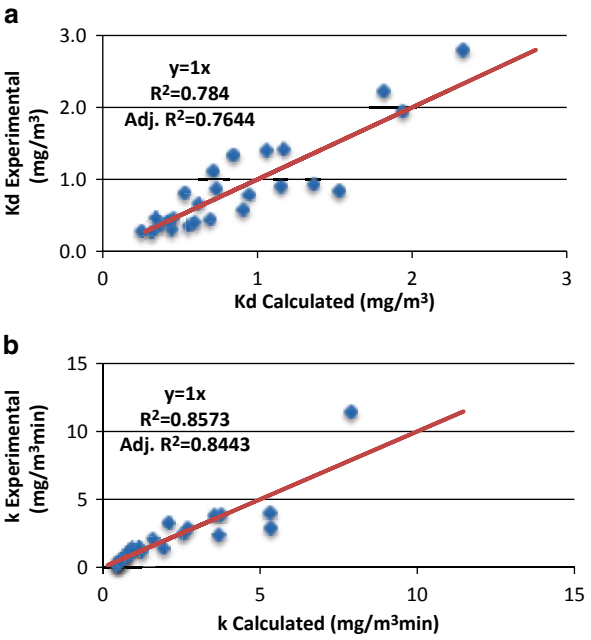

Fig. 1 Comparison of experimental L-H reaction constants to predicted L-H reaction constants (**a**) L-H equilibrium adsorption constant (**b**) L-H reaction rate constant

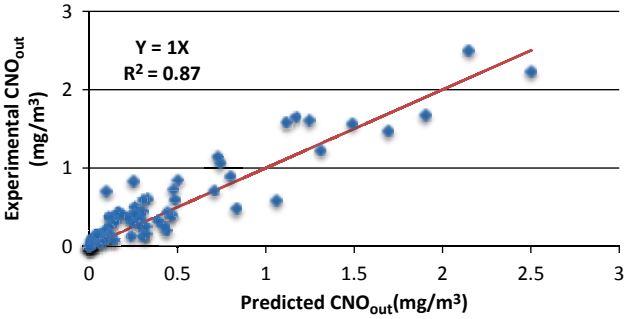

Fig. 2 Comparison of experimental NO concentrations after photocatalytic reduction compared to predicted NO concentrations

The validity of the NO photooxidation rate model, r_{NO}, was evaluated by comparing predicted NO concentration out (CNO_{out}) results with the additional observed data, which was recorded but not used to build the models. An additional 83 runs were completed at random environmental conditions within the defined variable ranges. Using a mass balance for the experimental setup, the reaction rate model was used to predict the outlet concentration. The predicted outlet concentration was compared to the actual outlet concentration measured to evaluate accuracy of the photodegradation reaction rate model. The CNO_{out} was estimated using the Taylors Series Expansion of Eq. 2, whereby Eqs. 3 and 4 predicted Kd and k, respectively. Figure 2 compares the resulting predicted CNO_{out} to the actual experimental CNO_{out}. From the results, the modified apparent reaction rate model explained about 87 % of the total variance.

3.2 Model Limitations

As recently stated, the model is only a function of relative humidity and irradiance and is limited to the ranges used to develop the model as previously noted in Table 1. The model was created for a 5 cm slit height with an air velocity of 0.003 m/s. The NO concentration was varied from 250 to 3,000 ppb. The degradation of the intermediate, nitrogen dioxide, and its possible interaction was not investigated as part of this study and is part of future work.

4 Conclusion

Air pollution modeling approaches incorporating the photocatalytic reaction kinetics, are a promising approach to understanding the efficiency of photocatalytic pavements in real world settings. Using findings from a previous study, the L-H

equilibrium adsorption constant and the L-H reaction rate were modeled using statistical techniques. Whereby the resulting model for L-H equilibrium adsorption constant is a function of the humidity and the interaction variable (humidity multiplied by irradiance), the L-H reaction rate model is a function of irradiance and the interaction variable. The resulting model for Kd explained 76 % of the variance in the data, whereas the model for k explained 84 % of the variance in the data. Substituting these two models into the apparent reaction rate model for heterogeneous reactions, a global NO photocatalytic reaction rate model was created in terms of humidity and irradiance. The NO photocatalytic reaction rate model was validated by comparing the predicted NO reduction to NO reductions measured from additional experimental runs that were not used in the model creation, determining that the global model describes 87 % of the data variability. These results can be incorporated into Lavoisier mass balance models for roadway microenvironments with photocatalytic pavements in order to study the significance of NO reductions in real world environments.

References

1. Ballari, M. M., Hunger, M., Husken, G., & Brouwers, H. J. H. (2010). NOx photocatalytic degradation employing concrete pavement containing titanium dioxide. *Applied Catalysis B: Environmental, 95*, 245–254.
2. Beeldens, A. (2006, June). *An environmental friendly solution for air purification and self-cleaning effect: The application of TiO2 as photocatalyst in concrete*. Belgian Road Research Centre. Proceedings of Transport Research Arena, Europe – TRA, Göteborg.
3. Berdahl, P., & Akbari, H. (2008). *Evaluation of titanium dioxide as a photocatalyst for removing air pollutants* (CEC-500-2007-112). California Energy Commission, PIER Energy-Related Environmental Research Program. Lawrence Berkeley National Laboratory. http://www.titan-shield.com/pdf/E/articles/PS_500-02-004-06_AKBARI.PDF. Accessed 05/2014.
4. Cassar, L. (2004, May). Photocatalysis of cementitious materials: clean buildings and clean air. *MRS Bulletin*, 29(5), 328–331. Published online by Cambridge University Press: January 2011 doi:http://dx.doi.org/10.1557/mrs2004.99.
5. Chen, D. H., & Li, K. (2007, January 26). Photocatalytic coating on road pavements/structures for NOx abatement. Beaumont: Texas Air Research Center, Lamar University.
6. Dylla, H., Hassan, M. M., Mohammad, L., Rupnow, T., & Wright, E. (2010). Evaluation of the environmental effectiveness of titanium dioxide photocatalyst coating for concrete pavements. *Journal of the Transportation Research Record, 2164*, 46–51.
7. Dylla, H., Hassan, M. M., & Thibodeaux, L. (2014). Kinetic study of photocatalytic degradation of nitrogen monoxide using concrete pavements. Paper # 14-2717. *Journal of the Transportation Research Record, 2441*, 38–47. Concrete Materials 2014, National Research Council, ISSN:0361-198.
8. Hassan, M. M., Dylla, H., Mohammad, L., & Rupnow, T. (2012). *Methods for application of titanium dioxide coatings to concrete pavement*. International Journal of Pavement Research and Technology, 5(1), 12–20, Taylor and Francis.
9. Poon, C. S., & Cheung, E. (2007). NO removal efficiency of photocatalytic paving blocks prepared with recycled materials. *Construction and Building Materials, 21*, 1746–1753. Elsevier.

Environmental Effects on the Photocatalytic Efficiency (NO_x Reduction) of Nanotitania in Portland Cement Mortar

Cezar A. Casagrande, Wellington L. Repette, Philippe J.P. Gleize, Glicerio Trichês, Joao V.S. Melo, and Dachamir Hotza

Abstract This work shows the feasibility of using nanotitania in cementitious mortars for photocatalysis of NO_x gases. Portland cement mortar samples with 3 % of nanotitania (Degussa P25) by mass of cement were made. The NO_x degradation test was performed varying three climatic conditions: relative humidity, intensity of UV radiation and NO_x (g) flow rate. There was a 50 % increase in the photocatalytic efficiency with the change from 60 ± 5 to 35 ± 5 % relative humidity. A 95 % increase of degradation efficiency with increasing radiation intensity from 10 to 60 w/m^2 was verified. It was revealed that variations in key climate conditions such as relative humidity and radiation levels are extremely impactful when it comes to efficiency in photocatalysis NO_x. Incorporating nanotitania in cementitious matrix showed great potential to contribute to the control of pollution from nitrogen oxide gases, showing an alternative low-complexity for the improvement of air quality.

Keywords Nanotitania particles • Photocatalysis • Titanium dioxide (TiO_2) • Cementitious mortars • Nitrogen oxides (NO_x)

1 Introduction

The increase of gas emissions by combustion has intensified the development of alternatives to reduce pollutant gas levels. Particularly, nitrogen gases (NO_x) react with the atmosphere resulting in compounds of nitric oxides (NO) and nitrogen dioxide (NO_2). One alternative to lower the levels of NO_x in the atmosphere is the use of Advanced Oxidation Processes, those processes are based on formation and

C.A. Casagrande (✉) • W.L. Repette • P.J.P. Gleize • G. Trichês • J.V.S. Melo
Department of Civil Engineering (ECV), Federal University of Santa Catarina (UFSC), Florianópolis, SC 88040-900, Brazil
e-mail: cezar.acasa@gmail.com

D. Hotza
Department of Chemical Engineering (EQA), Federal University of Santa Catarina (UFSC), Florianópolis, SC 88040-900, Brazil

K. Sobolev, S.P. Shah (eds.), *Nanotechnology in Construction*,
DOI 10.1007/978-3-319-17088-6_45

reaction of hydroxyl radicals (*OH) as main oxidizing agent in the degradation of pollutants with aid of a semiconductor [1–3]. When exposed to ultraviolet (UV) radiation, TiO_2 is led to an electronically excited state, responsible for the production of electron-hole pairs. As a result, reactive radicals such as hydroxyl are formed [4, 5]. From the absorption of ultraviolet light photon (hv) by TiO_2 a gap (h^+) is generated in the valence band (BV), at same time, an electron is deposited on a conducting layer (BC). As water molecule from humid air is exposed to activated TiO_2, it is adsorbed at its surface and reacts with the gap left in valence band, by electron that migrated to the conducting layer, for formation of hydroxyl radicals (*OH). When nitrogen gases come into contact with the hydroxyl radical, compounds are converted into nitrate ions (NO_3^-) and can also produce two other intermediates, such as nitrous acid (HNO_2) and nitrite anions (NO_2^-) [6]. The addition of titanium dioxide to construction materials has been shown as an alternative to reduction of polluting gases. Researchers report that photocatalytic efficiency of titanium dioxide is highly affected by the conditions in which reactions occur. The most important parameters that control the success of reaction are: gas flow subjected to the reaction, UV intensity, relative humidity of atmosphere and the concentration of nitrogen gas [7, 8].

This work presents results of the influence of variation of environment conditions (intensity of UV radiation, relative humidity and gas flow) on the photocatalytic efficiency in cement mortars with added nanotitania.

2 Experimental

A commercial ready mixed rendering mortar was used (Votorantim, Brazil) as basic material. The chemical composition of the cement used in the mortar is shown in Table 1. A commercial titania nanopowder was used (P25 Degussa, Germany) with 80 wt% anatase and 20 wt% rutile, average particle size of 20 nm and BET specific area of 50 m^2/g. The chemical composition determined by XRF analysis (Phillips PW 2,400 spectrometer) is presented in Table 1. Photocatalytic mortar samples content 3 wt% by cement were made with an absolute area (without considering the surface roughness) of 800 cm^2 (20 × 40 × 2 cm) on top of concrete bricks. The samples were cured for 7 days at a temperature of 25 ± 2 °C under >95 % of relative humidity before being transferred to a temperature and humidity controlled room at 25 ± 2 °C and relative humidity of 60 ± 5 % for 120 days.

For analysis of NO_x degradation, a photocatalysis testing chamber was used (Fig. 1), which comprises a cylinder of synthetic air (79.5 vol% N_2 and 20.5 vol% O_2) and a cylinder of nitric oxide (NO) 500 ppmv, an air humidifier, two flowmeters and flow controllers along the pipe. Lamps of 30 W with 90 cm length which emit UV-A radiation of λ 315–400 nm. A digital thermo-hygrometer sensor was used to measure air humidity. The data acquisition was performed every 2 s by a NO_x gas analyzer (Madur, GA-12) with a resolution of 1 ppmv coupled to pipe after the photoreactor.

Table 1 Chemical composition of materials

Oxides (%)	CPII-F cement	TiO_2 P25
CaO	60.26	<0.05
SiO_2	18.7	<0.05
MgO	4.86	0.10
Al_2O_3	4.27	<0.05
Fe_2O_3	2.73	<0.05
SO_3	2.7	–
K_2O	0.72[a]	<0.05
Na_2O	[a]	0.09
BaO	–	0.09
TiO_2	–	97.83
Insoluble residue	1.09	–
Loss on ignition	4.28	1.81

[a]Sum of Na_2O and K_2O

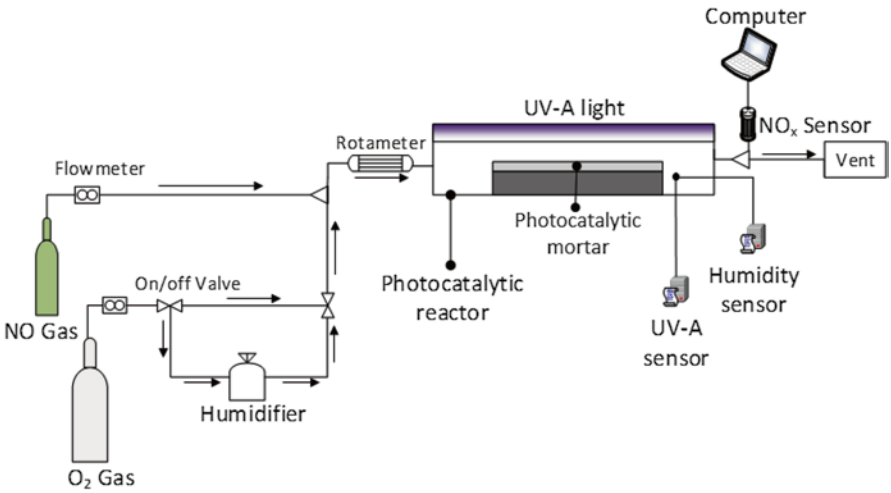

Fig. 1 Measurement setup for photocatalytic degradation of NO_x

The test was divided into three stages. First, during the initial 5 min, a gas flow of 20 ppmv of NO_x was forced within the apparatus; no UV-A radiation was imposed. In second stage, during the next 30 min, UV-radiation was supplied together with the gas flow. In third stage, UV-A radiation was stopped until the initial concentration of the stream of gas of 20 ppmv was obtained. The efficiency of NO_x removal (%) was measured from the amount related to the NO_x reading at the end of second stage (before the UV light was turned off), and was calculated according to Eq. 1.

$$\text{Efficiency of NO}_x\text{ removal}_{(\%)} = \left(\frac{\text{NO}_{x[\text{initial}]} - \text{NO}_{x[\text{final}]}}{\text{NO}_{x[\text{initial}]}} \right) \times 100 \quad (1)$$

where: $NO_{x\ [initial]}$: initial concentration of NO_x at second stage of the test, in ppmv; $NO_{x\ [final]}$: final concentration of NO_x after 30 min of photocatalysis reaction at end of the second stage of test, in ppmv.

Equation 2 was used to convert the results of NO_x degradation from parts per million by volume (ppmv) to NO_x degradation rate in mg/h/m^2. It was considered that the all NO gas flow through the chamber was oxidized to NO_2.

$$NO_x\ \text{degradation rate}_{\left[mg/h/m^2\right]} = \frac{\left(NO_{x\ \text{removal}[ppmv]} \times M_{[g/mol]} \times V_{\left[m^3/h\right]}\right)}{\left(R_{[atm]} \times T_{[K]} \times A_{\left[m^2\right]}\right)} \quad (2)$$

where: NO_x removal [ppmv] is maximum NO_x removal after 30 min of photocatalysis reaction, at the end of second stage of test, in ppmv; M is molecular concentration of NO_2, in g/mol; V is volumetric gas flow, in m^3/h; R is ideal gas constant, in atm (0.08205); T is temperature, in K; A is area of sample, in m^2.

3 Results

3.1 Flow Rate

The higher the gaseous flow, the smaller was the degradation of NO_x (ppmv) (Fig. 2). With the increase in gas flow from 1 to 5 l/min there was a 45 % loss in the photocatalytic efficiency. This is attributed to fact that the NO_x molecules require a minimum residence time onto the photocatalytic surface to interact with titanium dioxide. Thus, higher flow rates corresponded to a reduced residence time on the surface and less NO_x reacted. Therefore, the volumetric flow rate influences directly the residence in the time of NO_x on surface of sample and, thus, the performance of functional surface. These results are in agreement with the literature [7, 8].

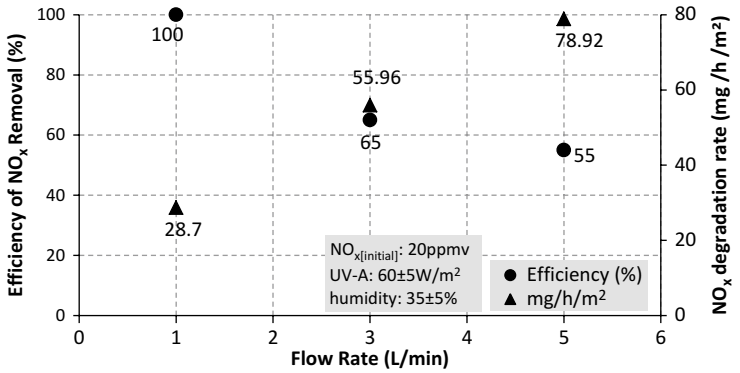

Fig. 2 Influence of flow rate on photocatalysis

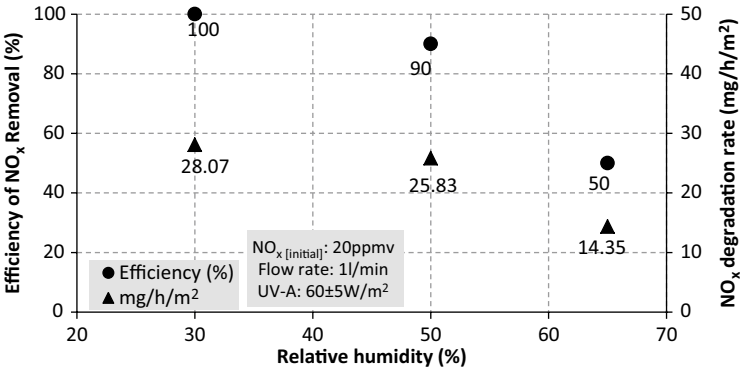

Fig. 3 Influence of humidity on the degradation of NO_x

3.2 *Relative Humidity*

The variation of relative humidity clearly shows a significant interference on the process. This can be attributed to competition of NO_x molecules and water molecules to gaps generated in titanium dioxide of the sample surface. Figure 3 shows a significant loss of photocatalytic effect when the humidity increases. A 50 % loss of photocatalytic efficiency was recorded when relative humidity increased from 30 to 65 %. Based on these results, a trend would be advanced in which the photocatalytic efficiency would rise with lowering the relative humidity. However, a minimum level of humidity is required for generation of hydroxyl radicals, and, therefore, for the photocatalytic reaction to occur. In fact, it has been shown [9–11] that at low levels of relative humidity the photocatalytic efficiency is highly reduced. Considering this, it is possible to propose that for each system there is an optimal relative humidity associated with efficiency of the photocatalytic reaction.

3.3 *Intensity of UV-A Radiation*

As can be seen in Fig. 4, increasing UV-A intensity enhances photocatalytic activity, what is attributed to fact that reactive sites on the titanium dioxide surface particles are more intensively excited and in a larger number. This higher potential for oxidation was also reported in literature [12, 13]. Figure 4 shows that increasing radiation intensity from 30 to 60 W/m^2 increased the NO_x degradation in 7 ppmv. However, this trend tends to stabilize, because at some point all possible sites of photocatalytic titanium dioxide which will be excited. In tests performed with the intensity of UV-A radiation of 60 W/m^2 an efficiency of 100 % was measured for degradation of NO_x, due to a combination of factors such as low relative humidity and low gas flow.

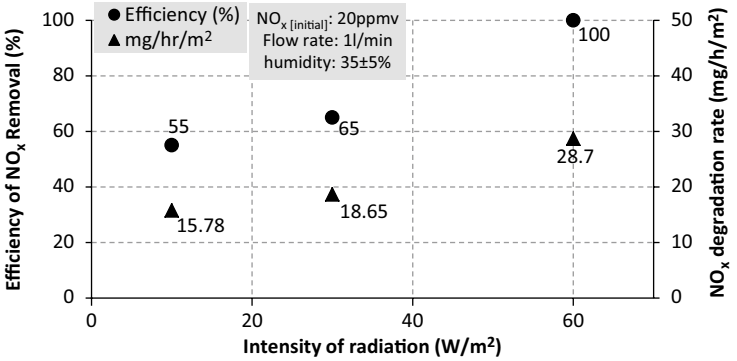

Fig. 4 Influence of UV radiation on degradation of NO_x

4 Conclusions

The results of photocatalytic mortars with incorporation of nanotitania showed that it is possible to obtain efficiency in degradation of NO_x up to 100 %, depending on test conditions. Photocatalysis was more efficient at low gas flow due to greater interaction NO_x/TiO_2. The humidity is a major interfering factor in photocatalysis, as water molecules compete with NO_x molecules for a contact on the mortar surface, reducing their photocatalytic efficiency. In most cases, the higher radiation intensities cause higher photodegradation due to the higher number of sites on surface of photocatalytic titanium dioxide. Photocatalytic mortars containing nanotitania proved to be a promising alternative for degrading NO_x molecules and hindering environmental pollution.

Acknowledgments The authors would like to thank the Votorantim Cements Company, CAPES and FAPESC for financial support of research.

References

1. Van Gerven, T., Mul, G., Moulijn, J., & Stankiewicz, A. (2007). A review of intensification of photocatalytic processes. *Chemical Engineering and Processing: Process Intensification, 46*, 781–789. doi:10.1016/j.cep.2007.05.012.
2. Thiruvenkatachari, R., Vigneswaran, S., & Moon, I. S. (2008). A review on UV/TiO2 photocatalytic oxidation process (Journal Review). *Korean Journal of Chemical Engineering, 25*, 64–72. doi:10.1007/s11814-008-0011-8.
3. Fonseca, A. J., Pina, F., Macedo, M. F., et al. (2010). Anatase as an alternative application for preventing biodeterioration of mortars: Evaluation and comparison with other biocides. *International Biodeterioration & Biodegradation, 64*, 388–396. doi:10.1016/j.ibiod.2010.04.006.
4. Fu, G., Vary, P. S., & Lin, C.-T. (2005). Anatase TiO2 nanocomposites for antimicrobial coatings. *The Journal of Physical Chemistry B, 109*, 8889–8898. doi:10.1021/jp0502196.

5. Rego, E., Marto, J., Marcos, P. S., & Labrincha, J. A. (2009). Decolouration of orange II solutions by TiO2 and ZnO active layers screen-printed on ceramic tiles under sunlight irradiation. *Applied Catalysis A: General, 355*, 109–114. doi:10.1016/j.apcata.2008.12.005.
6. Ângelo, J., Andrade, L., Madeira, L. M., & Mendes, A. (2013). An overview of photocatalysis phenomena applied to NOx abatement. *Journal of Environmental Management, 129*, 522–539. doi:10.1016/j.jenvman.2013.08.006.
7. Hüsken, G., Hunger, M., & Brouwers, H. J. H. (2009). Experimental study of photocatalytic concrete products for air purification. *Building and Environment, 44*, 2463–2474. doi:10.1016/j.buildenv.2009.04.010.
8. De Melo, J. V. S., & Trichês, G. (2012). Evaluation of the influence of environmental conditions on the efficiency of photocatalytic coatings in the degradation of nitrogen oxides (NOx). *Building and Environment, 49*, 117–123. doi:10.1016/j.buildenv.2011.09.016.
9. Devahasdin, S., Fan, C., Li, K., & Chen, D. H. (2003). TiO2 photocatalytic oxidation of nitric oxide: transient behavior and reaction kinetics. *Journal of Photochemistry and Photobiology A: Chemistry, 156*, 161–170. doi:10.1016/S1010-6030(03)00005-4.
10. Hunger, M., Hüsken, G., & Brouwers, H. J. H. (2010). Photocatalytic degradation of air pollutants — From modeling to large scale application. *Cement and Concrete Research, 40*, 313–320. doi:10.1016/j.cemconres.2009.09.013.
11. Laufs, S., Burgeth, G., Duttlinger, W., et al. (2010). Conversion of nitrogen oxides on commercial photocatalytic dispersion paints. *Atmospheric Environment, 44*, 2341–2349. doi:10.1016/j.atmosenv.2010.03.038.
12. Carp, O. (2004). Photoinduced reactivity of titanium dioxide. *Progress in Solid State Chemistry, 32*, 33–177. doi:10.1016/j.progsolidstchem.2004.08.001.
13. Beeldens, A. (2008). *Air purification by pavement blocks: Final results of the research at the BRRC*. 0–7. doi:http://www.brrc.be/pdf/tra/2008_Beeldens.pdf

Part IX
Self-Healing and Smart Materials

An Innovative Self-Healing System in Ultra-high Strength Concrete Under Freeze-Thaw Cycles

Ana Guerrero, Jose Luis García Calvo, Pedro Carballosa, Gloria Perez, Virginia R. Allegro, Edurne Erkizia, and Juan Jose Gaitero

Abstract The development of cementitious materials with self-healing properties is currently a very active research line in order to increase the service life of structures and reduce the costs associated to maintenance and repair. A combination of silica microcapsules containing an epoxy sealing compound and nanosilica particles functionalized with amine groups has been developed to confer self-healing properties to an ultra-high performance concrete. The durability of the self-healing system under severe climatic conditions is considered in this work. Cylindrical concrete specimens were made with and without the self-healing additions. After a curing time of 28 days, micro-cracks with a controlled width were created in the specimens that were subsequently subjected to a freeze-thaw test consisting of four cycles per day between −20 and +20 °C. The results from capillary water absorption test after 150 cycles confirm the efficiency of the sealing system even under the aggressive conditions considered in this study.

Keywords Self-healing concrete • Microcapsule • Nanosilica • Durability • Freeze-thaw cycles

A. Guerrero (✉)
Institute of Construction Science "Eduardo Torroja" CSIC,
calle Serrano Galvache, 4, Madrid E-28033, Spain

MATCON, Associated Unit Tecnalia-CSIC, Madrid, Spain
e-mail: aguerrero@ietcc.csic.es

J.L. García Calvo • P. Carballosa • G. Perez • V.R. Allegro
Institute of Construction Science "Eduardo Torroja" CSIC,
calle Serrano Galvache, 4, Madrid E-28033, Spain
e-mail: jolgac@ietcc.csic.es; carballosa@ietcc.csic.es; gperezaq@ietcc.csic.es; allegro@ietcc.csic.es

E. Erkizia • J.J. Gaitero
Sustainable Construction Division, Tecnalia, Materials,
calle Geldo, Edificio 700, Parque Tecnológico de Bizkaia, Derio E-48160, Spain

MATCON, Associated Unit Tecnalia-CSIC, Madrid, Spain
e-mail: edurne.erkizia@tecnalia.com; juanjose.gaitero@tecnalia.com

K. Sobolev, S.P. Shah (eds.), *Nanotechnology in Construction*,
DOI 10.1007/978-3-319-17088-6_46

1 Introduction

Self-healing concrete is one of the most promising smart materials under development by the construction materials scientific community. Several research groups have devoted their efforts to this issue [1] in order to obtain a cementitious material that can autonomously detect and repair the appearing cracks while in the micrometric scale, thus preventing macroscopic damage and reducing the maintenance and repair costs. Our group has proposed an innovative self-healing system formed by the combined action of two additions: epoxy-containing silica microcapsules (CAP) and amine-functionalized silica nanoparticles (NS). In previous works, the compatibility and stability of these additions within the cementitious matrix, their effect on the hydration of cement paste and the efficiency of the self-healing system have been confirmed in ultra-high performance concrete with special characteristics such as very low maximum particle size (micro-concrete) [2, 3]. As another step in the development of a reliable and durable material, the behavior of the self-healing micro-concrete exposed to severe temperature changes (freeze-thaw cycles) is presented in this work.

2 Experimental Methods

Cylindrical specimens of 100 mm in diameter and 25 mm thick were prepared with a water/cement ratio of 0.3 and the compositions shown in Table 1, for the reference and the self-healing micro-concretes. For the preparation of the specimens, the silica fume Elkem Grade 940-U undensified (SF), the microcapsules encapsulating the epoxy Epothin® from Buehler (CAP), the aggregates and the cement were mixed slowly for 1 min. The amine-functionalized nanosilica (NS), previously dispersed for 5 min in distilled water with the superplastizicer Structuro 351 from Fosrocusing an ultrasonic probe, was then added to the solids. The paste was mixed 1 min slow, 3 min fast and the mixing was halted for 2 min. The mixing proceeded fast for two more minutes and then half of the steel fibers (OL13/0.16) were added and mixed fast for 1 min followed by the addition of the other half and fast mixing for another minute. The specimens were stored for 24 h in a controlled chamber at 20 ± 1.0 °C and 100 % relative humidity and after that time they were unmolded and introduced in fresh water baths at 20.0 ± 1.0 °C, according to UNE-EN 196–1.

At 28 days of curing, four cylindrical specimens of each matrix were cracked to a specified crack mouth opening displacement (CMOD) of 150 μm and four to 300 μm using the Brazilian splitting tension test. The CMOD was measured with an

Table 1 Amounts of additions used in the micro-concrete specimens (per 680 g of CEMI 52.5N, 204 g of water, 510 g of siliceous aggregates (Ø < 1 mm) and 510 g of limestone (Ø < 0.5 mm) aggregates, 27.2 g of superplastizicer and 119 g of fibers)

	SF (g)	CAP (g)	NS (g)
Reference (REF)	170	0	0
Self-healing (SH)	11	68	91

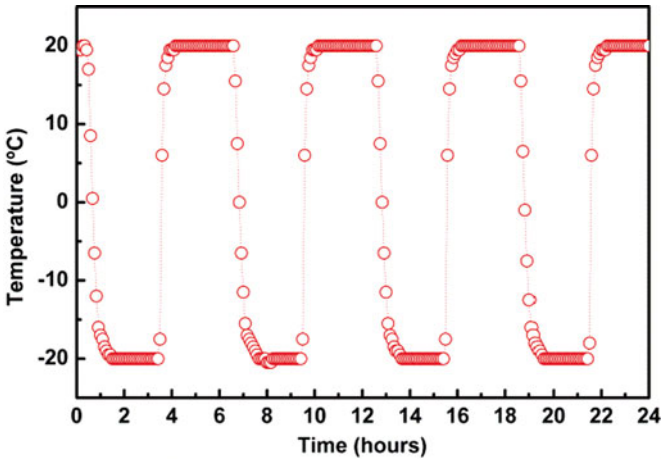

Fig. 1 Temperature profile during 24 h of the freeze-thaw test

extensometer placed between two steel plates stuck on one face of the specimen and the tests were performed at a constant crack mouth opening rate of 0.5 μm/s. Once cracked, the specimens were weighted before placing them on a metal support grating inside a climate chamber to be subjected to a freeze and thaw durability test consisting of cycles of 3 h in dry ambient at −20 °C and 3 h under water at 20 °C. Figure 1 shows the temperature profile during 24 h, as measured by a sensor positioned at the same support as the samples. Taking into account the high durability expected in the ultra-high performance micro-concretes fabricated, 150 cycles have been considered and the weight of the specimens was controlled several times during the test.

After the 150 freeze-thaw cycles the samples of the reference concrete (REF-FT) and the self-healing concrete (SH-FT) were preconditioned for the measurement of water absorption rate by means of capillarity test by drying them at 50 °C up to constant weight. Only one face of the specimens was put in contact with water up to a level of 5 mm and the samples were periodically weighed in order to measure the water absorption rate. The same procedure was followed for a set of specimens of both micro-concretes that were not subjected to the freeze-thaw cycles, but were stored in sealed plastic bags after cracking, in order to prevent carbonation, during a healing period of 28 days. These samples healed at laboratory conditions (REF-LC and SH-LC) were considered as the reference to evaluate the effect of the freeze-thaw cycles on the efficiency of the self-healing system proposed.

3 Results and Discussion

The weight of the specimens of reference (REF) and self-healing (SH) micro-concretes was measured during the thawing phase after 50, 72, 109 and 150 cycles. The resulting values for the samples considered in the test are depicted in Fig. 2.

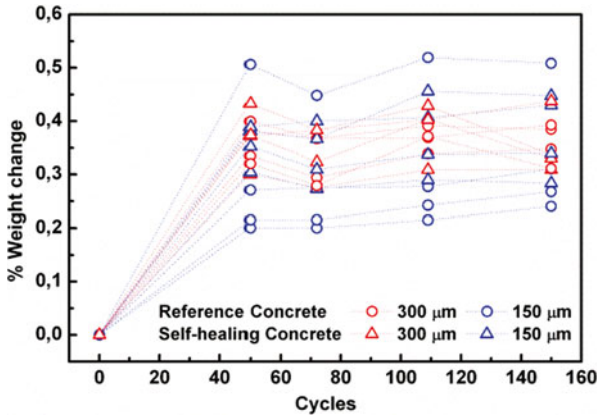

Fig. 2 Percent weight change of the specimens with respect to their initial weight during the freeze-thaw durability test

A clear increase of weight is observed after the initial 50 cycles that must be associated to the water saturation during the under-water step at 20 °C. The range seen in this initial increase (0.2–0.5 %) may be related to the variability in the obtained crack width when the load is removed from the specimens. However, between 50 and 150 cycles a variation in percent weight change lower than 0.1 % is observed for all the samples, thus indicating a constant weight of the specimens. Moreover, the physical aspect of the samples was also controlled during the test and no significant external damage was observed. Thus, it may be concluded that the two types of micro-concrete analyzed show no scaling due to the cycles. The results in Fig. 2 are in good agreement with Mu and co-workers [4] who report that the previous external loading does not give rise to an increase of scaling of concrete specimens subjected to freeze-thaw cycles. Nevertheless, they observed that pre-loading clearly accelerates the internal damage of the material due to the acceleration of the initiation and propagation of cracking.

In order to determine the effect of the internal damage probably produced by the freeze-thaw cycles on the samples and, more specifically, on the healing system in SH concrete, the results of the subsequent capillary absorption test have been collected in Fig. 3. The mean data of the specimens subjected to the freeze-thaw cycles (REF-FT and SH-FT) are compared to those corresponding to the samples stored in plastic bags at standard laboratory conditions during 28 days after cracking (REF-LC and SH-LC). The results of the same test for uncracked samples as presented previously [3] are also included for comparison.

In Fig. 3a it is observed that for the reference micro-concrete the initial water absorption rate of the cracked specimens is significantly higher than that observed in uncracked samples and increasing with the increase of the nominal crack width from 150 to 300 μm. The behavior of the samples with CMOD of 150 μm under the capillary absorption test (Fig. 3a) shows no significant influence of the freeze-thaw cycles. In fact, the capillary absorption coefficient (K) calculated using the mass

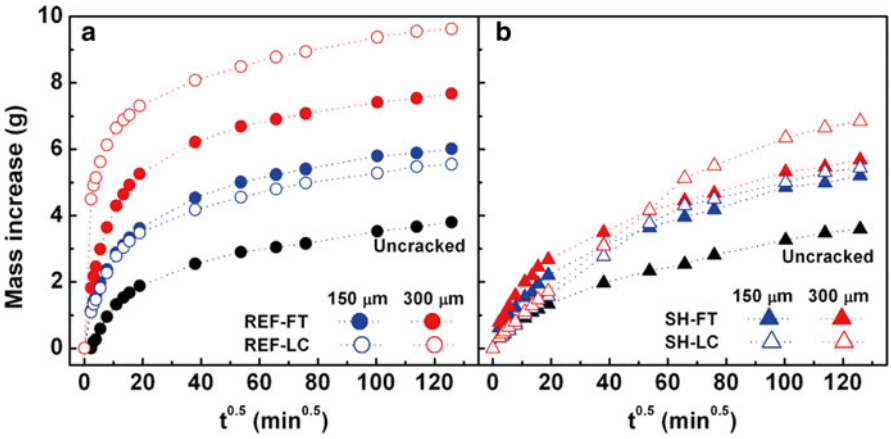

Fig. 3 Mean water absorption rate of the cracked specimens subjected to freeze-thaw test (*FT*) and stored in laboratory conditions (*LC*). (**a**) Reference (*REF*) concrete. (**b**) Self-healing (*SH*) concrete. Values of uncracked samples are included for comparison

increase after 24 h is 0.015 and 0.017 kg/m^2 min$^{0.5}$ for samples REF-FT and REF-LC, respectively. In the case of the specimens cracked up to a CMOD of 300 μm, a clearly lower absorption rate is observed in the sample subjected to the freeze-thaw cycles (REF-FT), with a lower mass increase and a value of K equal to 0.021 Kg/m^2 min$^{0.5}$, compared to 0.027 Kg/m^2 min$^{0.5}$ of the equivalent sample stored in laboratory conditions (REF-LC). This result suggests a lower content of pores in the material REF-FT, probably due to an enhancement of cement hydration in the under-water thawing periods giving rise to autogenous crack healing [5], more effective due to the low water/cement ratio of the concrete.

The initial mass increase rate of the uncracked self-healing concrete upon the capillary water absorption test (Fig. 3b) is significantly lower than that of corresponding sample of reference concrete in Fig. 3a, suggesting that the former would be denser probably due to the presence of nanosilica in the cement matrix. More interesting is the fact that the initial water absorption rate of the cracked samples stored in laboratory conditions (SH-LC) is very similar to that observed in the uncracked sample and almost insensitive to the crack width. This confirms the presence of an additional crack healing process, not present in the reference material and consequently, associated to the addition of the innovative system formed by CAP and NS.

Regarding the efficiency of this self-healing process under the freeze-thaw cycles, no effect is observed in the case of specimens cracked up to 150 μm. In fact, the values of K obtained after 24 h from the capillary water absorption test are 0.009 and 0.010 kg/ m^2 min$^{0.5}$ for the samples SH-LC and SH-FT, respectively. In the case of the specimens cracked up to 300 μm (Fig. 3b), the final mass increase observed for the sample subjected to the freeze-thaw test, SH-FT, is lower than the corresponding to the analogue sample stored in laboratory conditions, SH-LC, as already observed for the reference material (Fig. 3a). On the contrary, the absorption rate in

the first part of the experiment is in this case higher for sample SH-FT. This can be explained in terms of a combined autonomic and autogenous self-healing effect. Upon formation of the crack, epoxy containing capsules (CAP) break down partially sealing it (autonomic self-healing) [5]. If the samples are then subjected to freeze-thaw cycles, liquid water will enter the crack as far as the resin allows it. During the freezing part of the cycle, ice will exert a pressure on the material that may give rise to the appearance of internal microcracks and also probably a compression of the resin into pores and hollow microcapsules. In any case, during the subsequent thawing cycle water will find less resistance to enter the crack and a higher mass increase is observed than in samples SH-LC where there is no effect of ice. Moreover, water entering the crack in SH-FT reacts with anhydrous cement particles inside and provides a more effective autogenous healing [5] than in SH-LC. The resulting denser structure explains the lower total weight gain after the test.

4 Conclusions

In summary, the presence of the innovative self-healing system formed by CAP and NS in the cement matrix gives rise to a self-healing capacity of the resulting concrete that is not lost in the aggressive conditions of the freeze-thaw cycles considered (four freeze-thaw cycles per day from −20 to +20 °C). A minor effect of the freeze-thaw cycles is observed in the case of CMOD of 300 μm that may be related to a combined autonomic and autogenous self-healing effect.

Acknowledgement Acknowledgment is due to J. A. Sánchez and the Technical Evaluation of Innovative Products Unit of IETcc for their help in the experimental work and to the financial support of the BIA2011-29234-C02 Project (Spanish Government) and the P2012-23 project (Basque Government).

References

1. Van Tittelboom, K., & De Belie, N. (2013). Self-healing cementitious materials – A review. *Materials, 6*, 2182–2217.
2. Perez, G., Erkizia, E., Gaitero, J. J., et al. (2014). Effect of different amounts of innovative self-healing additions on the microstructure of cement pastes. In K. Van Bruegel, E. Koenders (Eds.), *Proceedings of the 1st Ageing of Materials & Structures conference* (pp. 628–634). Delft. Printed by Siecarepro.nl.
3. Garcia Calvo, J. L., Carballosa, P., Perez, G., et al. (2014). *Effect of self-healing nano-additions on the performance and the durability properties of ultra-high strength concretes*. Oral presentation in 1st Concrete Innovation conference, Oslo.
4. Mu, R., Miao, C., Luo, X., & Sun, W. (2002). Interaction between loading, freeze-thaw cycles and chloride salt attack of concrete with and without steel fiber reinforcement. *Cement and Concrete Research, 32*, 1061–1066.
5. Rooij, M., et al. (2013). In M. de Rooij, K. Van Tittelboom, N. De Belie, & E. Schlangen (Eds.), *Self-healing phenomena in cement-based materials. State-of-the-art report of RILEM technical committee 221-SHC: Self-healing phenomena in cement-based materials* (RILEM State-of-the-arts reports, Vol. 11). Dordrecht: Springer Netherlands.

Self Sensing Capability of Multifunctional Cementitious Nanocomposites

Chrysoula A. Aza, Panagiotis A. Danoglidis, and Maria S. Konsta-Gdoutos

Abstract Carbon nanotubes (CNTs) exhibit excellent electrical properties and can be used to produce multifunctional nanocomposite cement based materials with exceptional self sensing capabilities. The self sensing behavior of cementitious nanocomposite materials, their ability to sense strain, stress and cracking, while achieving superior mechanical properties, can be closely related to the electrical and piezoresistive properties of the material. In this research, the piezoresistive behavior of novel multifunctional cementitious nanocomposites was investigated in order to determine the carbon nanotube electrical percolation threshold. Carbon nanotube cement composites with different percentages of CNTs for w/c = 0.485 were prepared. The electrical resistance was initially measured using direct current (DC), followed by piezoresistivity measurements under cyclic compressive loading. The 4-pole method was employed for both conductivity and piezoresistivity measurements. Results demonstrate that carbon nanotubes can be used to successfully create a conductive network for stress/damage detection in advanced, multifunctional cement based nanocomposites.

Keywords Carbon nanotubes • Piezoresistivity • Strain sensing • Flexural strength • Multifunctional

1 Introduction

Carbon nanotubes are materials that exhibit excellent mechanical [1] and electrical properties. When subjected to stress/strain, their electrical properties change [2]. This piezoresistive behavior triggers the potential of creating smart cementitious composites for structural health monitoring and damage detection, alongside with improved mechanical performance. Recent research studies on the electrical properties and sensing ability of cementitious nanocomposites reinforced with CNTs

C.A. Aza, MSc (✉) • P.A. Danoglidis, PhD • M.S. Konsta-Gdoutos
Department of Civil Engineering, Democritus University of Thrace,
Vas. Sofias 12, Xanthi 67100, Greece
e-mail: azachrysoula@gmail.com; pdanogli@civil.duth.gr

K. Sobolev, S.P. Shah (eds.), *Nanotechnology in Construction*,
DOI 10.1007/978-3-319-17088-6_47

[3–7] indicated that CNTs can reduce the electrical resistance of the cementitious composites, and that by imposing compressive load the electrical resistance of the nanocomposite changes inversely; decreases upon loading and increases upon unloading [3–5]. Further studies on the piezoresistive properties have shown that the piezoresistive sensitivity of the nanocomposites is greatly affected by the amount of CNTs as well as by the water/cement (*w/c*) ratio [6, 7]. Moreover, recent studies have shown that by reinforcing the weak cementitious matrices with CNTs, the mechanical properties of the nanocomposites can be significantly improved [8–12], provided that CNTs are effectively dispersed in the matrix [10, 11]. In this study, the development of advanced, multifunctional with self sensing capabilities cement mortar nanocomposites, reinforced with well dispersed multiwall carbon nanotubes (MWCNTs) was investigated. Different amounts of carbon nanotubes were examined to study the piezoresistive behavior and determine the carbon nanotube electrical percolation threshold. Fracture mechanics tests were also performed to evaluate the mechanical properties of these nanocomposites.

2 Experimental Program

2.1 Materials and Mortar Preparation

Mortar specimens 20×20×80 mm were prepared using ordinary portland cement (OPC), fine aggregate sand and multiwall carbon nanotubes (MWCNTs) of 20–40 nm diameter and length >10 μm. To achieve homogeneous dispersion of MWCNTs, suspensions were prepared by adding the MWCNTs in an aqueous surfactant solution and applying sonication at room temperature following the method described in Konsta-Gdoutos et al. [10]. Next, OPC and sand were added into the MWCNT suspensions at a water to cement ratio *(w/c)* 0.485 and sand to cement ratio *(s/c)* 2.75. The materials were mixed according to ASTM 305. Metallic grids were inserted into the specimens, immediately after casting, serving as electrodes for measuring the electrical resistivity of the nanocomposites. The samples were cured in lime-saturated water for 3, 7 and 28 days. The piezoresistivity specimens were put in an oven before testing to dry at 95 °C for 3 days, to eliminate the effect of polarization.

2.2 Piezoresistivity Testing

To measure the electrical resistance of the cementitious nanocomposites two digital multimeters with the ability to measure μA and V, and a power supply unit capable of supplying direct current (DC) up to 30 V were used. According to the four-pole method followed, the multimeter connected with the inner electrodes was used to measure the voltage difference while the one connected with the outer electrodes and the power supply unit was used for current intensity measurements. For the piezoresistive behavior of the cement-based nanocomposites the change in

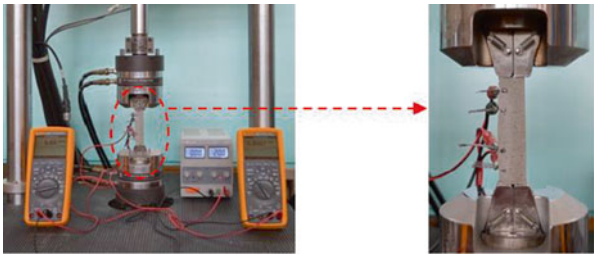

Fig. 1 Experimental setup for measuring the electrical resistance under compressive load

electrical resistance was measured using the aforementioned procedure, while a compressive cyclic load was simultaneously applied from a servohydraulic testing machine (MTS) of maximum operating strain ability 25 kN. A cyclic compressive loading of maximum 2 kN (load within the elastic region) was performed in each specimen and every cycle of loading-unloading had duration of approximately 120 s. The setup is shown in Fig. 1.

2.3 Fracture Mechanics Testing

The mechanical performance of the nanocomposites was evaluated by fracture mechanics tests. Tests were conducted on notched specimens of 20×20×80 mm at the age of 3, 7 and 28 days, using a closed-loop MTS servohydraulic testing machine with a 25 kN capacity. The crack mouth opening displacement (CMOD) at the notch, set at a rate of 0.012 mm/min, was used as the feedback control signal for running the test. The ASTM C348 was followed to determine the average values of the flexural strength and Young's modulus. Young's modulus was calculated from the load versus CMOD graphs using the two-parameter fracture model by Jenq and Shah [13].

3 Results and Discussion

3.1 Mechanical Performance

The results of the average flexural strength and Young's modulus of cement mortar nanocomposites are presented in Fig. 2 and Table 1, respectively. In all cases, the samples reinforced with 0.1 wt% MWCNTs exhibited the highest increase both in flexural strength and Young's modulus, estimated to 86.8 and 92.3 % respectively at 28 days. The samples containing 0.5 wt% MWCNTs showed improved mechanical properties compared to plain cement mortar, however, these samples demonstrated a smaller increase than the nanocomposites with 0.1 wt% MWCNTs. The results suggest that there is a threshold and an optimal amount of CNTs to achieve superior reinforcing effect.

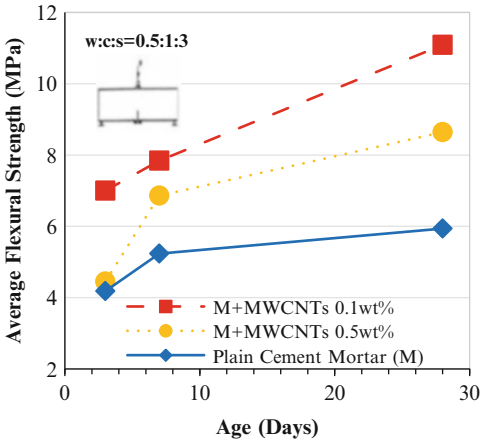

Fig. 2 Flexural strength of cement mortar and cement mortar nanocomposites

Table 1 Young's modulus (GPa)

Sample	Young's modulus (GPa)		
	3 days	7 days	28 days
Plain Cement Mortar	9.89	12.00	14.28
M+MWCNTs 0.1 wt%	16.68	18.43	27.47
M+MWCNTs 0.5 wt%	10.27	13.24	20.14

3.2 Piezoresistive Behavior

In order to further investigate the effect of the different CNTs loading and determine the CNT electrical percolation threshold, electrical resistance measurements were performed at 28 days specimens with different amounts of MWCNTs. The average values of resistivity of the different samples examined are illustrated in Fig. 3. It is observed that the resistivity of 0.1 wt% MWCNT composite significantly exceeds the average resistivity of all other mixtures, while increasing the MWCNT content further than 0.1 wt% a notable decrease in resistivity is observed.

Results of the piezoresistive response of 0.1 wt% MWCNT mortar composites are shown in Fig. 4. The graph reflects the cycles of loading-unloading performed and the corresponding change in resistivity. The fractional change of resistivity (%) is obtained by dividing the difference in values of resistivity each time and initial resistivity, $\Delta\rho$, to the initial resistivity, ρ_0. It is observed that resistivity decreases during loading and increases during unloading. Comparing the average resistivity change of all mixes (Table 2), it is observed that the 0.1 wt% MWCNT mortar nanocomposite exhibits a more pronounced piezoresistive response, up to 10.4 %. An increased resistivity change indicates that the sample exhibits better sensing response to the change in the applied stress, therefore the material could be used as a sensor.

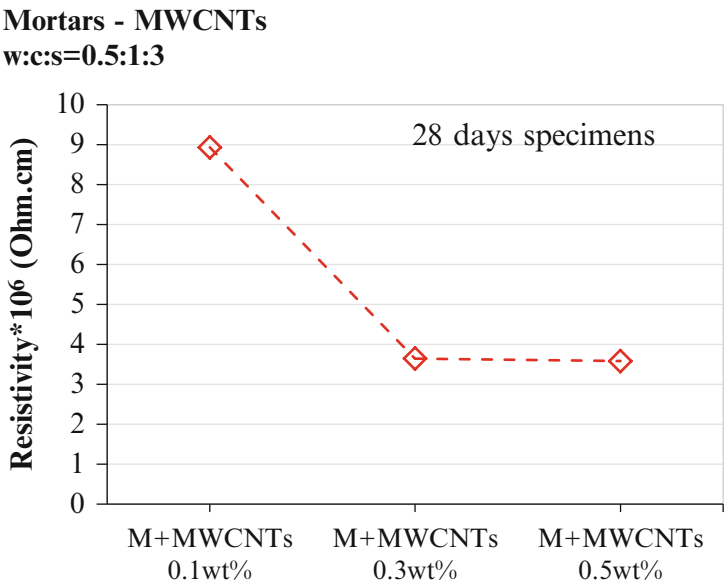

Fig. 3 Resistivity percolation threshold of cement mortars reinforced with MWCNTs

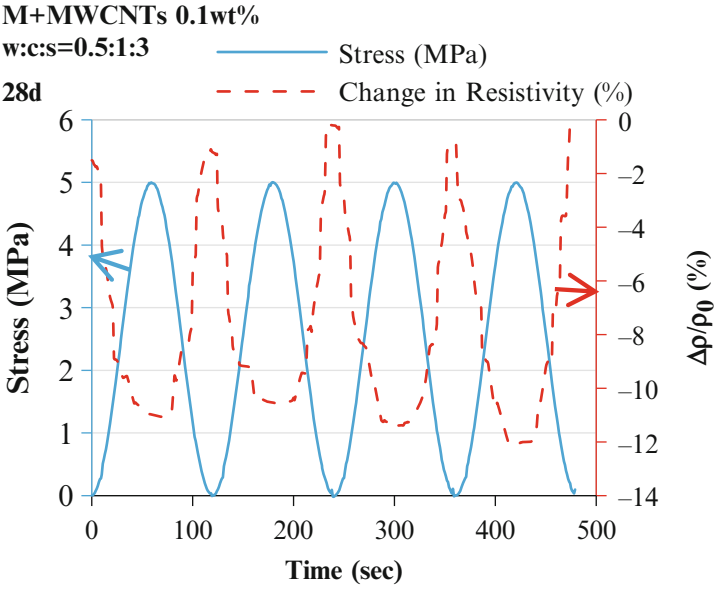

Fig. 4 Piezoresistive behavior of cement mortars reinforced with MWCNTs

Table 2 Average resistivity change of cement mortars reinforced with MWCNTs

Nanocomposite	Average resistivity change (%)
M + MWCNTs **0.1** wt%	10.4
M + MWCNTs **0.3** wt%	2.4
M + MWCNTs **0.5** wt%	3.2

4 Conclusions

The self sensing capability of multifunctional cementitious nanocomposites was investigated. The piezoresistive sensitivity and mechanical characteristics of cement mortar composites reinforced with different loadings of well dispersed MWCNTs were determined. Resistivity measurements were performed on 28 days old specimens with different contents of MWCNTs showed that the addition of MWCNTs was proven to induce a decrease in electrical resistance, with the mortar nanocomposites containing 0.3 and 0.5 wt% MWCNTs yielding better electrical properties. However, a content of 0.1 wt% MWCNTs was found to exhibit a better piezoresistive response while a further increase of the MWCNT content produced a lower sensing response. In addition, the three-point bending results indicated that the mechanical properties of cement mortar reinforced with different amounts of MWCNTs are remarkably improved. A MWCNT content of 0.1 wt% is able to almost double both the flexural strength and Young's modulus. The results suggest that an amount of 0.1 wt% MWCNTs provides both an amplified sensitivity in strain sensing and a superior reinforcing effect.

Acknowledgements The authors would like to acknowledge the financial support of the National Strategic Reference Framework (NSRF) – Research Funding Program "SYNERGASIA 2011 – Nano-Modified Smart Concrete (NSC) (11SYN_5_1430)", Partnerships of Production and Research Institutions in Focused Research and Technology Sectors, funded by the European Union (European Social Fund – ESF) and Greek national funds through the Operational Program "Competitiveness and Entrepreneurship and Regions in Transition (EPAN II)".

References

1. Salvetat, J. P., Bonard, J. M., Thomson, N. H., Kulik, A. J., Forro, L., Benoit, W., et al. (1999). Mechanical properties of carbon nanotubes. *Applied Physics A, 69*, 255–260.
2. Tombler, T. W., Zhou, C., Alexseyev, L., Kong, J., Dai, H., Liu, L., et al. (2000). Reversible electromechanical characteristics of carbon nanotubes under local-probe manipulation. *Nature, 405*, 769–772.
3. Li, G. Y., Wang, P. M., & Zhao, X. (2007). Pressure-sensitive properties and microstructure of carbon nanotube reinforced cement composites. *Cement and Concrete Composites, 29*, 377–382.
4. Yu, X., & Kwon, E. (2009). A carbon nanotube/cement composite with piezoresistive properties. *Smart Materials and Structures, 18*, 055010.

5. Konsta-Gdoutos, M. S., & Aza, C. A. (2014). Self sensing carbon nanotube (CNT) and nanofiber (CNF) cementitious composites for real time damage assessment in smart structures. *Cement and Concrete Composites, 53*, 162–169.
6. Han, B., Yu, X., Kwon, E., & Ou, J. (2012). Effects of CNT concentration level and water/cement ratio on the piezoresistivity of CNT/cement composites. *Journal of Composite Materials, 46*(1), 19–25.
7. Luo, J., Duan, Z., Zhao, T., & Li, Q. (2011). Effect of compressive strain on electrical resistivity of carbon nanotube cement-based composites. *Key Engineering Materials, 483*, 579–583.
8. Li, G. Y., Wang, P. M., & Zhao, X. (2005). Mechanical behavior and microstructure of cement composites incorporating surface-treated multi-walled carbon nanotubes. *Carbon, 43*, 1239–1245.
9. Cwirzen, A., Habermehl-Chirzen, K., & Penttala, V. (2008). Surface decoration of carbon nanotubes and mechanical properties of cement/carbon nanotube composites. *Advances in Cement Research, 20*, 65–73.
10. Konsta-Gdoutos, M. S., Metaxa, Z. S., & Shah, S. P. (2010). Highly dispersed carbon nanotubes reinforced cement based materials. *Cement and Concrete Research, 40*, 1052–1059.
11. Konsta-Gdoutos, M. S., Metaxa, Z. S., & Shah, S. P. (2010). Multi-scale mechanical and fracture characteristics and early-age strain capacity of high performance carbon nanotube/cement nanocomposites. *Cement and Concrete Composites, 32*, 110–115.
12. Metaxa, Z. S., Konsta-Gdoutos, M. S., & Shah, S. P. (2009). Carbon nanotube reinforced concrete. *ACI Special Publication, 267*, 11–20.
13. Shah, S. P., Swartz, S. E., & Ouyang, C. (1995). *Fracture mechanics of concrete: Application of fracture mechanics to concrete, rock and other quasi-brittle materials*. New York: Willey.

Effects of Ultra-low Concentrations of Carbon Nanotubes on the Electromechanical Properties of Cement Paste

Isaac Wong, Kenneth J. Loh, Rongzong Wu, and Navneet Garg

Abstract This study analyzed the effects of ultra-low concentrations of multi-walled carbon nanotubes (MWNT) on the electromechanical properties of cement paste. Here, 0.025 and 0.050 *wt%* of MWNTs were dispersed using a poly(sodium 4-styrenesulfonate) aqueous solution, which was then used for casting specimens. Because these concentrations make large-scale applications much more feasible, sample consistency and effects of saturation were also studied. Their resistivity ranges and strain sensing properties (*i.e.*, gage factors) were characterized.

Keywords Cement paste • Carbon nanotubes • Sensing • Smart concrete • Structural health monitoring

1 Introduction

Recent research in developing self-sensing cementitious composites focused on dispersing carbon nanotubes (CNT) to form percolated conductive networks in cement mixes [1–3]. Sensing was achieved, since applied stresses/strains would change the physical morphology of the embedded CNT network to produce a corresponding change in resistivity. Given their nano-scale dimensions, different intrinsic properties, processing techniques, and the uncertain effects on the bulk cementitious compound, a broad range of concentrations were explored, typically between 0.1 and 1.0 *wt%* of cementitious material [1–4]. These factors also affected their sensing properties and led to different results reported in the literature.

I. Wong • K.J. Loh • R. Wu (✉)
Department of Civil & Environmental Engineering,
University of California, Davis, CA 95616, USA
e-mail: kjloh@ucdavis.edu

N. Garg
Airport Pavement R&D Section, William J. Hughes Technical Center,
Federal Aviation Administration (FAA), Atlantic City, NJ 08405, USA

K. Sobolev, S.P. Shah (eds.), *Nanotechnology in Construction*,
DOI 10.1007/978-3-319-17088-6_48

As research in self-sensing cementitious composites matures, their applications would extend beyond small, lab-scale specimens to large, field-based implementations. For instance, Han et al. [4] installed mortar sensing blocks in a test pavement using 1.0 *wt%* multi-walled carbon nanotubes (MWNT) for traffic flow monitoring. While this study demonstrated the possibility of using this technology in real-world conditions, future applications would require self-sensing cementitious composites to be larger and fabricated at lower cost. Possible applications include full roadways, runways, and airport pavements. Thus, the objective of this study was to characterize the effects of ultra-low concentrations of MWNTs in cement paste, with emphasis on their electromechanical properties and sample consistency, in hopes of supporting future large-scale applications.

2 Experimental Details

The three batches of cementitious composites cast for this work differed in the amount of MWNTs incorporated (*i.e.*, calculated based on *wt%* of cementitious material), namely 0, 0.025, and 0.050 %. Recent findings showed mechanical improvements at these low concentrations [5]. In addition, four cement paste samples were made from each mix design/batch, with dimensions $35 \times 17.5 \times 17.5$ mm^3 ($1.38 \times 0.65 \times 0.65$ in^3). This section discusses the MWNT dispersion process, mix design, cementitious composite casting, and testing protocol.

2.1 Sample Preparation

Dispersion of the MWNTs (diameter <8 nm, 10–30 μm length, and purity >95 %) was achieved using a 1 *wt%* poly(sodium 4-styrenesulfonate) (PSS) solution and by following a procedure used in a previous study [6]. Appropriate amounts of MWNTs were measured to obtain 0.025 and 0.050 % of the weight of cementitious material, and they were mixed with the PSS solution. Dispersion was achieved by subjecting the MWNT-PSS solution to 3 h of bath sonication, followed by 45 min of high-energy tip sonication. The control batch used no PSS.

The cementitious mix was 75 % conventional Type I/II cement and 25 % ground granulated blast furnace slag. Hand mixing was used due to the small sample volumes. The solutions were gradually added and mixed into the dry components for ~3 min and until uniform. The low concentrations of MWNTs had minimal effects on mix rheology. Thus, a water/cement (w/c) ratio of 0.40 was used for all samples. The paste was poured into molds lined with aluminum foil, which was sanded off during demolding in order to eliminate possible contamination by a demolding agent. Two pieces of copper wire mesh were inserted in the fresh cement paste, ~23.5 mm (0.925 in) apart to establish embedded electrodes for two-point probe resistance measurements. Then, the molds were covered and kept at room temperature

for 24 h before demolding. The samples were cured in saturated lime solution for desired periods of times until it was necessary to conduct low-load testing. The samples were re-saturated in between tests.

2.2 Electromechanical Testing Procedure

Load testing was conducted using a Test Resources 150R electromechanical load frame and was performed at three time instances: shortly after removal from the lime solution, 13 days, and 25 days after removal. After removing from the lime solution, the samples were kept in the laboratory, at room temperature, and at an average humidity between 15 and 30 %. Saturated testing consisted of applying two consecutive loading patterns of 25 cycles to 0.89 kN (200 lbf) at a loading rate of 3.81 mm/min (0.15 in/min); the pause between each of the two load patterns was ~15 s. Two-point probe or direct current (DC) resistance was measured using an Agilent 34401A digital multimeter sampling at 2 Hz. Resistance was measured throughout loading and for 30–40 s before each load pattern was executed. At the other two degrees of saturation, loading tests were rearranged into five loading patterns, each with 10 cycles to the same 0.89 kN peak load. Samples of similar mix designs broke at 1.56 kN (350 lbf).

3 Results and Discussions

Table 1 summarizes the average resistivity ranges of all the samples tested. From Table 1, it can be observed that all of the samples exhibited resistivity drift, increasing with additional time and as DC current was injected (for measuring resistance), which was due to sample polarization. With longer periods of drying, Table 1 also shows that the same set of samples exhibited an increase in resistivity. This was expected due to purging of water. Besides this, samples with MWNTs were expected to have lower resistivity as compared to the control (*i.e.*, 0 %). This was not represented by the data, although it might be because PSS was not used for the control case; had PSS been used, the samples might have shown higher resistivity.

Although the temperature and humidity of the environment were not intentionally controlled, a closer look at the masses of the samples over the course of testing revealed that water loss occurred at different rates. By the 25th day of drying,

Table 1 Range of sample resistivity [Ω-m] over the course of testing

Concentration [*wt%*]	Saturated	13 Days	25 Days
0	100–850	900–1,200	1,200–2,200
0.025	100–900	1,000–2,200	3,100–3,700
0.050	80–140	1,600–2,500	2,700–3,300

Table 2 Summary of sample gauge factors (or strain sensitivities)

Sample set	Sample #	Saturated	13 Days	25 Days
0 %	1	NR	COMP	*0.35–0.45*
	2	NR	0.12	0.11–0.115
	3	NR	COMP	0.45
0.025 %	1	NR	COMP	COMP
	2	NR	*2–2.4*	*6–9*
	3	NR	*1.6–2.3*	*3–6.5*
	4	NR	*1.5–2.4*	*1.4–1.6*
0.050 %	1	0.2–0.3	*17–20*	*3.2–3.4*
	2	NR	0.55–0.6	*1.2–1.6*
	3	NR	COMP	COMP

NR no pattern or very noisy respon; *COMP* complex response and patterned

samples with MWNTs, namely the 0.025 % and 0.050 % sets, lost 9.2 % of their saturated mass with standard deviations of 0.22 % and 0.28 %, respectively. However, the control samples lost 8.1 ± 0.21 %. In addition, the 0.050 % samples lost 95.7 % of this water in the first 13 days, while the 0.025 and 0 % sample sets lost 93.3 % and 90.7 %, respectively. These results indicated that ultra-low concentrations of MWNTs could significantly increase the drying rate of cementitious composites, although further investigations are needed to confirm this.

Upon conducting the load tests described in Sect. 2.2, Table 2 summarizes the calculated gage factors (or strain sensitivities) of the different samples after different periods of drying. It should be mentioned that gage factor (*GF*) was calculated using Eq. 1 and by fitting a least-squares linear regression line to the fractional change in resistance ($\Delta R/R$) versus strain (ε) raw data.

$$GF = \frac{\Delta R / R_0}{\varepsilon} \tag{1}$$

The nominal resistance (R_0) was taken as the resistance at the beginning of applied load. Because all of the samples exhibited polarization and nominal resistivity drift, their responses varied. However, where *GF* values are reported in Table 2, the *GF* became consistent within that range. A least-squares linear best-fit was occasionally used to estimate the sample's nominal resistance drift, which was then subtracted from the data before signal processing. In order to provide distinction, italicized values in Table 2 indicate very minimal drift, such that no linear fitting of nominal resistance was performed or needed.

It can be observed from Table 2 that the cementitious composites did not exhibit stable electromechanical response until the 25th day of drying. Most of the saturated samples' measurements returned seemingly random or noisy responses. On the other hand, the majority of testing on the 25th day of drying produced data suitable for calculating *GF*. However, from Table 2, it can be seen that no strong trends could be observed, except that samples with MWNTs exhibited larger *GFs* than the control set.

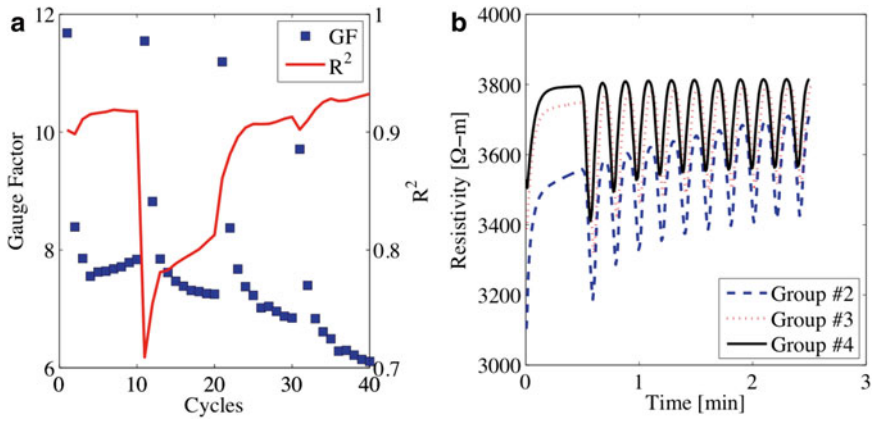

Fig. 1 Sample #2 of the 0.025 % MWNT set was tested on the 25th day of curing, and the (**a**) gage factor variations and (**b**) resistivity time histories are shown

For the two cases with MWNTs, there appeared to be non-uniform dispersion of carbon nanotubes. This could be attributed to a number of causes, namely segregation of the fresh paste as it was being poured into the molds, possible stratification of the paste during the first few hours of curing, potential reorganization of the material near the electrodes as the meshes were inserted in the fresh state, or random arrangement of nanotubes in a relatively small sample.

In addition to the samples exhibiting a spectrum of *GF*, there were variations observed even with the same sample tested and for consecutive load cycles, as can be seen in Fig. 1a. Figure 1a shows how *GF* varied with each loading cycle, as well as the corresponding R^2 or coefficient of determination. Each group of 10 tensile cyclic loads applied corresponded to a different load test group. As can be seen in each 10-cycle loading group, *GF* exhibited a consistent decrease, which was caused by the decrease in the sample's sensitivity to strain with increasing loading (see Fig. 1b). Nevertheless, it can also be seen from Fig. 1b that the sample's nominal resistance did not stabilize until the last loading group, which then produced consistent strain-sensitive electromechanical behavior; drift was minimal during the last 10-cycle loading group, as can be seen in Fig. 1b. It should be mentioned that most other *GF* ranges were more consistent with narrower *GF* ranges (see Table 2).

4 Conclusions

Although this research was able to disperse MWNTs in solutions, and they appeared very uniform in the fresh cement paste, the casted samples showed variations in their electromechanical response. This might be a result of the chosen dispersing agent (*i.e.*, PSS) and its unknown effects on the interaction of MWNTs with cement.

However, the samples showed consistent resistivity ranges and rates of drying, which were faster than the control samples. In addition, most of the samples showed strain-sensitive electromechanical behavior even when ultra-low concentrations of MWNTs were used. Their strain-sensitive response seemed to be significantly higher than samples without nanotubes. The large variations in gauge factors indicated a potential danger of having pockets of uneven conductivity or sensitivity to stress/strain. However, most of the samples using 0.025 and 0.050 % MWNTs showed improved electromechanical properties.

Acknowledgements The authors gratefully acknowledge financial support from the Federal Aviation Administration (FAA) under cooperative agreement no. 13-G-017. The 2013 Dwight David Eisenhower Graduate Fellowship Program provided additional support for this work.

References

1. Andrawes, B., & Chan, L. Y. (2012). Compression and tension stress-sensing of carbon nanotube-reinforced cement. *Magazine of Concrete Research, 64*, 253–258.
2. Han, B., Yu, X., Kwon, E., & Ou, J. (2012). Effects of CNT concentration level and water/cement ratio on the piezoresistivity of CNT/cement composites. *Journal of Composite Materials, 46*, 19–25.
3. Han, B., Yu, X., & Ou, J. (2010). Effect of water content on the piezoresistivity of mwnt/cement composites. *Journal of Materials Science, 45*, 3714–3719.
4. Han, B., Zhang, K., Burnham, T., Kwon, E., & Yu, X. (2013). Integration and road tests of a self-sensing CNT concrete pavement system for traffic detection. *Smart Materials and Structures, 22*, 015020.
5. Konsta-Gdoutos, M. S., Metaxa, Z. S., & Shah, S. P. (2010). Highly dispersed carbon nanotube reinforced cement based materials. *Cement and Concrete Research, 40*, 1052–1059.
6. Wille, K., & Loh, K. J. (2010). Nanoengineering ultra-high-performance concrete with multi-walled carbon nanotubes. *Transportation Research Record: Journal of the Transportation Research Board, 2142*, 119–126.

Mechanical Response and Strain Sensing of Cement Composites Added with Graphene Nanoplatelet Under Tension

Hongjian Du and Sze Dai Pang

Abstract The piezoresistivity-based strain sensing behavior of cement composites, incorporated with a two-dimensional nano-material was demonstrated under tensile loading. Graphene nanoplatelet (GNP) is electrically conductive nano-particle and thus can be potentially used as an admixture into the cement matrix to lower the electrical resistivity of the composites. Test results indicated that the mechanical performances can be enhanced by the addition of GNP up to 2.4 % due to the nano-filler and micro-crack arrest effects. Beyond this critical content, no further improvement can be noticed partially because of the weak pockets caused by the agglomeration of GNP particles. To depict the relation between mechanical and electrical response of the GNP-specimen, fraction change in resistance (FCR) is introduced to correlate with the tensile strain. It is noticed that FCR continuously increases until failure, with a gentle slope at the first stage (smaller than 100 micro-strains) and a steep slope at the second stage. With more GNP, this slope becomes higher revealing that the GNP-mortar can be used as smart material to sense its own tensile strain. The gage factor can be above 100 when more than 1.2 % GNP was added.

Keywords Nanotechnology • Percolation • Piezoresistivity • Structural Health Monitoring

1 Introduction

The demand for smart structures, capable of being sensitive and responding properly to certain stimulus, has led to the development of a new kind of smart building materials. Apart from having adequate structural properties and sufficient durability, smart building materials also represent additional functional applications, such as strain sensing, temperature sensing and vibration damping. One area of that is strain sensing ability of cement-based composites. The concept is based on the

H. Du (✉) • S.D. Pang
Department of Civil and Environmental Engineering, National University of Singapore, Singapore, Singapore
e-mail: ceedh@nus.edu.sg; ceepsd@nus.edu.sg
http://www.eng.nus.edu.sg/civil/people/cvepsd/cvepsd.html

K. Sobolev, S.P. Shah (eds.), *Nanotechnology in Construction*,
DOI 10.1007/978-3-319-17088-6_49

phenomenon of piezoresistivity, which is the change in electrical resistivity with relation to the applied strain. The advantages of self-sensing materials include reduced cost, larger sensing volume, greater durability and absence of mechanical property degradation. Previous research has demonstrated the suitability of some conductive materials in cement composites for the strain sensing purpose, such as carbon fiber, carbon black, carbon nanotube and carbon nanofiber [1–3].

However, a common limitation for their wide application is their relative high cost. Until recently, a much cheaper alternative, graphene nanoplatelet (GNP) was found to exhibit similar piezoresistive behaviors [4]. In addition, GNP does not have entanglement problem which exist in carbon fiber, carbon nanotube or carbon nanofiber. Previous studies have shown the damage detection and strain sensing for GNP-cement composites under compression [5, 6]. There is yet any study on the piezoresistive behavior of GNP-cement composites under tension. Tensile response of cement materials is important as tensile stress often develops in structural members, which might cause cracks or damage. The objective of this study is to investigate the feasibility of GNP-mortar as a smart material which is capable of strain sensing under tension while maintaining adequate mechanical properties.

2 Materials and Methods

Type I ordinary Portland cement (OPC) with a specific gravity of 3.15 was used to prepare the mortar specimens. The fineness modulus and specific gravity of natural sand used was and 2.80 and 2.65, respectively. Asbury TC307 was used in this study, with its physical properties shown in Table 1. Naphthalene sulfonate based superplasticizer, Darex Super 20, was used as dispersant. Prior to the casting of mortar mixtures, GNP was dispersed in water and Darex Super 20, followed by two hours of ultrasonication. This aims to exfoliate the GNP particles by breaking weak bonds between graphene layers and agglomerations. During sonication, the beaker was placed in an ice water bath to cool the suspension as it got heated up during the process.

The mix proportion for the reference mortar is water: cement: sand = 0.485: 1: 2.75, by weight, according to ASTM C 109 [7]. GNP was added to mortar at volume fraction of 1.2 %, 2.4 %, 3.6 % and 4.8 %, respectively. The amount of Darex Super 20 was approximately 50 % of added GNP by weight to achieve sufficient flowability. For monotonic direct tensile test, 10 × 60 × 240 mm plate specimens were prepared for each mortar mix. The specimens were embedded with four steel meshes and sandwiched with four aluminum plates using Devcon 2-Ton epoxy at the two

Table 1 Physical properties of GNP TC307

Density (g/cc)	Surface area (m^2/g)	Diameter (μm)	Thickness (nm)	Aspect ratio	Purity (%)
2.16	352	2.6	2.6	1,000	99.92

ends to prevent premature failure due to local stress concentration. For cyclic tensile test, Ø60 × 120 mm cylinders were prepared, with a Ø13 mm steel bar running through the center which helps transfer tensile loads to the mortar bar. For each specimen, two strain gauges were installed on the opposite sides, along the longitudinal direction.

Monotonic tensile loading was applied by using Instron Actuator I 1334 at a constant rate of 0.01 mm/min, until failure. For cyclic testing, Shimadzu Autograph was used to apply tensile loads on the steel bar. Each specimen was subjected to three cycles of loading to an applied strain of about 30 micro-strains. Four-probe method was used to measure the electrical resistance during the mechanical loading.

3 Results and Discussion

3.1 Mechanical Performances

The tensile strength of the specimen was obtained from the stress-strain curve at the maximum tensile stress point. The average ultimate tensile strength of GNP-mortar is shown in Fig. 1. It was observed that the addition of GNP, up to 3.6 vol.%, improved the tensile strength in comparison with the reference mortar. The highest tensile strength was observed for mortar containing 2.4 vol.%, after which the strength started to decrease. The improvement in strength could be due to the porosity reduction and pore refinement effect. Elastic modulus was obtained from the tangential slope of the linear portion of the stress-strain curve under tension, and shown in Fig. 1. The modulus increased consistently with higher GNP dosage up to 2.4 vol.%. Hence, it can be concluded that the addition of GNP enhances the mechanical properties of mortar under tension. However, there exists a threshold level of 2.4 vol.% above which no further improvement could be noticed. This could be due to the difficulty with dispersion of GNP particles at high dosages.

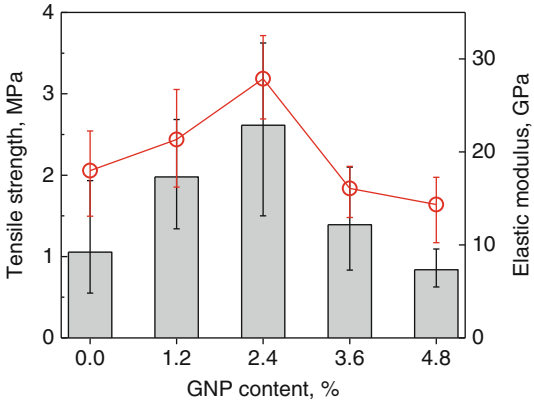

Fig. 1 Effect of GNP on mechanical properties of cement mortar under tension

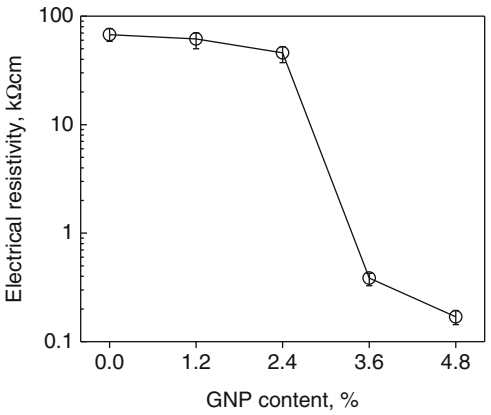

Fig. 2 Effect of GNP on the electrical resistivity of cement mortar

3.2 Electrical Resistivity

The electrical resistivity of GNP-mortar was measured before applying loads and the results are shown in Fig. 2. The addition of conductive GNP in cement matrix resulted in a decrease in electrical resistivity of mortar. With higher GNP addition, the distance between the adjacent GNP particles would be shorter, leading to the formation of shorter conductive pathways and a continuous network which resulted in a significant decrease resistivity. A great drop was observed between 2.4 and 3.6 vol.%. This critical amount of GNP was thus known as the percolation threshold above which a continuous electrical network was formed by the conductive GNP fillers throughout the specimen. Above this percolation threshold, resistivity continued to decrease but with a much smaller amount since an extensive electrical network has already established.

3.3 Strain Sensing Under Cyclical Loadings

A distinctive relationship between the fractional change in resistance (FCR) and cyclic tensile strain was observed for GNP mortar with 3.6 vol.% GNP for each loading cycle, as shown in Fig. 3a. However, no trend was noticed between FCR and applied strain. This implied that the addition of conductive GNP has imparted piezoresistive characteristics to cement composites. During each loading cycle, FCR increased with an increase in tensile strain, resulting in positive FCR. Upon unloading, FCR returned back to approximately zero. The reversible change confirms the ability of GNP-cement mortar for tensile strain sensing under cyclic loadings. The similar results have been previously reported [8], which only reported the FCR response within the elastic regime for cement paste with 0.5 vol.% carbon fiber (Fig. 3b).

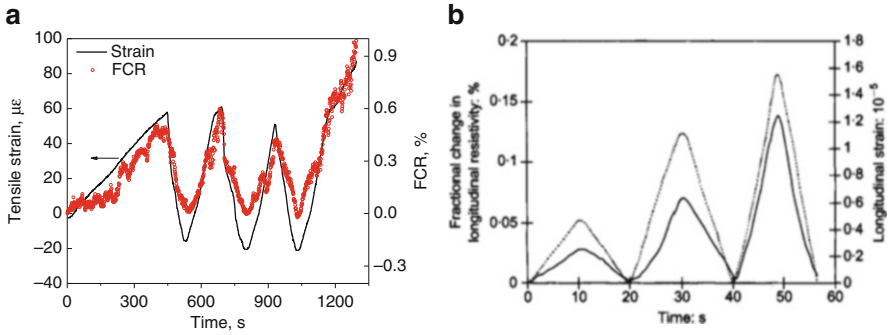

Fig. 3 (**a**) Electrical response of mortar subjected to cyclic tensile loading, and (**b**) Comparative work by Wen and Chung [8]

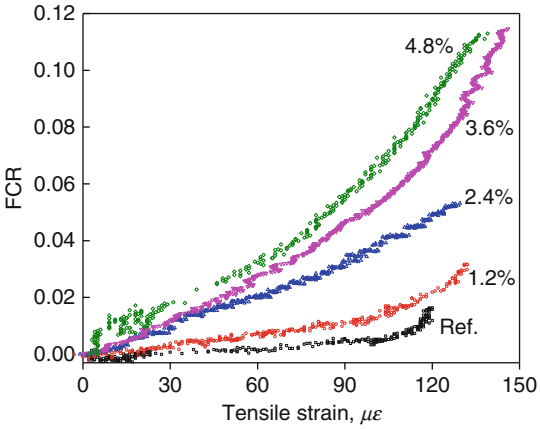

Fig. 4 Electrical response of mortar subjected to monotonic tensile loading

3.4 Strain Sensing Under Monotonic Loading

A plot of FCR against strain for mortar with different GNP dosages under monotonic tensile loading is shown in Fig. 4. For each GNP content, the slope was smaller initially but increased rapid when the tensile strain exceeded 100 micro-strain. It can be seen that for the same amount of applied strain, FCR increased with higher GNP content. With no GNP, there is little change in FCR. With an increase in GNP content, the number of interfaces between GNP and cement matrix increased which account for the increases in initial FCR when the specimen was subjected to tension. This indicated that GNP-cement mortar is more sensitive to the applied strain at higher GNP dosage.

4 Conclusions

The mechanical properties and capability of strain sensing of GNP-cement mortar under tensile loading are reported. It was found that the addition of GNP helps to increase the tensile strength and elastic modulus because of the pore refinement. However, exceeding a threshold level of 2.4 vol.%, GNP would not further improvement in mechanical properties was observed. Regarding electrical resistivity, the percolation threshold for GNP was also found to be 2.4 vol.%. It was demonstrated that GNP-mortar exhibited obvious strain sensing capability regardless of tensile loading schemes. Moreover, this sensitivity increased with higher GNP content.

Acknowledgements This work was financially supported by Singapore A*STAR R-302-000-034-305. Asbury Graphite Mills, USA, is kindly acknowledged for providing GNP. The authors are grateful to Miss Chunying Xu for her great assistance in laboratory.

References

1. Azhari, F., & Banthia, N. (2012). Cement-based sensors with carbon fibers and carbon nanotubes for piezoresistive sensing. *Cement and Concrete Composites, 34*, 866–873.
2. Chen, P. W., & Chung, D. D. L. (1993). Carbon fiber reinforced concrete for smart structures capable of nano-destructive flaw detection. *Smart Materials and Structures, 2*, 22–30.
3. Konsta-Gdoutos, M. S., & Aza, C. A. (2014). Self sensing carbon nanotube (CNT) and nanofiber (CNF) cementitious composites for real time damage assessment in smart structures. *Cement and Concrete Composites*. doi:10.1016/j.cemconcomp.2014.07.003.
4. Du, H., Quek, S.T., & Pang, S.D. (2013). Smart multifunctional cement mortar containing graphite nanoplatelet. *Proceedings of SPIE – The International Society for Optical Engineering, 8692*. doi: 10.1117/12.2009005.
5. Le, J.-L., Du, H., & Pang, S. D. (2014). Use of 2-D Graphene nanoplatelet (GNP) in cement composites for structural health evaluation. *Compos Part B: Engineering, 67*, 555–563.
6. Pang, S.D., Gao, H., Xu, C., Quek, S.T., & Du, H. (2014). Strain and damage self-sensing cement composites with conductive graphene nanoplatelet. *Proceedings of SPIE – The International Society for Optical Engineering, 9061*. doi: 10.1117/12.2045329.
7. ASTM C 109 (2005) *Standard test method for compressive strength of hydraulic cement mortars (using 2-in. [50 mm] cube specimens)*. American Society Testing & Materials. West Conshohocken, USA.
8. Wen, S., & Chung, D. D. L. (2003). A comparative study of steel- and carbon-fibre cement as piezoresistive strain sensors. *Advances in Cement Research, 15*, 119–128.

Nanosensors for Embedded Monitoring of Construction Materials: The "2D Conformable" Route

Bérengère Lebental, Boutheina Ghaddab, and Fulvio Michelis

Abstract We propose an approach to embedded monitoring of construction materials relying on 2D, conformable architectures that are expected to be lower cost and more robust than their 3D counterparts. In this article, we present two examples: a RFID-enabled carbon nanotube strain sensor on plastic for microcrack monitoring in concrete and a nanoparticle-asphalt sandwich for weigh-in-motion applications.

Keywords Embedded sensors • Flexible electronics • Nanoparticles • Carbon nanotubes • RFID • Concrete • Bitumen

1 Advances in Embedded Monitoring of Construction Materials

Complementary to surface-based health monitoring systems [1, 2], the concept of "embedded monitoring" is quickly making headway in civil engineering. Based on sensors within the construction materials themselves, it yields real-time localized volume information on the infrastructure, enabling early detection of degradation and lifetime prediction [1–3]. Related challenges include (1) proving the correct operation of *in situ* sensing devices, (2) exploiting localized, volume data for infrastructure management, (3) enabling wireless communication through electromagnetically opaque materials, (4) creating compact, fully autonomous power management systems (including hardware – harvesting and storage – and software), (5) minimizing perturbations between sensor and material, and (6) guaranteeing a sensor lifetime compatible with that of the monitored structure.[1]

[1] We do not address in the present paper issues related to optic-fiber based monitoring systems, though optic fibers may also be buried within the materials. Indeed, the monitoring principles are significantly different (for instance long-distance deported electronics, multiple measurement points with the same fiber…).

B. Lebental (✉) • B. Ghaddab • F. Michelis
LISIS, Université Paris-Est, IFSTTAR, Cosys, 14 – 20 Bd Newton,
Champs-Sur-Marne, Marne-la-Vallée F-77447, France

LPICM, Ecole Polytechnique - CNRS - UMR7647,
Route de Saclay, 91128 Palaiseau Cedex, France
e-mail: berengere.lebental@ifsttar.fr

K. Sobolev, S.P. Shah (eds.), *Nanotechnology in Construction*,
DOI 10.1007/978-3-319-17088-6_50

The most widespread approach entails the direct monitoring of volume indicators such as temperature (hydration), moisture (hydration, reinforcement corrosion, freeze-thaw process, carbonation, alkali-silica reactions), pH (reinforcement corrosion) and strain (shrinkage and swelling, cracking). Early work dealt mostly with wired devices incorporated directly during the casting process or positioned after casting into drilled holes filled with plaster [1]. They proved both the capability of pre-packaged sensors to operate inside the materials and the relevance of the measurements for monitoring purposes.

Embedded sensors for monitoring corrosion of reinforcements are also available. Exploiting electrochemistry principles (linearly polarized redox electrodes, half-cell potentials, electrode scales) or resistivity (two- or four-probe) measurements, these sensors are usually wired and mounted directly on the reinforcements before casting [4, 5].

A recent approach involves burying acoustic emitters and receivers to monitor hardening behavior in real-time as well as mechanical and morphological properties (thickness, structural defects, delamination, cracking). Wired, carefully packaged commercial PZT-based piezoelectric sensors are embedded in volume [3]. New sensing elements such as MEMS [6] or nanosensors [2] have also appeared, among those a large variety of strain, force and temperature sensors based on piezoresistive nanocomposite materials[2] [7].

A very strong focus lies on the demonstration of wireless communication through concrete with passive or battery operated devices (passive RFID tags, 802.15.4 nodes) to create the so-called "smart pebble" [8], or "smart aggregate" devices: wireless sensor nodes which incorporate several sensing elements, computing and communication capabilities, power supply and storage, and roughly sized like a concrete aggregate.

Altogether, with the exception of a few tag-based systems, existing embedded monitoring systems are based on rigid, non-conformable technologies where devices generally form rigid, 3D nodes in a pebble-like configuration. In the present paper, expanding on the tag-based route, we advocate an approach based on the development of conformable, 2D systems, through two practical examples.

2 A Conformable Carbon Nanotube Strain Sensor for Crack Detection

To achieve volume monitoring of strain fields and microcrack opening in concrete materials, we have developed a new type of strain sensor, namely a flexible carbon nanotube based strain sensor (Fig. 1).

[2] Piezoresistive nanocomposite materials: materials such as concrete and bitumen functionalized *en masse* with conducting nanoparticles such as carbon nanotubes or graphite; the material resistivity has been shown to depend on strain.

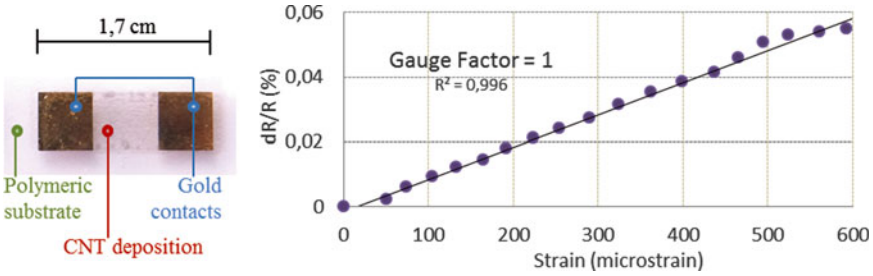

Fig. 1 Carbon nanotube strain sensor: (*left*) image and (*right*) piezoresistive response

Using a dedicated batch-process enabling high device reproducibility, we inkjet print a carbon nanotube ink (developed in-house) on a flexible, 150 µm thick ETFE substrate[3] with gold electrodes. The resulting devices are covered with epoxy for additional protection. They feature a linear piezoresistive response up to 700 microstrain, corresponding to 10 µm displacement (capability to detect crack opening up to 10 µm).

For the application, the sensors are combined with dedicated low-power, low-temperature-dependence conditioning electronics and with battery-powered and RFID-based communication capabilities [9]. RFID reading of the wireless, battery-powered embedded sensors has been demonstrated in 160×320 mm cylindrical concrete samples. Response of the embedded sensors under compression and three-point bending of the samples is under study.

To summarize, the sensing devices are flexible and ultra-thin, while conditioning and RFID electronics are planar but rigid.[4] Performances are comparable to metallic gauges. The conformability is expected to limit perturbation of the material by the sensor, while limiting degradation of the sensor during casting and early age. Thanks to the choice of low-cost technologies, the fabrication cost (labor included) is estimated at below 100€ in small series, below 10€ in larger series. These elements strongly support the 2D conformable route for embedded concrete monitoring.

3 A Nanoparticle-Asphalt Sandwich as Force Sensor

Weigh-in-motion (WIM) technologies are used for traffic management, overloading monitoring, weight enforcement or weight-based tolling. They are based on force sensors such as bending plates, strain gauges, load cells, fiber optic or piezoelectric sensors [10], which feature various issues such as insufficient accuracy, high cost and short lifetime.

[3] ETFE: Ethylene tetrafluoroethylene. This material was selected for its capability to withstand the chemical conditions inside concrete.

[4] Full conformability is planned for the next stage of development.

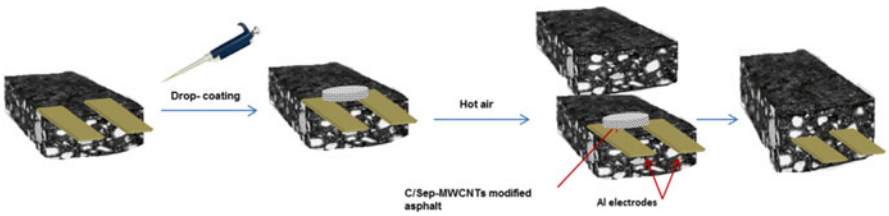

Fig. 2 Fabrication process for the nanoparticle-asphalt sandwich: from left to right, (1) a pair of electrodes is fixed on an asphalt slab; (2) the nanoparticle dispersion is drop-coated, then dried under hot air; (3) a second slab covers the deposition, (4) forming an asphalt sandwich

Force sensors based on piezoresistive nanocomposites have revealed themselves as a promising alternative [11] as they directly use construction materials, are expected to be low cost even for large areas and have good road compatibility, enhancing lifetime. However, they raise some concerns: large volumes of materials are required to replace the full pavement thickness so that significant quantities of (expensive) nanoparticles are required. In addition, material fabrication is complicated because of well-known nanoparticle dispersion issues, which may prevent on-site fabrication. The presence of nanoparticles directly on the road surface raises health and environmental issues.

As a promising substitute, we propose a 2D architecture based on a nanoparticle-asphalt sandwich [12]: a thin piezoresistive layer of carbon-clay nanoparticles is deposited between two pre-heated asphalt slabs in a process compatible with on-site fabrication.

The active material is a black powder composed of micro and nanoparticles of graphene-supported-on-sepiolite[5] assembled with multi-walled carbon nanotubes (MWNTs) at low weight ratio. This asphalt sandwich is obtained by high temperature annealing of liquid caramel mixed with sepiolite and MWNTs. The fabrication process is summarized in Fig. 2. Firstly, aluminum electrodes are fixed on an asphalt slab using epoxy glue. The material is dispersed in water with sodium dodecyl benzene sulfonate surfactant. The resulting suspension is then deposited by drop casting between and on the electrodes, forming a thin conducting layer. The layer is air dried at room temperature for 2 h then by hot air flow at 200 °C. The upper surface of a second asphalt slab is then heated up for enhanced adhesion capability and deposited on the first slab.

Compressive stress is applied over a 10 cm^2 surface area in the direction normal to the slab surface using a MTS 318.10 load unit. The devices are placed in a Wheatstone bridge loaded at 12 V_{DC} (bridge resistances are tuned device by device). The bridge output voltage is fed to an in-house, tunable conditioning module including a programmable gain amplifier, offset null stage, and third order low pass filter. The voltage generated by the conditioning chain is fed to the differential input of a digital multimeter. Acquisition rate is 2 s.

[5] Sepiolite: a fibrous clay mineral with $Mg_4Si_6O_{15}(OH)_2 \cdot 6H_2O$ as ideal formula.

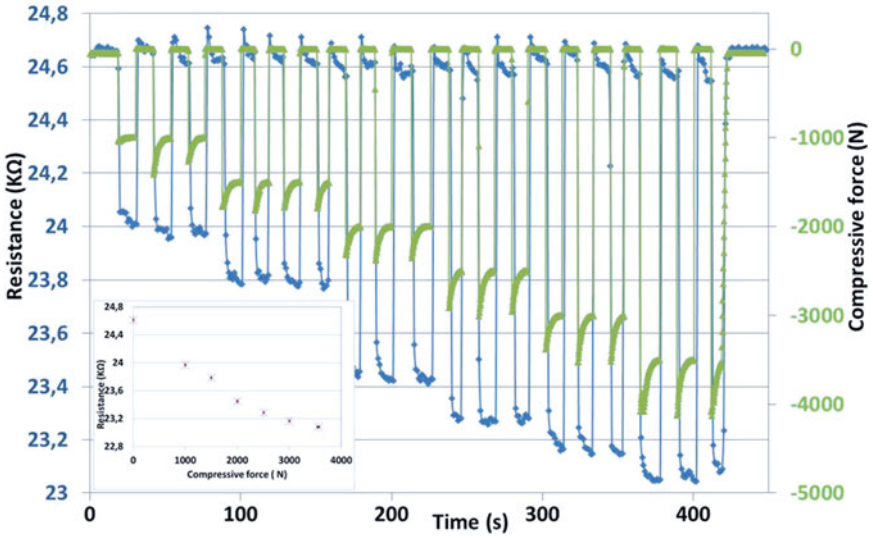

Fig. 3 Response of the asphalt sandwich to compressive force

Figure 3 shows the change in resistance of one device during compressive loading cycles up to 3,500 N (3.5 MPa). The resistance decreases reversibly by 6 % from 0 to 3,500 N. The response is linear until about 2,000 N, with sensitivity 0.6 Ω/kN. The response time is below 7 s. Additional experiments have also proved the sensitivity of the device to tensile strain and cracking.

These results show the promise of our asphalt sandwich architecture: functionalizing the inner layer of a pavement structure with very small amounts of nanoparticles is easily achievable and enables compressive force monitoring. Resulting devices are expected to have very low fabrication cost. They should conform naturally to structural deformation of the pavement layers, which will enhance their robustness. Moreover, the public and the environment will not be directly exposed to the nanoparticles.

4 Conclusions

We have developed a carbon nanotube strain sensor for embedded crack monitoring in concrete and a nanoparticle-asphalt sandwich based force sensor for weigh-in-motion. The two sensors feature conformability and are expected to be low cost, even in small series. We deem both characteristics essential for future industrial development of theses sensors for embedded monitoring.

Acknowledgments The authors acknowledge funding from FUI (France) for project SIPRIS and from ANR (France) for project Sense-City (ANR-10-EQPX-48). The authors also thank Vincent Gaudefroy, Eduardo Ruiz, Aranda Pilar, Cristina Garcia-Ruiz, Yvan Bonnassieux, Jean-Marc Laheurte, Laurence Bodelot, Fadi Zaki, Erick Merliot, Olivier Burban, Jean-Philippe Terrier, William Guillemaud and Jean-Luc Sorin for their help and support.

References

1. Lynch, J. P., et al. (2006). A summary review of wireless sensors and sensor networks for structural health monitoring. *The Shock and Vibration Digest, 38*(2), 91–130.
2. Ubertini, F., et al. (2014). Novel nanocomposite technologies for dynamic monitoring of structures. *Smart Materials and Structures, 23*, 045023.
3. Hu, B., et al. (2013). Embedded piezoelectric sensors for health monitoring of concrete structures. *ACI Materials Journal*, *110*(2), 149–158.
4. Bhadra, S., et al. (2013). A wireless passive sensor for temperature compensated remote pH monitoring. *IEEE Sensors Journal, 13*(6), 2428–2436.
5. Broomfield, J. P., et al. (2002). The use of permanent corrosion monitoring in new and existing reinforced concrete structures. *Cement and Concrete Composites, 24*(1), 27–34.
6. Lebental, B., et al. (2010). *Instrumentation of cementitious materials by embedded ultrasonic micro-transducers made of carbone nanotubes*. Ph.D. thesis, East Paris University, Paris.
7. Barroca, N., et al. (2013). Wireless sensor networks for temperature and humidity monitoring within concrete structures. *Construction and Building Materials, 40*, 1156–1166.
8. Watters, D. G., et al. (2003). Smart Pebble: Wireless sensors for structural health monitoring of bridge decks. *Proceedings – SPIE the International Society for Optical Engineering*, *5057*, 20. doi:10.1117/12.482397
9. Michelis, F., et al. (2014). *Wireless flexible strain sensor based on carbon nanotube piezoresistive networks for embedded measurement of strain in concrete*. EWSHM – 7th European Workshop on Structural Health Monitoring, Nantes.
10. Yannis, G. (2005). Integration of weigh-in-motion technologies in road infrastructure management. *ITE Journal, 75*(1), 39–43.
11. Liu, X. M., et al. (2009). Properties evaluation of asphalt-based composites with graphite and mine powder. *Construction and Building Materials, 22*, 121–126.
12. Lebental, B., et al. (2014). Capteur pour la chaussée à base de couches minces piézorésistives de nanoparticules noyées dans le matériau de chaussée. *FR Patent*, 01-04-2014.

Wireless Nanosensors for Embedded Measurement in Concrete Structures

Fulvio Michelis, Laurence Bodelot, Jean-Marc Laheurte, Fadi Zaki, Yvan Bonnassieux, and Bérengère Lebental

Abstract In this work we propose a wireless architecture for embedded monitoring in concrete. The modular structure of the system allows it to be adapted to different types of sensors. We present the application of such architecture for the detection of microcracks in concrete. A carbon nanotube strain sensor recently developed by the group is used to track mechanical deformations. Full temperature compensation is achieved by a specific conditioning circuit.

Keywords Wirelss SHM • Embedded monitoring • Carbon nanotubes • Nanosensors • Microcracks in concrete • RFID sensor

1 Introduction

In the domain of structural health monitoring (SHM), there is an increasing demand for embeddable devices capable of providing information on several physical parameters indicative of the health of a structure from within the structure itself. Parameters of interest may be humidity, temperature, strain and pH [1]. Several papers show the feasibility of embedding sensors in concrete [2–4]. The most

F. Michelis • F. Zaki • B. Lebental (✉)
Université Paris-Est, IFSTTAR, Cosys,
14 – 20 Bd Newton, Champs-Sur-Marne, F-77447 Marne-la-Vallée, France

Laboratoire de physique des interfaces et des couches minces (LPICM),
CNRS: UMR7647 – Polytechnique, Route de Saclay, 91128 Palaiseau Cedex, France
e-mail: berengere.lebental@ifsttar.fr

L. Bodelot
Laboratoire de Mécanique des Solides (LMS), CNRS: UMR7649 – Polytechnique,
Route de Saclay, 91128 Palaiseau Cedex, France

J.-M. Laheurte
ESYCOM, Université Paris-Est, Marne-la-Vallée, 77454 Marne-la-Vallée cedex 2, France

Y. Bonnassieux
Laboratoire de physique des interfaces et des couches minces (LPICM),
CNRS: UMR7647 – Polytechnique, Route de Saclay, 91128 Palaiseau Cedex, France

K. Sobolev, S.P. Shah (eds.), *Nanotechnology in Construction*,
DOI 10.1007/978-3-319-17088-6_51

common approach for the communication of sensors' readings is the wireless measurement the impedance of the sensor [5]. This technique presents few inconveniences. Firstly, the wireless element has to be specifically tailored for each sensing element and its specific characteristics. Secondly, it requires sensors to be physically far from each other or set on different resonant frequencies to avoid interference that would impede communication. Thirdly, the retrieved information is limited to only one physical parameter at the time, whereas studies [1] show the benefits of having access to a greater variety of information.

In this work, we propose an architecture designed to address these difficulties. Firstly, the sensing element is coupled with a conditioning circuit that adapts the sensory output to the input requirements of the wireless element. This interface between the two elements avoids the need to design specifically the wireless element for each sensor. Secondly, a commercial device is used to manage the (Radio-frequency identification) RFID communication protocol in order to handle collisions in environments with multiple devices. Thirdly, the choice of the components in the system allows the expansion of the board by the integration of multiple sensors.

We present the deployment of such platform in the context of crack detection in concrete. The sensing element is an innovative strain gauge based on carbon nanotube strain sensor that can be better suited then commercial solutions for embedded use in concrete.

2 Wireless Architecture for Embedded Nanosensors

Wireless communication can be achieved using several communication protocols such as Bluetooth, WiFi and ZigBee, but for the presented work, RFID presents itself as the optimal solution since it allows wireless power supply over Radio Frequency, along with communication capabilities and collision-handling protocols. The RFID system is based on two modules: the interrogator and the tag. In this work, we propose a system in which an interrogator is outside the concrete structure and wirelessly interrogates a tag that has sensing capabilities and is embedded inside the structure. The proposed architecture is shown in Fig. 1. The present paper focuses on the design of the Tag.

The tag is organized in four segments: the sensing elements, the conditioning circuits, the digital circuit for the digital acquisition and for the management of the com-

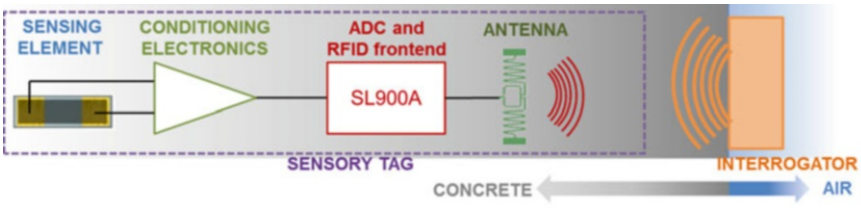

Fig. 1 Schematic structure of the proposed platform

munication protocol and, finally, the antenna. The sensing element translates the measured parameter into an electrical signal. The conditioning circuit converts this electrical signal into an analog signal compatible with the input requirement of the digital circuit. The tasks of digitalizing the analog signals of the sensors as well as managing RFID wireless communication are handled by the commercial device SL900A by AMS [6]. Finally, the antenna is customized for the communication through concrete increasing its communication range. The system is currently powered by a battery. Future developments of the sensor will include an energy harvester. Since the SL900A allows the digital acquisition of the temperature and two external sensors, the system will be further improved for the implementation of a multisensory system.

3 Customization of the Architecture for Crack Detection in Concrete

3.1 Carbon Nanotube Strain Sensor

Strain gauges are traditionally exploited as surface sensors for the monitoring of macro deformations of concrete structures [7]. Recent developments show that the use of strain gauges could be extended for volume analysis of microcracking events [8] to assess the risk for structural failures [9]. For instance, micro-cracking occurring near the reinforcement bars is symptomatic of alkaline reactions; microcracking also enhances permeability to chloride ions and other chemicals and is associated to general ageing [10]. We have developed a low cost, flexible strain sensor that promises to be better suited than commercial metallic strain gauges for embedded sensing in concrete. The polymeric substrate makes the proposed device highly conformable and adaptable to the inhomogeneous environment that is concrete. Moreover the device shows excellent compatibility to pH as high as 13, confirming the compatibility to concrete. The strain gauge exploits the piezoresistive behaviour of a percolated carbon nanotube (CNT) network ink-jet printed on a polymer substrate. The substrate, Ethylene tetrafluoroethylene (ETFE), is 125 μm thick and flexible. Gold electrodes are deposited atop it by evaporation and 20 layers of CNTs are then inkjet-printed in between and atop the electrodes. The size of the device is adjustable: we selected the following dimensions: 5×17 mm for a thickness of 0.15 mm (see Fig. 2). The fabrication process is detailed in [11].

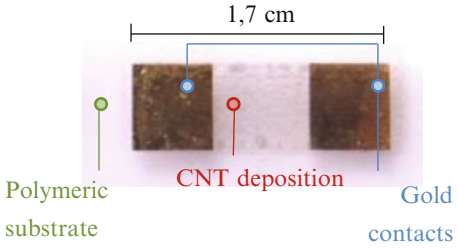

Fig. 2 Layout of the fabricated device

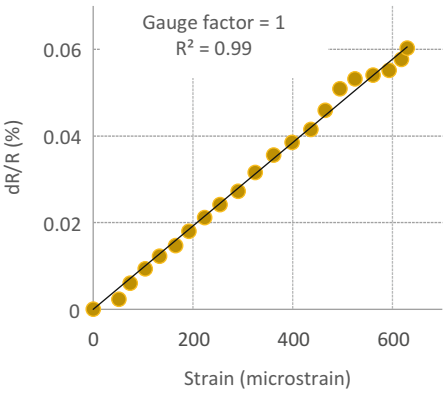

Fig. 3 Piezoresistive behaviour of the strain sensor

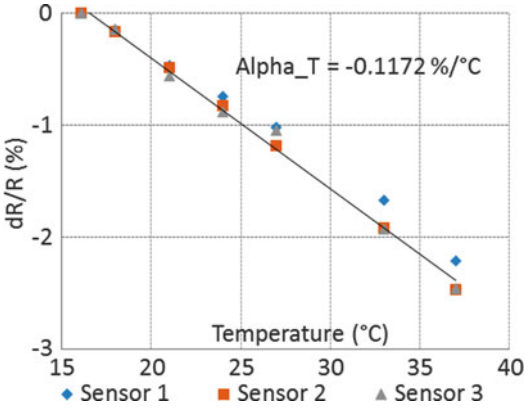

Fig. 4 Temperature dependence of three different sensors

High reproducibility of fabrication was achieved, suggesting the possibility of serial production. With the use of low-cost materials and low-cost technologies, the fabrication cost (labor included) is estimated at below €100 in small series and below €10 in larger series. For characterization of the sensors under strain, mechanical loading is achieved by gluing both extremities of the substrate to two clamps, mounted on stepper motors equipped with force sensors. The loading is force-controlled; force and strain are monitored simultaneously during test.

The resulting resistance/strain relationship is shown to be linear up to 600 microstrain (Fig. 3), with Gauge Factor = 1.0. For comparison, the average GF of commercial metallic strain gauge is 2. The device is sensitive to deformation as small as 1 µm, suggesting the possibility of using it to detect micro deformations and micro deformations inside concrete due to drying shrinkage [12]. To address real-life applications we analysed the influence of temperature on the sensors and their cycling capability. Figure 4 shows the influence of the temperature on 3 different sensors; it shows that different sensors react identically to temperature changes,

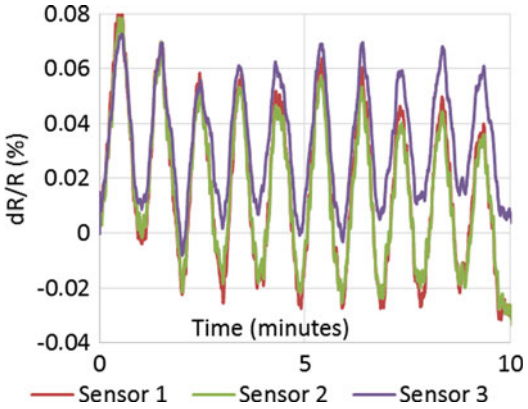

Fig. 5 Response of three different sensors to multiple loading cycles

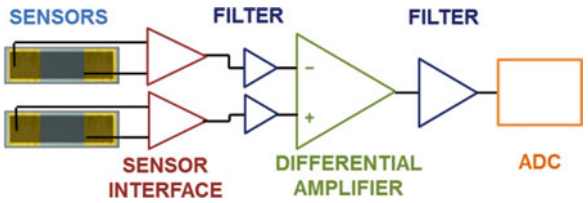

Fig. 6 Structure of the conditioning circuit

enabling systematic compensation for temperature changes. Figure 5 shows how three different devices respond to multiple elongation cycles. The sensors show analogous behaviour without obvious hysteresis, especially for the first three cycles. Additional work is under progress to improve cyclability. It is crucial for real-life applications that the sensor can withstand multiple cycles of elongation and relaxation (mainly due to freeze and thaw cycles).

3.2 Conditioning Circuit for the CNT Strain Sensor

Figure 6 shows the structure of the conditioning circuit bridging the strain sensor to the digital section of the device. The acquisition chain has built-in temperature compensation capabilities. We use two sensors, the first subject to both mechanical and thermal loadings, the second, glued to a rigid substrate, is subject only to the same thermal loadings as the first sensor. The sensor interface converts the change in resistance of both sensors into voltage change. After a filtering stage aimed at minimizing the high frequency noise, the signals enter a differential amplifier. It subtracts the contribution of both sensors, amplifies the resulting signal and matches it to the input dynamic of the ADC. The last stage is a second order low pass filter, with a cut-off frequency of 5 Hz. Figure 7 shows the fabricated printed circuit board (PCB). The circuit was operated for signal conditioning during a cyclic deformation

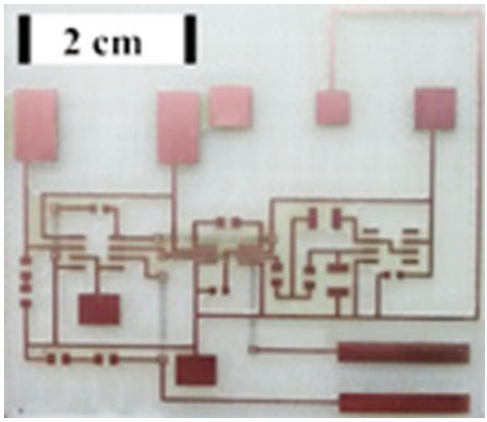

Fig. 7 Fabrication of the PCB

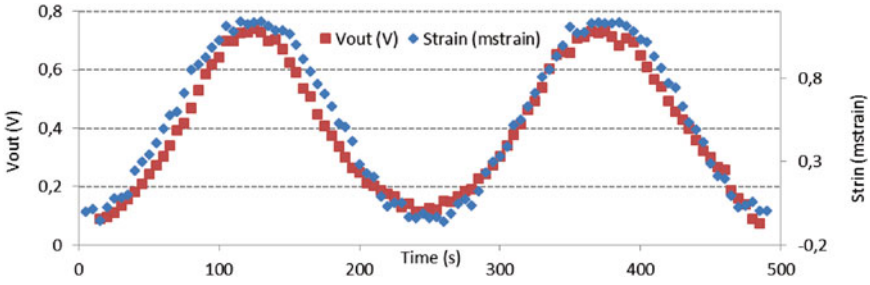

Fig. 8 Filtered output of the conditioning chain for a cyclic deformation

of the substrate and Fig. 8 shows the result of the characterization. At the current stage of development the circuit has an estimated power consumption of 0.36 mW and is powered by a button cell battery with capacity 225 mAh. The battery powers the digital acquisition as well, but the communication is totally passive thanks to the use of a semi-passive RFID device. Under these conditions the systems has an expected lifetime of 163 h of continuous operation. The possibility to hibernate and wake the system at command allows extending the lifetime of the device to several years. Future development of the circuit will include an energy harvester.

3.3 Digital Circuit and RFID Frontend

In the current version of the project, the commercial SL900A was selected to perform the digital tasks. This device can perform the acquisition of three different physical parameters by means of its internal temperature sensor and its two analog inputs.

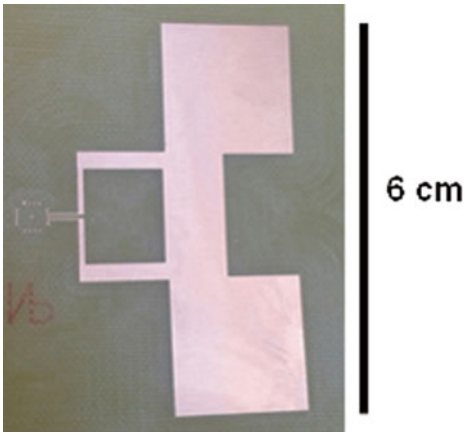

Fig. 9 The patch antenna

The SL900A chip manages the communication protocol as well. The protocol in use is the RFID EPS Gen2 Class 3. The frequency range selected for the application is UHF RFID band (860–960 MHz), a good compromise between size of the antenna and penetration depth in concrete. Lower frequencies would allow higher penetration, but the resulting bigger antennas would not be compatible with the application. We designed and fabricated a patch antenna (Fig. 9) taking into consideration the electromagnetic properties of concrete. The antenna was tested embedding it in a block of concrete at a depth of 2.5 cm: it showed full functionality and communication capabilities. The transmitted power used by the interrogator was 30 dBm.

4 Implementation

The proposed solution is currently under assembly. A real-scale outdoor experiment is planned for autumn 2014 within the Sense-City "mini-city" experiment. Several sensors will be installed in a new experimental concrete structure and their performance in real life conditions will be tested. The focus will be on the possibility to detect drying-associated shrinkage and stress applied to the structure.

5 Conclusions

We developed a flexible architecture for instrumentation of concrete structures with nanosensors. We presented the application of this architecture for the detection of micro-cracks in concrete. Future work will focus on the test of the system in real conditions and the implementation of a multisensory platform.

References

1. Lynch, J. P., et al. (2006). A summary review of wireless sensors and sensor networks for structural health monitoring. *The Shock and Vibration Digest, 38*(2), 91–130.
2. Harms, T., et al. (2010). Structural health monitoring of bridges using wireless sensor networks. *IEEE Instrumentation and Measurement Magazine, 13*(6), 14–18.
3. Hu, B., et al. (2013). Embedded piezoelectric sensors for health monitoring of concrete structures. *ACI Materials Journal*, *110*, 149–158.
4. Lebental, B., et al. (2010). *Instrumentation of cementitious materials by embedded ultrasonic micro-transducers made of carbone nanotubes*. Ph.D. thesis, East Paris University, Paris.
5. Quinn, W., et al. (2012). Development of an embedded wireless sensing system for the monitoring of concrete. *Structural Health Monitoring, 11*(4), 381–392.
6. AMS. (2015). SL900A EPC Sensor Enterprise. Retrieved from: http://ams. com/eng%20/Products/UHF-RFID/UHF-Interface-and-Sensor-Tag/SL900A. Accessed on 26 April 2015
7. Wenzel, H. (2009). *Health monitoring of bridges*. New York: Wiley.
8. Poornachandra, P., et al. (2013). Experimental investigation on corroded reinforced concrete beam in coastal environment using strain gauges. *International Journal of Engineering and Innovative Technology, 3*(5), 416–422.
9. Haksoo, C., et al. (2008). Structural health monitoring system based on strain gauge enabled wireless sensor nodes. *Proceeding of the Networked Sensing Systems*, 211–214.
10. Yang, W., et al. (2004). *Interaction between micro-cracking, cracking, and reduced durability of concrete*. Indiana: Purdue University.
11. Michelis, F., et al. (2014). *Wireless flexible strain sensor based on Carbon Nanotube piezoresistive networks for embedded measurement of strain in concrete*. Proceedings of the EWSHM14, Nantes, pp. 1780–1787.
12. Grassl, P., et al. (2010). Influence of aggregate size and volume fraction on shrinkage induced micro-cracking of concrete and mortar. *Cement and Concrete Research, 40*, 85–93.

Part X
Green Materials and By-product Utilization

The Role of Nano Silica in Modifying the Early Age Hydration Kinetics of Binders Containing High Volume Fly Ashes

Tesfamichael Yehdego and Sulapha Peethamparan

Abstract This paper outlines the development of several sustainable binders made with 70 % replacement of ordinary portland cement (OPC) with class F and C fly ashes. The early age strength and hydration kinetics of high-volume fly ash (HVFA) binders formulated with water/binder mass ratio of 0.3 were evaluated. Additions of nano-silica (NS) were used to modify the early-age hydration kinetics, microstructure, and strength development of HVFA binders. Nano-silica-modified HVFA binders developed 1-day compressive strengths nearly double those of un-modified HVFA binders. Modification with nano-silica promoted faster nucleation and higher heat of hydration over un-modified binders. The 28-day compressive strength and density of the microstructure at late age were also improved by nano-silica modification.

Keywords High volume fly ash • Nano-silica • Hydration kinetics • Microstructure

Abbreviations

70FC	70 % class C fly ash
70FF	70 % class F fly ash
HVFA	High volume fly ash
NS	Nano-silica
OPC	Ordinary portland cement
SCMs	Supplementary cementitious materials

T. Yehdego
Department of Civil and Environmental Engineering, Clarkson University, 8 Clarkson Avenue, Box 5712, Potsdam, NY 13699, USA
e-mail: yehdegtz@clarkson.edu

S. Peethamparan (✉)
Department of Civil and Environmental Engineering, Clarkson University, 8 Clarkson Avenue, Box 5710, Potsdam, NY 13699, USA
e-mail: speetham@clarkson.edu

K. Sobolev, S.P. Shah (eds.), *Nanotechnology in Construction*,
DOI 10.1007/978-3-319-17088-6_52

1 Introduction

Cement production is an energy-intensive and expensive process [1]. Fly ash is one of the most commonly used SCMs, but is typically limited to 25 % replacement of OPC [2]. Fly ash reacts with the calcium hydroxide (CH) produced during the hydration of OPC, forming secondary calcium silicate hydrate (C-S-H). These secondary products reduce the porosity and permeability of concrete, resulting in improved ultimate strength and durability [3]. Despite these benefits, the use of fly ash to replace high proportions of OPC in concrete is still limited due to the lack of binding property of fly ash when mixed with water. This results in slow early-age strength development, which is the main drawback of high volume cement replacement with fly ash [4].

One of the ways of improving the early age strength of SCMs is using nano-silica (NS) as a concrete ingredient. It has been well established that the addition of SiO_2 in the form of nano-silica improves the mechanical strength and stiffness of concrete [5]. The high surface area of nano-silica, which acts as nucleation site for cement hydration, and its pozzolanic reactivity are responsible for these improvements. It has been reported that the addition of nano-silica accelerates the hydration of cement, especially at the early ages of cement hydration [6]. When incorporated into concrete, nano-silica reacts with calcium hydroxide; the size and abundances of calcium hydroxide crystals therefore significantly decreases, resulting in a more refined and less porous gel matrix. This pore refinement results in a denser, less permeable concrete and improves the early-age strength of the binder [7].

Though several studies have been investigated the effect of nano-silica on cement properties, there are few studies on the effect of nano-silica on high volume supplementary cementitious materials (SCMs) [8–11]. In general, the use of nano-silica with SCMs and OPC blends resulted in higher particle dissociation, up to 45 % increase in compressive strength [8, 9], and reduced setting time [11].

The main objective of the present study is to formulate sustainable binders for concrete with very low portland cement and high fly ash contents (30 % and 70 %, respectively) with adequate strength and durability. The effect of nano-silica addition on the compressive strength, hydration kinetics and microstructural development are also evaluated.

2 Materials and Experimental Methods

2.1 Materials

The binders used in this study were high-volume fly ash (HVFA) mixtures of 70 % class F fly ash (FF) or 70 % class C fly ash (FC) and 30 % portland cement (OPC). Binder pastes were prepared with 0.3 water-to-binder ratio (by mass). A commercially-available powder nano-silica with particle size of 12 nm also used at dosages of 0.5, 1, and 2 %.

2.2 Experimental Methods

2.2.1 Compressive Strength

Pastes were prepared according to a strict procedure in order to minimize in-sample variation. Nano-silica incorporation was performed by first adding the nano-silica to water and dispersing it for 10 min. Dispersing was performed by (1) blending the nano-silica and half of the mixing water in a Hobart mixer at 285 rpm and, (2) electrical sonication of nano-silica and the mixing water in an ultrasonicator. The same compressive strength was obtained using both methods of dispersion, so the first method was adopted considering the ease of application. After 10 min of dispersing the nano-silica with the mixing water in the mixing bowl, the binder was added to the mixing bowl within 30 s while mixing at slow speed. This was followed by 30 s mixing at slow speed, 30 s rest, and 60 s mixing at high speed. Cylindrical paste specimens measuring 4 in. in length and 2 in. in diameter were cast for the determination of compressive strength. Specimens were demolded after 24 h and cured in saturated lime water solution. Compressive strength was determined in accordance with the specifications of ASTM C 39 at various ages.

2.2.2 Hydration Kinetics

TAM-AIR isothermal conduction calorimetry was used to study the hydration kinetics. Paste specimens were prepared for calorimetric evaluation at 25 °C isothermal condition and heat flow evolved by the paste was then recorded.

2.2.3 Microstructure Evaluation

Secondary mode scanning electron microscopy was used to analyze the microstructure of nano-silica-modified HVFA binders. At a specified curing period, the hardened paste samples were soaked in acetone to stop the hydration reaction followed by drying in an oven at 50 °C. Dried samples were examined under a JEOL JSM-7400F electron microscope.

3 Result and Discussion

3.1 Compressive Strength

The compressive strengths of nano-silica-modified HVFA binders at 1, 7, and 28 days are presented in Fig. 1. X-axis and Y-axis represents the dosage of nano-silica and compressive strength, respectively. High-volume class F (70 %FF) binders are shown in Fig. 1a, and class C (70 %FC) binders are shown in Fig. 1b. These data represent the average compressive strength of three specimens. Significant

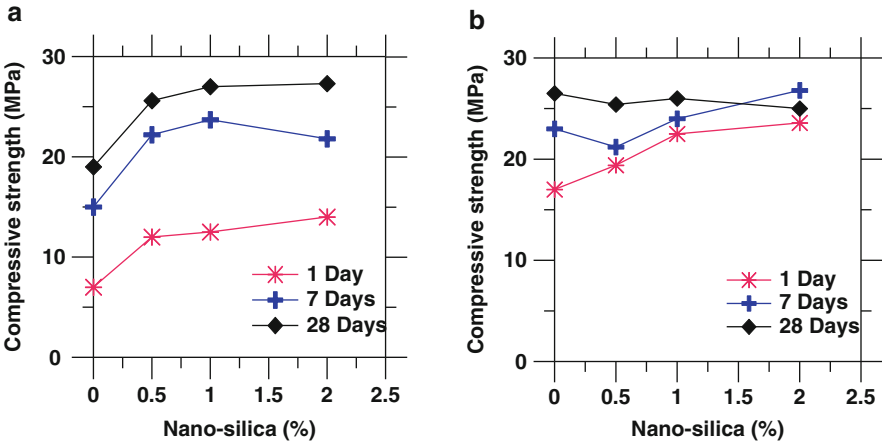

Fig. 1 Compressive strength of nano-silica-modified high volume (**a**) Class F and (**b**) Class C fly ash binders at 1, 7, and 28 days

differences in the compressive strengths of modified and unmodified class F binders are evident at all ages, with strength improvements at all nano-silica dosages evaluated. Class F binder containing 2 % nano-silica developed about twice the compressive strength of the control binder after 1 day, and had 43 % higher strength than the control after 28 days. In general, increased nano-silica dosage resulted in improved compressive strength, which is likely due to the increase in reactivity of fly ash caused by the additional nucleation sites provided by nano-silica.

Similarly, high-volume class C binders exhibited improved compressive strength when modified with nano-silica. Class C binder containing 2 % nano-silica developed its ultimate strength in 1 day, which was 40 % higher than the control. Class C binders, however, do not show significant change in compressive strength when modified with nano-silica as in the case of class F. This difference could be due to a lower pozzolanic and higher cementitious reactivity of class C fly ash compared with Class F fly ash. The slight decrease in compressive strength of modified class C binders could be due to conversion reduction which is very common for high alumina cement.

3.2 Hydration Kinetics

The heat evolution in nano-silica modified HVFA binders is presented in Fig. 2. Figure 2a shows the heat evolution in high-volume class F (70FF) binders. The maximum instantaneous heat evolution in the class F control binder was 1.2 mW/g; 2 % nano-silica increased this value by about 25 %. In general, the rate of heat evolution during very early hydration increased with dosage of nano-silica. Modification with nano-silica resulted in shorter induction periods, with the onset of the acceleration stage occurring earliest with additions of 2 % nano-silica. Increased heat evolution

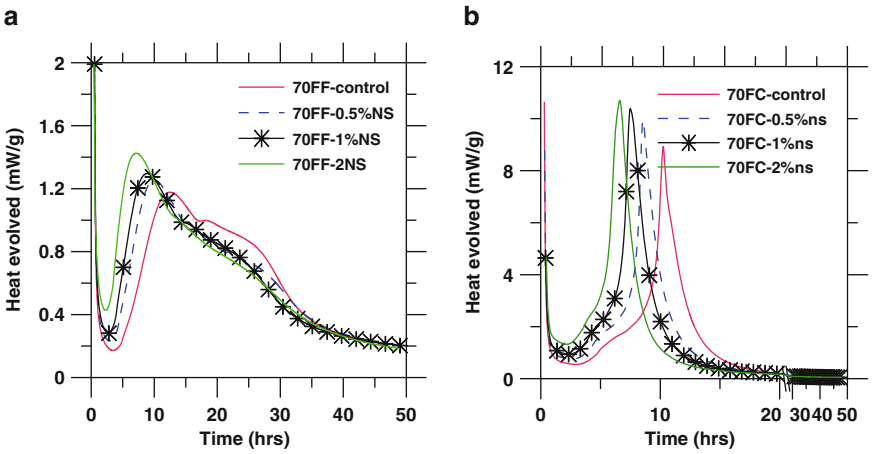

Fig. 2 Heat evolution in nano-silica-modified high-volume (**a**) class F and (**b**) class C fly ash binders at 25 °C

and rapid reaction progression with additions of nano-silica are mainly due to the acceleration of the pozzolanic reaction with increased surface area and nucleation sites [7]. Similarly, high-volume class C (70FC), Fig. 2b, binders exhibited higher heat evolution and more rapid reaction progression when modified with nano-silica.

3.3 Microstructure

Scanning electron micrographs of HVFA binders are presented in Fig. 3. High-volume class F control binder and 2 % nano-silica-modified binder are shown in Fig. 3a, b, respectively, and class C control and 2 % nano-silica-modified binders are shown in Fig. 3c, d, respectively. For both class F fly ash, the control binder shows significantly more porous and less dense microstructure and higher traces of $Ca(OH)_2$ than modified binders. Modification with 2 % nano-silica resulted in more hydration product formation and denser microstructure. Similarly, class C binders exhibited more product formation and denser microstructure when modified with nano-silica. Modification with nano-silica resulted in dense and complete product formation in a honeycomb pattern, visible in Fig. 3c, d.

4 Conclusions

- Modification of HVFA binders with nano-silica improved strength.
- The compressive strength of nano-silica-modified HVFA binders increased as the dosage of nano-silica increased.

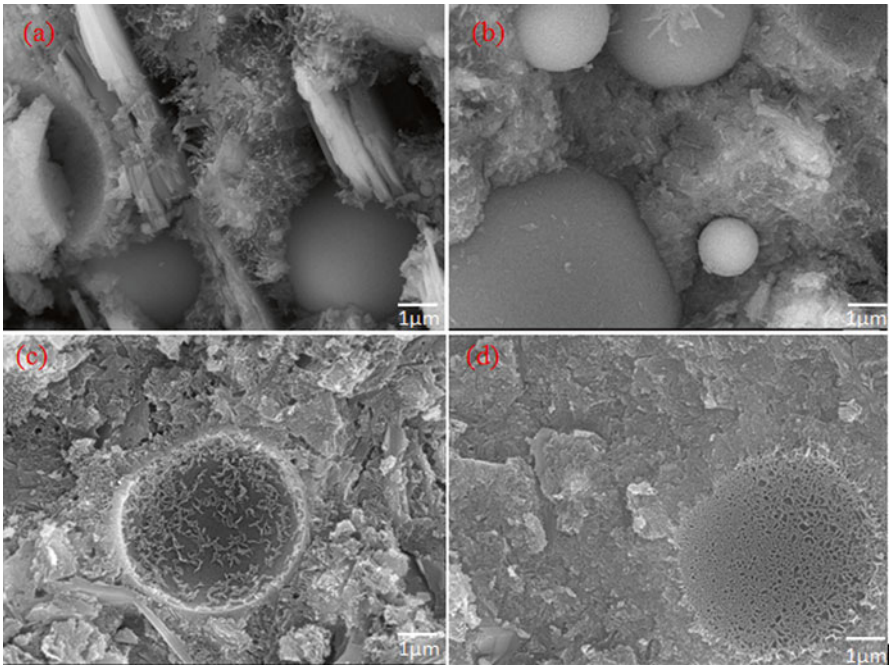

Fig. 3 Effect of nano-silica on the microstructure of HVFA (**a**) 70 %FF, (**b**) 70 %FF-2 %NS, (**c**) 70 %FC and (**d**) 70 %FC-2 %NS

- Nano-silica-modified HVFA binders exhibited an accelerated rate of hydration compared to unmodified HVFA binders.
- Nucleation and product formation were faster and more complete in all nano-silica modified HVFA binders.
- The effect of nano-silica on compressive strength was more significant in both class F and class C fly ash binders, but at 28 days it was more significant on class F fly ash binders.

Acknowledgement The authors gratefully acknowledge the financial support from the National Science Foundation (NSF) under CMMI Award no. 1055641. Any opinions, findings, and conclusions or recommendations expressed in this article are those of the authors and do not necessarily reflect the views of the NSF.

References

1. Mehta, P. K. (1998) Role of pozzolanic & cementitious by-products in sustainable development of the concrete industry. *Sixth CANMET/ACI/JCI conference: Fly ash, silica fume, slag & natural pozzolans in concrete*, Tokushima, Japan.
2. Mehta, P. K. (2001). Reducing the environmental impact of concrete. *Concrete International, 23*, 61–66.

3. Giaccio, G. M., & Malhotra, V. M. L. (1988). Concrete incorporating high volumes of ASTM class F fly ash. *Cement, Concrete and Aggregates, 10*, 88–95.
4. Sakai, E., Miyahara, S., Ohsawa, S., Lee, S. H., Diamond, S. M., et al. (2005). Hydration of fly ash cement. *Cement and Concrete Research, 35*, 1135–1140.
5. Byung-Wan, J., Chang-Hyun, K., Gh-ho, T., & Jogn-Bin, P. (2007). Characteristics of cement mortar with nano-SiO2 particles. *Construction and Building Materials, 21*, 1351–1355.
6. Land, D., & Stephan, D. (2000). Influence of nano-silica on the hydration of ordinary Portland cement. *Journal of Materials Science*. doi:10.1007/s10853-011-5881-1.
7. Qing, Y., Zenan, Z., Deyu, K., & Rongshen, C. (2007). Influence of nano-SiO2 addition on the properties of hardened cement paste compared with silica fume. *Construction and Building Materials, 21*, 537–542.
8. Pengkun, H., Shiho, K., Deyu, K., David, J., Jueshi, Q., & Surendra, P. (2013). Modification effects of colloidal nanoSiO2 on cement hydration and its gel property. *Composites Part B: Engineering, 45*, 440–448.
9. Pengkun, H., Kejin, W., & Jueshi, Q. (2012). Effect of colloidal nano-silica on hydration of fly ash. *Cement and Concrete Research, 34*, 1095–1103.
10. Lucino, S., Joao, A. L., Victor, M. F., Dachamir, H., & Wellington, L. R. (2009). Effect of colloidal nano-silica on rheological and fresh properties of cement paste. *Construction and Building Materials, 23*, 2487–2491.
11. Min-Hong, Z., & Jahidul, I. (2012). Use of nano-silica to reduce setting time and increase early strength of concretes with high volumes of fly ash or slag. *Construction and Building Materials, 29*, 573–580.

New Silica Fume from Recycled Glass

David Harbec, Hanane Bahri, Arezki Tagnit-Hamou, and François Gitzhofer

Abstract Based on its high content of amorphous silica (SiO_2), waste glass represents a good material for reclamation as glass nanoparticles ("glass fume"). When mixed into a cement paste, glass fume offer nucleation sites for portlandite and has both pozzolanic and filler behaviors. When adequately dispersed, glass fume increases slump of the cement pastes and mechanical properties of mortars. Moreover, it has been tested in high performance concrete (water-to-binder ratio (W/B) of 0.35). The evolutions of the compressive strength and of the permeability of the glass fume concrete are comparable of those of a high performance concrete mixed using silica fume.

Keywords Waste glass • RF plasma spheroidization • Glass nanoparticles • Pozzolanic reaction • High performance concrete • Concrete permeability • Microstructure densification • C-S-H gel rim

1 Introduction

Because of its pozzolanic reactivity and filler effect, submicron amorphous silica, has been added to in high- [1] and ultra-high-performance [2] concrete, in particular, for the past 30 years. For instance, silica fume (SF) is a supplementary cementitious material (SCM) used for cement replacement that improves mechanical performance, decreases porosity, and densifies microstructure [3, 4]. Today, with the emergence of nanotechnologies, new concrete materials with improved properties could be developed with nanomaterials, especially nanosilica [5–7].

Nanoparticles can be manufactured according to two main approaches: (i) the "top-down" approach, in which structures are reduced in size to the nanoscale and

D. Harbec (✉) • H. Bahri • A. Tagnit-Hamou
CRIB, Department of Civil Engineering, Université de Sherbrooke, Sherbrooke, QC, Canada
e-mail: david.harbec@usherbrooke.ca; hanane.bahri@usherbrooke.ca; a.tagnit@usherbrooke.ca

F. Gitzhofer
CREPE, Department of Chemical Engineering and Biotechnological Engineering,
Université de Sherbrooke, Sherbrooke, QC, Canada
e-mail: francois.gitzhofer@usherbrooke.ca

K. Sobolev, S.P. Shah (eds.), *Nanotechnology in Construction*,
DOI 10.1007/978-3-319-17088-6_53

(ii) the "bottom-up" approach, in which materials are engineered from atoms or molecular components through a process of assembly or self-assembly into nanoparticles [6]. Based on its high content in silica ($SiO_2 > 70$ wt%), waste glass with an added value can be transformed into amorphous silica-based nanoparticles using both "top-down" and sustainable-development approaches.

In a situation in which the use of high- and ultra-high-performance concrete is limited due to the scarcity and high cost of SF, glass fume (GF) is now being produced and tested in construction materials as a viable alternative to SF.

2 Materials and Methodology

Harbec et al. [8] identified the bi-modal particle-size distribution of GF. Engineering improvements to the GF production process increased the nanometric content by up to 97–98 %. GF can be observed with transmission electron microscopy (TEM: *Hitachi H-7500*) on a carbon-coated copper grid. Chemical and mineral compositions can be determined, respectively, with X-ray fluorescence (XRF: *Panalytical Axios*) and X-ray diffraction (XRD: *Panalytical X'pert Pro MRD*) techniques in the 10–70° 2θ range.

A comparative study of the influence of GF when blended in high-performance concrete (HPC) was conducted. For this study, 7 HPC were blended in two distinct series of batches with a water-to-binder ratio (W/B) of 0.35. One General Use (GU) cement, one siliceous sand (0–5 mm), and two crushed coarse limestone aggregates (5–14 and 10–20 mm) were used for the HPC mixes. The use of an air-entraining admixture and a polycarboxylate-type superplasticizer (SP) enabled to closely control the air content between 6 and 8 % and yield an initial slump of 180–220 mm. In the first series, performances of the HPC with 10 % GF and 10 % SF (labelled GF 10 % and SF 10 %) as cement replacement were compared to a control HPC, labelled Control 1. These HPCs were mixed with a binder dosage of 430 kg/m^3. In the second series, the performance of HPC with 1 %, 3 % and 5 % GF HPCs labelled: GF 1 %, GF 3 %, GF 5 % as cement addition were compared to a control HPC, labelled Control 2. These HPCs were mixed with a binder dosage of 434.3, 442.9, 451.5, and 430 kg/m^3, respectively. The fresh properties (density, air content, and slump) were determined and the concrete cast as cylinders 100 mm in diameter × 200 mm in length for compressive-strength testing (ASTM C39) and resistance to chloride-ion penetration testing (RCPT: ASTM C1202).

To achieve the desired slump, Control 1, SF 10 %, GF 10 %, Control 2, and GF 1 %, 3 %, and 5 % required SP dosages (dry extract) of 0.19 %, 0.26 %, 0.21 %, 0.13 %, 0.14 %, 0.15 %, and 0.17 % respectively. GF 10 % required 19 % less SP than SF 10 %. The SP requirement, however, increased as did the GF content in the HPCs.

The polished surfaces of the HPCs was also observed with variable pressure scanning electron microscopy (VP-SEM: *Hitachi S-3400N*) coupled with energy dispersive spectroscopy (EDS: *Oxford Inca*).

3 Characterization of GF

Figure 1 shows as-produced GF. GF has a spherical morphology: it is composed of a large fraction of nanoparticles of 30–200 nm in diameter. Table 1 shows the chemical compositions of the oxide basis and the loss on ignition (LOI) of GF and SF. As for FS, GF keeps its amorphous microstructure from waste glass. In Fig. 2, the XRD diffractogram shows a hump between $2\theta = 15°$ and $2\theta = 40°$ centered at the location of the main peak of cristobalite (one form of crystallized SiO_2 stable at high temperature) and no distinguishable crystalline line from the background noise from $2\theta = 40°$ to $2\theta = 70°$.

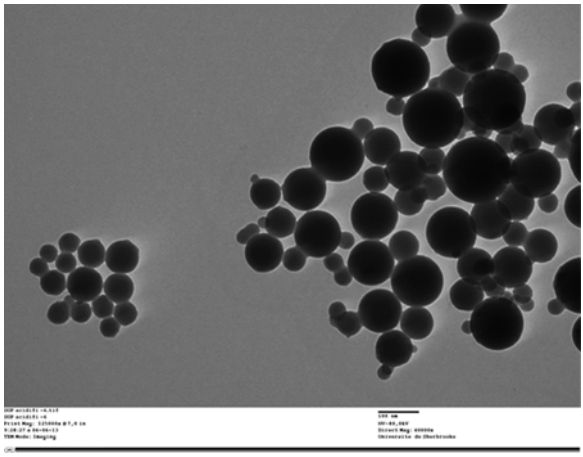

Fig. 1 TEM micrographs of GF

Table 1 Chemical composition and LOI of GF and SF determined with XRF

Metal oxide	GF	SF
SiO_2	72.05	99.81
TiO_2	0.05	0.00
Al_2O_3	1.61	0.12
Fe_2O_3	0.27	0.10
Mn_3O_4	0.02	0.02
MgO	0.69	0.25
CaO	10.80	0.38
Na_2O	11.96	0.00
K_2O	0.53	0.54
LOI (%)	1.794	0.00

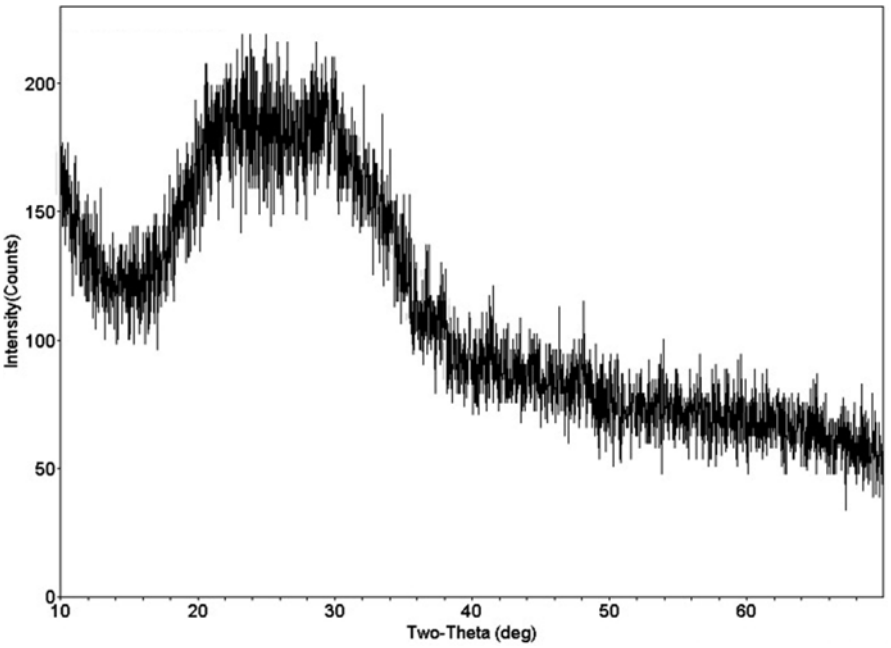

Fig. 2 XRD diffractogram of GF

4 Structuration of High-Performance Concrete (HPC)

Figure 3 shows the evolution of the HPC's compressive strength as function of curing time for the first and second series. Figure 3a shows that the introduction of fine amorphous silica particles as a cement replacement increases compressive strength with respect to the control HPC. SF 10 % and GF 10 % HPC displayed a rapid increase in compressive strength after 7 days of curing. The compressive strength of SF 10 % continued to increase rapidly and plateaued at ≈72 MPa after 56 days of curing. The compressive strength of GF 10 % increased quasi-linearly from 7 days to 91 days of curing to reach the strength of the SF 10 %.

Figure 3b shows that the early age compressive strength (<28 days) of the HPC increased with increasing GF addition. The evolution of the compressive strength of GF 1 % was similar to that of Control 2. A low amount of GF addition (3 %) yielded a slight increase in compressive strength up to 28 days of curing. For the GF 5 %, the compressive strength increased rapidly within the first 28 days and continues to increase quasi-linearly from 56 to 182 days. The compressive strengths at 28 days of GF 3 % and GF 5 % were 64 MPa and 72 MPa, respectively. At 91 days, the compressive strengths of Control 2, GF 1 % and GF 3 % plateaued at around 67 MPa, while that of GF 5 % continued to increase to 82 MPa after 182 days. At 182 days, the compressive strength of Control 2 and GF 3 % decreased by

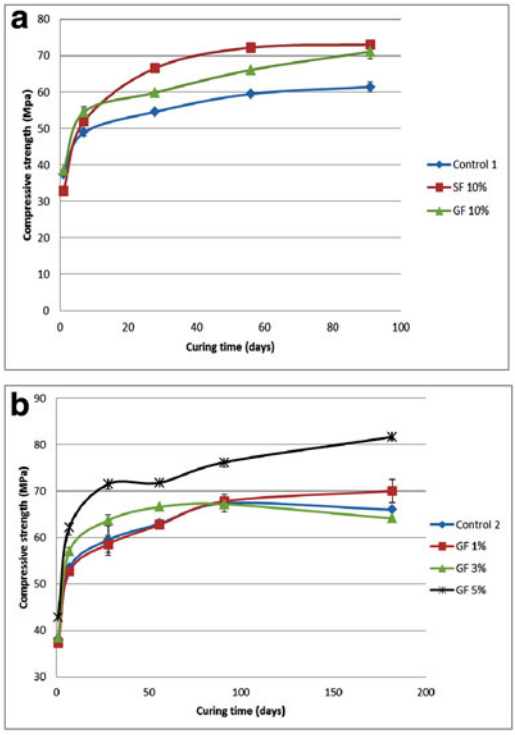

Fig. 3 Evolution of the compressive strength of HPC for (**a**) the first series and (**b**) the second series

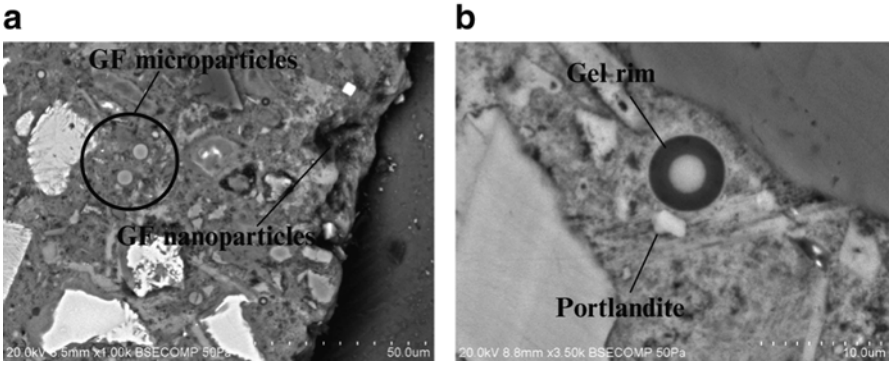

Fig. 4 (**a**) SEM micrographs showing the hydration of GF and the microstructure densification in GF 10 % after 182 days of curing. (**b**) Generation of a C-S-H gel rim around a GF microparticle in the vicinity of a portlandite crystal

1–3 MPa with respect to the 91 day values. It should be noted that only 1 cylinder was tested at 182 days for these HPCs.

The SEM micrographs in Fig. 4 show hydrating GF micro- and nanoparticles within a dense cement paste in GF 10 % HPC after 182 days of curing. One of the microparticles is magnified by 3.5 k times in Fig. 4b. A rim of gel formed around

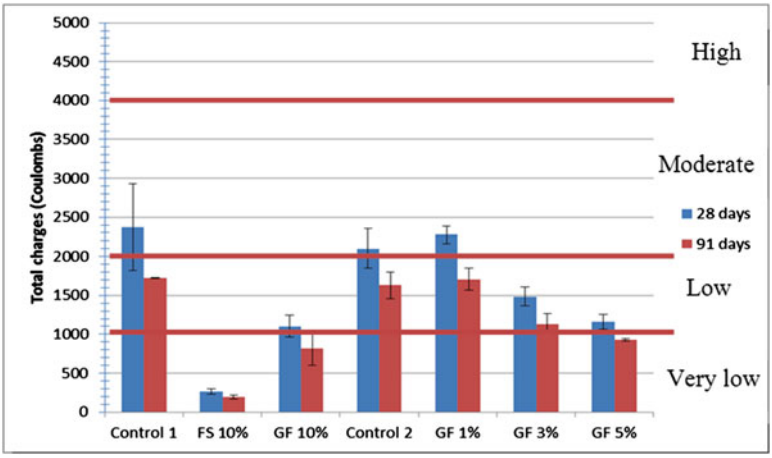

Fig. 5 Resistance to chloride-ion penetration of HPC (ASTM C1202)

the particle during its hydration in the vicinity of portlandite crystal. Compared to GF, this gel is enriched of calcium. The GF nanoparticles seem to fill the interfacial transition zone (ITZ).

The histogram in Fig. 5 presents the results of the RCPT after 28 and 91 days of curing. While Control 1 and 2 exhibited moderate and low penetration at 28 days and 91 days according to ASTM C1202, the introduction of fine amorphous silica particles in the HPC as a cement replacement and addition reduced the RCPT values. In the case of GF, penetration decreased as the amount of GF used increased. As for the compressive strength results, the results of RCPT of GF 1 % mirrored those of the control HPC. While FS 10 % had very low penetration at 28 and 91 days, GF 3 % displayed low values at 28 and 91 days, whereas GF 5 % and GF 10 % went from low penetration at 28 days to very low penetration at 91 days.

5 Discussion

The fresh-state properties of the HPC revealed that GF required less SP than SF. This fact is attributed to the weak water absorption of glass [9]. More water was thus available to fluidize and hydrate cement.

In the hardened state, GF achieves comparable compressive strengths and RCPT in the same charge range than SF after 91 days when used as a cement replacement in the HPC. The compressive strengths of the HPC increased and RCPT values decreased as the GF content increased. Previous NICOM contribution [10] stated the nucleation effect at early age and the pozzolanic effect of GF at the hardened

stated. Early-age performance of GF can be attributed to its nucleation and filler effects, while the increased long-term compressive strength to its pozzolanic effect. Dissolved lime when cement is put in contact with water can nucleate on the GF nanoparticles. This mechanism shortens the induction period and favor a higher degree of hydration of cement. Slower development of the compressive strengths of GF at early age (<28 days) with respect to SF may be attributed to the slower pozzolanic reactivity of GF. SEM micrographs show reacting GF micro- and nanoparticles after 182 days and a densification of the cement paste. The lower amorphous silica content and higher loss on ignition of GF may contribute to the slower reactivity.

6 Conclusion

This paper presented the effect of introducing GF as a cement replacement and addition in HPC. GF consists of amorphous glass nanoparticles with a PSD within 30–200 nm and microparticles with a PSD within 1–10 μm.

The fresh-state properties of the HPC revealed that GF required less SP than SF. This fact is attributed the weak water absorption of glass [9]. More water was thus available to fluidize and hydrate cement.

In the hardened state, GF generated compressive strengths and RCPT comparable to SF at late age (>91 days) in HPC. The compressive strengths of the HPC increased and RCPT decreased as the GF content increased. Early-age performance of GF can be attributed to its nucleation and filler effects, while the increased long-term compressive strength to its pozzolanic effect.

References

1. Adam, N., & Aïtcin, P. C. (1998). High performance concrete. An overview. *Materials and Structures, 31*(206), 111–117.
2. Richard, P., & Cheyrezy, M. (1995). Composition of reactive powder concretes. *Cement and Concrete Research, 25*(7), 1501–1511.
3. Aïtcin, P. C., & Laplante, P. (1990). Long-term compressive strength of silica-fume concrete. *Journal of Materials in Civil Engineering, 2*, 164–170.
4. Gjorv, O. E., Monteiro, P. J. M., et al. (1990). Effect of condensed silica fume on the steel-concrete bond. *ACI Materials Journal, 87*, 573–580.
5. Porro, A., & Dolado, J. S., et al. (2010). Nanotechnology and concrete: Concepts and approach. *Transportation Research Record 2142* (Nanotechnology in Cement and Concrete 2010) *2*, 127–129.
6. Sanchez, F., & Sobolev, K. (2010). Nanotechnology in concrete – A review. *Construction and Building Materials, 24*, 2060–2071.
7. Gaitero, J. J., Campillo, I., et al. (2010). Small change can make a great difference. *Transportation Research Record 2141* (Nanotechnology in Cement and Concrete) *1,* 1–5.

8. Harbec, D., Gitzhofer, F., et al. (2011). Induction plasma synthesis of nanometric glass powder (NSGP) for use in cementitious materials. *Powder Technology, 214*, 356–364.
9. Zidol, A., Pavoine, A., et al. (2012). *Effect of glass powder on concrete durability*. International congress on Durability of Concrete 2012, Trondheim, ICDC2012-D-11-00153.
10. Harbec, D., Tagnit-Hamou, A., & Gitzhofer, F., (2012). Influence of spheroidized glass nanoparticles on the early age reactivity mechanism. *4th International symposium on Nanotechnology in Construction (NICOM4),* Agios Nikolaos, Crete.

Study of the Interaction Between Nanoclay and Fly Ash and Its Impact on the Enhancement of the Rheological Properties of Geopolymer Binders

Carlos Montes, Anupam Joshi, Saeid Salehi, Yuri Lvov, and Erez Allouche

Abstract Naturally occurring nanoclays, such as halloysite nanotubes (HNTs) are relatively cheap and abundant materials with interesting applications in the construction industry. Recently, an electrostatic interaction was discovered between halloysite and fly ash particles, which has the potential to beneficially alter the properties of some hardened products of fly ash, such as geopolymer binders. Additionally, layer-by-layer deposition can be used to enhance even further the benefits of the fly ash-nanoclay interaction. This paper describes the nature of the interaction of the nanoclay particles with fly ash and the results of mechanical and rheological testing conducted on geopolymer produced from such nanocomposites, and the implications of this discovery for construction materials.

Keywords Geopolymer • Halloysite • Nanoclay • Layer-by-layer encapsulation

1 Introduction

Geopolymer binder is an inorganic alumino-silicate polymer that offers corrosion and high temperature resistance properties as well as low carbon footprint, which may be produced out of fly ash [1]. These properties make geopolymer candidate for high performance cement applications, such as oil well casing grouts, acid resistant concrete containers, and even proppant sands. However, its rheological or fresh properties are not always easy to control, especially at the environments in which these oil well grouts must be applied, which is in the range of 50–300 °C and 70–210 MPa.

The geopolymer-halloysite composite properties were characterized by SEM and Zeta-potential and their dynamic viscosity at high temperatures determined. The layer-by-layer (LbL) encapsulation approach was utilized in addition to direct halloysite/kaolin deposition for positively charge fly ash microparticles. LbL multilayer shell assembly helped to densify and thicken the nanoclay shell deposited on

C. Montes (✉) • A. Joshi • S. Salehi • Y. Lvov • E. Allouche
Institute for Micromanufacturing, Louisiana Tech University, Ruston, LA, USA
e-mail: cmontes@latech.edu; arj019@latech.edu

K. Sobolev, S.P. Shah (eds.), *Nanotechnology in Construction*,
DOI 10.1007/978-3-319-17088-6_54

fly ash microparticles. Halloysite is a naturally occurring aluminosilicate mineral with a chemical formula $Al_2Si_2O_5 \cdot 2H_2O$. Halloysite nanoshells allowed for more efficient control of setting time which is very important for practical applications for the oil well construction industry.

2 Experimental

2.1 Materials

Two class F fly ash sources were utilized. The chemical and phase composition, location and other characteristics of these fly ash sources are detailed in Table 1.

Halloysite nanotubes with a length of 1–1.5 μm, with inner lumen of ca. 15 nm and outer diameter of 50–60 nm from Applied Minerals Co., NY were utilized for this study. Halloysite specific gravity is 2.53. Figure 1 is an image of halloysite nanotubes and fly ash. Table 2 summarizes the surface properties of fly ashes.

Sodium silicate used was a liquid silicate with a SiO_2/Na_2O ratio of 3.2 in 37 wt% aqueous solution. Also, 10 and 12 M sodium hydroxide solutions were utilized.

Polyethyleneimine (positively charged below pKa 11.5) and polyacrylic acids (negatively charged above pKa 3.5), both of medium molecular weight purchased from Aldrich-Sigma, were utilized for the layer-by-layer nanoassembly.

2.2 Equipment and Methods

Viscosity measurements were conducted on a Brookfield DV-III Ultra Rheometer. A small sample adapter and a SV4-27 spindle were selected for all the experiments. A Hitachi S-4800 Field Emission Scanning Electron Microscope (SEM) was used

Table 1 Chemical composition of fly ash sources utilized in the study

Oxide	DH, LA	MO, TX	Halloysite
SiO_2	59.32 %	55.61 %	46.55 %
Al_2O_3	19.72	19.87	39.50 %
CaO	6.95	12.93	–
Fe_2O_3	7.22	4.52	–
MgO	2.23	2.49	–
SO_3	0.36	0.49	–
Na_2O	1.11	0.67	–
K_2O	1.27	0.86	–
TiO_2	1.00	0.89	–
MnO_2, SrO, BaO, LOI	<0.80	<0.80	–
H_2O	–	–	13.60 %

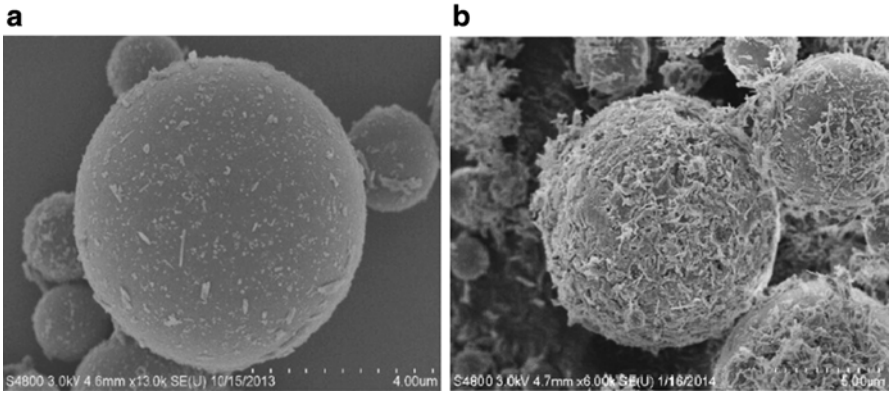

Fig. 1 (**a**, **b**) SEM images of dry MO fly ash mixed with 6 wt% pristine halloysite and after LbL fly ash coating with PAA/PEI/halloysite

Table 2 Specific gravity, fineness and ξ-potential of raw materials

	DH, LA	MO, TX
Specific gravity (g/cm^3)	2.23 ± 0.02	3.28 ± 0.02
Fineness (<45 μm)	62.97 ± 0.03	68.75 ± 0.03
Ash ξ-potential	+22 ± 1 mV	−21 ± 1 mV

for microstructural characterization. Zeta-potential (ξ-potential) and dynamic light scattering (DLS) measurements were carried out with microelectrophoretic ZetaPlus Potential Analyzer (Brookhaven Instruments) at 25.0 ± 0.5 °C. For LbL film thickness measurements 9 MHz Quartz Crystal Microbalance (QCM, USI-system, Japan) instrument with silver electrode resonators was used.

To prepare paste specimens, the alkaline activators were mixed first, and then fly ash was added and mixed for 60 s. The halloysite nanotubes were premixed in dry condition with the fly ash. To measure viscosity, approximately 20 ml of paste was poured on a small sample container, which was attached to the rheometer. Then, the spindle was inserted, and rotated constantly at a speed of 5 rpm.

Two approaches were used for fly ash microparticle coating: (1) for positively charged ash microparticles (Dolet Hills type), the fly ash was mixed with negatively charged halloysite in dispersion. (2) For negatively charged ash (Monticello type) the layer-by-layer assembly was used: first, adsorbing on ash microcores cationic polyelectrolyte – polyethyleneimine, followed by adsorption of anionic nanoclays (halloysite or kaolin). To increase thickness of the shell, this polycation/polyanion alternate adsorption was repeated two times [3, 5–7].

3 Results and Discussion

3.1 Zeta Potential and Nanoarchitectural Shell Assembly in Fly Ash Microparticles (LbL Method)

In the case of positive fly ash (DH) some halloysite deposition was achieved when mixed dry with the fly ash. In order to increase the thickness of the coating of the halloysite on the fly ash surface this LbL approach was implemented. In the case of positively charged DH, fly ash was first coated with the polyanion-PAA, followed by a layer of polycation-PEI. After each deposition surface charge was measured to ensure successful coating with potential alternation. Figure 1 shows SEM images of Monticello (MO) and Dolet Hills (DH) fly ash particles coated with 6 wt% halloysite with and without layer-by-layer treatment.

It can be seen how the LbL treatment enhanced the coating of the fly ash particles by halloysite. This is especially noticeable for the Monticello fly ash. With QCM control we measured thickness of PEI/halloysite bilayer as 50 ± 10 nm; this estimation may be used for a similar architecture coating on fly ash microcores.

The zeta potential for halloysite and kaolin was found to be -30 ± 5 mV and -25 ± 5 mV respectively. Table 3 shows the potential monitoring of the fly ash particles during LbL assembly process: a regular positive/negative charge alternation confirms planned polycation/polyanion adsorption.

3.2 Rheological Tests

In Fig. 2 it can be seen the dynamic viscosity vs. time of Monticello fly ash geopolymer (a) and Dolet Hills fly ash geopolymer (b). MO geopolymer paste was tested at ambient temperature because its moderate CaO content would cause flash set at higher temperature. Results show that the sample that was treated LbL exhibited a significantly longer setting time compared to pure and dry added halloysite.

Table 3 Surface ξ-potential of positive DH and negative MO fly ash microparticles in the process of the LbL shell assembly

Layer	ξ-Potential (mV), error ±1
Control DH[a] fly ash	+21 (±3)
DH FA/PAA[b]	−43 (±4)
DH FA/PAA/PEI[c]	+55 (±4)
Control MO[a] fly ash	−22 (±3)
MO FA/PEI	+21 (±4)
MO FA/PEI/PAA	−33 (±4)
MO FA/PEI/PAA/PEI	+49 (±4)

[a]*DH* Dolet hill fly ash, *MO* Monticello fly ash
[b]*PAA* polyacrylic acid
[c]*PEI* polyethylenimine

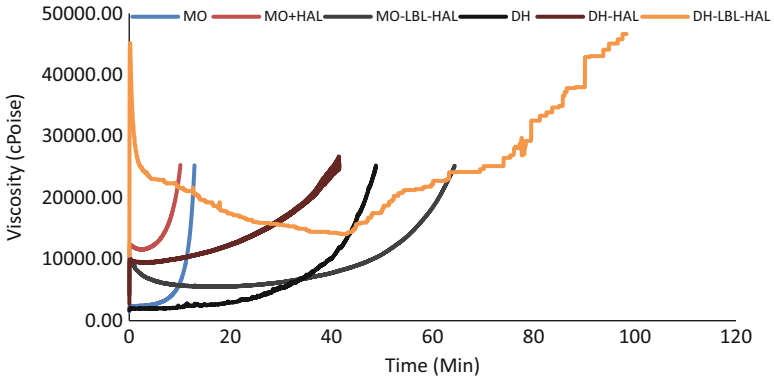

Fig. 2 Dynamic viscosity of Monticello fly ash and Dolet Hills fly ash geopolymer at ambient temperature and at 50 °C respectively: pure (*MO*), with 6 % halloysite(*HAL*) and treated LbL with 6 % halloysite (*LBL + HAL*), Dolet Hills fly ash geopolymer at 50 °C: pure (*DH*), with 6 % halloysite (*HAL*) and treated LbL with 6 % halloysite (*LBL + HAL*)

The results were similar for the DH sample that was tested at 50 °C. The results were obtained after conducting 3 tests, and are found to be repeatable.

4 Conclusions

The modification of the rheology of geopolymer paste at moderately high temperatures is an important aspect of the present work, which may find applications such as the cementing of oil and gas exploration and production wells. For the enhancement of rheology and viscosity of fly ash formulations for geopolymers, the ash particles were coated with polycation/nanoclay multilayers using LbL approach. The fly ash microcores were coated sequentially with oppositely charged polyelectrolytes and clays. Results show that after the LbL treatment geopolymer samples exhibited a significatively larger setting time both in ambient and high temperatures.

References

1. Davidovits, J. (2008). *Geopolymer chemistry and applications* (2nd ed., pp. 1–367). Saint Quintin: Geopolymer Institute.
2. Lvov, Y., Decher, G., & Möhwald, H. (1993). Assembly, structural characterization and thermal behavior of layer-by-layer deposited ultrathin films of polyvinylsulfonate and polyallylamine. *Langmuir, 9*, 481–486. doi:10.1021/la00026a020.
3. Ariga, K., McShane, M., Lvov, Y., Ji, Q., Vinu, A., & Hill, J. P. (2012). Inorganic nanoarchitechtonics for biological applications. *Chemistry of Materials, 24*, 728–737. doi:10.1021/cm202281m.

4. Decher, G. (1997). Fuzzy nanoassemblies: Toward layered polymeric multicomposites. *Science, 277*, 1232–1237. doi:10.1126/science.277.5330.1232.
5. Caruso, F., Caruso, R., & Möhwald, H. (1998). Nanoengineering of inorganic and hybrid hollow spheres by colloidal templating. *Science, 282*, 1111–1114. doi:10.1126/science.282.5391.1111.
6. Lvov, Y., Eadula, S., Zhang, Z., Lu, Z., & Grozdits, G. (2006). Layer-by-layer nanocoating of mill broken fibers for improved paper. *Journal of Nordic Pulp and Paper Research, 21*, 552–559. doi:10.3183/NPPRJ-2006-21-05-p552-557.
7. Bantchev, G., Lu, Z., & Lvov, Y. (2009). Layer-by-layer nanoshell assembly on colloids through simplified washless process. *Journal of Nanoscience and Nanotechnology*, *9*, 396–403. doi: http://dx.doi.org/10.1166/jnn.2009.J055.

The Effect of Nano Materials on HVFA Mixtures

Jussara Tanesi, Jose Munoz, Haejin Kim, and Ahmad Ardani

Abstract The interest in more sustainable concrete mixtures with the supplementary cementitious materials like fly ash has increased significantly in the past few years. Nevertheless, the early age properties development (setting and strength gain) of these mixtures still remains a challenge and, in most cases, prevents their efficient use in practice. In this paper, nano-aluminosilicates were used to improve early age properties of high volume fly ash (HVFA) mixtures. This paper presents results of several different paste and mortar mixtures where 60 % (by volume) of the portland cement was replaced by fly ash (Class C or Class F) and 1 % of amorphous nano-aluminosilicates with different silicon-aluminum ratios. Paste mixtures were characterized by measuring heat release and setting times and the compressive strength was evaluated in mortar mixtures in order to determine the optimal silicon-aluminum ratio for the cementitious materials used in the study.

Keywords High volume fly ash mixtures • Nano aluminosilicates • Nano materials • Setting • Compressive strength • Heat release

1 Introduction

Fly Ash is considered an excellent replacement for portland cement to reduce the embodied energy of concrete mixtures [1]. Because of the problems encountered in early hydration reaction of concrete mixtures with high volumes of fly ash (HVFA), scientific bibliography recommends, as suitable replacement, a maximum of 35 % of fly ash by mass [1]. However, data from U.S. ready mix concrete producers

J. Tanesi (✉) • H. Kim
TFHRC- concrete laboratory, SES Group & Associates LLC, Chesapeake City, MD, USA
e-mail: jussara.tanesi.ctr@dot.gov; haejin.kim.ctr@dot.gov

J. Munoz
TFHRC - chemistry laboratory, SES Group & Associates LLC, Chesapeake City, MD, USA
e-mail: jose.munoz.ctr@dot.gov

A. Ardani
TFHRC- concrete laboratory, FHWA, Washington, DC, USA
e-mail: ahmad.ardani@dot.gov

K. Sobolev, S.P. Shah (eds.), *Nanotechnology in Construction*,
DOI 10.1007/978-3-319-17088-6_55

indicate that the actual average replacement is reduced to 12 % by mass in pavements and transportation infrastructures [2]. Delayed setting times, reduced early-age strengths and increased sensitivity to curing conditions are common problems encountered in HVFA mixtures. The dilution effect and the delay in the hydration reaction of fly ash are the principal causes of these problems. Previous efforts, such as adding alkali activators, gypsum, calcium hydroxide, cement kiln dust, silica fume, limestone [3, 4], nano-silica [5], or lowering water to cementitious materials ratio [6], were found to be effective in order to ameliorate the problems due to slow early hydration reaction in HVFA mixtures.

This paper presents results on the application of a new type of nanoaluminosilicate with different silicon to aluminum ratios used to improve the early age properties of HVFA mixtures. The effects on the early hydration reaction of these nano-additives in the HVFA mixtures were investigated using isothermal calorimetry and setting time. Finally, the compressive strength of HVFA mortar mixtures was evaluated.

2 Materials and Testing

2.1 Production of Nano-particles

The following reagent grade chemicals were used in the preparation of the nanoparticles: tetra-ethyl orthosilicate (TEOS), aluminum-tri-sec-butoxide (ATSB), aluminum ethoxide (AE), sec-butyl alcohol ($C_4H_{10}O$), nitric acid (HNO_3) and deionized water (18.2 MΩ cm). The nanosilica (nano SiO_2) and nanoboehmite (nano AlO(OH)) were synthesized following sol-gel process described elsewhere [7]. The two nanoaluminosilicates sols were synthesized by mixing 1 mol of TEOS with 2.1 and 0.9 mol of ATSB for silicon-aluminum ratio of 0.64 (Si/Al0.64) and 1.3 (Si/Al1.3), respectively, at water to alkoxides molar ratio of 70. The silica precursor was allowed to "prehydrolyze" in water at pH 3 for a period of 10 min at room temperature [8]. After this prehydrolysis step, the aluminum precursor, previously dissolved in 7 mL of sec-butyl alcohol, was added and stirred until complete homogenization was achieved. Following the synthesis, all sols were dialyzed to remove side impurities and determine the concentrations [7].

2.2 Paste and Mortar Mixtures

The portland cement and fly ashes in this research were the same used in previous studies [4, 10]. The cement (Type I/II) had a reported Blaine fineness of 378 m^2/kg and a calculated Bogue phase composition of 52.5 % C3S, 15.5 % C2S, 7.1 % C3A, and 10.7 % C4AF, with a reported limestone content of 3.7 %, all mass fractions. Its density was measured to be 3,270 kg/m^3. Fly ashes chemical compositions, measured densities (ρ in kg/m^3), and particle size characteristics (d(50) is

Table 1 Oxide composition percent by mass and physical characteristics of the class C and class F fly ashes

Fly ash	SiO_2	Al_2O_3	Fe_2O_3	CaO	MgO	SO_3	Na_2O	K_2O	ρ	$(50)^d$
Class C	38.38	18.72	5.06	24.63	5.08	1.37	1.71	0.56	2,630	10.30
Class F	59.73	30.18	2.80	0.73	0.83	0.02	0.24	2.42	2,160	25.34

median-diameter in μm) are provided in Table 1. The class C and F fly ash had a LOI 0.26 and 0.79 % of LOI, respectively. The class C fly ash has been observed to produce considerable delays in setting times when used with a variety of portland cements in the past [4, 6].

The mixture designs were based on a previous study [10]. All cement replacements were made on a volumetric basis, based on the measured specific gravities of the cement and fly ashes. All mixtures were designed to maintain **constant volume fractions** of water and powders. No admixtures were used. The water content was 221 lb/yd^3 and the sand content was 2,455 lb/yd^3 for all mixtures. The *w/c* of the plain mixture (only portland cement) was 0.40. 60 % of the cement volume was replaced by either fly ash or a combination of 59 % of fly ash and 1 % of different nano-particles. Since the water content was kept constant and the two fly ashes had different specific gravities, mixtures containing class F fly ash had a *w/cm* of 0.50, while the mixtures containing class C fly ash had a *w/cm* of 0.46. Paste mixtures were prepared according to ASTM C1738 and mortar mixtures according to ASTM C305, except for the size of mixer used. Setting time (ASTM C192), isothermal calorimetry (ASTM C1679 and ASTM C1702) and compressive strength (ASTM C109) were carried out.

3 Results and Discussion

3.1 Setting Time

Figure 1 shows the test results of initial setting times. Both fly ashes caused initial setting time delays, due to dilution effect (class F and class C) and a retardation effect (class C), as observed by Gurney et al. [4]. The initial setting time for class F and class C fly ash mixtures were delayed by 125 min and 335 min, respectively.

For the ternary mixtures when compared with the binary mixtures, i.e., the ones containing either fly ash F or fly ash C only, different behaviors were observed, depending on the type of nano-particle and fly ash used. For example, nano-silica particles were not able to accelerate setting time in the class F mixture but accelerated in the class C mixture by 75 min. Nano-boehmite retarded setting time by 60 min in the class F mixture and by 95 min in the class C mixture. The Si/Al1.3 nano-aluminosilicate delayed setting time by 35 min in the class F mixture and delayed setting by 20 min in the class C mixture. Nevertheless, the Si/Al0.64 nano-aluminosilicate accelerated setting time for both fly ash mixtures, 75 min in the class F fly ash mixture and 180 min in the class C fly ash mixture.

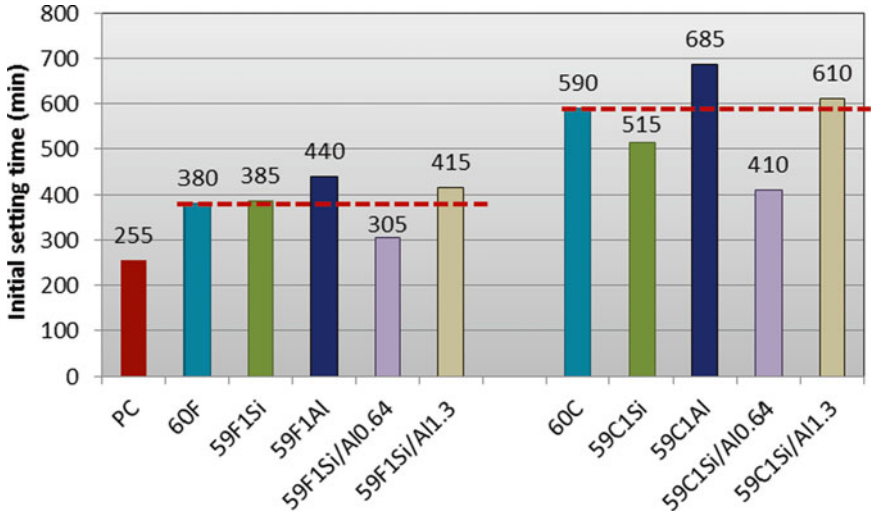

Fig. 1 Initial setting time. *PC* represents the plain mixture (only portland cement). For the other 9 mixtures, the first number indicates the percentage of fly ash (as relates to the total cementitious volume), followed by a letter that represents the class of fly ash used followed by volumetric percentage and type of nano-particle

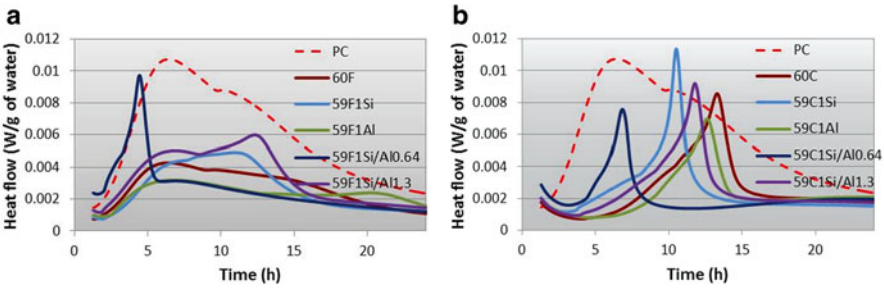

Fig. 2 Heat flow, through isothermal calorimetry, of Portland cement paste mixture and fly ash paste mixtures with nano-aluminosilicates. Heat flow was normalized by the mass of water. (**a**) Class F fly ash mixtures and (**b**) Class C fly ash mixtures

3.2 Isothermal Calorimetry

Figure 2 illustrates the heat flow over time for the portland cement mixture, the binary and ternary mixtures. Heat flow is shown only for the first 24 h to give better visualization, although it was collected for a total of 72 h.

As it can be seen in Fig. 2a, 60F mixture shows much lower peaks than the PC mixture and the peaks are shifted to the right, indicating setting time delay mainly due to the dilution effect, since most of the fly ash is normally inert during the first few hours.

All the nano-particles in Fig. 2a, with exception of nanoboehmite, promoted an amplification of the aluminate peak with respect of 60F mixture. In the case of 59F1Si/Al0.64 mixture, there is a significant shift of the curve to the left. This mixture also showed the most significant aluminate peak amplification of all mixtures, with a peak higher than the portland cement mixture. Muñoz et al. [7] suggest that nano-aluminosilicate particles in addition to serving as nucleation sites to form calcium silicate hydrates (C-S-H) and potentially calcium aluminate silicate hydrates (C-A-S-H), also deplete sulfates due to adsorption and/or to precipitation of monosulfate. The latter characteristic of the nano-aluminosilicate particles may explain the observed acceleration of the aluminate peak. The 59F1Si mixture curve shows a slight delay comparing to the 60F. Although the silicate peaks in 59F1Al and 59F1Si/Al1.3 mixtures occur about the same time as the one in 60F, the aluminate peaks in both 59F1Al and 59F1Si/Al1.3 mixtures are delayed in comparison with 60F.

In Fig. 2b, all the nano-particles showed acceleration of reactions of class C fly ash mixture with respect of 60C mixture. Mixtures 59C1Si and 59C1Si/Al1.3 showed amplification of aluminate peak. Due to the reactive aluminate content of the class C fly ash, mixtures containing the class C fly ash presented a sharper amplification of the second peak in comparison with the class F fly ash mixtures. In both class F and class C fly ash mixtures, there appear to be an optimum Si/Al ratio of 0.64 in terms of acceleration of reactions.

3.3 *Compressive Strength*

Mortar compressive strength was determined on cubes at different ages from 1 to 28 days at different age intervals.

In Fig. 3a, mixtures containing class F fly ash and boehmite and nanoaluminosilicates with Si/Al of 0.64 and 1.3 presented similar compressive strength. Mixture containing nano-silica presented slightly higher strength than the mixtures with other nano particles but presented lower strength than the binary mixture.

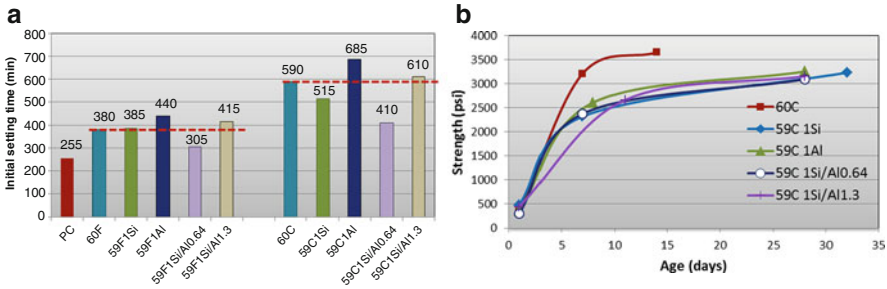

Fig. 3 Compressive strength development of mortars containing fly ash and nanoaluminosilicates. (**a**) Class F fly ash mixtures and (**b**) Class C fly ash mixtures

In Fig. 3b, mixtures containing class C fly ash, the same behavior is observed: mixtures containing nano-aluminosilicates presented lower compressive strength than the control binary mixture. In the case of class C fly ash mixtures, the compressive strength of all mixtures containing nano-aluminosilicates was similar.

4 Summary and Conclusions

In this study, pastes with a total of 60 % volume of the portland cement replaced by either class F or class C fly ash and different nano-particles were investigated. Based on the results obtained, following conclusion can be drawn. The nanosilica accelerates setting only of class C fly ash mixture, provides nucleation sites and forms C-S-H. The nano-boehmite delayed setting even further when compared with the binary mixtures setting, provides nucleation sites and may be forming C-A-S-H. The effect on setting and acceleration of the hydration reaction of the amorphous nano-aluminosilicate depends on the Si/Al ratio, with an optimum at 0.64. They provide nucleation sites and may be forming C-A-S-H. All the nanoparticles tested show lower compressive strength than the control mixture with 60 % fly ash.

References

1. American Concrete Institute Committee 232. (2004). *Use of fly ash in concrete* (ACI committee Report ACI 232.2R-03, 41 pages). Farmington Hills: American Concrete Institute. ISBN: 9780870311376.
2. Obla, K., Lobo, C., & Kim, H. (2012). *Greatly increased use of fly ash in hydraulic cement concrete (HCC) for pavement layers and transportation structures-volume I*. (Final report). MD: NRMCA.
3. Niemuth, M. D. (2012). *Effect of fly ash on the optimum sulfate of Portland Cement*. Ph.D. dissertation, Purdue University, publication number 3556556, advisor Jason Weiss.
4. Gurney, L., Bentz, D. P., Sato, T., & Weiss, W. J. (2012). Reducing set retardation in high-volume fly ash mixtures with the use of limestone, improving constructability for sustainability. *Transportation Research Record*, 2290, 139–146.
5. Zhang, M. H., & Islam, J. (2012). Use of nano-silica to reduce setting time and increase early strength of concretes with high volumes of fly ash or slag. *Construction and Building Materials, 29*, 573–580.
6. De la Varga, I., Castro, J., Bentz, D., & Weiss, J. (2012). Application of internal curing for mixtures containing high volumes of fly ash. *Cement and Concrete Composites, 34*(9), 1001–1008.
7. Muñoz, J. F., Yao, Y., Youtcheff, J., & Arnold, T. (2014). Mixtures of silicon and aluminum oxides to optimize the performance of nanoporous thin films in concrete. *Cement and Concrete Composites, 48*, 140–149.
8. Pozarnsky, G. A., & McCormick, A. V. (1995). Multinuclear NMR study of aluminosilicate sol-gel synthesis using the prehydrolysis method. *Journal of Non-Crystalline Solids, 190*(3), 212–225.
9. Schneider, J. F., Hasparyk, N. P., Silva, D. A., & Monteiro, P. J. (2008). Effect of lithium nitrate on the alkali-silica reaction gel. *Journal of the American Ceramic Society, 91*(10), 3370–3374.
10. Tanesi, J., Bentz, D. P., & Ardani, A. (2013). Enhancing high volume fly ash concretes using fine limestone powder. In SP-294: *Advances in green binder systems*. Farmington Hills: American Concrete Institute.

Part XI
Light-Weight Materials for Energy Efficient Construction

Development of Nano Insulation Materials for Building Constructions

Bjørn Petter Jelle, Tao Gao, Linn Ingunn Christie Sandberg, Serina Ng, Bente Gilbu Tilset, Mathieu Grandcolas, and Arild Gustavsen

Abstract The application of superinsulation materials (SIM) reaching thermal conductivities far below 20 mW/(mK) allows the construction of relatively thin building envelopes while still maintaining a high thermal resistance, which also increases the architectural design possibilities for both new buildings and refurbishment of existing ones. To accomplish such a task without applying vacuum solutions and their inherit weaknesses may be possible from theoretical principles by utilizing the Knudsen effect for reduced thermal gas conductance in nanopores. This study presents the attempts to develop nano insulation materials (NIM) through the synthesis of hollow silica nanospheres (HSNS), indicating that HSNS may represent a promising candidate or stepping-stone for achieving SIM. Furthermore, initial experiments with aerogel-incorporated concrete and the conceptual work concerning NanoCon are presented.

Keywords Nano insulation material • NIM • NanoCon • Building • Construction

B.P. Jelle (✉)
Department of Materials and Structures, SINTEF Building and Infrastructure, NO-7465 Trondheim, Norway

Department of Civil and Transport Engineering, Norwegian University of Science and Technology (NTNU), NO-7491 Trondheim, Norway
e-mail: bjorn.petter.jelle@sintef.no; bjorn.petter.jelle@ntnu.no

T. Gao • A. Gustavsen
Department of Architectural Design, History and Technology, Norwegian University of Science and Technology (NTNU), NO-7491 Trondheim, Norway

L.I.C. Sandberg
Department of Civil and Transport Engineering, Norwegian University of Science and Technology (NTNU), NO-7491 Trondheim, Norway

S. Ng
Department of Materials and Structures, SINTEF Building and Infrastructure, NO-7465 Trondheim, Norway

B.G. Tilset • M. Grandcolas
Materials and Nanotechnology Sector, SINTEF Materials and Chemistry, NO-0314 Oslo, Norway

K. Sobolev, S.P. Shah (eds.), *Nanotechnology in Construction*,
DOI 10.1007/978-3-319-17088-6_56

1 Introduction

Today energy-efficiency and zero emissions in the building sector represent a major mean on the path towards a more sustainable world, where thermal insulation for both new and existing buildings has an important role [1, 2]. Very thick building envelopes are not desirable due to several reasons, e.g. considering space issues with respect to economy, floor area, transport volumes, architectural restrictions and other limitations, material usage and existing building techniques. Vacuum insulation panels (VIP) represent a state-of-the-art thermal insulation solution [3–6], however due to the risk of loss of vacuum caused by perforation or moisture and air diffusion during many years, the VIP is not a robust solution [2–4, 7]. Thus, there is a demand to develop high performance thermal superinsulation materials (SIM). The objective of this work is to summarize the path from concepts to experimental investigations for tailor-making the high performance thermal building insulation materials of beyond tomorrow like e.g. nano insulation materials (NIM) and NanoCon. A special focus is given on our current attempts to manufacture NIM based on hollow silica nanospheres (HSNS).

2 Nano Insulation Materials and the Knudsen Effect

In order to make a thermal insulation material reaching very low values, the concept of nano insulation materials (NIM) has been conceived. A NIM is defined as basically a homogeneous material with a closed or open small nano pore structure with an overall thermal conductivity of less than 4 mW/(mK) in the pristine condition [2]. Hence, a NIM achieves its low thermal conductivity, without applying a vacuum in the pores, by utilizing the so-called Knudsen effect. The gas thermal conductivity λ_{gas} taking into account the Knudsen effect may be written in a simplified way as the following [2–4, 7]:

$$\lambda_{gas} = \frac{\lambda_{gas,0}}{1 + 2\beta Kn} = \frac{\lambda_{gas,0}}{1 + \frac{\sqrt{2}\beta k_B T}{\pi d^2 p \delta}} \tag{1}$$

where

$$Kn = \frac{\sigma_{mean}}{\delta} = \frac{k_B T}{\sqrt{2}\pi d^2 p \delta} \tag{2}$$

where λ_{gas} is the gas thermal conductivity in the pores, $\lambda_{gas,0}$ is the gas thermal conductivity in the pores at standard temperature and pressure, β is a coefficient characterizing the molecule-wall collision energy transfer (in)efficiency (between 1.5 and 2.0), $k_B \approx 1.38 \cdot 10^{-23}$ J/K is Boltzmann's constant, T is the temperature, d is the gas molecule collision diameter, p is the gas pressure in pores, δ is the characteristic pore diameter, and σ_{mean} is the mean free path of gas molecules. When the pore size within a material is decreased below a certain level, i.e. a pore diameter of the order of 40 nm or below

for air, the gas thermal conductivity, and thereby also the overall thermal conductivity, becomes very low (<4 mW/(mK) with an adequate low-conductivity grid structure) even with air-filled pores. This is explained by the Knudsen effect where the mean free path of the gas molecules is larger than the pore diameter. That is, a gas molecule located inside a pore will hit the pore wall and not another gas molecule, where the solid state and gas interaction is taken care of by the β coefficient. The resulting gas thermal conductivity λ_{gas}, thus also including the gas and pore wall interaction, versus pore diameter and pore gas pressure, may be calculated in this simplified model.

3 Concrete, Aerogel, NIM and NanoCon

Initial investigations are currently being performed with aerogel in various cement and concrete mixtures to improve the thermal resistance of concrete while attempting to maintain as much as possible of the mechanical strength properties (Fig. 1) [8, 9]. However, as long as relatively high-conducting materials like e.g. cement and water are applied in mixtures, it may be rather difficult to reach low thermal conductivity values comparable to traditional insulation materials (<40 mW/(mK)) and at least comparable to superinsulation (<20 mW/(mK)).

To be able to make a structural material which also inherits thermal insulation properties would revolutionize the building sector. That is, a construction material with strong mechanical strength properties like e.g. concrete, stone or steel, while possessing a similar or lower thermal conductivity than e.g. mineral wool, expanded or extruded polystyrene, or polyurethane, will have a huge potential. Normally, this is contradictory as large mechanical strength implies a compact solid state material with strong bonds, thus also with a large thermal conductivity. Nevertheless, one may envision a strong solid skeleton within a porous material with satisfactory mechanical strength and sufficient low conductivity. Hence, a new material is introduced on a conceptual basis: NanoCon is basically a homogeneous material with a closed or open small nano pore structure with an overall thermal conductivity of less

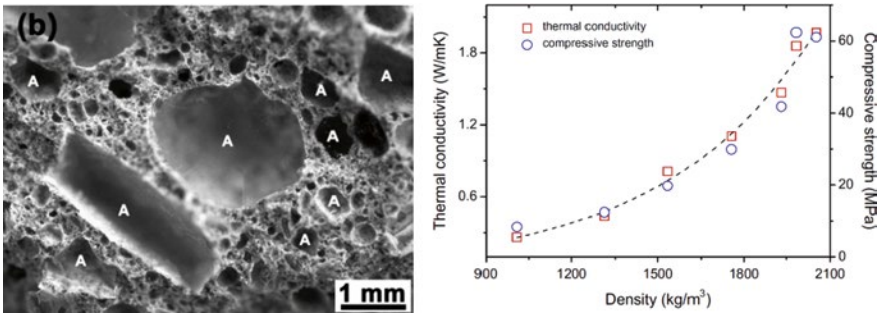

Fig. 1 Cured aerogel-incorporated concrete sample after mechanical test where A denotes the aerogel particles (*left*). Variation of thermal conductivity and compressive strength with density of aerogel-incorporated concrete, where the highest and lowest densities depicted correspond to 0 vol% and 60 vol% aerogel content, respectively (*right*) [8]

than 4 mW/(mK) (or another low value) and exhibits the crucial construction properties that are as good as or better than concrete [4, 10]. Essentially, NanoCon is a NIM with construction properties matching or surpassing those of concrete. In the above definition of NanoCon, a homogeneous material is stated, although the first attempts to reach such a material might be tried by piecing or mixing several different materials together, i.e. with a final material product which on a nanoscale is not homogeneous. For example, joining NIM and carbon nanotubes (CNT) in one single material might enable a very low conductivity due to the NIM part and a very large tensile strength due to the CNT part. In this respect it should be noted that CNT have a very large thermal conductivity along the tube axis. Furthermore, it is noted that the extremely large tensile strength of CNT (63 GPa measured and 300 GPa theoretical limit) surpasses that of steel rebars (500 MPa) by more than two orders. In comparison, the bare ordinary concrete without rebars has a tensile strength of 3 MPa and a compressive strength of 30 MPa. Thus, the potential impact of NanoCon is tremendously huge.

4 Hollow Silica Nanospheres

Various experimental pathways may be followed for attempting to make nano insulation materials (NIM), e.g. membrane foaming, gas release and templating [11], where we in the following will focus on the template method. Miscellaneous detailed experimental information and procedures concerning the various fabrications of hollow silica nanospheres (HSNS) are found in our earlier studies [11–17]. Basically, the HSNS manufacturing applies the template method with either polyacrylic acid (PAA) or polystyrene (PS) as sacrificial templates, where PAA and PS have been removed by a washing and a heating process, respectively (the template materials diffuse and evaporate through the silica shell), see Fig. 2.

Scanning electron microscope (SEM) images of fabricated spherical PS templates are shown in Fig. 3 (left). The PS templates were thereafter coated with small silica particles, where an example is depicted in Fig. 3 (middle). By removal of the PS templates, HSNS are formed, depicted in Fig. 3 (right).

The thermal conductivity has been measured for various powder samples of HSNS, where the conductivity values are typically in the range 20–90 mW/(mK), though some uncertainties in the Hot Disk apparatus measurement method have to be further clarified [15, 16]. Regarding thermal conductivity measurements, the specific powder

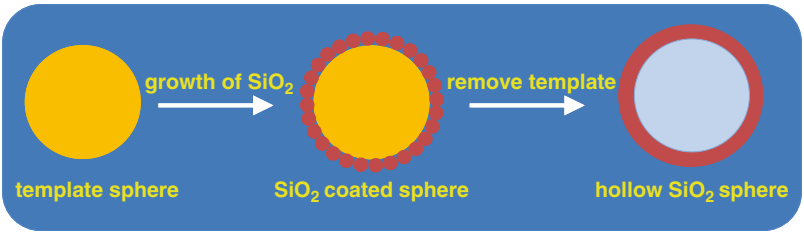

Fig. 2 Principle drawing of the sacrificial template method for manufacturing of HSNS

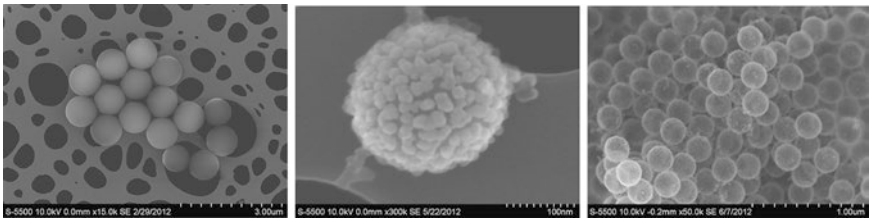

Fig. 3 SEM image of (*left*) spherical PS templates, (*middle*) small silica particles coated around a spherical PS template, and (*right*) HSNS after removal of PS. See also Fig. 2

packing of the HSNS in the bulk condition is also an issue to be addressed. At the moment, the thermal conductivity is being attempted lowered by a parameter variation and optimization of the hollow silica sphere inner diameter and wall thickness. In addition, aspects like e.g. thermal radiation, mesoporosity, powder packing at bulk scale and nanosphere packing at nano scale should be addressed. Assembling the HSNS into a homogeneous bulk material is yet another issue to be studied. In general, it is of major importance to investigate the durability of building materials and components, also newly developed ones, e.g. by carrying out accelerated climate ageing in the laboratory [18]. Thus, performing a robustness assessment of these materials and components may also be found to be beneficial [19]. That is, a durability and robustness evaluation of the new superinsulation materials (when ready) should be carried out. Life cycle analysis (LCA) of NIM as HSNS has also been performed [13, 17, 20].

5 Conclusions

Application of nanotechnology utilizing the Knudsen effect for making superinsulation materials is being investigated. A possible stepping-stone towards this goal is to make nano insulation materials through the synthesis of hollow silica nanospheres. Furthermore, studies for improving the thermal resistance of concrete are also being carried out, including initial investigations utilizing aerogels. Ultimately one may envision to make a material with low thermal conductivity and construction properties matching or surpassing those of concrete, i.e. NanoCon.

Acknowledgements This work has been supported by the Research Council of Norway and several partners through the "*Concrete Innovation Centre*" (COIN) and "*The Research Centre on Zero Emission Buildings*" (ZEB).

References

1. McKinsey. (2009). *Pathways to a low-carbon economy. Version 2 of the global greenhouse gas abatement cost curve*. McKinsey & Company.
2. Jelle, B. P., Gustavsen, A., & Baetens, R. (2010). The path to the high performance thermal building insulation materials and solutions of tomorrow. *Journal of Building Physics, 34*, 99–123.

3. Baetens, R., Jelle, B. P., Thue, J. V., Tenpierik, M. J., Grynning, S., Uvsløkk, S., & Gustavsen, A. (2010). Vacuum insulation panels for building applications: A review and beyond. *Energy and Buildings, 42*, 147–172.
4. Jelle, B. P. (2011). Traditional, state-of-the-art and future thermal building insulation materials and solutions – Properties, requirements and possibilities. *Energy and Buildings, 43*, 2549–2563.
5. Alam, M., Singh, H., & Limbachiya, M. C. (2011). Vacuum insulation panels (VIPs) for building construction industry – A review of the contemporary developments and future directions. *Applied Energy, 88*, 3592–3602.
6. Kalnæs, S. E., & Jelle, B. P. (2014). Vacuum insulation panel products: A state-of-the-art review and future research pathways. *Applied Energy, 116*, 355–375.
7. Wegger, E., Jelle, B. P., Sveipe, E., Grynning, S., Gustavsen, A., Baetens, R., & Thue, J. V. (2011). Aging effects on thermal properties and service life of vacuum insulation panels. *Journal of Building Physics, 35*, 128–167.
8. Gao, T., Jelle, B. P., Gustavsen, A., & Jacobsen, S. (2014). Aerogel-incorporated concrete: An experimental study. *Construction and Building Materials, 52*, 130–136.
9. Ng, S., Jelle, B. P., Sandberg, L. I. C., Gao, T., & Wallevik, O. H. (2015). Experimental investigations of aerogel-incorporated ultra-high performance concrete. *Construction and Building Materials*, *77*, 307–316.
10. Jelle, B. P., Gustavsen, A., & Baetens, R. (2010, December 5–9). *The high performance thermal building insulation materials and solutions of tomorrow*. Proceedings of the Thermal Performance of the Exterior Envelopes of Whole Buildings XI International Conference (Buildings XI), Clearwater Beach, Florida, USA.
11. Jelle, B. P., Tilset, B. G., Jahren, S., Gao, T., & Gustavsen, A. (2011, September 15–16). *Vacuum and nanotechnologies for the thermal insulation materials of beyond tomorrow – From concept to experimental investigations*. Proceedings of the 10th International Vacuum Insulation Symposium (IVIS-X) (pp. 171–178), Ottawa, Canada.
12. Gao, T., Sandberg, L. I. C., Jelle, B. P., & Gustavsen, A. (2012). Nano insulation materials for energy efficient buildings: A case study on hollow silica nanospheres. In A. Mendez-Vilas (Ed.), *Fuelling the future: Advances in science and technologies for energy generation, transmission and storage* (pp. 535–539). Boca Raton: BrownWalker Press.
13. Gao, T., Jelle, B. P., Sandberg, L. I. C., & Gustavsen, A. (2013). Monodisperse hollow silica nanospheres for nano insulation materials: Synthesis, characterization, and life cycle assessment. *ACS Applied Materials and Interfaces, 5*, 761–767.
14. Sandberg, L. I. C., Gao, T., Jelle, B. P., & Gustavsen, A. (2013). Synthesis of hollow silica nanospheres by sacrificial polystyrene templates for thermal insulation applications. *Advances in Materials Science and Engineering,* 2013, Article ID 483651, 6 p.
15. Grandcolas, M., Etienne, G., Tilset, B. G., Gao, T., Sandberg, L. I. C., Gustavsen, A., & Jelle, B. P. (2013, September 19–20). *Hollow silica nanospheres as a superinsulating material*. Proceedings of the 11th International Vacuum Insulation Symposium (IVIS 2013) (pp. 43–44), Dübendorf, Switzerland.
16. Jelle, B. P., Gao, T., Tilset, B. G., Sandberg, L. I. C., Grandcolas, M., Simon, C., & Gustavsen, A. (2013, September 19–20). *Experimental pathways for achieving superinsulation through nano insulation materials*. Proceedings of the 11th International Vacuum Insulation Symposium (IVIS 2013) (pp. 99–100), Dübendorf, Switzerland.
17. Gao, T., Sandberg, L. I. C., & Jelle, B. P. (2014). Nano insulation materials: Synthesis and life cycle assessment. *Procedia CIRP, 15*, 490–495.
18. Jelle, B. P. (2012). Accelerated climate ageing of building materials, components and structures in the laboratory. *Journal of Materials Science, 47*, 6475–6496.
19. Jelle, B. P., Sveipe, E., Wegger, E., Gustavsen, A., Grynning, S., Thue, J. V., Time, B., & Lisø, K. R. (2014). Robustness classification of materials, assemblies and buildings. *Journal of Building Physics, 37*, 213–245.
20. Schlanbusch, R. D., Jelle, B. P., Sandberg, L. I. C., Fufa, S. M., & Gao, T. (2014). Integration of life cycle assessment in the design of hollow silica nanospheres for thermal insulation applications. *Building and Environment, 80*, 115–124.

Three-Phase-Foams as New Lightweight Materials and Their Use in Foam Concretes

Christina Krämer, Torsten Kowald, and Reinhard Trettin

Abstract Lightweight materials are very important due to material and cost saving with simultaneous combination of thermal insulation and sustainability. A biomimetic approach is the creation of foams based on three phases whereas in our study the third phase consists of pozzolanic active nanomaterials. These nanomaterials can be varied, surface treated and also combined with other strength improving aids or materials. Beside the higher stability of three-phase-foams, a further advantage over two-phase-foams is the ability to improve the strength of foam concrete by a pozzolanic reaction. Aim of the developments is to build foam concretes which have comparable or improved performance compared to aerated concrete. This would reduce cost in production of lightweight concretes. Additionally, the three-phase-foams gave a better control over foam homogeneity and pore size. The reactive solid phase enables also hardening of the three-phase-foams due to pozzolanic reaction in solution and strengthening caused by the formation of other reaction products.

Keywords Foam Concrete • Nanoparticles • Three-phase-foams • Pozzolans • Inorganic foams

1 Introduction

Natural lightweight materials as bamboo or bone structures show in various aspects advantages due to effective use of material. With the help of biomimetic approaches in material science new materials are developed. These construction and building materials should be shaped such that a weight and cost saving results [1]. Further the materials can be designed to have good thermal insulation and can be used for static relevant application which is important for construction industry. Nowadays this goal is achieved in form of lightweight concrete, especially aerated and foam concrete [2]. While for production of foam concrete foaming agents are used, the

C. Krämer (✉) • T. Kowald • R. Trettin
Institut für Bau- und Werkstoffchemie, University of Siegen, Siegen, Germany
e-mail: kraemer@chemie.uni-siegen.de
http://www.chemie-biologie.uni-siegen.de/bwc

K. Sobolev, S.P. Shah (eds.), *Nanotechnology in Construction*,
DOI 10.1007/978-3-319-17088-6_57

pore entry of aerated concrete is achieved by the generation of hydrogen, which is built during the reaction of aluminum powder at high pH values. In case of aerated concrete energy consuming and strength increasing autoclaving process is used. This treatment is usually not applied in foam concrete production. A comparison of foam concrete with aerated concrete shows, that there are advantages due to the cost saving, sustainability and environmental compatibility [2, 3]. In production, a controlled and homogeneous pore entry is essential. The borders of the pores should be thin but still show high strength. This can be achieved by a very dense microstructure inside the borders and adjusted foaming process or production [2]. Our approach is to incorporate three-phase-foams based on pozzolans to achieve strength improvement and stabilization of the pore structure in foam concrete. The researchers Gonzenbach et al. were the first who showed a simple preparation method for high volume particle-stabilized foams with low densities. In this foams metalloid or metal based nanoparticles are introduced in the water-air-interface (continuous-disperse-interface) by partial hydrophobation due to sorption of surfactants on the particle surface. Van der Waals interaction between nanoparticle surface and surfactants are used for foam stabilization. This is possible by functionalizing the surface groups of the solid oxides and functional groups of the surfactants at a specific pH value [4]. Three-phase-foams were incorporated in cement paste for production of foam concrete and hardened due to pozzolanic reaction in $Ca(OH)_2$ solution. Additionally, nanostructured additives can be incorporated in the foam system and also used for the production of foam concrete or hardened in solution which provides a noticeably strengthening. The studies of microstructure and phase development of the produced lightweight materials will be shown and explained.

2 Results

The total drainage of the continuous phase of the produced three-phase-foams over 60 min was examined. As foaming agents betaine (B) and n-hexylamine (HA) were used. The nanoparticles were dispersed in water at the specific pH determined by electrophoretic light scattering. The dispersions consisted of 30 % w/w mixed oxide (MO) or 35 % w/w nanosilica (NS). In every case three-phase-foams were more stable than two-phase-foams with same betaine concentration. The foaming in case of n-hexylamine without solid content was not possible. Three-phase-foams with B (NS B) and HA (NS HA) could be further stabilized by an additional nanostructured additive (NA), that no drainage within 60 min occurred. The densities of the three-phase-foams before addition to concrete were between 0.06 and 0.12 g/cm^3. After foaming, the foams were added to the cement paste and stirred again before storage for 7 days at 20 °C and 98 % relative air humidity.

The study of microstructure was done by scanning electron microscopy (SEM) and light microscopy (LM). Comparisons of the average pore radii of the incorporated foams with the resulting foam concretes showed that the pore sizes were similar. The average pore radii of the foam concretes were in a range of 150–200 µm. Those of the three-phase-foams were 10–30 µm smaller (MO B) or larger (NS B). Thus the

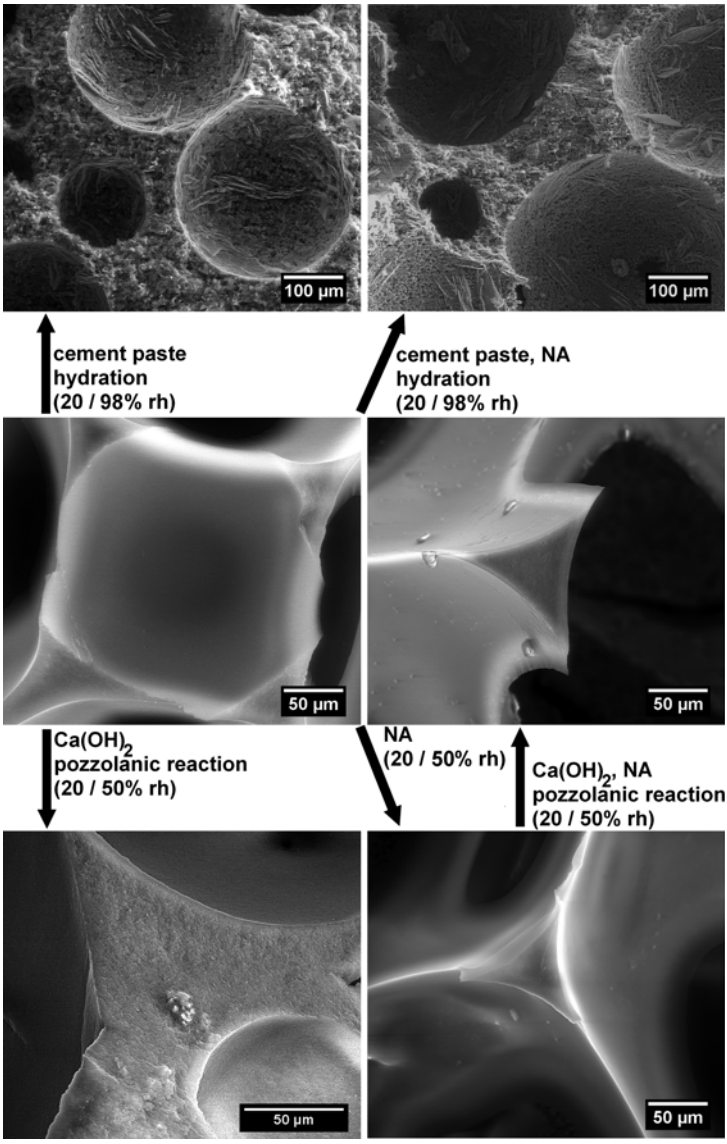

Fig. 1 Microstructure investigations by SEM. Three-phase-foam NS B (*middle left*), foam concrete NS B (*top left*), foam concrete NS B with NA (*top right*), hardened NS B (*bottom left*), NA stabilized NS B foam (*bottom right*) and hardened NS B with NA (*middle right*)

pore size distribution can be controlled by the incorporated foams. The bigger pores inside foam concrete can be explained by shear forces during the production process and the effect of Ostwald ripening.

For SEM sample preparation no sputtering was used and the fracture surfaces were investigated. Figure 1 gives an overview of the different materials that were produced based on the three-phase-foam NS B. This foam had border widths in the

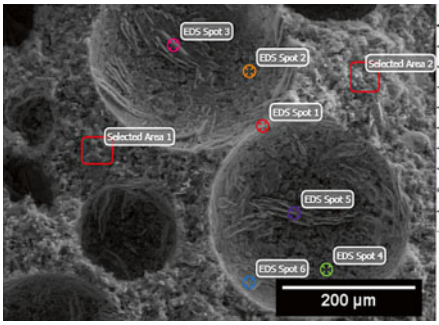

Element	areas/dots of EDX analysis			
	1	2	Spot 3	Spot4
C	5,15	6,44	5,33	5,43
O	69,89	72,26	67,03	70,04
Al	0,97	1,28	0,29	0,9
Si	5,39	5,45	1,39	5,44
S	0,48	0,48	0,19	0,59
Ca	17,27	13,14	25,45	16,95
Fe	0,85	0,95	0,31	0,64
Ca/Si	3	2	18	3
Ca/Al	18	10	88	19

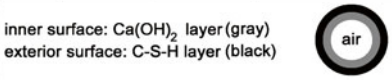

Fig. 2 Element mapping of foam concrete NS B after 7 day by EDX analysis (*left*), calcium-to-silicon- and calcium-to-aluminum-ratio and theoretical pore structure (*right*)

range of 25–400 µm and lamellae widths of ~1.0 µm (Fig. 1, middle left). After pozzolanic hardening border and lamellae widths were between 150 and 400 µm and 1–2 µm (Fig. 1, bottom left). The addition of NA to NS B lead to border and lamellae widths of 100–200 µm and 0.5–1.0 µm before hardening (Fig. 1, bottom right) and of 25–300 µm and 1.0–1.5 µm after hardening (Fig. 1, middle right). Comparisons of the foams with and without NA show that the border and lamellae widths of the NA stabilized foams are smaller. Both hardened foams showed densified borders due to the pozzolanic reaction and $Ca(OH)_2$ and $CaCO_3$ inside air pores.

Foam concretes showed a dense microstructure in the borders but inhomogeneity with respect to the pore size distribution and the border widths. In this study the production process was done with a w/c-ratio of 0.5 due to the high water demand of the pozzolans. A further optimization of the concrete can provide a better homogeneity. Additionally, a layer of reaction products can be seen inside the air pores (Fig. 1, top left and right). In EDX analysis an element mapping showed that the thin layer consists of $Ca(OH)_2$ (Fig. 2, spot 3) and underneath this layer and in the borders mainly C-S-H-phases were formed (Fig. 2, area 1 and 2 and spot 4). This layer was built due to the influence of surfactants, which occupy a specific crystal surface and interfere the crystallization of $Ca(OH)_2$. The interference leads to smaller crystals and changes in the shape with respect to the space direction.

3 Summary and Conclusions

In summary, the investigations show an approach to create inorganic foams as self-containing materials. This enables waiving on cementitious binders and produce lightweight materials in low density ranges below 100 kg/m^3. Another approach is to incorporate the three-phase-foams in cement paste due to the amount of pozzolans and a given stable pore structure to achieve a strengthening and performance of foam concrete. After incorporation of the foams a specific pore structure and

preferred formation of hydration products can be observed in the pores of the foam concretes. The nanoparticles and surfactants preserved a local sourcing or the sorption of the surfactant is so strong that a physical bonding to the particles still occurs. Therefore the surfactants have an influence on the crystallization of $Ca(OH)_2$ due to the occupation on the crystal surface. This leads to the formation of a thin layer consisting of small particles of $Ca(OH)_2$ at the pore inner surface. The nanoparticles accumulate in the borders so that C-S-H-phases were formed underneath the $Ca(OH)_2$. Additionally, the results show a stable pore structure which can be controlled by the incorporated foams. Incorporation of NA in the foam structure shows a complete stabilization of the foams after production. NA stabilized foams can reach densities down to only 60 kg/m^3. Additionally, the combination of the NA stabilized foams and pozzolanic hardening results in a further stabilization due to a dense package in the borders and the formation of strength increasing reaction products. The NA stabilized foams can also be incorporated in foam concrete and could enable strength improvement.

References

1. Lakes, R. (1993). Materials with structural hierarchy. *Nature [Online], 361*(6412), 511–515.
2. Schauerte, M., & Trettin, R. (2012). *Neue Schaumbetone mit gesteigerten mechanischen und physikalischen Eigenschaften*; 18th Ibausil, Tagungsband (pp. 2-0066–2-0072). Weimar.
3. Schauerte, M., Krämer, C., Trettin, R. (2013). *Modified tenside foams for foam concrete applications*, 1st. International Bauchemie Tagung, Tagungsband (p. 477). Berlin.
4. Gonzenbach, U. T., Studart, A. R., Tervoort, E., & Gauckler, L. J. (2006). Ultrastable particle-stabilized foams. *Angewandte Chemie International Edition, 45*(21), 3526–3530.

Part XII
Durability

Nano-engineered Superhydrophobic and Overhydrophobic Concrete

Scott W. Muzenski, Ismael Flores-Vivian, Marina I. Kozhukhova, Sunil Rao, Michael Nosonovsky, and Konstantin Sobolev

Abstract The use of superhydrophobicity and overhydrophobicity in cementitious materials can lead to improved durability performance. Ingress of water with dissolved chemicals can have detrimental effects on the performance of cementitious materials. Additionally, reducing the amount of water and ice on concrete surfaces can improve the reduction of scaling, thereby preserving the pore system and integrity of concrete. The hydrophobic, overhydrophobic, and superhydrophobic surfaces can be realized by using particle deposition and siloxane coatings. Thin layers of such water repellant material can create a strong barrier to water. Another method to improve the durability of concrete is based on the addition of superhydrophobic admixtures of polymethyl hydrosiloxane emulsions and nano particles. These admixtures can produce a 3-dimensional volume hydrophobization by releasing hydrogen in alkali environments enabling the formation of air voids throughout a cementitious matrix. The walls of these voids are then coated with varying size particles producing the surface roughness required for superhydrophobicity. This paper compares different approaches and benefits of superhydrophobic concrete and discusses the improved durability properties and the future applications.

Keywords Superhydrophobicity • Overhydrophobicity • Hydrophobic concrete • Hierarchical roughness

S.W. Muzenski (✉) • S. Rao • K. Sobolev
Department of Civil and Environmental Engineering, University of Wisconsin-Milwaukee, Milwaukee, WI, USA
e-mail: swm@uwm.edu

I. Flores-Vivian
Materials Development Department, OVNIVER, Monterrey, NL, Mexico

M.I. Kozhukhova
Belgorod State Technological University, Belgorod, Russia

Department of Civil and Environmental Engineering, University of Wisconsin-Milwaukee, Milwaukee, WI, USA

M. Nosonovsky
Department of Mechanical Engineering, University of Wisconsin-Milwaukee, Milwaukee, WI, USA

K. Sobolev, S.P. Shah (eds.), *Nanotechnology in Construction*,
DOI 10.1007/978-3-319-17088-6_58

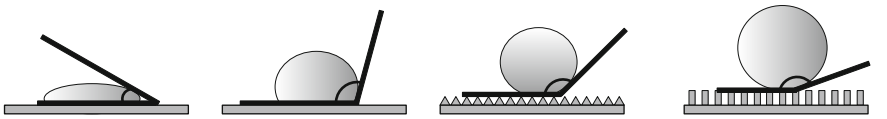

Fig. 1 Hydrophilic, hydrophobic, overhydrophobic, and superhydrophobic surfaces [3]

1 Introduction

The hydrophobicity of a material is defined as the ability of the material to repel water and depends on the surface chemical composition and the surface geometry (micro- and nano-structural morphology) [1]. The contact angle between a droplet of water and the surface is generally used as an indicator of hydrophobicity or wettability. The contact angles of hydrophilic, hydrophobic, over-hydrophobic, and superhydrophobic surfaces as shown in Fig. 1 can be measured by a goniometer or tensiometer [2]. Common concrete is an example of a hydrophilic mesoporous material which absorbs water.

Superhydrophobic surfaces with hierarchical patterns imposed over larger roughness surfaces have generated interest due to their potential in industrial applications (mainly, for self-cleaning). These surfaces mimic the lotus leaf surface, which is well known for its superhydrophobicity and self-cleaning properties, (lotus-effect). Mimicking living nature for engineering applications is called "biomimetics," and biomimetic approaches can be used to synthesize hydrophobic and superhydrophobic concrete [4–9].

Waterproofing and the incorporation of hydrophobic additives into the concrete matrix are two approaches used to improve the physical properties of concrete. The first approach consists of using hydrophobic materials on the surface of concrete to repel water [10]. The type of material and quantity used affects its concrete protecting efficiency [11]. The second approach consists on creating a hydrophobic concrete or cement matrix using admixtures [5, 12–14]. These polymethyl-hydrosiloxane (PMHS) based admixtures react with cement based systems to release hydrogen and create small, well dispersed air voids (10–100 μm) throughout the cementitious matrix which can be tailored to provide optimal size and spacing for exceptional freeze-thaw resistance while resulting in little to no reduction in compressive strength [15]. The walls of these voids can also be coated with sub-micro and nano-sized particles to produce the hierarchical surface roughness to achieve superhydrophobic properties (Fig. 2) providing a good alternative to conventional air entraining admixtures.

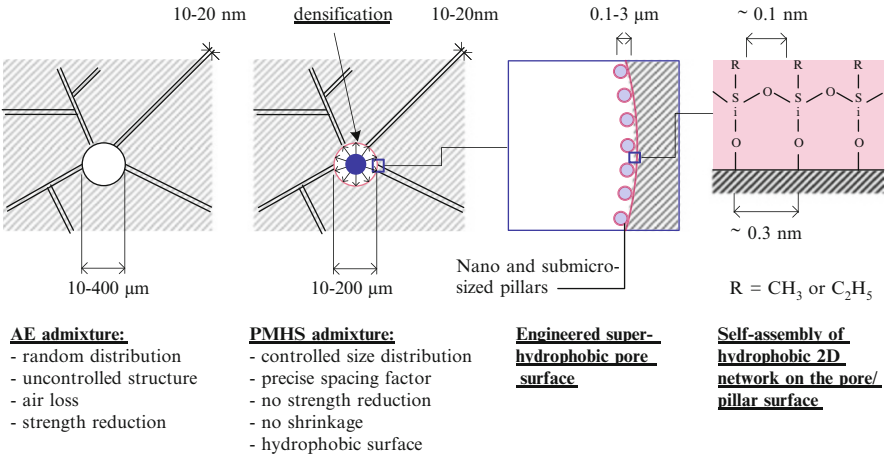

Fig. 2 How the superhydrophobic hybridization of concrete works [15]

2 Materials and Methods

To create hydrophobic coatings, emulsions are produced, which are based on PMHS oil (specific gravity of 0.997 at 25 °C and viscosity of 30 cSt) and water soluble polyvinyl alcohol (PVA) for emulsion stabilization (98 % hydrolyzed with a molecular weight of 16,000) because of its nonionic properties and compatibility with concrete materials [16]. Nano-SiO_2 with a purity of 99.5 % and average particle size of 15 nm was used as nano-particles. Silica fume or metakaolin were used as the sub-micro particles in the composition of the emulsion.

To prepare the emulsions, de-ionized water was used as a dispersion medium, water-soluble PVA as surfactant and PMHS as the dispersion phase. Micro-particles of silica fume or metakaolin were used to stabilize [17] and modify the emulsion using two different approaches: "shell" and "core" as described in CFIRE 07-03 [18] and explained in detail in Flores-Vivian et al. [3]. First, the application of superhydrophobic emulsions was considered as surface treatment. For these surface treatments (E1S), the concentrations of surfactant, PMHS, and silica fume were used at 3.485, 25.0, and 5.0 % by weight of the emulsion, respectively. Another set of emulsions (E1SR) for surface treatment were produced by diluting one part of E1S into four parts of DI water. Finally, for internal hydrophobization, the emulsion was composed of surfactant, PMHS, metakaolin, and nano- SiO_2 at 3.50, 25.0, 0.4, and 0.1 % by weight of the emulsion respectively.

The surface treatments were applied on five different mortars with varying water to cement (W/C) and sand to cement (S/C) ratios produced in accordance with ASTM C305. Each mortar also had 1 % (by volume) of polyvinyl alcohol fibers (RECS 15 × 12 mm). The W/C of 0.25, 0.30, 0.40, 0.45, and 0.50 were used in M1,

M2, M3, M4, and M5 mortars, respectively. The S/C of 0.0, 1.0, 2.0, 2.5, and 3.0 were used in M1, M2, M3, M4, and M5, respectively. A polycarboxalate ether superplasticizer (PCE) solid content of 0.10 % by weight of cement was used in each mix with the exception of M1 where a PCE content of 0.14 % was used. These samples were then tested for contact and roll-off angles using a goniometer. Mixtures for internal hydrophobization were produced with 2.75 % (by volume) PVA fibers and 50 % ground granulated blast furnace slag as a replacement for Type I portland cement. The W/CM of 0.30, S/CM of 0.50, and PCE content of 0.125 % were used for mixes E30 and REF30 while a W/CM of 0.45, S/CM of 1.0, and PCE content of 0.050 % were used for mixes E45 and REF45. Mixes E30 and E45 contained a single dose of hydrophobic emulsions (0.25 g of siloxane to 1 L of entire composite mix) while REF30 and REF 45 contained no entrained air. These samples were tested for compressive strength (ASTM C109), accelerated freeze-thaw cycling (tested between −50 and 20 °C in 5 % NaCl solution) [5], and water absorption (ASTM C642).

3 Results and Discussion

Results from the contact and roll-off angle tests can be seen in Table 1. It can be seen that uncoated samples provided small water contact angles (0–20°) because of their high absorption. Because of this, no roll-off angles were able to be recorded because the entire water droplet was absorbed in the sample. Coated samples increased the contact angles for all specimens with engineered micro/nano-roughness and hierarchical structure required for superhydrophobicity. The diluted emulsion (E1SR) demonstrated a reduced contact angle when the W/C and S/C was increased. The samples produced with high W/C ratio and S/C ratio had higher porosity and thus the hydrophobic agent may be absorbed by the porous network. Non diluted emulsions (E1S) produce a thicker coating therefore eliminating the effects on contact angle due to the surface roughness of the tile itself when lower W/C ratio and S/C ratio is considered. The surface roughness of samples with higher W/C and S/C were still able to contribute to the contact angle for this non-diluted samples which is why there is an incremental increase in contact angle for E_{1S} emulsions. The hydrophobic properties of treated surfaces were highly evident when the

Table 1 Contact and roll off angles of coated and uncoated mortars

			Contact/roll off angle, degrees		
Sample ID	W/C	S/C	Uncoated	E1SR	E1S
M01	0.25	0.0	5.90/NA	143.75/2.4	120.05/90.0
M02	0.30	1.0	10.00/NA	145.45/1.0	118.60/81.2
M03	0.40	2.0	0.00/NA	141.40/5.9	121.65/66.0
M04	0.45	2.5	0.00/NA	123.60/7.9	128.20/58.5
M05	0.50	3.0	28.05/NA	132.65/11.7	129.40/62.4

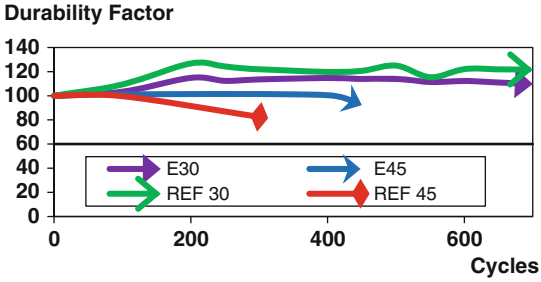

Fig. 3 The durability factor for samples tested for freezing (at −50 °C) and thawing in 5 % NaCl solution

roll-off angle was measured. The concentration of the cementitious material and sand had a smaller effect on the roll-off angle than the concentration of the hydrophobic agent.

Results from internal hydrophobization demonstrate improved behavior as well. The 28-day compressive strengths of 122.8, 88.7, 118.0, and 88.0 MPa for REF30, REF45, E30, and E45, respectively show only slight reductions when hydrophobic air bubbles are incorporated. If conventional air entraining admixtures were used to generate the same quantity of air, a more significant reduction in strength is commonly observed. The addition of hydrophobic air voids generates higher air content in the samples; however absorption tests show improved results when these admixtures are used to generate voids with values of 10.5, 13.8, 9.7, and 12.7 % for REF30, REF45, E30, and E45, respectively. This indicates that the walls of the voids are in fact hydrophobic and are capable of repelling water and reducing the absorption in close to fully saturated states. Freezing and thawing tests show promising results as seen by improved durability factor (as calculated by ASTM C215) of the sample with hydrophobic admixtures when used at a high W/C (E45 vs. REF 45) as seen in Fig. 3. Samples with a low W/C both displayed exceptional results through 700 accelerated (at −50 °C) freeze-thaw cycles. Additionally, they resulted in increasing durability factors through 200 cycles because the samples were still gaining strength as they were placed in the freeze-thaw chamber after only 14 days in accordance with ASTM C666. The likely cause of this is from the dense and higher strength matrix; however the addition of hydrophobic admixtures may display improved results similar to those seen in higher W/C samples if the samples would be tested for even longer periods.

4 Conclusion

The application of hydrophobic emulsions as a coating on mortar tiles proved to result in high contact and low roll-off angles, especially when diluted emulsions were applied on a stronger cementitious matrix (low W/C and low S/C). This could be attributed to the fact that when more porous samples are used in combination

with diluted emulsions, the emulsions become absorbed in the tiles and thus reduce the surface hydrophobicity. The opposite effect occurs when undiluted emulsions are used in combination with rougher tile surfaces (high W/C and high S/C) as the excess of hydrophobic agents produce a thicker coat and eliminate the effects of hydrophobicity from the surface roughness of the tile itself.

Based on the durability factor results, it is clear that a lower W/C provides a better freeze-thaw response demonstrating a durability factor of more than 100 through as many as 700 freezing (at −50 °C) and thawing cycles. Samples with superhydrophobic admixtures may also prove to demonstrate superior performance if tested longer. This is evident as these samples have lower absorption due to their superhydrophobic air voids and thus better freezing and thawing resistance.

Based on these results, it can be envisioned that the combination of internal and surface hydrophobization techniques should result in an ultra-durable cementitious material. Further research may need to be performed to demonstrate this hypothesis. Further research may also be required to improve the hydrophobicity of emulsions to achieve higher contact angles of more than 150°.

Acknowledgements The authors thank the CFIRE for funding this project through grants CFIRE 04-09, CFIRE 05-10, CFIRE 06-03, and CFIRE 07-03. The authors also thank Kuraray, Lafarge, and Handy Chemicals for donation of materials.

References

1. Liu, Y. (2006). Super hydrophobic surfaces from a simple coating method: A bionic nanoengineering approach. *Nanotechnology, 17*, 3259–3263.
2. Nosonovsky, M. (2007). Multiscale roughness and stability of superhydrophobic biomimetic interfaces. *Langmuir, 23*(6), 3157–3161.
3. Flores-Vivian, I., Hejazi, V., Kozhukhova, M., Nosonovsky, M., & Sobolev, K. (2013). Self-assembling particle-siloxane coatings for superhydrophobic concrete. *ACS Applied Materials and Interfaces, 5*(24), 13284–13294.
4. Sobolev, K., & Ferrada-Gutiérrez, M. (2005). How nanotechnology can change the concrete world: Part 2. *American Ceramic Society Bulletin, 11*, 16–19.
5. Sobolev, K., & Batrakov, V. (2007). The effect of a PEHSO on the durability of concrete with supplementary cementitious materials. *ASCE Journal of Materials, 19*(10), 809–819.
6. Poole, B. *Biomimetics: Borrowing from biology*. http://www.thenakedscientists.com
7. Nosonovsky, M. (2011). Slippery when wetted. *Nature, 477*, 412–413.
8. Nosonovsky, M., & Bhushan, B. (2009). Superhydrophobic surfaces and emerging applications: Non-adhesion, energy, green engineering. *Current Opinions in Colloid and Interface Science, 14*, 270–280.
9. Hejazi, V., Sobolev, K., & Nosonovsky, M. (2013). From superhydrophobicity to icephobicity: Forces and interaction analysis. *Nature Scientific Reports, 3*, 2194.
10. Moriconi, G., & Tittareli, F. (2009). Effectiveness of surface or bulk hydrophobic treatments in cementitious materials. In *Protection of historical buildings*, CRC Press Rome, Italy (PROHITECH, 09, pp. 1071–1075).
11. Raupach, M., & Wolff, L. (2005). Investigations on long-term durability of hydrophobic treatment on concrete. *Surface Coatings International Part B: Coatings Transactions, 99*(2), 127–133.
12. Popovics, S. (1982). *Fundamentals of portland cement concrete* (Fresh Concrete, Vol. 1). New York: John Wiley and Sons Inc.

13. Hekal, E. E., & Abd-El-Khalek, M. (1999). Mechanical and physico-chemical properties of hardened portland cement pastes containing hydrophobic admixtures part 1: Compressive strength and hydration kinetics. *ZKG International, 52*(12), 697–700.
14. Hekal, E. E., & Abd-El-Khalek, M. (2000). Mechanical and physico-chemical properties of hardened portland cement pastes containing hydrophobic admixtures part 2: Physical properties and micro-structure. *ZKG International, 53*(3), 152–158.
15. Sobolev, K., et al. (2013, May). *Superhydrophobic engineered cementitious composites for highway bridge applications: Phase I*. Madison: Center for Freight and Infrastructure Research and Education (CFIRE).
16. Kim, J. H., & Robertson, R. E. (1999). Structure and properties of poly(vinyl alcohol)-modified mortar and concrete. *Cement and Concrete Research, 29*(3), 407–415.
17. Aveyard, R., Binks, B. P., & Clint, J. H. (2003). Emulsions stabilised solely by colloidal particles. *Advances in Colloid and Interface Science, 100–102*, 503–546.
18. Sobolev et al. (2013). *Anti-icing and de-icing superhydrophobic concrete to improve the safety on critical elements on roadway pavements*, Center for Freight and Infrastructure Research and Education (CFIRE) Madison, WI.

Chloride Ion Monitoring in Etched Nanochannels in Glass Using MQAE and Development of Microchannels in Hardened Cement Paste

Yuya Sakai, Choji Nakamura, and Toshiharu Kishi

Abstract In this study, nanochannels were prepared on a glass plate and the dependence of the chloride ion transport rate on the channel size was investigated. The nanochannels were etched using acidic etching agents, and the fluorescent reagent N-[ethoxycarbonylmethyl]-6-methoxy-quinolinium bromide (MQAE) was used to measure the concentration of the chloride ions. A decrease of the chloride ion transport rate with decreasing cross-sectional channel size was confirmed. The obtained results are, however, not directly applicable to concrete because glass and concrete have different surface properties. As such, a hardened cement paste (HCP) plate with a smooth surface and an absence of detected pores was prepared by high pressure curing. A microchannel was machined on the plate surface and a glass plate was bonded to this surface by autoclave treatment.

1 Introduction

Thus far, there have been many attempts at developing models to evaluate chloride ion ingress into concrete; however, they have met with only limited success. The difficulty lies in the fact that models are typically developed on the basis of the macroscopic measurement results. One promising approach involves direct observation of the chloride ion transport in an artificially prepared pore. In this study, we prepared microscopic pores, or channels, in two stages. In the first stage, we prepared micro/nanochannels on a glass plate and developed a method for directly observing chloride ion transport in the channels optically. However, the surface properties of glass and the pore walls of cementitious materials are very different.

Y. Sakai (✉) • T. Kishi
Institute of Industrial Science, The University of Tokyo, Tokyo, Japan
e-mail: ysakai@iis.u-tokyo.ac.jp
http://wdnsword.iis.u-tokyo.ac.jp/sakai/sakaitope.html

C. Nakamura
School of Engineering, The University of Tokyo, Tokyo, Japan
e-mail: Choji@iis.u-tokyo.ac.jp

K. Sobolev, S.P. Shah (eds.), *Nanotechnology in Construction*,
DOI 10.1007/978-3-319-17088-6_59

Therefore, in the second stage, we attempted to prepare microchannels on a smooth plate of hardened cement paste (HCP) in the absence of pores. The distribution of the surface potential of the plate was evaluated using scanning probe microscopy (SPM) because it is important to develop a physical model for comparing experimental results with those derived from theory.

2 Experimental Procedure

2.1 Preparation of the Glass Plate with Micro/Nanochannels

In this study, N-[ethoxycarbonylmethyl]-6-methoxy-quinolinium bromide (MQAE) is used to detect Cl^- concentration. MQAE is a fluorophore, and its fluorescence intensity decreases with increasing Cl^- concentration. In order to evaluate the Cl^- concentration with respect to fluorescence intensity, we measured the intensity of 0.25 mM MQAE added to KCl solutions of various concentrations. The fluorescence intensity of MQAE was obtained using a fluorescence microscope (Leica DM IRM, Leica Microsystems, Wetzlar, Germany) and evaluated by imaging analysis. The result is shown in Fig. 1. The vertical axis indicates the ratio of the fluorescence intensity of the MQAE solution (F_0) to that of the MQAE with KCl solution (F_{KCl}). The micro/nanoetched plate consisted of two U-shaped microchannels (depth: 30 μm; width: 500 μm) and 32 nanochannels (depth: 95 nm, 28 nm or 16 nm; width: 5 μm; length: 500 μm) that bridge the microchannels, as shown in Fig. 2.

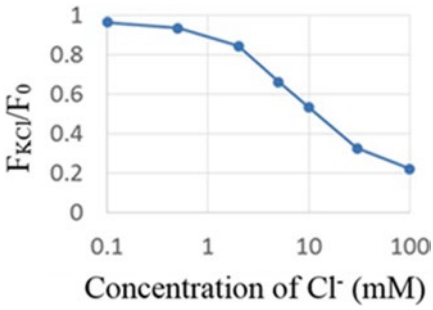

Fig. 1 Quenching plot of MQAE

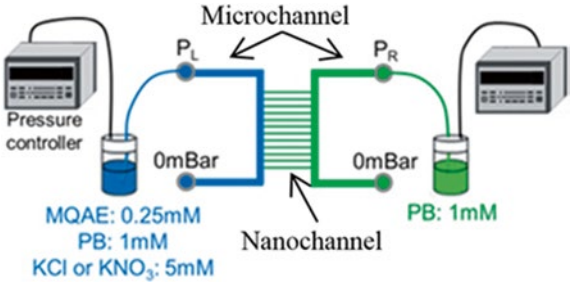

Fig. 2 Experimental setup and channel design

The chip was fabricated by photolithography and wet etching. After etching the microchannels on the upper substrate and nanochannels on the bottom substrate, the substrates were joined by thermal bonding. The microchannel inlets were connected to the pressure controller to control the flow of the solution. To avoid a decrease in pH, a phosphate buffer solution (PB) was used. The experimental procedure is as following. First, the right microchannel was filled with 1 mM PB under a pressure of $P_R = 200$ mBar for 30 min. Next, the left microchannel was filled with 0.25 mM MQAE solution, 1 mM PB, and 5 mM KCl solution (mixed in a 1:1:1 volume ratio) under a pressure $P_L = 100$ mBar. After observance of fluorescence from the left microchannel, we ceased the flow by setting $P_R = P_L = 0$ and obtained microscope photographs over regular time intervals. The fluorescence intensity from the nanochannels was measured by imaging analysis of these photographs. We then replaced the KCl solution with KNO_3 solution and conducted the same measurements to compare their fluorescence intensity.

2.2 Preparation of Cementitious Material with Microchannels

First, the cement paste with a water to cement ratio of 25 % was cast on a glass plate after 1 min of mixing with a mixer (ARE-30, THINKY, Tokyo, Japan). The cast was then wrapped with a plastic film and wiper and packed in a vacuumed plastic bag. The cast was cured for 3 days under a hydrostatic pressure of 400 MPa and immersed in acetone for 1 h. Photo 1 shows the sample (1.5 × 3.0 × 0.3 cm) after acetone immersion. A small piece was removed from the sample and examined by a scanning electron microscope, as shown in Fig. 3. The surface is shown to be very smooth, and no holes were observed even when the image was magnified 7,000 times. After the imaging, as shown in Photo 2, the sample was immersed in acetone for 24 h and dried at a temperature of 20 °C and relative humidity (RH) of 20 % for 5 days. At this stage, the surface morphology was evaluated by the dynamic force

Photo 1 Press-cured HCP

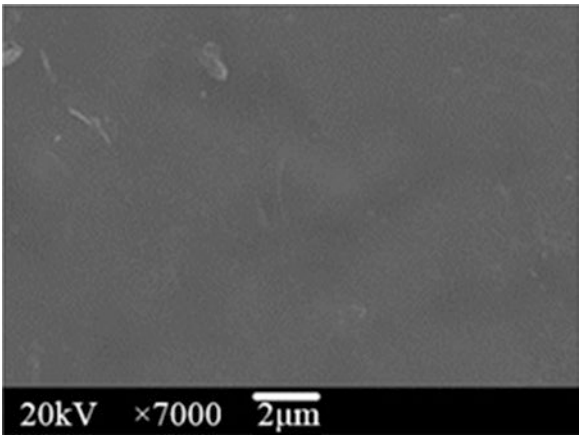

Fig. 3 SEM image of press-cured HCP

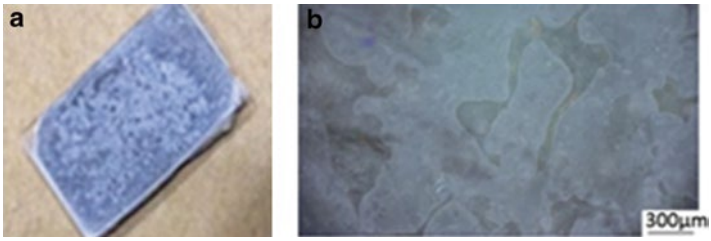

Photo 2 Bonded glass and HCP by autoclave. (**a**) With digital camera. (**b**) With microscope

mode, one of the measuring modes of SPM (AFM5200S, Hitachi High-Tech Science Corporation, Tokyo, Japan). The result is shown in Fig. 4, where the degree of brightness indicates the measured height. In Fig. 4, the brighter components of the image represent elevated features. In the measurement field of Fig. 4, the maximum height difference is 25 nm and no holes are observed. Next, a microchannel was prepared mechanically using a microprocessing machine. Figure 5 shows a digital microscope image of the prepared microchannel. The depth and width measured by digital microscope were 120 and 200 μm, respectively.

Finally, the channel was covered by a glass plate. Calcium hydroxide is produced in the interface between aggregate and cement paste and changes into C-S-H by autoclave treatment. Based on these reports, the HCP prepared with 400 MPa was immersed in water, with its surface in contact with a glass plate for 5 days. Then, autoclave treatment of 150 °C was applied for 3 h. The result is shown in Photo 2a, indicating that a strong bond was formed between the HCP surface and the glass plate. However, as shown in Photo 2b, the bonding hydrates are not uniform, and leakage is expected to occur. We are presently developing a method to achieve uniform bonding.

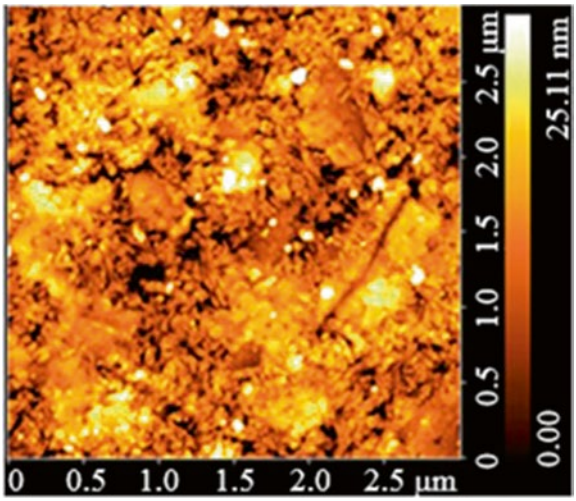

Fig. 4 Surface shape scanned with SPM

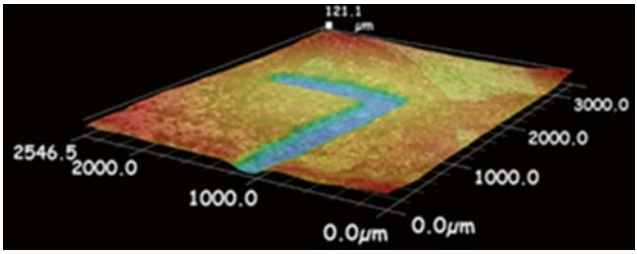

Fig. 5 Prepared channel on HCP

3 Results and Discussion

3.1 Evaluation of Chloride Transport in Nanochannels

Figure 6 shows the comparison between the fluorescence intensity of KCl (F_{KCl}) and KNO_3 (F_{KNO3}) for the channel depths of 95 nm, 28 nm, and 16 nm after 45 min. In the figure, MQAE and KCl or KNO_3 are observed to be diffused over the length of the nanochannels. By this time, MQAE diffusion has attained a steady state.

In the case of the 95-nm deep channels, F_{KCl} is less than F_{KNO3}, which indicates that Cl^- has entered into the nanochannels. The ratio of the fluorescence intensity is $F_{KNO3}/F_{KCl} = 1.36$. In the case of the 16-nm deep channels, the ratio is reduced to $F_{KNO3}/F_{KCl} = 1.06$, indicating that a substantially fewer number of Cl^- have entered into the nanochannels owing to electrical exclusion. Plecis et al. [1] defined the

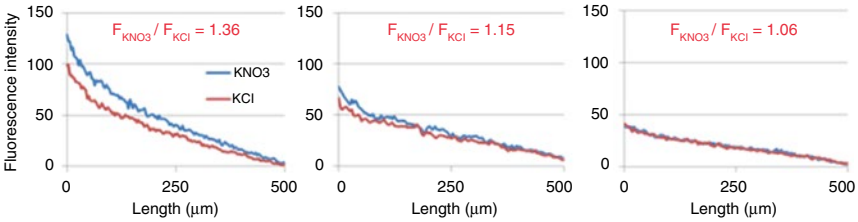

Fig. 6 Comparison between F_{KCl} and F_{KNO3} after 45 min for channel depths of 95 nm (*on left*), 28 nm (*on middle*), and 16 nm (*on right*)

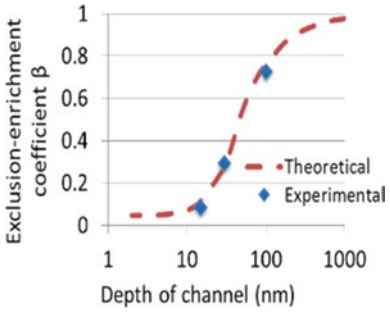

Fig. 7 Comparison. (**a**) 24 h after preparation. (**b**) 1 month after preparation between β_{exp} and β_{pre}

exclusion-enrichment coefficient β to quantify the effect of electrical interaction on Cl^- behavior in a nanoscale space according to Eq. (1):

$$\beta = \frac{C_{eff}(x)}{C^*(x)} = \frac{C(x,z)_z}{C^*(x)}, \tag{1}$$

where $C_{eff}(x)$ is the concentration of ions undergoing electrical interaction and $C^*(x)$ is the concentration of ions without electrical interaction. First, an experimental value for β (β_{exp}) should be obtained from our results. The concentration of Cl^- in nanochannels can be obtained by the quenching plot given in Fig. 1 and the fluorescence intensity ratio F_{KNO3}/F_{KCl}. The experimental value β_{exp} can be obtained by dividing these by the bulk concentration of Cl^-, which was 5 mM. Then, the theoretical value of β (β_{pre}) can be expressed by Eq. (2) [1].

$$\beta_{pre} = \frac{1}{h}\int_0^h \exp\left(-q\frac{\zeta\cosh\left((h/2-z)/\lambda_D\right)}{\cosh\left(h/2\lambda_D\right)}/k_BT\right)dz \tag{2}$$

Here, λ_D, q, h, and ζ are the Debye length, the net charge of the diffusing species, the channel depth, and the zeta potential. The zeta potential of the glass surface used in this experiment was determined according to a report by Kirby et al. [2]. Using the experimental conditions comprised of a pH of 7.4 and temperature of 25 °C, we obtained $\zeta = 80$ mV. Figure 7 shows the comparison between β_{exp} and β_{pre}.

Although we have only three experimental values, it is confirmed that these experimental values agree well with the theoretical curve. Therefore, it is considered that this information verifies the reliability of the experimental results and the possibility of quantification of ionic behavior under the effect of exclusion and enrichment in a nanoscale space.

3.2 Surface Potential of HCP with Smooth Surface and No Holes

SPM analysis was conducted on the HCP prepared by the same procedure as discussed in Sect. 2.2. However, the curing time under pressure in this case was 24 h and the sample was immersed in acetone for 24 h. The sample was subsequently maintained at a temperature of 20 °C and RH of 20 % for either 24 h or 1 month until the SPM analysis was conducted. Here, an absolute value for the surface potential has no meaning and the results are only valid from a relative perspective. The measured field was 10 × 10 μm. The results of the sample held for 24 h prior to the test are shown in Fig. 8a, b shows the results of the sample cured for 1 month. In Fig. 8, the brighter regions indicate a larger surface potential. The measurement of surface potential is affected by the surface morphology. In Fig. 8a, the regions of highest brightness are along the edges of the hydrates, and the difference is considered to be due to the surface morphology.

As such, it can be said that the surface potential is not different between hydrates. Dark spots of an approximate diameter of 1 μm are observed. It has been reported that carbonated HCP has a lower zeta potential [3], indicating that the darker spots are probably carbonated hydrates. As shown above, SPM can evaluate the distribution of the surface potential, which has not yet been well investigated. The information is important for comparison of the experimental results with theoretical values or to develop a model to evaluate mass transfer.

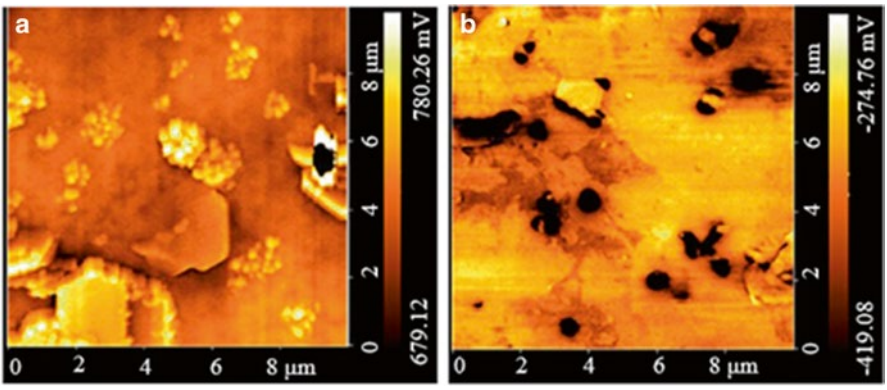

Fig. 8 Surface potential of the HCP surface evaluated with SPM

4 Conclusion

The results of this study are summarized in the following points.

A method to measure the chloride ion concentration in nanochannels using a fluorophore has been developed and the obtained results agree well with those derived from theory. A HCP plate with a very smooth surface was prepared and micromachined. The HCP was bonded to a glass plate by autoclave treatment; however, the bonding was not uniform and leakage was expected.

Acknowledgement Some of the experimental work reported in this study was conducted with financial support from the Japan Cement Association. We thank Associate Prof. Hibara and Ms. Fukuyama of the Tokyo Institute of Technology and Prof. Eijkel of the University of Twente for their experimental instruction and discussion.

References

1. Plecis, A., Schoch, R. B., & Renaud, P. (2005). Ionic transport phenomena in nanofluidics: Experimental and theoretical study of the exclusion-enrichment effect on a chip. *Nano Letters, 5*, 1147–1155.
2. Kirby, B. J., & Hasselbrink, E. F. (2004). Zeta potential of microfluidic substrates: 1. Theory, experimental techniques, and effects on separations. *Electrophoresis, 25*, 187–202.
3. Castellote, M., Llorente, I., & Andrade, C. (2006). Influence of the composition of the binder and the carbonation on the zeta potential values of hardened cementitious materials. *Cement and Concrete Research, 36*(10), 1915–1921.

Alkali-Silica Reaction Mitigation Using Nano-silica and Fly Ash

Mohamed Zeidan and Aly Said

Abstract Alkali-aggregate reaction was first observed in the US during 1920s. In the last several decades, several studies investigated the mechanisms of alkali-silica reaction in concrete and the extent of damage it may cause to the cementitious matrix. Research on alkali-silica reaction mitigation covers mainly the use of supplementary cementitious materials and lithium compounds. Meanwhile, nano-silica has proved its capacity to enhance concrete properties. Nano-silica consists of highly reactive high surface area particles generally available dispersed in a solution. The addition of nano-silica to concrete can significantly enhance the overall cementitious matrix and the interfacial transition zone in specific. Such enhancements can lead to refined pore structure, lower overall permeability and higher strength. The use of nano-silica in infrastructure project promises longer service life with low maintenance activities resulting in substantial economic savings. In the current study, the use of effect of nano-silica on the alkali-silica reaction will be investigated. Results show that nano-silica can help mitigate the effect of alkali-silica reaction.

Keywords Alkali-silica reaction • Concrete • Nano-silica • Durability • Mitigation • Supplementary cementitious materials

1 Introduction

Unlike natural rocks, concrete is an alkaline material due to the presence of hydroxides generated during the hydration reaction of cement. This highly alkaline medium promotes reactions between components of certain types of aggregates and cement hydration products. Generally, three main types of alkali-aggregate reactions (ARR)

M. Zeidan
Department of Computer Science and Industrial Technology, Southeastern Louisiana University, Hammond, LA 70402, USA
e-mail: mohamed.zeidan@selu.edu

A. Said (✉)
Department of Architectural Engineering, The Pennsylvania State University, University Park, PA 16802, USA
e-mail: aly.said@engr.psu.edu

K. Sobolev, S.P. Shah (eds.), *Nanotechnology in Construction*,
DOI 10.1007/978-3-319-17088-6_60

are believed to cause concrete cracking and deterioration. These reactions are known as (i) alkali-silicate, (ii) alkali-carbonate, and (iii) alkali-silica reactions, according to Hobbs [1]. Alkali-silica reaction, being the most common type, is usually mitigated using supplementary cementitious materials. The pozzolanic reaction consumes the calcium hydroxide, a by-product of the hydration reaction, thus reducing the alkali content in the concrete matrix.

Experimental results indicate that the addition of nano-silica promotes both hydration and pozzolanic reaction in concrete and cement mortars [2–5]. The acceleration of these reactions leads to enhancement at the microstructure level, improving concrete mechanical properties and durability [6]. On the other hand, the effect of nano-silica on ASR has not been investigated sufficiently to date. In a recent study, accelerated mortar-bar testing showed that using nano-silica reduced expansion caused by ASR in waste-glass cement mortars [7]. However, using nano-silica as an ASR mitigation technique is not recognized adequately, so far. This study aims mainly to present better understanding of the effect of nano-silica on ASR and to access its mitigation efficiency compared to other known techniques.

2 Experimental Program

An experimental program was designed to investigate the effect of nano-silica on ASR, either solely or combined with class F fly ash. This effect will be investigated in terms of expansion of mortars made with ASR-reactive aggregate. To achieve these goals, the accelerated mortar-bar method was used to measure the expansion caused by ASR for different mixtures. Class F fly ash was solely used in one mixture in order to compare its effect as a well-known effective ASR mitigation techniques.

For the mortar specimens, type II/VI portland cement that met ASTM C150 [8] specifications was used in all the mixtures. Nano-silica used in this study was a commercial type supplied by a European manufacturer. The product is a milky white, odorless, aqueous-suspended solution with a SiO_2 content of 50 % by weight. According to the data provided by the manufacturer, the density of the solution was 87.4 lb/ft^3, its pH value was 9.5, and the average particle size was 35 nm.

To study the expansion caused by ASR, the accelerated mortar bars test was used according to ASTM C1260 [9] and ASTM C1567 [10]. For the different combinations of cementitious materials, the mortar was prepared with a proportion of 1 part of cementitious material to 2.25 parts of graded aggregate by mass (dry materials), with a water-to-cement ratio of 0.47. Mortar bars of dimensions $1'' \times 1'' \times 11''$ were molded and compacted according to ASTM standards. After that, the molds were kept in a moisture cabinet with a relative humidity of not less than 90 % for 24 h. After unmolding, the bars were soaked in tap water and placed in an oven with a temperature of 80°C for 24 h for conditioning. Then, the zero reading of the bars length was measured by using a length-comparing device with an accuracy of 0.0001 in. Immediately after measurement, specimens were immersed in a 1 N

Table 1 Combinations of cementitious materials for mortar mixtures

Mixture	Cement	Fly ash	Nano-silica
C0	100 %	0 %	0 %
CN1	97 %	0 %	3 %
CN2	94 %	0 %	6 %
CF	70 %	30 %	0 %
CFN1	83 %	14 %	3 %
CFN2	68 %	29 %	3 %

sodium hydroxide (NaOH) solution in sealed containers, which were stored inside a convection oven of temperature 80°C ± 2°C. The expansion in the bars was measured and recoded every 3–4 days for the first 14 days of exposure, and every 7–10 days after that. According to ASTM standards, the expansion values should be recorded at 14 days of exposure. However, in order to understand better the long-term behavior of ASR, the expansion was monitored continuously for up to 80 days.

Different combinations of cementitious materials and nano-silica were used as binders for mortar mixtures. Besides the control mixture (100 % cement), five different combinations of cementitious materials and nano-silica were used to prepare the mortar bars. Table 1 presents the combinations of cementitious material used for the six mortar mixtures that were tested. At least three mortar bars were prepared and tested for each of the six mixtures.

3 Results

The expansion in mortars bars immersed in NaOH solution at 80°C was monitored for approximately 80 days, and the expansion ratios were calculated. The main expansion ratio readings, taken at 14 days of exposure, were compared to the limits recommended in the standard appendix of ASTM C1260 [9] and C1567 [10]. These standards consider the aggregate and/or the cementitious materials combination to be indicative of innocuous ASR behavior if the expansion percentage was less than 0.10 % and potentially deleterious if it is more than 20 %. For expansions between those two limits, further testing is needed to define the causes of expansion.

The expansion values presented in Table 2 indicate that the aggregates used in this study can be considered as potentially reactive. This can be revealed, basically, through the 14 days' expansion value and the guidance limits recommended by the ASTM standards, as previously described. Based on the results from 14 days of expansion, the efficiency of the different pozzolans dosages used can be judged by comparing them to the reference values.

It was noticed that the 30 % of Class F fly ash (mixture CF) could reduce the expansion values to nearly the acceptable limits. Also, 6 % of nano-silica (mixture CN2) could achieve the same or slightly better performance in terms of ASR mitigation. However, the most efficient mitigation performance, measured in terms of

Table 2 Expansion ratios in mortar bars

Mixture	Cement	Fly ash	Nano-silica
	14 days	28 days	80 days
C0	0.335 %	0.638 %	1.055 %
CN1	0.190 %	0.381 %	1.117 %
CN2	0.094 %	0.253 %	0.903 %
CF	0.103 %	0.258 %	0.882 %
CFN1	0.108 %	0.247 %	0.788 %
CFN2	0.036 %	0.165 %	0.496 %

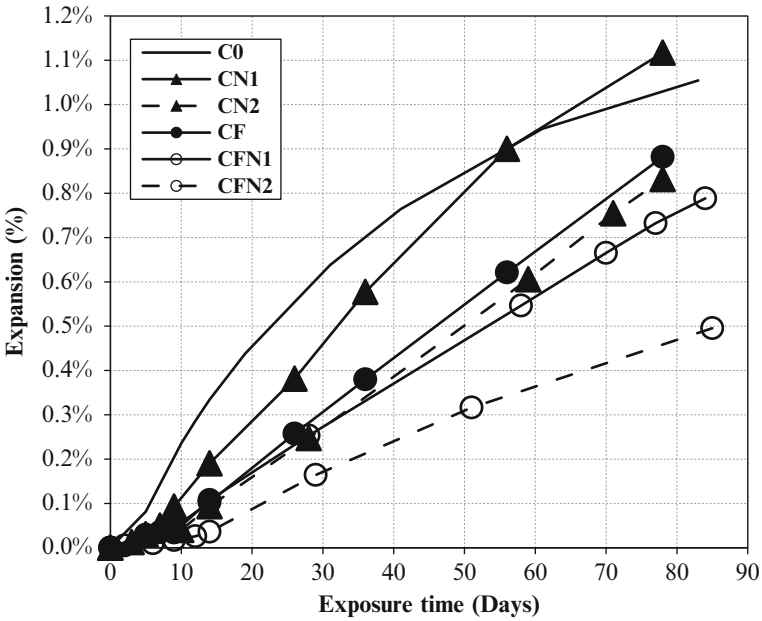

Fig. 1 Expansion in mortar bars at different exposure ages

reducing the 14 days expansion, was achieved by combining the classical mitigation using fly ash with 3 % of nano-silica. This could be observed by means of the significantly lower expansion values for mixtures CFN2.

Further, the long term expansion caused by ASR was investigated in this study, as shown in Table 2 and Fig. 1. Such data illustrates the expansion in mortar bars for up to 80 days. It should be noted that this long exposure period combined with the accelerated conditions simulated a very long period of ASR in actual service conditions. This period might even exceed the design service life for most structures; therefore, these very high expansion values might not be observed in practice.

The results of long-term expansion indicate that the rate of expansion was significantly reduced when fly ash was used. Generally, the control mixture (C0), containing only portland cement, represented the upper limit of the expansions at all ages of

exposure, except for mixture CN1, which had a slightly higher expansion at the end of the exposure period. For the control mixture, the rate of increase in expansion was higher during the first 30 days of the exposure; it started gradually declining after 30 days, and tended to reach a constant maximum value. For the other five mixtures, the expansion increase tended to follow almost a linear behavior after the first 14 days and up to the end of the exposure.

This study indicates that incorporating nano silica with fly ash performed significantly better than using fly ash only. In terms of reducing expansion and strength loss caused by ASR, the best results were achieved in case of using fly ash combined with nano-silica. This phenomenon may be explained by the rapid acceleration of the pozzolanic reaction in presence of nano silica particles, as confirmed by the results of thermo-gravimetric analysis performed on concrete sample incorporating nano-silica in a previous study [6].

4 Summary and Conclusions

Generally, the effect of nano-silica conforms to the literature about using silica fume for ASR mitigation. However, relatively low dosages of nano-silica (as low as 3 % of cementitious materials) were effective in terms of ASR mitigation, compared to higher addition rates normally used for micro-silica.

Considering the materials, mixture designs, and testing methods implemented in the present study, the following conclusions may be drawn. Nano-silica could mitigate the effect of ASR on concrete and mortar expansion. However, combining nano-silica with fly ash showed the best performance was due to ASR in terms of reducing expansion or preventing strength reduction. This was attributed to the accelerated pozzolanic reaction caused by the nano-silica.

ASR could have a considerable impact on mechanical properties of concrete, especially in cases of long exposure, high temperatures, or highly reactive aggregates. However, the studied supplementary cementitious materials along with nano-silica could prevent strength loss due to ASR for the studied exposure periods.

References

1. Hobbs, D. W. (1988). *Alkali-silica reaction in concrete*. London: Telford.
2. Sobolev, K., Flores, I., Torres-Martinez, L. M., Valdez, P. L., Zarazua, E., & Cullar, E. L. (2009, May 31–June 2). *Engineering of SiO_2 nano-particles for optimal performance in nano cement-based materials* (pp. 139–148). Proceedings of the 3rd international symposium on Nanotechnology in Construction (NICOM3). Prague: Czech Republic.
3. Jo, B. W., Kim, C. H., Tae, G., & Park, J. B. (2007). Characteristics of cement mortar with nano-SiO_2 particles. *Construction and Building Materials, 21*(6), 1351–1355.
4. Li, H., Xiao, H., Yuan, J., & Ou, J. (2004). Microstructure of cement mortar with nano-particles. *Composites Part B: Engineering, 35*(2), 185–189.

5. Said, A. M., & Zeidan, M. S. (2009). Enhancing the reactivity of normal and fly ash concrete using colloidal nano-silica. *ACI Special Publication SP, 267*(07), 75–86.
6. Said, A. M., Zeidan, M. S., Bassuoni, M. T., & Tian, Y. (2012). Properties of concrete incorporating nano-silica. *Construction and Building Materials, 36*, 838–844.
7. Aly, M., Hashmi, M. S. J., Olabi, A. G., Messeiry, M., Abadir, E. F., & Hussain, A. I. (2012). Effect of colloidal nano-silica on the mechanical and physical behaviour of waste-glass cement mortar. *Materials and Design, 33*, 127–135.
8. American Society for Testing and Materials, ASTM C150. (2007). *Standard specification for portland cement*. Annual Book of ASTM Standards, V.04.01, West Conshohocken.
9. American Society for Testing and Materials, ASTM C1260. (2001). *Standard test method for potential alkali reactivity of aggregates (mortar-bar method)*. Annual Book of ASTM Standards, V.04.02, West Conshohocken.
10. American Society for Testing and Materials, ASTM C1567. (2008). In M. Zeidan, & A. Said (Eds.), *Determining the potential alkali-silica reactivity of combinations of cementitious materials and aggregate (accelerated mortar-bar method)*. Annual Book of ASTM Standards, V.04.02, West Conshohocken.

Application of Nanotechnology to Control ASR in Portland Cement Concrete

Anol K. Mukhopadhyay and Kai-Wei Liu

Abstract Nanotechnology applications to control ASR can be broadly classified in three categories, i.e., (i) mechanical controls, (ii) chemical controls and (iii) combination of both physical and chemical controls. Control of crack growth and propagation by adding carbon nano-fibers and nano-tubes is considered as the main approach under the category of mechanical control. On the other hand, adding nano-particles (e.g., nano-silica and others) in different dosages (e.g., 0.5, 1.0, and 2 %) with and without conventional SCMs (e.g., fly ash) to control availability of alkalis and $Ca(OH)_2$ is the main approach under chemical measures. Different concrete mixtures containing nanosilica, fly ash and carbon-nanofibers were developed. An accelerated concrete cylinder test (ACCT) was used to test all the concrete mixtures, measure expansion due to ASR and verify the efficacy of each control measure to control ASR.

Keywords Alkali-silica reaction (ASR) • Accelerated concrete cylinder test • Concrete ASR expansion • Nanosilica • Fly ash

1 Introduction

Alkali-silica reaction (ASR) is a deleterious chemical reaction between hydroxyl (OH^-) ions associated with alkalis (sodium and potassium) present in cement or other sources and certain reactive siliceous components that may be present in coarse and/or fine aggregates. The product of this reaction is a gel known as ASR gel. In the presence of sufficient moisture (>80 % RH), the gel absorbs moisture due to its hygroscopic nature and swells and create tensile stresses in concrete. When these stresses exceed the tensile strength of concrete, cracks develop both in aggregate particles as well as in the cement paste in concrete.

A.K. Mukhopadhyay (✉)
Materials and Pavement, Texas A&M Transportation Institute (TTI),
Texas A&M University, College Station, TX 77843, USA
e-mail: anol@tamu.edu

K.-W. Liu
Zachry Department of Civil Engineering, Texas A&M University,
College Station, TX 77843, USA
e-mail: kaiwei@tamu.edu

K. Sobolev, S.P. Shah (eds.), *Nanotechnology in Construction*,
DOI 10.1007/978-3-319-17088-6_61

In general, supplementary cementitious materials (SCMs) such as fly ash, ground granulated blastfurnace slag (GGBS), and condensed silica fume are all used to reduce ASR expansion in concrete. Class F fly ash (20–25 %) is more effective in controlling ASR than Class C fly ash [1–4]. A higher replacement level (>25 %) may be needed for certain F ashes in order to avoid ASR distress/reduce ASR to a safe level. A higher fly ash replacement level (i.e., >25 %) may not be permissible in certain applications where early strength requirement is very important. Determination of optimum fly ash content depending on the quality of fly ash and level of protection needed is a very important aspect and the current test methods are not fully capable to address this aspect.

Nanotechnology applications to control ASR can be broadly classified in three categories, i.e., (i) mechanical controls, (ii) chemical controls and (iii) combination of both physical and chemical controls. Control of crack growth and propagation by adding carbon nano-fibers and nano-tubes is considered as the main approach under the category of mechanical control. On the other hand, adding nano-particles (e.g., nano-silica and others) in different dosages (e.g., 0.5, 1.0, and 2 %) with and without conventional SCMs (e.g., fly ash) to control availability of alkalis and $Ca(OH)_2$ is the main approach under chemical measures. Reductions in permeability through pore refinements, developments of uniform and homogeneous microstructures with improved interfacial transition zone (ITZ) are the additional benefits from adding nanomaterials to control ASR indirectly. A combined approach of both mechanical and chemical controls is anticipated to be the best control measure in order to provide a long term solution without any ASR distress. In chemical controls, nano-silica and SCMs (e.g., fly ash and/or other SCMS) together can control ASR effectively and can be economical. In cases where high fly ash content is required to control ASR but not allowed because of strength restrictions, adding certain percentages of nanomaterials (e.g., nanosilica) along with the permissible level of fly ash replacement should be sufficient to control ASR chemically. Another approach could be adding suitable nanomaterials to improve the early strength of high fly ash content (required to control ASR) mixtures.

2 Materials and Methods

2.1 Materials

The reactivity of the aggregates used are tested by ASTM C 295 [5], ASTM C 1260 [6], and ASTM C 1293 [7]. The authors have developed a device called volumetric change measuring device (VCMD) as a rapid chemical method to determine alkali silica reactivity of aggregate [8] in terms of measuring compound activation energy (CAE). The VCMD-based test was also used to determine the reactivity of these aggregates. The reactivity data by the different methods is summarized in Table 1.

A high-alkali ($Na_2O_e = 0.82$ %) portland cement was selected in order to achieve the desired alkali levels of 4.5 lbs/yd^3 (i.e., using cement alone without any alkali boosting). The carbon nanofibers (CNFs) used for the test were factory treated to

Table 1 List of aggregate with relevant material data

Aggregate	ASTM C 1260 (14-day expansion, %)	ASTM C 1293 (1-year expansion, %)	ASTM C 295 (reactive constituents)	CAE (KJ/mol)
Coarse	0.012 (NR)	0.027 (NR)	Few siliceous (e.g., Chert) inclusions	61.70 (NR)
Fine	0.381 (HR)	0.391 (HR)	Acid volcanic, Chert	26.96 (HR)

QTZ quartz, *NR* nonreactive, *HR* highly reactive

Table 2 Concrete mix design for conducting ACCT

Mix	Alkali (kg/m^3)	Na_2O_e (%)	w/c	CAF	CF (kg/m^3)	Nanosilica (wt% of cement)	Fly ash replacement (wt% of cement)	CNF (wt% of cement)
1	2.7	0.82	0.45	0.76	3.5	–	–	–
2						–	–	0.5
3						0.5	–	–
4						–	20	–
5						–	25	–
6						0.5	25	–
7							25	0.5
8						–	35	–

w/c water to cement ratio, *CAF* coarse aggregate factor

remove any remaining polyaromatic hydrocarbons from the surface. The CNFs have a diameter ranging from 60 to 150 nm, a length of 30–100 μm, and a specific surface area of 56–60 m^2/g. Class F fly ash was used as a conventional method to control ASR. The nanosilica particles with a surface area of 41.3 m^2/g were mixed with deionized (DI) water and dispersed at 3,800 rpm with amplitude of 50 % for 5 min before use. The final concentration of total solids in DI water is around 3.64 %.

2.2 Mix Design and Specimen Preparation

Table 2 presents the concrete mix designs. The control mix is a straight cement mix without any alkali boosting. Concretes were mixed by hand following ASTM C 192 [9] procedures. Concrete cylinders using the mix shown in Table 2 were cast for ACCT.

2.3 Pore Solution Extraction

The cement paste cylinders (51 mm × 102 mm) corresponding to the mix in Table 2 were cast and covered with plastic foil, and then stored under 100 % relative humidity (RH) at 25 ± 2 °C for 7 days. After the 7-day curing, the specimens were

Table 3 Concentration of the extracted pore solution from cement paste

Mix (Table 2)	Na^+ (N)	K^+ (N)	Na^+_e (N)
1, 2	0.18	0.81	0.66
3	0.09	0.70	0.51
4	0.10	0.58	0.44
5, 7	0.10	0.56	0.43
6	0.09	0.50	0.39
8	0.08	0.43	0.33

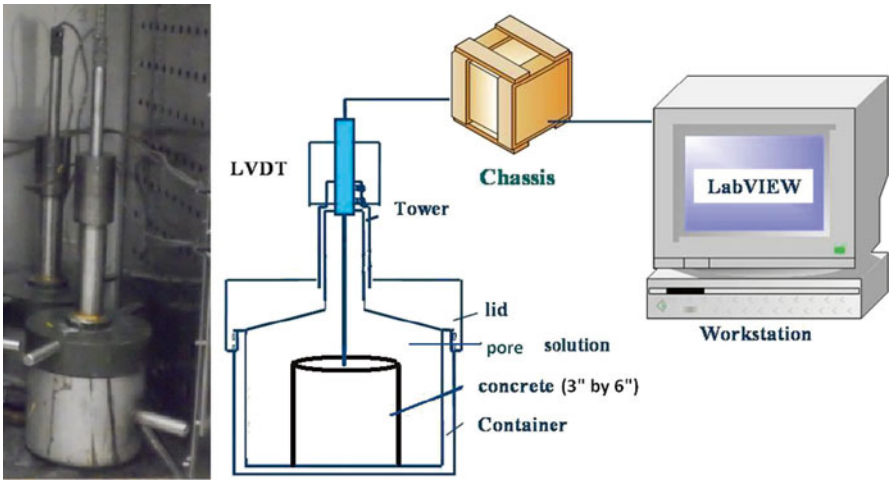

Fig. 1 The test set up for ACCT

de-molded and pore solutions were extracted from each paste specimen by applying a high-pressure squeezing method. The extracted pore solution was analyzed by Atomic Absorption Spectrometer to determine Na^+ and K^+ ion concentration. Table 3 presents the composition (Na^+ and K^+) of pore solution extracted from the studied cement pastes. The Na equivalent (Na^+_e) [10] represents the total alkali levels of pore solution in normality for each mix in this study.

The pore solution concentrations in Table 3 were used to generate the soak solutions (soak solution alkalinity = pore solution alkalinity) for the concrete cylinder tests according to the mix designs in Table 2. Calcium hydroxide crystals were added (above saturation level, i.e., 1 g/L solution) to each soak solution.

3 Test Equipment and Test Procedure

An accelerated concrete cylinder test (ACCT) has recently developed by the authors [11] to measure concrete ASR expansion and was used to test all the concrete mixtures in this study. Figure 1 shows the ACCT setup. A 5.1 by 10.2 cm concrete

cylinder (after 7 days curing @100 % RH) with cast-in place threaded rod (2.5 cm inside from the top) is placed inside the container followed by immersing the specimen with a soak solution of chemistry equal to the concrete pore solution alkalinity. The purpose of creating soak solution chemistry equals to pore solution chemistry is to prevent alkali leaching from the specimen. Each VCMD was tightly closed and placed inside an oven at 60 °C. The LVDT rod is connected to the threaded rod attached to the specimen, which moves inside the LVDT during ASR expansion of the specimen and creates electrical signals. These signals are converted to LVDT displacements (inch) through the data acquisition system and recorded (every 15 min) by the attached computer through the LabVIEW program. An expansion limit of 0.04 % after a testing period of 28 days is proposed for the ACCT as a criterion to diagnose aggregate alkali silica reactivity [11].

4 Results and Discussion

The selected mixes in Table 2 were tested by the ACCT. Figure 2 shows the expansion curves over time (28 days) for different mixes. The important observations are summarized below:

- The original mix shows an expansion of around 0.31 % at 28 days. This indicates that the tested concrete mix is highly reactive.
- A fly ash content of 20 or 25 % was not sufficient to control ASR. However, 35 % fly ash was sufficient to control ASR.

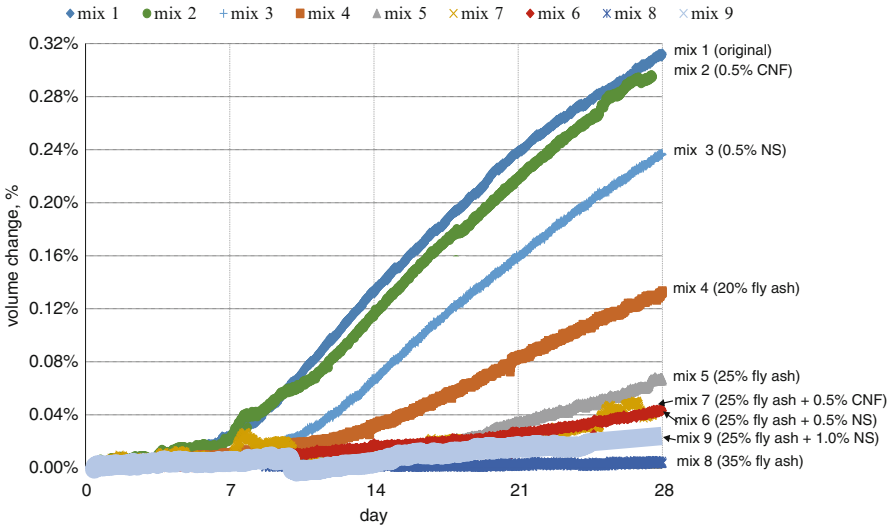

Fig. 2 ACCT expansion over time for the studied concrete mixes

- Adding 0.5 % nano-silica alone was not sufficient to reduce the expansion below 0.04 %. However, 0.5 % nano-silica addition was effective to reduce the expansion by 26 %. It is to be noted that 0.5 % nano-silica addition reduce the alkalinity from 0.66 to 0.51 N. This is not a considerable reduction and the alkalinity is still higher than threshold alkalinity (0.35 N). It seems 0.5 % nano-silica alone is not sufficient to reduce the expansion significantly.
- Adding 0.5 % CNF has caused a slight reduction of expansion. The main role of CNF is to control crack propagation and minimize crack formation. The original specimen is still expanding without any break in the expansion trend. The specimen doesn't show any visible crack outside. It seems the effect of CNF may not be manifested at this early age of expansion.
- However, 0.5 % nano-silica along with 25 % fly ash was good enough to reduce the expansion close to 0.04 %. It is anticipated that a slightly more nano-silica addition (higher than 0.5 %) will make the expansion below 0.04 % at 28 days and will produce a safe mix. A mix with 25 % fly ash and 1 % nano-silica (Mix 9 in Fig. 2) was subsequently developed and tested by the ACCT method. The Fig. 2 shows that the 28 days expansion of Mix 9 is 0.034 %. The pore solution alkalinity of mix 9 is 0.35N which is similar to the threshold alkalinity (0.35N). Therefore, 1 % addition of nano-silica along with 25 % class F ash is sufficient to make the studied mix a ASR resistant safe mix.
- The results show that 35 % of the studied fly ash is sufficient to control ASR. However, 35 % fly ash may not satisfy the early age strength requirement for certain applications and may not be allowed. The addition of appropriate percentage of suitable nano-materials can enhance the early strength gain and overcome the limitations.

Therefore, two options can be recommended here. In option one, add nano-silica (more than 0.5 %) with 25 % fly ash and control ASR chemically. In option two, add nanomaterials (e.g., nano-SiO_2, nano-TiO_2, Nano-Al_2O_3 etc.) with 35 % fly ash and overcome the limitations of low early strength gain. A most appropriate option needs to be selected based on cost benefit analysis matching with specific case.

The mix with 25 % fly ash +0.5 % CNF didn't make much difference and shows only slight reduction in expansion in comparison with the mix with 25 % fly ash.

5 Conclusions

- Different concrete mixtures containing nano-silica ± fly ash (chemical control), carbon-nanofibers (mechanical control) and nano-silica ± fly ash ± carbon-nanofibers (both mechanical and chemical control) were developed and tested by the ACCT method.
- ACCT method was found to be effective to optimize fly ash content and determine the effectiveness of adding different nanomaterials to control ASR.

- The addition of nanomaterials can play a significant role to control ASR if the allowable level of fly ash replacement alone sometimes can't control ASR.
- A practical nanotechnology based approach to control ASR is suggested.

Acknowledgment The authors acknowledge and thank Drs. Konstantin Sobolev and Ismael Flores Vivian for supplying the nanomaterials and other guidance in this study.

References

1. Diamond, S. (1981). Effect of two Danish fly ashes on alkali contents of pore solutions of cement-fly ash pastes. *Cement and Concrete Research, 11*(3), 383–394.
2. Shehata, M. H., & Thomas, M. D. A. (2000). The effect of fly ash composition on the expansion of concrete due to alkali silica reaction. *Cement and Concrete Research, 60*(7), 1063–1072.
3. Shon, C. S., Zollinger, D. G., Sarkar, S. L., et al. (2003). Application of modified ASTM C 1260 test for fly ash-cement mixtures. *Journal of Translational Research Board, 1834*, 93–106.
4. Shon, C. S., Sarkar, S. L., Zollinger, D. G., et al. (2004). Testing the effectiveness of class C and class F fly ash in controlling expansion due to alkali-silica reaction using modified ASTM C 1260 test method. *Journal of Materials in Civil Engineering, 16*(1), 20–27.
5. ASTM C 295–03. (2008). *Standard guide for petrographic examination of aggregate for concrete* (Annual Book of ASTM Standards 04.02, pp. 199–206). West Conshohocken: American Society for Testing Materials.
6. ASTM C 1260–07. (2008). *Standard test method for potential alkali reactivity of aggregates (Mortar-Bar Method)* (Annual Book of ASTM Standards 04.02, pp. 677–681). West Conshohocken: American Society for Testing Materials.
7. ASTM C 1293-08a. (2008). *Standard test method for determination of length change of concrete due to alkali-silica reaction* (Annual Book of ASTM Standards 04.02, pp. 682–688). West Conshohocken: American Society for Testing Materials.
8. Liu, K. W., & Mukhopadhyay, A. (2014). A kinetic-based ASR aggregate classification system. *Construction and Building Materials, 68*, 525–534.
9. ASTM C 192–07. (2008). *Standard practice for making and curing concrete test specimens in the laboratory* (Annual Book of ASTM Standards 04.02, pp. 137–144). West Conshohocken: American Society for Testing Materials.
10. French, W. J. (1980). Reactions between aggregates and cement paste – An interpretation of the pessimum. *Quarterly Journal of Engineering Geology, 13*(4), 231–247.
11. Liu, K. W., & Mukhopadhyay, A. (2014). An accelerated concrete cylinder test for alkali-silica reaction. *Journal of Testing Evaluation, 44*(3), 1–10.

Effect of Iron-Oxide Nanoparticles on the Durability of Fly Ash Cement Paste

Linoshka Soto-Pérez, Natalia Vázquez, Omar Molina, Minju Jo, and Sangchul Hwang

Abstract A two-factor, two-level factorial design was developed to assess the chemical resistance of cement paste containing fly ash (FA) and engineered iron oxide nanoparticles ($ENP_{Fe\text{-}surf}$) in acetic and sulfuric acid at pH 3. Weight loss and increment of the specimens was recorded during 90-day exposure to acid solutions and then compressive strength was measured. Results showed a slight weight increment for the specimens submerged in sulfuric acid due to the hydration of cement and to the expansive products formed by the reaction between calcium hydroxide/calcium aluminate (ferrite) hydrates and sulfates. Weight increment of those specimens was not as significant as those only exposed to tap water due to the calcium hydroxide dissolution and the calcium silicate hydrate decalcification by the acid. Exposure to acetic acid resulted in weight loss in all specimens due to the formation of soluble calcium salts. Compressive strength of the specimens exposed only to tap water was not changed by the $ENP_{Fe\text{-}surf}$ addition, although its addition to the specimens containing FA positively affected compressive strength. When exposed to sulfuric acid solutions, the specimens containing FA had lower compressive strength with the $ENP_{Fe\text{-}surf}$ presence. The specimens placed in acetic acid always showed decreases in strength with the $ENP_{Fe\text{-}surf}$ addition.

Keywords Acetic acid • Chemical resistance • Compressive strength • Sulfuric acid

1 Introduction

Compressive strength and chemical resistance are very important properties of structural concrete. Portland cement concrete does not possess good resistance to acid attack since one of its principal hydration products is calcium hydroxide (CH). CH is highly soluble in water and contributes to the high alkalinity of concrete [1]. Sulfates dissolved in water can react with the CH to form expansive products

L. Soto-Pérez (✉) • N. Vázquez • O. Molina • M. Jo • S. Hwang
Department of Civil Engineering and Surveying, University of Puerto Rico at Mayagüez, Mayagüez, Puerto Rico
e-mail: linoshka.soto@upr.edu; natalia.vazquez1@upr.edu; omar.molina1@upr.edu; minju.jo@upr.edu; sangchul.hwang@upr.edu

K. Sobolev, S.P. Shah (eds.), *Nanotechnology in Construction*,
DOI 10.1007/978-3-319-17088-6_62

(e.g., gypsum and ettringite), causing cracking and spalling of the cement paste and thus reducing the compressive strength and durability of concrete [1]. The amount of CH in the hardened cement paste can be lowered by replacing part of the cement with pozzolanic materials, such as fly ash (FA), which reacts with the CH in concrete to form the CSH gel, the principal hydration product of cement. This contributes to the densification of the specimen, preventing the penetration of aggressive agents such as sulfates.

In this study, a two-factor, two-level factorial design was used to assess the durability of cement paste containing FA and engineered iron oxide nanoparticles coated with surfactants ($ENP_{Fe\text{-}surf}$). Weight gain/loss of the specimens during 90-days of exposure to acetic and sulfuric acids and the compressive strength after 90 days in acids was determined as a means of chemical resistance of the specimens.

2 Experimental

2.1 Materials

Portland cement Type IP according to ASTM C595 was purchased at a local supplier in Puerto Rico and FA was obtained from a local coal-fueled power plant (AES Puerto Rico) (Table 1). $ENP_{Fe\text{-}surf}$ was purchased from the Ferrotec (Bedford, NH) and were composed of (in % vol.) nominal 10-nm magnetite (2.8–3.5), proprietary surfactant(s) (2.0–4.0), and water (92.5–95.2). Certified ACS-grade sulfuric acid and acetic acid were purchased from the Fisher Scientific.

2.2 Specimen Design and Preparation

Cement paste specimens were made in a two-factor, two-level (2^2) factorial design. The factors were the ratios of FA substitution and $ENP_{Fe\text{-}surf}$ addition to the binding materials (i.e., cement + FA). Low and high levels for FA/B ratio were 0.0 and 0.40 and those for ENP/B ratio were 0.0 and 0.03. The water-to-binder (W/B) ratio was fixed at 0.35 with which high compressive strengths were developed in the preliminary studies. $ENP_{Fe\text{-}surf}$ solution was first added to water and then the liquid was poured to the binding materials and mixed in a mechanical mixer for 3 min. No plasticizers were used. The paste was cast into plastic molds of 2-in in diameter and 4-in in height. After 24 h, the specimens were demolded and cured in a tank filled with calcium-saturated tap water at ambient temperature.

Table 1 Chemical composition of Portland cement and fly ash used in the study

	Oxide content (wt%)									
	SiO_2	Al_2O_3	Fe_2O_3	CaO	MgO	SO_3	Na_2O	K_2O	TiO_2	P_2O_5
PC	27.14	6.68	3.71	55.47	1.62	3.48	0.59	0.48	0.32	0.11
FA	30.84	9.93	5.01	39.61	0.35	11.43	0.90	1.01	0.45	0.11

2.3 Durability Test in Terms of Chemical Resistance

Chemical resistance of the specimens in terms of changes in the weight and compressive strength was tested by exposing the specimens in tap water and two different acid solutions at pH 3: sulfuric acid and acetic acid. Two specimens per mixture were placed in a container filled with 6 L of the test solution. Weight monitoring was done after 1, 3, 7, 28, 56, and 90 days of immersion. Saturated weight was recorded and cumulative mass loss was calculated between each monitoring period. After 90 days of exposure to the acid solutions, compressive strength was tested by a 3,000 kN Forney universal testing machine.

3 Results and Discussion

3.1 Weight Change of the Specimens

From the previous studies it was found that the specimens containing FA significantly increased its compressive strength after 28 days of curing, while the specimens with no FA addition continued to gain strength but in a slower rate. This behavior was observed since pozzolanic reactions are slow at low curing times and start developing at higher rates after long curing times. Since all specimens were cured in calcium-saturated tap water for 28 days prior to the durability test, specimens containing FA showed a faster weight gain than those without FA from the beginning of the experiment (Fig. 1a). After 90 days of exposure, specimens containing FA significantly gained more weight than those without FA. The weight increase can be ascribed to the ongoing hydration of cement and to the pozzolanic reactions to form more CSH gel. A higher and faster weight gain in the specimens containing natural pozzolana resulted in a denser material due to pore reduction, thus enhancing the durability of the concrete specimens [2]. A greater weight gain was observed for the specimens containing $ENP_{Fe\text{-}surf}$ than the specimens without $ENP_{Fe\text{-}surf}$, independently on the FA addition.

Similar to the specimens exposed to tap water, the specimens containing FA immediately had a faster weight gain than those without FA (Fig. 1a). After a long-term exposure, a greater weight gain was observed for the specimens containing either FA or $ENP_{Fe\text{-}surf}$, or both than the specimens containing Portland cement only. Besides the ongoing hydration of cement and pozzolanic reactions to form CSH gel, the weight increase in these specimens can also be ascribed to the formation of expansive products such as ettringite due to sulfate attack. The magnitude of the weight increment was significantly lower than the specimens placed in tap water. The dissolution of CH with sulfuric acid for calcium sulfate was faster than the formation of CSH gel. Additionally, the additives that reacted with CH to increase cement densification consumed the leachable CH available to react with the acid, thus leaving the CSH gel to expose to acid attack so as to increase deterioration after a long-term exposure [3]. Weight reduction was only observed for specimens without $ENP_{Fe\text{-}surf}$ addition, which shows that $ENP_{Fe\text{-}surf}$ increased the durability of the specimens in terms of weight loss. This could be due to the substitution of calcium with iron in the

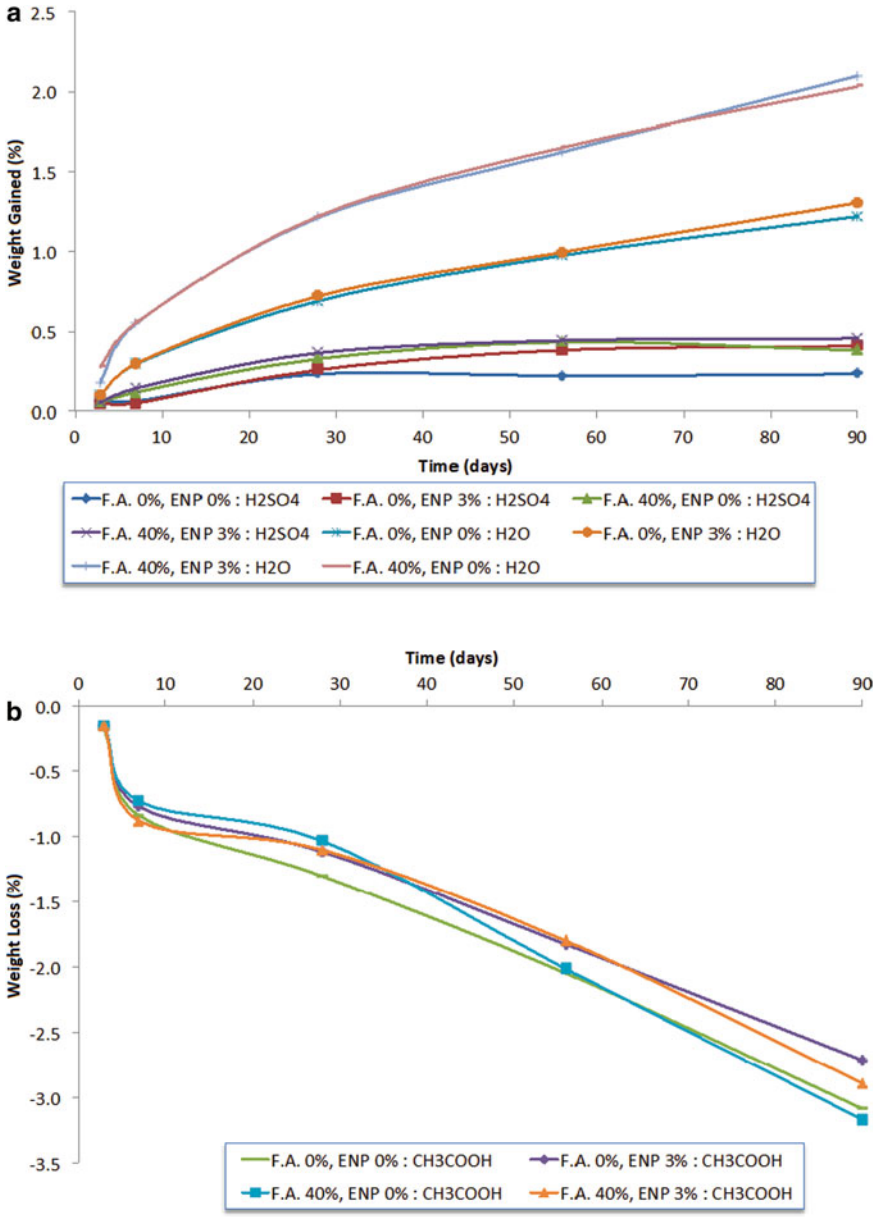

Fig. 1 Weight change in sulfuric acid and water (**a**) and acetic acid (**b**)

CSH gel when paste was decalcified, reducing the dissolution rate of the gel, thus incrementing the durability of the specimen [4]. In addition, the formation of calcium aluminoferrite hydrate may be favored due to high alumina content (12.59 %) in FA (Table 1) and $ENP_{Fe\text{-}surf}$ addition [1]. This hydrate is more resistant than other hydration products to acidic environments, similar to calcium aluminates [5].

After 90 days of exposure to sulfuric acid, the surface of the specimens was more porous, and spalling and cracking on the surface of the specimens was observed. Makhloufi et al. (2012) reported weight loss after 90-day exposure to sulfuric acid at pH 1.3, which was attributed to the formation of expansive products such as ettringite. The ettringite formation was caused by the reaction of calcium monosulfatoaluminate with sulfate ions, which was responsible for the weight increase at the beginning of the exposure but resulted in cracking at a later time due to internal stress in the specimen [2].

All the specimens exposed to acetic acid at pH 3 immediately started to lose weight, as shown in Fig. 1b. Since acetic acid tended to only form calcium salts, which are highly soluble in water [1], weight loss was observed for all the specimens since the beginning of the exposure to the acid. Senhadji et al. (2014) also found that when products of the acidic reaction were soluble calcium salts, it was more likely to obtain a higher weight reduction in concrete specimens [5]. After 90 days in acetic acid, the specimens with $ENP_{Fe\text{-}surf}$ showed slightly less weight loss. This implies again that $ENP_{Fe\text{-}surf}$ helped to improve the durability of the specimens when exposed to acids due to pore size reduction. In addition, spalling was clearly noticed in the surface of all the specimens, although the specimens with $ENP_{Fe\text{-}surf}$ addition showed less deterioration.

3.2 Compressive Strength After 90-Day Exposure to Acids

Compressive strength for the specimens exposed to sulfuric acid was lower than those that were only exposed to water, followed by the specimens exposed to acetic acid (Table 2). Acetic acid solutions produced a harsher environment due to decalcification of CH and CSH to form highly soluble calcium and aluminum salts [4]. This facilitated leaching of these products out of the specimen, leaving a more porous material, and therefore reducing its compressive strength.

In general, specimens containing FA resulted in lower compressive strength, due to the short curing time of 28 days prior to acidic attack, thus pozzolanic reaction was not fully achieved, leaving a more porous material susceptible to acid attack. Contrary to the results obtained from the durability test, the specimens containing $ENP_{Fe\text{-}surf}$ resulted in lower compressive strengths when exposed to acids. Since the formation of calcium aluminoferrites was very similar to the formation of calcium aluminates, this reaction occurred very fast at the beginning of the hydration process [1]. As this hydration product decalcified slower than calcium silicate hydrates, weight reduction rate was decreased (Fig. 1). Although the formation of this hydrates does not contribute to the strength of concrete but to its durability and depends on the availability of sulfates during the early setting and hardening reactions of concrete [1]. Similar to the formation of monosulfoaluminates, $C_4A(F)SH_{18}$ is likely to be formed when the availability of sulfates is limited. This represents a problem for the durability of concrete when exposed to sulfate ions after the solidification of the paste because an expansive product similar to ettringite might form, and increase the internal stresses of the concrete leading to micro-cracking, spalling of the concrete and decreasing the strength. It is believed that this was the reason why specimens containing both FA and $ENP_{Fe\text{-}surf}$ resulted in such low compressive strengths while its weight reduction

Table 2 Compressive strength of specimens after 90 days of acid exposure

Mixture composition	Average compressive strength (MPa)		
	Tap water	Sulfuric acid	Acetic acid
F.A. 0 %, ENP 0 %	73.3	71.2	64.6
F.A. 0 %, ENP 3 %	68.8	71.1	56.8
F.A. 40 %, ENP 0 %	63.7	51.0	44.8
F.A. 40 %, ENP 3 %	69.5	45.9	41.6

was the lowest of all the specimens exposed to sulfuric acid. On the other hand, $ENP_{Fe\text{-}surf}$ addition to the specimens containing FA and only exposed to tap water positively affected the compressive strength of the specimen.

4 Conclusions

The conclusions drawn from the experimental results are:

- Exposure to water and sulfuric acid resulted in weight increment for all specimens, whereas all specimens in acetic acid experienced a reduction in weight, regardless of its composition. The $ENP_{Fe\text{-}surf}$ addition resulted in higher weight gain or lower weight loss than the Portland cement specimens.
- Compressive strength of the specimens exposed only to tap water was not changed by the $ENP_{Fe\text{-}surf}$ addition, although its addition to the specimens containing FA positively affected its compressive strength.
- Compressive strength was higher for specimens submerged in sulfuric acid than the specimens in acetic acid.
- When exposed to sulfuric acid solutions, the specimens containing FA had lower compressive strength with the $ENP_{Fe\text{-}surf}$ presence, while for those placed in acetic acid showed decreases in strength with the $ENP_{Fe\text{-}surf}$ addition.

Acknowledgments Financial supports, in part, by AES Puerto Rico, LLC, the USGS 104B Program through the USVI Water Resources Institute, the NSF (DMR-0934115), and the PR NASA Space Grant Scholarship to Linoshka Soto are appreciated. We thank Eng. Ruben Segarra (Essroc San Juan) for characterization of cement and fly ash.

References

1. Metha, P., & Monteiro, P. (2014). *Concrete microstructure, properties and materials* (4th ed.). New York: McGraw-Hill Education.
2. Makholoufi, Z., Kadri, E. H., Bouhicha, M., & Benaissa, A. (2012). Resistance of limestone mortars with quaternary binders to sulfuric acid solution. *Construction and Building Materials, 26*, 497–504.
3. Girardi, F., & Di Maggio, R. (2011). Resistance of concrete mixtures to cyclic sulfuric acid exposure and mixed sulfates: Effect of the type of aggregate. *Cement and Concrete Research , 33*, 276–285.
4. Bertron, A., Duchesne, J., & Escadeillas, G. (2005). Attack of cement pastes exposed to organic acids in manure. *Cement and Concrete Composites, 27*, 898–909.
5. Shehadji, Y., Escadeillas, G., Mouli, M., Khelafi, H., & Benosman, A. (2014). Influence of natural pozzolan, silica fume and limestone fine on strength, acid resistance and microstructure of mortar. *Powder Technology, 254*, 314–323.

Nano-scale Investigation of Interactions of Chlorides with Oxides That Form on Carbon Steel in Concrete Pore Solutions

Pouria Ghods, O. Burkan Isgor, and H. Burak Gunay

Abstract Passivation and chloride-induced depassivation of carbon steel in concrete are processes that take place in nano scale. Spectroscopic and microscopic studies in this scale demonstrate that the thickness of the oxide films that form on carbon steel in the passivating environment of concrete pore solutions is typically in the range of 3–15 nm. Nano-scale analytical studies show that oxide films that form on carbon steel exposed to simulated concrete pore solutions consist of two layers separated with an indistinct border. The thinner Fe^{II}-rich inner oxide film is protective but unstable in the presence of chlorides. The thicker Fe^{III}-rich outer oxide film is unprotective and likely porous. Chloride exposure decreases the thickness of the oxide films and changes their stoichiometry such that near the film/substrate interface Fe^{III}/Fe^{II} ratio increases. Electrochemical quartz crystal nano-balance studies coupled with electrochemical observations provide kinetic evidence of how chlorides interact with these two layers and transform protective oxides into unprotective ones.

Keywords Corrosion • Passive film • Rebar • Chloride • Concrete

1 Introduction

Since the depassivation of steel plays an important role as to when and how the corrosion will start and progress, it is important to understand its mechanism accurately. Although significant progress has been made on the evaluation and the

P. Ghods
Giatec Scientific Inc., Ottawa, ON, Canada

Carleton University, Civil and Environmental Engineering Department, Ottawa, ON, Canada
e-mail: pouria@giatec.ca; pouria.ghods@carleton.ca
http://www.giatec.ca

O.B. Isgor (✉)
Oregon State University, School of Civil and Construction Engineering, Corvallis, OR, USA
e-mail: Burkan.Isgor@oregonstate.edu

H.B. Gunay
Carleton University, Department of Civil and Environmental Engineering, Ottawa, ON, Canada
e-mail: hgunay@connect.carleton.ca

K. Sobolev, S.P. Shah (eds.), *Nanotechnology in Construction*,
DOI 10.1007/978-3-319-17088-6_63

mitigation of corrosion problems in concrete structures, the exact breakdown mechanism of the passive film by chlorides has not been well defined because of the difficulties in examining the process in nano-scale level on thin passive layers [1].

Until recently, the studies on passive films that form on carbon steel in environments similar to typical concrete pore solutions remained at the macroscale level; therefore, nano-scale structural and compositional characteristics of these films remained highly speculative. It has been recently shown that the passive film that forms on carbon steel in the highly alkaline environment of concrete pore solution is 3–15 nm thick and near the film/substrate interface the concentration of the Fe^{II} oxides is higher than the concentration of the Fe^{III} oxides; the layers near the free surface of the film mostly contain Fe^{III} oxides [2, 3].

In this paper basic findings of these recent nano-scale analytical studies [1–3, 5] using focused ion beam/ transmission electron microscopy (FIB/TEM), X-Ray photoelectron spectroscopy (XPS), and electron energy loss spectroscopy (EELS) are summarized to demonstrate possible mechanisms of the chloride-induced transformation of passive film. Selected results from a parallel study [4] using the electrochemical quartz crystal nano-balance (EQCN) technique is also presented to provide kinetic evidence of how chlorides interact with these two layers and transform protective oxides into unprotective ones. The fundamental understanding developed in the summarized studies has implications in the development of new corrosion-resistant steels and corrosion inhibitors.

2 Experimental Programs

Samples for the XPS, TEM and EELS studies were taken from the cross sections of 10 mm long rebar specimens cut from as-received deformed carbon steel rebar with 10 mm nominal diameter. The cross sections of each sample were polished to 1 μm using anhydrous (water-free) isopropyl alcohol. After polishing, all samples were kept in anhydrous alcohol to avoid exposure to air until they were transferred to the beakers containing the test solution. The details of sample preparation for each analytical technique including the chemical composition of the steel rebar is given in [1].

The EQCN and electrochemical tests were conducted on commercially available 10 MHz AT-cut 13.67 mm diameter quartz crystals (QC). One side of the QC was sputtered with ~100 nm-thick iron (Fe) layer that served as the working electrode. The iron layer was directly deposited on the etched QC surface; the other side of the QC was sputtered with ~100 nm-thick gold (Au). These QC samples were mounted on a typical beaker-type EQCN cell such that only iron layer was exposed to the test solutions. The details of the EQCN test setup can be found in [4].

Two types of passivating solutions were prepared by dissolving calcium hydroxide, sodium hydroxide, potassium hydroxide and calcium sulfate in distilled water: CH: saturated calcium hydroxide solution (pH 12.4); CP: simulated concrete pore solution (pH 13.3). The chemical composition and properties of these two solutions are presented in [1]. All the test samples were exposed to the two passivating solutions (CH and CP solutions) for extended period of time (minimum 10 days) to

Table 1 Sample designation and corresponding chloride concentration

Specimen	CH-0	CH-1	CH-2	CP-0	CP-1	CP-2
Chloride concentration (M)	0	0.05	0.45	0	0.45	3.0

ensure the formation of a stable passive film on the surface of the samples. Chloride was incrementally added to each solution at the concentrations presented in Table 1. At each level of chloride concentration some samples were removed from the solutions and kept in nitrogen chamber for the nano-scale studies described above. For TEM and EELS analysis, electron-transparent samples were extracted using the focused ion beam (FIB) method. The details of the TEM, EELS, XPS and EQCN techniques and their test setup are presented elsewhere [2–5].

3 Results and Discussions

TEM micrographs of the CH-0 and CP-0 samples exposed to chloride-free CH and CP passivating solutions are shown in Fig. 1a, b, respectively. A thin oxide film between the steel substrate and the gold layer is visible in both TEM samples. Both oxide films had relatively uniform thicknesses; however, the oxide film formed in the CP solution was slightly thicker than the one in the CH solution. From these images, the thicknesses of the oxide films on the CH-0 and CP-0 samples were 5–8 and 8–13 nm, respectively.

TEM micrographs of the CH-2 and CP-2 samples exposed to chloride concentrations above the depassivation thresholds are shown in Fig. 1c, d, respectively. Figure 1c shows that the oxide film of the CH-2 sample can be much thinner and less uniform than the oxide films of the CH-0 sample (Fig. 1a): the oxide film still covers the CH-2 steel surface, but with varying thickness that ranges from 2 to 10 nm. Figure 1c shows part of the oxide film that appears thinner than other parts of the film (< ~3 nm). The oxide films on the CP-2 sample (Fig. 1d) is also much thinner and less uniform than the oxide film of the CP-0 (Fig. 1b). Some parts of the oxide film still cover the steel surface, albeit with varying thickness; however, unlike the CH-2 sample, there are also parts of the CP-2 steel surface without any oxide film at all, which is confirmed by EDS analysis.

The EELS analysis was carried out at three different locations of the oxide film in each sample as shown in Fig. 2. The fingerprints obtained from the EELS spectra are summarized in Table 2. Oxide film matches were identified by comparing these fingerprints with those from various iron oxide signatures [5]. The results suggest that although the chemical compositions of the oxide films vary in different pore solutions, the change in oxidation state along the oxide film follows a particular pattern; the inner oxide-film compounds resemble Fe^{II} oxidation state and the outer oxide-film compounds are at Fe^{III} oxidation state.

From inside to the outside of the oxide film, Fe^{II}/ Fe^{III} ratio decreases. In the presence of chloride the variation of the chemical compositions of the iron oxide diminishes with distance from the Fe substrate, especially in the CH-1 specimen. This is

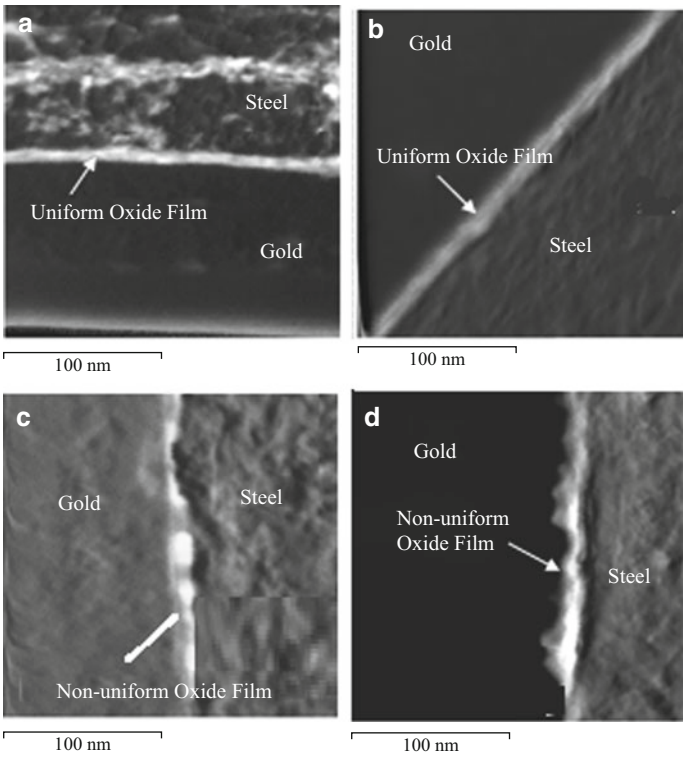

Fig. 1 TEM micrographs of samples exposed to CH and CP solutions: (**a**) CH-0; (**b**) CP-0; (**c**) CH-2; (**d**) CP-2

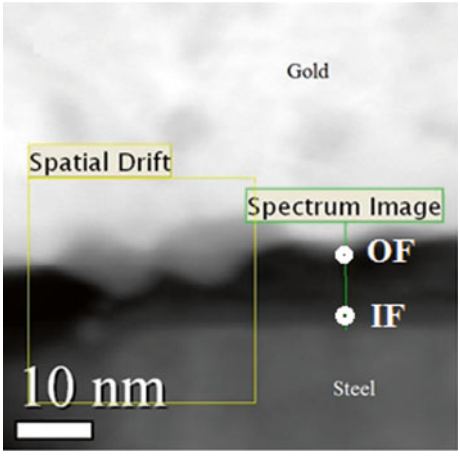

Fig. 2 A typical annular dark field STEM image where the EELS study was carried out (i.e., outer layer of oxide film, OF, and inner layer of oxide film, IF)

Table 2 Summary of fingerprints acquired from the EELS results

Sample	CH-0		CH-1		CP-0		CP-1	
Test location	IF	OF	IF	OF	IF	OF	IF	OF
Fe-I(L_3)/I(L_2) (±0.3)	4.3	5.4	6.1	7.5	4.3	5.3	4.2	6.9
Δ(O-$K_{peak,prepeak}$) (eV) (±0.2)	9.2	10.5	9.5	10.6	9	9.6	9.1	10.4
O-I($K_{prepeak}$)/I (K_{peak}) (±0.01)	0.11	0.15	0.17	0.21	0.1	0.16	0.07	0.19
Iron oxide match	Fe^{II}	Fe^{II} /Fe^{III}	Fe^{III}	Fe^{III}	Fe^{II}	Fe^{III}	Fe^{II} /Fe^{III}	Fe^{III}

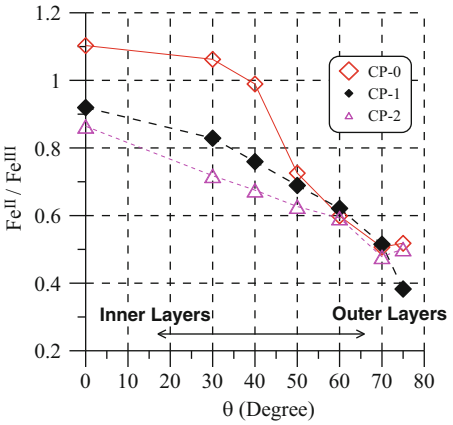

Fig. 3 Comparison of the Fe^{II}/Fe^{III} at inner and outer layers of oxide film

mostly related to the changes in the ionic state of the inner layer of the oxide film. In samples exposed to the CH-1 solution, the fingerprints of Fe^{II} were not observed in the inner oxide film. Instead, the fingerprints corresponding to Fe^{III} were revealed (Table 2). In the CP-1 solution, the fingerprints of Fe^{III} were also revealed in addition to the fingerprints of Fe^{II} in the inner oxide film.

Therefore, it is inferred that the role of chloride is related to the change in the oxidation state of the film. The oxidation state of the outer oxide-film, despite remaining relatively unaffected in the chloride media, does not prevent the chloride ingress. Hence, the inner oxide-film is likely responsible for the passivity and the porous outer oxide-film solely controls the time required for chloride to reach the inner layer of the film.

The EELS observations are in line with the results of the XPS studies shown in Fig. 3. Using the XPS spectra, the ratio between the concentration of Fe^{II} and Fe^{III} iron oxide was obtained at various emission angles corresponding to various depth of oxide film. For all samples, the Fe^{II}/Fe^{III} ratio generally decreases by increasing the emission angle, which indicates that within the outer regions of the film the concentration of Fe^{III} oxides is higher than that of the inner regions that are closer to the steel substrate. It is also observed that the Fe^{II}/Fe^{III} ratios close to the surface of oxide film are similar in all three samples, whereas at the regions closer to the steel substrate, Fe^{II}/Fe^{III} of the CP-0 specimen is greater than that of the chloride-exposed samples CP-1 and CP-2.

EQCN and electrochemical test results also provided additional information on the mechanism of chloride-induced depassivation process. Initially, a mass gain was observed in the EQCN data; in absence of any electrochemical evidence of corrosion, this mass change was attributed to the chloride ingress through the porous unprotective oxide film. During this period the samples remained passive, which can be interpreted as the induction time. This was followed by a mass loss trend indicating the onset of passivity breakdown. After the onset of mass loss trend, the electrochemical indicators changed drastically such that the open circuit potential (OCP) and low frequency impedance dropped while low frequency phase angle diverged from −90°. This can be explained as passive film breakdown and pit initiation.

4 Conclusions

This research summary provided insights into the mechanism of passive film formation and chloride-induced depassivation of oxide film in concrete, which can have implication in the development of new corrosion-resistant steels and corrosion inhibitors in the future.

References

1. Ghods, P. (2010). *Multi-scale investigation of the formation and breakdown of passive films on carbon steel rebar in concrete*. Doctoral dissertation, Carleton University.
2. Ghods, P., Isgor, O. B., Carpenter, G. J., Li, J., McRae, G. A., & Gu, G. P. (2013). Nano-scale study of passive films and chloride-induced depassivation of carbon steel rebar in simulated concrete pore solutions using FIB/TEM. *Cement and Concrete Research, 47*, 55–68.
3. Ghods, P., Isgor, O. B., Bensebaa, F., & Kingston, D. (2012). Angle-resolved XPS study of carbon steel passivity and chloride-induced depassivation in simulated concrete pore solution. *Corrosion Science, 58*, 159–167.
4. Gunay, H. B. (2011). *Electrochemical and microscopic investigation of the passivation and depassivation processes of iron and steel in simulated concrete pore solutions*. M.Sc. thesis, Carleton University.
5. Gunay, H. B., Ghods, P., Isgor, O. B., Carpenter, G. J., & Wu, X. (2013). Characterization of atomic structure of oxide films on carbon steel in simulated concrete pore solutions using EELS. *Applied Surface Science, 274*, 195–202.

Part XIII
Self-consolidating Concrete

Effect of Particle Size and Amount of Nanosilica and Microsilica on Early Age and Hardened Structure of Self Compacting Concrete

Gonzalo Barluenga, Javier Puentes, and Irene Palomar

Abstract The paper presents an analysis of the experimental results of Self Compacting Concretes (SCC) with limestone filler and two types and up to three amounts of active silica-based additions, as microsilica and nanosilica, to evaluate the influence of the size particle and amount of silica-based additions. The experimental program combined early age monitoring of temperature, UPV, evaporation rate and free drying shrinkage, assessing early age drying cracking risk and evaluating hardened porosity, permeability and mechanical performance. At early ages, the pozzolanic effect was detected in the temperature profile after cement hydration is generalized, although the size effect of the additions facilitate hydrated products nucleation and accelerated solid microstructure development, bringing forward the interconnection among the solid particles. The smaller the particle size, the faster the UPV evolution and the earlier shrinkage began. Both effects together can increase the risk of early age cracking due to drying shrinkage.

In the hardened state, the mixtures with silica-based additions improved the mechanical properties as compressive strength and UPV. Larger amount and finer particle size produced larger improvement. It was also observed that nanosilica produced finer porous network than microsilica.

Keywords SCC • Nano-silica • Microsilica • Early age • Porous structure

1 Introduction

The use of low amounts of active mineral additions in SCC compositions is an effective way to improve material hardened performance without increasing either the embodied energy or the economic cost of moderate strength SCC [1]. As a general rule, SCC is considered to be a conventional concrete with a large filling ability, although further differences have been found for both the early age behavior [1] and the hardened performance [1, 2]. The main changes are due to the large

G. Barluenga (✉) • J. Puentes • I. Palomar
Department of Architecture, University of Alcala, Madrid, Spain
e-mail: gonzalo.barluenga@uah.es; xmojica@hotmail.com; Irene.palomar@uah.es

K. Sobolev, S.P. Shah (eds.), *Nanotechnology in Construction*,
DOI 10.1007/978-3-319-17088-6_64

amount of fine particle mineral additions used in their composition [3, 4], which leads to a different speed on the plastic-to-solid evolution [1], and an increase of early age cracking risks [5]. The assessment of the early age evolution of any cement-based material (CBM) requires of the simultaneous monitoring of several parameters related to cement hydration, microstructure formation, mechanical capacity development and dimensional stability [6–10].

The particle size of the additions plays a main role in their effectiveness. In general terms, it has been shown that the smaller the particle size the larger the effectiveness. Accordingly, nanoparticles have been pointed out as the next generation additions for CBM [11]. Among the nano-components available, amorphous nanosilica has proved to be a cost effective component for SCC [12]. Although some research has been done on the size effects of silica-based additions on CBM [13, 14] their influence on the early age parameters and hardened performance of moderate strength SCC still needs to be studied.

2 Experimental Program

Six concrete compositions, which are summarized in Table 1, were tested. A reference SCC with limestone filler was designed (CA). This reference composition was modified substituting 2.5–10 % of the filler by two silica-based mineral additions: microsilica (CAMS) and nanosilica (CANS). The water to fines ratio (w/f) remained at 0.36 and the amount of paste was constant for all the compositions. The chemical compositions of cement, limestone filler, microsilica (MS) and nanosilica (NS) have been previously described [10].

Table 1 Compositions of the SCC mixtures under study (components in kg/m^3)

Compositions	CA	CAMS10	CAMS5	CAMS25	CANS5	CANS25
Cement CEM I 42,5 R	350	350	350	350	350	350
Gravel (4–20 mm)	790	790	790	790	790	790
Sand (0–4 mm) Humidity 6.25 %	691	691	691	691	691	691
Limestone filler (Betocarb P1)	350	315	332.5	341.25	332.50	341.25
Micro-silica (MEYCO MS 610)	–	35	17.5	8.75	–	
Nano-silica (MEYCO MS 685)	–	–			79.45	39.77
Water[a]	204	204	204	204	142	173
HRWRA (Glenium ACE425)	5.25	5.25	5.25	5.25	5.25	5.25
Water/cement[b]	0.71	0.71	0.71	0.71	0.71	0.71
W/fines (cem + additions)[b]	0.36	0.36	0.36	0.36	0.36	0.36
Slump Cone (mm)	–	–			–	
J-ring djf[c] (mm)	815	750			795	
CbE[c] (%)	29	36			79	

djf spread diameter, *CbE* blocking coefficient
[a]Liquid water added
[b]Included water in the components (sand, HRWRA and nano-silica)
[c]UNE 83362:2007- Self-compacting concrete. Characterization of the flowability through rebars. Slump-flow test with J-ring

Table 1 also records the average slump spread diameter and the blocking coefficient of some of the compositions for J-ring test.

The experimental program involved monitoring early age temperature, UPV, evaporation rate and free drying shrinkage, assessing early age drying cracking risk and evaluating hardened porosity, vapor permeability and mechanical performance. The aim was to evaluate the influence of the size particle and amount of silica-based additions on material formation process and properties. The experimental setup for early age monitoring [10] and the tests for hardened SCC evaluation [1] have been described previously. Evaporation, drying shrinkage and early age cracking were forced by airflow of 3 m/s during 6 h [1].

3 Experimental Results and Analysis

Temperature evolution of CBM during early ages is related to cement hydration and subsequent pozzolanic and latent hydraulic reactions of active additions. However, the variations in SCC composition leads to time shifting of the temperature evolution, due to both physical effects [3] and addition's reactivity [9]. In order to allow a direct comparison of the early parameters, a Reaction index ($I_{r,\,24}$) was defined as the amount of heat produced by a sample regarding to the total heat at 24 h [1]. Figure 1 plots $I_{r,\,24}$ of the compositions. A S-curve pattern is followed by all the samples, although the use of additions reduced $I_{r,\,24}$, as pozzolanic reactions takes place after cement hydration was generalized.

Figure 2 plots UPV and early age free drying shrinkage. According to the UPV curves, the compositions with NS showed the change from plastic to pseudo-rigid state the earliest, which indicates a larger nucleation effect due to the smaller particle size than MS. The same effect can be observed for shrinkage. The results obtained for 10 % of MS were very similar than those of 5 % NS, which also points out that the effectiveness of NS is larger than MS.

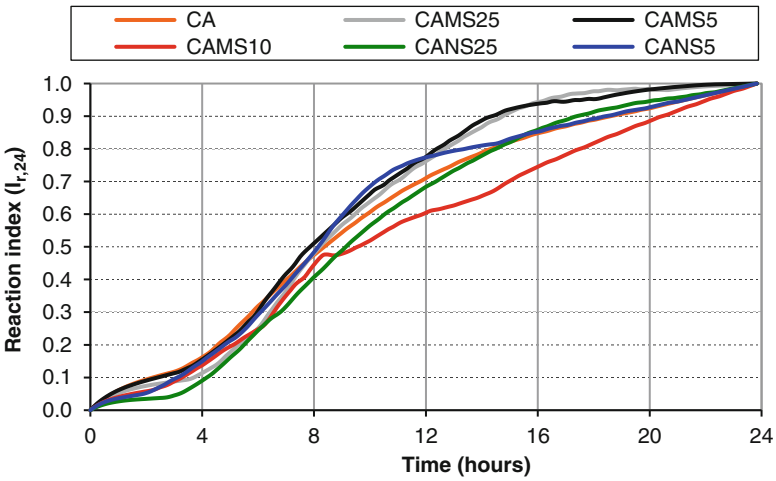

Fig. 1 Reaction index ($I_{r,24}$)

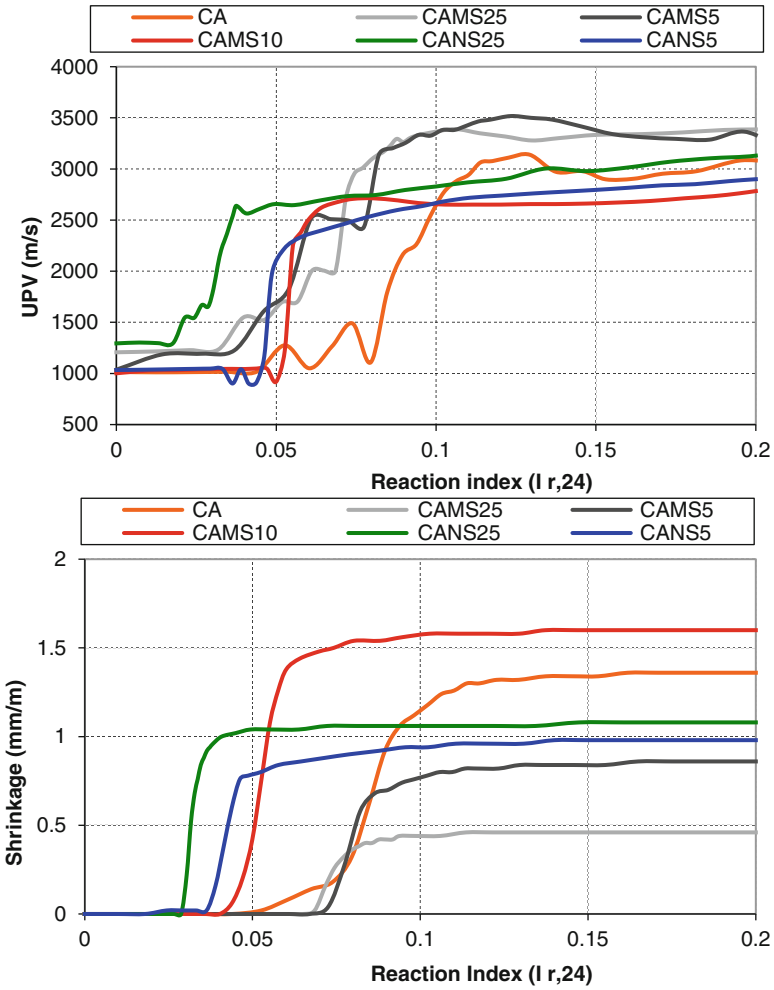

Fig. 2 UPV and EA Shrinkage evolution regarding to Reaction index

Table 2 summarizes the experimental results of early age evaporation rate, free drying shrinkage and cracking; mercury porosimetry, vapor permeability and compressive strength and UPV at 28 days.

It can be observed that there was no direct relation among evaporation rate, shrinkage and early age cracking, as far as larger evaporation did not mean larger shrinkage or cracking area. However, larger amounts of addition produced larger cracking area. NS produced larger evaporation, shrinkage and cracking than MS.

Regarding hardened physical properties, the increase of addition content reduced the average pore diameter although increased vapor permeability. Increasing MS amount also increased pore index (total accessible porosity in % of volume). Again, NS effectiveness was larger than MS. Compressive strength increased with the amount of addition and 5 % of NS improved strength by 25 %, while 10 % of MS barely improved strength by 8 %.

Table 2 SCC properties

	CA	CAMS25	CAMS5	CAMS10	CANS25	CANS5
Evaporation at 24 h (kg/m^2)	1.64	1.92	2.56	1.22	2.68	2.48
EA Shrinkage (mm/m)	1.36	0.46	0.88	1.62	1.08	1.02
EA cracked area (mm^2/m^2)	345	70.93	365.37	1,270.74	110.00	1,923.15
Pore index (%) (MIP)	8.92	7.67	8.08	8.83	9.00	5.02
Av Pore diameter (μm) (MIP)	0.58	0.65	0.59	0.59	0.66	0.42
Permeability coefficient (g/m^2 · 24 h · mmHg) (VP)	0.61	0.29	0.49	0.58	0.48	0.44
Permeability (g/m^2 · h cm) (VP)	4.47	1.60	2.75	5.94	1.83	3.06
Comp. Strength (28 days) (MPa)	31.0	31.75	32.0	33.5	38.75	39.0
UPV (28 days) (m/s)	4,660	4,975	4,890	4,757	4,914	4,369

EA shrinkage and cracking, *MIP* mercury intrusion porosimetry, *VP* vapor permeability of pastes; *SCC* mechanical properties at 28 days

4 Discussion and Conclusions

The effects of two silica-based additions, nanosilica (NS) and microsilica (MS), on early age and hardened performance of a moderate strength SCC with limestone filler have been evaluated. The main objective was to assess the influence of particle size and addition amount on the material properties.

The use of silica-based additions modified the early age behavior in two main ways: the small particle size facilitated the nucleation of hydrated products and the pozzolanic effect of amorphous silica was recorded after 8 h. The main consequences were the acceleration of the interconnected structure growth and the earlier occurrence of drying shrinkage, which increased early age cracking risk. These effects were larger for NS than for MS. Larger amounts of addition did not mean larger evaporation or shrinkage, although, larger amounts of addition recorded larger early age cracking in both cases. It can be highlighted that early age evaporation, drying shrinkage and early age cracking are not directly related, although there is a physical connection among them.

In the hardened state, NS produced a more compact solid structure and a finer pore network than MS. The effect of this structure on hardened properties can be summarized as larger compressive strength and smaller average pore diameter. Unexpectedly, the reduction of pore diameter did not lead to a reduction of vapor permeability, which suggests that permeability is related to pore interconnectivity rather than to pore diameter.

Acknowledgements The authors gratefully acknowledge the contribution of the students Alvaro Mozas and Hector Arenas, the technical support of R. Tascón, G. Sánchez and I. Pajares, the components supplied by BASF Construction Chemicals España S.L., Omya Clariana SL and Cementos Portland Valderrivas and the funding grants: CCG-08-UAH/MAT 40, co-funded by the University of Alcalá and Community of Madrid; PI3-2008-0499, funded by the Spanish Ministry of Science and Innovation; PPII11-0167-3491 funded by J C Castilla-La Mancha and SCC_Pump (BIA2013-48480-C2-2-R and BIA2013-48480-C2-1-R) funded by the Spanish Ministry of Economy and Competitiveness.

References

1. Barluenga, G., Palomar, I., Puentes, J. (2013). *Early age monitoring and hardened properties of SCC with limestone filler and active mineral additions*. Fifth North American conference on the Design and Use of Self-Consolidating Concrete, Chicago.
2. Bermejo, E. B., Moragues, A., Galvez, J. C., & Fernandez Canovas, M. (2010). Permeability and pore size distribution in medium strength self-compacting concrete. *Materiales de Construcción, 60*(299), 37–51.
3. Ye, G., Liu, X., Poppe, A. M., et al. (2007). Numerical simulation of the hydration process and the development of microstructure of self-compacting cement paste containing limestone as filler. *Materials and Structures, 40*, 865–875.
4. Darquennes, A., Khokhar, M. I. A., Rozière, E., et al. (2011). Early age deformations of concrete with high content of mineral additions. *Construction and Building Materials, 25*, 1836–1847.
5. Barluenga, G., & Hernandez-Olivares, F. (2007). Cracking control of concretes modified with short AR-glass fibers at early age: Experimental results on standard concrete and SCC. *Cement and Concrete Research, 37*(12), 1624–1638.
6. Boumiz, A., Vernet, C., & Cohen, F. (1996). Mechanical properties of cement pastes and mortars at early ages – Evolution with time and degree of hydration. *Advanced Cement Based Materials, 3*, 94–106.
7. Hammer, T. A. (2006). *The use of pore water pressure to follow the evolution from fresh to hardened concrete*. 2nd International symposium on Advances in Concrete through Science and Engineering, Quebec City.
8. Desmet, B., Atitung, K. C., Abril, M. A., et al. (2011). Monitoring the early-age hydration of self-compacting concrete using ultrasonic p-wave transmission and isothermal calorimetry. *Materials and Structures, 44*, 1537–1558.
9. Barluenga, G., Palomar, I., & Puentes, J. (2013). Early age and hardened performance of fluid cement pastes combining mineral additions. *Materials and Structures, 46*(6), 921–941.
10. Barluenga, G., Puentes, J., & Palomar, I. (2014). Early age testing of self-compacting concrete for structural repair. In M. C. Forde (Ed.), *Structural faults and repair 2014*. Edinburgh: Engineering Technics Press.
11. Kawashima, S., Hou, P., Corr, D. J., & Shah, S. P. (2013). Modification of cement-based materials with nanoparticles. *Cement and Concrete Composites, 36*, 8–15.
12. Quercia, G., Spiesz, P., Hüsken, G., & Brouwers, H. J. H. (2014). SCC modification by use of amorphous nano-silica. *Cement and Concrete Composites, 45*, 69–81.
13. Senff, L., Hotza, D., Repette, W. L., et al. (2010). Mortars with nano-SiO2 and micro-SiO2 investigated by experimental design. *Construction and Building Materials, 24*, 1432–1437.
14. Jalal, M., Mansouri, E., Sharifipour, M., & Pouladkhan, A. R. (2012). Mechanical, rheological, durability and microstructural properties of high performance self-compacting concrete containing SiO2 micro and nanoparticles. *Materials and Design, 34*, 389–400.

Self-Compacting Concrete with Nanosilica and Carbon Nanofibers

Javier Puentes, Gonzalo Barluenga, and Irene Palomar

Abstract This study aimed to assess the changes of behavior due to the addition of nanosilica and carbon nanofibers in SCC. The target was to identify variations at early ages and in the hardened state due to the addition of nano-size components. The setting process and early ages were monitored during the first 24 h, combining several experimental techniques as ultrasonic pulse velocity, temperature, capillary pressure, free shrinkage, cracking, and mass loss. In addition, the porous microstructure in the hardened state was evaluated measuring vapor permeability, mercury intrusion porosimetry and a mechanical characterization.

The results pointed out that the size of the nano-components affected capillary pressure development at early ages and reduced vapor permeability in the hardened state. The reactivity of the component also affected evaporation, drying shrinkage and cracking risks at early ages and pore and solid structure in the hardened state. On the other hand, the use of carbon nanofibers produced larger cracking risk at early ages, which can be mitigated by the addition of low amounts of polypropylene microfibers.

Keywords SCC • Nanosilica • Carbon-nanofibers • Polypropylene fibers • Early age cracking

1 Introduction

Nano-additions and nano-fibers can modify the rigid structure of Ordinary Portland Concrete (OPC), improving its hardened performance [1]. Self compacting concrete (SCC) is an efficient material characterized by its large fluidity in fresh state compared to a OPC, although a similar hardened behavior has been described [2]. Several studies on SCC with nanosilica (NS) and carbon nanofibers (CNF) have been carried out in order to identify their advantages in the fresh and hardened performance [3, 4].

J. Puentes (✉) • G. Barluenga • I. Palomar
Department of Architecture, University of Alcala, Madrid, Spain
e-mail: xmojica@hotmail.com; gonzalo.barluenga@uah.es; irene.palomar@uah.es

K. Sobolev, S.P. Shah (eds.), *Nanotechnology in Construction*,
DOI 10.1007/978-3-319-17088-6_65

The fluidity of SCC is achieved by the use of a large amount of fine particles and a High range water reducing admixture (HRWRA), also called superplasticizer [5]. Due to these differences in composition, SCC show an increases of Early Age (EA) shrinkage [6, 7] and a cracking risk increase, due to the larger paste volume [7, 8] regarding to OPC [9]. Some experimental techniques have been used to assess the evolution of the characteristics during the setting process and EA, identifying the key-points of the process and the relationships among the hydration parameters during 24 h after mixing [9–11]. The tests are related to the activity of water in the hydration and its role in the solid structure and pore formation. The lack of water in the pores produces tension stresses that are absorbed by the deformation of the sample. If the strain is restrained and the stress exceeds the material strength, it would crack. Accordingly, EA cracking of restrained displacement concrete members is related to the cement hydration, the formation of the microstructure and the environmental conditions [11, 12].

Theoretically, nano-fibers should be good candidates to control EA cracking, as the addition of CNF increased 30 % flexural strength of fluid pastes [9]. However, it has been shown that CNF does not control cracking and even increased it [9]. In order to mitigate EA cracking, small amounts of micro-fibers can be incorporated [13, 14].

2 Experimental Program

Four SCC mixes were tested and the compositions are summarized in Table 1. A conventional SCC mix reference with limestone filler (CA), with a high range water reducing admixture (HRWRA), was designed. This reference composition was modified using 1 % volume fraction of a different HRWRA with a nanosilica dispersion in a single product (CAu). Then, 0.09 % volume fraction of carbon nanofibers (CNF) with nominal dimensions of 20–80 nm of diameter and a 30 μm in length, prepared in an aqueous suspension, was added (CAu + C). Finally, 0.1 % volume fraction of polypropylene microfibers (PPF) of 19 mm in length was included (CAu + CP). Table 1 also records the average slump spread diameter (djf) and blocking coefficient (CbE) of the SCC mixtures.

The evolution of the mixtures during EA was evaluated by the simultaneous monitoring of temperature, ultrasonic pulse velocity (UPV), capillary pressure, water evaporation (mass loss) and shrinkage [11]. The laboratory conditions were constant during the tests (25–26 °C and 50–55 % RH). For the Temperature and Ultrasonic pulse velocity a plastic mold (150 × 100 × 70 mm) was used. The 54 kHz ultrasonic transducers were placed in direct contact to fresh concrete at 140 mm of distance. Inside of the same sample, a needle thermometer and four −15 kPa pressure transducers located at two different depths (15 and 35 mm) were placed. Free shrinkage and mass loss were monitored on other sample placed in a 500 × 100 × 50 mm metal tray. An air flow of 3 m/s was applied during the first 6 h to maximize water evaporation and shrinkage. EA drying cracking risk was assessed

Table 1 Compositions of the SCC mixtures under study (components in Kg/m^3)

	CA	CAu	CAu + C	CAu + CP
Cement CEM I 42,5 R	350	350	350	350
Limestone Filler (Betocarb P1-DA)	350	350	350	350
Water[a]	204	206	206.5	215
HRWRA (Glenium ACE425)	5.25	–	–	–
HRWRA + NS (Ulmix NS SCC)	–	3.5	3.5	3.5
CNF (Carbon-Nano-Fibers)	–	–	58.3	58.3
PPF (Polypropylene fibers)	–	–	–	0.9
Coarse aggregate (4–20 mm)	790	790	790	790
Sand (0–4 mm)	693	691	691	683
W/c[b]	0.71	0.71	0.71	0.71
W/fines (cement + additions)[b]	0.36	0.36	0.36	0.36
djf[c] mm	815	825	765	725
CbE[c] %	28	62	94	85

[a]Liquid water added
[b]The amount of water included in the sand and minor components (HRWRA & CNF) were also taken into account
[c]UNE 83362: 2007 – SCC Characterization of flowability through rebars. Slump-flow test with J-ring

on double restrained slabs casted in a 600 × 900 × 50 mm mold submitted to the same air flow (Kraai slab modified test) [12].

In the hardened state, apparent density (Dap) and open porosity (accessible water) of SCC samples were evaluated and calculated at 7 days. Porosimetry, ASTM D4404-84 (2004), and vapor permeability of paste samples, UNE EN 15803, were also assessed. Characterization included compressive strength of 100 mm cubic specimens, flexural strength on 400 × 100 × 100 mm specimens and UPV.

3 Experimental Results and Analysis

Figure 1 shows the evolution of EA parameters as temperature, UPV and EA shrinkage, which are related to cement hydration, solid structure evolution and pore network formation, respectively [11]. The time dependency of those parameters makes difficult the direct comparison of the compositions under study [9].

The effect of the environment on the samples can be observed in Fig. 2 that plots water evaporation rate and capillary pressure. The relation of water content both with cement hydration and environmental conditions during setting can be observed [10].

Mercury porosimetry and permeability test results of pastes are shown in Table 2. The incorporation of nano-sized components decreased the porosimetry index. However, the size of the average pore diameter is very different in the two dosages (pCAu and pCAu + C) as well as permeability, which depends on the component type. CNF reduced water vapor permeability.

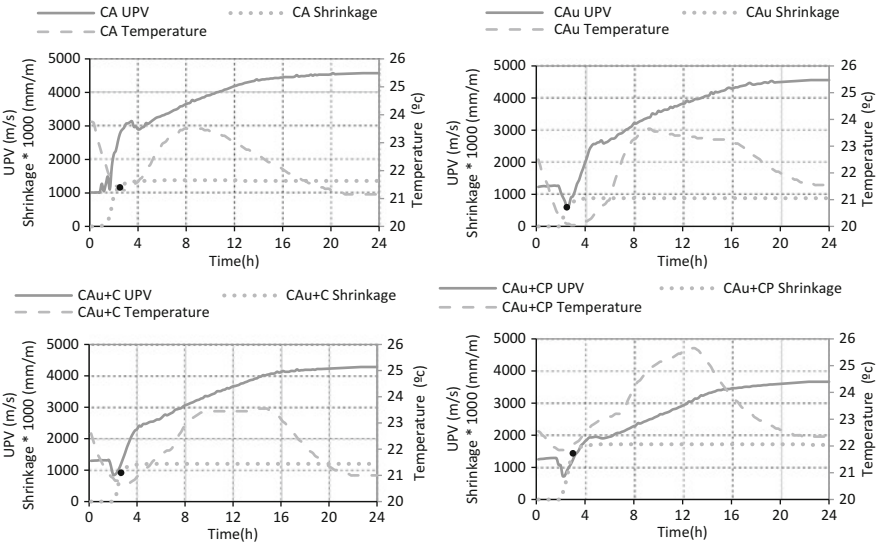

Fig. 1 Evolution of UPV, temperature and drying shrinkage during 24 h

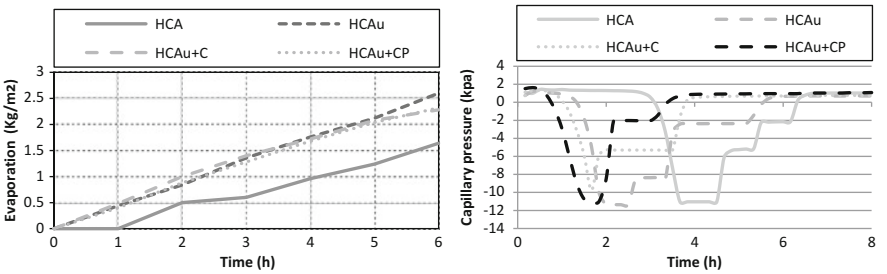

Fig. 2 Evaporation rate and capillary pressure evolution

Table 2 Mercury intrusion porosimetry (MIP) and Vapor permeability (VP) of pastes

	pCA	pCAu	pCAu+C
Pore index (%) (MIP)	8.92	7.42	7.73
Pore diameter 4 V/A (μm) (MIP)	0.5839	0.7882	0.5986
Permeability coefficient g/m^2 · 24 h · mmHg (VP)	0.61	0.58	0.47
Permeability g/m^2 · h cm(VP)	4.47	3.76	3.98

EA shrinkage and cracking, apparent density and open porosity at 7 days and mechanical properties are summarized in Table 3. The largest EA cracking was measured for the SCC reference mixture (CA). Contrary to expectations, CNF did not reduce shrinkage and increased the EA cracking regarding the composition with

Table 3 Properties of hardened SCC

	HCA	HCAu	HCAu + C	HCAu + CP
Apparent density (g/cm^3)	2.31	2.30	2.26	2.21
Open porosity (%)	2.35	2.89	2.18	3,28
EA shrinkage (mm/m)	1.36	0.88	1.20	1.70
EA cracked area (mm^2/m^2)	345	0.00	296	0.00
Compressive strength (MPa) 7 days	25.50	24.00	24.00	25.00
Flexural strength (MPa) 120 day	5.03	5.49	5.11	–
UPV (m/s)	4,392.67	4,854.00	4,454.00	4,338.50
E_s (GPa)	44.57	54.19	44.83	41.60

NS (CAu). Moreover, PPF obtained the largest shrinkage but it did not crack. PPF reduced density and increased open porosity. NS increased UPV values regarding the reference mixture which is related to concrete compactness.

4 Discussion and Conclusions

The use of different nano-components in SCC have produced different effects on the early age and hardened behavior of the samples under study.

The addition of 1 % volume fraction of a HRWRA with a nanosilica dispersion in a single product accelerated the increase of capillary pressure, increased evaporation rate, reduced early age drying shrinkage and cracked area, at early ages. In the hardened state, it reduced pore index and vapor permeability, although increased average pore diameter, open porosity and UPV.

The addition of 0.09 % volume fraction of carbon nanofibers (CNF) accelerated capillary pressure development and increased drying shrinkage and cracked area at early ages. The use of 0.1 % volume fraction of Polypropylene fibers mitigated the early age cracking risks. In the hardened state, CNF increased pore index and reduced average pore diameter, vapor permeability, open porosity and UPV.

Accordingly, it can be concluded that the size of the nano-components affected capillary pressure development at early ages and reduces vapor permeability in the hardened state. The reactivity of the component can also affect evaporation, drying shrinkage and cracking risks at early ages and pore and solid structure in the hardened state.

Acknowledgements The authors want to acknowledge R. Tascón, G. Sanchez, A. Delgado, P. Soto Lozada, David Gonzalez and I. Pajares for their technical support. Some components were supplied by BASF Construction Chemicals España S.L., Omya Clariana SL., Ulmen S.L., Grace S.A., Grupo Antolin and Cementos Portland Valderrivas. They also acknowledge the financial support of the grants CCG-08-UAH/MAT 40, co-funded by the Univeristy of Alcalá and Community of Madrid; PI3-2008-0499, funded by the Spanish Ministry of Science and Innovation; PPII11-0167-3491 funded by J C Castilla-La Mancha and SCC_Pump (BIA2013-48480-C2-2-R and BIA2013-48480-C2-1-R) funded by the Spanish Ministry of Economy and Competitiveness.

References

1. Sobolev, K., & Ferrada, M. (2005). How nanotechnology can change the concrete world. Part one. *American Ceramic Society Bulletin, 84*(10), 14–18.
2. Persson, B. (2001). A comparison between mechanical properties of self-compacting concrete and the corresponding properties of normal concrete. *Cement and Concrete Research, 31*, 193–198.
3. Jalal, M., Mansouri, E., Sharifipour, M., & Pouladkhan, A. R. (2012). Mechanical, rheological, durability and microstructural properties of high performance self-compacting concrete containing SiO2 micro and nanoparticles. *Materials & Design, 34*, 389–400.
4. Kawashima, S., Hou, P., Corr, D. J., & Shah, S. P. (2013). Modification of cement-based materials with nanoparticles. *Cement and Concrete Composites, 36*, 8–15.
5. Scrivener, K. L., & Kirkpatrick, J. R. (2008). Innovation in use and research on cementitious material. *Cement and Concrete Research, 38*(2), 128–136.
6. Bissonnette, B., Pierre, P., & Pigeon, M. (1999). Influence of key parameters on drying shrinkage of cementitious materials. *Cement and Concrete Research, 29*, 1655–1662.
7. Roziere, E., Granger, S., Turcry, P., & Loukili, A. (2007). Influence of paste volume on shrinkage cracking and fracture properties of self-compacting concrete. *Cement and Concrete Composites, 29*, 626–636.
8. Loser, R., & Leemann, A. (2009). Shrinkage and restrained shrinkage cracking of SCC compared to conventionally vibrated concrete. *Materials and Structures, 42*, 71–82.
9. Puentes, J., Barluenga, G., & Palomar, I. (2012). Early age behaviour of self-compacting concrete with polypropylene fibers and carbon nanofibers. In: J. Barros (Ed.), *Fibre reinforced concrete: Challenges and opportunities BEFIB 2012 Proceedings RILEM PRO 88* (pp. 611–623). Bagneux: Rilem Publications.
10. Hammer, T. A. (2006). The use of pore water pressure to follow the evolution from fresh to hardened concrete. In J. Marchand (Ed.), *2nd international RILEM symposium on Advances in Concrete through Science and Engineering Proceedings RILEM PRO 51* (pp. 207–224). Bagneux: Rilem Publications.
11. Barluenga, G., Palomar, I., & Puentes, J. (2013). Early age and hardened performance of cement pastes combining mineral additions. *Materials and Structures, 46*(6), 921–941.
12. Kraii, P. (1985). Proposed test to determine the cracking potential due to drying shrinkage of concrete. *Concrete Construction, 30*, 775–778.
13. Metaxa, Z., Kosta-Gdoutos, M. S., & Shah, S. P. (2010). Mechanical properties and nanostructure of cement-based materials reinforced with carbon nanofibers and polyvinyl alcohol (PVA) microfibers. *ACI Special Publication, 270*, 115–124.
14. Barluenga, G. (2010). Fiber–matrix interaction at early ages of concrete with short fibers. *Cement and Concrete Research, 40*, 802–809.

Part XIV
Field Applications

Utility of Colloidal Nano-silica in Processing of Fiber Reinforced Cementitious Composites

Bekir Y. Pekmezci

Abstract In this study, colloidal nano silica (CNS) was utilized for modifying green state properties of processed cement mortars. Fly ash was used as supplementary cementitious material in the mixtures. Contribution of CNS to mechanical properties of processed composites was also studied. Short fiber reinforced cementitious mixtures were processed by calender extrusion. Influence of CNS due to modification on rheology of fresh paste was determined during processing. Flexural strength tests were carried out on hardened composites. As the main results of the study; using CNS helped to obtain more shape stable fly ash mixtures during processing. Amount of water retaining admixture was decreased due to use of fly ash and CNS simultaneously. Surface quality was much better than the reference cement composite mixture. CNS improved the mechanical properties of processed SFRCC's including fly ash at 3 days of curing.

Keywords Colloidal nano silica • Processing • Cement • Composite • Grass fiber

1 Introduction

The method of processing plays a significant role in the production of cement based composites. Processing method influences the cost and the production speed. Extrusion is an efficient method for the production of short fiber reinforced cementitious composites (SFRCC). In order to have a successful extrusion, an optimization should be done on the mixture. The mixture should be plastic, enough to be taken from the die properly, and stiff enough to hold its shape after extrusion. Agents modifying rheology of fresh paste should be used in order to achieve this phenomenon. This method is generally used for production of relatively thicker products due to the slip resistance along die generated during extrusion [1–5]. Processing becomes very hard due to wall slip resistance at narrow dies. For example, extrusion of $3 \times 1{,}000 \times 3{,}000$ mm panel is extremely hard. Since excessive processing pressures are generated during conventional extrusion, a novel method calendar

B.Y. Pekmezci (✉)
Faculty of Civil Engineering, Istanbul Technical University, Istanbul, Turkey
e-mail: pekmezcib1@itu.edu.tr

K. Sobolev, S.P. Shah (eds.), *Nanotechnology in Construction*,
DOI 10.1007/978-3-319-17088-6_66

extrusion was developed to produce high performance fiberboards. This study describes the utility of CNS in fiberboard processing by calender extrusion.

CNS contains spread particles and is in a discrete spherical shape ranging 5–100 nm in size. The maximum concentration depends on particle size. Five nanometer particles constitute 15 % of weight, 8 nm particles constitute 30 % of weight and 100 nm particles constitute 50 % of its weight. The appearance of CNS depends on the size of its particles and its concentration ratio. If the size of the particles are large and has a high concentration ratio, it is milky-white, if the particles are medium in size then the color is opaque and if the particles are small it appears to be colorless [6–8]. CNS is widely being used in cementitious mixtures to improve strength and rheology of the mixtures in laboratory studies.

2 Experimental Study

Calender extrusion production technique was applied for production of fiber reinforced cementitious composites. Figure 1 show perspective schematic representation of the system. In this method, first the dry substances, except the fibers, are weighed according to a proper mix design and poured into a mixer. The dry mix is then prepared. Next, half of the total amount of water to be introduced into the mix is added to moisten the mix and mixed for 5 min. Meanwhile, the plasticizer, liquid materials, and other chemical additives, as well as the remaining portion of water, are mixed in a dosing unit and taken into the mixer. Finally, the fibers are added to the mix. During processing, the first band takes the fiber included in the fresh mortar from the feeding unit and delivers it to the first roller set, which then compresses the cementitious mortar to a 3–5 cm thickness. The material is then passed to a second band and the second band transfers the material to a second roller set. The thickness of the material is further decreased in the second roller set to 1–3 cm. The thinned material is taken from the rollers and passed to a third band, and the third

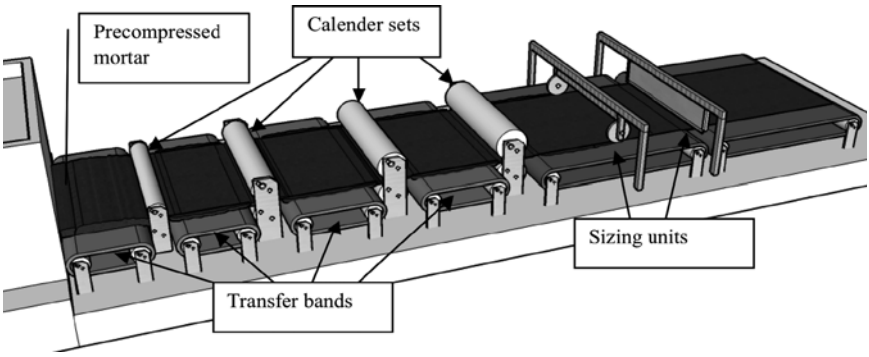

Fig. 1 Calender extrusion line perspective

Table 1 Properties of cement

Property	Value
Setting time, initial (min)	115
Le chatelier opening (mm)	1.0
Compressive strength, 2 days, MPa	37.0
Compressive strength, 28 days, MPa	60.0
SO_3 (%)	3.45
Unsoluble residue (%)	0.16
Ignition loss (%)	3.10
Cl^- (%)	0.011

band transfers the material to a third roller set. The third and the fourth roller sets decrease the fresh material thickness to 0.6–1.0 and 0.2–0.4 cm, respectively. During the processing, the green state composite should keep its unity. There should not be any cracks, cleavages on the material while it is in green state. In order to keep the unity of whole structure, an optimum rheology should be determined. The water retaining additives are added to the mixture to obtain optimum viscosity.

CNS was used as a double functional material in this experimental study. The first function of the material was to improve the rheology to help keeping the unity and the shape stability of green state composite structure during processing. The second function of CNS was to improve 3 days mechanical properties of the fly ash included hardened composite. Cement was White Cement obtained from Cimsa Cement Factory Turkey. Superplasticizer was obtained from SIKA Turkey. The properties of Cimsa White Cement is given in Table 1.

Composites were produced in factory scale production system. Glass fibers were used as reinforcement. Two different glass fiber usage ratios applied on the mixes. Lower glass fiber ratio was 1.5 % while the higher ratio was 2.5 % by weight of the total mix. Water to binder ratio of the composites was kept as 0.35. Superplasticizer was used in order to keep the water to cement ratio constant. A water-retaining admixture was used in order to keep the shape stable during processing. Fly ash was used in order to reduce water retaining agent and have better surface characteristics. 2.5 % of CNS was added in the mixtures. One cubic meter cement binder control mix contained 700 kg of cement and 200 kg of silicious quartz dust, plus 650 kg of silicious sand. The maximum size of sand was 400 μm and quartz dust was 100 μm. Water-retaining cohesion-enhancing agent was used with the ratio of 1.0 % of cement by weight in plain mixture not containing fly ash. Fly ash content was 25 % of cement by weight. Water-retaining admixture reduced 0.5 % of binder by inclusion of fly ash to the mixture. In order to help to keep shape stability and unity of the fresh state mortar in production line, 2.5 % of CNS added to the mixture as well. Totally six mixes produced as, plain cement mix, fly ash mix with 25 % of replacement by weight of cement, CNS including fly ash mixes.

The thicknesses of the composites were 15 mm. The dimensions of the composite specimens produced for experimental study was 100 × 200 cm. All samples were cured under laboratory conditions of 20 °C temperature and 65 % relative humidity. The curing time was 3 days. One day before the tests started, the panel samples were

cut using a diamond saw into 5 × 35 cm pieces for flexural tests. The samples taken from longitudinal direction along processing were tested.

Visual inspections made during production. The thicknesses of the panels were measured at 10 points along the cross-section to determine the stability of the thickness. Flexural properties of the glass fiber-reinforced cement-based composite samples were determined using simple beam four-point loading, where the span length was selected as 300 mm. A closed-loop testing machine, the Instron 5500R, was used for the flexural tests. The crosshead rate was 1 mm/min.

Green strengths of the composites were determined by measuring compressive resistance of fresh samples. Flexural strength tests were applied on hardened specimens.

3 Test Results and Discussion

Visual inspections during production showed a plastic behavior of the processed material while it is in the green state. The material can be shaped into any form without any cracks or visual defects. Thickness stability of the composite was determined by measuring the thickness from 10 points along the cross section. The average thickness of the panel was 15.02 mm while maximum, minimum, and standard deviations were 15.05, 14.92, and 0.1 mm, respectively. Average unit weight of the composite was measured as 1.81 kg/dm^3. Average compressive strength of the plain matrix was 37.5. Influence of fly ash and CNS on fresh properties (green strength) is given in Table 2.

Best mix was found to be FA mix with CNS in determining fresh properties of the mixture. Replacing fly ash with cement by decreasing water retaining agent in the mixture decreased the green strength value of the mixture. Shape stability of the fresh composite was decreased depending on its own green strength loss. With addition of CNS to the matrix mixture, again shape stability of the fresh composite retained due to the increase in the green strength. Flexural strength test results are given in Table 3. Using fly ash in processed fiber reinforced composites caused a

Table 2 Green strength of the materials

Mixture	Green strength, KPa
Plain-matrix	3.7
FA-matrix	3.0
FA/CNS-matrix	3.5

Table 3 Flexural strength test results

Mixture	Flexural strength, MPa
Plain 1.5 F	9.36
Plain 2.5 F	14.62
FA/1.5 F	7.73
FA/2.5 F	12.12
FA/CNS/1.5 F	8.45
FA/CNS/2.5 F	12.90

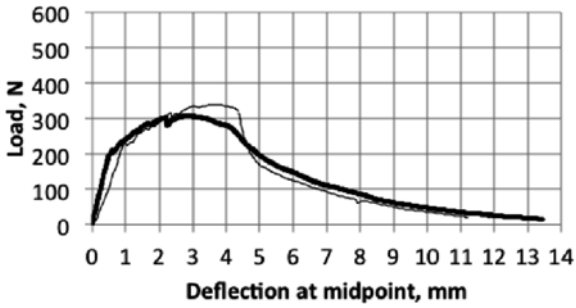

Fig. 2 Load-deflection at mid-span relations of fly ash and fly ash CNS mixes with 1.5 % glass fiber

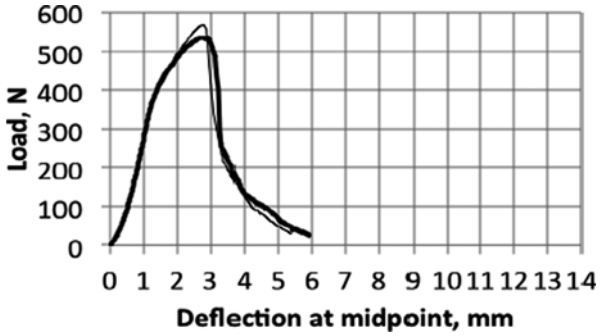

Fig. 3 Load-deflection at mid-span relations of fly ash and fly ash CNS mixes with 2.5 % glass fiber

decrease in flexural strength values. The decrement was 21 % for the mixtures having 1.5 % of glass fiber while it was 16 % for the mixtures having 2.5 % of glass fiber. Adding CNS to fly ash mixtures increased flexural strength 9 % for 1.5 % glass fiber mixtures while the increment was under 1 % for 2.5 % of glass fiber addition. CNS increased 3 days flexural strength of processed fly ash glass fiber composites particularly for the mixes having lower glass fiber amounts. The increment is possibly due to the early pozzolanic reaction. It is emphasized in the literature, that the type and chemical composition of fly ash is very important for early age reactivity [9].

Load-deflection at mid-span relations of the hardened composites are given in Figs. 2 and 3 for glass fiber ratios of 1.5 and 2.5 % respectively.

Samples having two different amount of fiber amount showed similar behavior under flexural loads. Toughness, which is the area under the load deflection curve, implies the energy absorption capacity. The influence of CNS to the toughness of the glass fiber reinforced composites was not drastic. Addition of CNS to the composites increased the fracture energy very slightly depending on the increment on the strength. Cement fly ash composites exhibited strain-hardening behavior. Multiple fine cracks were observed on samples that exhibited strain-hardening behavior during testing. With multiple fine cracks, the crack arresting and bridging mechanism worked and mechanical properties, especially energy absorption, were improved. Fibers pulled out during loading. The fibers pulling out, instead of rupturing, improved the

toughness of the composite. A single macro crack formed approximately at half the total deformation. After a bend-over point softening began as a result of the crack-bridging activity of the fibers. The descending part of the load deflection curve was linear and no sharp decrease was observed. The behavior was still ductile.

Using CNS in fly ash composites slightly increased the toughness of 1.5 % glass fiber composite.

4 Conclusions

CNS was used in order to improve rheological properties of glass fiber reinforced composites during processing. The influence of CNS on flexural strength of processed fly ash glass fiber composites was also studied. Based on the results obtained from experimental studies, the following results can be drawn:

Use of CNS found to be helpful to reduce amount of the water-retaining agent in the mixtures. Satisfactory shape stability and surface characteristics of the composite were obtained by using less amount of water retaining agent in the mixtures. The amount of water retaining agent reduced to the half amount by adding 25 % of fly ash and 2.5 % of CNS in the mixture.

Strength loss in early curing ages (3 days) may partially be tolerated by adding CNS to the processed fly ash glass fiber composites.

Flexural strength of the processed composite having CNS has 9 % higher flexural strength than composite not having CNS for 1.5 % of glass fiber.

References

1. Kuder, K. G., & Shah, S. P. (2011). Processing of high performance fiber reinforced cement based composites. *Construction and Building Materials, 24*, 181–186.
2. Shao, Y., Marikunte, S., & Shah, S. P. (1995). Extruded fiber-reinforced composites. *Concrete International, 17*, 48–52.
3. Peled, A., Cyr, M., & Shah, S. P. (2000). High content of fly ash (Class F) in extruded cementitious composites. *ACI Materials Journal, 97*, 509–517.
4. Aldea, C., Marikunte, S., & Shah, S. P. (1998). Extruded fiber reinforced cement pressure pipe. *Advanced Cement Based Materials, 8*, 47–55.
5. Pekmezci, B. Y. (2014). Properties of PVA reinforced cement bonded fiberboards produced with calender extrusion. *Science and Engineering of Composite Materials*. doi:10.1515/secm-2014-30.
6. Otterstedtand, J. E., & Greenwood, P. (2006). *Some important, fairly new uses of colloidal silica/silica sol*. In E. Horacio, H. E. Gergna, & W. O. Roberts (Eds.), *Colloidal silica fundamentals and applications* (pp. 738–741). Boca Ration: CRC Press, Taylor & Francis Group.
7. Gundogdu, D., Pekmezci, B. Y., & Atahan, H. N. (2010). *Influence of nano SiO_2 on mechanical properties of mortars containing fly ash*. Proceedings of international conference on Material Science and 64th RILEM annual week, Aachen, Germany.
8. Gundogdu, D. (2010). *Influence of nano SiO2 on mechanical properties of mortars containing fly ash*. MSc thesis, Istanbul Technical University, Istanbul.
9. Hou, P., Kawashima, S., Wang, K., Corr, D., Qian, J., & Shah, S. P. (2013). Effects of colloidal nanosilica on rheological and mechanical properties of fly ash–cement mortar. *Cement and Concrete Composites, 35*, 12–22.

Index

K. Sobolev, S.P. Shah (eds.), *Nanotechnology in Construction*,
DOI 10.1007/978-3-319-17088-6